Université catholique de Louvain

Institut de la Matière Condensée
et des Nanosciences (IMCN)

Molécules, Solides et Réactivité (MOST)

Photophysics and photochemistry of trischelate Ir(III) complexes: towards the development of novel photoactive supramolecules

Cédric LENTZ

Promoteur : Professeur Benjamin ELIAS

Thèse de doctorat présentée en vue de l'obtention

du diplôme de Docteur en Sciences

Louvain-la-Neuve

2018

Members of the Jury

Prof. Yann GARCIA (***Chairperson***)
Université catholique de Louvain

Prof. Sophie LAURENT
Université de Mons

Dr Ali ATES
UCB

Prof. Giovanni POLI
Université Pierre et Marie Curie (France)

Prof. Olivier RIANT
Université catholique de Louvain

Prof. Raphaël ROBIETTE
Université catholique de Louvain

Prof. Benjamin ELIAS (***Supervisor***)
Université catholique de Louvain

Remerciements

Tout d'abord, je tiens à remercier très sincèrement le Professeur Benjamin Elias ("The Boss") de m'avoir débauché de mon ancien laboratoire et ouvert les portes du monde magique des complexes d'Iridium. Je le remercie en plus de son apport scientifique indéniable et ses conseils pour la liberté qu'il m'aura laissé, de sa présence dans les bons et les mauvais moments et de sa patience vis-à-vis de mon caractère de merde. Il aurait souhaité que je prolonge mon doctorat de quelques années, peut-être jusqu'à ce qu'il atteigne enfin l'âge de trente ans, mais toutes les bonnes choses ont une fin ! Comme promis, je ferai ce qu'il faut pour qu'un autre Lentz prenne ma place un jour.

Lors de cette thèse de doctorat, j'ai été amené à collaborer avec plusieurs chimistes de haut niveau qui m'auront chacun apporté des clés pour mener à bien un travail de qualité.

Je remercie ainsi le Professeur Michel Luhmer (ULB) qui m'aura guidé sur le chemin sinueux que constitue l'apprentissage de la photo-CIDNP. Son incroyable sens de la précision et son sens du travail si méticuleux me sont encore utiles à ce jour. Je ne peux évidemment pas oublier Luca et son aide dans les expériences de CIDNP toutes les discussions que nous avons eues sur le sujet, ni Rita pour sa gentillesse et sa disponibilité ! Les remerciements à ces gens bizarres d'une autre université ne pourraient être complets sans mentionner Fanny pour nos discussions enrichissantes et évidemment Lio pour tellement de choses que je vais résumer en disant « incroyable support scientifique » et « pote de billard ».

J'adresse ensuite mes plus sincères remerciements au Professeur Giovanni Poli (Université Pierre et Marie Curie) pour l'accueil au sein de son

laboratoire pendant ces dix semaines et pour la découverte d'une (infime) partie de la catalyse au Palladium. Je garderai en mémoire sa disponibilité, ses conseils avisés et surtout sa bonne humeur permanente ! Je remercie également Julie et Farès pour l'aide pratique dans les synthèses.

Je souhaite également remercier le Professeur Garry Hanan (Université de Montréal) de son accueil pour ces quelques semaines dans cette belle ville de Montréal. Au-delà des résultats que nous avons obtenus, son sens pratique, sa vision d'un projet abouti et sa sympathie seront d'excellents souvenirs que je garderai de notre collaboration. Ces remerciements sont également adressés à Oli pour son aide dans la mise en place des manipulations, nos parties de PMU devant l'écran de la GC et sa « rapidité » d'action et à Thomas pour les calculs théoriques et les discussions.

*Je souhaite évidemment remercier les membres du labo qui m'auront accompagné durant toutes ces années : Georges que je n'aurai connu qu'un mois mais qui m'aura marqué par son sens de la mode et de la coiffure, Alex et son amour pour Gérard Depardieu, Guims et son rire tonitruant si agréable (et ses résolutions de problèmes d'ordi), Christophe ainsi que Chris et Tophe qui ne sont jamais loin dans sa tête, Johan et son amour pour cette radio de m**** qu'est Radio Nova, Simon et son raffinement concernant les PSJ sur les filles VM, Robin le Portugais de caractère mais toujours prêt pour un bon verre, Justin et sa volonté de fer de 30 secondes pour ne pas manger de frites, Akin pour son franglais et surtout son hit planétaire « Là c'est die », Martin pour ses blagues que seuls lui et le Boss comprennent, le p'tit Alex pour la plus belle histoire d'amour qu'on ait vue à Blankenbergue et évidemment Poupoule, notre bouteille d'oxygène (oui, toujours sur notre dos) en permanence là pour notre sécurité, accomplir tous les petits services qu'on peut lui demander et ça, dans la bonne humeur ! Parmi les membres plus*

éphémères du labo, je remercie Diamante et Nathalie que j'aurai traumatisées pendant des mois. Ca aura néanmoins été un plaisir de vous aider à réaliser votre stage.

Deux membres de ce labo méritent des remerciements tous particuliers. Il y a tout d'abord Quentin qui m'aura accompagné dans tellement de délires pendant plus de onze ans dès le début de nos études. Je sais que ça aura été très dur de me supporter mais aller jusqu'à me présenter Florence et faire ce qu'il faut pour que j'aille jusqu'à l'épouser… je ne méritais pas une telle vengeance ! Le second larron est bien évidemment Mika, mon Pilou ! Je ne pensais pas connaître quelqu'un qui prendrait un réel plaisir à me faire sortir de mes gonds et qui aurait un humour aussi pourri que le mien. Un jour je me vengerai car après tout : « Qui casse paie ». Je n'ai qu'une dernière chose à dire : « Ma princesse… T'enlèves la tristesse de mon être. A tes côtés, je touche le ciel rempli de joie et de merveilles ».

La vie au labo n'aurait pas été la même sans Elle… ma Déesse… Merci à ma belle Chanchan pour toutes les aides administratives, la bonne humeur communicative et sa capacité à trouver tous les surnoms les plus pourris pour tout le monde ! Une fois que sa paresse l'a emporté et qu'elle a malheureusement pris sa pension, j'ai eu la chance de rencontrer Audrey avec sa gentillesse rare et sa capacité à se faire offrir des chocolats chauds par tout le monde et par la suite Corinne, que je n'ai connue que brièvement mais qui a su me guider dans les méandres administratifs que représente une défense de thèse.

Ils restent dans l'ombre mais méritent également des remerciements de ma part : Jessica (magasin), Sabrina (support technique) Raoul (spectrométrie de masse), Cécile et Alain (RMN), Laurent (HPLC), Brigitte

(serviettes hygiéniques dans les toilettes), Axel et Hubert (réparation « rapide » et outillage).

Une fois ma vie d'étudiant terminée et que je suis passé du côté obscur en endossant un poste d'assistant, j'ai eu la chance de travailler dans un cadre totalement différent avec des personnes remarquables. Je commencerai par remercier tous ces Professeurs pour qui j'ai donné d'innombrables heures d'exercices et de travaux pratiques, à savoir les Professeurs Michel Devillers, Bernard Tinant, Istvan Marko, Yann Garcia, Alexandru Vlad, Jean-François Gohy et Benjamin Elias.

Toutes ces séances de travaux pratiques, de monitorat,… étaient chapeautées d'une main de fer par les trois Drôles de Dames que sont Marianne Van de Wiel, Catherine Liégeois et Agnès Gnagnarella. Merci pour la liberté que vous m'avez laissée pour inculquer un semblant de savoir à ceux que je surnommais affectueusement les Touristes et pour les corrections de leurs copies, souvent sources de fous rires ou d'intense séances de « mais à quoi on sert ». Tous ces moments n'auraient pas été aussi bien orchestrés sans la bonne humeur et l'aide bienveillante de nos chers techniciens, à savoir Nadine, Marie-Jo, Edouard, François, Anne, Pascale et Richard. Je remercie évidemment l'ensemble des assistants avec qui j'ai eu la chance de donner ces cours : Nadia, Madeleine, Akina, Claire Sophie, Nathalie, Pierre, Antoine, Samuel, Simon, Guillaume, Thomas, Corentin, Quentin et Mika.

Et comment oublier ceux qui ont fait que le job d'assistant était tantôt une pénitence, tantôt un grand moment de plaisir ? Je remercie très sincèrement tous ces touristes, tous ces glandeurs qui participaient aux cours. J'espère avoir pu en aider voire en motiver certains.

Je remercie tous ces amis d'hier et d'aujourd'hui pour leur présence tout au long de ces années, avec un remerciement plus particulier à ceux qui peuvent se considérer comme de la famille actuellement, David et Kevin. Merci à tous les deux pour ces moments de partage et aux nombreux délires qu'on a eus et qu'on aura encore.

J'adresse un remerciement particulier à Marc et Michèle, sans doute les seuls Parisiens avec véritablement le cœur sur la main, pour m'avoir accueilli chez eux durant mon séjour à Paris, alors que je n'avais pas encore la chance de les connaître et sans jamais rien me demander en retour.

Merci à mes parents pour leur soutien sans faille même si le résumé de ma thèse décrit par mon cher Papa se limite à : « Oui bah en gros, tu niques des molécules quoi ». J'espère les avoir rendus fiers.

Pour terminer, je remercie les personnes les plus chères à mon cœur, à savoir ma chère épouse Florence pour son amour inconditionnel et son soutien depuis toutes ces années où je lui ai bien pourri la vie, à mes filleuls Scott et Alex dont c'est autant un privilège qu'un plaisir de vous voir évoluer ainsi et surtout mes enfants Noah et Jade. Vous êtes une source intarissable de bonheur au quotidien et tout ce que je fais sera toujours dans le but que vous soyez fiers de votre Papa.

Abbreviations

μs	microsecond
2244tpy	2,2';4',4''-terpyridine
2254tpy	2,2';5',4''-terpyridine
6-iPr-bpy	6-isopropyl-2,2′-bipyridine
Å	Angström
a.u.	arbitrary unit
acac	acetylacetonate
ACN	acetonitrile
AcOEt	ethyl acetate
AcOH	acetic acid
AO	Atomic Orbital
Ar	Argon
atm	atmosphere
bpy	2,2′-bipyridine
bpytBu$_2$	4,4′-di-*tert*-butyl-2,2′-bipyridine
bpz	2,2′-bipyrazine
bt	2-phenylbenzothiazole
Cat	Catalyst
CIDNP	Chemically Induced Dynamic Nuclear Polarization
COSY	COrrelation SpectroscopY
DFT	Density Functional Theory

dGMP	2'-deoxyguanosine-5′-monophosphate
DMA	N,N-dimethylacetamide
DMF	N,N-dimethylformamide
dmgH	dimethylglyoximate
$dmgH_2$	dimethylglyoxime
DMSO	dimethyl sulfoxide
dphphen	4,7-diphenyl-1,10-phenanthroline
dtbbpy	4,4′-di-*tert*-butyl-2,2′-bipyridine
EDTA	ethylenediaminetetraacetic acid
EPR	Electron Paramagnetic Resonance
ESI	ElectroSpray Ionization
Et_3N	triethylamine
ETM	Electron Transfer Mediator
FID	Free Induction Decay
FMN	flavin mononucleotide
GC	Gas Chromatography
GMP	guanosine-5′-monophosphate
h	hour
HAT	1,4,5,8,9,12-hexaazatriphenylene
HER	Hydrogen Evolution Reaction
HF	HyperFine interaction
His	histidine
HMBC	Heteronuclear Multiple Bond Correlation

HOMO	Highest Occupied Molecular Orbital
HSQC	Heteronuclear Single Quantum Correlation
HT	Proton transfer
Hz	Hertz
IC	Internal Conversion
ISC	InterSystem Crossing
kJ	kilojoule
knr	Non-radiative rate constant
kr	Radiative rate constant
LC	Ligand Centered
LED	Light-Emitting Diode
LLCT	Ligand-to-Ligand Charge Transfer
LMCT	Ligand-to-Metal Charge Transfer
LUMO	Lowest Unoccupied Molecular Orbital
M	mole of compound per liter of solution
MC	Metal Centered
min	minute
MLCT	Metal-to-Ligand Charge Transfer
MLLCT	Metal-Ligand-to-Ligand Charge Transfer
mmol	millimole
MO	Molecular Orbital
mol	mole
N-Ac-Tyr	N-acetyl tyrosine

NHC	N-Heterocyclic Carbene
nm	nanometer
NMDA	N-methyl-D-aspartate
NMP	N-methyl-2-pyrrolidone
NMR	Nuclear Magnetic Resonance
NOESY	Nuclear Overhauser Effect SpectroscopY
ns	nanosecond
OLED	Organic Light-Emitting Diode
pc	phtalocyanine
PET	Photoinduced Electron Transfer
Ph	phenyl
piqH	1-phenylisoquinoline
ppy(OMe)$_2$H	2-(3',5'-dimethoxyphenyl)pyridine
ppy(OMe)H	2-(3'-methoxyphenyl)pyridine
ppyCF$_3$H	2-(3′-trifluoromethyl)-phenylpyridine
ppyH	2-phenylpyridine
ppytBu$_2$H	4-*tert*-butyl-2-(4'-*tert*-butylphenyl)pyridine
ppytBuH	2-(4′-*tert*-butyl)-phenylpyridine
Pro	proline
PS	PhotoSensitizer
Pyr	pyridine
Q	Quencher
quant.	quantitative

Rnase A	Ribonuclease A
ROESY	Rotating-frame Overhauser Effect SpectroscopY
RT	Room Temperature
SCE	Saturated Calomel Electrode
SOC	Spin-Orbit Coupling interaction
tap	1,4,5,8-tetraazaphenanthrene
TD-DFT	Time Dependent - Density Functional Theory
TEOA	triethanolamine
TFA	trifluoroacetic acid
THF	tetrahydrofuran
TOF	TurnOver Frequency
TON	TurnOver Number
tpp	tetraphenylporphyrin
Trp	tryptophan
Tyr	tyrosine
UV	Ultra-Violet
Vis	Visible
VR	Vibrational Relaxation
WRC	Water Reduction Catalyst
ε	Molar extinction coefficient
τ	Lifetime of the excited state
ϕ	Quantum yield

Publications

Lentz C., Schott O., Auvray T., Hanan G., Elias B., Photocatalytic H_2 production using a red-absorbing Ir(III)-Co(III) complex, *Inorg. Chem.* **2018**, *56*, 10875-10881
(***Cover article***)

Lentz C., Marcelis L., Cauet E., Kirsch A., Elias B., Twisted bpy ligand for pH-sensitive Ir(III) complex: switching from ^{3}MLLCT to ^{3}LC, *to be submitted*

Lentz C., Fusaro L., Marcelis L., Luhmer M., Elias B., pH dependency of photoreactions between a protonable polyazaaromatic Ir(III) complex and a nucleobase: a photo-CIDNP study, *to be submitted*

Lentz C., Schott O., Auvray T., Hanan G., Elias B., Design and photophysical studies of Iridium(III)-Cobalt(III) dyads and their application for dihydrogen photo-evolution, *to be submitted*

Lentz C., Roudesly F., Oble J., Poli G., Elias B., Oxidative palladocatalyzed reactions: photooxidation of Pd(0) to Pd(II) by Ir(III) complexes in Wacker oxidation and acetoxylation, *in preparation*

Abstract

Our entire world is in the grip of rapidly increasing environmental pollution and this issue is supported by global warming and energy crisis. This is mainly due to the use of chemicals to fulfill multiple demands of materials with various applications such as polymers, agriculture, pharmaceuticals,… which induce the production of different kinds of pollutants. There is an obvious demand over the world to reduce the amounts of these harmful materials. In that purpose, photoredox catalysis is emerging as a powerful tool in green chemistry and Ir(III) complexes represent one of the most promising solutions because of their high tunability and ability to absorb and convert light into chemical energy.

During this Ph.D. thesis, we aimed to develop photoactivatable Ir(III) cocatalysts to regenerate Pd(II) and Co(III) catalysts and, hence, avoid the use of stoichiometric harmful additives. Ir(III) complexes with varying first coordination sphere were deeply investigated to select the best photosensitizers. Thereafter, some of the investigated Ir(III) photosensitizers have shown valuable improvements when coupled to Pd(II) catalysts compared to well-known systems. In addition, several Ir(III)-Co(III) dyads were designed and their photophysical properties were tuned to favor H_2 photocatalytic production.

Résumé

Notre monde entier est en proie à une pollution environnementale en perpétuelle croissance et cette situation est soutenue par le réchauffement climatique et la crise énergétique. Ceci est principalement dû à l'utilisation de produits chimiques pour répondre à des demandes conséquentes de matériaux pour applications diverses telles que les polymères, l'agriculture, les produits pharmaceutiques, ... qui induisent la production de différents types de polluants. Il existe une demande évidente à travers le monde pour réduire les quantités de ces matériaux nocifs. Dans ce but, la catalyse photoredox apparaît comme un outil puissant dans la chimie verte et les complexes d'Iridium (III) représentent l'une des solutions les plus prometteuses en raison de leur haute modulabilité et de leur capacité à absorber et convertir la lumière en énergie chimique

Durant cette thèse de doctorat, notre but a été de développer des cocatalyseurs photoactivables à base d'Iridium(III) pour régénérer des catalyseurs Pd(II) et Co(III) et ainsi éviter l'utilisation d'additifs stoechiométriques nocifs. Des complexes d'Ir(III) présentant une variation de la première sphère de coordination ont ainsi été étudiés en profondeur pour sélectionner les meilleurs photosensibilisateurs. Par la suite, certains photosensibilisateurs d'Ir(III) étudiés ont montré des améliorations intéressantes lorsqu'ils étaient couplés à des catalyseurs de Pd(II) dans le cadre de réactions oxydatives. Enfin, plusieurs dyades Ir(III)-Co(III) ont été conçues et leurs propriétés photophysiques ajustées afin de favoriser la production photocatalytique de H_2.

Table of contents

CHAPTER 1

Introduction

1.1 General introduction

A sufficient, clean and sustainable energy supply, as alternative to fossil fuels is one of the Holy Grails nowadays. Indeed, the global annual energy consumption is estimated approximately to 4.58×10^{20} J, which corresponds to an average energy consumption rate of 14.5 TJ/s.[1] To give an idea on how much energy we are using, running a complete cycle of an energy-efficient washing machine corresponds to the continuous muscular work of 15 human beings, while 1.6 million people are required to taking off a fully loaded Boeing 747.[2] Interestingly, the sun provides an annual global intensity of about 3×10^{24} J *i.e.* exceeding by almost 10000 times the current annual energy demand. Therefore, solar energy conversion into clean chemical fuels is an area full of promises and represents one of the most important breakthrough in modern science.

One approach to convert solar energy into a fuel is to use it to split water into molecular hydrogen H_2 and oxygen O_2 as their recombination into water releases 119 kJ/g H_2.[1]

$$2\ H_2O \xrightarrow{\Delta G^0 = 238\ \text{kJ/mol}\ H_2} \mathbf{O_2} + 2\ \mathbf{H_2} \qquad \text{eq 1.1}$$

Hence, electrochemical decomposition of water requires a potential difference of more than 1.23 V which is the necessary potential between the cathode (where the two-electron reduction of protons takes place – equation 1.2), and the anode (where the four-electron oxidation of water occurs – equation 1.3) to provide H_2 and O_2, respectively.

$$2\,H^+ + 2\,e^- \longrightarrow H_2 \qquad \text{eq 1.2}$$

$$2\,H_2O \longrightarrow O_2 + 4\,H^+ + 4\,e^- \qquad \text{eq 1.3}$$

This energy corresponds to a wavelength of approximately 1000 nm *i.e.* in the near-infrared region. Therefore, if the energy of light is efficiently used in an electrochemical system, it should be possible to decompose water with the energy associated to visible light.

One of the most pioneering experiments in water splitting upon irradiation was performed in 1972 by Fujishima and Honda using TiO_2 as a semiconductor photocatalyst.[3] In that system, light triggers electrons and holes migration to the surface of the semiconductor where charges accumulation favors the occurrence of multielectron redox processes. However, the energy gap of TiO_2 corresponds to a threshold of about 3.2 V (Figure 1.1), *i.e.* an irradiation wavelength of 390 nm, meaning that visible light (sunlight) is almost useless.

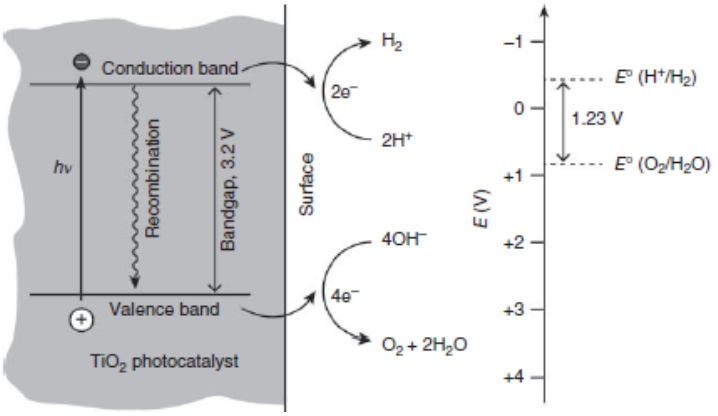

Figure 1.1 – Water splitting by solid-state photocatalysis with TiO_2 (from [3])

Since then, numerous other heterogeneous systems have been developed and, among them, UV-activatable photocatalysts have emerged.[4-7] However, their efficiency strongly depends on many interfacial parameters that are difficult to control. The development of homogeneous molecular devices allowed to solve these interfacial issues.[8-15]

As the overall water splitting is generally difficult to achieve due to the uphill nature of the reaction, each half reaction *i.e.* reduction of protons (equation 1.2) and oxidation of water (equation 1.3) has usually been developed separately. In our laboratory, the research in this field is mainly focused on the photocatalyzed hydrogen evolution reaction (HER). The key feature of our systems is the charge separation: each absorbed photon leads to the transfer of one electron in a given direction. The main components of these photochemical H_2-evolving systems are a light-harvesting photosensitizer (PS), a proton-reduction catalyst (Cat) and an electron bridge (B) linking them (Figure 1.2). An additional sacrificial electron donor such as EDTA, Et_3N, triethanolamine (TEOA), sodium ascorbate,… is also required to regenerate the oxidized charge injector photosensitizer once the process has been triggered.[16] With respect to HERs, covalent linkage of the photosensitizer to the catalyst affording a monocomponent system gives in general rise to enhanced H_2 production when compared to dissociated, bimolecular systems[9, 17-18]

In the literature, several systems for dihydrogen photoproduction based on transition metal complexes such as ruthenium,[10-11, 19] osmium[20] or iridium[21-23] as photosensitizers and platinum[13, 24-25] or palladium[25-26] as catalytic centers have been synthesized and investigated. Their ability to produce hydrogen is

characterized by two main features *i.e.* the turnover number (TON) defined as the number of moles of substrate that a mole of catalyst can convert before becoming inactivated, and the turnover frequency (TOF) corresponding to the number of revolutions of the catalytic cycle per unit time.

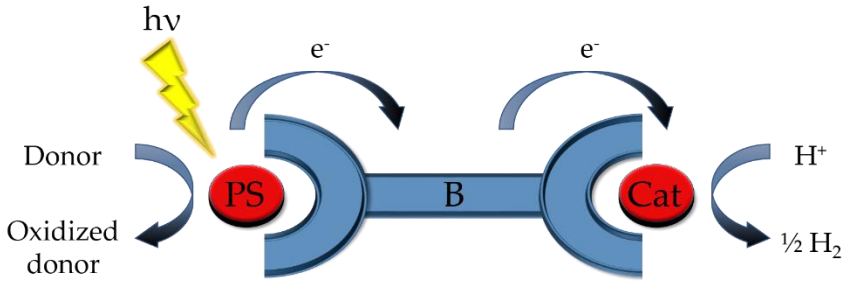

Figure 1.2 – Simplified scheme of a monocomponent system for H_2 photoproduction using a light-harvesting photosensitizer (PS), a reduction catalyst (Cat) and an electron bridge (B)

Elements of photochemistry are essential to understand the electron transfer pathway since the key process relies on light-triggered reaction. As a consequence, general information about photochemistry is now provided.

1.2 Elements of photochemistry

1.2.1 Molecular orbitals

Molecular orbital (MO) theory is necessary for a better understanding of electronic transitions resulting from the absorption of light by a coordination complex. Organic molecules display several MOs depending on the combination of the atomic orbitals (AO):

- σ MOs arising from the combination of s or p atomic orbitals;
- π MOs formed from the transversal combination of p atomic orbitals;
- n MOs corresponding to lone pairs.

In addition to these MOs found in organic molecules, organometallic compounds involve d orbitals combinations (dσ and dπ) between the metal center and its ligands.

1.2.2 Absorption of light

The simplest interaction between molecules and light arises from the absorption of *one* photon by *one* molecule. By doing so, a molecule is promoted from the ground to the excited electronic state, reflecting the relative energy of the molecular orbitals. The necessary condition to observe this transition is that the absorbed energy must be strictly the same than the energetic difference between HOMO and LUMO. In addition, the spin of the electrons is also important. In the ground state, according to Pauli's rule, the HOMO is usually occupied by two electrons with opposite spins ($+^1/_2$; $-^1/_2$); the spin multiplicity (= 2S +1 ; S = sum of the spin quantum numbers) is equal to 1 and the state

is termed singlet (S_0). When one of the two electrons is promoted to a molecular orbital of higher energy, its spin remains unchanged, so as the multiplicity (Figure 1.3). As a result, both the ground and the excited states are called *singlet state* (S_0 for the ground state and S_1, S_2,… for the excited states). Once on the singlet state, the spin can be inverted yielding to the more stable *triplet state* (*vide infra*).

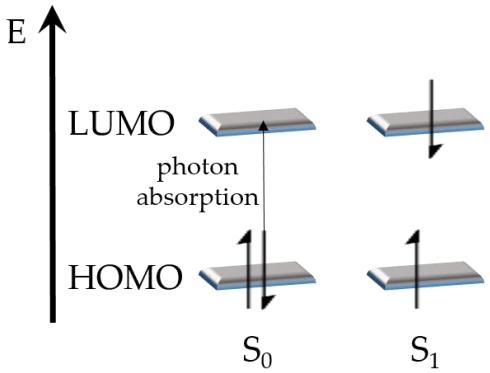

Figure 1.3 – General scheme for the formation of excited singlet state S_1 after the absorption of a photon

As promotion of the electron to its excited state (10^{-15} s) is fast with respect to nuclear motion (10^{-13}-10^{-11} s), such electronic transition is likely to occur without any change in the position of the nuclei of the irradiated compound and its environment. In other words, when a photon is absorbed, the excited state S_1 still possesses the same geometry and solvation as S_0. This is termed the *Franck-Condon principle* (*vide infra*) (Figure 1.4).

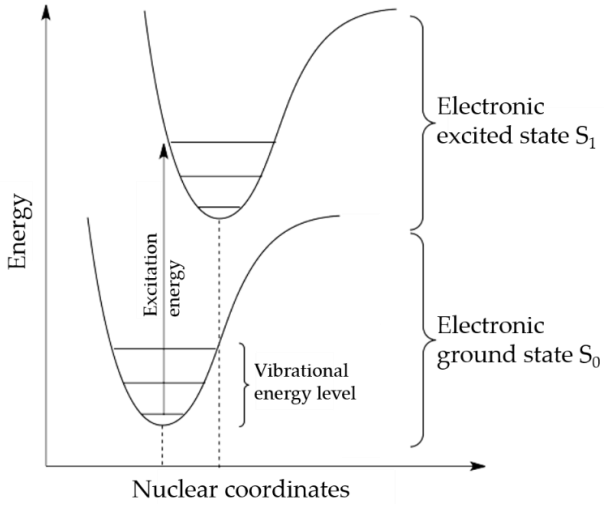

Figure 1.4 – Franck-Condon principle energy diagram

1.2.2.1 Beer-Lambert law

In 1817, Theodor von Grotthuss stated the first principle of photochemistry: *only the light absorbed is effective in producing photochemical change*.[27] Hence, measuring the amount of absorbed light by the investigated system is essential. The absorption of light at wavelength λ by a substance dissolved in a transparent medium is described by the Beer-Lambert law (equation 1.4),

$$A(\lambda) = log \frac{I_0}{I} = \varepsilon \, l \, C \qquad \text{eq 1.4}$$

where $A(\lambda)$ is the absorbance at the considered wavelength, I_0 and I are the intensities of incident and transmitted light, respectively, ε is the molar absorption coefficient, l is the optical path length and C is the solution molar concentration. The molar absorption coefficient ε represents the ability of a compound to absorb light at a given wavelength of the incident light.

1.2.2.2 Selection rules

Selection rules constrain the possible transitions of a system from one quantum state to another. The selection rules governing transitions between electronic energy levels of a system are:

- ***Spin rule***: allowed transitions must only involve the promotions of electrons without a change in their spin *i.e.* only singlet-to-singlet and triplet-to-triplet transitions are allowed whereas singlet-to-triplet and triplet-to-singlet transitions are forbidden ($\Delta S = 0$). However, there is a weak interaction between states of different multiplicities via *spin-orbit coupling*. This phenomenon describes the interaction between the spin of a particle with its motion. As a result, a "real" singlet (triplet) state always contains a small fraction of a triplet (singlet) state, allowing a non-negligible transition between a singlet state and a triplet state. This effect is increased by the presence of a heavy atom such as a transition metal. Intersystem crossing *i.e.* crossing from a singlet excited state to a triplet state, is thus the result from spin-orbit coupling.[28]

- ***Symmetry rule (Laporte's rule)***: in a centrosymmetric molecule, transitions between states of the same symmetry with respect to inversion are forbidden *i.e.* pure p-p or d-d transitions are forbidden whereas s-p, p-d or d-f transitions are allowed ($\Delta l = \pm 1$ where l is the orbital quantum number). In other words, a transition is forbidden if it implies a redistribution of the electrons within the same set of orbitals. However, due to vibrations, a centrosymmetric

compound may temporarily lose its symmetry and allow absorption of light from forbidden transitions. Another relaxation of Laporte's rule implies transition metal complexes in which π-orbitals from the ligands can mix with the d-orbitals from the metal yielding to transitions that are no longer purely d-d.[28]

1.2.3 Deactivation of excited compounds

Once the excited state is formed after the absorption of a photon, a given compound can undergo several processes to release the excess of energy which can be either radiative or non-radiative (Figure 1.5).

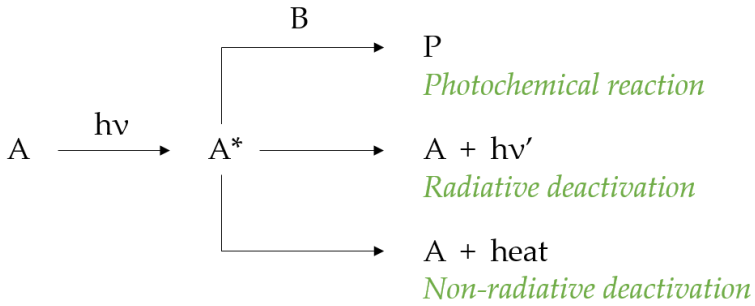

Figure 1.5 – General pathways for the deactivation of the excited compound A*

1.2.3.1 Photophysical deactivation

1.2.3.1.1 Jablonski diagram

Following the absorption of a photon yielding to an excited state S_n (n = 1, 2, 3…) (Figure 1.6 – blue arrows), the system by itself can

undergo different radiative or non-radiative pathways in order to recover its ground state. The so-called photophysical processes are conveniently described using the Jablonski diagram (Figure 1.6).

Shortly after excitation, the geometry of the excited state S_n fastly decays (10^{-13}-10^{-11} s) from the Franck-Condon state to its most stable state, followed by a change in the solvation of the excited compound (10^{-11}-10^{-10} s) (except for isolated compounds in gas phase), decreasing the energy of the excited compound without changing the multiplicity. This phenomenon is called *vibrational relaxation* (VR – Figure 1.6 – vertical wavy arrows). Once the lowest vibrational state of an excited state S_n is reached, the electron can undergo two distinct non-radiative transitions:

- *Internal Conversion* (IC – Figure 1.6): Transition of the excited electron to a lowest electronic state with the same multiplicity S_{n-1};
- *InterSystem Crossing* (ISC – Figure 1.6): Transition of the electron to an isoenergetic vibrational state with a different multiplicity T_n.

These pathways ultimately lead to the lowest excited state S_1 (or T_1) according to Kasha's rule.[29] At this step, the ground state recovery occurs by:

- *non-radiative deexcitation* through internal conversion;
- *radiative deexcitation* by emission of a photon from either the singlet state S_1 yielding to fluorescence (Figure 1.6 – orange arrows) or the triplet state T_1 yielding to phosphorescence (Figure 1.6 – green arrows).

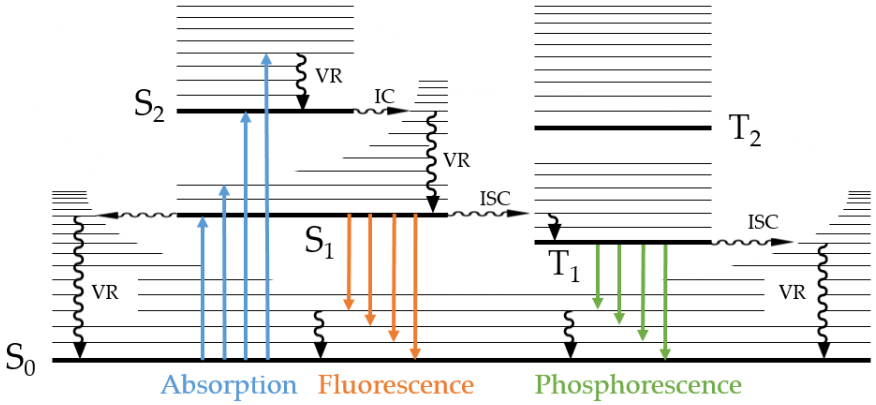

Figure 1.6 – Jablonski diagram describing absorption of a photon (blue arrows) followed by radiative deactivation through fluorescence (orange arrows) and phosphorescence (green arrows) and non-radiative deactivation

1.2.3.1.2 Excited state lifetime

Just as a rate constant of a reaction is a significant measure of the ground state reactivity of a molecule, the rate constant for the deactivation of the excited state provides a good idea of its reactivity, keeping in mind that the excited state lifetime τ depends on several photophysical (Figure 1.7) and photochemical (*vide infra*) processes. Photophysical deactivation is a combination of rate constants associated to radiative (k_r) and non-radiative (k_{nr}) processes involving both singlet S_1 (k^S) and triplet T_1 (k^T) excited states and the ground state S_0 as well as the intersystem crossing process (k_{ISC}).

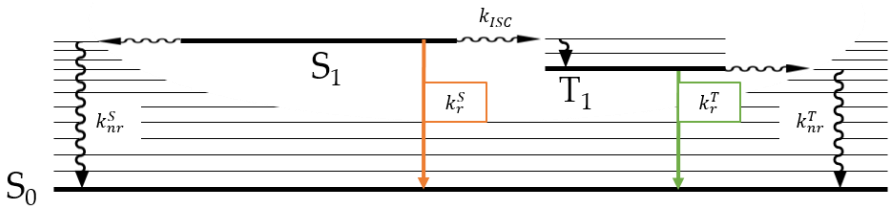

Figure 1.7 – Radiative and non-radiative rate constants for the deactivation of the first excited state S_1

After a short light pulse, a certain number of ground state compounds A are promoted to their excited state S_1 and the deactivation kinetics of these excited A* can therefore be defined according to:

$$-\frac{d[A^*]}{dt} = (k_r + k_{nr})[A^*] \qquad \text{eq 1.5}$$

where k_r is the global radiative rate constant (*i.e.* including both fluorescence and phosphorescence phenomena), k_{nr} is the sum of all of the non-radiative rate constants and $[A^*]$ is the concentration of the excited species A*.

Integration of equation 1.5 provides the time evolution of the concentration of A*,

$$[A^*]_t = [A^*]_0 exp[-(k_r + k_{nr})t] = [A^*]_0 exp\left(-\frac{t}{\tau}\right) \qquad \text{eq 1.6}$$

where $[A^*]_0$ is the concentration of the excited molecules just after the light pulse (*i.e.* t = 0) and τ is the lifetime of the excited state.

It is noteworthy that the intensity of luminescence, *i.e.* the emissive radiation including both fluorescence and phosphorescence contributions, is proportional at any time to the transient concentration of the excited compounds [A*], with a proportionality factor corresponding to the radiative deexcitation rate constant k_r (equation 1.5). This relationship allows to have direct experimental access to the lifetime of the investigated compound.

$$I_t = k_r[A^*]_t = k_r[A^*]_0 exp\left(-\frac{t}{\tau}\right) \qquad \text{eq 1.7}$$

For organic molecules, the lifetime of the singlet state yielding to fluorescence ranges from 10^{-11} s to 10^{-7} s whereas the triplet state deexcitation through phosphorescence is much longer due to the spin-

forbidden transition *i.e.* from 10^{-6} s to seconds. On the other hand, for organometallic compounds, the distinction is not easy to make due to the presence of a heavy element facilitating spin-orbit coupling and, hence, a mix up of both fluorescence and phosphorescence phenomena.

1.2.3.1.3 Quantum yield

The emission quantum yield Φ coincides with the efficiency of the process *i.e.* the fraction of excited molecules that returns back to the ground state with emission of photons, and thus its value ranges from zero to unity. In other words, the emission quantum yield corresponds to the ratio between the number of emitted photons and the number of absorbed photons (over the whole duration of the process). Hence, if the radiative deactivation pathways are much shorter than non-radiative ones ($k_r >> k_{nr}$), the emission quantum yield will be higher according to equation 1.8.

$$\Phi = \frac{k_r}{k_r + k_{nr}} = k_r \tau \qquad \text{eq 1.8}$$

It is worth mentioning that according to equation 1.8, the emission quantum yield of a compound alone in solution is constant (within the same solvent).

The simplest method to determine the emission quantum yield of a compound is based on the comparison of the luminescence spectrum of the investigated compound with the spectrum of standard species with well-studied quantum yield at a specific excitation wavelength (Table 1.1). Hence, the luminescence quantum yield can be obtained from:

$$\frac{\Phi}{\Phi_{ref}} = \frac{I}{I_{ref}} \frac{A_{ref}}{A} \frac{n^2}{n_{ref}^2} \qquad \text{eq 1.9}$$

where Φ and Φ_{ref} are the luminescence quantum yields of the investigated and reference compounds, respectively, I and I_{ref} are the luminescence emission areas of the investigated and reference compounds, respectively, A and A_{ref} are the absorbances of the investigated and reference compounds, respectively, and n and n_{ref} are the refraction indexes of the investigated and reference media, respectively.

Table 1.1 – Examples of standard species for the determination of the emission quantum yield[30]

Compound	Emission range (nm)	Excitation (nm)[a]	Solvent	Quantum yield[b]
Anthracene	370-450	340	EtOH	0.28
Quinine sulfate	380-580	366	H_2SO_4 0.5 M	0.546
Fluorescein	490-620	496	NaOH 0.1 M	0.95
$[Ru(bpy)_3]^{2+}$	550-700	436	H_2O	0.042
Rhodamine B	560-590	348	MeOH	0.70

[a] Maximum of the considered absorption band of the compounds
[b] Room temperature values in deoxygenated solutions

1.2.3.2 Photochemical deactivation

In addition to the photophysical processes describing the radiative and non-radiative deactivations of an excited state, photochemical processes can occur between a luminescent molecule A* in the presence of a quencher Q *i.e.* a competitor to intramolecular photophysical deactivation yielding to the formation of new species

mainly through electron or energy transfer but also proton transfer, excimer or exciplex formation, etc… (Figure 1.8). An excited molecule A* can undergo a photochemical deactivation through intramolecular reactions but these pathways will not be detailed hereafter.

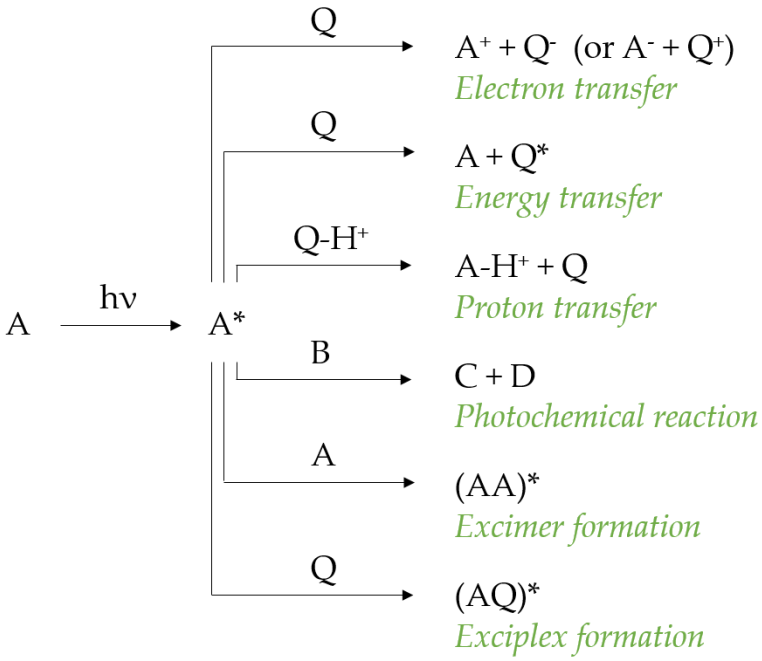

Figure 1.8 – General intermolecular pathways for photochemical deactivation

All these above mentioned pathways will lead to luminescence quenching. In terms of molecular dynamics, depending on the experimental conditions, several quenching mechanisms can occur:

- *Dynamic quenching*: the quencher Q is not in large excess compared to the excited compound A* and the excited state lifetime is long enough to allow a diffusional approach of both species (Figure 1.9 – red pathway with k_d as the

diffusion rate constant between A* and Q and k_R as the reaction rate constant);

- *Long-range quenching*: the quencher Q is not in large excess compared to the excited compound A* but diffusional approach is not possible due to short excited state lifetime or viscosity of the medium. Such quenching is effective only if the interaction is significant at distance longer than the collisional distance *i.e.* up to 80-100 Å. This non-radiative transfer usually results from dipole-dipole interaction.[28]

- *Static quenching*: the quencher Q is in large excess compared to the excited compound A* inducing a high probability that A and Q interact before the excitation process (*i.e.* at the ground state), forming a complex A···Q (Figure 1.9 – blue pathway with k_d' as the diffusion rate constant between A and Q). As both compounds are associated to the time of excitation, diffusion is not required.

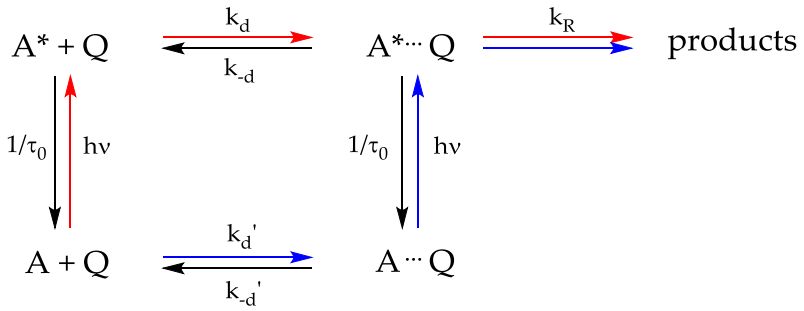

Figure 1.9 – Luminescence inhibition of compound A* by quencher Q through dynamic quenching (*red pathway*) and static quenching (*blue pathway*)

1.2.3.2.1 Dynamic quenching

In experimental conditions favoring a dynamic quenching of compound A* by quencher Q (Figure 1.9), the decrease of the concentration of A* by photochemical intermolecular deactivation is represented by:

$$-\frac{d[A^*]}{dt} = k_Q[A^*][Q] \qquad \text{eq 1.10}$$

where k_Q is the rate constant for the quenching process. When combined to equation 1.5, the overall decrease of A* concentration as a function of time corresponds to:

$$-\frac{d[A^*]}{dt} = \left(k_r + k_{nr} + k_Q[Q]\right)[A^*] = \left(\frac{1}{\tau_0} + k_Q[Q]\right)[A^*] \qquad \text{eq 1.11}$$

where τ_0 is the excited state lifetime in the absence of the quencher. Integration of equation 1.11 provides the time evolution of the concentration of the compound A*,

$$[A^*]_t = [A^*]_0 exp\left[-\left(k_r + k_{nr} + k_Q[Q]\right)t\right] = [A^*]_0 exp\left[-\frac{t}{\tau}\right] \qquad \text{eq 1.12}$$

where τ is the excited state lifetime in the presence of the quencher. Therefore, the ratio between the lifetime in the absence and in the presence of the quencher Q is provided by the equation 1.13, known as the *Stern-Volmer equation*,

$$\frac{\tau_0}{\tau} = 1 + \tau_0 k_Q[Q] = 1 + K_{SV}[Q] \qquad \text{eq 1.13}$$

where K_{SV} is the Stern-Volmer constant. Hence, as τ_0 is constant, this linear equation allows the direct determination of the quenching rate constant k_Q by studying the variation of the ratio τ_0/τ as a function of the concentration of the quencher. Equation 1.13 can also be expressed as the ratio between the quantum yield in the absence and in the

presence of the quencher (Φ_0 and Φ, respectively – equation 1.14) and, by taking into account the possible variation of concentration of the compound A (equation 1.9), between the emission intensity in the absence and in the presence of the quencher (I_0 and I, respectively – equation 1.15).

$$\frac{\Phi_0}{\Phi} = 1 + \tau_0 k_Q[Q] = 1 + K_{SV}[Q] \qquad \text{eq 1.14}$$

$$\frac{I_0}{I} = 1 + \tau_0 k_Q[Q] = 1 + K_{SV}[Q] \qquad \text{eq 1.15}$$

The addition of a large amount of quencher Q can lead to a deviation from linearity of the Stern-Volmer equation due to the induced change of polarity of the medium or, more importantly, to an interaction between ground state compound A and quencher Q forming a complex A···Q yielding to static quenching (*vide infra*).

As observed in Figure 1.9 (red pathway), the quenching process can be viewed as two distinct processes *i.e.* (i) a diffusion constant k_d describing the equilibrium association between A* and the quencher Q yielding to the transient complex A*···Q and (ii) the reaction rate constant k_R describing the interaction between both compounds within the association complex giving rise to the quenching process. As the diffusion of both compounds is reversible, the rate of the decrease of A* concentration by intermolecular deactivation (equation 1.9) can be re-expressed according to:

$$-\frac{d[A^*]}{dt} = k_Q[A^*][Q] = k_R[A^{*\cdots}Q] \qquad \text{eq 1.16}$$

As the concentration of the complex [A*···Q] is considered as constant after a short induction period because its rate of formation is balanced by the rates of dissociation and reaction between A* and Q (equation 1.17),

$$\frac{d[A^{*\cdots}Q]}{dt} = k_d[A^*][Q] - k_{-d}[A^{*\cdots}Q] - k_R[A^{*\cdots}Q] = 0 \quad \text{eq 1.17}$$

the combination of equations 1.16 and 1.17 yields to:

$$k_Q = \left[\frac{k_R}{k_{-d}+k_R}\right] k_d = \eta k_d \quad \text{eq 1.18}$$

where η is the factor describing the efficiency of the collisions between A* and Q as well as the luminescence quenching of A* by Q inside the association complex. Therefore, two limiting cases can be distinguished from equation 1.18 (Figure 1.10):

- $k_R \ll k_{-d}$ (or $k_R \approx k_{-d}$): The quenching process is controlled by the interaction between A* and Q meaning that the rate of quenching is sensitive to the factors that affect the interaction, yielding to $k_Q = K.k_R$ (with $K = {}^{k_d}/_{k_{-d}}$).

- $k_R \gg k_{-d}$: The quenching process is controlled by diffusion meaning that every time A* and Q encounter, luminescence quenching takes place, yielding to $k_Q = k_d$.

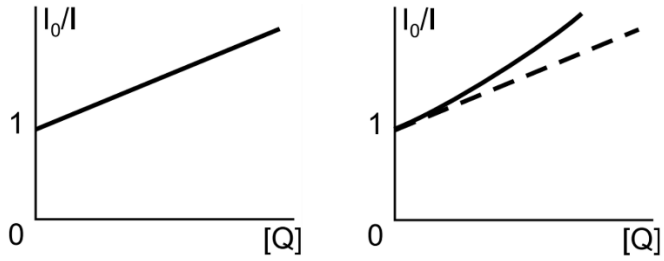

Figure 1.10 – Distinction between dynamic quenching controlled by reaction (*left*) and diffusion (*right*)

1.2.3.2.2 Static quenching

A static quenching implies that excited compound A* and quencher Q cannot change their positions in space relative to each other during the excited state lifetime of A*. Luminescence quenching generated by the interaction with Q can thus arise from two distinct processes, the sphere of effective quenching model (also known as *Perrin's model*) and the formation of a non-luminescent complex at the ground state (Figure 1.11).

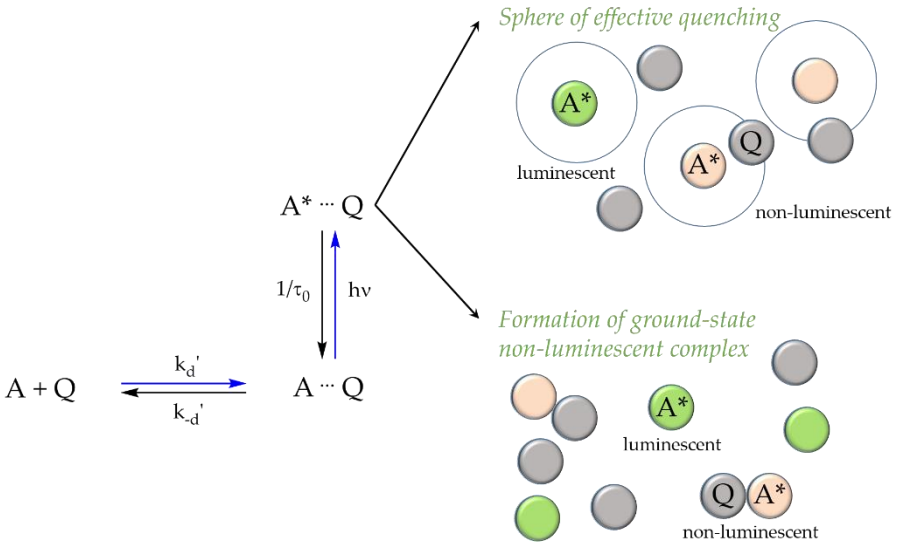

Figure 1.11 – Static quenching of luminescent excited compound A* (green sphere) by a quencher Q (grey sphere) yielding to non-luminescent compound (orange sphere) either using the Perrin's model (*up*) or upon the formation of a complex A···Q at the ground state (*down*)

- ***Formation of a non-luminescent ground state complex***

For a certain concentration of quencher Q, a fraction of ground state compound A is associated to Q according to the corresponding

equilibrium characterized by an association constant K_{ass} (equation 1.19).

$$A + Q \rightleftharpoons A\cdots Q$$

$$K_{ass} = \frac{[A\cdots Q]}{[A][Q]} \qquad \text{eq 1.19}$$

If the obtained complex A···Q is not luminescent (and no dynamic quenching occurs), then the residual luminescence arises from the fraction of compound A that is not complexed to the quencher according to:

$$\frac{I}{I_0} = \frac{[A]}{[A]_0} \qquad \text{eq 1.20}$$

where $[A]_0$ is the total concentration of compound A, nam ely $[A]_0 = [A] + [A\cdots Q]$. Therefore, equations 1.19 and 1.20 can be combined into:

$$\frac{I_0}{I} = \frac{[A]_0}{[A]} = \frac{[A]+[A\cdots Q]}{[A]} = 1 + \frac{[A\cdots Q]}{[A]} = 1 + K_{ass}[Q] \qquad \text{eq 1.21}$$

Accordingly, the plot of the ratio between luminescence intensities in the absence (I_0) and in the presence (I) of the quencher versus the concentration of the quencher is linear, as reported for dynamic quenching (equation 1.15). It is noteworthy that, unlike the previous observation on the dynamic quenching (equation 1.14), the plot of the ratio between luminescence lifetime in the absence (τ_0) and in the presence (τ) of the quencher cannot be superposed to that of I_0/I. Indeed, upon excitation of compound A, the fraction of A associated to Q is not luminescent whereas the fraction of A free in solution is not quenched and, hence, its excited state lifetime is not altered.

While pure static quenching via the formation of the ground state complex can be observed in viscous media or in a rigid matrix, a

small fraction of compound A can be associated to the quencher in non-viscous media where dynamic quenching takes place. Therefore, the residual luminescence is given by the product of the fraction of A not associated to Q and the fraction of excited A* not quenched by collisions with Q (equation 1.22).

$$\frac{I_0}{I} = (1 + K_{ass}[Q])\left(1 + \tau_0 k_Q[Q]\right) \qquad \text{eq 1.22}$$

Therefore, the plot of $^{I_0}/_{I}$ versus the concentration of the quencher displays an upward curvature while, as the excited state lifetime is not related to the concentration of the quencher, the plot of $^{\tau_0}/_{\tau}$ is linear, according to the Stern-Volmer equation (equation 1.13).

- ***Sphere of effective quenching***

While the formation of a non-luminescent complex at the ground state implies strong interactions between one compound A and one quencher Q, Perrin's model provides a better understanding of the reality for "complexes" with weak interactions or having a different stoechiometry ratio than 1:1. According to this model, the luminescence quenching of excited compound A* is complete if a quencher Q is located even partially inside a quenching sphere surrounding the luminophore A. If the quencher is outside of this sphere, it does not alter the luminescence of A*. As a result, as previously developed for the formation of non-luminescent complexes, the luminescence intensity decreases upon the addition of quencher whereas the excited state lifetime of A* remains unchanged.

1.2.3.2.3 Photoinduced electron transfer

As mentioned above, luminescence quenching characterized by Stern-Volmer equation may arise from different phenomena (see Figure 1.8). Nevertheless, as this work highlights the photoinduced production of dihydrogen from a proton source through electron transfer, our attention will focus on photoinduced electron transfer (PET). Photoinduced electron transfer is an active area in research as it is the key phenomenon for a wide range of natural[31] and artificial applications. In PET reactions, absorption of light activates the donor or acceptor for electron transfer. Indeed, in 1945, it has been recognized by Rabinowitch that *an electronically excited molecule has an increased tendency to give away an electron, as well as the capacity to replace the one which was removed from its normal level*.[32] In other words, oxidation and reduction properties of a light-absorbing compound are enhanced upon irradiation within the excited state lifetime window (Figure 1.12). Despite the different electronic configurations, both ground and excited states obey the same rules in redox reactions *i.e.* the reduction of the compound occurs with the transfer of an electron from a donor to the lowest energetic orbital vacancy whereas the oxidation takes place when the highest energetic electron is removed from the compound by an acceptor.

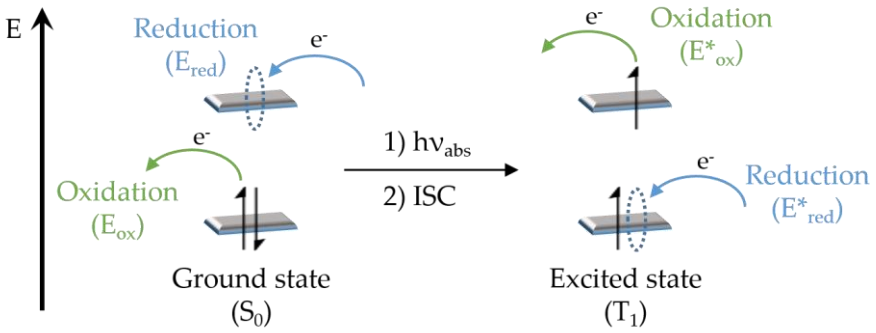

Figure 1.12 – Enhanced reductive and oxidative electron transfer potential of a compound upon light absorption

The extra amount of energy carried by the excited state ΔG(A*/A) consists of an enthalpic and an entropic term, ΔH(A*/A) and ΔS(A*/A), respectively (equation 1.23).

$$\Delta G(A^*/A) = \Delta H(A^*/A) - T\Delta S(A^*/A) \qquad \text{eq 1.23}$$

At absolute zero, ΔH(A*/A) is equal to the energy between the lowest vibrational state of the excited and ground states, and considered as approximately equal at room temperature. The entropic term ΔS(A*/A) is a combination of three different contributions *i.e.* (i) change in solvation, (ii) change in the internal degrees of freedom and (iii) change in orbital and spin degeneracy, which is difficult to evaluate. These changes in solvation, size and shape induce a shift between absorption and emission spectra called the *Stokes shift*. When the Stokes shift is small, these changes are also small and the difference in entropy between ground and excited states can be neglected. Therefore, the reduction and oxidation potentials at the excited state ($E_{red}^*(A^*/A)$ and $E_{ox}^*(A^*/A)$, respectively) can be approximated by:

$$\Delta E_{red}^*(A^+/A^*) = E_{red}^0(A^+/A) + E_{00}(A^*/A) \qquad \text{eq 1.24}$$

$$\Delta E_{ox}^*(A^*/A^-) = E_{ox}^0(A/A^-) - E_{00}(A^*/A) \qquad \text{eq 1.25}$$

where $E_{00}(A^*/A)$ is the potential corresponding to the energy between the lowest vibrational state of the excited and ground states which can be approximated to the emission energy if the entropy term of equation 1.23 is neglected.

When a compound in its excited state encounters a ground state electron donor or acceptor within its excited state lifetime, an electron transfer can occur. The feasibility of such process can be predicted by the *Rehm-Weller equation*:[33]

$$\Delta G_{ET} = \left(E_{D^+/D} - E_{A/A^-}\right) - \Delta E_{00} - \frac{e^2}{\varepsilon d} \qquad \text{eq 1.26}$$

where $e^2/\varepsilon d$ is the free enthalpy associated with the coulombic interaction between oxidated donor D^+ and reduced acceptor A^-. This term is negligible for polar solvent due to high dielectric constant value.

As shown in the next section, properties such as (i) long excited state lifetimes, (ii) highly oxidizing and reducing excited states and (iii) insensitivity towards changes of structure or environment[34] render Iridium(III) complexes superior to other previously used transition metal complexes such as Ruthenium(II), Osmium(II) or Rhodium(III) complexes for the photoinduced electron transfer required for H_2 production.

1.3 Ir(III) complexes in photoinduced H_2 production

Iridium photosensitizers are supramolecular assemblies made of a central metal cation chelated by several ligands with one or more chelating sites. As a consequence of this association, supramolecular complexes display different properties compared to separated building blocks. Ir(III) complexes were first considered for hydrogen evolution in 1979 by Lehn and Sauvage who found out that an $[Ir(bpy)_3]^{3+}$ (bpy = 2,2'-bipyridine) derivative evolves some hydrogen with platinum catalyst and TEOA as sacrificial electron donor.[35] Although not pursued at the time, this work allowed Ir(III) photosensitizers to be revisited two decades ago after their popularity as emitters for OLEDs exploded.[36-38] Bernhard's group first described the potential of bis-cyclometalated Ir(III) complexes having the architecture $[Ir(N^C)_2(N^N)]^+$ (N^C = cyclometalated ligand ; N^N = neutral ancillary ligand).[23, 39-40] Due to its two-step synthesis and high efficiency to photoinduce an electron transfer, this class of Ir(III) complexes represents ideal photosensitizers for photoinduced hydrogen production.

1.3.1 Fundamentals of Ir(III) photosensitizers

1.3.1.1 Synthesis of the $[Ir(N^C)_2(N^N)]^+$ complexes

The $[Ir(N^C)_2(N^N)]^+$ structure is prepared in a two-step synthesis in which the cyclometalated ligand is added to $IrCl_3$ (or derivative) to form a dichloro-bridged dimer and then this dimer is splitted into two cationic complexes by the addition of the neutral N^N ligand (Figure 1.13).

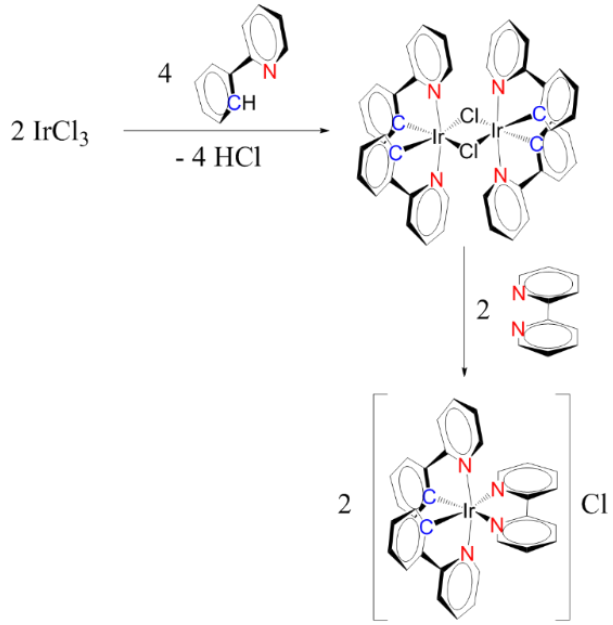

Figure 1.13 – General synthetic pathway of the $[Ir(N^C)_2(N^N)]^+$ photosensitizer illustrated with 2-phenylpyridine (ppyH) as N^CH ligand and 2,2′-bipyridine (bpy) as N^N ligand

1.3.1.2 Photophysics and electrochemistry

d^6 transition metal complexes such as Iridium(III), Ruthenium(II) or Rhodium(III) complexes display an octahedral coordination site around the metal center. Interactions between the metal and the ligands induce a donating and a retro-donating interaction *i.e.* σ-donation from the atoms of the ligands directly linked to the metal center and partial delocalization of the electrons from the metal to the non-bonding orbitals π* of the ligands, respectively. Linear combination of these atomic and molecular orbitals leads to the general diagram for the molecular orbital energy levels associated to an octahedral transition metal complex (Figure 1.14).

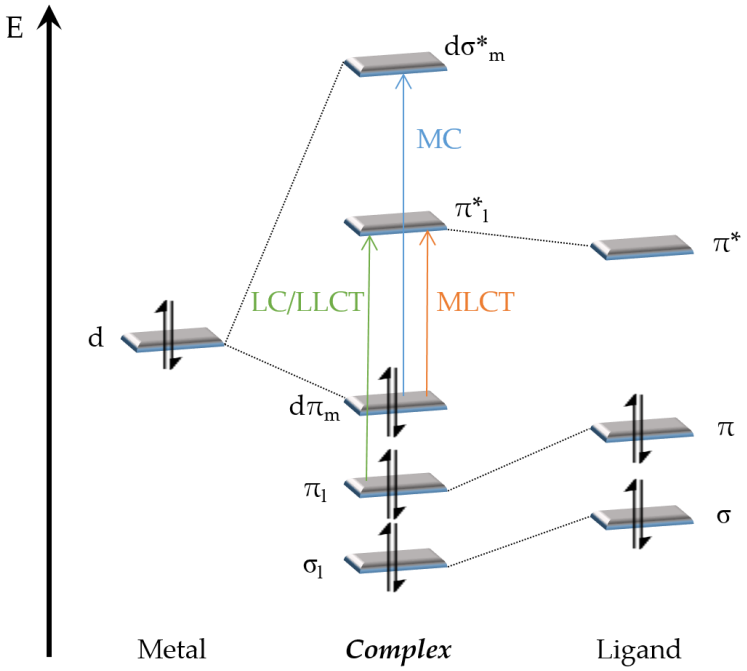

Figure 1.14 – General molecular orbital diagram of an octahedral transition metal complex and electronic transitions upon light absorption

Upon absorption of a photon, several electronic transitions involving orbitals of the metal and/or orbitals of the ligands can thus in principle be observed:

- *MC* (*Metal Centered*): this transition implies the transfer of one electron from the orbital $d\pi_m$ to the non-bonding orbital $d\pi^*_m$ of the metal center (*m* stands for "*metal*") (Figure 1.14 – blue arrow). Due to the high energy of the non-bonding orbital, this transition usually lies in the UV range and the return of the electron to the ground state is not emissive.[34]
- *LC* (*Ligand Centered*): this transition implies the transfer of one electron from the orbital π_l to the non-bonding orbital π^*_l of the same ligand (*l* stands for "*ligand*") (Figure 1.14 –

green arrow) and can be observed in the near-UV region. As the metal center is not involved in the process, such transition can be found for the free ligand in the same area of the UV spectrum with an extinction coefficient equal to about 10^5 $M^{-1}.cm^{-1}$.

- *MLCT* (*Metal-to-Ligand Charge Transfer)*: this transition implies the transfer of one electron from the orbital $d\pi_m$ of the metal center to the non-bonding orbital π^*_l of a ligand (Figure 1.14 – orange arrow). Thus, a MLCT results in oxidation of the metal center and reduction of a ligand implying a change in the polarity of the complex due to charge separation process (equation 1.27).

$$[M(L)_n]^{m+} + h\nu \rightarrow [M^{\bullet+}(L)_{n-1}(L)^{\bullet-}]^{m+} \qquad \text{eq 1.27}$$

This type of transition can be observed in the visible region of the electromagnetic spectrum with an extinction coefficient of *ca* 10^3-10^4 $M^{-1}.cm^{-1}$.

- *LLCT* (*Ligand-to-Ligand Charge Transfer):* this transition implies the transfer of one electron from the orbital π_l to the non-bonding orbital π^*_l of the different ligand (Figure 1.14 – green arrow) implying, as observed for MLCT, a charge separation within the complex (equation 1.28).

$$[M(L)_n]^{m+} + h\nu \rightarrow [M(L)_{n-2}(L)^{\bullet+}(L)^{\bullet-}]^{m+} \qquad \text{eq 1.28}$$

This type of transition can be observed in the visible region of the electromagnetic spectrum with an extinction coefficient equal to about 10^3-10^4 $M^{-1}.cm^{-1}$.

Early photophysical characterization of $[Ir(N^C)_2(N^N)]^+$ structures was first achieved by Watts[41-43] and Güdel.[44] The

combination of their research with more recent techniques such as Density Functional Theory (DFT) computations[45-46] revealed a unique electronic structure with mixing of triplet states once irradiated. Indeed, both ^{1}MLCT and ^{1}LLCT states resulting respectively from d → $\pi^*_{N^N}$ and π_{N^C} → $\pi^*_{N^N}$ promotions are less energetic than high energy ^{1}LC states from the π → π^* transitions on both N^C and N^N ligands (Figure 1.15 – left). Nevertheless, significant ISC stabilization in LC states brings the N^C centered ^{3}LC state down to the energy of ^{3}MLCT resulting in an overlap (Figure 1.15 – right).[34, 44, 47] As a result, while the lowest singlet excitation is a mixture between ^{1}MLCT and ^{1}LLCT states, emission from the bis-cyclometalated complexes is best described as a mixing between ^{3}MLCT and ^{3}LC states.

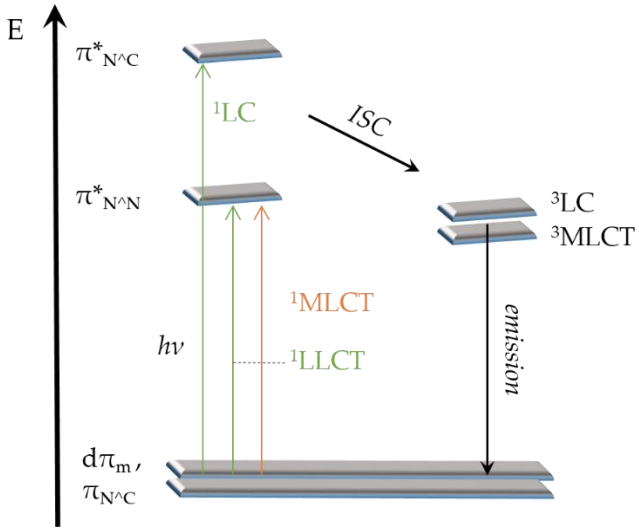

Figure 1.15 – Main electronic transitions for cyclometalated Ir(III) complexes during absorption (*left*) and emission (*right*) of light

The electrochemistry of the bis-cyclometalated complexes usually shows reversible processes. The first reduction is a reversible process consistent with an N^N centered LUMO (Figure 1.16 – up). In

complexes chelated by electrodeficient cyclometalated N^C ligands, a second reversible reduction can also be observed and attributed to the corresponding low-lying $\pi^*_{N^C}$ orbitals. The oxidation is quasi-reversible and involves the Ir(III)/Ir(IV) redox couple with a strong influence from the N^C ligand (Figure 1.16 – down), implying an evident mixing of $d\pi_m$ and π_{N^C} orbitals in the HOMO. From the potentials of the oxidation and reduction processes, corresponding excited state potentials can be deduced (*vide supra*).

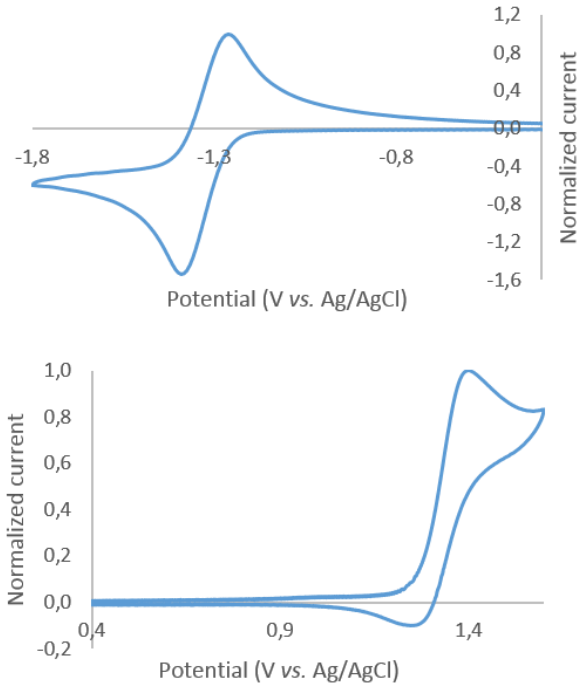

Figure 1.16 – Voltammograms of the $[Ir(N^C)_2(N^N)]^+$ photosensitizer (illustrated with 2-phenylpyridine as N^CH ligand and 2,2′-bipyridine as N^N ligand) measured by cyclic voltammetry in dry acetonitrile for reduction (*up*) and oxidation (*down*).

Such photophysical and electronic configurations offer the possibility of fine tuning of $[Ir(N^C)_2(N^N)]^+$ properties. Indeed, the

participation of a different ligand in each of the mixed state frontier orbitals *i.e.* N^C ligand for HOMO and N^N ligand for LUMO allows them to be independently tuned upon strategic ligand modification. This tuning is a master key to the success of bis-cyclometalated Ir(III) complexes in photocatalytic water splitting. Indeed, because bpy ligand is the site of the LUMO, addition of electron-donating groups destabilizes the LUMO while electron-withdrawing groups induce the opposite effect. On the ppy ligand, electron-donating substituents raise the π_{N^C} orbitals to destabilize the HOMO whereas electron-withdrawing groups stabilize the HOMO.[23, 39, 48] All substituents on the ppy moiety are also more effective when added to the phenyl side of the ligand, which is the main contributor of π orbitals to the HOMO.

1.3.2 Application of Ir(III) complexes in photocatalytic water reduction

1.3.2.1 Initial exploration

In 2005, the enhanced photophysical and electrochemical properties of $[Ir(N^C)_2(N^N)]^+$ photosensitizers lead Goldsmith and coworkers to begin exploring those complexes for photosensitization of sacrificial hydrogen evolution.[39] They employed a combinatorial approach to synthesize a library of 32 bis-cyclometalated Ir(III) complexes. Out of these, six complexes with N^C ligands as ppy or F-mppy (F-mppyH = 5-methyl-2-(4-fluorophenyl)pyridine) and N^N ligand as bpy, phen (phen = 1,10-phenanthroline) or dphphen (dphphen = 4,7-diphenyl-1,10-phenanthroline) having the longest excited state lifetimes and largest molar absorption coefficients were chosen for H_2 evolution studies. $[Co(bpy)_3]^{2+}$, previously known to

catalyze proton reduction, was used along with TEOA as sacrificial electron donor in an acetonitrile/water solution to form a three-component system with the Ir(III) photosensitizers following a precise oxidative quenching mechanism (Figure 1.17 – up).[49-50]

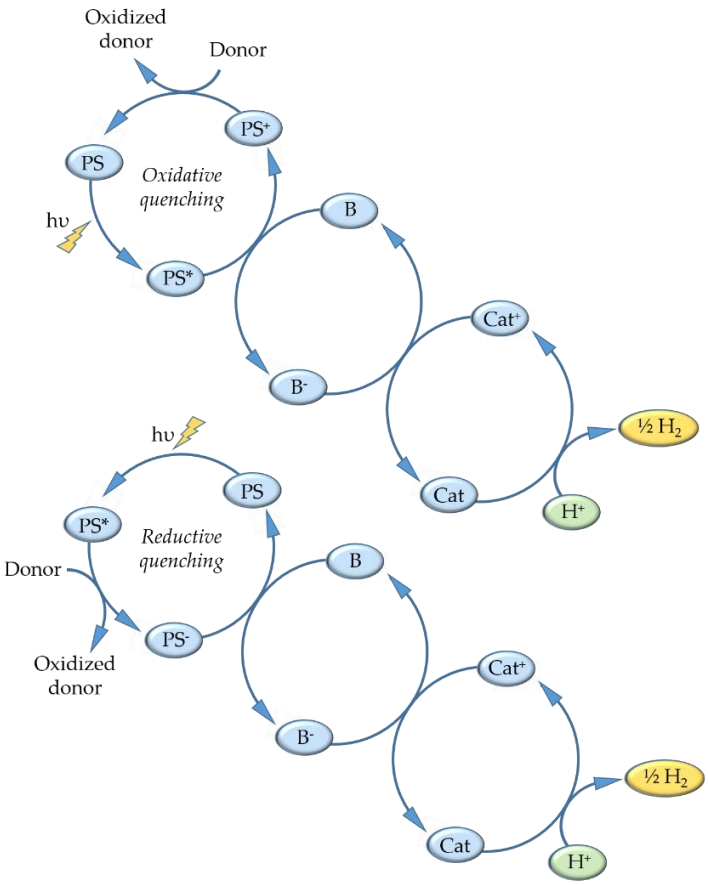

Figure 1.17 – Oxidative (*up*) and reductive (*down*) quenching mechanisms for the photoproduction of hydrogen using a photosensitizer (PS), an electron bridge (B) and a sacrificial electron donor

In this first system, the selected Ir(III) complexes appeared to outperform well-known Ru(II) chromophores with relative H_2 quantum yield above 20 times larger than $[Ru(bpy)_3]^{2+}$. This

improvement in performance stems from the highly negative excited state oxidation potentials of the Ir(III) photosensitizers. All the iridium-based photosensitizers lead to a similar photoproduction of hydrogen, even if F-mppy-containing complexes are slightly better performers than complexes bearing ppy ligands. Lowry and coworkers showed that a further addition of fluorine groups to the ppy core allowed even more dramatic improvement in performance.[23] Nevertheless, this trend to produce roughly the same amount of hydrogen was explained by the possible existence of some processes that limit one (or more) of the reaction steps that leads to hydrogen production (*vide supra*). Because TEOA is also able to reductively quench the excited Ir(III) photosensitizers, such three-component system might yield to a lower H_2 production. Nevertheless, quenching studies showed that the rate of reductive quenching by TEOA is more than one order of magnitude slower than the $[Co(bpy)_3]^{2+}$ oxidative quenching rate.

One approach to overcome the hydrogen production catalyst degradation is to use highly active proton reduction catalysts that can handle a two-electron oxidation state change. The catalysts offering this desired ability include precious metals such as colloidal platinum and palladium catalysts.[13, 51] Tinker and coworkers first reported the use of such catalysts coupled to an Ir(III) photosensitizer and TEOA as sacrificial reductant.[52] In this system, besides the observation previously made with $[Co(bpy)_3]^{2+}$ as hydrogen production catalyst, reductive quenching of the Ir(III) chromophore by TEOA (Figure 1.17 – down) is the dominant pathway for H_2 generation. Only modest turnover numbers were achieved *i.e.* 63 TON, but, more importantly, the robustness of the water reduction catalysts allowed the study of the photosensitizer degradation. Indeed, displacement of the N^N ligand

was evidenced, representing the major pathway for degradation in the presence of coordinating solvents such as acetonitrile.

To explore more deeply the structure-activity relationship for Ir(III) photosensitizers and, thus, address the photosensitizer degradation, Curtin and coworkers synthesized and studied a series of $[Ir(N^C)_2(N^N)]^+$ complexes in combination to a robust colloidal Pd catalyst.[53] It appeared that bulky substituents on all ligands (Figure 1.18) shielded the Iridium center from the solvent, preventing N^N ligand dissociation and increasing the activity. Furthermore, beyond steric effects, the electronic influence of the substituents also played a key role in the performance of the catalytic system towards the photoproduction rate of hydrogen. Indeed, photosensitizers with an electron-donating N^N ligand to raise the LUMO and electron-withdrawing N^C ligands to lower the HOMO display better turnover frequencies (TOF). Lifetime and molar absorptivity are not the only keys to efficient photosensitizer performance. Indeed, when both $[Ir(F\text{-}mppy)_2(N^N)]^+$ and $[Ir(MeO\text{-}mppy)_2(N^N)]^+$ families are compared, the latter displays a much shorter lifetime and much more negative redox potentials but higher molar absorptivity compared to the former leading to similar hydrogen photoproduction.

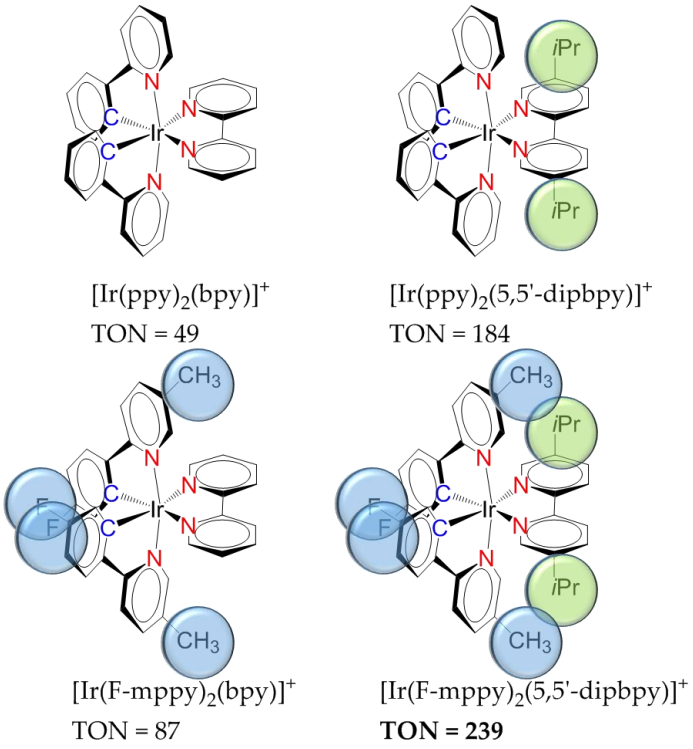

Figure 1.18 – Increase of the hydrogen photoproduction with bulky substituents on N^C and N^N ligands
(with 5,5′-dipbpy as 5,5′-diisopropyl-2,2′-bipyridine)

1.3.2.2 Systems with first row components

In order to be commercially available for solar fuel generation, cheap and earth-abundant materials must be used for the design of the photocatalysts. Hence, non-precious cobalt-, iron- and nickel-based catalysts were explored in early water reduction catalyst (WRC) systems, together with ruthenium-, rhenium-, or porphyrin-based photosensitizers.[54-59] These systems exhibited low activities. More robust Ir(III) photosensitizers drastically improve the performance of the hydrogen photoproduction with costless water reduction catalysts and are thus a promising area of research.

As mentioned previously, first investigation of Ir(III) chromophores were conducted with $[Co(bpy)_3]^{2+}$ reduction catalyst. Due to catalyst degradation, a library of ligands have been explored to improve the stability of the Cobalt catalyst. For instance, a Co(III) diimine-dioxime complex (Figure 1.19 – structure A) was used with common $[Ir(ppy)_2(bpy)]^+$ to achieve a 307 catalyst TON after 4 h of irradiation. This, for example, represents a huge improvement over the low TON (< 1) obtained with $[Ru(bpy)_3]^{2+}$ as photosensitizer.[60] This was further increased to ~700 TON by adding triphenylphosphine to the system which was used to stabilize the Co(I) intermediate, which in turn acts as the active species. Other ligands such as quaterpyridine were investigated with Co(II) (Figure 1.19 – structure B), with $[Ir(dF(CF_3)ppy)_2(dtbbpy)]^+$ (dF(CF_3)ppyH = bis[3,5-difluoro-2-(5-trifluoromethyl)-2-pyridinyl]benzene ; dtbbpy = 4,4'-bis(*tert*-butyl)-2,2'-bipyridine) as photosensitizer and two proton sources, *i.e.* an anilinium salt and water, displaying TON of 1013 and 890 photosensitizer turnovers, respectively.[61] Similarly to the observations made by Curtin and coworkers (Figure 1.18),[53] steric ligands as well as HOMO stabilization again appear to be critical in the Ir(III) photosensitizer because pairing the Co(II) quaterpyridine complex with common $[Ir(ppy)_2(bpy)]^+$ as chromophore gives only 530 photosensitizer TON. On the Co(II) catalyst, the stabilizing effect of the tetradentate ligand on the redox state of the metal plays a key role in proton reduction. As the obtained results outperform the hydrogen production of the system using $[Co(bpy)_3]^{2+}$, new cobalt catalysts are still developed nowadays like Co(II) complexes containing pentadentate ligands (Figure 1.19 – structure C) which achieved 690 catalyst TON together with $[Ir(ppy)_2(bpy)]^+$.[62]

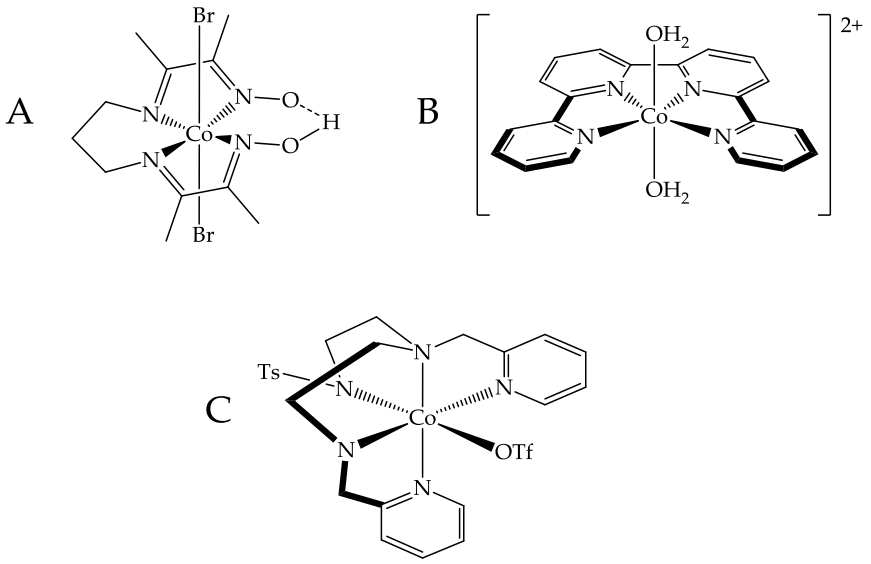

Figure 1.19 – Selected Cobalt-based WRCs used with Iridium photosensitizers

Iron-based catalysts have also shown promising results as water reduction catalysts when coupled with Ir(III) photosensitizer. For example, visible light irradiation of iron mononuclear and oligomeric carbonyl complexes with $[Ir(ppy)_2(bpy)]^+$ afforded ~400 catalyst TON which was an outstanding performance for iron as water reduction catalyst.[63] As mechanistic studies revealed the presence of $Fe(CO)_5$ as the active species, other researchers used triiron clusters $[Fe_3(CO)_{12}]$ in the presence of a phosphine to stabilize the catalyst (Figure 1.20 – structure A), raising catalyst turnovers to ~1500.[64] Biomimetic diiron-dithiolate complex $[Fe_2S_2]$ (Figure 1.20 – structure B) also achieved a significant performance in the presence of $[Ir(ppy)_2(bpy)]^+$, with 466 catalysts TON.[65] As the quantum yield was low, Yu and coworkers designed four hydrogenase mimics with the $[Fe_2S_2]$ core surrounded by well-defined dendrimers for encapsulation and stabilization of the catalyst as well as the regulation of the electron-

transfer process.[22] Tremendous catalytic activity was observed for the four catalysts, until 22200 catalyst TON for the catalyst with the most widespread dendrimer skeleton (Figure 1.20 – structure C).

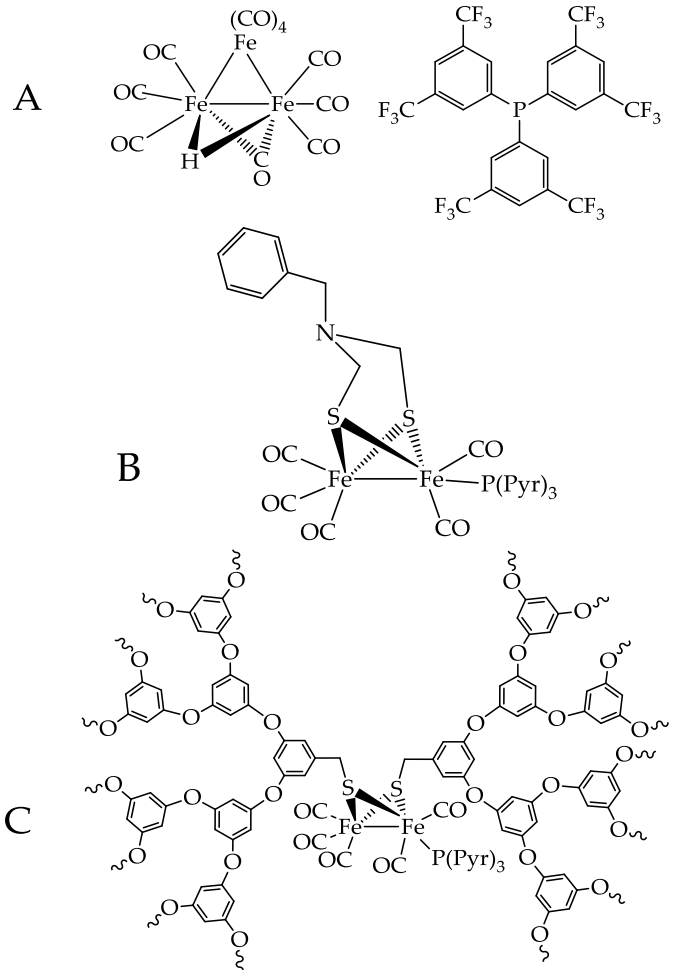

Figure 1.20 – Selected Iron-based WRCs used with Iridium photosensitizers

In addition to iron and cobalt, nickel water reduction catalysts have been successfully tested with Ir(III) chromophores. A nickel-thiolate hexameric cluster (Figure 1.21 – structure A) was used to form an impressive hydrogen production system producing 3750 TON per

Ni_6 cluster while up to 30000 TON per Ni_6 cluster could be obtained at low catalyst concentration.[66] Other kinds of catalysts such as tetranickel cluster [Ni_4O_{14}] coupled with polyoxotungstate demonstrated, on the other hand, a long-lived catalyst, generating hydrogen for a period of seven days in the presence of $[Ir(ppy)_2(bpy)]^+$ with a TON reaching ~6500.[67] Other Ni(II) complexes bearing tetradentate macrocyclic N^N^N^N, N^N^N^S and N^N^N^P ligands turned out to be highly promising water reduction catalysts. Studies of these catalysts revealed that the nature of the ligand proves critical and the phosphorus-containing complex (Figure 1.21 – structure B) gives the best performance with ~5000 catalyst TON.[68] Nevertheless, these complexes may not be truly homogeneous as mercury poisoning studies revealed the presence of *in situ* generated Ni nanoparticles.

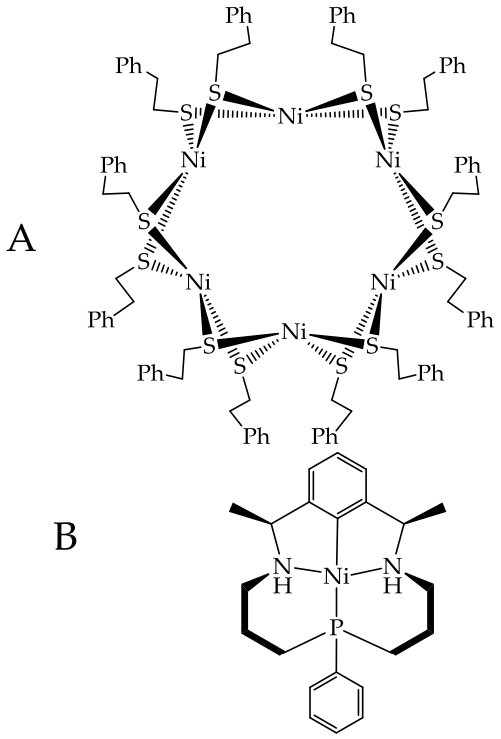

Figure 1.21 – Selected Nickel-based WRCs used with Iridium photosensitizers

1.3.2.3 Strategies for improved photosensitizers efficiency

Despite its great potential in the establishment of multicomponent supramolecular systems, $[Ir(ppy)_2(bpy)]^+$ suffers from major drawbacks that limit its use as photosensitizer with WRCs:

- dissociation of the bpy ligand (or displacement by the solvent) due to accumulation of the electron density on the antibonding orbital of the bpy ligand when the electron transfer to the proton reduction catalyst is not sufficiently rapid or efficient;
- short excited state lifetime and absorption coefficients in the visible region;
- low solubility in aqueous media.

To address these disadvantages, efforts have been mainly focused on the alteration of the ligand structure of the common architecture $[Ir(N^C)_2(N^N)]^+$. Modification of both N^C and N^N ligands has been explored with some of the new N^N ligands being specifically designed to trigger an intramolecular electron transfer *i.e.* synthesize novel monocomponent systems.

1.3.2.3.1 New N^CH ligands

- ***Phenylazole derivatives***

Phenylazole derivatives have gained interest as alternatives to ppy ligands because of the presence of intraligand electron-rich heteroatoms raising the HOMO *i.e.* allowing a red-shift in absorbance and increasing the LC character of emission yielding to a longer excited

state lifetime. Gärtner and coworkers synthesized and evaluated the photocatalytic behavior of a family of Ir(III) complexes bearing phenylazole as cyclometalated ligands (Figure 1.22).[68] They generally display longer excited state lifetime and higher photoluminescence quantum yields than standard $[Ir(ppy)_2(bpy)]^+$. All the investigated complexes turned out to be efficient water reduction photosensitizers when used with the iron-based reduction catalyst [Fe-S] (Figure 1.20 – structure A). Although a direct correlation between the photophysics and the performance as a photosensitizer cannot be easily established, the longer lifetime might induce a slightly better performance of the most active phenylazole complex (Figure 1.22 – framed structure) *i.e.* 1614 TON as compared to $[Ir(ppy)_2(bpy)]^+$ under similar conditions.

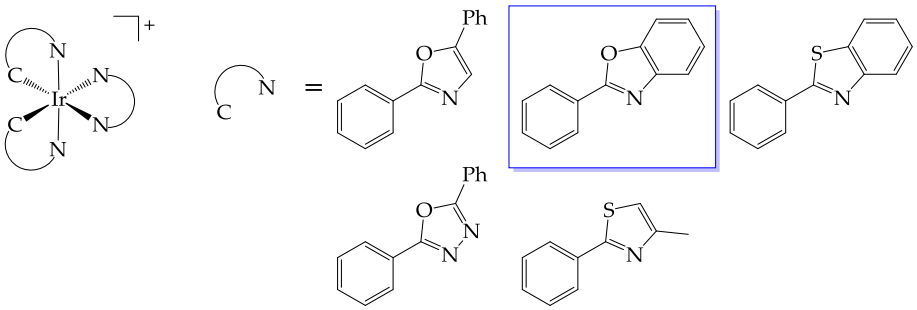

Figure 1.22 – Phenylazole-based Ir(III) photosensitizers used for photocatalytic water reduction (with bpy as N^N ligand)[68]

In further works performed by Yuan and coworkers using 2-phenylbenzothiazole (bt) derivative ligands,[69] a family of compounds was obtained by adding a trifluoromethyl group on various positions (Figure 1.23) to increase steric hindrance, in turn leading to decreased self-quenching (*vide supra*).[70] Such derivatives with 2-phenylbenzothiazole as cyclometalated ligands display similar features than those with phenylazole ones *i.e.* enhanced photochemical

stability and redshifted absorption spectra. Surprisingly, the position of the CF_3- group on the phenyl moiety and even its removal do not alter dramatically the energy of the HOMO or the absorbance of the complexes. When tethered on the thiazole moiety, the emission bands are redshifted and more structured, probably resulting from an increased contribution of a N^C intraligand charge transfer from the phenyl ring to the electron-poor benzothiazole ring. This hypothesis was supported by the addition of an amine functional group on the phenyl ring enhancing the disparity between the two rings. As a result, the latter complex has an intense red absorption band and is almost non-emissive under air. In water reduction reaction with colloidal Platinum, both complexes displaying mainly intraligand charge transfer are poor photosensitizers. Other Ir(III) complexes with a CF_3- group on the benzothiazole moiety showed significantly higher performances for proton reduction, the most active complex yielding ~1500 TON (Figure 1.23 – framed structure).

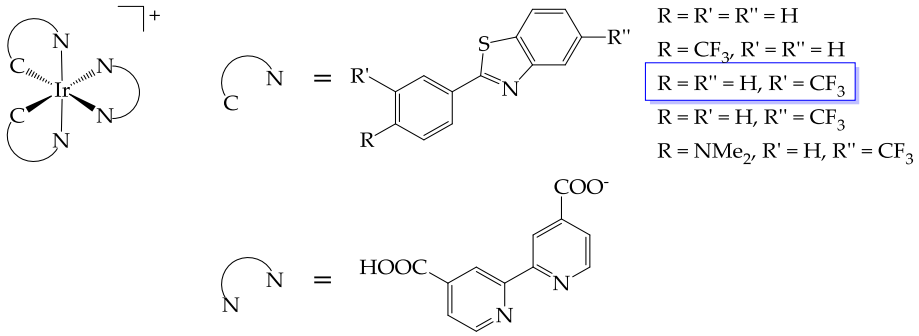

Figure 1.23 – 2-phenylbenzothiazole-based Ir(III) photosensitizers used for photocatalytic water reduction[69]

- ***Coumarin derivatives***

In order to increase visible light absorption, dye-based ligands have also been used to replace simple ppy ligands. Takizawa and

coworkers explored this approach by substituting the phenyl moiety of a benzothiazole ligand by a coumarin fragment (Figure 1.24).[71] This substitution led to a dramatic enhancement in the absorption spectrum, with all the complexes displaying intense bands in the visible region with an unprecedented extinction coefficient of 1.29 x10^5 $M^{-1}.cm^{-1}$ at 483 nm for the complex bearing a bpy as diimine ligand. All the emissive coumarin-based compounds display a pure ^{3}LC emitting state rather than the typical mixture of ^{3}LC and ^{3}MLCT, affording longer excited states lifetimes compared to reference $[Ir(ppy)_2(bpy)]^+$. Using an acetonitrile/water mixture as solvent, $[Co(bpy)_3]^{3+}$ as WRC and triethylamine (NEt_3) as sacrificial electron donor, the coumarin-based complexes yield TON of 1500, to be compared to a TON of 315 for $[Ir(ppy)_2(bpy)]^+$ or 1 for $[Ru(bpy)_3]^{2+}$ under similar conditions.

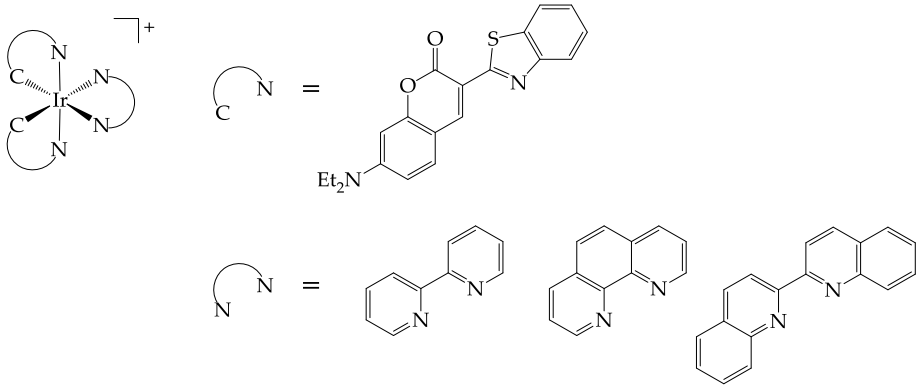

Figure 1.24 – Coumarin-based Ir(III) photosensitizers used for photocatalytic water reduction[71]

1.3.2.3.2 Towards new N^N ligands

Some efforts to modify the bpy ligand have also been reported by Gärtner and coworkers by either adding substituents at the 6 or the 6 and 6′ positions (Figure 1.25 – group A), or varying the 1,4-bis-imine

structures by the addition of heteroatoms (Figure 1.25 – group B).[72] The resulting effects are dramatic when the complexes are used as photosensitizers together with the previously described [Fe-S] cluster (Figure 1.20 – structure A) and NEt_3. Indeed, only complexes bearing bpy-based ligands yield reasonable amounts of H_2. Such disparity in performance stands in photophysical and electrochemical properties. Only bpy-based complexes display strong emissive excited states that can be quenched by the sacrificial electron donor following a reductive quenching mechanism (Figure 1.17).

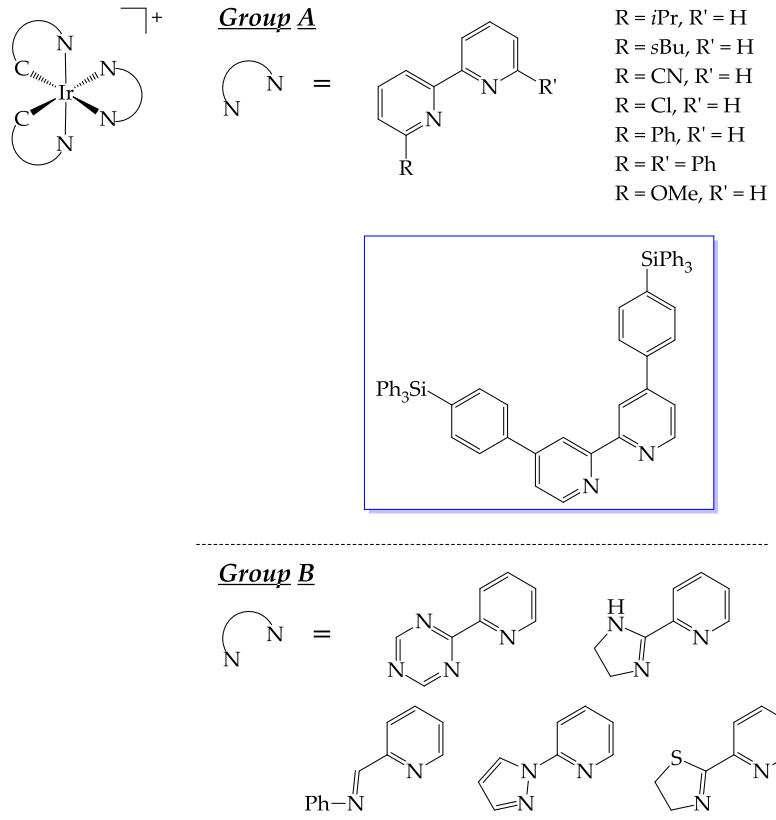

Figure 1.25 – bpy derivatives (*group* A) and novel 1,4-bis-imine-based (*group* B) Ir(III) photosensitizers used for photocatalytic water reduction (with ppyH as N^CH ligand)[21, 72]

Amongst the bpy-based photosensitizers, $[Ir(ppy)_2(6\text{-}iPr\text{-}bpy)]^+$ (6-iPr-bpy = 6-isopropyl-2,2'-bipyridine) yields a TON of 1840 and is one of the few new photosensitizers to overcome the hydrogen generation of standard $[Ir(ppy)_2(bpy)]^+$ (1590 TON). Further improvement in experimental conditions allowed the combination of the former complex with the [Fe-S] cluster to achieve 2770 TON. This performance is at least partially due to the steric bulk of the isopropyl group on the bpy ligand preventing solvent molecules access to the ligand and, hence, degradation of the complex through bpy dissociation. Whang and coworkers explored this steric effect by anchoring large triphenylsilyl groups to a diphenyl-bpy ligand (Figure 1.25 – framed structure) and found out a remarkable improvement in stability.[21] The new photosensitizer achieved up to 17000 TON with a Platinum catalyst over a period of 144 h whereas reference complex $[Ir(ppy)_2(bpy)]^+$ only reached 530 TON after 24 h under similar conditions.

1.4 Objectives

This Ph.D. thesis is aimed to develop new ways for reliable systems in the field of sustainable chemistry using Ir(III) complexes as photosensitizers. The results presented in each of the next four chapters have been published in at least one publication in peer reviewed journals or are currently being submitted.

The first part (Chapter 2) is dedicated to the synthesis and the full photophysical study of Ir(III) complexes with varying N/C ratio of the first coordination sphere (Figure 1.26). Indeed, despite the numerous studies of Ir(III) complexes as photosensitizers, no clear comparative study of the role of the first coordination sphere on the photoinduced properties has been performed. In order to determine their behavior in the presence of redox systems, all these complexes will be studied upon addition of hydroquinone (H_2Q) and benzoquinone (BQ).

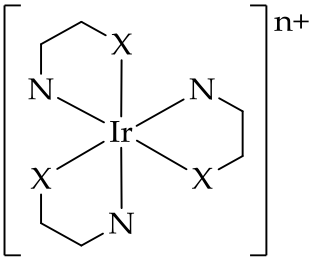

$[IrN_{3+n}C_{3-n}]$ (n = 0, 1, 2, 3)
X = N or C

Figure 1.26 – General structure of the investigated Ir(III) complexes with varying N/C ratio

As these studies lead to the design of a novel Ir(III) complex, namely $[Ir(N,N'\text{-bpy})_2(N,C^3\text{-bpy})]^{2+}$, Chapter 3 is aimed at the

unambiguous determination of the nature of its excited state. To reach that goal, photo-CIDNP ^{1}HNMR spectroscopy will be used as an efficient tool for the study of its behavior upon irradiation in the presence of a well-known redox system such as 2'-deoxyguanosine-5′-monophosphate (dGMP) upon variation of pH.

Finally, solar energy conversion of light to usable forms of energy is the ideal alternative to fossil fuels. However, one of the main disadvantages of such systems is the efficient storage of the energy produced. As a result, new solar energy conversion systems that can convert light into chemical energy may improve the energy storage efficiency. The most promising approach towards this goal is the conversion of solar energy into storable fuels such as molecular hydrogen. In that purpose, several new covalent photoactive dyads including Ir(III) photosensitizers and a cobaloxime catalyst combined by a terpyridine ligand, *i.e.* 2,2′;4′,4′′-terpyridine (2244tpy) and 2,2′;5′,4′′-terpyridine (2254tpy) are reported in Chapter 4 (Figure 1.27). All these compounds as well as the corresponding Ir(III) photosensitizers are synthesized and studied, and are shown to efficiently produce dihydrogen under visible light irradiation.

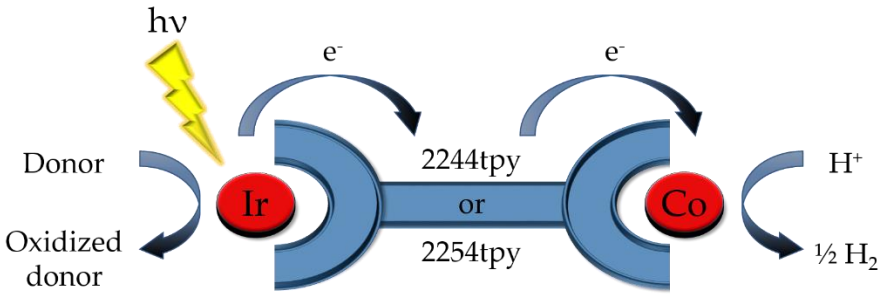

Figure 1.27 – Structure of the [Ir-Co] dyads for H_2 photoproduction

Although our laboratory is interested in hydrogen photoproduction, high stability of Ir(III) complexes towards harsh thermal, photochemical and chemical conditions make them relevant candidates for various other applications. For example, despite Palladium(II) catalysis being one of the most utilized catalysis in the industry, the regeneration of the catalyst still remains a challenge as it is highly atom expensive. The evolution of selective reoxidation routes from Pd(0) to Pd(II) is one of the ultimate goals of present-day chemical research. Chapter 5 presents a preliminary study of a novel multicomponent system for photoinduced Palladium(II) regeneration from Iridium(III) photosensitizers, in particular for the Pd-catalyzed Wacker oxidation and acetoxylation of terminal olefins (Figure 1.28).

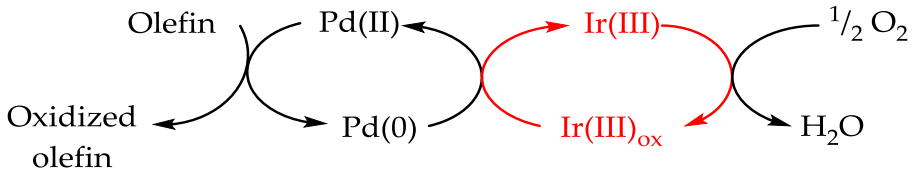

Figure 1.28 – Use of a photoactivatable Ir(III) complex in Pd(0) reoxidation

1.5 References

1. Schulz, M.; Karnahl, M.; Schwalbe, M.; Vos, J. G., The role of the bridging ligand in photocatalytic supramolecular assemblies for the reduction of protons and carbon dioxide. *Coord. Chem. Rev.* **2012**, *256*, 1682-1705.
2. Armaroli, N.; Balzani, V., The future of energy supply: Challenges and opportunities. *Angew. Chem. Int. Ed.* **2007**, *46*, 52-66.
3. Fujishima, A.; Honda, K., Electrochemical Photolysis of Water at a Semiconductor Electrode. *Nature* **1972**, *238*, 37-38.
4. Osterloh, F. E., Inorganic Materials as Catalysts for Photochemical Splitting of Water. *Chem. Mater.* **2008**, *20*, 35-54.
5. Brancho, J. J.; Bartlett, B. M., Challenges in Co-Alloyed Titanium Oxynitrides, a Promising Class of Photochemically Active Materials. *Chem. Mater.* **2015**, *27*, 7207-7217.
6. Ran, J.; Zhang, J.; Yu, J.; Jaroniec, M.; Qiao, S. Z., Earth-abundant cocatalysts for semiconductor-based photocatalytic water splitting. *Chem. Soc. Rev.* **2014**, *43*, 7787-7812.
7. Fushimi, K.; Lill, K. A.; Habazaki, H., Heterogeneous hydrogen evolution on corroding Fe–3at.% Si surface observed by scanning electrochemical microscopy. *Electrochim. Acta* **2007**, *52*, 4246-4253.
8. Natali, M.; Argazzi, R.; Chiorboli, C.; Iengo, E.; Scandola, F., Photocatalytic hydrogen evolution with a self-assembling reductant-sensitizer-catalyst system. *Chem. Eur. J.* **2013**, *19*, 9261-9271.
9. Fihri, A.; Artero, V.; Pereira, A.; Fontecave, M., Efficient H2-producing photocatalytic systems based on cyclometalated iridium- and tricarbonylrhenium-diimine photosensitizers and cobaloxime catalysts. *Dalton Trans.* **2008**, 5567-5569.
10. Ozawa, H.; Yokoyama, Y.; Haga, M. A.; Sakai, K., Syntheses, characterization, and photo-hydrogen-evolving properties of tris(2,2'-bipyridine)ruthenium(II) derivatives tethered to a cis-Pt(II)Cl2 unit: insights into the structure-activity relationship. *Dalton Trans.* **2007**, 1197-1206.
11. Rau, S.; Schafer, B.; Gleich, D.; Anders, E.; Rudolph, M.; Friedrich, M.; Gorls, H.; Henry, W.; Vos, J. G., A supramolecular photocatalyst for the production of hydrogen and the selective hydrogenation of tolane. *Angew. Chem. Int. Ed.* **2006**, *45*, 6215-6218.
12. Artero, V.; Chavarot-Kerlidou, M.; Fontecave, M., Splitting water with cobalt. *Angew. Chem. Int. Ed.* **2011**, *50*, 7238-7266.
13. Sakai, K.; Ozawa, H., Homogeneous catalysis of platinum(II) complexes in photochemical hydrogen production from water. *Coord. Chem. Rev.* **2007**, *251*, 2753-2766.

14. Zarkadoulas, A.; Koutsouri, E.; Kefalidi, C.; Mitsopoulou, C. A., Rhenium complexes in homogeneous hydrogen evolution. *Coord. Chem. Rev.* **2015**, *304-305*, 55-72.
15. Lazarides, T.; McCormick, T.; Du, P.; Luo, G.; Lindley, B.; Eisenberg, R., Making hydrogen from water using a homogeneous system without noble metals. *J. Am. Chem. Soc.* **2009**, *131*, 9192-9194.
16. Esswein, A. J.; Nocera, D. G., Hydrogen production by molecular photocatalysis. *Chem. Rev.* **2007**, *107*, 4022-4047.
17. Rousset, E.; Chartrand, D.; Ciofini, I.; Marvaud, V.; Hanan, G. S., Red-light-driven photocatalytic hydrogen evolution using a ruthenium quaterpyridine complex. *Chem. Commun.* **2015**, *51*, 9261-9264.
18. Jacques, A.; Schott, O.; Robeyns, K.; Hanan, G. S.; Elias, B., Hydrogen Photoevolution from a Green-Absorbing Iridium(III)-Cobalt(III) Dyad. *Eur. J. Inorg. Chem.* **2016**, *2016*, 1779-1783.
19. Ozawa, H.; Haga, M. A.; Sakai, K., A photo-hydrogen-evolving molecular device driving visible-light-induced EDTA-reduction of water into molecular hydrogen. *J. Am. Chem. Soc.* **2006**, *128*, 4926-4927.
20. Arachchige, S. M.; Brown, J. R.; Chang, E.; Jain, A.; Zigler, D. F.; Rangan, K.; Brewer, K. J., Design considerations for a system for photocatalytic hydrogen production from water employing mixed-metal photochemical molecular devices for photoinitiated electron collection. *Inorg. Chem.* **2009**, *48*, 1989-2000.
21. Whang, D. R.; Sakai, K.; Park, S. Y., Highly efficient photocatalytic water reduction with robust iridium(III) photosensitizers containing arylsilyl substituents. *Angew. Chem. Int. Ed.* **2013**, *52*, 11612-11615.
22. Yu, T.; Zeng, Y.; Chen, J.; Li, Y. Y.; Yang, G.; Li, Y., Exceptional dendrimer-based mimics of diiron hydrogenase for the photochemical production of hydrogen. *Angew. Chem. Int. Ed.* **2013**, *52*, 5631-5635.
23. Lowry, M. S.; Goldsmith, J. I.; Slinker, J. D.; Rohl, R.; Pascal, R. A., Jr.; Malliaras, G. G.; Bernhard, S., Single-Layer Electroluminescent Devices and Photoinduced Hydrogen Production from an Ionic Iridium(III) Complex. *Chem. Mater.* **2005**, *17*, 5712-5719.
24. Kobayashi, M.; Masaoka, S.; Sakai, K., Photoinduced hydrogen evolution from water by a simple platinum(II) terpyridine derivative: a Z-scheme photosynthesis. *Angew. Chem. Int. Ed.* **2012**, *51*, 7431-7434.
25. Pfeffer, M. G.; Kowacs, T.; Wachtler, M.; Guthmuller, J.; Dietzek, B.; Vos, J. G.; Rau, S., Optimization of hydrogen-evolving photochemical molecular devices. *Angew. Chem. Int. Ed.* **2015**, *54*, 6627-6631.
26. Tschierlei, S.; Presselt, M.; Kuhnt, C.; Yartsev, A.; Pascher, T.; Sundstrom, V.; Karnahl, M.; Schwalbe, M.; Schafer, B.; Rau, S.; Schmitt, M.; Dietzek, B.; Popp, J., Photophysics of an intramolecular hydrogen-evolving Ru-Pd photocatalyst. *Chem. Eur. J.* **2009**, *15*, 7678-7688.

27. Helbling, E. W. Z., H., *UV Effects in Aquatic Organisms and Ecosystems*. Royal Society of Chemistry: **2007**.
28. Valeur, B.; Berberan-Santos, M. N., *Molecular Fluorescence: Principles and Applications*. 2nd ed.; Wiley-VCH: **2012**.
29. Kasha, M., Characterization of electronic transitions in complex molecules. *Discuss. Faraday Soc.* **1950**, *9*, 14-19.
30. Brouwer, A. M., Standards for photoluminescence quantum yield measurements in solution (IUPAC Technical Report). *Pure Appl. Chem.* **2011**, *83*.
31. Rutherford, A. W.; Boussac, A., Biochemistry. Water photolysis in biology. *Science* **2004**, *303*, 1782-1784.
32. Rabinowitch, E. I., *Photosynthesis and related processes*. Interscience Publishers, inc.: New York, N.Y., **1945**.
33. Rehm, D.; Weller, A., Kinetik und Mechanismus der Elektronübertragung bei der Fluoreszenzlöschung in Acetonitril. *Ber. Bunsenges Phys. Chem.* **1969**, *73*, 834-839.
34. Flamigni, L.; Barbieri, A.; Sabatini, C.; Ventura, B.; Barigelletti, F., Photochemistry and Photophysics of Coordination Compounds: Iridium. *Top. Curr. Chem.* **2007**, *281*, 143-203.
35. Kirch, M.; Lehn, J.-M.; Sauvage, J.-P., Hydrogen Generation by Visible Light Irradiation of Aqueous Solutions of Metal Complexes. An approach to the photochemical conversion and storage of solar energy. *Helv. Chim. Acta* **1979**, *62*, 1345-1384.
36. Tsuboyama, A.; Iwawaki, H.; Furugori, M.; Mukaide, T.; Kamatani, J.; Igawa, S.; Moriyama, T.; Miura, S.; Takiguchi, T.; Okada, S.; Hoshino, M.; Ueno, K., Homoleptic cyclometalated iridium complexes with highly efficient red phosphorescence and application to organic light-emitting diode. *J. Am. Chem. Soc.* **2003**, *125*, 12971-12979.
37. Baldo, M. A.; Lamansky, S.; Burrows, P. E.; Thompson, M. E.; Forrest, S. R., Very high-efficiency green organic light-emitting devices based on electrophosphorescence. *Appl. Phys. Lett.* **1999**, *75*, 4-6.
38. Adachi, C.; Baldo, M. A.; Thompson, M. E.; Forrest, S. R., Nearly 100% internal phosphorescence efficiency in an organic light-emitting device. *J. Appl. Phys.* **2001**, *90*, 5048-5051.
39. Goldsmith, J. I.; Hudson, W. R.; Lowry, M. S.; Anderson, T. H.; Bernhard, S., Discovery and High-Throughput Screening of Heteroleptic Iridium Complexes for Photoinduced Hydrogen Production. *J. Am. Chem. Soc.* **2005**, *127*, 7502-7510.
40. Cline, E. D.; Adamson, S. E.; Bernhard, S., Homogeneous catalytic system for photoinduced hydrogen production utilizing iridium and rhodium complexes. *Inorg. Chem.* **2008**, *47*, 10378-10388.

41. Ohsawa, Y.; Sprouse, S.; King, K. A.; DeArmond, M. K.; Hanck, K. W.; Watts, R. J., Electrochemistry and spectroscopy of ortho-metalated complexes of iridium(III) and rhodium(III). *J. Phys. Chem.* **1987**, *91*, 1047-1054.
42. Ichimura, K.; Kobayashi, T.; King, K. A.; Watts, R. J., Excited-state absorption spectroscopy of ortho-metalated iridium(III) complexes. *J. Phys. Chem.* **1987**, *91*, 6104-6106.
43. Garces, F. O.; King, K. A.; Watts, R. J., Synthesis, structure, electrochemistry, and photophysics of methyl-substituted phenylpyridine ortho-metalated iridium(III) complexes. *Inorg. Chem.* **1988**, *27*, 3464-3471.
44. Colombo, M. G.; Hauser, A.; Guedel, H. U., Evidence for strong mixing between the LC and MLCT excited states in bis(2-phenylpyridinato-C2,N')(2,2'-bipyridine)iridium(III). *Inorg. Chem.* **1993**, *32*, 3088-3092.
45. Bolink, H. J.; Cappelli, L.; Cheylan, S.; Coronado, E.; Costa, R. D.; Lardiés, N.; Nazeeruddin, M. K.; Ortí, E., Origin of the large spectral shift in electroluminescence in a blue light emitting cationic iridium(iii) complex. *J. Mater. Chem.* **2007**, *17*, 5032-5041.
46. De Angelis, F.; Fantacci, S.; Evans, N.; Klein, C.; Zakeeruddin, S. M.; Moser, J. E.; Kalyanasundaram, K.; Bolink, H. J.; Gratzel, M.; Nazeeruddin, M. K., Controlling phosphorescence color and quantum yields in cationic iridium complexes: a combined experimental and theoretical study. *Inorg. Chem.* **2007**, *46*, 5989-6001.
47. Lowry, M. S.; Bernhard, S., Synthetically tailored excited states: phosphorescent, cyclometalated iridium(III) complexes and their applications. *Chem. Eur. J.* **2006**, *12*, 7970-7977.
48. Tamayo, A. B.; Garon, S.; Sajoto, T.; Djurovich, P. I.; Tsyba, I. M.; Bau, R.; Thompson, M. E., Cationic bis-cyclometalated iridium(III) diimine complexes and their use in efficient blue, green, and red electroluminescent devices. *Inorg. Chem.* **2005**, *44*, 8723-8732.
49. Ziessel, R.; Hawecker, J.; Lehn, J.-M., Photogeneration of Carbon Monoxide and of Hydrogen via Simultaneous Photochemical Reduction of Carbon Dioxide and Water by Visible-Light Irradiation of Organic Solutions Containing Tris(2,2'-bipyridine)ruthenium(II) and Cobalt(II) Species as Homogeneous Catalysts. *Helv. Chim. Acta* **1986**, *69*, 1065-1084.
50. Chan, S. F.; Chou, M.; Creutz, C.; Matsubara, T.; Sutin, N., Mechanism of the formation of dihydrogen from the photoinduced reactions of poly(pyridine)ruthenium(II) and poly(pyridine)rhodium(III) complexes. *J. Am. Chem. Soc.* **1981**, *103*, 369-379.
51. Amouyal, E.; Koffi, P., Photochemical production of hydrogen from water. *Journal of Photochemistry* **1985**, *29*, 227-242.

52. Tinker, L. L.; McDaniel, N. D.; Curtin, P. N.; Smith, C. K.; Ireland, M. J.; Bernhard, S., Visible light induced catalytic water reduction without an electron relay. *Chem. Eur. J.* **2007**, *13*, 8726-8732.
53. Curtin, P. N.; Tinker, L. L.; Burgess, C. M.; Cline, E. D.; Bernhard, S., Structure−Activity Correlations Among Iridium(III) Photosensitizers in a Robust Water-Reducing System. *Inorg. Chem.* **2009**, *48*, 10498-10506.
54. Creutz, C.; Sutin, N., Photogeneration and reactions of cobalt(I) complexes. *Coord. Chem. Rev.* **1985**, *64*, 321-341.
55. Sun, L.; Akermark, B.; Ott, S., Iron hydrogenase active site mimics in supramolecular systems aiming for light-driven hydrogen production. *Coord. Chem. Rev.* **2005**, *249*, 1653-1663.
56. Lomoth, R.; Ott, S., Introducing a dark reaction to photochemistry: photocatalytic hydrogen from [FeFe] hydrogenase active site model complexes. *Dalton Trans.* **2009**, 9952-9959.
57. Zhang, P.; Wang, M.; Li, C.; Li, X.; Dong, J.; Sun, L., Photochemical H2 with noble-metal-free molecular devices comprising a porphyrin photosensitizer and a cobaloxime catalyst. *Chem. Commun.* **2010**, *46*, 8806-8808.
58. Probst, B.; Rodenberg, A.; Guttentag, M.; Hamm, P.; Alberto, R., A highly stable rhenium-cobalt system for photocatalytic H2 production: unraveling the performance-limiting steps. *Inorg. Chem.* **2010**, *49*, 6453-6460.
59. McLaughlin, M. P.; McCormick, T. M.; Eisenberg, R.; Holland, P. L., A stable molecular nickel catalyst for the homogeneous photogeneration of hydrogen in aqueous solution. *Chem. Commun.* **2011**, *47*, 7989-7991.
60. Zhang, P.; Jacques, P. A.; Chavarot-Kerlidou, M.; Wang, M.; Sun, L.; Fontecave, M.; Artero, V., Phosphine coordination to a cobalt diimine-dioxime catalyst increases stability during light-driven H2 production. *Inorg. Chem.* **2012**, *51*, 2115-2120.
61. Leung, C.-F.; Ng, S.-M.; Ko, C.-C.; Man, W.-L.; Wu, J.; Chen, L.; Lau, T.-C., A cobalt(II) quaterpyridine complex as a visible light-driven catalyst for both water oxidation and reduction. *Energy Environ. Sci* **2012**, *5*, 7903-7907.
62. Call, A.; Codola, Z.; Acuna-Pares, F.; Lloret-Fillol, J., Photo- and electrocatalytic H2 production by new first-row transition-metal complexes based on an aminopyridine pentadentate ligand. *Chem. Eur. J.* **2014**, *20*, 6171-6183.
63. Gartner, F.; Sundararaju, B.; Surkus, A. E.; Boddien, A.; Loges, B.; Junge, H.; Dixneuf, P. H.; Beller, M., Light-driven hydrogen generation: efficient iron-based water reduction catalysts. *Angew. Chem. Int. Ed.* **2009**, *48*, 9962-9965.
64. Gartner, F.; Boddien, A.; Barsch, E.; Fumino, K.; Losse, S.; Junge, H.; Hollmann, D.; Bruckner, A.; Ludwig, R.; Beller, M., Photocatalytic hydrogen

generation from water with iron carbonyl phosphine complexes: improved water reduction catalysts and mechanistic insights. *Chem. Eur. J.* **2011**, *17*, 6425-6436.
65. Zhang, P.; Wang, M.; Na, Y.; Li, X.; Jiang, Y.; Sun, L., Homogeneous photocatalytic production of hydrogen from water by a bioinspired [Fe(2)S(2)] catalyst with high turnover numbers. *Dalton Trans.* **2010**, *39*, 1204-1206.
66. Kagalwala, H. N.; Gottlieb, E.; Li, G.; Li, T.; Jin, R.; Bernhard, S., Photocatalytic hydrogen generation system using a nickel-thiolate hexameric cluster. *Inorg. Chem.* **2013**, *52*, 9094-9101.
67. Lv, H.; Guo, W.; Wu, K.; Chen, Z.; Bacsa, J.; Musaev, D. G.; Geletii, Y. V.; Lauinger, S. M.; Lian, T.; Hill, C. L., A noble-metal-free, tetra-nickel polyoxotungstate catalyst for efficient photocatalytic hydrogen evolution. *J. Am. Chem. Soc.* **2014**, *136*, 14015-14018.
68. Gartner, F.; Denurra, S.; Losse, S.; Neubauer, A.; Boddien, A.; Gopinathan, A.; Spannenberg, A.; Junge, H.; Lochbrunner, S.; Blug, M.; Hoch, S.; Busse, J.; Gladiali, S.; Beller, M., Synthesis and characterization of new iridium photosensitizers for catalytic hydrogen generation from water. *Chem. Eur. J.* **2012**, *18*, 3220-3225.
69. Yuan, Y. J.; Zhang, J. Y.; Yu, Z. T.; Feng, J. Y.; Luo, W. J.; Ye, J. H.; Zou, Z. G., Impact of ligand modification on hydrogen photogeneration and light-harvesting applications using cyclometalated iridium complexes. *Inorg. Chem.* **2012**, *51*, 4123-4133.
70. Ho, C.-L.; Wong, W.-Y.; Yao, B.; Xie, Z.; Wang, L.; Lin, Z., Synthesis, characterization, photophysics and electrophosphorescent applications of phosphorescent platinum cyclometalated complexes with 9-arylcarbazole moieties. *J. Organomet. Chem.* **2009**, *694*, 2735-2749.
71. Takizawa, S.-y.; Pérez-Bolívar, C.; Anzenbacher, P.; Murata, S., Cationic Iridium Complexes Coordinated with Coumarin Dyes - Sensitizers for Visible-Light-Driven Hydrogen Generation. *Eur. J. Inorg. Chem.* **2012**, *2012*, 3975-3979.
72. Gärtner, F.; Cozzula, D.; Losse, S.; Boddien, A.; Anilkumar, G.; Junge, H.; Schulz, T.; Marquet, N.; Spannenberg, A.; Gladiali, S.; Beller, M., Synthesis, Characterisation and Application of Iridium(III) Photosensitisers for Catalytic Water Reduction. *Chem. Eur. J.* **2011**, *17*, 6998-7006.

CHAPTER 2

Tris-bidentate Ir(III) polypyridyl and cyclometalated complexes: synthesis and comparative photoredox behavior

2.1 Foreword

As previously mentioned, Ir(III) complexes display unique photophysical and electrochemical properties compared to other transition metal complexes such as high tunability upon change of a ligand[1] and the possibility of forming up to three cyclometalated bonds between the metal center and the coordinating ligands.[2-3] So the C/N (C-chelation *vs.* N-chelation) ratio in the first coordination sphere can vary from 0/6 to 3/3 which gives rise to high versatility of luminescent and (photo-)redox properties.

Among all N-chelated and cyclometalated complexes, a vast majority of the trischelate complexes described in the literature are derived from $[Ir(N,N'\text{-bpy})(ppy)_2]^+$ [4-10] (ppyH = 2-phenylpyridine ; N,N'-bpy = 2,2'-bipyridine) and *fac*-$[Ir(ppy)_3]$ (respectively termed $[IrN_4C_2]^+$ and $[IrN_3C_3]$ hereafter for sake of clarity – Figure 2.1a-b).[9, 11-15] The photophysics of these complexes are well reported in the literature; the lowest excited state is attributed to MLCT (Metal-to-Ligand Charge Transfer) and MLLCT (Metal-Ligand-to-Ligand Charge Transfer) transition for $[IrN_3C_3]$ and $[IrN_4C_2]^+$, respectively. In contrast, $[Ir(N,N'\text{-bpy})_3]^{3+}$ (termed $[IrN_6]^{3+}$ hereafter – Figure 2.1d) derivatives are scarcely described[16-18] and $[Ir(N,N'\text{-bpy})_2(ppy)]^{2+}$ (termed $[IrN_5C_1]^{2+}$ hereafter – Figure 2.1c) ones are almost not reported in the literature despite their expected interesting properties.[19-20] The lack of extensive studies on these two latter Ir(III) derivatives probably comes from the difficulty of obtaining pure compounds and reproducible synthetic protocols.

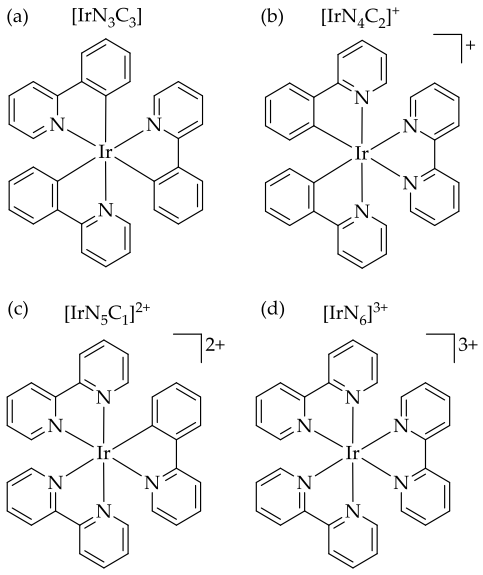

Figure 2.1 – Structures of the trischelate Ir(III) complexes: (a) *fac*-$[Ir(ppy)_3]$ ($[IrN_3C_3]$) ; (b) $[Ir(N,N'\text{-}bpy)(ppy)_2]^+$ ($[IrN_4C_2]^+$) ; (c) $[Ir(N,N'\text{-}bpy)_2(ppy)]^{2+}$ ($[IrN_5C_1]^{2+}$) ; (d) $[Ir(N,N'\text{-}bpy)_3]^{3+}$ ($[IrN_6]^{3+}$)

In this chapter, we report (i) the synthesis, via a key intermediate $[Ir(N,N'\text{-}bpy)_2Cl_2]^+$ (termed $[IrN_4Cl_2]^+$ – Figure 2.2a), with the full characterization of both $[IrN_5C_1]^{2+}$ and $[IrN_6]^{3+}$ and (ii) the comprehensive photophysical studies of the full series of trischelate Ir(III) complexes with a C/N coordination sphere gradually ranging from 0/6 to 3/3 by successive chelation of ppyH and/or bpy onto the metal center. Interestingly, we also managed to synthesize an intermediate between $[IrN_5C_1]^{2+}$ and $[IrN_6]^{3+}$ barely described in the literature[21-23] which is $[Ir(N,N'\text{-}bpy)_2(N,C^3\text{-}bpy)]^{2+}$ (termed $[R\text{-}IrN_5C_1]^{2+}$ hereafter for sake of clarity – "R-" stands for "roll-over" – Figure 2.2b) made from the roll-over derivative of the precursor $[IrN_4Cl_2]^+$, *i.e.* $[Ir(N,N'\text{-}bpy)(N,C^3\text{-}bpy)Cl_2]$ (termed $[IrN_3CCl_2]$ hereafter for sake of clarity – Figure 2.2a). This compound is made out of three bpy ligands but has

C/N = 1/5 as one pyridine ring is twisted, providing a cyclometalating Ir-C bond. The main interest of this $[R\text{-}IrN_5C_1]^{2+}$ complex lies in the presence of a non-chelating nitrogen atom on the twisted bpy ligand. Since this nitrogen can be easily protonated, it allowed us to investigate the influence of this protonation on the spectroscopic properties of $[R\text{-}IrN_5C_1]^{2+}$. Therefore, changes resulting from the derivatization of the second coordination sphere, *i.e.* the substitution of the C^6 of the ppy moiety by a N of the cyclometalated N,C^3-bpy, can be also extensively investigated.

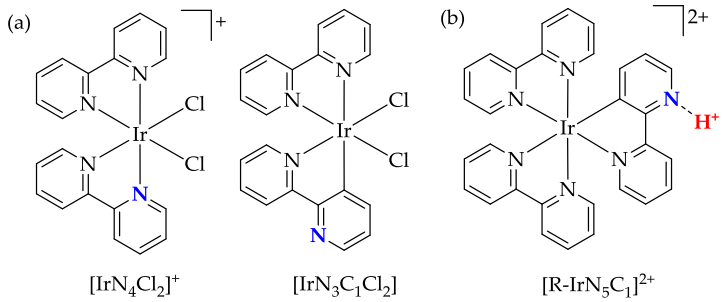

Figure 2.2 – (a) Structures of the two precursors $[Ir(N,N'\text{-}bpy)_2Cl_2]^+$ ($[IrN_4Cl_2]^+$) and $[Ir(N,N'\text{-}bpy)(N,C^3\text{-}bpy)Cl_2]$ ($[IrN_3CCl_2]$). (b) Structure of the roll-over $[R\text{-}IrN_5C_1]^{2+}$ complex and its protonated form (*red*)

(iii) Finally, based on the electrochemical and photophysical properties of the complexes, their photochemical properties are investigated. Indeed, we present hereafter a comprehensive experimental photophysical study on the behavior of these complexes and a photochemical study in the presence of well-known redox system, *i.e.* benzoquinone (BQ) / hydroquinone (H_2Q). We included the $[R\text{-}IrN_5C_1]^{2+}$ complex and

its protonated form in this comparative study, which can be considered as intermediates between $[IrN_5C_1]^{2+}$ and $[IrN_6]^{3+}$.

2.2 Synthesis

2.2.1 Synthesis of the Ir(III) precursors

In contrast to the $[IrN_3C_3]$ and $[IrN_4C_2]^+$ complexes which can be obtained from common $[(ppy)_2Ir(\mu\text{-}Cl)_2Ir(ppy)_2]$ dimer intermediate (obtained from Nonoyama's procedure[24]) (Figure 2.3b) rather easily, the synthesis of $[IrN_5C_1]^{2+}$ and $[IrN_6]^{3+}$ complexes is more challenging; the lack of an efficient procedure to obtain these two complexes is responsible for their limited occurrence in the literature. In order to tackle this issue, an optimization of a reaction pathway based on the $[IrN_4Cl_2]^+$ precursor was investigated (Figure 2.3a).

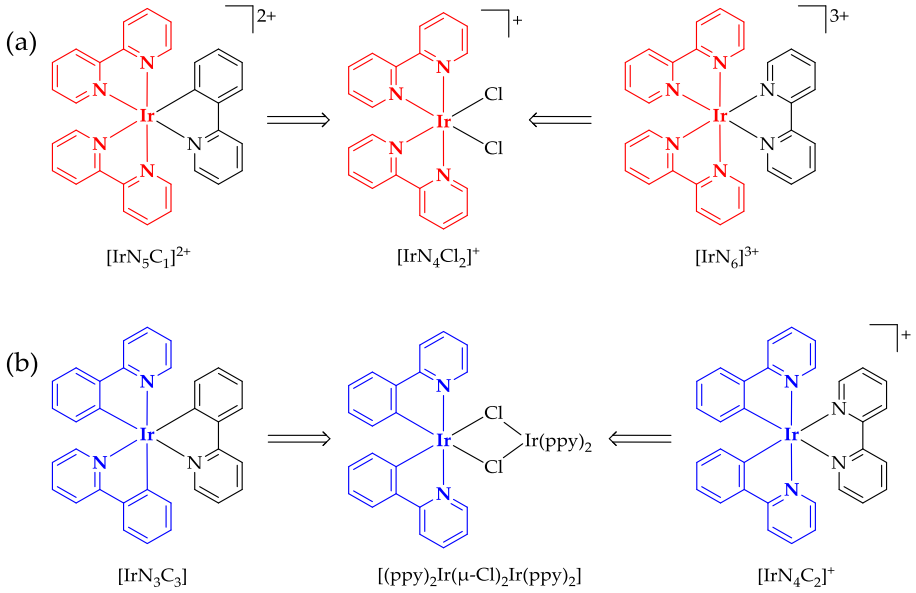

Figure 2.3 – Schematic pathway for the retrosynthesis of all trischelate complexes from (a) $[IrN_4Cl_2]^+$ and (b) $[(ppy)_2Ir(\mu\text{-}Cl)_2Ir(ppy)_2]$

An optimized synthesis of this $[IrN_4Cl_2]^+$ precursor using a microwave assisted procedure allowed to obtain the $[IrN_4Cl_2]^+$ with a 59% yield (equation 2.1). The structure of this precursor has been confirmed by X-ray crystallography (Table 2.1 and Figure 2.4a). During the synthesis of the precursor $[IrN_4Cl_2]^+$, its cyclometalated analogue $[IrN_3C_1Cl_2]$ was obtained as a side product (equation 2.1).

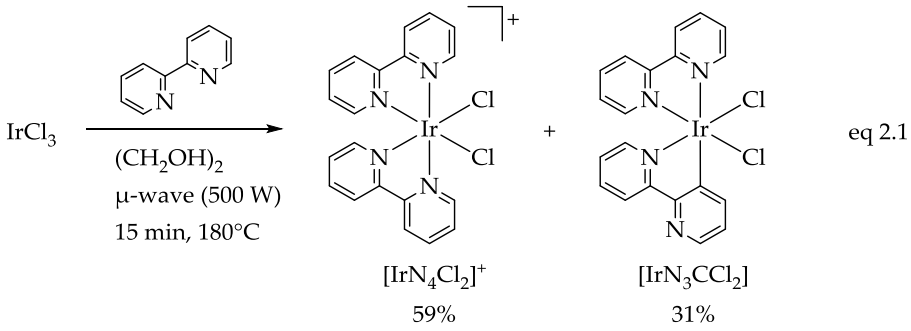

This precursor, with a twisted pyridine ring, has only been described once in the literature by Watts and coworkers, but solely as a dimer.[25] In our case, the developed reaction conditions allowed the isolation of the mononuclear $[IrN_3C_1Cl_2]$ precursor with a 31% yield. X-ray crystallography of this new Iridium precursor is depicted in Figure 2.4b (and Table 2.1).

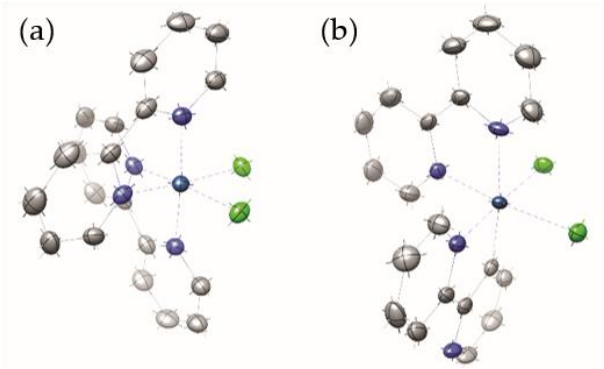

Figure 2.4 – X-ray structures of (a) $[IrN_4Cl_2]^+$ and (b) $[IrN_3CCl_2]$

As expected for $[IrN_4Cl_2]^+$, the Iridium center displays an octahedral geometry though slightly distorted. Four of the six coordinating sites are occupied by the two bpy ligands while the remaining sites bear chloride ligands in *cis* position relative to each other. The $[IrN_4Cl_2]^+$ cation is found to crystallize in the monoclinic *C*2/*c* space group with the Iridium metal located on the rotation axis, imposing 2-fold symmetry on the complex. All four Ir-N distances were found to be equal *i.e.* 2.050 Å.

Table 2.1 – Crystallographic and refinement details for $[IrN_4Cl_2]^+$ and $[IrN_3CCl_2]$.

	$[IrN_4Cl_2]^+$	$[IrN_3CCl_2]$
Empirical formula	$C_{21}H_{16}Cl_2F_3IrN_4O_3S$	$C_{22}H_{18}Cl_2IrN_5$
Formula weight, g/mol	724.54	615.51
Temperature, K	150(2)	120(2)
Wavelength, Å	0.71073 Å	0.71073 Å
Crystal system	Monoclinic	Monoclinic
Space group	*C*2/c	$P2_1/c$
a, Å	15.1486(3)	14.1710(4)
b, Å	13.8258(3)	10.7695(3)
c, Å	12.3879(2)	13.8541(4)
β, °	109.316(2)	92.082(3)
Volume, Å³	2448.49(9)	2112.95(11)
Z	4	4
ρ (calc.), $g.cm^{-3}$	1.965	1.935
μ, mm^{-1}	5.811	6.591
F(000)	1392	1184
Reflections collected	10350	28702
Independent reflections	2239 [R(int) = 0.0321]	3921 [R(int) = 0.0403]
Completeness to theta = 25.242°	99.6%	99.9%
Data / restr. / param.	2239 / 31 / 195	3921 / 0 / 272
Goodness-of-fit on F2	1.009	1.081
Final R indices [I>2σ(I)]	R1 = 0.0271, wR2 = 0.0721	R1 = 0.0243, wR2 = 0.0625
R indices (all data)	R1 = 0.0283, wR2 = 0.0729	R1 = 0.0260, wR2 = 0.0635
$\Delta\rho_{max,min}$ 0($eÅ^{-3}$)	1.767 and -1.639	0.825 and -1.135

On the other hand, the neutral $[IrN_3C_1Cl_2]$ complex shows a $P2_1/c$ packing where the iridium center displays a slightly distorted octahedral geometry. It could be noted that one of the bonds to the chelating atoms is significantly longer than the others (2.136 Å *vs.* 2.016 Å, 2.031 Å and 2.046 Å). X-ray refinement indicates that the longest bond corresponds to an Ir-N bond in

trans of the shortest bond, assigned to the Ir-C bond of the twisted pyridine. A search in the CSD database for octahedral Ir(III) complexes with *trans* N-Ir-C bonds reveals average bond lengths for the Ir-C and Ir-N bonds of 2.012Å and 2.150Å, respectively, which is in line with the reported structure. These observations are also in agreement with the crystallographic data of the $[Ir(ppy)_2Cl]_2$ dimer where Ir-C and Ir-N were separated by a distance of 2.052 Å and 2.111 Å, respectively.[26] These observations clearly suggest that the formation Ir-C bond is favored in *trans* with respect to the pyridine of the second N,N'-bpy ligand with a stronger π-acceptor character than the chloride ion.

$[IrN_4Cl_2]^+$ precursor can be successfully used to synthesize the trischelate complexes $[IrN_5C_1]^{2+}$ and $[IrN_6]^{3+}$ after the chelation of an additional 2-phenylpyridine or a third 2,2'-bipyridine ligand, respectively. It is worth mentioning that $[IrN_4Cl_2]^+$ being less prone to complexation than precursors such as $[Ir(ppy)_2Cl]_2$, it had to be converted into the bis-triflate derivative to allow the chelation of a third bidentate ligand for the synthesis of $[IrN_5C_1]^{2+}$ and $[IrN_6]^{3+}$ (*vide infra*). $[IrN_3CCl_2]$ precursor can be directly used to afford the trischelate roll-over $[R\text{-}IrN_5C_1]^{2+}$ complex by chelation of a 2,2'-bipyridine ligand. Under acidic conditions, the protonated form of the complexes, $[IrN_3C_1Cl_2\text{-}H]^+$ and $[R\text{-}IrN_5C_1\text{-}H]^{3+}$, can be generated. These protonated species will, of course, display particular photophysical properties. Stable protonated species can be isolated by addition of trifluoroacetic acid in a solution of the corresponding neutral complexes in acetonitrile, followed by evaporation of the solvent.

2.2.2 Synthesis of the [IrN_3C_3] complex

According to literature, tris-cyclometalated Ir(III) complexes can typically be prepared by four different synthetic pathways. The first method involves treating precursor [$Ir(acac)_3$] (acacH = acetylacetone) with three equivalents of the free N^CH ligand (here N^CH = ppyH) in refluxing glycerol (equation 2.2).[27] These complexes can also be prepared from the appropriate β-diketonate derivative (equation 2.3) or well-known dichloro-bridged dimer [$(N^C)_2Ir(\mu\text{-}Cl)_2Ir(N^C)_2$] (equation 2.4), by heating the Ir(III) complex with an excess of cyclometalating ligand in glycerol. Finally, the cyclometalated complexes can be obtained from the key intermediate [$(N^C)_2Ir(CH_3CN)_2]^+$ in *o*-dichlorobenzene at 100°C (equation 2.5).[26] Previous routes to make tris-cyclometalated Ir(III) complexes also utilize $IrCl_3.H_2O$ as starting material but it requires huge amounts of cyclometalating ligand as solvent making it necessary to prepare the N^CH ligand on a large scale.[28]

$$[Ir(acac)_3] \xrightarrow[\text{glycerol}]{\text{3 N^CH}} [Ir(N^C)_3] + 3\ \text{acacH} \qquad \text{eq 2.2}$$

$$[(N^C)_2Ir(O^O)] \xrightarrow[\text{glycerol}]{\text{1 N^CH}} [Ir(N^C)_3] + 1\ \text{O^OH} \qquad \text{eq 2.3}$$

$$[(N^C)_2Ir(\mu\text{-}Cl)_2Ir(N^C)_2] \xrightarrow[\substack{K_2CO_3\\ \text{glycerol}}]{\text{2 N^CH}} [Ir(N^C)_3] + 2\ KCl + H_2O + CO_2 \qquad \text{eq 2.4}$$

$$[Ir(N^C)_2(CH_3CN)_2]Cl \xrightarrow[o\text{-dichlorobenzene}]{\text{1 N^CH}} [Ir(N^C)_3] + 2\ CH_3CN + HCl \qquad \text{eq 2.5}$$

The last method described in equation 2.5 offers the huge advantage over others to be performed in milder conditions and

avoid the presence of the meridional isomer as side product. Indeed, this isomer can be obtained only in the presence of a sufficient concentration of added base. Hence, the $[(N^C)_2Ir(CH_3CN)_2]^+$ undergoes replacement of one acetonitrile ligand with the nitrogen end of the incoming bidentate N^CH ligand to form an intermediate, which is the same to both facial and meridional isomers (Figure 2.5 – step 1). In the presence of a base, the carbon end of the ligand is deprotonated and coordinates with removal of the second acetonitrile ligand (Figure 2.5 – step 2'). The net result of this path is the formation of the meridional isomer. In the case of the absence of the base, the formation of the facial isomer is completed by decomplexation of one of the mutually *trans* Nitrogen atoms of the intermediate, proton transfer from the carbon of the incoming ligand, coordination of this carbon to the Iridium center (Figure 2.5 – step 2) and finally replacement of the remaining acetonitrile ligand (Figure 2.5 – step 3).

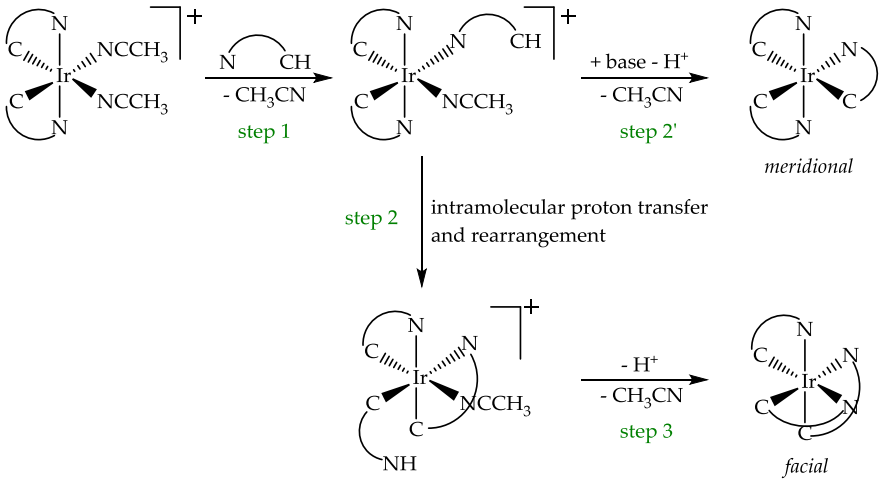

Figure 2.5 – Mechanism for the formation of facial and meridional isomers of $[Ir(N^C)_3]$ from $[(N^C)_2Ir(CH_3CN)_2]^+$

Despite their apparent similarity, facial and meridional isomers of cyclometalated Ir(III) complexes display markedly different photophysical properties.[29] Typically, the facial isomers have one order of magnitude longer lifetimes and quantum yields than the meridional ones at room temperature, making them much better candidates for photoinduced electron transfer (PET) applications. With that in mind, the choice to synthesize the facial isomer according to the method described in Figure 2.6 was made for this work.

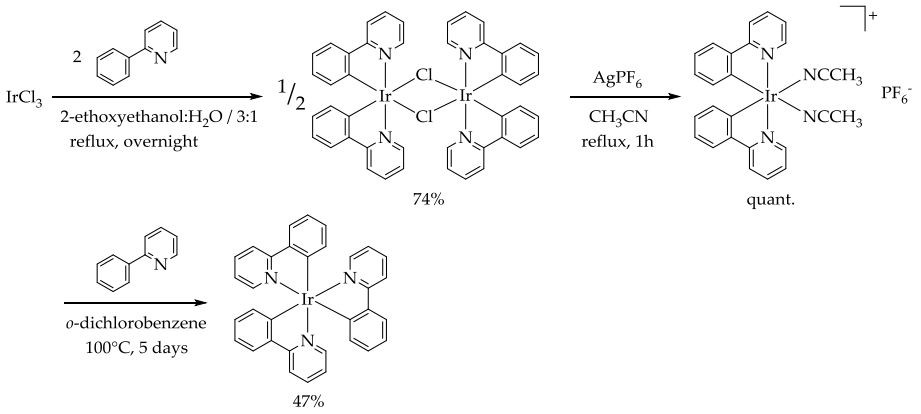

Figure 2.6 – Synthetic pathway for $[IrN_3C_3]$ complex followed in this work.

2.2.3 Synthesis of the $[IrN_4C_2]^+$ complex

As previously described, the $[IrN_4C_2]^+$ skeleton is easily prepared from the chelation of the neutral N^N ligand (here N^N = bpy) on the dichloro-bridged dimer $[(N^C)_2Ir(\mu\text{-}Cl)_2Ir(N^C)_2]$ (here N^CH = ppyH) obtained from Nonoyama's method[24] (Figure 2.7). Despite three different geometrical isomers of the bis-cyclometalated structure are theoretically possible, the strong *trans* effect of the cyclometalating carbons induces the exclusive formation of the isomer

placing both Ir-C bonds trans with respect to the neutral ancillary N^N ligand. As this high yield route is the only one described for the $[Ir(N^C)_2(N^N)]^+$ structure, no additional investigation or improvement have been performed.

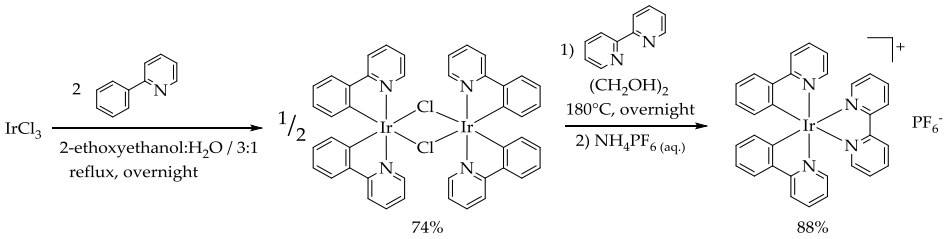

Figure 2.7 – Synthetic pathway for $[IrN_4C_2]^+$ complex followed in this work.

2.2.4 Synthesis of the $[IrN_5C_1]^{2+}$ complex

As $[IrN_5C_1]^{2+}$ complex is barely known in the literature, numerous synthetic pathways have been investigated in this Ph.D. thesis and are summarized hereafter:

- Initially, we tried the reaction between $[IrN_4Cl_2]^+$ precursor and 2-phenylpyridine in the presence of either a base able to deprotonate the 2-phenylpyridine or a silver salt promoting the chloride ions substitution (equation 2.6).

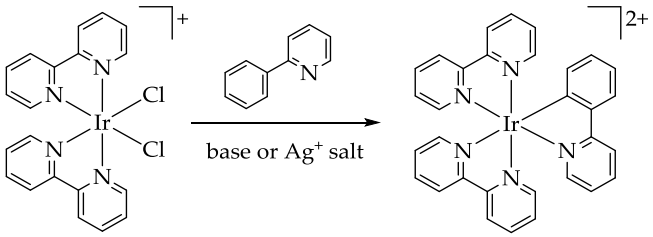

eq 2.6

In the presence of a base (usually carbonate salt), only starting materials could be recovered at the end of the reaction while under harsher conditions *i.e.* when submitted to microwaves, only decomposition products were isolated. When a silver salt was associated with 2-phenylpyridine, either decomposition products were obtained at high temperature (> 100°C) (even under microwaves) while at lower temperature, no product could be observed.

- As 2-phenylpyridine seems to be unreactive towards $[IrN_4Cl_2]^+$ precursor, transmetalation between this complex and activated 2-phenylpyridine by chelation to a transition metal was investigated (equation 2.7).

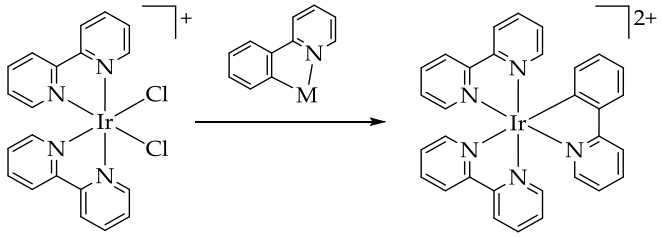

eq 2.7

According to the literature, Constable and coworkers managed the synthesis of $[IrN_5C_1]^{2+}$ by transmetalation between the same Iridium precursor and an organomercury complex *i.e.* [Hg(ppy)OAc].[20] Despite all the attempts and multiple changes in experimental conditions, the product could never be obtained. The likely high stability of the $[IrN_4Cl_2]^+$ precursor being the reason for the inertness of the system, the organomercury complex was put in reaction with more reactive $[(ppy)_2Ir(\mu\text{-}Cl)_2Ir(ppy)_2]$ dimer in order to confirm its reactivity. Not surprisingly, $[IrN_3C_3]$ was obtained pure. The same reaction with other transition metals such as Palladium derivative $[Pd(ppy)OAc]_2$ was attempted but unsuccessful.

- As [Hg(ppy)OAc] complex was able to transfer a 2-phenylpyridine ligand, a more sequential pathway *i.e.* one ligand chelated after another, was investigated. Matsumoto and coworkers managed the synthesis of $[Ir(N,N'\text{-bpy})Cl_4]^-$ precursor[30] on which one 2-phenylpyridine ligand and a second 2,2'-bipyridine ligand could theoretically be chelated (equation 2.8).

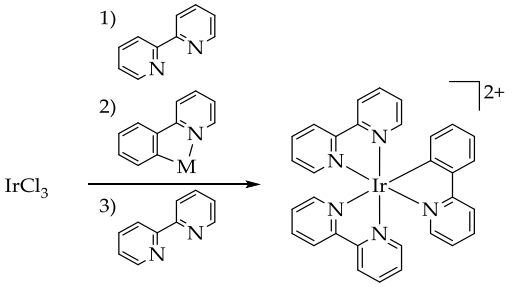

eq 2.8

$[Ir(N,N'\text{-bpy})Cl_4]^-$ precursor was efficiently obtained but subsequent chelation of a 2-phenylpyridine ligand by using either $[Pd(ppy)OAc]_2$ or [Hg(ppy)OAc] complexes afforded multiple products, probably corresponding to the three isomers of $[Ir(N,N'\text{-bpy})(ppy)Cl_2]$ precursor, which could not be separated from each other.

- Finally, the substitution of chloride ions by more labile ligands with respect to 2-phenylpyridine has been investigated (equation 2.9).

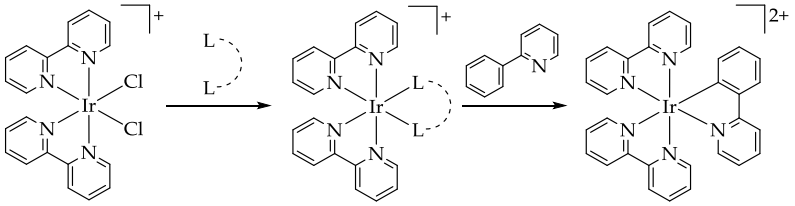

eq 2.9

Although the chelation of ligands such as acetonitrile and acetylacetonate ion on $[(N\hat{}C)_2Ir(\mu\text{-}Cl)_2Ir(N\hat{}C)_2]$ dimer is useful for the synthesis of $[Ir(N\hat{}C)_3]$ skeleton, only starting materials

were recovered when $[IrN_4Cl_2]^+$ precursor was combined to those compounds. Using harsher conditions *e.g.* a boiling solution of triflic acid and $[IrN_4Cl_2]^+$ precursor in *o*-dichlorobenzene, allowed the substitution reaction to occur, affording the expected $[Ir(N,N'\text{-bpy})_2(CF_3SO_3)_2]^+$ intermediate. This complex was then refluxed with 2-phenylpyridine in 2-ethoxyethanol yielding to the desired $[IrN_5C_1]^{2+}$ complex (Figure 2.8).

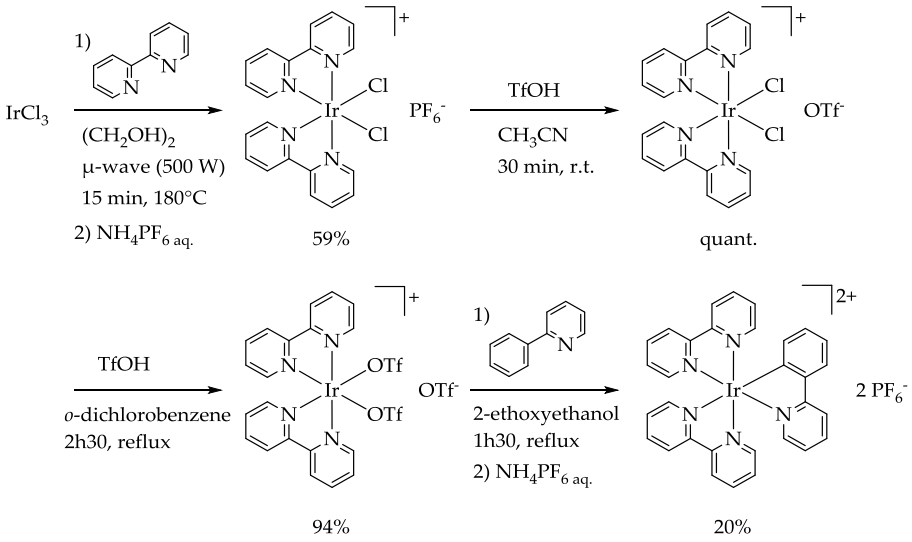

Figure 2.8 – Optimized synthetic pathway for $[IrN_5C_1]^{2+}$ complex followed in this work.

2.2.5 Synthesis of the $[IrN_6]^{3+}$ complex

As $[IrN_6]^{3+}$ complex is barely described in the literature, different synthetic pathways have been investigated during this Ph.D. work and are summarized hereafter:

- Matsumura-Inoue and coworkers published a synthesis of $[IrN_6]^{3+}$ from the direct chelation of three 2,2'-bipyridine ligands on an Iridium center under microwave activation (equation 2.10).[31]

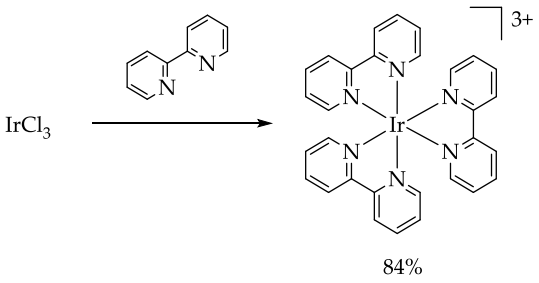

84% eq 2.10

We tried these conditions but could only obtain the $[IrN_4Cl_2]^+$ precursor, even when silver salts were added to the reaction mixture.

- In view of $[Ir(N,N'\text{-bpy})_2(CF_3SO_3)_2]^+$ complex reactivity, a refluxing solution of this precursor with 2,2'-bipyridine in ethyleneglycol allowed to yield the desired $[IrN_6]^{3+}$ complex (Figure 2.9).

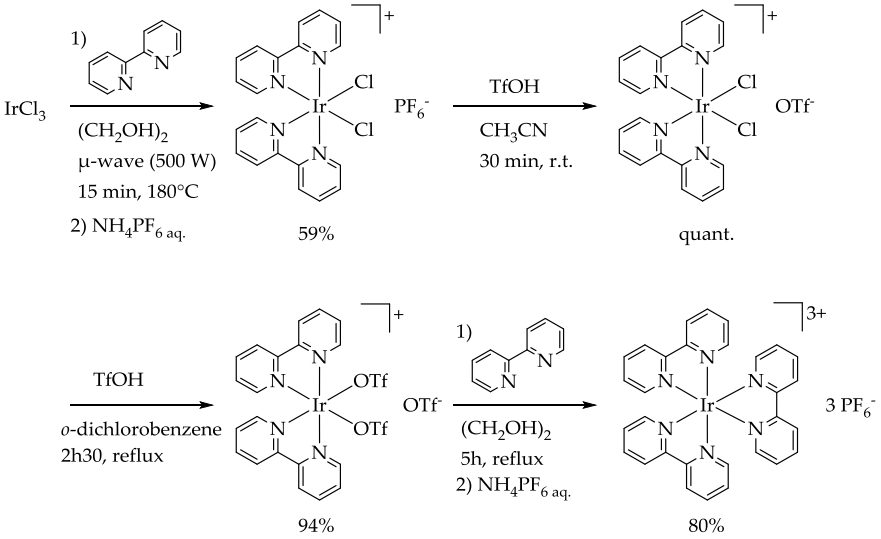

Figure 2.9 – Synthetic pathway for $[IrN_6]^{3+}$ complex followed in this work.

2.3 Photophysical and electrochemical studies

2.3.1 Photophysics of the Ir(III) precursors

The obtention of the mononuclear $[IrN_4Cl_2]^+$ and $[IrN_3C_1Cl_2]$ precursors, as well as the protonated form $[IrN_3C_1Cl_2\text{-}H]^+$ allows to achieve a comparative study of their electrochemical and spectroscopic properties. The oxidation and reduction potential for the two precursors, as well as the protonated form of the roll-over species, measured by cyclic voltammetry are gathered in Table 2.2 and the corresponding voltammograms are displayed in the supporting information (Figures S2.1-S2.3). The photophysical data of these species are gathered in Table 2.3 and Figure 2.10 shows the absorption and emission spectra at 298 K or 77 K for all the Ir(III) precursors. The more structured and blueshifting profiles observed at 77 K are due to a rigidochromism caused by the change in solvent stabilization of the excited states. In liquid, solvent molecules can reorder to accommodate the newly increased dipole moment of the photo-excited complex. In contrast, when the solvent is frozen, this effect cannot occur and the excited state is effectively destabilized. This destabilization leads to the observed shift of emission to shorter wavelengths and reduction in Stokes shift.[32]

Table 2.2 – Electrochemical data for the Iridium(III) precursors at the ground state

Precursor	E_{ox} (V)[a]	E_{red} (V)[a]
$[IrN_4Cl_2]^+$	> +2.0	-1.08[r] (ΔE_p = 126 mV),
		-1.32[r] (ΔE_p = 160 mV)
$[IrN_3C_1Cl_2]$	+1.38[r] (ΔE_p = 75 mV)	-1.29[r] (ΔE_p = 100 mV)
$[IrN_3C_1Cl_2\text{-}H]^+$	+1.60[ir]	-1.04[ir], -1.36[ir]

[a]The measurements were made using Ag/AgCl as reference electrode in acetonitrile with 0.1 M Bu_4NClO_4 as a supporting electrolyte. [b]ΔE_p stands for the peak-to-peak separation

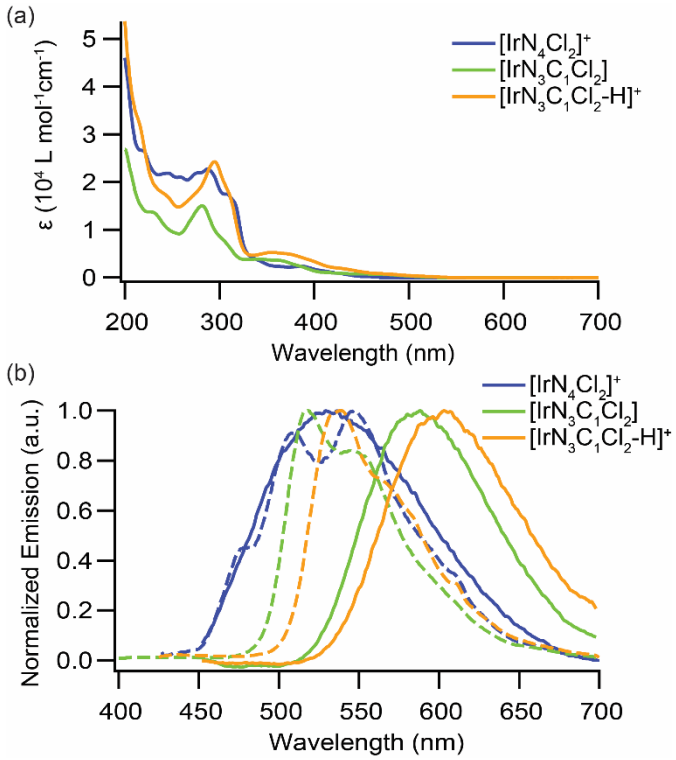

Figure 2.10 – (a) Absorption and (b) emission spectra at 298 K (solid line) or 77 K (dashed line) of the iridium precursors.

Table 2.3 – Absorption and luminescence data for the Iridium(III) precursors in acetonitrile under air at RT

	$[IrN_4Cl_2]^+$	$[IrN_3C_1Cl_2]$	$[IrN_3C_1Cl_2\text{-}H]^+$
$\lambda_{max,\ abs}$ [nm] (ε x 10^3 $M^{-1}.cm^{-1}$)	219 (27.2), 246 (22.4), 259 (21.5), 275 (22.4), 288 (23.2), 308 (17.9), 362 (2.4), 386 (2.5), 412 (1.4), 426 (0.9), 457 (0.2)	230 (14.5), 282 (16.2), 342 (4.0), 363 (3.7), 420 (1.0), 474 (0.7)	214 (33.7), 242 (17.8), 295 (24.7), 355 (5.4), 372 (5.1), 432 (1.9), 478 (0.8), 520 (0.3)
$\lambda_{max,\ em}$[a] [nm] at 298 K	533	586	602
$\lambda_{max,\ em}$[a,b] [nm] at 77 K	477, 509, 547	518, 548	537, 569
τ [ns] under air	296	19	87
ϕ[c]	0.011	0.002	0.008
k_r [d]($x10^3$ s^{-1})	37.2	107.5	92.0
τ [ns] under Ar	296	19	87
ϕ[e]	0.011	0.002	0.008
k_r [f]($x10^3$ s^{-1})	37.2	107.5	92.0
Proposed excited state assignment	^{3}LC	^{3}MLLCT	^{3}MLLCT
HOMO	π(N,N'-bpy)	Ir-C (N,C^3-bpy)	Ir-C (N,C^3-bpy-H^+)
LUMO	π^*(bpy)	π^*(N,N'-bpy)	π^*(N,N'-bpy)

[a]λ_{exc} = 400 nm. [b]Emission at 77 K measured in EtOH:MeOH / 4:1. [c]The quantum yield (+/- 5%) was measured under air using $[Ru(bpy)_3]^{2+}$ as reference; ϕ_{ref} = 0.028 in H_2O, λ_{exc}= 400 nm, and 298 K. [d]Radiative rate constant at 298 K ($k_r = \phi/\tau$). [e]The quantum yield (+/- 5%) was measured under Argon using $[Ru(bpy)_3]^{2+}$ as reference ; ϕ_{ref} = 0.042 in H_2O, λ_{exc}= 400 nm, and 298 K. [f]Radiative rate constant under Argon at 298 K ($k_r = \phi/\tau$).

The roll-over geometry of $[IrN_3C_1Cl_2]$ implies that the two bpy units are no longer equivalent and that two ligands with an uneven electron density are present in the precursor. In cyclic voltammetry, the roll-over $[IrN_3C_1Cl_2]$ exhibits a single reversible reduction wave at -1.29 V *vs.* Ag/AgCl and an oxidation wave at

+1.38 V *vs.* Ag/AgCl. The reduction can reasonably be assigned to the reduction of the π-deficient ligand, *i.e.* the N,N'-bpy moiety; the higher potential required to reduce the N,N'-bpy unit in $[IrN_3C_1Cl_2]$ compared to the $[IrN_4Cl_2]^+$ can be rationalized by the Ir-C trans effect observed in the X-ray structure, which increases the energy of the π*(N,N'-bpy). This assignation is confirmed by the reduction potential measured for the protonated $[IrN_3C_1Cl_2\text{-}H]^+$, where the Ir-C trans effect induced by the protonated $N,C^3\text{-bpy-}H^+$ is weaker, inducing a reduction potential close to $[IrN_4Cl_2]^+$ for the protonated roll-over precursor. The presence of these two non-equivalent bpy ligands should allow a CT transition to take place. Indeed, the emission spectra of the $[IrN_3C_1Cl_2]$ and its protonated analog undergo a hypsochromic shift and get more structured at 77 K. The protonation of $[IrN_3C_1Cl_2]$ also induces a bathochromic shift of *ca* 10-15 nm in absorption and in emission (from 586 nm to 602 nm), suggesting that the orbitals involved in the spectroscopic processes are sensitive to protonation. Excited state lifetimes are measured, which are too short to be assigned to a pure ligand-centered transition. In addition k_r values (Table 2.3) are relatively high compared to usual values for pure ^{3}LC transitions. The excited state of $[IrN_3C_1Cl_2]$ should thus correspond to a ^{3}MLLCT transition between the "Ir-C(N,C^3-bpy)" fragment and the N,N'-bpy ligand. Upon protonation, despite the electron impoverishment on the cyclometalated $N,C^3\text{-bpy-}H^+$, the LUMO of $[IrN_3C_1Cl_2\text{-}H]^+$ is still believed to be localized on the N,N'-bpy ligand because of the CT character observed in spectroscopic studies, and the excited state of the $[IrN_3C_1Cl_2\text{-}H]^+$ assigned to a similar ^{3}MLLCT transition.

2.3.2 Photophysics of the Ir(III) trischelate complexes

Trischelate Iridium(III) complexes are well-known to display various photophysical properties depending on the nature of the ancillary ligands.[3] In contrast to Ru(II) complexes for which the emission always lies in the orange-red region, the emission of Ir(III) complexes can be tuned from blue to red by appending the appropriate ligands to the metal center.[33-36] But, in contrast to Ru(II) complexes, because of a strong spin-orbit interaction and the important influence of the ligands, the deactivation of Ir(III) complexes usually involves a mixture of excited states.[2-3] Besides the classical way *via* introduction of electron-donating or electron-withdrawing group on ligands, the coordination sphere around the Ir(III) center can be modified, which is scarcely the case for Ru(II) complexes. According to the literature, substitution of a ppy by a N,N'-bpy in the series $[Ir(N,N'\text{-bpy})_n(ppy)_{3-n}]^{n+}$ (n = 0, 1, 2, 3), *i.e.* increasing the N/C ratio in the first coordination sphere of the metal center, leads to compounds that are less prone to oxidation and more to reduction.[4, 6, 31]

The redox potentials for the five complexes, as well as for the protonated form of the roll-over species, measured by cyclic voltammetry are gathered in Table 2.4 and the corresponding voltammograms are displayed in the supporting information (Figures S2.4-S2.9).

Not surprisingly, the potential of the oxidation wave for the complexes are anodically shifted when the ratio N/C varies from 3/3 to 5/1, *i.e.* 0.80 V, 1.33 V and 1.78 V *vs.* Ag/AgCl for $[IrN_3C_3]$, $[IrN_4C_2]^+$ and $[IrN_5C_1]^{2+}$, respectively. The oxidation

potential for $[R\text{-}IrN_5C_1]^{2+}$ (and its protonated analog $[R\text{-}IrN_5C_1\text{-}H]^{3+}$) and $[IrN_6]^{3+}$ is higher than 2.0 V *vs.* Ag/AgCl and can thus not be determined. Following a similar trend, the potential for the first reduction process shifts towards less negative values upon increasing the number of N atoms chelating the metallic center, *i.e.* < -2.0 V, -1.32 V, -1.04 V and -0.81 V *vs.* Ag/AgCl for $[IrN_3C_3]$, $[IrN_4C_2]^+$, $[IrN_5C_1]^{2+}$ and $[IrN_6]^{3+}$, respectively. The $[R\text{-}IrN_5C_1]^{2+}$ complex displays two reversible reduction processes at -1.07 V and -1.27 V *vs.* Ag/AgCl, respectively, similar to those of $[IrN_5C_1]^{2+}$. Upon protonation, both reduction waves of $[R\text{-}IrN_5C_1]^{2+}$ are slightly anodically shifted at -0.95 V and -1.16 V *vs.* Ag/AgCl, respectively.

Table 2.4 – Electrochemical data for the Iridium(III) complexes at the ground state

Complex	E_{ox} (V)[a]	E_{red} (V)[a]
$[IrN_3C_3]$	$+0.80^r$ (ΔE_p = 61 mV)	< -2.0
$[IrN_4C_2]^+$	$+1.33^r$ (ΔE_p = 136 mV)	-1.32^r (ΔE_p = 119 mV)
$[IrN_5C_1]^{2+}$	$+1.78^{ir}$	-1.04^r (ΔE_p = 63 mV), -1.24^r (ΔE_p = 59 mV)
$[R\text{-}IrN_5C_1]^{2+}$	> +2.0	-1.07^r (ΔE_p = 87 mV), -1.27^r (ΔE_p = 93 mV)
$[R\text{-}IrN_5C_1\text{-}H]^{3+}$	> +2.0	-0.95^r (ΔE_p = 72 mV), -1.16^r (ΔE_p = 81 mV)
$[IrN_6]^{3+}$	> +2.0	-0.81^r (ΔE_p = 128 mV), -1.03^{ir}, -1.22^{ir}

[a] The measurements were made using Ag/AgCl as reference electrode in acetonitrile with 0.1 M Bu_4NClO_4 as a supporting electrolyte. [b] ΔE_p stands for the peak-to-peak separation.

The absorption and emission data for the series of trischelate complexes are reported in Table 2.5 and Figures 2.11 and 2.12.

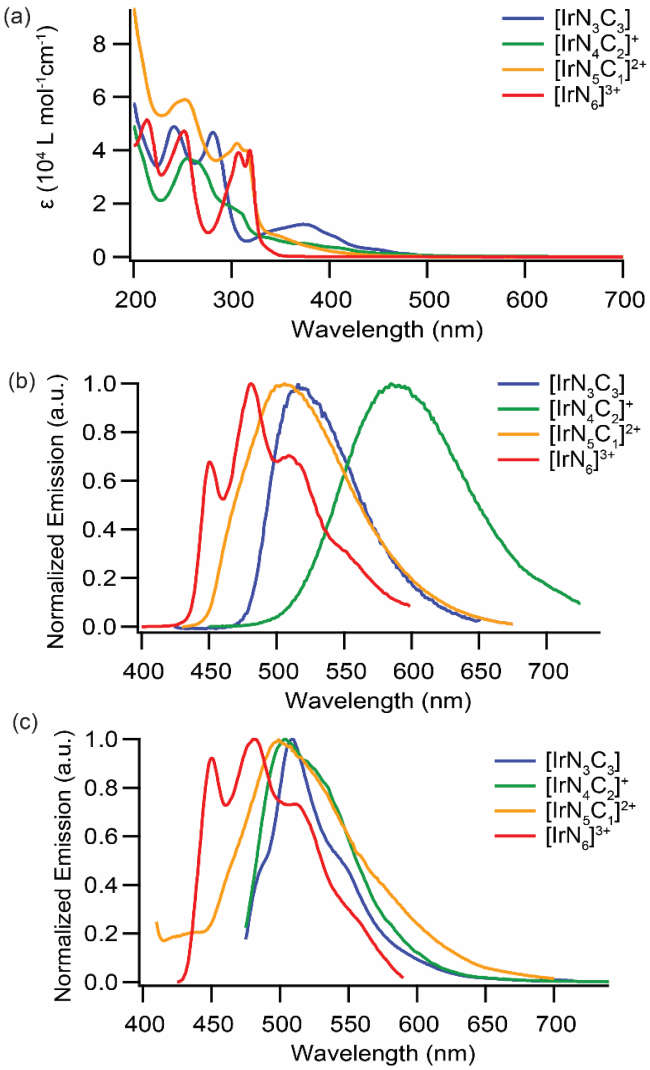

Figure 2.11 – (a) Absorption spectra of Iridium complexes in acetonitrile ; emission spectra of Iridium(III) trischelate complexes (b) at 298 K in acetonitrile and (c) at 77 K in EtOH:MeOH / 4:1

Table 2.5 – Absorption and luminescence data for the Iridium(III) precursors in acetonitrile under air at RT

	$[IrN_3C_3]$	$[IrN_4C_2]^+$	$[IrN_5C_1]^{2+}$	$[R\text{-}IrN_5C_1]^{2+}$	$[R\text{-}IrN_5C_1\text{-}H]^{3+}$	$[IrN_6]^{3+}$
$\lambda_{max,\,abs}$ [nm] (ε x 10^3 $M^{-1}.cm^{-1}$)	241 (48.8), 281 (46.7), 339 (9.6), 376 (12.2), 408 (7.1), 473 (1.3), 486 (0.9)	257 (512), 267 (487), 310 (227), 339 (96), 376 (64), 412 (36), 467 (7)	243 (57.6), 253 (59.0), 305 (42.6), 312 (39.9), 352 (7.4), 392 (2.8), 427 (1.1)	252 (58.3), 305 (35.6), 312 (33.0), 346 (9.8), 363 (7.5), 454 (1.3)	253 (49.1), 304 (38.1), 315 (37.7), 344 (9.8), 363 (6.7), 387 (3.4)	213 (51.5), 251 (47.2), 307 (39.1), 319 (39.9), 390 (0.1)
$\lambda_{max,\,em}$ [a] [nm]	517	587	507	464, 493, 523	484, 516 , 557	452, 484, 514
$\lambda_{max,\,em}$ [a,b] H_2O [nm]	-[c]	600	503	461, 491, 521	482, 513, 552	452, 484, 514
$\lambda_{max,\,em}$ [a,d] [nm] at 77 K	486, 510, 549	507	490	453, 483, 515	469, 502, 533	451, 483, 515
τ [ns]	20	63	595	282	1034	1238
ϕ [e]	0.023	0.0165	0.099	0.063	0.021	0.053
k_r [f] ($x10^3$ s^{-1})	1150	261.9	166.4	223.1	20.3	42.8
τ [ns] under Ar	864 [g]	307	2770	298	5780	6340
ϕ [h]	0.040	0.035	0.139	0.182	0.021	0.129
k_r [i] ($x10^3$ s^{-1})	46.3	114.0	50.2	611.8	3.63	20.3
Proposed excited state assignment	^{3}MLLCT	^{3}MLLCT/^{3}LC	^{3}MLLCT/^{3}LC	^{3}MLLCT/^{3}LC	^{3}LC	^{3}LC
HOMO	Ir-C(ppy)	Ir-C(ppy) /π(N,N′-bpy)	Ir-C(ppy)	Ir-C(N,C^3-bpy)	nd[j]	π(N,N′-bpy)
LUMO	π^*(ppy)	π^*(N,N′-bpy)	π^*(N,N′-bpy)	π^*(N,N′-bpy)	nd[j]	π^*(N,N′-bpy)

[a]λ_{exc} = 400 nm. [b]Measured in phosphate buffer 50 mM in H_2O milliQ , pH=7.0. [c]$[IrN_3C_3]$ is not soluble in aqueous media. [d]Emission at 77 K measured in EtOH:MeOH / 4:1. [e]The quantum yield (+/- 5%) was measured under air using $[Ru(bpy)_3]^{2+}$ as reference; ϕ_{ref} = 0.028 in H_2O, λ_{exc}= 400 nm, and 298 K. [f]Radiative rate constant at 298 K ($k_r = \phi/\tau$). [g]Self-quenching process due to aggregation of $[IrN_3C_3]$ complex is occurring in acetonitrile. The luminescence lifetime of $[IrN_3C_3]$ isolated in acetonitrile is reported as 1.74 μs.[37] [h]The quantum yield (+/- 5%) was measured under Argon using $[Ru(bpy)_3]^{2+}$ as reference ; ϕ_{ref} = 0.042 in H_2O, λ_{exc}= 400 nm, 298 K. [i]Radiative rate constant under Argon at 298 K ($k_r = \phi/\tau$). [j]Not determined (see text).

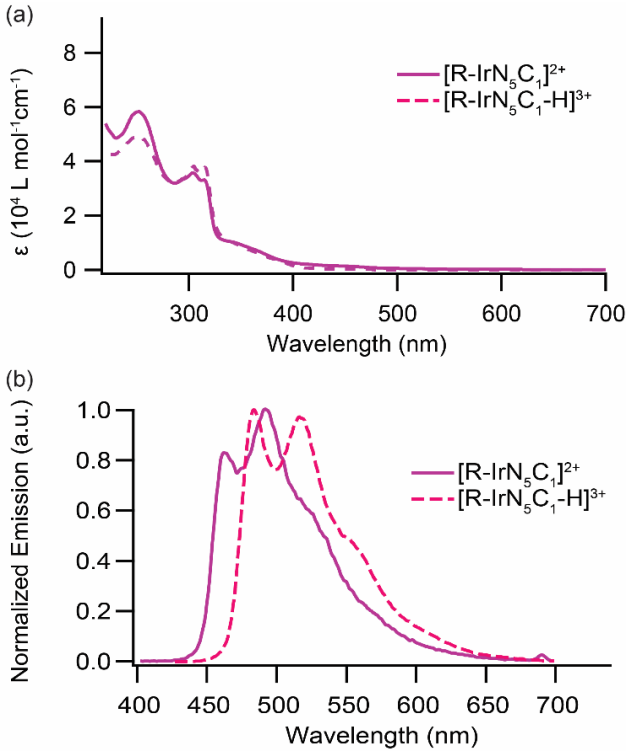

Figure 2.12 – (a) Absorption and (b) emission spectra of the rolled-over Iridium complex $[R\text{-}IrN_5C_1]^{2+}$ (solid line) and its protonated form (dashed line) at 298 K in acetonitrile

If the effect of the modification of the coordination sphere is easily rationalized for the electrochemical properties of the series of Ir(III) complexes, the situation is more puzzling in absorption and emission spectroscopy. Indeed, spectroscopically, it is generally accepted that a manifold of excited states contributes to the overall photophysics of the complex. Usually, a dominant character (like LC, MLCT, MLLCT) is used to describe the behavior of this manifold of excited states. The attribution of these excited states (listed in Table 2.5) are discussed in the following paragraphs for each complex.

[IrN_3C_3] displays a broad emission spectrum with a maximum at 517 nm. Cooling to 77 K leads to a more structured blue-shifted spectrum centered at 510 nm with the occurrence of two shoulders at 486 nm and 549 nm. The excited state of the complex lasts only 20 ns at room temperature which is consistent with a ^{3}MLCT involving π^*(ppy) as confirmed in the literature.[38-39]

As for [IrN_3C_3], [IrN_4C_2]$^+$ displays a broad emission spectrum centered at 587 nm. The complex undergoes positive solvatochromism when dissolved in water ($\lambda_{max,\ water}$ = 600 nm). An intense hypsochromic shift is detected at 77 K attesting the CT character of the excited state. However, the longer lifetime of the complex compared to [IrN_3C_3] suggests a slight contribution of a ^{3}LC on the diimine ligand as previously described.[40-41] Consequently, [IrN_4C_2]$^+$ is characterized by a ^{3}LC/^{3}MLLCT combination, with the LUMO localized on the π^*(N,N'-bpy).

[IrN_5C_1]$^{2+}$ displays a broad emission spectrum centered at 507 nm and, surprisingly, undergoes a weak negative solvatochromic effect when solubilized in water ($\lambda_{max,\ water}$ = 503 nm), implying that several excited states should be involved in the emission process, and that at least one of them does not correspond to a charge transfer. The partial ^{3}CT character of the excited state is nevertheless confirmed by the hypsochromic shift ($\lambda_{max,\ 77\ K}$ = 490 nm) measured when the sample is cooled to 77 K. However, this shift is relatively small compared to [IrN_4C_2]$^+$, implying a non-negligeable ^{3}LC contribution, consistent with the increase of N/C ratio on the coordination sphere compared to [IrN_4C_2]$^+$. Furthermore, the lifetime of the excited state close to 600

ns and the relatively weak radiative rate constant (k_r = 166.4 10^3 s^{-1}) are also in disagreement with a pure ^{3}CT. It is thus expected that excited states involved in the deactivation of $[IrN_5C_1]^{2+}$ correspond to a mixture of a ^{3}LC state centered on the cyclometalated ligand and a ^{3}MLLCT state between the Ir-C fragment and π*(N,N'-bpy) (Table 2.5).

In contrast, $[IrN_6]^{3+}$ exhibits a different photophysical behavior; the luminescence displays a structured three-banded emission spectrum at 452 nm, 484 nm and 514 nm and decays in about 1.2 μs under air. Neither a solvatochromism effect is observed upon the change of solvent polarity (*i.e.* from acetonitrile to water) nor at 77 K where the emission only shows a slightly more structured spectrum, which is in favor of a ^{3}LC excited state, as described in the literature,[38] localized on the N,N'-bpy (Table 2.5).

The roll-over $[R\text{-}IrN_5C_1]^{2+}$ can be considered as an intermediate complex between $[IrN_5C_1]^{2+}$ and $[IrN_6]^{3+}$ as it has the same coordination sphere as the former (N/C ratio equal to 5/1) but is built with the same ligands as the latter. The three-banded emission spectrum of $[R\text{-}IrN_5C_1]^{2+}$ is blue-shifted compared to $[IrN_5C_1]^{2+}$, due to the electron-withdrawing character of the non-chelating nitrogen atom stabilizing the HOMO; indeed, the oxidation wave for $[R\text{-}IrN_5C_1]^{2+}$ is anodically shifted compared to $[IrN_5C_1]^{2+}$. As it was observed for this latter, when the solvent is switched from acetonitrile to water, a small solvatochromic effect is noted, consistent with a minor contribution of a ^{3}CT excited state. Thus, the excited states of non-protonated $[R\text{-}IrN_5C_1]^{2+}$ correspond to a mixture of a ^{3}LC centered on the cyclometalated

N,C^3-bpy and a ^{3}MLLCT transition between the Ir-C fragment and π^*(N,N'-bpy) (Table 2.5).

Emission spectrum for $[R\text{-}IrN_5C_1\text{-}H]^{3+}$ is red-shifted compared to the non-protonated $[R\text{-}IrN_5C_1]^{2+}$ complex. It should be noted that the two reduction processes are anodically shifted compared to the unprotonated complex. This might be due to the fact that once the cyclometalated ligand is protonated, it reduces the trans Ir-C effect to the N,N'-bpy ligand, easying the reduction of the latter. The protonation also induces a stabilization of the π and π^* orbitals located on the twisted N,C^3-bpy. A ^{3}LC transition should thus still correspond to the most predominant lowest excited state. This attribution is in agreement with the long lifetime of the excited state, measured in the same range as $[IrN_6]^{3+}$ *i.e.* 1.0 μs for $[R\text{-}IrN_5C_1]^{2+}$ and 1.2 μs for $[IrN_6]^{3+}$. A ^{3}LC character is also supported by the absence of important shift when the complex is solubilized in a more polar solvent or cooled to 77 K, and by the weak radiative rate constant (k_r = 20.3 10^3 s^{-1}). Nevertheless, as all ligands display electron-poor character, the attribution of the excited state is challenging with common techniques and requires more specific measurements such as photo-CIDNP measurements (*vide infra*).

2.4 Photochemistry

The oxidation and reduction potentials of the excited states, namely E_{ox}^* and E_{red}^*, can be estimated using the redox potentials in the ground state (Table 2.4) and the E_{00} transition (evaluated by Franck-Condon line-shape analysis shown in Table S2.1) are gathered in Table 2.6. Based on these data, it appears, not surprinsingly, that the excited state of $[IrN_6]^{3+}$ is the most oxidizing (E_{red}^* = +1.86 V) whereas the excited state of $[IrN_3C_3]$ is the most reducing (E_{ox}^* = -1.71 V) above all investigated complexes.

Table 2.6 – Calculated electrochemical data for the Iridium(III) complexes at the excited state

Complex	E_{00} (nm)[a]	E_{ox}^* (V)[b]	E_{red}^* (V)[b]
$[IrN_3C_3]$	493	-1.71	< +0.51
$[IrN_4C_2]^+$	570	-0.85	+0.86
$[IrN_5C_1]^{2+}$	471	-0.85	+1.59
$[R\text{-}IrN_5C_1]^{2+}$	464	> -0.66	+1.59
$[R\text{-}IrN_5C_1\text{-}H]^{3+}$	483	> -0.55	+1.57
$[IrN_6]^{3+}$	451	> -0.73	+1.86

[a]The energy of the excited state is evaluated by Franck-Condon line-shape analysis according to equation S2.1 (see Supporting Information) at 298 K in acetonitrile. [b]Excited state potentials calculated according to equations $E^*_{ox} = E_{½\,ox} - E_{00} \approx E_{½\,ox} - \Delta E_{\lambda max}$ and $E^*_{red} = E_{½\,red} + E_{00} \approx E_{½\,red} + \Delta E_{\lambda max}$

Nevertheless, the photoreactivity of all complexes towards a model electron donor or acceptor, *i.e.* hydroquinone (H_2Q – equation 2.11) or benzoquinone (BQ – equation 2.12) has been investigated in acetonitrile[3] by Stern-Volmer steady-state luminescence quenching experiments. The associated quenching rate constants, *i.e.* when photoinduced electron transfer (PET) is operative, are reported in Table 2.7. An idea on the

thermodynamics of the possible reductive PET by H_2Q or oxidative PET by BQ with the excited states of each complexes are also provided in Table 2.7, according to equations 2.11 and 2.12.

$$[Ir]^{n+*} \xrightarrow{BQ} [Ir]^{(n+1)+} \qquad \Delta G_{PET} = -nF\left(E^{*}_{ox\,[Ir]} - E_{BQ}\right) \qquad \text{eq 2.11}$$

$$[Ir]^{n+*} \xrightarrow{H_2Q} [Ir]^{(n-1)+} \qquad \Delta G_{PET} = -nF\left(E_{H_2Q} - E^{*}_{red\,[Ir]}\right) \qquad \text{eq 2.12}$$

Table 2.7 – Calculated ΔG_{PET} and associated measured rate constants for the PET between Iridium(III) complexes and H_2Q and BQ in acetonitrile under air atmosphere at room temperature

	ΔG_{PET} (kJ/mol)[a]		k_Q ($M^{-1}.s^{-1}$)	
	H_2Q	BQ	H_2Q	BQ
$[IrN_3C_3]$	> +82.01	-111,92	-	$2.68\ 10^{10}$
$[IrN_4C_2]^+$	+44,38	-32,81	-	$1.19\ 10^{9}$ [b]
$[IrN_5C_1]^{2+}$	-16,40	-23,16	$8.01\ 10^{9}$	$9.76\ 10^{9}$
$[R\text{-}IrN_5C_1]^{2+}$	-33,70	> -22,19	$3.06\ 10^{10}$	$3.51\ 10^{10}$
$[R\text{-}IrN_5C_1\text{-}H]^{3+}$	-31,84	> -11,58	$1.55\ 10^{10}$	$1.00\ 10^{10}$
$[IrN_6]^{3+}$	-59,82	> -28,95	$5.76\ 10^{9}$	$1.15\ 10^{10}$

[a] The ΔG_{PET} associated to the PET processes are evaluated using equations 2.11 and 2.12, using E_{ox} = 1.24 V *vs.* Ag/AgCl in acetonitrile for H_2Q, and E_{red} = -0.43 V *vs.* Ag/AgCl in acetonitrile for BQ. [b] For $[IrN_4C_2]^+$, a static contribution to the quenching in presence of BQ is detected, with an association constant of K = 267 M^{-1}.

Both $[IrN_3C_3]$ and $[IrN_4C_2]^+$ are not quenched by H_2Q as expected from the estimated endergonicity of the PET (Table 2.7). In contrast, the highly photooxidizing $[IrN_6]^{3+}$ complex as well as $[IrN_5C_1]^{2+}$ and $[R\text{-}IrN_5C_1]^{2+}$ can be photoreduced by H_2Q. In the presence of BQ, except for $[IrN_4C_2]^+$, the luminescence quenching of all trischelate Ir(III) complexes corresponds to a purely

dynamic process with a high quenching rate constant close to the diffusion limit, showing that all irradiated complexes can be oxidized by BQ. Strikingly, from these quenching experiments, it should be stressed that $[IrN_5C_1]^{2+}$, $[R\text{-}IrN_5C_1]^{2+}$ and its protonated form, and $[IrN_6]^{3+}$ complexes can be used as both efficient photooxidizing or photoreducing agents towards H_2Q or BQ, respectively.

2.5 Conclusion

A family of Iridium(III) complexes with C/N ratio of the first coordination sphere varying from 0/6 to 3/3 could be obtained. Although the synthesis of $[IrN_3C_3]$ and $[IrN_4C_2]^+$ was well established in the literature, $[IrN_5C_1]^{2+}$ and $[IrN_6]^{3+}$ were scarcely described, limiting comprehensive and comparative studies within this family of complexes. In addition, improved synthetic protocols allowed to obtain key intermediates, *i.e.* $[IrN_3C_1Cl_2]$ and $[IrN_4Cl_2]^+$, affording a roll-over species $[R\text{-}IrN_5C_1]^{2+}$ whose protonated form can also be isolated and investigated independently. Thanks to electrochemical and photophysical comparative studies, the rich photophysics of this family of Iridium(III) complexes is highlighted. Clearly, a manifold of excited states have to be taken into account for most of the studied complexes, ranging from ^{3}LC to ^{3}MLLCT depending on the C/N ratio (Figure 2.13). The ability of all complexes to undergo PET has been investigated through quenching experiments with a well-known redox system, BQ/H_2Q in acetonitrile. Surprisingly, all complexes were able to photoreduce BQ, even $[IrN_6]^{3+}$ which is known in the literature as a very poor electron-donor. In contrast, the excited states of $[IrN_3C_3]$ and $[IrN_4C_2]^+$ were not oxidizing enough to react with H_2Q. Strikingly, $[IrN_5C_1]^{2+}$, $[R\text{-}IrN_5C_1]^{2+}$ and its protonated form, and $[IrN_6]^{3+}$ complexes are efficient photooxidizing and photoreducing agents towards H_2Q or BQ.

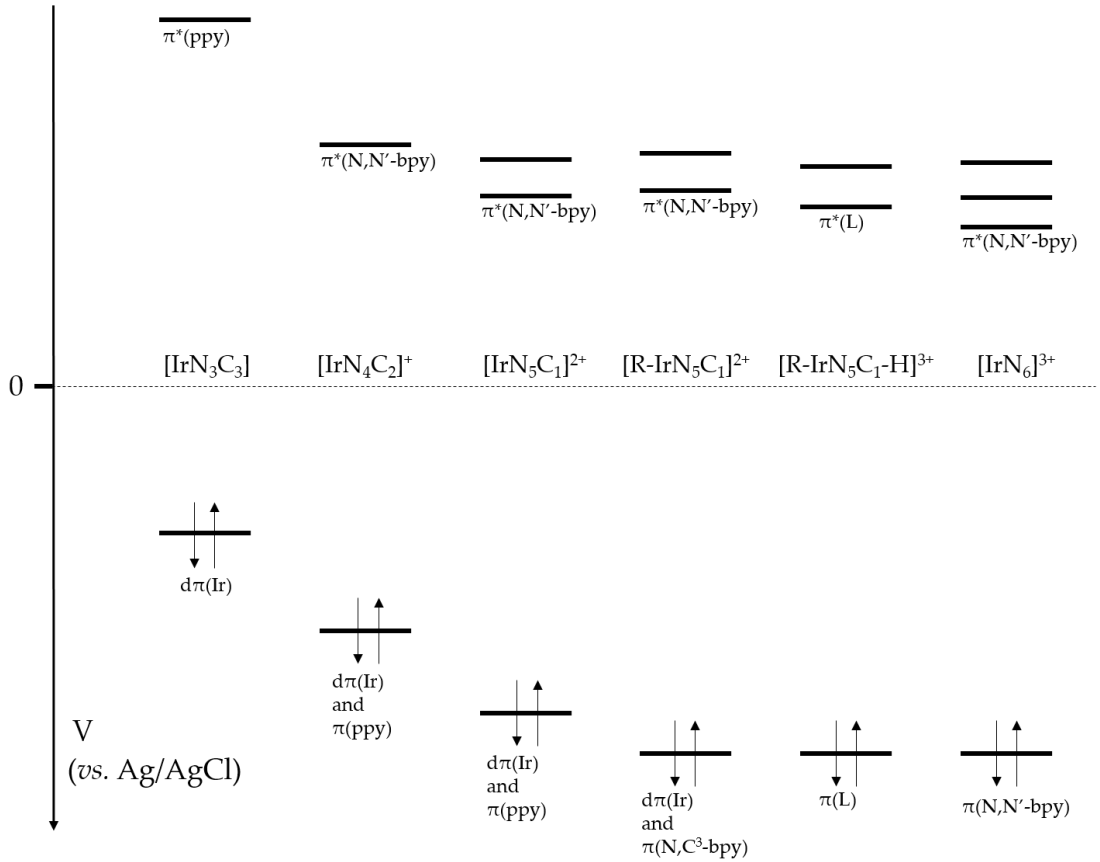

Figure 2.13 – Proposed photophysical scheme for all the investigated trischelate Ir(III) complexes

2.6 Synthetic procedures

All the reaction mixtures were protected from direct light during the synthesis to prevent photochemical degradation and the reactions were conducted under Argon. After synthesis and purification, the compounds were characterized by ^{1}H NMR spectroscopy (500 MHz) and by high resolution mass spectrometry unless otherwise indicated.

Iridium (III) bis(2-phenylpyridine-N,C³) dichloro-bridged dimer. Iridium(III) chloride hydrate (694.3 mg, 1.96 mmol) was suspended in a 2-ethoxyethanol:H_2O / 3:1 mixture (31.6 mL) followed by 2-phenylpyridine (0.608 mL, 4.25 mmol). The system was kept under Argon atmosphere and heated to reflux overnight. The obtained yellow solid was centrifuged, washed successively with ethanol and acetone and dissolved in dichloromethane to remove impurities. The solvents were evaporated under reduced pressure to provide a yellow solid (781.0 mg, 74% yield). ^{1}H NMR ($CDCl_3$), δ/ppm: 9.24 (dd, 4H, *H-1*, J_{1-2} = 5.8 Hz, J_{1-3} = 1.2 Hz), 7.87 (dd, 4H, *H-4*, J_{4-3} = 8.0 Hz, J_{4-2} = 1.2 Hz), 7.73 (ddd, 4H, *H-3*, J_{3-4} = 8.0 Hz, J_{3-2} = 7.5 Hz, J_{3-1} = 1.2 Hz), 7.49 (dd, 4H, *H-5*, J_{5-6} = 8.2 Hz, J_{5-7} = 1.2 Hz), 6.75 (m, 8H, *H-2* + *H-6*), 6.56 (ddd, 4H, *H-7*, J_{7-8} = 7.9 Hz, J_{7-6} = 7.2 Hz, J_{7-5} = 1.2 Hz), 5.93 (dd, 4H, *H-8*, J_{8-7} = 7.9 Hz, J_{8-6} = 0.8 Hz).

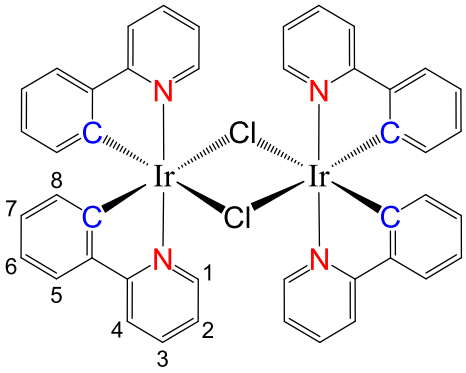

Bis (2-phenylpyridine-N,C³) bis (acetonitrile-N) iridium(III) hexafluorophosphate. $[Ir(ppy)_2(\mu\text{-}Cl)]_2$ (27.9 mg, 0.0260 mmol) was suspended in CH_3CN (15.0 mL) and the mixture was kept under Argon atmosphere and heated to 60°C. A solution of $AgPF_6$ (14.3 mg, 0.0567 mmol) in CH_3CN (5.0 mL) was added and the mixture was stirred at 60°C for 2h. The reaction mixture was cooled to room temperature and then centrifuged. The solid was washed with CH_3CN and the filtrate was evaporated under reduced pressure to afford a light yellow solid (37.9 mg, quantitative yield). ^1H NMR ($CDCl_3$), δ/ppm: 8.98 (dd, 2H, *H-1*, J_{1-2} = 5.8 Hz, J_{1-3} = 1.2 Hz), 7.92 (m, 4H, *H-3* + *H-4*), 7.54 (dd, 2H, *H-5*, J_{5-6} = 7.7 Hz, J_{5-7} = 1.3 Hz), 7.40 (dd, 2H, *H-2*, J_{2-1} = 5.8 Hz, J_{2-3} = 3.2 Hz), 6.86 (ddd, 2H, *H-6*, J_{6-5} = 7.7 Hz, J_{6-7} = 7.5 Hz, J_{6-8} = 1.2 Hz), 6.71 (ddd, 2H, *H-7*, J_{7-6} = J_{7-8} = 7.5 Hz, J_{7-5} = 1.3 Hz), 6.03 (dd, 2H, *H-8*, J_{8-7} = 7.5 Hz, J_{8-6} = 1.2 Hz), 2.26 (s, 6H, *H-Me*).

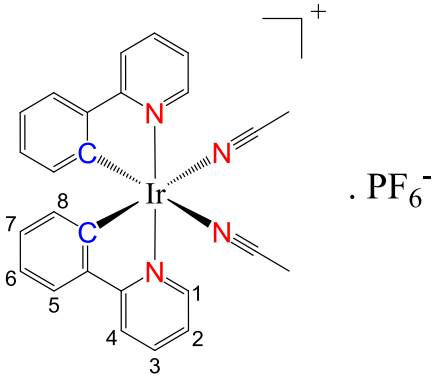

Tris (2-phenylpyridine-N,C³) iridium(III) *[IrN₃C₃]*. $[Ir(ppy)_2(CH_3CN)_2]PF_6$ (37.9 mg, 0.0521 mmol) was suspended in a solution of 2-phenylpyridine (8.9 μL, 0.0625 mmol) in *o*-dichlorobenzene (5.0 mL). The mixture was then kept under Argon atmosphere and heated to 100°C for 5 days. The solution was cooled to room temperature and directly put on a column chromatography on silica gel using hexane as eluent to remove the solvent and then dichloromethane. Evaporation of the solvents afforded a bright yellow solid (16.1 mg, 47%). ^{1}H NMR (CD_3CN), δ/ppm: 8.01 (dd, 3H, *H-4*, J_{4-3} = 8.3 Hz, J_{4-2} = 1.1 Hz), 7.72 (m, 6H, *H-3* + *H-5*), 7.60 (dd, 3H, *H-1*, J_{1-2} = 5.6 Hz, J_{1-3} = 1.7 Hz), 7.00 (ddd, 3H, *H-2*, J_{2-3} = 7.4 Hz, J_{2-1} = 5.6 Hz, J_{2-4} = 1.1 Hz), 6.86 (ddd, 3H, *H-6*, J_{6-7} = 7.7 Hz, J_{6-5} = 7.1 Hz, J_{6-8} = 1.4 Hz), 6.74 (ddd, 3H, *H-7*, J_{7-6} = 7.7 Hz, J_{7-8} = 7.5 Hz, J_{7-5} = 1.4 Hz), 6.68 (ddd, 3H, *H-8*, J_{8-7} = 7.5 Hz, J_{8-6} = 1.4 Hz).

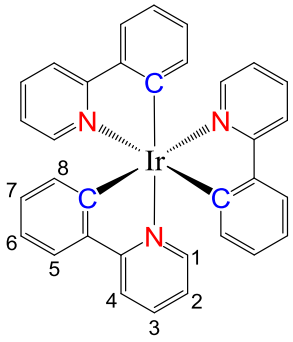

Bis (2-phenylpyridine-N,C³) (2,2′-bipyridine-N,N′) iridium(III) hexafluorophosphate *[IrN₄C₂]*⁺. [Ir(ppy)₂(μ-Cl)]₂ (15.5 mg, 0.0145 mmol) was mixed with 2,2′-bipyridine (5.4 mg, 0.0347 mmol) and NH_4PF_6 (35.4 mg, 0.217 mmol) in a CH_3CN:EtOH / 3:1 mixture (2.5 mL). The mixture was kept under Argon atmosphere and refluxed for 24 h. The reaction mixture was cooled to room temperature and water was added. The precipitate was centrifuged, washed successively with water, ethanol and diethylether and dried under reduced pressure to afford a yellow solid (20.4 mg, 88%). ^{1}H NMR (CD_3CN), δ/ppm: 8.53 (dd, 2H, *H-12*, $J_{12\text{-}11}$ = 8.1 Hz, $J_{12\text{-}10}$ = 1.3 Hz), 8.12 (ddd, 2H, *H-11*, $J_{11\text{-}12}$ = 8.1 Hz, $J_{11\text{-}10}$ = 7.9 Hz, $J_{11\text{-}9}$ = 1.7 Hz), 8.06 (dd, 2H, *H-4*, $J_{4\text{-}3}$ = 8.5 Hz, $J_{4\text{-}2}$ = 1.6 Hz), 7.98 (dd, 2H, *H-9*, $J_{9\text{-}10}$ = 5.5 Hz, $J_{9\text{-}11}$ = 1.7 Hz), 7.85 (ddd, 2H, *H-3*, $J_{3\text{-}4}$ = 8.5 Hz, $J_{3\text{-}2}$ = 7.6 Hz, $J_{3\text{-}1}$ = 1.6 Hz), 7.80 (dd, 2H, *H-5*, $J_{5\text{-}6}$ = 7.8 Hz, $J_{5\text{-}7}$ = 1.4 Hz), 7.60 (dd, 2H, *H-1*, $J_{1\text{-}2}$ = 5.8 Hz, $J_{1\text{-}3}$ = 1.6 Hz), 7.50 (ddd, 2H, *H-10*, $J_{10\text{-}11}$ = 7.9 Hz, $J_{10\text{-}9}$ = 5.5 Hz, $J_{10\text{-}12}$ = 1.3 Hz), 7.04 (ddd, 2H, *H-6*, $J_{6\text{-}5}$ = 7.8 Hz, $J_{6\text{-}7}$ = 7.5 Hz, $J_{6\text{-}8}$ = 1.3 Hz), 7.02 (ddd, 2H, *H-2*, $J_{2\text{-}3}$ = 7.6 Hz, $J_{2\text{-}1}$ = 5.8 Hz, $J_{2\text{-}4}$ = 1.6 Hz), 6.92 (ddd, 2H, *H-7*, $J_{7\text{-}6}$ = $J_{7\text{-}8}$ = 7.5 Hz, $J_{7\text{-}5}$ = 1.4 Hz), 6.28 (dd, 2H, *H-8*, $J_{8\text{-}7}$ = 7.5 Hz, $J_{8\text{-}6}$ = 1.3 Hz).

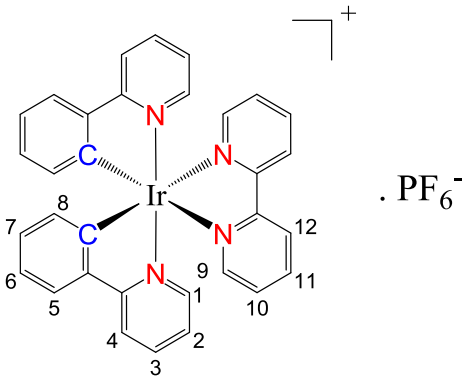

Bis (2,2′-bipyridine-N,N′) dichloroiridium(III) hexafluorophosphate *[IrN$_4$Cl$_2$]$^+$*. Ammonium hexachloroiridate (III) hydrate (51.1 mg, 0.111 mmol) and 2,2′-bipyridine (33.1 mg, 0.212 mmol) were suspended in ethyleneglycol (4.0 mL). After being purged with Argon, the suspended mixture was stirred and heated to 180°C in a microwave (500W) for 15 min. The solution was cooled to room temperature and an aqueous solution (3 mL) of KPF_6 (389.6 mg, 2.12 mmol) was added for the precipitation. The orange solid was washed successively with excess water, ethanol and diethylether to afford the desired product as an orange solid (46.9 mg, 59%). HRMS (ESI): m/z calculated for $[C_{20}H_{16}Cl_2{}^{193}IrN_4 - PF_6]^+$, 575.03758 ; found: 575.03619, m/z calculated for $[C_{20}H_{15}Cl^{193}IrN_4 - PF_6 - HCl]^+$, 539.06090; found: 539.05982, m/z calculated for $[C_{20}H_{14}{}^{193}IrN_4 - PF_6 - 2HCl]^+$, 503.08422 ; found: 503.08599. ^{1}H NMR (CD_3CN), δ/ppm: 9.78 (dd, 2H, *H-1*, J_{1-2} = 5.7 Hz, J_{1-3} = 1.5 Hz), 8.55 (dd, 2H, *H-4*, J_{4-3} = 8.2 Hz, J_{4-2} = 1.4 Hz), 8.44 (dd, 2H, *H-5*, J_{5-6} = 8.2 Hz, J_{5-7} = 1.4 Hz), 8.37 (ddd, 2H, *H-3*, J_{3-4} = 8.2 Hz, J_{3-2}=7.8 Hz, J_{3-1} = 1.5 Hz), 8.06 (ddd, 2H, *H-6*, J_{6-5} = 8.2 Hz, J_{6-7} = 7.7 Hz, J_{6-8} = 1.4 Hz), 7.98 (ddd, 2H, *H-2*, J_{2-3} = 7.8 Hz, J_{2-1} = 5.7 Hz, J_{2-4} = 1.4 Hz), 7.70 (dd, 2H, *H-8*, J_{8-7} = 5.8 Hz, J_{8-6} = 1.4 Hz), 7.38 (ddd, 2H, *H-7*, J_{7-6} = 7.7 Hz, J_{7-8} = 5.8 Hz, J_{7-5} = 1.4 Hz).

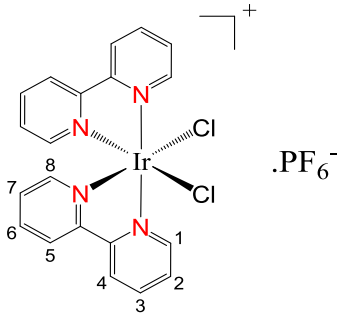

Bis (2,2′-bipyridine-N,N′) bis triflate iridium(III) triflate. $[Ir(bpy)_2Cl_2]PF_6$ (18.8 mg, 0.0260 mmol) was suspended in *o*-dichlorobenzene (1.7 mL) and triflic acid (100 µL, 1.13 mmol) was added. The mixture was stirred and refluxed under Argon atmosphere for 1 h. After this period, the solution was cooled to room temperature and another portion of triflic acid (100 µL, 1.13 mmol) was added. The mixture was brought again to reflux for 2 h. When the solution was cooled to room temperature, diethylether was added dropwise for precipitation. The obtained solid was isolated and washed with diethylether (105.0 mg, 94%). HRMS (ESI): m/z calculated for $[C_{22}H_{16}F_6IrN_4O_6S_2 - OTf]^+$, 803.00392; found: 803.00332. ^1H NMR (CD_3CN), δ/ppm: 9.21 (dd, 2H, *H-1*, J_{1-2} = 5.7 Hz, J_{1-3} = 1.4 Hz), 8.65 (dd, 2H, *H-4*, J_{4-3} = 8.2 Hz, J_{4-2} = 1.4 Hz), 8.53 (ddd, 2H, *H-3*, J_{3-4} = 8.2 Hz, J_{3-2}=7.9 Hz, J_{3-1} = 1.4 Hz), 8.47 (dd, 2H, *H-5*, J_{5-6} = 8.1 Hz, J_{5-7} = 1.5 Hz), 8.17 (ddd, 2H, *H-2*, J_{2-3} = 7.9 Hz, J_{2-1} = 5.7 Hz, J_{2-4} = 1.4 Hz), 8.11 (ddd, 2H, *H-6*, J_{6-5} = 8.1 Hz, J_{6-7} = 7.8 Hz, J_{6-8} = 1.4 Hz), 7.52 (dd, 2H, *H-8*, J_{8-7} = 6.0 Hz, J_{8-6} = 1.4 Hz), 7.43 (ddd, 2H, *H-7*, J_{7-6} = 7.8 Hz, J_{7-8} = 6.0 Hz, J_{7-5} = 1.5 Hz). ^{19}F NMR (CD_3CN), δ/ppm: -379.83 (s, 3F, free triflate), -380.18 (s, 6F, chelated triflate).

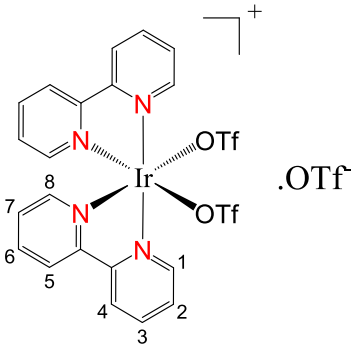

Bis (2,2′-bipyridine-N,N′) (2-phenylpyridine-N,C³) iridium(III) hexafluorophosphate *[IrN₅C₁]*²⁺. [Ir(bpy)₂(OTf)₂]OTf (29.7 mg, 0.0312 mmol) was mixed in a minimum amount of 2-ethoxyethanol (0.9 mL) and heated to reflux. At this step, 2-phenylpyridine (44.6 μL, 0.312 mmol) was added. The mixture was refluxed for 1 h under Argon atmosphere. The solution was cooled to room temperature and a saturated aqueous solution of KPF_6 (172.3 mg, 0.936 mmol) was added. After 2 days in the fridge, the solid was washed successively with water, ethanol and diethylether. The washings were put on a preparative plate on silica with CH_3CN:H_2O:$NH_4Cl_{(aq)}$ / 4:5:1 as eluent. The fraction with Rf = 0.3 was collected to afford a yellow solid (6.7 mg, 20%). HRMS (ESI): m/z calculated for $[C_{31}H_{24}F_6{}^{193}IrN_5P - PF_6]^+$, 804.1297; found: 804.1287, m/z calculated for $[C_{31}H_{24}IrN_5 - 2PF_6]^{2+}$, 329.5825; found: 329.5826. ^1H NMR (CD_3CN), δ/ppm: 8.62 (dd, 1H, *H-3.Pyr1*, $J_{3.Pyr1\text{-}4.Pyr1}$ = 8.0 Hz, $J_{3.Pyr1\text{-}5.Pyr1}$ = 0.6 Hz), 8.57 (dd, 1H, *H-3.Pyr2*, $J_{3.Pyr2\text{-}4.Pyr2}$ = 8.1 Hz, $J_{3.Pyr2\text{-}5.Pyr2}$ = 0.7 Hz), 8.53 (dd, 1H, *H-3.Pyr3*, $J_{3.Pyr3\text{-}4.Pyr3}$ = 7.8 Hz, $J_{3.Pyr3\text{-}5.Pyr3}$ = 0.6 Hz), 8.51 (dd, 1H, *H-3.Pyr4*, $J_{3.Pyr4\text{-}4.Pyr4}$ = 7.8 Hz, $J_{3.Pyr4\text{-}5.Pyr4}$ = 0.7 Hz), 8.30 (ddd, 1H, *H-4.Pyr1*, $J_{4.Pyr1\text{-}3.Pyr1}$ = 8.0 Hz, $J_{4.Pyr1\text{-}5.Pyr1}$ = 7.8 Hz, $J_{4.Pyr1\text{-}6.Pyr1}$ = 1.5 Hz), 8.25 (ddd, 1H, *H-4.Pyr3*, $J_{4.Pyr3\text{-}5.Pyr3}$ = 8.0 Hz, $J_{4.Pyr3\text{-}3.Pyr3}$ = 7.9 Hz, $J_{4.Pyr3\text{-}6.Pyr3}$ = 1.4 Hz), 8.22 (ddd, 1H, *H-4.Pyr4*, $J_{4.Pyr4\text{-}3.Pyr4}$ = $J_{4.Pyr4\text{-}5.Pyr4}$ = 7.8 Hz, $J_{4.Pyr4\text{-}6.Pyr4}$ = 1.4 Hz), 8.21 (dd, 1H, *H-3.Pyr5*, $J_{3.Pyr5\text{-}4.Pyr5}$ = 7.8 Hz, $J_{3.Pyr5\text{-}5.Pyr5}$ = 0.7 Hz), 8.20 (ddd, 1H, *H-4.Pyr2*, $J_{4.Pyr2\text{-}3.Pyr2}$ = 8.1 Hz, $J_{4.Pyr2\text{-}5.Pyr2}$ = 7.9 Hz, $J_{4.Pyr2\text{-}6.Pyr2}$ = 1.2 Hz), 8.00 (ddd, 1H, *H-4.Pyr5*, $J_{4.Pyr5\text{-}3.Pyr5}$ = 7.8 Hz, $J_{4.Pyr5\text{-}5.Pyr5}$ = 7.5 Hz, $J_{4.Pyr5\text{-}6.Pyr5}$ = 1.5 Hz), 7.97 (dd, 1H, *H-6.Pyr2*, $J_{6.Pyr2\text{-}5.Pyr2}$ = 6.0 Hz, $J_{6.Pyr2\text{-}4.Pyr2}$ = 1.2 Hz), 7.94 (dd, 1H, *H-4*, $J_{4\text{-}3}$ = 7.8 Hz, $J_{4\text{-}2}$ = 1.1 Hz), 7.90 (dd, 1H, *H-6.Pyr1*, $J_{6.Pyr1\text{-}5.Pyr1}$ = 5.5 Hz, $J_{6.Pyr1\text{-}4.Pyr1}$ = 1.5 Hz), 7.70 (m, 2H, *H-6.Pyr3* + *H-6.Pyr4*), 7.66 (ddd, 1H, *H-5.Pyr1*, $J_{5.Pyr1\text{-}4.Pyr1}$ = 7.8 Hz, $J_{5.Pyr1\text{-}6.Pyr1}$ = 5.5 Hz, $J_{5.Pyr1\text{-}3.Pyr1}$ = 0.6 Hz), 7.59 (dd, 1H, *H-6.Pyr5*, $J_{6.Pyr5\text{-}5.Pyr5}$ = 6.0 Hz, $J_{6.Pyr5\text{-}4.Pyr5}$

= 1.5 Hz), 7.53 (ddd, 1H, *H-5.Pyr3*, $J_{5.Pyr3\text{-}4.Pyr3}$ = 8.0 Hz, $J_{5.Pyr3\text{-}6.Pyr3}$ = 5.9 Hz, $J_{5.Pyr3\text{-}3.Pyr3}$ = 0.6 Hz), 7.51 (ddd, 1H, *H-5.Pyr4*, $J_{5.Pyr4\text{-}4.Pyr4}$ = 7.8 Hz, $J_{5.Pyr4\text{-}6.Pyr4}$ = 5.9 Hz, $J_{5.Pyr4\text{-}3.Pyr4}$ = 0.7 Hz), 7.50 (ddd, 1H, *H-5.Pyr2*, $J_{5.Pyr2\text{-}4.Pyr2}$ = 7.9 Hz, $J_{5.Pyr2\text{-}6.Pyr2}$ = 6.0 Hz, $J_{5.Pyr2\text{-}3.Pyr2}$ = 0.7 Hz), 7.23 (ddd, 1H, *H-3*, $J_{3\text{-}4}$ = 7.8 Hz, $J_{3\text{-}2}$ = 7.6 Hz, $J_{3\text{-}1}$ = 0.8 Hz), 7.19 (ddd, 1H, *H-5.Pyr5*, $J_{5.Pyr5\text{-}4.Pyr5}$ = 7.5 Hz, $J_{5.Pyr5\text{-}6.Pyr5}$ = 6.0 Hz, $J_{5.Pyr5\text{-}3.Pyr5}$ = 0.7 Hz), 7.06 (ddd, 1H, *H-2*, $J_{2\text{-}3}$ = $J_{2\text{-}1}$ = 7.6 Hz, $J_{2\text{-}4}$ = 1.1 Hz), 6.20 (dd, 1H, *H-1*, $J_{1\text{-}2}$ = 7.6 Hz, $J_{1\text{-}3}$ = 0.9 Hz).

Pyr1, Pyr2, Pyr3, Pyr4 and Pyr5 are undefined Pyridine residues

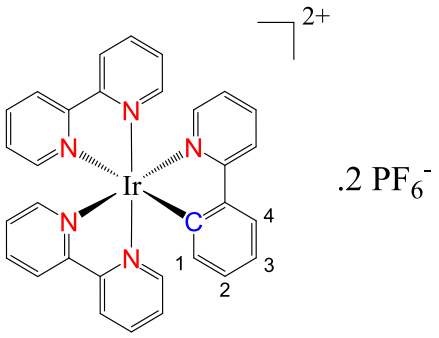

Tris (2,2′-bipyridine-N,N′) iridium(III) hexafluorophosphate ***[IrN$_6$]$^{3+}$*****.** 2,2′-bipyridine (0.1114, 0.713 mmol) was suspended in ethyleneglycol (6,5 mL) and the mixture was deoxygenated and kept under Argon atmosphere. [Ir(bpy)$_2$(OTf)$_2$]OTf (34.0 mg, 0.0357 mmol) was added and the suspension was heated to reflux for 5 h. The reaction mixture was cooled to room temperature. A saturated aqueous solution of KPF_6 (5 mL) was added for precipitation. The precipitate was washed with water and dried under vacuum. The remaining solid was washed with diethylether and dried (31.2 mg, 80%). HRMS (ESI): m/z calculated for [$C_{30}H_{24}F_{12}{}^{193}IrN_6P_2$ – PF_6]$^+$, 951.09698 ; found: 951.09651, m/z calculated for [$C_{30}H_{24}F_6{}^{193}IrN_6P$ – 2 PF_6]$^{2+}$, 403.06613 ; found: 403.06593. ^{1}H NMR (CD_3CN), δ/ppm: 8.66 (dd, 6H, *H-4*, $J_{4\text{-}3}$ = 8.3 Hz, $J_{4\text{-}2}$ = 1.3 Hz), 8.39 (ddd, 6H, *H-3*, $J_{3\text{-}4}$ = 8.3 Hz, $J_{3\text{-}2}$ = 7.4 Hz, $J_{3\text{-}1}$ = 1.4 Hz), 7.68 (m, 12H, *H-1* + *H-2*).

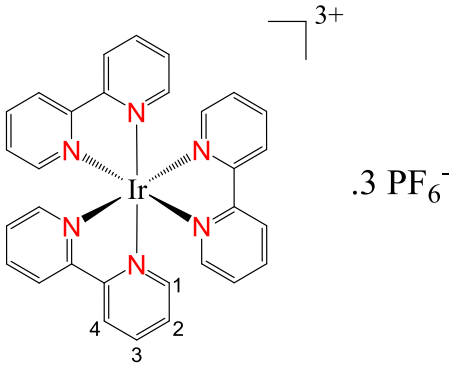

.3 PF_6^-

(2,2′-bipyridine-N,N′) (2,2′-bipyridine-N,C³) dichloroiridium(III) ***[IrN₃CCl₂]*****.** Ammonium hexachloroiridate (III) hydrate (61.3 mg, 0.128 mmol) and 2,2′-bipyridine (41.1 mg, 0.263 mmol) were suspended in ethyleneglycol (5.5 mL). After being purged with Argon, the suspended mixture was stirred and heated to 180°C in a microwave (500W) for 15 min. The solution was cooled to room temperature and a saturated aqueous solution of KPF_6 (360.1 mg, 1.96 mmol) was added for the precipitation. The orange solid was washed successively with water and dissolved in ethanol to remove the side products. The crude product was put on a column chromatography on alumina using acetone as eluent. The first collected fraction corresponded to the desired product (23.1 mg, 31%). HRMS (ESI): m/z calculated for $[C_{20}H_{16}{}^{193}IrN_4Cl_2 + H]^+$, 575.03758; found: 575.03652, m/z calculated for $[C_{20}H_{15}{}^{193}IrN_4Cl - Cl]^+$, 539.0609; found: 539.0583. ^1H NMR (CD_3CN), δ/ppm: 9.79 (dd, 1H, *H-1*, J_{1-2} = 5.4 Hz, J_{1-3} = 1.6 Hz), 8.59 (dd, 1H, *H-15*, J_{15-14} = 7.6 Hz, J_{15-13} = 1.7 Hz), 8.50 (dd, 1H, *H-4*, J_{4-3} = 7.9 Hz, J_{4-2} = 1.1 Hz), 8.38 (dd, 1H, *H-13*, J_{13-14} = 4.6 Hz, J_{13-15} = 1.7 Hz), 8.32 (dd, 1H, *H-5*, J_{5-6} = 8.2 Hz, J_{5-7} = 1.4 Hz), 8.28 (ddd, 1H, *H-3*, J_{3-4} = 7.9 Hz, J_{3-2} = 7.7 Hz, J_{3-1} = 1.6 Hz), 8.23 (dd, 1H, *H-12*, J_{12-11} = 8.0 Hz, J_{12-10} = 1.6 Hz), 7.98 (ddd, 1H, *H-2*, J_{2-3} = 7.7 Hz, J_{2-1} = 5.4 Hz, J_{2-4} = 1.1 Hz), 7.91 (dd, 1H, *H-8*, J_{8-7} = 5.8 Hz, J_{8-6} = 1.5 Hz), 7.81 (ddd, 1H, *H-6*, J_{6-5} = 8.2 Hz, J_{6-7} = 7.6 Hz, J_{6-8} = 1.5 Hz), 7.70 (ddd, 1H, *H-11*, J_{11-12} = 8.0 Hz, J_{11-10} = 7.5 Hz, J_{11-9} = 1.4 Hz), 7.58 (dd, 1H, *H-9*, J_{9-10} = 5.9 Hz, J_{9-11} = 1.4 Hz), 7.26 (dd, 1H, *H-14*, J_{14-15} = 7.6 Hz, J_{14-13} = 4.6 Hz), 7.16 (ddd, 1H, *H-7*, J_{7-6} = 7.6 Hz, J_{7-8} = 5.8 Hz, J_{7-5} = 1.4 Hz), 6.99 (ddd, 1H, *H-10*, J_{10-11} = 7.5 Hz, J_{10-9} = 5.9 Hz, J_{10-12} = 1.6 Hz).

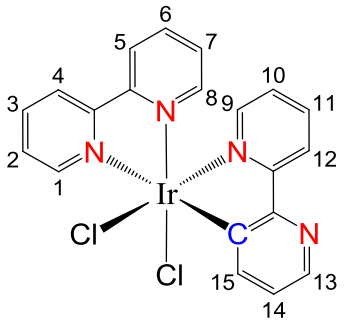
6
5
7
4
10
3
8
9
11
N
N
N
2
12
1
Ir
Cl
C
N
Cl
15
13
14

Bis (2,2′-bipyridine-N,N′) (2,2′-bipyridine-N,C³) iridium(III) hexafluorophosphate *[R-IrN₅C₁]*²⁺. **[**Ir(N,N′-bpy)(N,C³-bpy)Cl₂] (16.0 mg, 0.0279 mmol) and 2,2′-bipyridine (13.3 mg, 0.0852 mmol) were suspended in ethyleneglycol (2.1 mL). After being purged with Argon, the suspended mixture was stirred and heated to reflux overnight. The solution was cooled to room temperature and a saturated aqueous solution of KPF_6 (102.5 mg, 0.557 mmol) was added for the precipitation. The orange solid was washed successively with water, ethanol and diethylether to afford the desired product to afford the desired product (4.0 mg, 15%). HRMS (ESI): m/z calculated for $[C_{30}H_{23}F_6{}^{193}IrN_6P - PF_6]^+$, 805.12498; found: 805.12504, m/z calculated for $[C_{30}H_{23}IrN_6 - 2PF_6]^{2+}$, 330.08067; found: 330.07991. ^1H NMR (CD_3CN), δ/ppm: 8.63 (dd, 1H, *H-12*, $J_{12\text{-}11}$ = 8.1 Hz, $J_{12\text{-}10}$ = 1.1 Hz), 8.58 (dd, 1H, *H-13*, $J_{13\text{-}14}$ = 8.1 Hz, $J_{13\text{-}15}$ = 1.4 Hz), 8.54 (dd, 1H, *H-5*, $J_{5\text{-}6}$ = 8.1 Hz, $J_{5\text{-}7}$ = 1.2 Hz), 8.52 (dd, 1H, *H-4*, $J_{4\text{-}3}$ = 8.1 Hz, $J_{4\text{-}2}$ = 1.3 Hz), 8.47 (dd, 1H, *H-20*, $J_{20\text{-}19}$ = 8.0 Hz, $J_{20\text{-}18}$ = 1.6 Hz), 8.42 (dd, 1H, *H-21*, $J_{21\text{-}22}$ = 4.7 Hz, $J_{21\text{-}23}$ = 1.6 Hz), 8.32 (ddd, 1H, *H-11*, $J_{11\text{-}12}$ = 8.1 Hz, $J_{11\text{-}10}$ = 7.9 Hz, $J_{11\text{-}9}$ = 1.6 Hz), 8.26 (ddd, 1H, *H-6*, $J_{6\text{-}5}$ = 8.1 Hz, $J_{6\text{-}7}$ = 8.0 Hz, $J_{6\text{-}8}$ = 1.5 Hz), 8.24 (ddd, 1H, *H-3*, $J_{3\text{-}4}$ = 8.1 Hz, $J_{3\text{-}2}$ = 8.0 Hz, $J_{3\text{-}1}$ = 1.5 Hz), 8.22 (ddd, 1H, *H-14*, $J_{14\text{-}13}$ = 8.1 Hz, $J_{14\text{-}15}$ = 7.7 Hz, $J_{14\text{-}16}$ = 1.5 Hz), 8.09 (ddd, 1H, *H-19*, $J_{19\text{-}20}$ = 8.0 Hz, $J_{19\text{-}18}$ = 7.7 Hz, $J_{19\text{-}17}$ = 1.5 Hz), 8.00 (dd, 1H, *H-16*, $J_{16\text{-}15}$ = 5.8 Hz, $J_{16\text{-}14}$ = 1.5 Hz), 7.90 (dd, 1H, *H-9*, $J_{9\text{-}10}$ = 5.5 Hz, $J_{9\text{-}11}$ = 1.6 Hz), 7.71 (m, 2H, *H-8* + *H-1*), 7.68 (ddd, 1H, *H-10*, $J_{10\text{-}11}$ = 7.9 Hz, $J_{10\text{-}9}$ = 5.5 Hz, $J_{10\text{-}12}$ = 1.1 Hz), 7.60 (dd, 1H, *H-17*, $J_{17\text{-}18}$ = 5.8 Hz, $J_{17\text{-}19}$ = 1.5 Hz), 7.54 (m, 2H, *H-7* + *H-2*), 7.51 (ddd, 1H, *H-15*, $J_{15\text{-}14}$ = 7.7 Hz, $J_{15\text{-}16}$ = 5.8 Hz, $J_{15\text{-}13}$ = 1.4 Hz), 7.34 (ddd, 1H, *H-18*, $J_{18\text{-}19}$ = 7.7 Hz, $J_{18\text{-}17}$ = 5.8 Hz, $J_{18\text{-}20}$ = 1.6 Hz), 7.01 (dd, 1H, *H-22*, $J_{22\text{-}23}$ = 7.7 Hz, $J_{22\text{-}21}$ = 4.7 Hz), 6.63 (dd, 1H, *H-23*, $J_{23\text{-}22}$ = 7.7 Hz, $J_{23\text{-}21}$ = 1.6 Hz).

(for description of the ^1H NMR attribution, see next chapter)

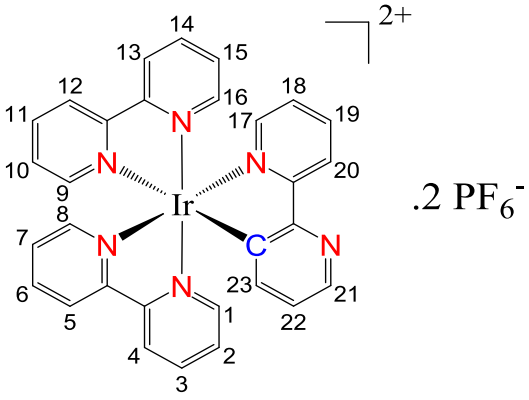
2+
14
13
15
12
16
18
11
17
19
N
N
N
10
9
20
Ir
8
7
N
C
N
6
N
23
21
5
1
22
4
2
3
.2 PF6-

2.7 References

1. Li, J.; Djurovich, P. I.; Alleyne, B. D.; Yousufuddin, M.; Ho, N. N.; Thomas, J. C.; Peters, J. C.; Bau, R.; Thompson, M. E., Synthetic control of excited-state properties in cyclometalated Ir(III) complexes using ancillary ligands. *Inorg. Chem.* **2005**, *44*, 1713-1727.
2. Dixon, I. M.; Collin, J.-P.; Sauvage, J.-P.; Flamigni, L.; Encinas, S.; Barigelletti, F., A family of luminescent coordination compounds: iridium(iii) polyimine complexes. *Chem. Soc. Rev.* **2000**, *29*, 385-391.
3. Flamigni, L.; Barbieri, A.; Sabatini, C.; Ventura, B.; Barigelletti, F., Photochemistry and Photophysics of Coordination Compounds: Iridium. *Top. Curr. Chem.* **2007**, *281*, 143-203.
4. Yu, T.; Zeng, Y.; Chen, J.; Li, Y. Y.; Yang, G.; Li, Y., Exceptional dendrimer-based mimics of diiron hydrogenase for the photochemical production of hydrogen. *Angew. Chem. Int. Ed.* **2013**, *52*, 5631-5635.
5. Constable, E. C.; Neuburger, M.; Rosel, P.; Schneider, G. E.; Zampese, J. A.; Housecroft, C. E.; Monti, F.; Armaroli, N.; Costa, R. D.; Orti, E., Ligand-based charge-transfer luminescence in ionic cyclometalated iridium(III) complexes bearing a pyrene-functionalized bipyridine ligand: a joint theoretical and experimental study. *Inorg. Chem.* **2013**, *52*, 885-897.
6. Shao, F.; Elias, B.; Lu, W.; Barton, J. K., Synthesis and characterization of iridium(III) cyclometalated complexes with oligonucleotides: insights into redox reactions with DNA. *Inorg. Chem.* **2007**, *46*, 10187-10199.
7. Whittle, V. L.; Williams, J. A., A new class of iridium complexes suitable for stepwise incorporation into linear assemblies: synthesis, electrochemistry, and luminescence. *Inorg. Chem.* **2008**, *47*, 6596-6607.
8. Goldsmith, J. I.; Hudson, W. R.; Lowry, M. S.; Anderson, T. H.; Bernhard, S., Discovery and High-Throughput Screening of Heteroleptic Iridium Complexes for Photoinduced Hydrogen Production. *J. Am. Chem. Soc.* **2005**, *127*, 7502-7510.
9. Kim, J. I.; Shin, I. S.; Kim, H.; Lee, J. K., Efficient electrogenerated chemiluminescence from cyclometalated iridium(III) complexes. *J. Am. Chem. Soc.* **2005**, *127*, 1614-1615.
10. Rueping, M.; Vila, C., Visible light photoredox-catalyzed multicomponent reactions. *Org. Lett.* **2013**, *15*, 2092-2095.
11. Ren, X.; Kondakova, M. E.; Giesen, D. J.; Rajeswaran, M.; Madaras, M.; Lenhart, W. C., Coumarin-based, electron-trapping iridium complexes as highly efficient and stable phosphorescent emitters for organic light-emitting diodes. *Inorg. Chem.* **2010**, *49*, 1301-1303.

12. Dedeian, K.; Shi, J.; Shepherd, N.; Forsythe, E.; Morton, D. C., Photophysical and electrochemical properties of heteroleptic tris-cyclometalated iridium(III) complexes. *Inorg. Chem.* **2005**, *44*, 4445-4447.
13. Sajoto, T.; Djurovich, P. I.; Tamayo, A. B.; Oxgaard, J.; Goddard, W. A., 3rd; Thompson, M. E., Temperature dependence of blue phosphorescent cyclometalated Ir(III) complexes. *J. Am. Chem. Soc.* **2009**, *131*, 9813-9822.
14. Yang, C. H.; Fang, K. H.; Chen, C. H.; Sun, I. W., High efficiency mer-iridium complexes for organic light-emitting diodes. *Chem. Commun.* **2004**, 2232-2233.
15. Aoki, S.; Matsuo, Y.; Ogura, S.; Ohwada, H.; Hisamatsu, Y.; Moromizato, S.; Shiro, M.; Kitamura, M., Regioselective aromatic substitution reactions of cyclometalated Ir(III) complexes: synthesis and photochemical properties of substituted Ir(III) complexes that exhibit blue, green, and red color luminescence emission. *Inorg. Chem.* **2011**, *50*, 806-818.
16. Finlayson, M. F.; Ford, P. C.; Watts, R. J., Excited states and transients formed in laser flash photolysis of iridium(III) complexes of 2,2'-bipyridine. *J. Phys. Chem.* **1986**, *90*, 3916-3922.
17. Minaev, B.; Ågren, H.; Angelis, F. D., Theoretical design of phosphorescence parameters for organic electro-luminescence devices based on iridium complexes. *Chem. Phys.* **2009**, *358*, 245-257.
18. Abdel-Shafi, A. A.; Bourdelande, J. L.; Ali, S. S., Photosensitized generation of singlet oxygen from rhenium(I) and iridium(III) complexes. *Dalton Trans.* **2007**, 2510-2516.
19. King, K. A.; Watts, R. J., Dual emission from an ortho-metalated iridium(III) complex. *J. Am. Chem. Soc.* **1987**, *109*, 1589-1590.
20. Constable, E. C.; Leese, T. A., Metal exchange in organomercury complexes; a facile route to cyclometallated transition metal complexes. *J. Organomet. Chem.* **1987**, *335*, 293-299.
21. Watts, R. J.; Harrington, J. S.; Van Houten, J., A stable monodentate 2,2'-bipyridine complex of iridium(III): a model for reactive intermediates in ligand displacement reactions of tris-2,2'-bipyridine metal complexes. *J. Am. Chem. Soc.* **1977**, *99*, 2179-2187.
22. Nord, G.; Hazell, A. C.; Hazell, R. G.; Farver, O., A carbon-bonded tris(2,2'-bipyridine)iridium(III) complex: (2,2'-bipyridinyl-C3,N')bis(2,2'-bipyridine-N,N')iridium(III) perchlorate-water (3/1). *Inorg. Chem.* **1983**, *22*, 3429-3434.
23. Braterman, P. S.; Heath, G. A.; MacKenzie, A. J.; Noble, B. C.; Peacock, R. D.; Yellowlees, L. J., Solution structure and properties of the [(2,2'-bipyridinyl-C3,N')bis(2,2'-bipyridine-N,N')iridium(III)](2+) hydrate ion, "pseudo-[Ir(bpy)3(OH)]2+". *Inorg. Chem.* **1984**, *23*, 3425-3426.
24. Nonoyama, M., Benzo[h]quinolin-10-yl-NIridium(III) Complexes. *Bull. Chem. Soc. Jpn.* **1974**, *47*, 767-768.

25. Garces, F. O.; Watts, R. J., A new ortho-metalated dichloro-bridged complex of iridium(III) with 2,2'-bipyridine: [{Ir(bpy-C3,N')(bpy-N,N')Cl}2][Cl]2. *Inorg. Chem.* **1990**, *29*, 582-584.
26. McGee, K. A.; Mann, K. R., Selective low-temperature syntheses of facial and meridional tris-cyclometalated iridium(III) complexes. *Inorg. Chem.* **2007**, *46*, 7800-7809.
27. Dedeian, K.; Djurovich, P. I.; Garces, F. O.; Carlson, G.; Watts, R. J., A new synthetic route to the preparation of a series of strong photoreducing agents: fac-tris-ortho-metalated complexes of iridium(III) with substituted 2-phenylpyridines. *Inorg. Chem.* **1991**, *30*, 1685-1687.
28. Grushin, V. V.; Herron, N.; LeCloux, D. D.; Marshall, W. J.; Petrov, V. A.; Wang, Y., New, efficient electroluminescent materials based on organometallic Ir complexes. *Chem. Commun.* **2001**, 1494-1495.
29. Tamayo, A. B.; Alleyne, B. D.; Djurovich, P. I.; Lamansky, S.; Tsyba, I.; Ho, N. N.; Bau, R.; Thompson, M. E., Synthesis and characterization of facial and meridional tris-cyclometalated iridium(III) complexes. *J. Am. Chem. Soc.* **2003**, *125*, 7377-7387.
30. Matsumoto, T.; Periana, R. A.; Taube, D. J.; Yoshida, H., Regioselective hydrophenylation of olefins catalyzed by an Ir(III) complex. *J. Mol. Catal. A: Chem.* **2002**, *180*, 1-18.
31. Yoshikawa, N.; Masuda, Y.; Matsumura-Inoue, T., Rapid Synthesis of New Emitting Ir(III) Polypyridine Complexes. *Chem. Lett.* **2000**, *29*, 1206-1207.
32. Tsuboyama, A.; Iwawaki, H.; Furugori, M.; Mukaide, T.; Kamatani, J.; Igawa, S.; Moriyama, T.; Miura, S.; Takiguchi, T.; Okada, S.; Hoshino, M.; Ueno, K., Homoleptic cyclometalated iridium complexes with highly efficient red phosphorescence and application to organic light-emitting diode. *J. Am. Chem. Soc.* **2003**, *125*, 12971-12979.
33. Lowry, M. S.; Hudson, W. R.; Pascal, R. A., Jr.; Bernhard, S., Accelerated luminophore discovery through combinatorial synthesis. *J. Am. Chem. Soc.* **2004**, *126*, 14129-14135.
34. Laskar, I. R.; Chen, T.-M., Tuning of Wavelengths: Synthesis and Photophysical Studies of Iridium Complexes and Their Applications in Organic Light Emitting Devices. *Chem. Mater.* **2004**, *16*, 111-117.
35. Lowry, M. S.; Bernhard, S., Synthetically tailored excited states: phosphorescent, cyclometalated iridium(III) complexes and their applications. *Chem. Eur. J.* **2006**, *12*, 7970-7977.
36. Zanoni, K. P.; Coppo, R. L.; Amaral, R. C.; Murakami Iha, N. Y., Ir(III) complexes designed for light-emitting devices: beyond the luminescence color array. *Dalton Trans.* **2015**, *44*, 14559-14573.

37. Takayasu, S.; Suzuki, T.; Shinozaki, K., Intermolecular interactions and aggregation of fac-tris(2-phenylpyridinato-C2,N)iridium(III) in nonpolar solvents. *J. Phys. Chem. B* **2013**, *117*, 9449-9456.
38. Watts, R. J., Photogeneration of Strong One- and Two-Electron Redox Agents from Transition Metal Complexes. *Comments Inorg. Chem.* **1991**, *11*, 303-337.
39. Hofbeck, T.; Yersin, H., The triplet state of fac-Ir(ppy)3. *Inorg. Chem.* **2010**, *49*, 9290-9299.
40. Garces, F. O.; King, K. A.; Watts, R. J., Synthesis, structure, electrochemistry, and photophysics of methyl-substituted phenylpyridine ortho-metalated iridium(III) complexes. *Inorg. Chem.* **1988**, *27*, 3464-3471.
41. Ohsawa, Y.; Sprouse, S.; King, K. A.; DeArmond, M. K.; Hanck, K. W.; Watts, R. J., Electrochemistry and spectroscopy of ortho-metalated complexes of iridium(III) and rhodium(III). *J. Phys. Chem.* **1987**, *91*, 1047-1054.

CHAPTER 3

Exploring photoreactions between pH sensitive $[R\text{-}IrN_5C_1]^{2+}$ and dGMP by photo-Chemically Induced Dynamic Nuclear Polarization (photo-CIDNP)

3.1 Foreword

CIDNP was discovered independently by Bargon, Fischer and Johnsen,[1] and by Ward and Lawler[2] in 1967. This method can monitor free radicals, even with short lifetimes (nanosecond timescale) by studying the NMR signals of the radical compound under specific acquisition conditions (*vide infra*). CIDNP has been widely used as a valuable tool to distinguish reaction pathways involving radicals,[3-7] and especially in the field of protein studies, in the scope of mapping surface accessibility of amino-acid residues for electron transfer reactions.[8-12] In this case, it uses a photosensitizer (usually flavins[8-12] or 2,2′-bipyridine[8-10, 12-13]) to generate a radical pair with an amino-acid the disappearance of which can be followed using CIDNP. It also allows the monitoring of the protein folding pathway as well as its interaction with some cofactors in solution.

Recently, photo-CIDNP NMR has gained interest to study the photoreactivity of Ru(II) complexes in the presence of biomolecules such as *N*-acetyl tyrosine (*N*-Ac-Tyr) or guanosine-5′-monophosphate (GMP).[14] Indeed, polypyridyl Ru(II) complexes are characterized by a unique combination of chemical stability, (photo-)redox properties, excited state reactivity, luminescence emission in the visible light spectrum and long excited state lifetime.[15-16] When the chelated ligands are highly π electron-deficient, *e.g.* 1,4,5,8-tetraazaphenanthrene (TAP), 2,2′-bipyrazine (bpz) or 1,4,5,8,9,12-hexaazatriphenylene (HAT), Ru(II) complexes are able to photooxidize some amino-acids, such as tyrosine and tryptophan, and the guanine nucleobases, yielding to radical pair occurrence (*vide infra*).[17-20] Recent photo-CIDNP studies were used to characterize the photoinduced electron transfer between Ru(II)-TAP complexes and GMP, in different pH conditions.[21]

To the best of our knowledge, such studies have never been performed using Ir(III) complexes as photosensitizer. In this chapter, we demonstrate, in collaboration with Prof. M. Luhmer (Université libre de Bruxelles) and Dr Luca Fusaro, the interest of photo-CIDNP NMR spectroscopy as an efficient tool to determine the nature of the excited state of $[R\text{-}IrN_5C_1]^{2+}$ as well as to probe its behavior in the presence of biological target (such as dGMP) upon variation of pH.

3.2 Introduction

3.2.1 Nuclear spin polarization

All nuclei are characterized by a nuclear spin quantum number, *I*, which may have values multiple of $^1/_2$ greater than or equal to zero (Table 3.1).

Table 3.1 – Selected examples of values of nuclear spin quantum numbers *I* with variation of parity in the atomic number Z and mass number A

A	Z	*I*	examples of nuclei
odd	even or odd	$I = {}^1/_2$	^{1}H, ^{19}F, ^{13}C
		$I = {}^3/_2$	^{11}B, ^{23}Na
		$I = {}^5/_2$	^{17}O, ^{27}Al
even	odd	$I = 1$	^{2}H, ^{14}N
		$I = 3$	^{10}B
even	even	$I = 0$	^{12}C, ^{16}O

All elements with $I \neq 0$ are able to absorb and re-emit electromagnetic radiation at a specific resonance frequency in the radio wave region, when they are in a magnetic field B_0. Indeed, in a static magnetic field, B_0, the 2xI nuclear spin states lose their degeneracy and become separated in energy, allowing to observe transitions between these splitted states. Namely, in a magnetic field B_0, a nucleus with a spin number $I = {}^1/_2$ possesses two different spin states corresponding to the different orientations of the magnetic moment m *i.e. parallel* (spin

"up" ; m = +1/2 ; ↑) or *anti-parallel* (spin "down" ; m = -1/2 ; ↓) to B_0 (Figure 3.1).

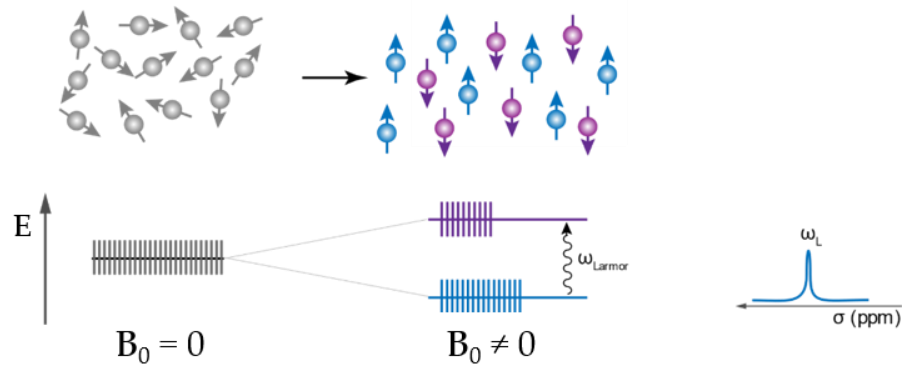

Figure 3.1 – Boltzmann distribution of proton spin when submitted to a static magnetic field B_0 yielding to ^1H NMR signal

The difference in energy between these nuclear spin states is weak, implying an extremely small difference of population in α and β states (Boltzmann distribution). The nuclear polarization by B_0 and, consequently, the observation of a nuclear magnetic resonance (NMR) signal result from this small difference in population (about 1 for 10^5 at 300 K in a field of 9.4 T for ^1H), according to equation 3.1 where $n_{+1/2}$ and $n_{-1/2}$ are the populations in α and β states, respectively.

$$\frac{n_{+1/2} - n_{-1/2}}{n_{+1/2} + n_{-1/2}} \qquad \text{eq 3.1}$$

3.2.2 Photo-CIDNP

3.2.2.1 Theory about photo-CIDNP

Under specific reaction conditions, NMR spectra can exhibit anomalous signal intensities, namely, enhanced absorption or emission. This phenomenon was recognized as spin polarization induced by a deviation from the Boltzmann distribution (Figure 3.2). The photo-Chemically Induced Dynamic Nuclear Polarization (photo-CIDNP) refers to non-Boltzmann spin state distributions in the product of photochemical reactions, involving radical intermediates. The commonly accepted radical-pair mechanism was proposed by Kaptein and Oosterhoff[22] and independently by Closs[23] in 1969. This mechanism is based on two key phenomena: (i) the unique interplay of nuclear-spin dependent intersystem crossing in the radical pairs, which is caused by hyperfine interaction between nuclear spins and the spin of the unpaired electron of the radical and (ii) the electron-spin dependent chemical reactivity of the pairs. (Photo-)CIDNP experiments can thus provide detailed information about reaction intermediates and the pathways of their formation (or disappearance).

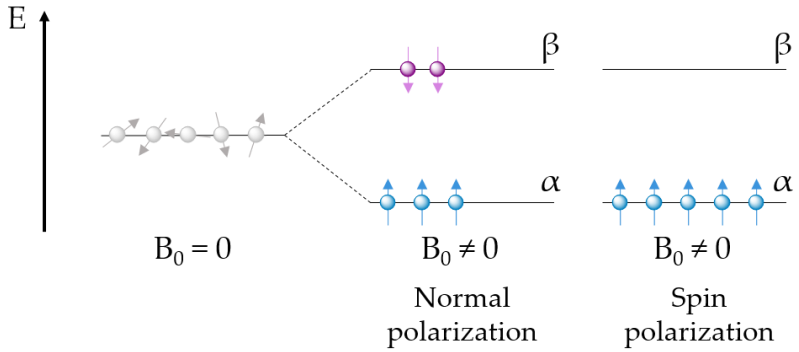

Figure 3.2 – Normal and spin polarization in a magnetic field B_0

The photo-CIDNP mechanism[14] is displayed in Figure 3.3. Photo-CIDNP involves a photosensitizer, P, which absorbs light and which, in its excited state, will react with a target, T.

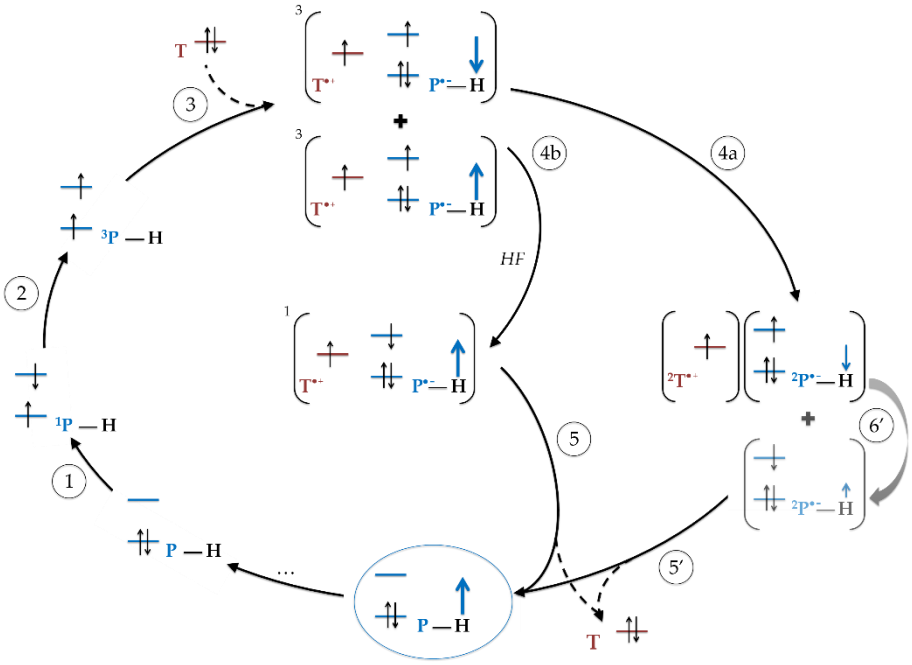

Figure 3.3 – Photo-CIDNP mechanism for the photoinduced electron transfer from the target T to the photosensitizer P

Photo-CIDNP measurements correspond to a difference between two NMR spectra, one recorded before an irradiation of the sample and the other recorded after. Light irradiation of the sample induces modifications of the intensity of NMR peaks,[A] which are called photo-CIDNP effects.

The process responsible for photo-CIDNP effect generation is based on several steps. (i) First, the photosensitizer P is irradiated by

[A] Despite the photo-CIDNP effect can be detected for both photosensitizer P and target T, our attention will be focused on the former.

UV-visible light yielding singlet state $^{1}P^{*}$ (Figure 3.3 – step 1) which undergoes subsequent intersystem crossing (ISC) providing the triplet state $^{3}P^{*}$ (Figure 3.3 – step 2). This ISC is mandatory as no photo-CIDNP effect can take place if the excited photosensitizer remains in a singlet excited state. (ii) Provided that the excited state lifetime of $^{3}P^{*}$ is long enough for a photoreaction to occur, excited $^{3}P^{*}$ and the target T can encounter and an intermolecular electron transfer between T and $^{3}P^{*}$ takes place, yielding to the formation of a radical pair in triplet state, $^{3}\{P^{\bullet-}\ldots\ T^{\bullet+}\}$ (Figure 3.3 – step 3).[B] (iii) The fate of the triplet radical pair, $^{3}\{P^{\bullet-}\ldots\ T^{\bullet+}\}$, is the key step of photo-CIDNP. Two processes are possible for the triplet radical pair; (a) either to dissociate into free radicals, $P^{\bullet-}$ and $T^{\bullet+}$, which are then involved in a back electron transfer (BET) at re-encounter, yielding the *escape products*, P and T (b) or undergo an ISC process yielding the singlet radical pair, $^{1}\{P^{\bullet-}\ldots\ T^{\bullet+}\}$, which undergoes an ultrafast BET, yielding the *geminate products*, P and T. The escape and the geminate products are chemically equivalents, but the reaction pathway is different and influence their respective nuclear spin populations. The key feature of this step is the *spin-sorting* effect; indeed, the probability of a given radical pair $^{3}\{P^{\bullet-}\ldots\ T^{\bullet+}\}$ to yield the geminate or the escape products depends on their nuclear spin state. Indeed, the ISC process is influenced by the nuclear spin state of the neighboring atoms of the radical electron due to *hyperfine coupling*.[C] The HF-ISC (hyperfine coupling intersystem

[B] In this explanation, an oxidative electron transfer of the target is considered but photo-CIDNP effects can also be observed in the case of a reductive photoinduced electron transfer.

[C] It is worth mentioning that another mechanism called *electron spin-orbit coupling interaction* (SOC) can also produce an intersystem crossing from triplet to singlet state for a geminate pair of radicals but, in this case, it thus not induce any spin-sorting and, consequently, no CIDNP effect.

crossing) favors the geminate pathway for one population of nuclear spin, the α state in the example presented in Figure 3.4.

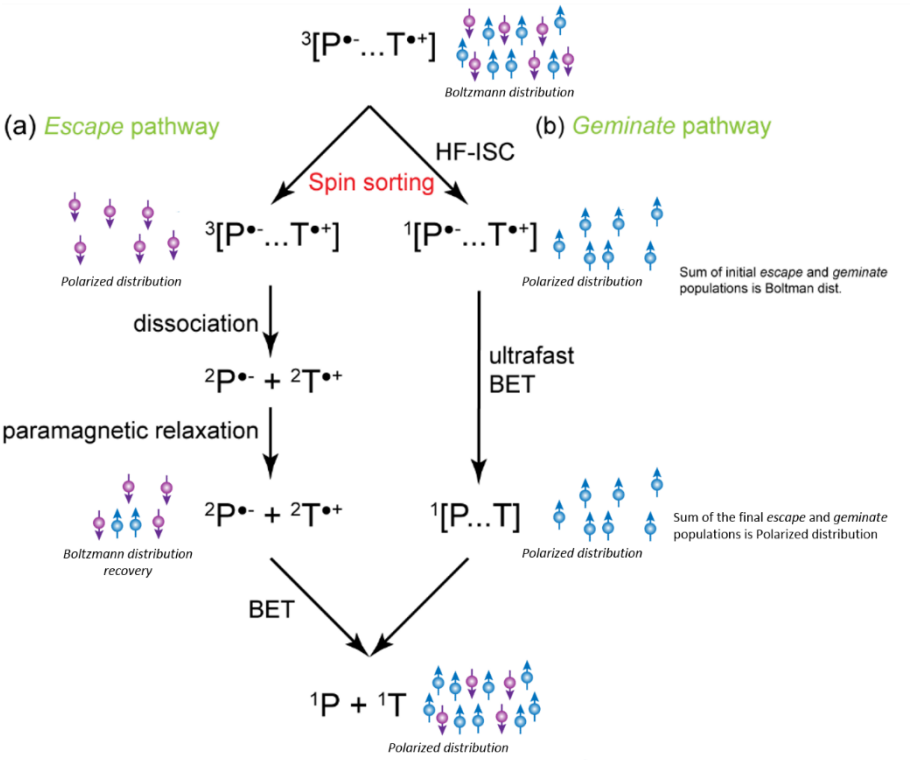

Figure 3.4 – Spin-sorting mechanism for CIDNP enhancements occurrence

As the reaction occurs in a magnetic field B_0, the nuclear spin populations of the original radical pair $^3\{P^{\bullet-}\ldots T^{\bullet+}\}$ obey the Boltzmann distribution. Due to the hyperfine interaction (HF) between the unpaired electrons (the one on the photosensitizer in this case) and the nuclear spin of the neighboring ^1H atom, the population of radical pairs entering in the geminate pathway will display an overrepresentation of α nuclear spin state compared to the Boltzmann distribution, and, reciprocally, the population of radical pairs entering the escape pathway will carry an over-representation of β nuclear

state. At this stage, the sum of the two populations (the one entering the geminate and the other entering the escape pathway) still obey the Boltzmann distribution.

As stated here-before, the radical pairs in the geminate pathway undergo an ultrafast back electron transfer leading to the so-called geminate recombination products, which are the diamagnetic parent compounds. As no process has influenced the nuclear spin state of this population, the geminate products possess a non-Boltzmannian distribution of population, *i.e.* in our case, more α nuclear spin state. In the escape pathway, the radical pair $^{3}\{P^{\bullet -}\ldots\ T^{\bullet +}\}$ dissociate, yielding free radical species. By diffusion, these radicals will eventually recombine and undergo a BET to yield the escape diamagnetic parent compounds. However, during their microsecond lifetime, escape radicals, $^{2}P^{\bullet -}$ and $^{2}T^{\bullet +}$, can undergo paramagnetic relaxation and partially recover the Boltzmann distribution. Paramagnetic relaxation takes place for free radicals in solution over a long timescale; therefore, it only affects escape polarization as the radical species in the geminate pathway have a lifetime shorter than few nanoseconds.

The final detected polarizations are the result of incomplete cancellation of geminate polarizations by escape polarizations (Figure 3.5). The efficiency of paramagnetic relaxation on escape products can be altered by degenerate exchange processes (if they are fast enough compared to relaxation), *i.e.* (i) degenerate electron exchange (equation 3.2) or (ii) degenerate deuterium atom exchange in the case of a protonation of the reduced photosensitizer (equation 3.3). These processes tend to rapidly convert free radicals with escape polarization into diamagnetic compounds.

$$\downarrow P^{\bullet -} + P \longrightarrow \downarrow P + P^{\bullet -} \qquad \text{eq 3.2}$$

$$\downarrow PD^{\bullet} + P \longrightarrow \downarrow P + PD^{\bullet} \qquad \text{eq 3.3}$$

Photo-CIDNP effects are very sensitive and may be not observable in the case of radical reaction; for example, too small hyperfine coupling constants, limited diffusion processes,… can prevent the occurrence of observable photo-CIDNP effects.

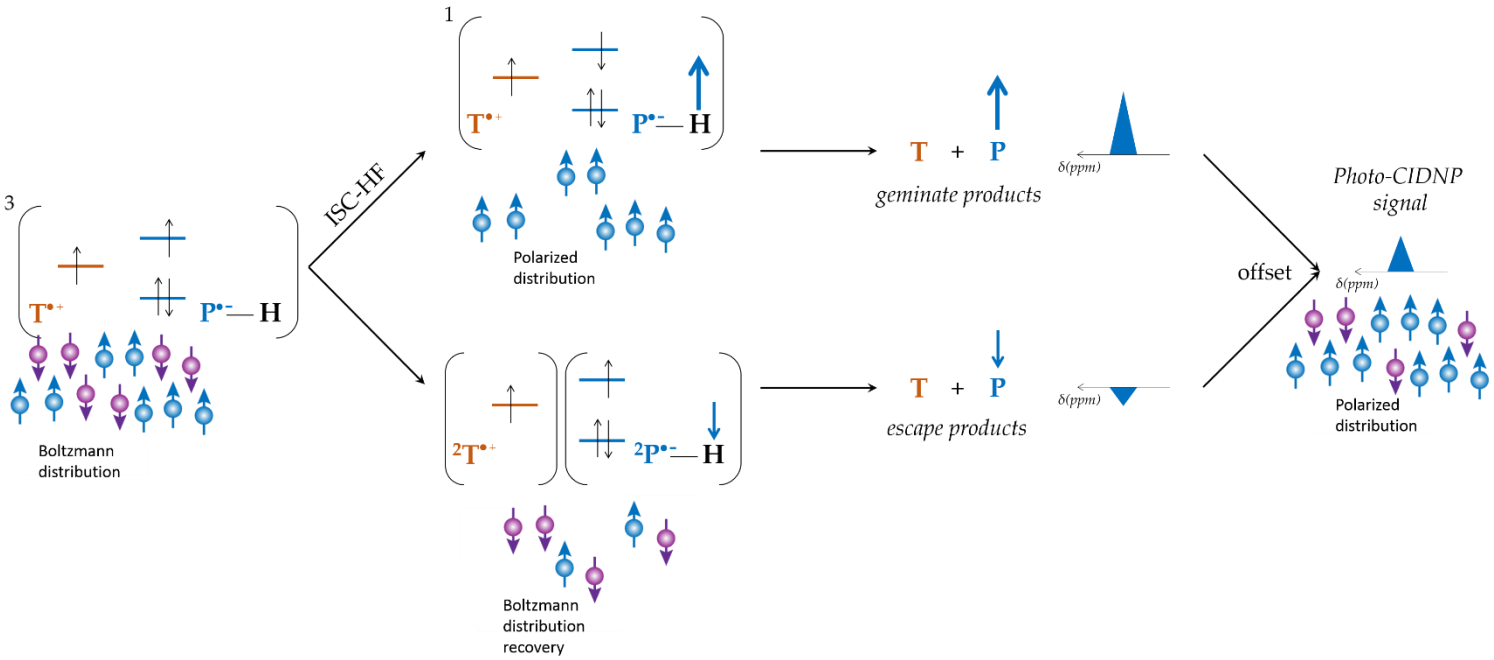

Figure 3.5 – Process for appearance of a photo-CIDNP signal
(where ISC-HF is the intersystem crossing induced by hyperfine interaction)

3.2.2.2 Applications of photo-CIDNP

Photo-CIDNP measurements can be performed with or without time resolution. Time-resolved CIDNP measurements allow the kinetic study of processes such as radical recombination or nuclear spin relaxation while steady-state CIDNP provides information on the compounds structure and their exposure to the surrounding environment. A well-known application of time-resolved CIDNP is the study of protein folding. The basic experiment involves laser irradiation of a solution of the protein and a photosensitizer (usually flavin mononucleotide – FMN) directly followed by detection of the nuclear polarization. The NMR signals of some solvent-accessible aromatic amino acid units *i.e.* tryptophan (Trp), tyrosine (Tyr) and histidine (His), are enhanced compared to equilibrium NMR intensities, giving information on the accessibility of side chains. Indeed, despite known X-ray structures of several proteins, steady-state photo-CIDNP allows direct monitoring of their structure in solution providing supplementary data about their active site. A recent example given by Hore and co-workers is shown with Ribonuclease A (*RNase A*) containing six tyrosine, six histidine and no tryptophan unit.[24] For native bovine pancreatic *RNase A*, four tyrosine (Tyr73, Tyr76, Tyr92 and Tyr115) and two histidine (His105 and His119) residues are found to be solvent accessible and, hence, able to react with a photosensitizer. However, the polarization intensity of a residue is not constant and is specific to the nature of the amino acid. A Stern-Volmer competition with all other accessible residues occurs. The rate constant for quenching of the triplet flavin photosensitizer by histidine is two orders of magnitude smaller than for tyrosine[25] and, therefore, a histidine unit must be highly solvent-accessible compared to tyrosine

units in order to be sufficiently polarized. Indeed, additional steady-state photo-CIDNP measurements reveal emissive enhancements for all the exposed tyrosine residues in native *RNase A* while histidine residues were not polarized yet accessible (Figure 3.6).

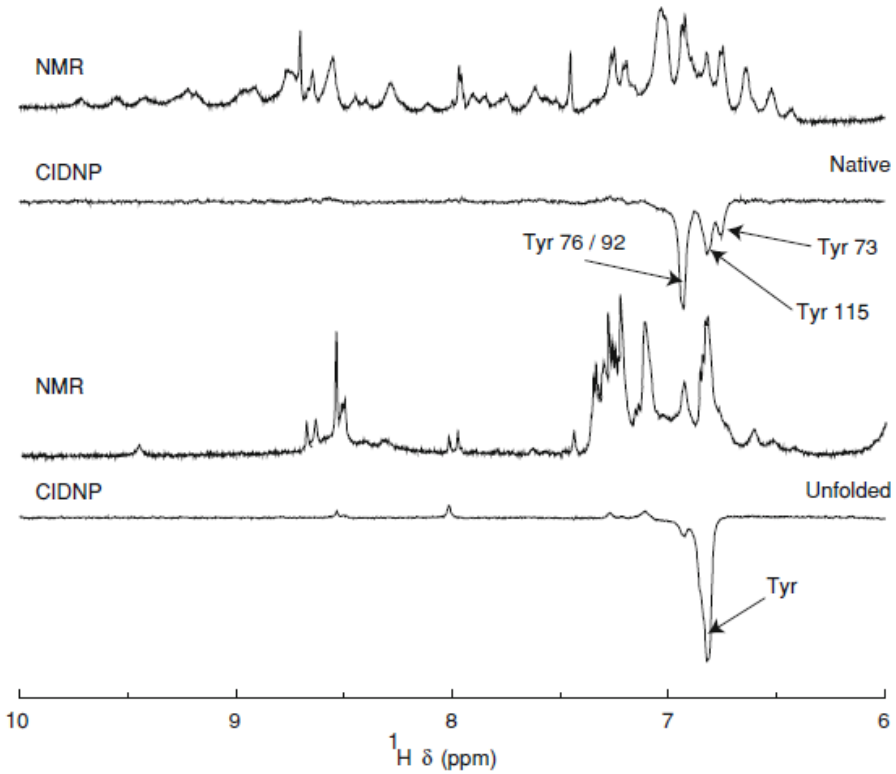

Figure 3.6 – Partial 600 MHz ^{1}H NMR in D_2O and steady-state photo-CIDNP spectra of *RNase A* in its native (*up*) and unfolded (*down*) states (from [24])

Molten proteins under refolding conditions are recorded in the same conditions after sample illumination spanning either 60 or 300 seconds in duration (Figure 3.7). The initial spectrum is close to the spectrum of the fully denaturated state shown in Figure 3.6. After 278 seconds, the spectrum shows all features expected of the native state of *RNase A* indicating that the protein has adopted its native three-

dimensional fold. NMR peak intensities as a function of the time, t, are correlated according to equation 3.4 providing the refolding time constant T_i and taking into account the time constant for the photobleaching of FMN, T^F.

$$s_i(t) = A_i exp(-t/T_i) - A^F exp(-t/T^F) \qquad \text{eq 3.4}$$

Interestingly, different time constant values are obtained for Tyr73/Tyr115 and Tyr76/Tyr92 *i.e.* 4.2 s (± 0.2 s) and 16.6 s (± 2.9 s). The slower constant is due to the presence of a proline (Pro) residue at position 93. In the native state, this residue is found on its *cis* conformation while it had time to undergo a *cis-trans* equilibration when *RNase A* was denatured.[26] Hence, the authors postulate that isomerization of the Tyr92 – Pro93 must occur before native conformation can be reached.

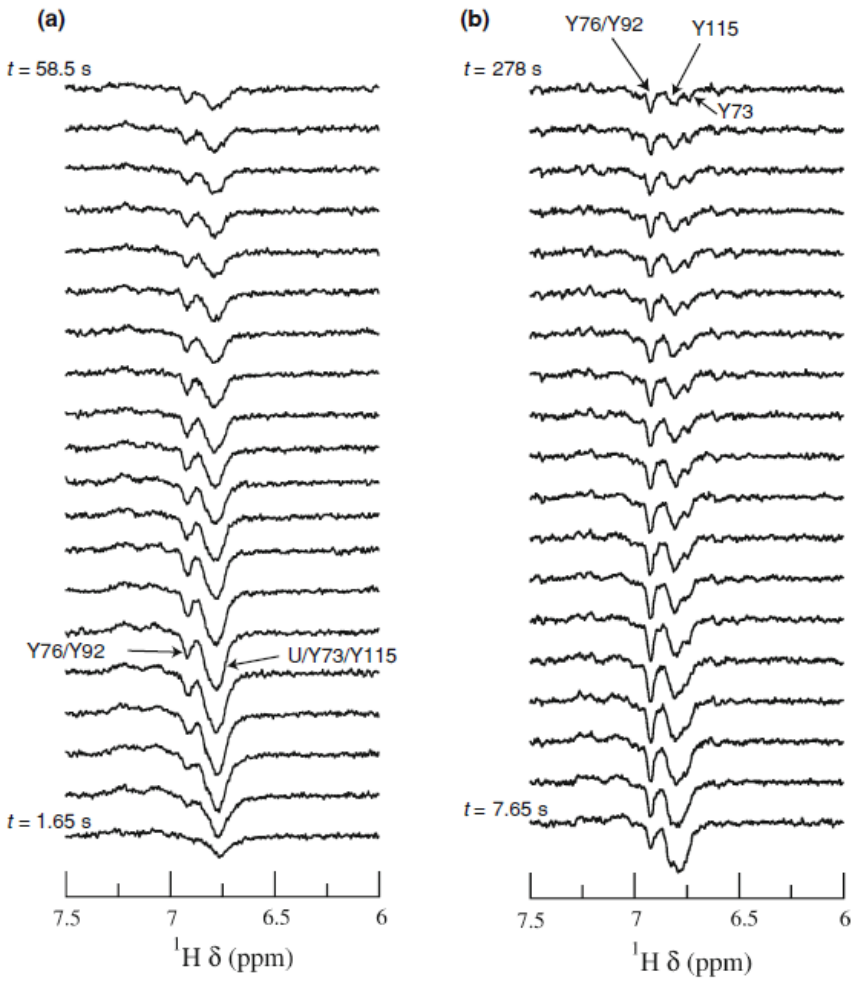

Figure 3.7 – Photo-CIDNP NMR spectra (600 MHz, D_2O) taken from (a) the Δt = 1.5 s and (b) the Δt = 7.5 s refolding experiments, with Y = Tyr and U = other unfolded state Tyr residues (from [24])

To the best of our knowledge, steady-state photo-CIDNP experiments implying a transition metal complex have only been performed on Ru(II) complexes.[14, 21, 27] CIDNP arising from photooxidation by polyazaaromatic Ru(II) complexes such as $[Ru(TAP)_2(phen)]^{2+}$ (phen = 1,10-phenanthroline), $[Ru(TAP)_3]^{2+}$ or $[Ru(TAP)_2(HAT)]^{2+}$ revealed the unpaired electron density in the

transient monoreduced complexes as well as the occurrence of a proton-coupled electron transfer at various pH. For example, the excited state quenching of $[Ru(TAP)_2(HAT)]^{2+}$ by reducing agents such as hydroquinone (H_2Q), N-acetyltyrosine and guanosine-5′-monophosphate was first investigated at several pH revealing that reductive quenching also occurs in strong acidic solution. Experimental data provided clear-cut evidence that blue-light irradiation of the complex yields two distinguishable photoinduced electron/proton- transfer processes depending on pH (Figure 3.8). At pH = 4.8, major photo-CIDNP enhancements are mainly observed on ^1H close to the proximal nitrogen atoms on the HAT ligand (*i.e.* close to the Ru(II) center). In contrast, at pH = 0.5, a striking enhancement is observed for the ^1H signals close to the distal nitrogen atoms on the HAT ligand. Such a variation at low pH could not be observed with $[Ru(TAP)_3]^{2+}$ or $[Ru(TAP)_2(phen)]^{2+}$.[21]

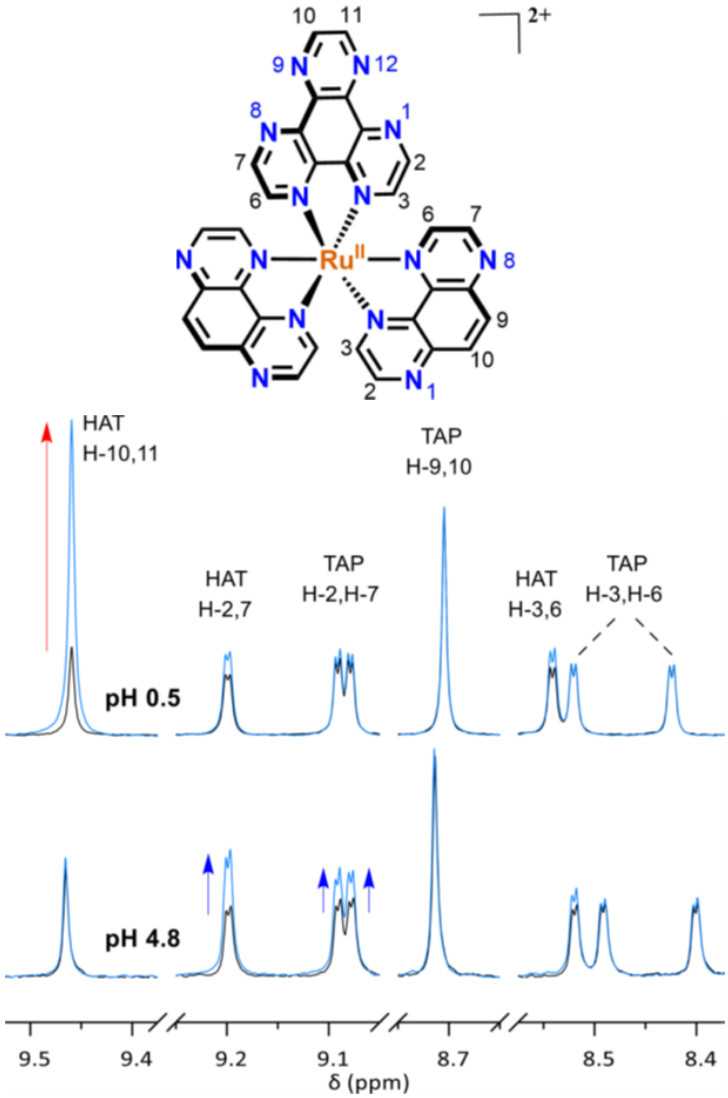

Figure 3.8 – Regions of ^{1}H NMR spectra showing the signals of $[Ru(TAP)_2(HAT)]^{2+}$ for samples containing 2 mM of H_2Q at pH = 4.8 (*down*) and pH = 0.5 (*up*). Equilibrium spectra are in black and the spectra recorded upon sample illumination are superimposed in blue

At pH > 1, it is thus the unprotonated excited state that undergoes electron transfer, and a subsequent proton transfer may take place within the geminate radical pair. In such a case, single

protonation preferentially occurs on proximal nitrogen atom of the HAT ligand (Figure 3.9 – pH > 1). At pH < 1, protonation of the excited state complex on distal nitrogen atom occurs first, and subsequent electron transfer yields the corresponding protonated reduced complex (Figure 3.9 – pH < 1).

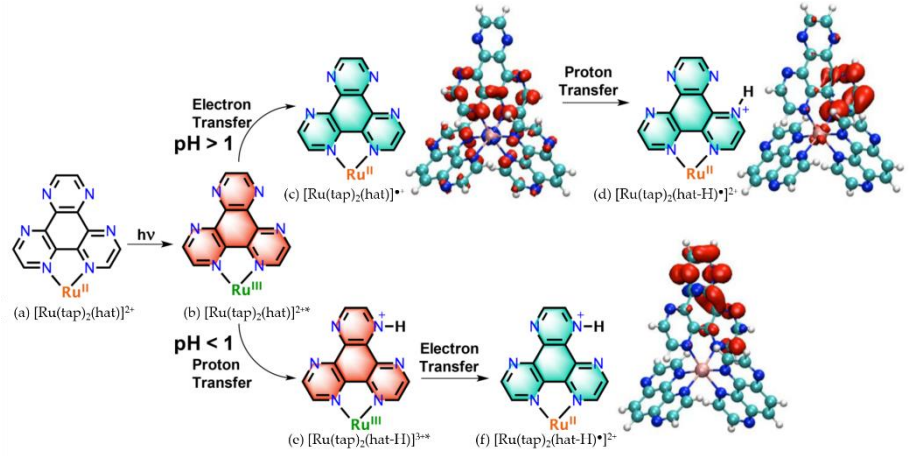

Figure 3.9 – Photoinduced electron-/proton-transfer processes with the protonatable Ru(II) polyazaaromatic complex $[Ru(TAP)_2(HAT)]^{2+}$ (with (a) the ground state complex, (b) unprotonated excited state complex, (c) unprotonated monoreduced complex, (d) monoreduced complex protonated on a proximal nitrogen atom of the HAT ligand, (e) excited state complex protonated on a distal nitrogen atom of the HAT ligand and (f) corresponding monoreduced complex) (from [27])

In the previous chapter, we have demonstrated that $[R\text{-}IrN_5C_1]^{2+}$ can be spectroscopically and electrochemically tuned upon protonation of the non-chelating N atom. According to these studies and in comparison with other Ir(III) trischelate complexes, we established that the nature of the excited state for the neutral complex corresponds to a mixture of a ^{3}LC π-π^* transition, centered on the N,C^3-bpy, and a ^{3}MLLCT transition between the dσ orbital of the Ir-C fragment and π^*(N,N′-bpy). However, no such clear-cut evidence

could be obtained in order to determine the exact nature of the excited state for the protonated $[R\text{-}IrN_5C_1\text{-}H]^{3+}$; we propose that it is likely a ^3LC transition involving $\pi(N,C^3\text{-bpy-H})$, but additional experimental data are needed in order to confirm this hypothesis.

One way to acquire more information on the nature of an excited state is to study its reactivity. In particular, since Ir(III) complexes can be involved in photoinduced electron transfer (PET) processes, we can study the reduced complex and its fate, which is obtained after irradiation of the complex in the presence of an electron donor. Our ability to study the reduced complex obtained after the PET depends on the rate of the BET process between this reduced complex and the oxidized electron donor; if the BET is slow enough, the obtained free radical can be monitored. In our case, the lifetime of the radical species are long enough to be probed by time-resolved photophysical techniques, but usually too short-lived for direct efficient detection by Electron Paramagnetic Resonance (EPR).[28-29] Nevertheless, photo-CIDNP measurements can be used to detect transient radicals in solution.

3.3 Results and discussion

3.3.1 ^{1}H NMR attribution for $[R\text{-}IrN_5C_1]^{2+}$

^{1}H NMR spectroscopy is commonly used for the characterization of polyazaaromatic Ir(III) complexes. However, despite the inherent symmetry of the unchelated bpy ligand, comprehensive ^{1}H assignment in complexes such as $[R\text{-}IrN_5C_1]^{2+}$ is not straightforward due to (i) the metal induced change in chemical and magnetic environment upon complexation and (ii) the inherent dissymmetry of the complex due to the presence of the cyclometalated bond between one of the pyridine unit and the Ir(III) center (Chart 3.1).

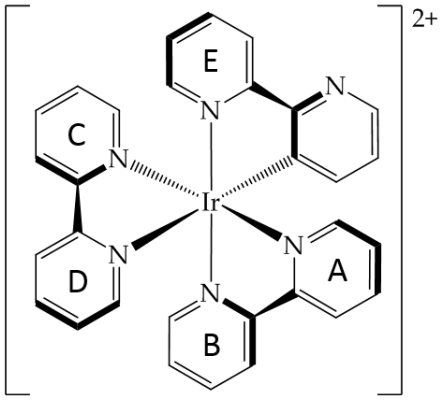

Chart 3.1 – Structure of the investigated $[R\text{-}IrN_5C_1]^{2+}$

The present section provides clear-cut and detailed ^{1}H assignment of $[R\text{-}IrN_5C_1]^{2+}$ type complexes using long-range interligand Nuclear Overhauser Effects (NOEs). Indeed, all the ^{1}H with the same relative position with respect to the N-chelated pyridine units present similar chemical shifts, unlike the signals of the cyclometalated one. As a result, $[R\text{-}IrN_5C_1]^{2+}$ displays five different N-chelated pyridine units (labelled A, B, C, D and E – Chart 3.1 and Figure 3.10), not always easy to distinguish. The same assignment method has

already been successfully applied to assign the ^{1}H chemical shifts of symmetric compounds, $[Ru(TAP)_2(phen)]^{2+}$ and $[Ru(TAP)_2(HAT)]^{2+}$ complexes.[30]

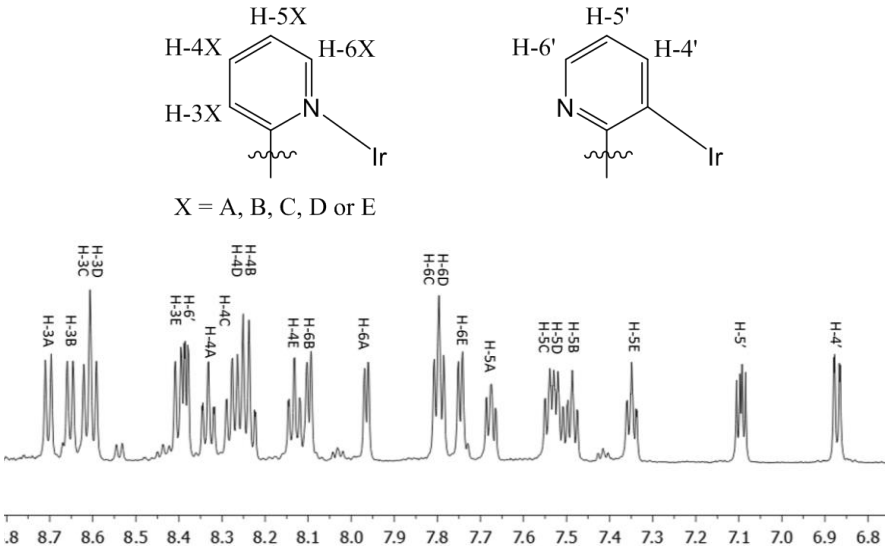

Figure 3.10 – ^{1}H NMR spectrum of $[R\text{-}IrN_5C_1]^{2+}$ in D_2O (25°C, 600 MHz) (*down*) and identification of the N-chelated (labeled A, B, C, D and E) and C-chelated pyridine units (*up*)

Although each ^{1}H of the pyridine units of $[R\text{-}IrN_5C_1]^{2+}$ displays a specific chemical shift, they all fall within the same chemical shift region (Table 3.2). Nevertheless, the signals could be attributed to all specific pyridine moieties. Indeed, the ^{1}H 1D (Figure 3.10) and 2D dqfCOSY (Figure 3.11) NMR spectra of $[R\text{-}IrN_5C_1]^{2+}$ clearly reveal the three-spin system of the cyclometalated pyridine unit (*i.e.* H-4', H-5' and H-6' ; Figure 3.10) and the four-spin systems for the N-chelated units (*i.e.* H-3A, H-4A, H-5A and H-6A ; H-3B, H-4B, H-5B and H-6B ; H-3C, H-4C, H-5C and H-6C ; H-3D, H-4D, H-5D and H-6D ; H-3E, H-4E, H-5E and H-6E ; Figure 3.10).

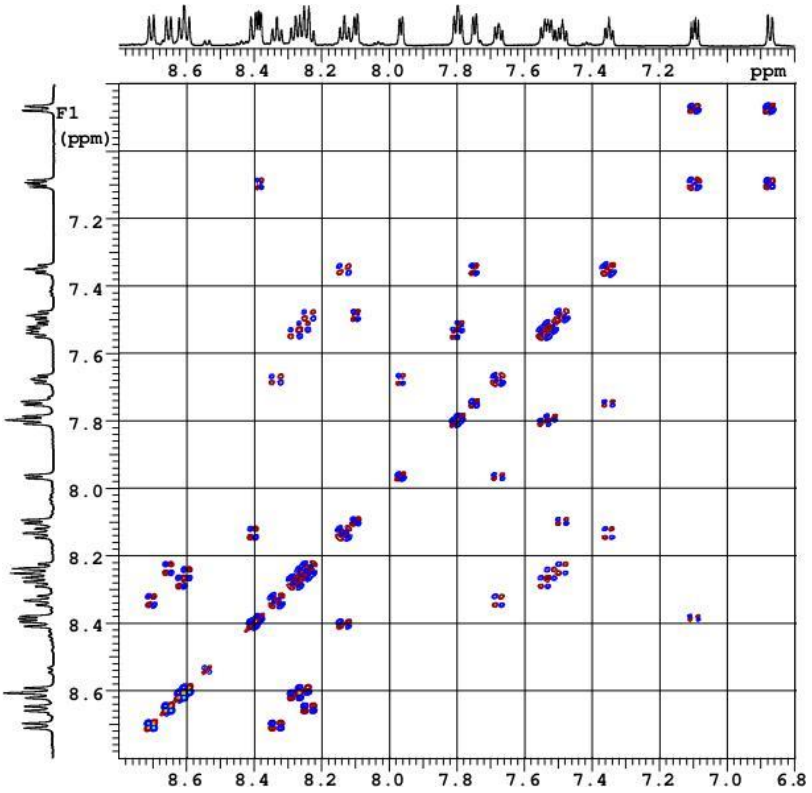

Figure 3.11 – dqfCOSY spectrum of the complex $[R\text{-}IrN_5C_1]^{2+}$ (D_2O, 14.1 T, 25°C).

Table 3.2 – (*left*) Chemical shift areas of the protons located on the N-chelated pyridine units and *(right)* chemical shifts of the protons located on the cyclometalated pyridine unit of $[R\text{-}IrN_5C_1]^{2+}$ (D_2O, 25°C, 600 MHz)

N-chelated units	Chemical shift area (ppm)	C-chelated unit	Chemical shift (ppm)
H-3	8.40-8.70		
H-4	8.13-8.33	H-4′	6.87
H-5	7.35-7.68	H-5′	7.10
H-6	7.75-8.10	H-6′	8.38

Beside ^1H and dqfCOSY NMR spectra, spatial interaction measurements are required to clearly differentiate each ligand with

respect to one another. Indeed, a strong intraligand interaction is expected between both H-3X of the same N,N'-bpy because of the short ^{1}H-^{1}H distance. The ^{1}H-^{1}H 2D ROESY analysis revealed interactions between H-3B and H-3A, and between H-3C and H-3D (Figure 3.12). It is noteworthy that the negative signals on the diagonal strongly affects the apparent intensity of these last correlations.

HSQC NMR analysis allowed to identify each carbon linked to the protons (Figure 3.13). Additional HMBC NMR analysis was in agreement with the ROESY data (Figure 3.14), *e.g.* some correlations being observed between the proton H-3X (X = A, B, C, D or E) of a unit and the adjacent quaternary carbon C_{β} and similarly with respect to C_{α} (Figure 3.15).

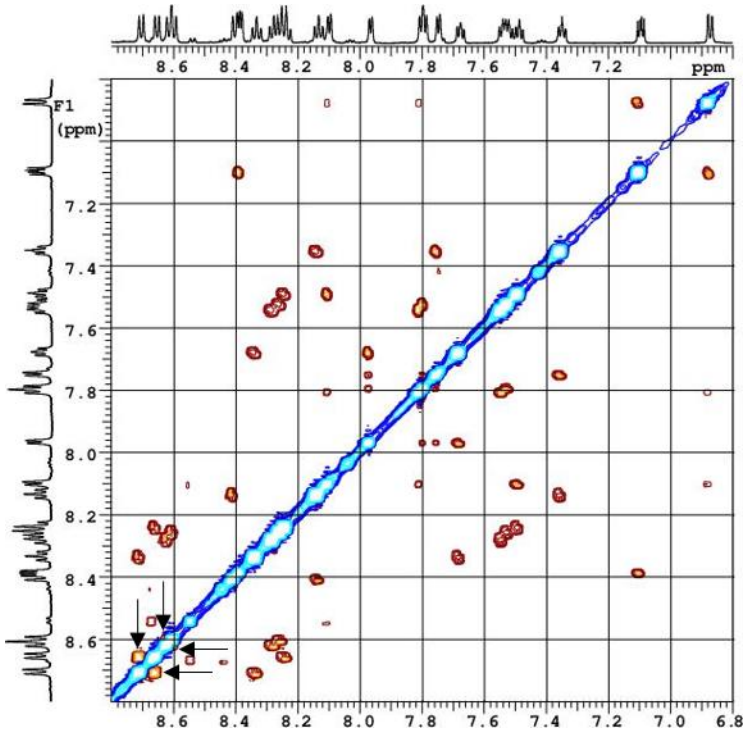

Figure 3.12 – ROESY spectrum of the complex $[R\text{-}IrN_5C_1]^{2+}$ (D_2O, 14.1 T, 25°C, τ_m = 500 ms) (Interunit correlations between bpy H-3C and H-3D as well as H-3B and H-3A are indicated by arrows)

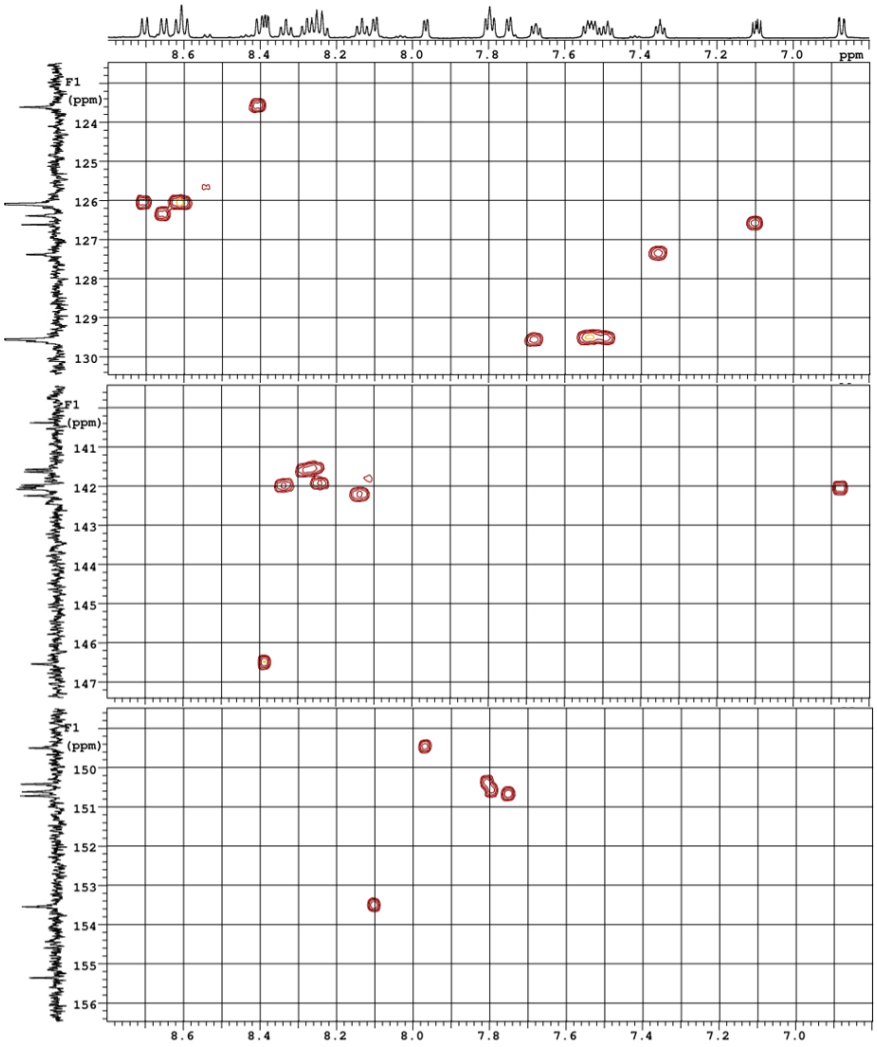

Figure 3.13 – HSQC spectrum of the complex $[R\text{-}IrN_5C_1]^{2+}$ (D_2O, 14.1 T, 25°C)

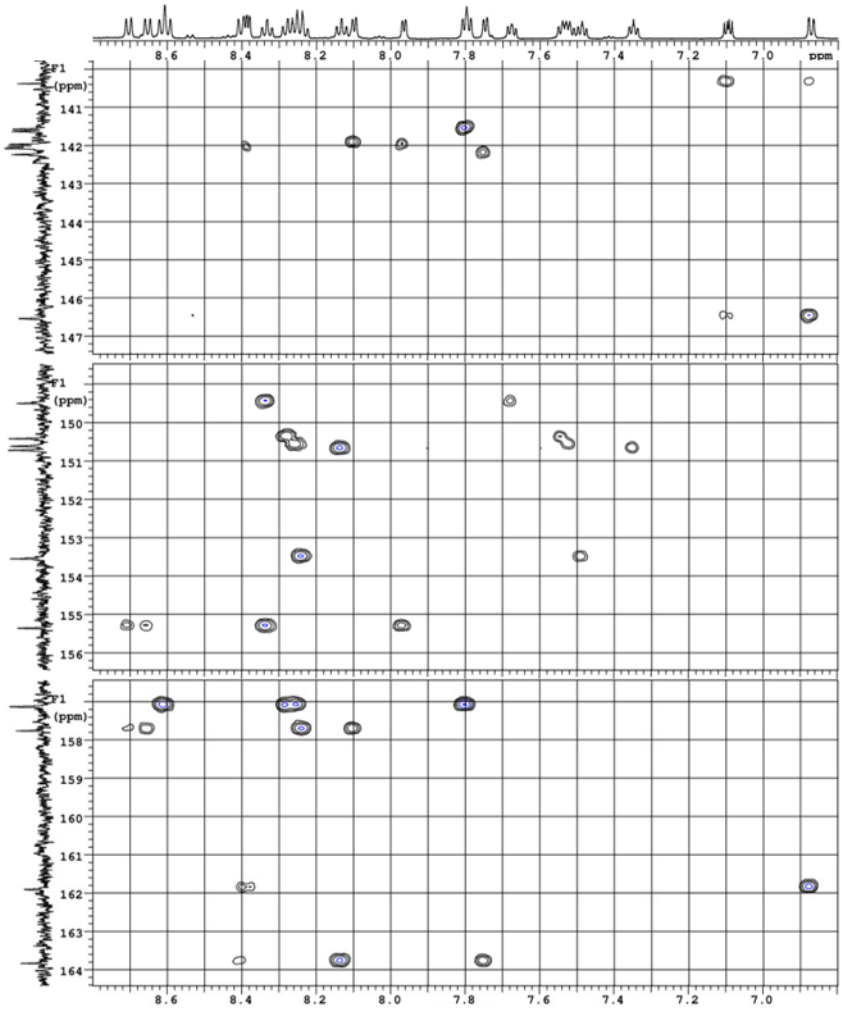

Figure 3.14 – HMBC spectrum of the complex $[R\text{-}IrN_5C_1]^{2+}$ (D_2O, 14.1 T, 25°C)

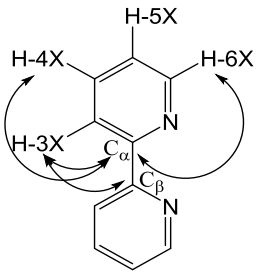

Figure 3.15 – ^2J and ^3J HMBC correlations used to assign the signals of the bpy ligands

Estimated distances between the ^{1}H in *ortho* or *meta* position of the coordination site of the N,N'-bpy and N,C^3-bpy ligands in the complex from X-ray structures[31] are gathered in Table 3.3. The shortest interligand distances are found between ^{1}H in *ortho* position of the chelating atom, *e.g.* H-6E and H-6A. Nevertheless, despite their ortho position of the chelating N, the distance between H-6E and H-6B is much longer than between H-6E and H-6A (4.823 Å *vs*. 3.369 Å, respectively). The ROESY experiments reveal an interaction between ^{1}H closer to each other *i.e.* between H-6E and H-6A. Similar conclusions can be drawn for other ^{1}H of the whole complex, *i.e.* H-6E with H-6D, H-6A with H-6D, H-4' with H-6B, H-4' with H-6C and H-6B with H-6C (Figure 3.12).

Table 3.3 – Distances between ^{1}H of the cyclometalated bpy and ^{1}H in *ortho* and *meta* position of the other bpy ligands[a,b,c]

	H-6E		*H-5E*		*H-4'*		*H-5'*	
	Att1	Att2	Att1	Att2	Att1	Att2	Att1	Att2
H-6B	4.823	5.589	6.127	7.666	**3.515**	**3.346**	**4.692**	5.504
H-5B	6.134	7.739	7.217	9.878	5.598	**4.140**	6.623	6.051
H-5A	**4.424**	5.476	6.253	6.391	7.875	6.403	9.984	7.399
H-6A	**3.369**	**3.340**	5.443	**4.412**	5.767	5.179	7.774	6.373
H-6C	5.589	4.823	7.666	6.127	**3.346**	**3.515**	5.504	**4.692**
H-5C	7.739	6.134	9.878	7.217	**4.140**	5.598	6.051	6.623
H-5D	5.476	**4.424**	6.391	6.253	6.403	7.875	7.399	9.984
H-6D	**3.340**	**3.369**	**4.412**	5.443	5.179	5.767	6.373	7.774

[a] "Att1" and "Att2" stand for Attribution 1 and Attribution 2, respectively (determined from the crystal structure of [Ir(ppy)$_2$(bpy)]PF$_6$ with ppy1 = N,C^3-bpy and ppy2 = N,N'-bpy "C+D" with Ir-N of the Pyr D replacing the Ir-C bond).[31]

[b] Interligand distances short enough to provide ROEs are indicated in bold

[c] The values that could discriminate pyridine unit B from unit C and unit A from unit D are underlined (*vide infra*)

Gathering all information and conclusions drawn from previous analysis, two possible peak assignments remain for the structure of the complex $[R\text{-}IrN_5C_1]^{2+}$ (Figure 3.16).

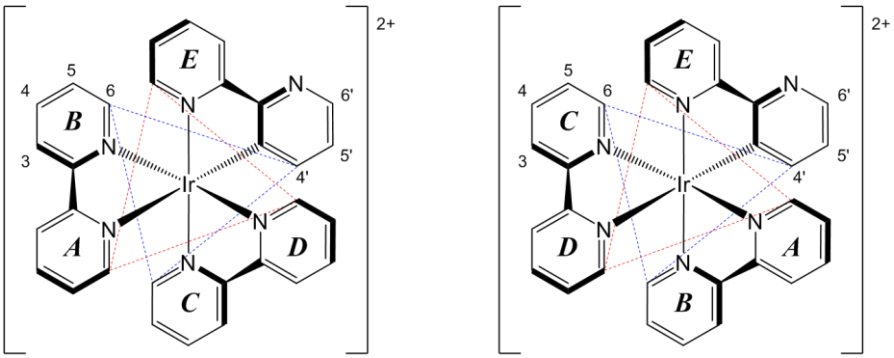

Figure 3.16 – Possible attributions for $[R\text{-}IrN_5C_1]^{2+}$ structure (*left*: Attribution 1 ; *right*: Attribution 2) with long-range interligand interactions between H-6E, H-6A and H-6D *(in red)* and H-4', H-6B and H-6C *(in blue)*

Interligand NOEs between ^1H in *ortho* and *meta* positions with respect to a chelating atom (nitrogen or carbon) should provide clear-cut distinction between the two possible assignments depicted in Figure 3.16. Indeed, the shortest distance between H-5' and H-6C is about 4.7 Å, whereas it is about 5.5 Å between H-5' and H-6B. Hence, a weak interligand NOE is expected between H-5' (in *meta* position of the Ir-C bond) and H-6C but not between H-5' and H-6B. Figure 3.17 shows a 1D ROESY spectrum of the complex $[R\text{-}IrN_5C_1]^{2+}$ recorded with selective excitation of H-5'. As expected, the strongest enhancement is detected for the vicinal protons H-4' and H-6'. These Overhauser effects were already detected in the 2D ROESY spectrum (Figure 3.12). In addition, a long-range interligand Overhauser effect is observed for the signal at 8.10 ppm. This enhanced signal is assigned to N,N'-bpy H-6B, *i.e.* the N,N'-bpy ^1H in *ortho* position with respect to the chelating N atom. 1D ROESY spectrum with selective excitation of

H-4′ was also performed in order to confirm the assignments (Figure 3.18). Based on these last results, the assignment of the ^{1}H NMR spectrum as depicted in Figure 3.19 is proposed.

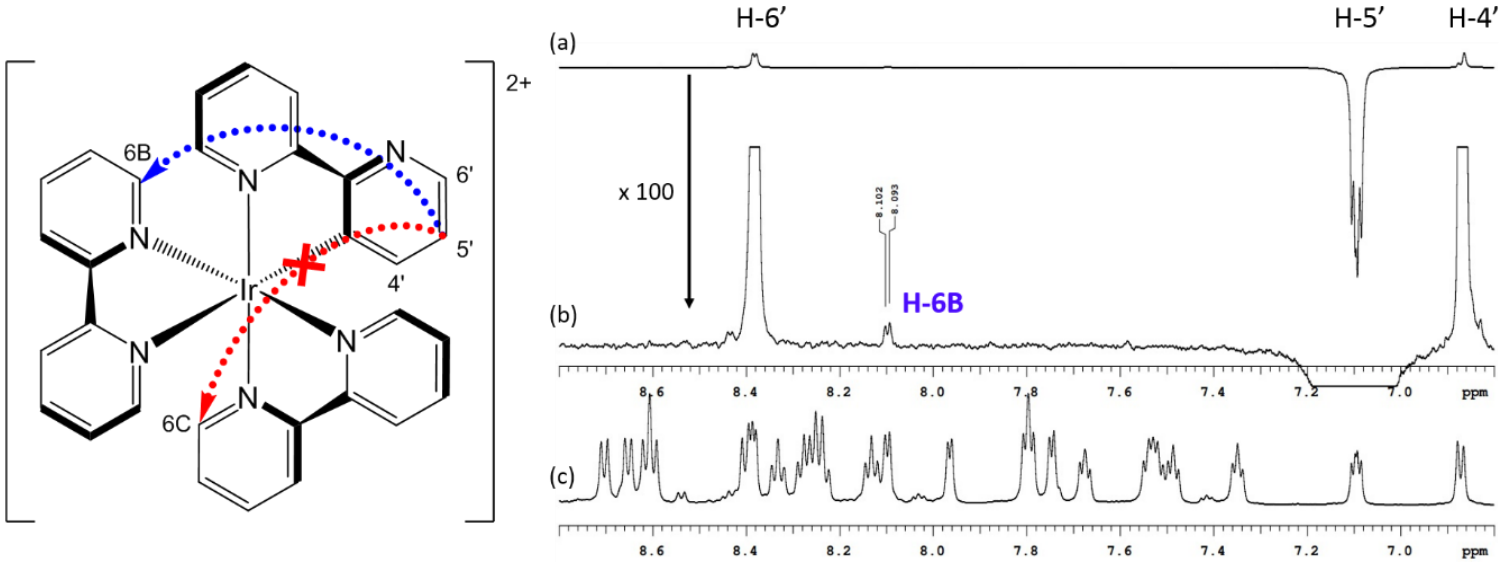

Figure 3.17 – Structure and (a,b) 1D ROESY spectrum of $[R\text{-}IrN_5C_1]^{2+}$ with selective excitation of N,C^3-bpy H-5′ (D_2O, 14.1 T, 25°C, τ_m = 500 ms) and (c) corresponding equilibrium ^1H spectrum

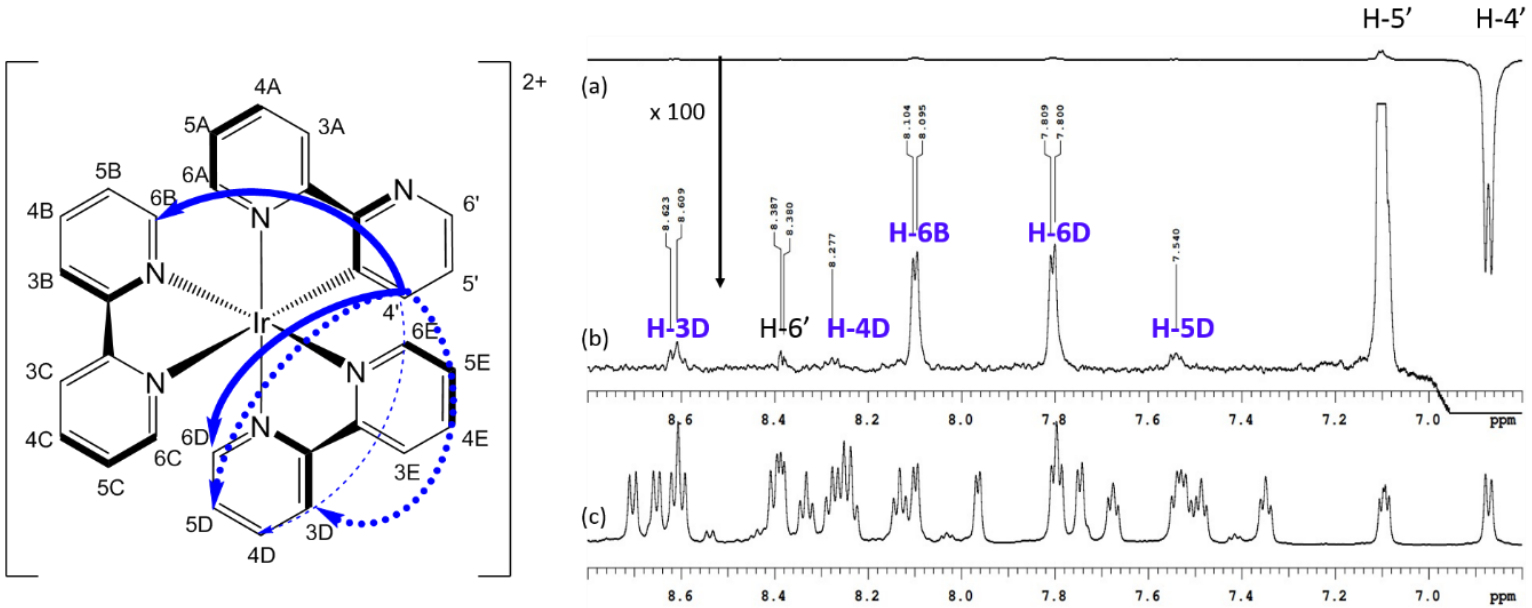

Figure 3.18 – Structure and (a,b) 1D ROESY spectrum of $[R\text{-}IrN_5C_1]^{2+}$ with selective excitation of N,C^3-bpy H-4′ (D_2O, 14.1 T, 25°C, τ_m = 500 ms) and (c) corresponding equilibrium ^1H spectrum

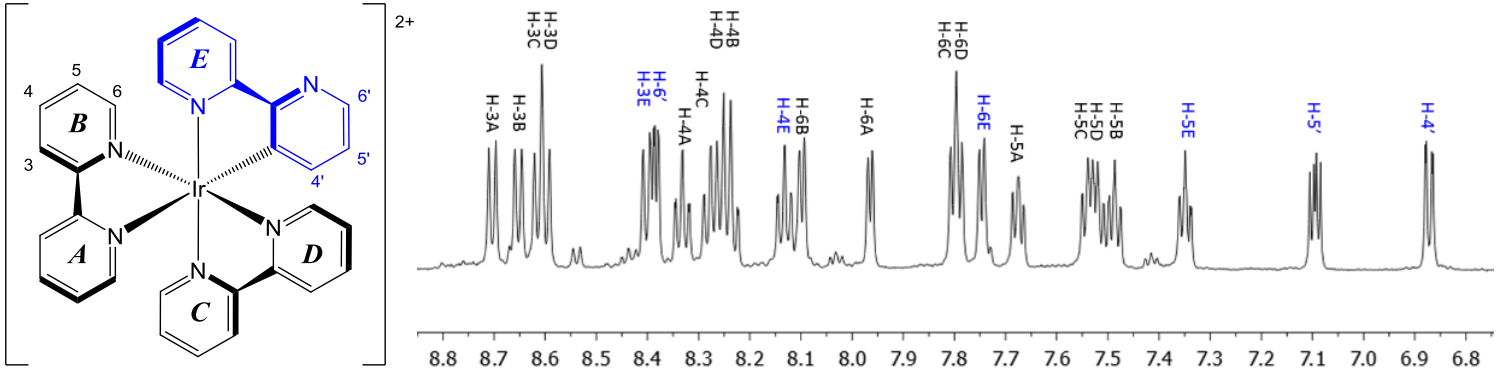

Figure 3.19 – Full ^{1}H attribution for $[R\text{-}IrN_5C_1]^{2+}$ in D_2O (with signals corresponding to th N,C^3-bpy depicted in blue) (25°C, 600 MHz)

3.3.2 pKa determination for ground state [R-IrN$_5$C$_1$-H]$^{3+}$

3.3.2.1 pKa determination for ground state [R-IrN$_5$C$_1$-H]$^{3+}$

The protonation state of the complex has an essential impact on its (photo)physical properties. Various experimental approaches such as UV-spectroscopy[32] or potentiometric measurements[33] are commonly used for the determination of the pKa. Nevertheless, the observation of tiny changes in UV-visible absorption upon variation of the pH leads to unprecise evaluation of the pKa. Hence, NMR spectroscopy represents a valuable alternative since the protonation state of a compound may directly alter the chemical shift of NMR-active nuclei. Furthermore, NMR spectroscopy allows an easy determination of several pKa values in the case of multiple protonation sites (*vide infra*). The pKa of a given species can therefore be obtained from the existing relation between pH change and chemical shifts (sigmoidal curves). Finally, precise values for pKa can be obtained despite the possible presence of impurities in the investigated sample. Noteworthy, as the ^{1}H NMR experiments are performed in D$_2$O with a pH meter calibrated in non-deuterated solvents, the measurements correspond to pH$^\#$ and pKa$^\#$ and can be respectively converted into pH and pKa according to equations 3.5 and 3.6.[34] The comparison of pH and pH$^\#$ is not straightforward due to the fact that binding affinities of protonating groups are different for H$^+$ and D$^+$.

$$pH = (0.929 \pm 0{,}001) \times pH^{\#} + (0.42 \pm 0.01) \qquad \text{eq 3.5}$$

$$pKa = (0.929 \pm 0{,}001) \times pKa^{\#} + (0.42 \pm 0.01) \qquad \text{eq 3.6}$$

The evolution of the ^{1}H NMR spectrum of [R-IrN$_5$C$_1$]$^{2+}$ against the variation of pH$^\#$ can be observed in Figure 3.20. As expected,

signals corresponding to the ^{1}H close to the protonation site (*e.g.* H-4′ ; Figure 3.20 – blue arrows) are dramatically altered upon pH# change. Similar effects, although less pronounced, are observed for the ^{1}H of the N,N′-bpy ligands (*e.g.* H-3B ; Figure 3.20 – red arrows). Changes of the chemical shift from the basic (δ_B) to the acidic form (δ_A) are less than 0.040 ppm for any ^{1}H of both N,N′- chelated bpy ligands while they are more than 0.120 ppm for all ^{1}H signals for the cyclometalated ligand. An internal reference, the nucleotide dGMP (dGMP = 2′-deoxyguanosine-5′-monophosphate – Chart 3.2), with well-known ^{1}H attribution and pKa, has been used to confirm the results. dGMP behaves the same way *i.e.* the protonation on the guanine moiety has more effect on the H-8 (Figure 3.20 – green arrows) than the protonation of the phosphate group (pKa = 2.69 and pKa = 6.29, respectively).[35]

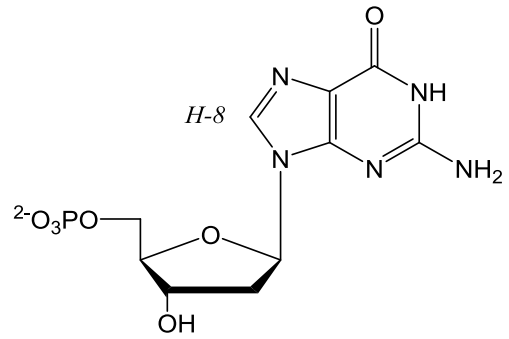

Chart 3.2 – Structure of the investigated dGMP

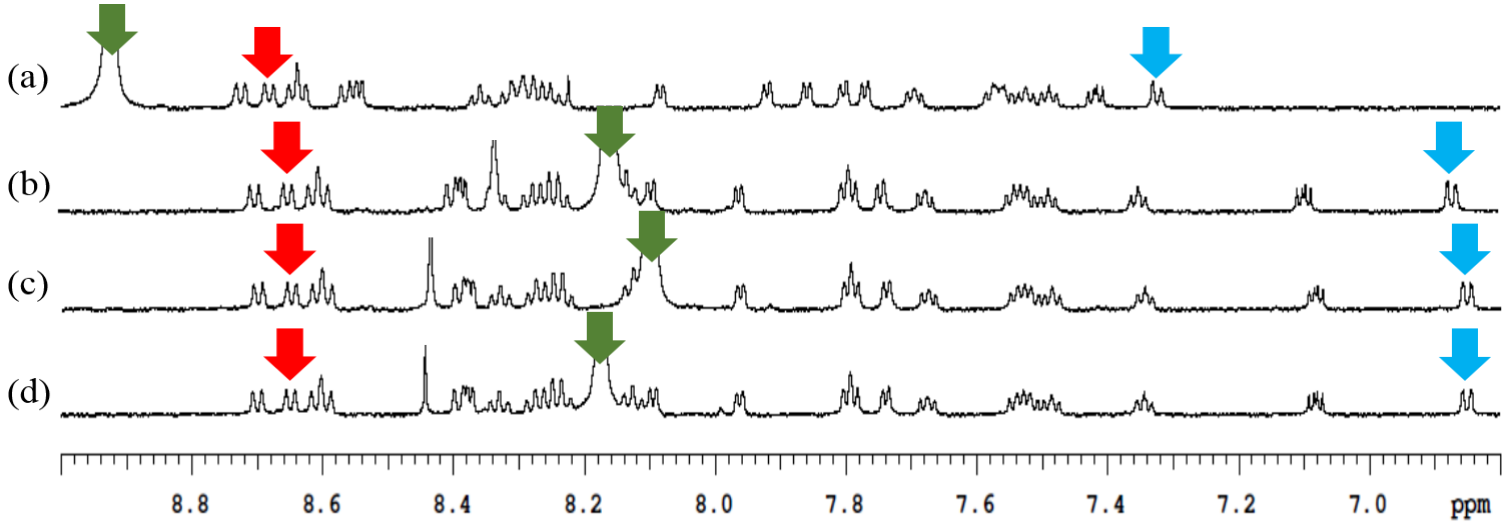

Figure 3.20 – ^{1}H NMR spectra (25°C, 600 MHz) of 0.1 mM [R-IrN$_5$C$_1$]$^{2+}$ and 2 mM dGMP recorded in deuterated 20 mM acetate-phopshate buffer at (a) pH$^{\#}$ = 1.56, (b) pH$^{\#}$ = 3.50, (c) pH$^{\#}$ = 4.99 and (d) pH$^{\#}$ = 7.00. Red arrows stand for H-3B, green arrows stand for H-8 and blue arrows stand for H-4'

Figure 3.21 depicts the chemical shift variations of H-3B and H-4' upon pH change ($0 < pH^{\#} < 5$) (for the numbering of the different protons, see Figure 3.19). The inflection point gives a $pKa^{\#}$ equals to 1.72 and 1.82, respectively, *i.e.* pKa of 2.02 and 2.11 after correction (equation 3.6). Therefore, based on these measurements, we will assume that our complex $[R\text{-}IrN_5C_1]^{2+}$ in its ground state presents a pKa value of 2.07.

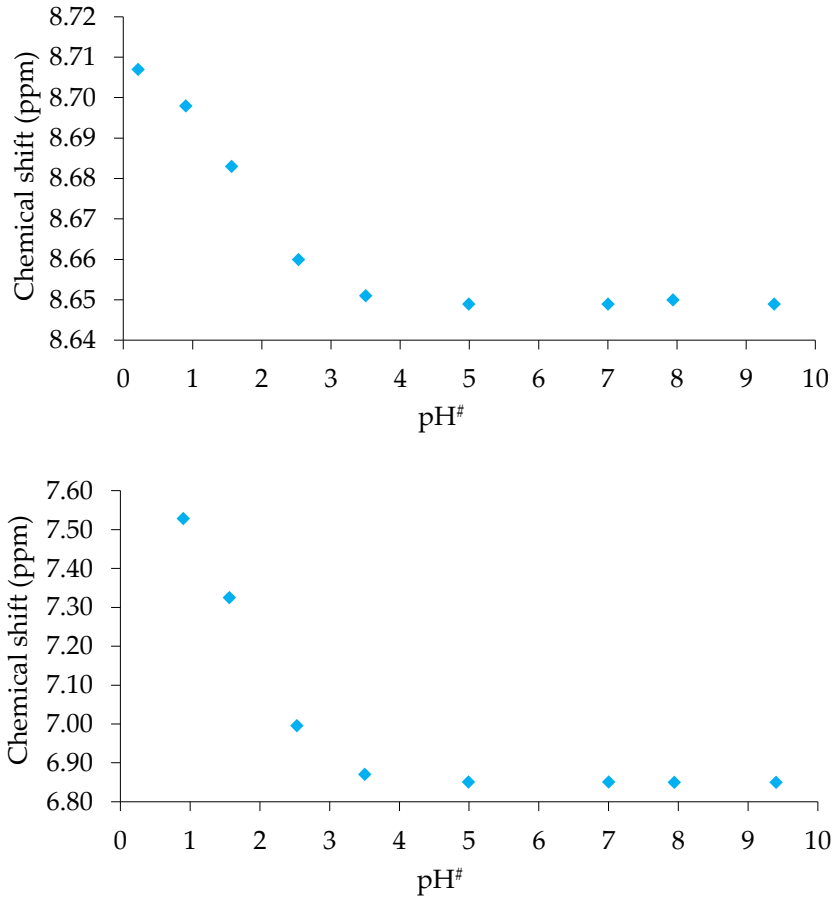

Figure 3.21 – Evolution of the chemical shift for H-3B (*up*) and H-4' (*down*) for complex $[R\text{-}IrN_5C_1]^{2+}$ against $pH^{\#}$

To further test the validity of our method, we measured the pKa of the guanine moiety and phosphate group using chemical shift variation upon $pH^{\#}$ change, and compared to literature data. Figure 3.22 depicts the chemical shift change for H-8 of dGMP from $pH^{\#}$ = 0 to $pH^{\#}$ = 10. Two inflection points are observed and estimated after correction to be pKa (guanine-H) = 2.63 and pKa ($-PO_3H^-$) = 6.32. These values are close to the previously measured pKa using potentiometric pH titration *i.e.* 2.69 and 6.29, respectively.[35]

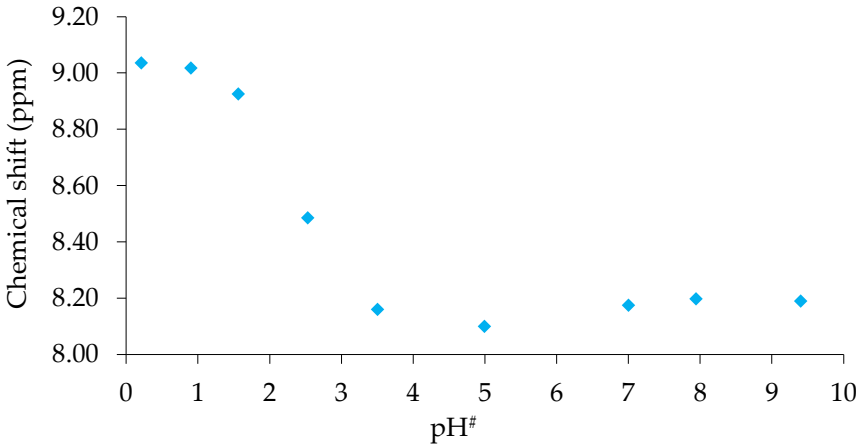

Figure 3.22 – Evolution of the chemical shift of H-8 of dGMP against $pH^{\#}$

3.3.2.2 pKa determination for excited $[R\text{-}IrN_5C_1\text{-}H]^{3+}$

Charge redistribution caused by photoinduced electron transfer influences the acid-base behavior of a molecule. Indeed, changes in acid (BH^+) and base (B) strength upon irradiation first introduced by Förster in 1949 can be very important if the base emits at a different wavelength after protonation. If BH^+ emits at a lower wavelength than B and if one then imagines a solution of same concentration in [BH^+] and [B] (*i.e.* pH equal to ground state pKa), then

upon excitation BH^+ will find itself at a higher energy level than excited B and will then exhibit a strong tendency to change to B. In other words, it will become a stronger acid (Figure 3.23). If the base B emits at a higher energy than BH^+, then B will become a stronger base upon excitation.

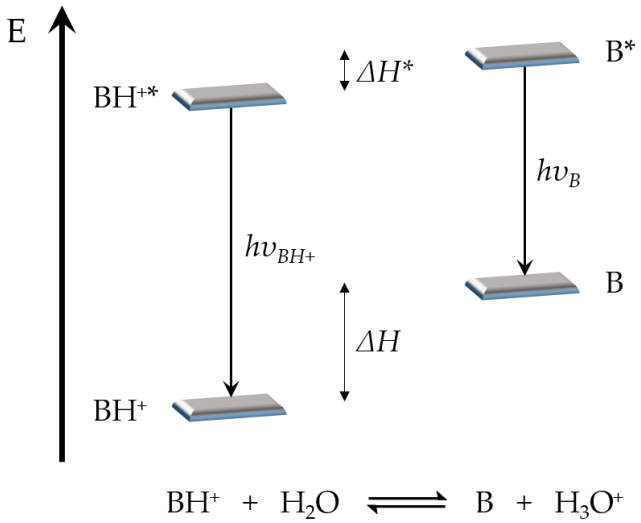

$$BH^+ + H_2O \rightleftharpoons B + H_3O^+$$

Figure 3.23 – Förster's relationship of energetic changes to electronic transitions

Assuming that the free energy between the ground and the excited states is given by the respective orbital energies, the acidity constant of the excited state can thus be obtained from the thermodynamic Förster cycle based on the influence of the acidity on emission data (in cm^{-1}) of both neutral and protonated complexes (461 nm / 21692 cm^{-1} and 482 nm / 20747 cm^{-1}, respectively, in aqueous solvent) and the pKa at the ground state, by use of equation 3.7 at 298 K. According to the measured pKa of the ground state, the Förster pKa of the excited state (pKa*(F)) value is estimated at 4.05. Emission maxima at the 0-0 transitions (see Supporting Information – Table S2.1)

for neutral and protonated complexes ($\bar{\upsilon}_B$ and $\bar{\upsilon}_{BH^+}$, respectively) were used.

$$pKa^*(F) = pKa + 2{,}1.10^{-3}(\bar{\vartheta}_B - \bar{\vartheta}_{BH^+}) \qquad \text{eq 3.7}$$

Another way to characterize the protonation state of the excited complex is to record steady-state luminescence spectra of $[R\text{-}IrN_5C_1]^{2+}$ at different pH. At pH > 5, in the emission spectra two maxima are observed at 482 nm and 513 nm. Interestingly, at lower pH, they are blue-shifted to 461 and 491 nm, respectively (Table 2.5). Global fitting analysis of the evolution of the emission spectra as function of the pH reveals an inflexion point at pH = 3.45 ± 0.02 corresponding to the apparent pKa at the excited state (pKa_{app}*) (Figures 3.24-3.25).

The higher value for excited state pKa*(F) and pKa_{app}* compared to ground state pKa is rationalized by a higher electronic density on the ligands because of the ^{3}MLLCT contribution to the excited state. As this contribution is weak compared to ^{3}LC, difference between pKa*(F)/pKa_{app}* and pKa of the ground state is small. As a comparison, $[Ru(TAP)_3]^{2+}$ complex characterized by pure ^{3}MLCT transition exhibits a pKa of -3.0 for the first protonation in the ground state and a pKa of 3.5/5.0 (apparent/Förster values) in the excited state.

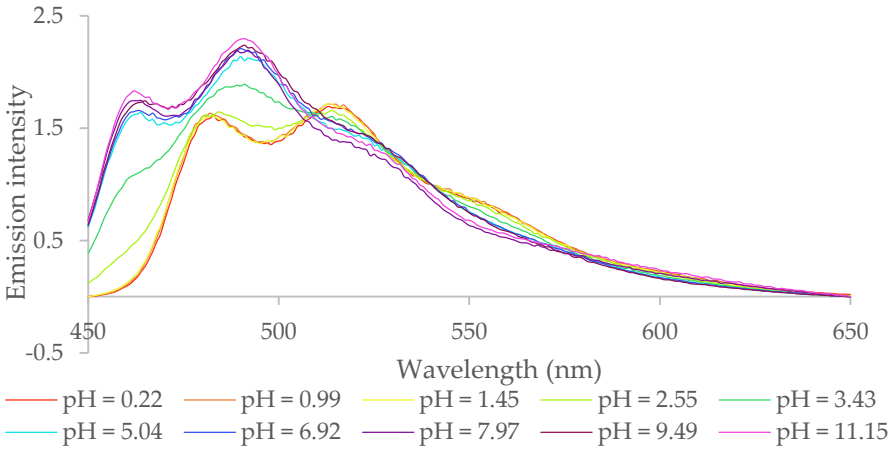

Figure 3.24 – Evolution of the emission spectra of $[R\text{-}IrN_5C_1]^{2+}$ at various pH

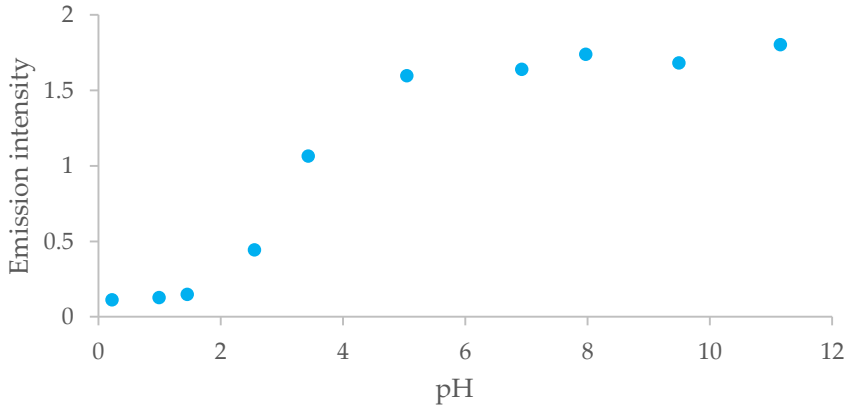

Figure 3.25 – Emission intensity of the hypsochromic band (461 nm) of neutral $[R\text{-}IrN_5C_1]^{2+}$ as a function of the pH

3.3.2.3 pKa determination for mono-reduced and mono-oxidized complexes

Photo-CIDNP experiments are direcly related to the behavior of the radical species generated by the initial photoreaction. As pH has an influence on the protonation state of the starting materials, *i.e.* the

ground state complex and dGMP, and on the excited complex, it can also affect the protonation state of the radical species generated by the PET. It is thus of prime interest to evaluate the pKa of the possible radical intermediates generated by a BET, as any protonation process of these species are likely to induce an important effect on the photo-CIDNP enhancements measured. Indeed, the PET will generate mono-reduced $[R\text{-}IrN_5C_1]^{\bullet+}$ (or mono-oxidized $[R\text{-}IrN_5C_1]^{\bullet 3+}$) complex which can be protonated depending on the pH of the solution. The protonation state of the starting material, *i.e.* the complex and dGMP, but also the protonation state of all the radical intermediates can have an influence on photo-CIDNP effects. Before discussing the photo-CIDNP experiments, we have evaluated the pKa of these entities.

Knowing reduction potentials of both neutral and protonated $[R\text{-}IrN_5C_1]^{2+}$ (E_{red} = -1.07 V *vs.* Ag/AgCl = ~-0.87 V *vs.* NHE and E_{red} = -0.95 V *vs.* Ag/AgCl = ~-0.75 V *vs.* NHE, respectively) and the ground state pKa of the complex determined at 2.07, the pKa of the mono-reduced complex can be evaluated at 6.14 thanks to Hess's cycle (Figure 3.26). In comparison, mono-reduced $[Ru(TAP)_3]^{\bullet+}$ complex displays a pKa of 7.6.

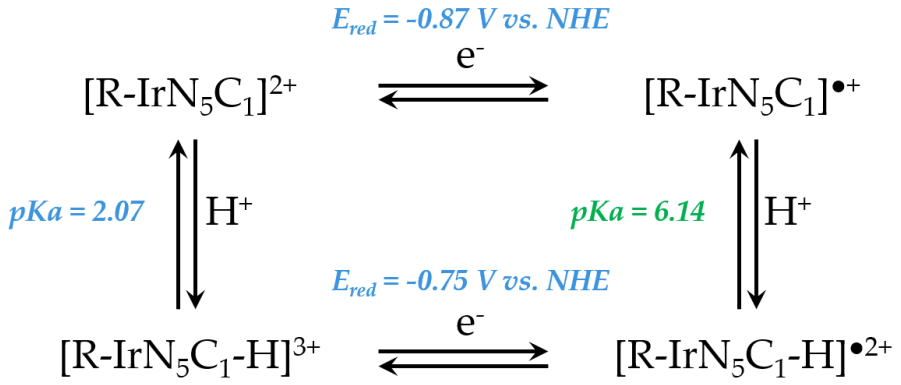

Figure 3.26 – Hess's cycle for the determination of the pKa of the mono-reduced $[R\text{-}IrN_5C_1\text{-}H]^{\bullet 2+}$ complex

As both neutral $[R\text{-}IrN_5C_1]^{2+}$ and protonated $[R\text{-}IrN_5C_1\text{-}H]^{3+}$ display oxidation wave outside the measurable range (E_{ox} > 2.0 V *vs.* Ag/AgCl), pKa for mono-oxidized $[R\text{-}IrN_5C_1\text{-}H]^{\bullet 4+}$ cannot be determined using Hess's cycle (Figure 3.27) but is expected to be lower than ground state pKa because of the enhanced electron-poor character of ligands on the protonated complex compared to the neutral one.

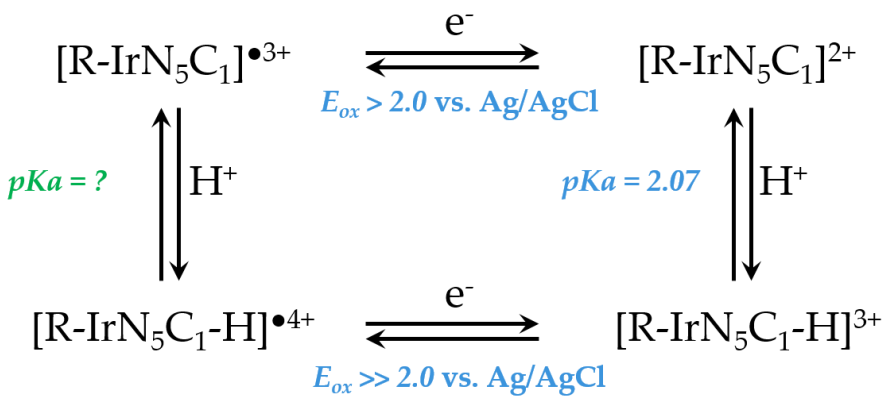

Figure 3.27 – Hess's cycle for the determination of the pKa of the mono-oxidized $[R\text{-}IrN_5C_1\text{-}H]^{\bullet 4+}$ complex

All the calculated pKa values suggest multiple and complex pH effects during luminescence quenching and photo-CIDNP experiments due to the influence of the pH on protonation states of (i) the ground state complex, (ii) the excited state complex and (iii) the reduced or oxidized complex obtained after the PET process.

The use of dGMP as redox system is expected to afford critical results as the nucleic base can be protonated and deprotonated on the purine moiety (pka(dGMP-H^+) = 2.69 ; pKa(dGMP) = 9.56),[35] enhancing respectively reduction and oxidation potentials and thus providing crucial information on the nature of the excited state of the Ir(III) complex via luminescence quenching. Photo-CIDNP enhancements

are expected to be highly influenced as protonation of the photosensitizer at ground and excited states is a key feature for CIDNP occurrence.[21] As these depend on electron transfer between the photosensitizer and the quencher, luminescence quenching of the Ir(III) complex by electron transfer with dGMP will thus be investigated.

3.3.4 Luminescence quenching of $[R\text{-}IrN_5C_1]^{2+}$ by dGMP at various pH

With respect to the excited state reduction potential of unprotonated $[R\text{-}IrN_5C_1]^{2+}$ (E_{red}^* = 1.59 V *vs.* Ag/AgCl) and the ability of dGMP to act as an electron donor (E_{ox}[guanine] = 1.10 V *vs.* Ag/AgCl),[36] a photoreductive electron transfer process is thermodynamically possible between $[R\text{-}IrN_5C_1]^{2+}$ and the nucleic base. Considering the oxidation power of the excited state of neutral $[R\text{-}IrN_5C_1]^{2+}$ as well as reduction potential of dGMP and using the empirical Rehm-Weller equation (equation 3.8 – where $E_{D^{\bullet+}/D}$ and $E_{A/A^{\bullet-}}$ are the reduction potentials, ΔE_{00} is the energy of transition *i.e.* the Stokes shift), it is expected that the process described in equation 3.9 will be exergonic by about 0.5 eV.

$$\Delta G_{ET} = \left(E_{D^{\bullet+}/D} - E_{A/A^{\bullet-}}\right) - \Delta E_{00} \qquad \text{eq 3.8}$$

$$[\text{R-Ir(III)}N_5C_1]^{2+*} + \text{dGMP} \rightarrow [\text{R-Ir(III)}N_5C_1^{\bullet}]^{+} + \text{dGMP}^{\bullet+} \qquad \text{eq 3.9}$$

As the Ir(III) complex emits in aqueous solutions, monitoring the luminescence in the presence of a gradually increasing concentration of the nucleic base can be performed. The luminescence quenching rate constants of $[R\text{-}IrN_5C_1]^{2+}$ complex by dGMP as a

function of the pH are reported in Table 3.4. All the experiments were carried out with dGMP concentrations far below the aggregation and self-association limit.[37]

Table 3.4 – Luminescence lifetime or the $[R\text{-}IrN_5C_1]^{2+}$ complex as function of the pH (τ_0) and quenching rate constant of the photoreaction with dGMP[a]

pH	τ_0 (μs)	k_Q (10^9 M^{-1} s^{-1})
0.22	2.63	0.271
0.99	3.19	0.298
1.45	3.45	0.724
2.55	3.00	1.766
3.43	2.42	2.153
5.04	2.07	2.451
6.92	2.53	2.104
7.97	2.18	2.606
9.49	2.10	2.296
11.15	1.82	4.959

[a]Measurements with 20 mM aqueous acetate-phosphate buffer under air atmosphere at 298 K.

Figure 3.28b shows the relative emission decrease for $[R\text{-}IrN_5C_1]^{2+}$ under neutral conditions (pH = 6.92) upon gradual addition of dGMP. As both emission bands are equally affected by the presence of the quencher, the observations will be focused on the most hypsochromic band, closer to the energy of transition ΔE_{00} of the complex. A linear Stern-Volmer relationship in the luminescence intensity can be obtained from these data (Figure 3.28b – inset) (Table 3.4) suggesting that pure dynamic quenching of the excited state of unprotonated $[R\text{-}IrN_5C_1]^{2+}$ is occurring in the presence of dGMP at pH = 6.92, with a quenching rate constant of 2.1×10^9 $M^{-1}.s^{-1}$.[38] As both compounds are influenced by pH (pKa [Ir] = 2.07 ; pKa_1 [guanine] =

2.69 ; pKa_2 [guanine] = 9.56),[35] the occurrence of a PET process has also been investigated in acidic and basic conditions (pH = 0.99 and 11.15, respectively) (Figures 3.28a and 3.28c). Strikingly, both protonations of the phosphate group (pKa_1 = 0.7 ; pKa_2 = 6.29)[35] do not affect the quenching rate constant. Under highly basic conditions, a faster PET between unprotonated $[R\text{-}IrN_5C_1]^{2+}$ and deprotonated dGMP is observed compared to neutral pH, in agreement with the electron-rich character of deprotonated dGMP (thus expected to display a lower oxidation potential) and the coulombic attraction between the Ir(III) complex and the negatively charged guanine moiety. Under highly acidic conditions, protonated $[R\text{-}IrN_5C_1\text{-}H]^{3+}$ displays a excited state reduction potential close to its neutral form (E_{red}^* = 1.57 V *vs.* Ag/AgCl) whereas oxidation potential of protonated dGMP is, to the best of our knowledge, unknown in the literature but expected to be high implying that a photoinduced electron transfer from the nucleic base to the Ir(III) complex is unlikely. Nevertheless, a slowed down luminescence quenching rate compared to neutral pH and, hence, slower PET, are observed between both protonated $[R\text{-}IrN_5C_1\text{-}H]^{3+}$ and dGMP-H^+. A valid hypothesis explaining this PET process is the transfer of the proton of dGMP-H^+ coupled to the electron transfer, *i.e.* a Proton-Coupled Electron Transfer (PCET) process, to some residual non-protonated $[R\text{-}IrN_5C_1]^{2+}$. Thus, control experiments implying electron transfer from dGMP-H^+ to unprotonable $[Ir(N,N'\text{-}bpy)_3]^{3+}$ at highly acidic and neutral pH (pH = 0.98 and pH = 6.93) have been performed. Unexpectedly, luminescence quenching was observed (Figures 3.29a and 3.29b, respectively), with an quenching rate constant increasing with pH as it could be expected because of the progressive deprotonation of the guanine residue and the inertness of $[Ir(N,N'\text{-}bpy)_3]^{3+}$ upon variation of the pH. These results thus attest that

no proton transfer was involved in the electron transfer process *i.e.* no PCET occurs between dGMP-H^+ and remaining protonable [R-IrN_5C_1]$^{2+}$ (equation 3.10).

$$[\text{R-Ir(III)N}_5\text{C}_1]^{2+*} + \text{dGMP-H}^+ \longrightarrow [\text{R-Ir(III)N}_5\text{C}_1\text{-H}^\bullet]^{2+} + \text{dGMP}^{\bullet+} \qquad \text{eq 3.10}$$

Consequently, luminescence quenching at low pH indicates that a PCET is unlikely (energy transfer between both compounds will be ruled out by CIDNP experiments – *vide infra*). Previous experiments in Chapter 2 brought out the fact that protonated [R-IrN_5C_1-H]$^{3+}$ and [Ir(N,N'-bpy)$_3$]$^{3+}$ are able to photoreduce benzoquinone (BQ). As protonated dGMP-H^+ more than likely displays a high reduction potential, an electron transfer from the excited protonated complex to dGMP-H^+ is thus expected. Although a photoreduction of both complexes by dGMP-H^+ cannot be entirely excluded, based on these experiments, a photoinduced reduction of the protonated nucleic base is more likely to occur.

In conclusion, on the basis of thermodynamic considerations and Stern-Volmer relationship between [R-IrN_5C_1]$^{2+}$ and dGMP at extreme pH, the luminescence quenching could be ascribed to a PET process between the guanine moiety and the excited complex playing the role of either the photooxidant at high pH or the photoreducer at low pH as described by equations 3.11 and 3.12, respectively.

$$[\text{R-Ir(III)N}_5\text{C}_1]^{2+*} + (\text{dGMP} - \text{H})^- \longrightarrow [\text{R-Ir(III)N}_5\text{C}_1]^{\bullet+} + (\text{dGMP} - \text{H})^\bullet \qquad \text{eq 3.11}$$

$$[\text{R-Ir(III)N}_5\text{C}_1\text{-H}]^{3+*} + \text{dGMP-H}^+ \longrightarrow [\text{R-Ir(III)N}_5\text{C}_1\text{-H}]^{\bullet 4+} + \text{dGMP-H}^\bullet \qquad \text{eq 3.12}$$

In order to gain insight into the exact nature of the electronic orbitals involved in PET processes at the different pH, photo-CIDNP

experiments have been achieved. Indeed, as stated in the introduction and according to Stern-Volmer plots at various pH, protonation of the cyclometalated ligand gave rise to changes in the complex properties leading to ambiguous description of the nature of the excited state.

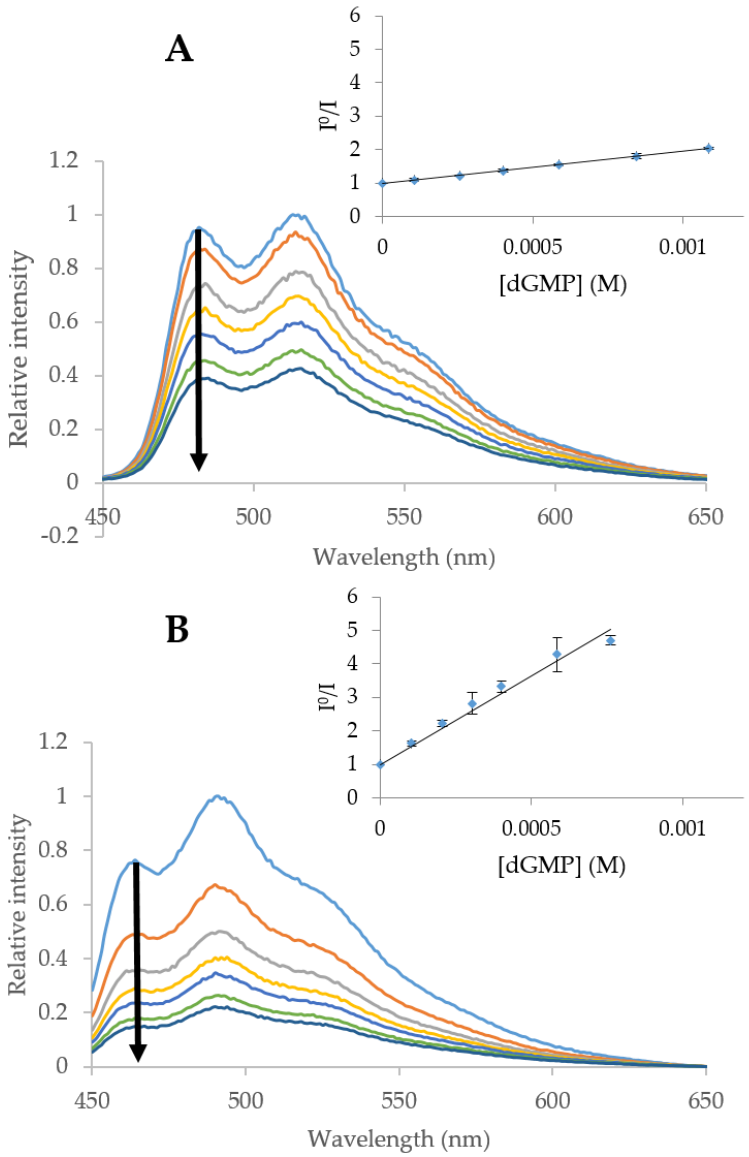

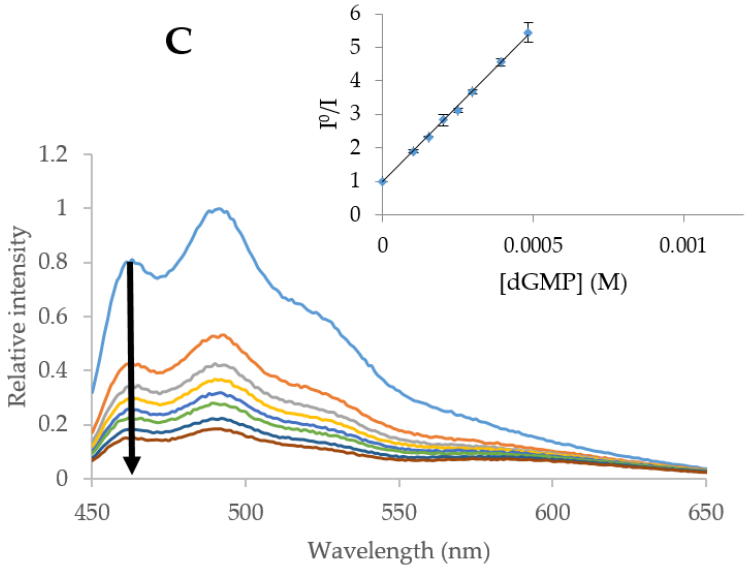

Figure 3.28 – Luminescence spectra (λ_{exc} = 405 nm) of $[R\text{-}IrN_5C_1]^{2+}$ upon increasing concentration of dGMP (20 mM acetate-phosphate buffer, air atmosphere, room temperature) at (A) pH = 0.99, (B) pH = 6.92 and (C) pH = 11.15. *Insets*: corresponding Stern-Volmer plots obtained upon the addition of dGMP measured at 482 nm for pH = 0.99 and at 461 nm for pH = 6.92 and pH = 11.15.

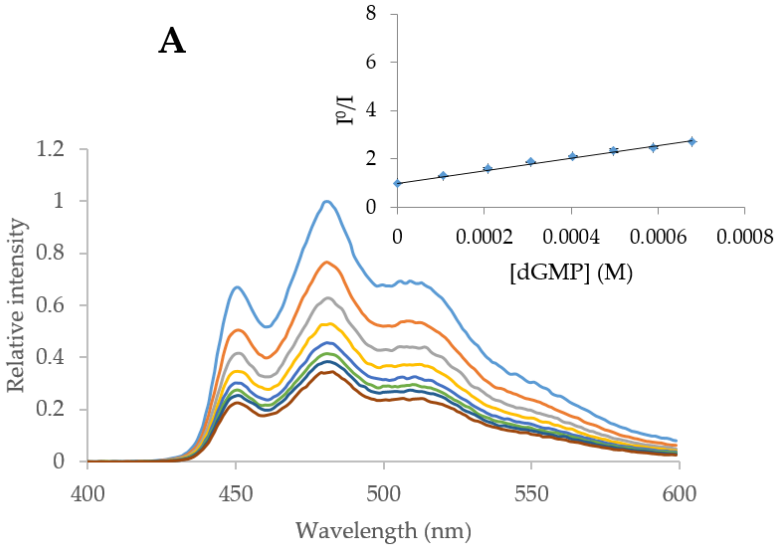

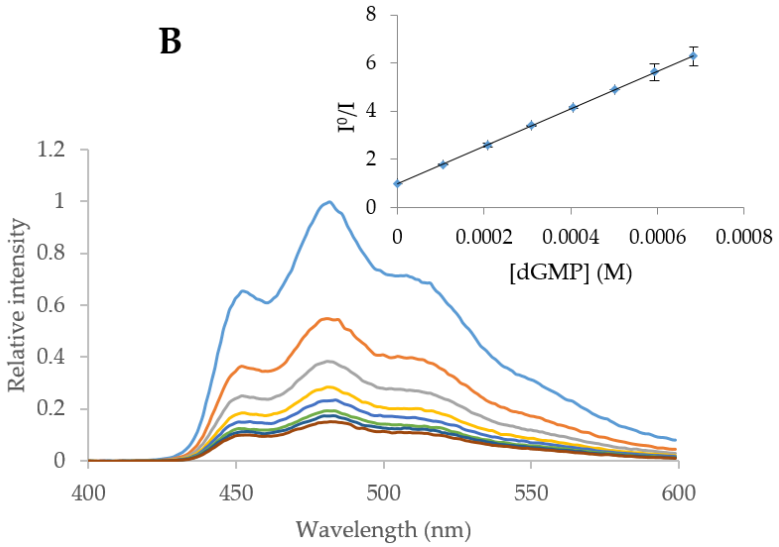

Figure 3.29 – Luminescence spectra (λ_{exc} = 405 nm) of $[Ir(N,N'\text{-bpy})_3]^{3+}$ upon increasing concentration of dGMP (20 mM acetate-phosphate buffer, air atmosphere, room temperature) at (A) pH = 0.98 and (B) pH = 6.93. *Insets*: corresponding Stern-Volmer plots obtained upon the addition of dGMP measured at 451 nm.

3.3.5 Photo-CIDNP measurements

Photo-CIDNP experiments were carried out using a 600 MHz spectrometer at 25°C for a total of 10 freshly prepared samples. At least 35 ^{1}H NMR spectra were recorded for each sample: a first series of 5 spectra without sample illumination, a subsequent series of 20 spectra with alternation between measurements with light illumination ("light" spectra referred as L1 to L10) and others without irradiation ("dark" spectra referred as D1 to D10), and finally a last series of 10 spectra without sample illumination to check the recovery of the ^{1}H signals. The illumination period of 300 ms was followed by a delay of

10 ms prior to the non-selective ^{1}H RF pulse and subsequent acquisition of the free induction decay (FID).

First, ^{1}H NMR spectra were recorded under the same illumination conditions for one type of control sample: the Ir(III) complex in the absence of the biomolecule at pH$^{\#}$ = 1.34 to confirm that no photo-CIDNP enhancement can arise in the absence of a redox quencher. Moreover, ^{1}H NMR spectra revealed a high photostability of [R-IrN$_5$C$_1$]$^{2+}$, even under highly acidic or basic conditions.

A fixed dGMP:[R-IrN$_5$C$_1$]$^{2+}$ / 20:1 ratio was used in order to have a major luminescence quenching (Φ_Q > 50%) at any pH according to Table 3.4 and equation 3.13.

$$\Phi_Q = 1 - \frac{I}{I_0} \quad \text{with} \quad \frac{I_0}{I} = 1 + k_Q \tau_0 [dGMP] \qquad \text{eq 3.13}$$

The photo-CIDNP enhancements were calculated using the integral data from spectra in the dark before sample illumination (D1), during sample illumination (L1) and in the dark after sample illumination (D2) according to equation 3.14 (with $I_D = \frac{(I_{D1}+I_{D2})}{2}$).

$$photo\text{-}CIDNP\ enhancement\ (\%) = 100\ x \frac{I_{L1}-I_D}{I_D} \qquad \text{eq 3.14}$$

For illustration purposes, the aromatic regions of ^{1}H NMR spectra showing the signals of [R-IrN$_5$C$_1$]$^{2+}$ and dGMP are displayed in Figure 3.30 for the sample at pH$^{\#}$ = 3.50 except H-4E which is superimposed on the aromatic proton of dGMP. As expected, the equilibrium spectrum before illumination (D1) exhibits Ir(III) complex signals of equal intensity (Figure 3.30a). In contrast, in the first spectrum recorded with illumination (L1), signals of unequal intensity are interestingly observed only for ^{1}H of the cyclometalated N,C^3-bpy-H ligand (Figure 3.29b). The integrated intensity of all these signals

except one corresponding to H-6E is increased compared to that in spectrum D1 (positive photo-CIDNP effect, absorptive polarization). The integrals observed in subsequent spectrum D2 (Figure 3.29c), which was recorded immediately after spectrum L1, are once again equal and not significantly different from the values observed in the equilibrium spectrum (prior to illumination).

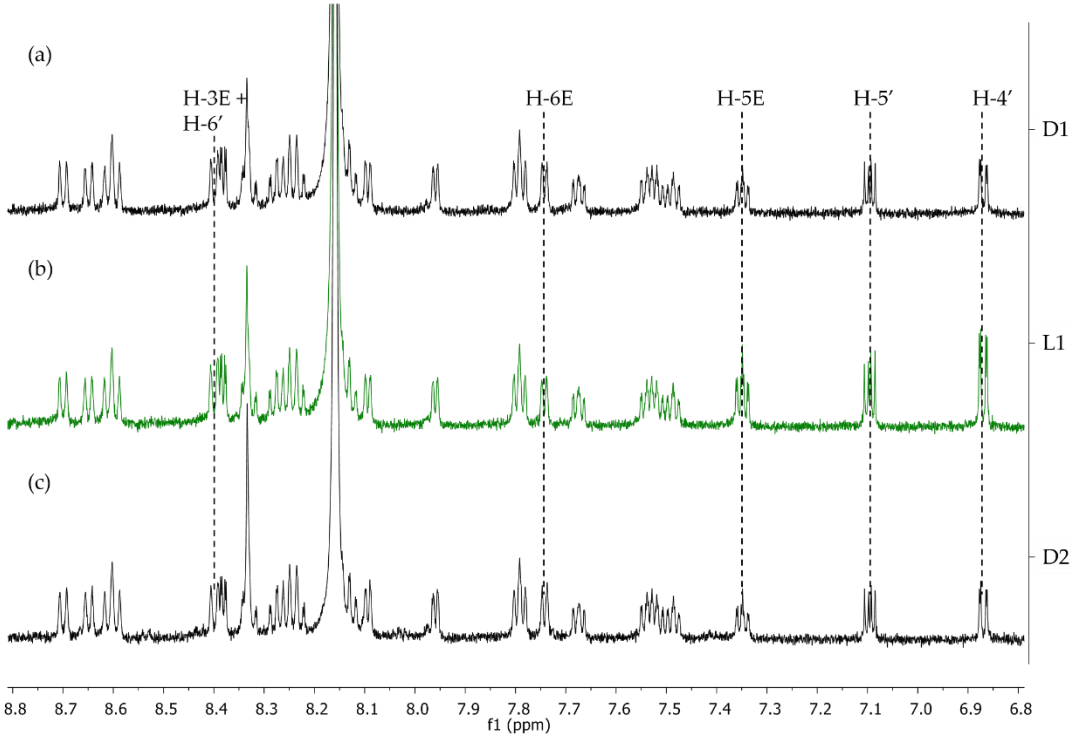

Figure 3.30 – ^{1}H NMR signals of $[R\text{-}IrN_5C_1]^{2+}$ observed for the sample at $pH^{\#}$ = 3.50: (a) equilibrium spectrum D1 recorded without illumination ; (b) spectrum L1 obtained with illumination at 405 nm ; (c) spectrum D2 recorded without illumination immediately after spectrum L1. All the ^{1}H signals exhibiting photo-CIDNP effects are displayed.

Photo-CIDNP enhancements measured for the aromatic ^{1}H of dGMP decreased from $pH^{\#}$ = 7.94 to reach a minimum at $pH^{\#}$ = 3.50 and then gradually increased again at lower $pH^{\#}$. These photo-CIDNP enhancements confirm the occurrence of a photoinduced electron transfer between the excited complex and dGMP and the generation of a radical pair following this PET reaction. Considering the photo-CIDNP effects on the structure of the complex, they are indicative of the presence of the unpaired radical electron on a specific portion of the complex *i.e.* located on the N,C^{3}-bpy rather than on one of the N,N'-bpy ligands.

Figures 3.31 and 3.32 display several measured CIDNP enhancements obtained in the whole range of $pH^{\#}$ investigated. Although no noticeable photo-CIDNP enhancement can be detected on the N,N'-bpy ligands (Figure 3.32), significant enhancements are observed on the cyclometalated N,C^{3}-bpy ligand (Figure 3.31). The evolution of the photo-CIDNP enhancements for this ligand as a function of $pH^{\#}$ can be separated in three distinct regions: (i) above $pH^{\#}$ = 5.0, no significant enhancement can be observed; (ii) below $pH^{\#}$ = 5.0, the photo-CIDNP enhancements increase dramatically up to a maximum value located around $pH^{\#}$ = 1.56; (iii) finally, in highly acidic conditions ($pH^{\#} \leq 1.56$), measured photo-CIDNP effects decrease for all the signals of the cyclometalated ligand. It is noteworthy that enhancements could not be determined for some ^{1}H signals at specific $pH^{\#}$ because of the recovery with other signals from the Ir(III) complex or dGMP.

For sake of clarity of the discussion, the analysis of the photo-CIDNP effects in these regions will be described successively.

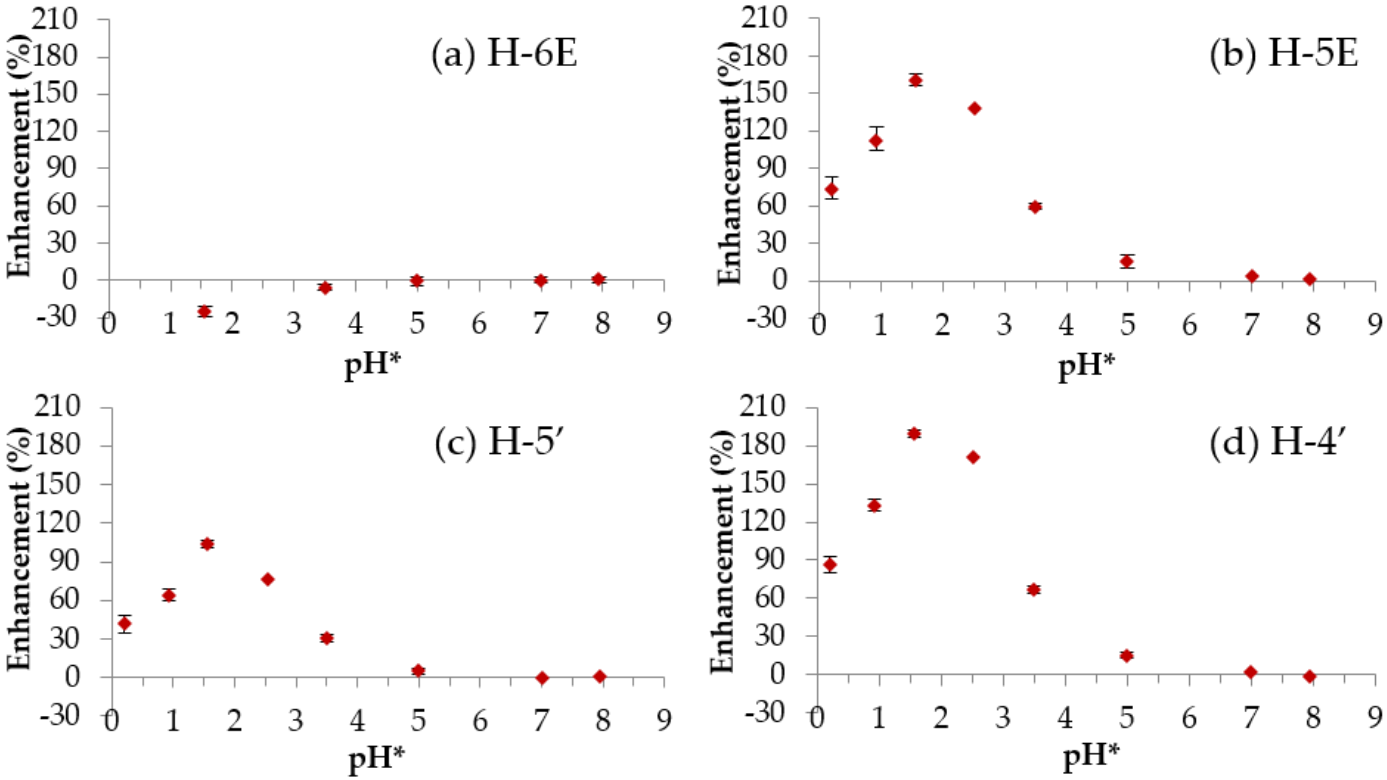

Figure 3.31 – $pH^{\#}$ effect on the ^{1}H photo-CIDNP enhancements observed for the complex $[R\text{-}IrN_5C_1]^{2+}$ in the presence of dGMP for the signals of the N,C^3-bpy ligand: (a) H-6E, (b) H-5E, (c) H-5′, (d) H-4′

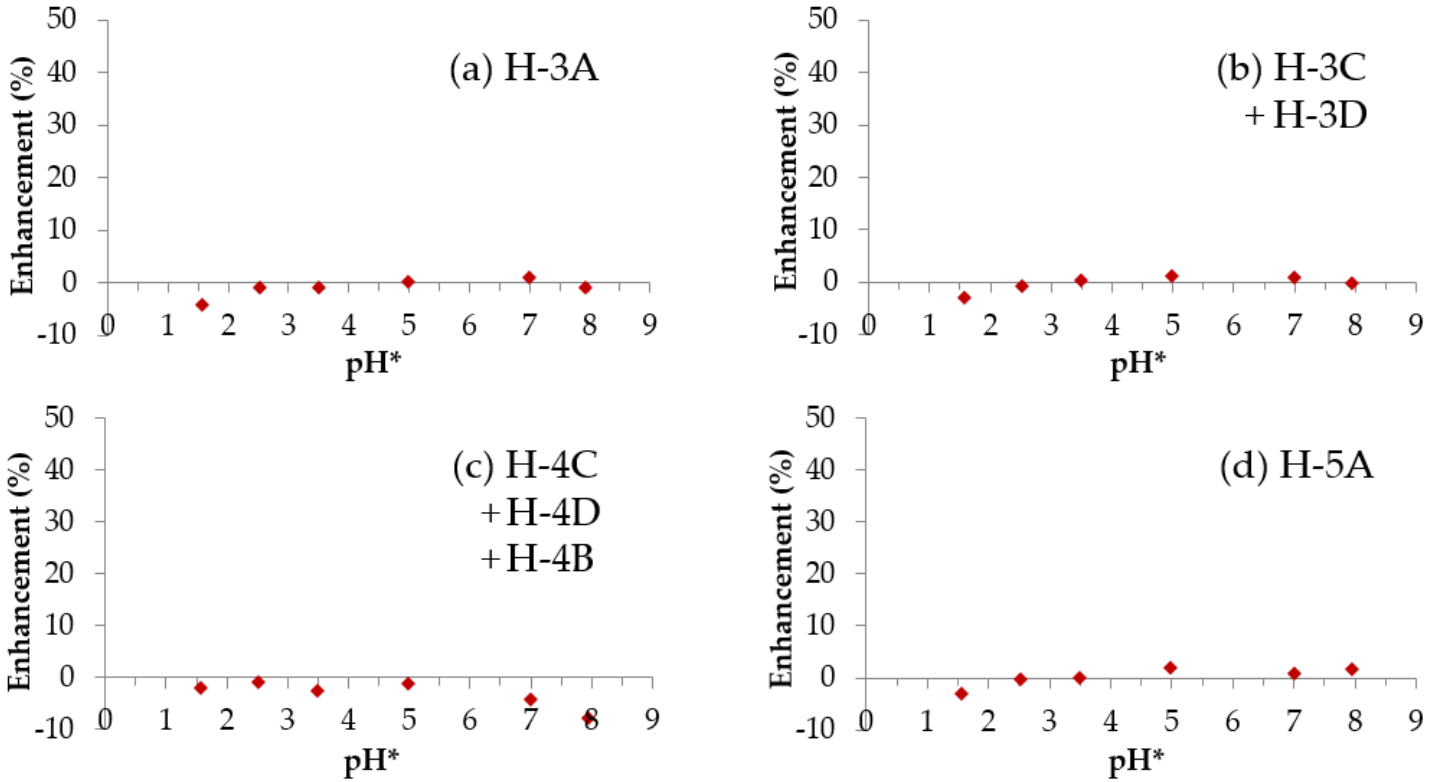

Figure 3.32 – pH# effect on the ^{1}H photo-CIDNP enhancements observed for the complex $[R\text{-}IrN_5C_1]^{2+}$ in the presence of dGMP for the signals of the N,N'-bpy ligand: (a) H-3A, (b) H-3C + H-3D, (c) H-4C + H-4D + H-4B, (d) H-5A

3.3.5.1 Photo-CIDNP enhancements at $pH^{\#}$ > 4.99

In this range of $pH^{\#}$, the complex is not protonated in its ground and excited states (*vide supra*). In the presence of dGMP, the luminescence of the complex is quenched, indicating that a photoinduced electron transfer should be at stake in these conditions.

Upon irradiation, an electron from dGMP is transferred to the Iridium centre. Based on the determined pKa of mono-reduced $[R\text{-}IrN_5C_1\text{-}H]^{\bullet 2+}$, it can be safely assumed that in this $pH^{\#}$ region, the mono-reduced complex will remain unprotonated on the whole $pH^{\#}$ range considered. We can thus consider that PET reactions depicted in equations 3.15 and 3.16 are occurring in highly basic and neutral conditions, respectively.

$$[\mathrm{Ir(III)}(N,N'\text{-bpy})(N,N'\text{-bpy})(N,C^3\text{-bpy})]^{2+*} + (\mathrm{dGMP}-\mathrm{H})^- \rightarrow [\mathrm{Ir(III)}(N,N'\text{-bpy})^{\bullet -}(N,N'\text{-bpy})(N,C^3\text{-bpy})]^{+} + (\mathrm{dGMP}-\mathrm{H})^{\bullet} \quad \text{eq 3.15}$$

$$[\mathrm{Ir(III)}(N,N'\text{-bpy})(N,N'\text{-bpy})(N,C^3\text{-bpy})]^{2+*} + \mathrm{dGMP} \rightarrow [\mathrm{Ir(III)}(N,N'\text{-bpy})^{\bullet -}(N,N'\text{-bpy})(N,C^3\text{-bpy})]^{+} + \mathrm{dGMP}^{\bullet +} \quad \text{eq 3.16}$$

Considering the LUMO centered on the N,N'-bpy ligands, one should expect that photo-CIDNP enhancements should be observed onto a N,N'-bpy ligand in the presence of dGMP. However, as stated earlier, no enhancement could be observed on the Iridium complex. Nevertheless, the aromatic ^1H of dGMP exhibits a negative photo-CIDNP effect confirming the presence of the photoinduced electron transfer. The absence of CIDNP effects on the complex can be rationalized by the occurrence of electron self-exchange between mono-reduced and ground state complexes, which are both at the same protonation state. Indeed, dissociation of the triplet radical-pairs generated by the PET (the so-called geminate radical pairs) yields non-

protonated free radicals of the mono-reduced Iridium complex in solution which can be involved in electron self-exchange with the parent diamagnetic complex as depicted in equation 3.17.[14]

$$[\mathbf{R\text{-}Ir(III)N_5C_1}]^{\bullet+} + [\text{R-Ir(III)N}_5\text{C}_1]^{2+} \rightleftharpoons [\mathbf{R\text{-}Ir(III)N_5C_1}]^{2+} + [\text{R-Ir(III)N}_5\text{C}_1]^{\bullet+} \quad \text{eq 3.17}$$

Electron self-exchange may effectively inhibit or even prevent the build-up of non-equilibrium nuclear polarization during steady-state illumination. The electron self-exchange is the most probable reason to explain the absence of photo-CIDNP effect; however, neither longer longitudinal relaxation time nor signal broadening for the Ir(III) complex to support this hypothesis can be observed.

3.3.5.2 Photo-CIDNP enhancements at 1.56 < pH# < 4.99

In the pH# range considered in this region, the situation is more complex. Indeed, we will deal with both protonated and unprotonated species. On the one hand, the protonation state of dGMP will vary in this region as the pKa of the guanine moiety is equal to 2.69. On the other hand, even if the Iridium complex will not be protonated in its ground state, the protonation of its excited state has to be taken into account, as we determined that the apparent pKa of the excited state of the complex is around 3.45. In addition, as presented earlier, the mono-reduced complex is expected to be protonated (Figure 3.26) due to the presence of an additional electron on one ligand of the complex that increases the basicity of the mono-reduced complex yielding to pKa = 6.14 (*vide supra*).

Unlike $[Ru(TAP)_3]^{2+}$ complex, $[R\text{-}IrN_5C_1]^{2+}$ does not show any symmetry elements yielding to a manifold of possible positions for the unpaired electron. Indeed, photo-CIDNP enhancements with different intensities were detected on each ^1H signal of the protonated cyclometalated N,C^3-bpy ligand as presented in Figure 3.31. These signals increase to reach their maximum at $pH^{\#} = 1.56$. An inflection point of the evolution of photo-CIDNP effect as a function of $pH^{\#}$ can be observed at $pH^{\#} \approx 3.25$. Taking into account the correction due to the use of D_2O (pH ≈ 3.44), this pH value is, interestingly, close to the apparent pKa of the excited complex ($pKa_{app}^* = 3.45$).

In contrast to higher $pH^{\#}$ region where photo-CIDNP effects are absent despite the occurrence of the PET, the detection of photo-CIDNP effects at $pH^{\#} < 4.99$ is possible thanks to the protonation of the mono-reduced complex generated by the PET. This protonation inhibits the electron self-exchange mechanism with ground state complex as they both display different protonation states. The dependence of the intensity of the observed photo-CIDNP enhancements as function of $pH^{\#}$ can be rationalized by considering not only the protonation state of the mono-reduced complex, but also the protonation of the excited complex. Indeed, since the apparent pKa of the excited complex is evaluated to be 3.45, protonation of the excited complex can occur prior to the electron transfer at lower $pH^{\#}$ value (*vide infra*).

Since the excited state of the neutral $[R\text{-}IrN_5C_1]^{2+}$ corresponds to a complex ^{3}MLLCT/^{3}LC mixture with the LUMO localized on all N,N'-bpy and N,C^3-bpy ligands (Figure 3.33 – step "hυ"), after PET from neutral dGMP to excited $[R\text{-}IrN_5C_1]^{2+*}$ has occurred (equation 3.18 and Figure 3.33 – step "PET"), the radical electron on the mono-reduced

complex is thus localized on these ligands. A proton transfer (HT) has to occur subsequently (equation 3.19 and Figure 3.33 – step "HT"), not only to inhibit electron self-exchange, but also to explain the occurrence of photo-CIDNP effects on the cyclometalated N,C^3-bpy ligand but not on N,N′-bpy ligands. Indeed, if it can be assumed that the radical electron on the unprotonated mono-reduced complex should be located on the N,N′-bpy ligand, this radical electron moves to the N,C^3-bpy ligand of the mono-reduced complex when protonated *i.e.* through a Ligand-to-Ligand Charge Transfer (LLCT) process (equation 3.20 and Figure 3.33 – step "LLCT"). It can be safely concluded that at 3.45 < pH$^{\#}$ < 5 (following a photoinduced electron transfer implying the ^{3}MLLCT excited state):

$$[\mathrm{Ir(III)}(N,N'\text{-bpy})(N,N'\text{-bpy})(N,C^3\text{-bpy})]^{2+*} + \mathrm{dGMP}$$

$$\xrightarrow{\mathrm{PET}} [\mathrm{Ir(III)}(N,N'\text{-bpy})^{\bullet-}(N,N'\text{-bpy})(N,C^3\text{-bpy})]^{+} + \mathrm{dGMP}^{\bullet+} \quad \text{eq 3.18}$$

$$[\mathrm{Ir(III)}(N,N'\text{-bpy})^{\bullet-}(N,N'\text{-bpy})(N,C^3\text{-bpy})]^{+} + \mathrm{H}^{+}$$

$$\xrightarrow{\mathrm{HT}} [\mathrm{Ir(III)}(N,N'\text{-bpy})^{\bullet-}(N,N'\text{-bpy})(N,C^3\text{-bpy-H})^{+}]^{2+} \quad \text{eq 3.19}$$

$$[\mathrm{Ir(III)}(N,N'\text{-bpy})^{\bullet-}(N,N'\text{-bpy})(N,C^3\text{-bpy-H})^{+}]^{2+}$$

$$\xrightarrow{\mathrm{LLCT}} [\mathrm{Ir(III)}(N,N'\text{-bpy})(N,N'\text{-bpy})(N,C^3\text{-bpy-H})^{\bullet}]^{+} + \mathrm{dGMP}^{\bullet+} \quad \text{eq 3.20}$$

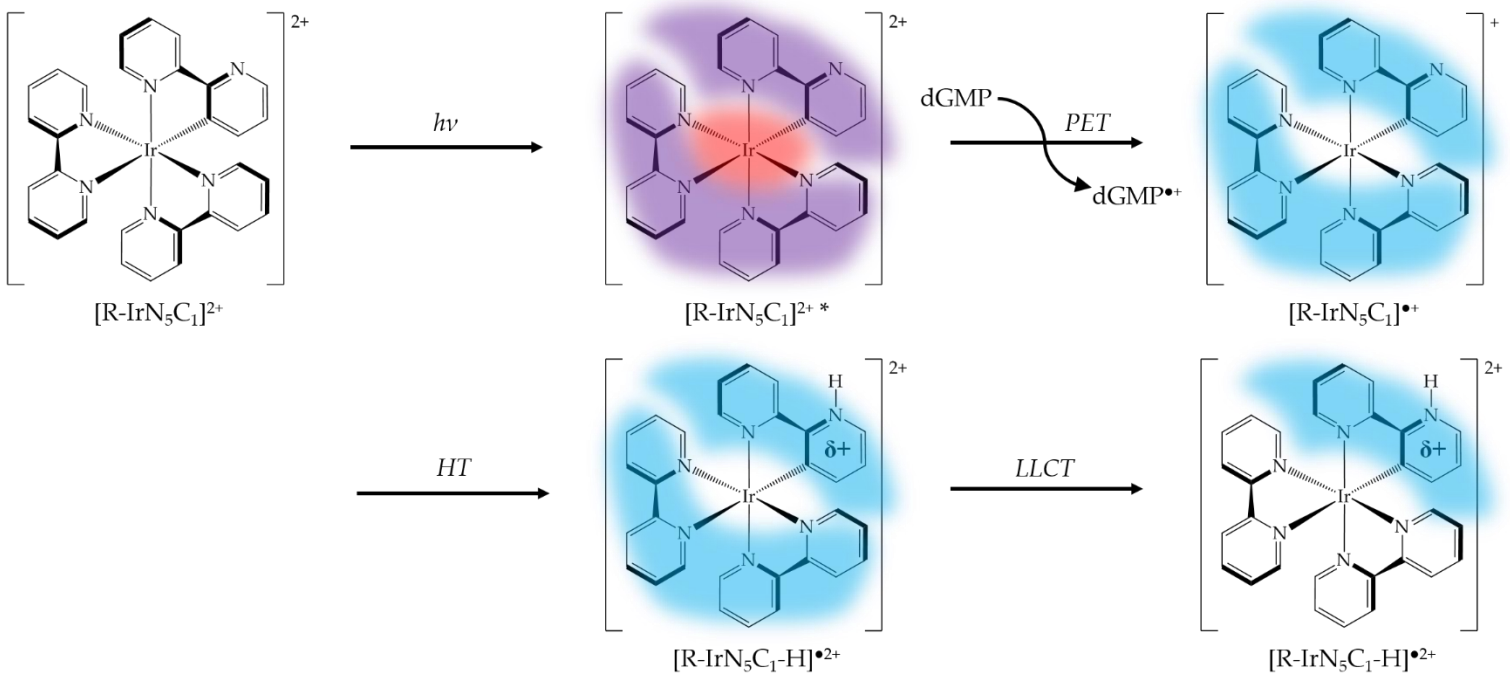

Figure 3.33 – Description of the electron transfers within $[R\text{-}IrN_5C_1]^{2+}$ during the photoreaction between the neutral photosensitizer and dGMP at $1.56 < pH^{\#} < 4.99$ with schematic localization of lone electrons on the former HOMO (*red*) and LUMO (*blue*).
(PET = Photoinduced Electron Transfer – HT = Proton Transfer – LLCT = Ligand-to-Ligand Charge Transfer)
(*purple* describes the presence of both lone electrons on HOMO and LUMO on the same part of the complex)

The intensity of photo-CIDNP effects are expected to be more important in the case of ET-HT as (i) ET is favored, generating more ion pairs, (ii) at this range of $pH^{\#}$, no unprotonated mono-reduced complex is present which could be involved in electron self-exchange, lowering the photo-CIDNP effects, and (iii) the hyperfine coupled ISC BET and the ion-pair splitting is not in competition with the proton transfer, enhancing the nuclear polarization.

As a conclusion, the excited state of the protonated $[R\text{-}IrN_5C_1\text{-}H]^{3+}$ complex has been attributed to a ^3LC transition localized on the cyclometalated protonated N,C^3-bpy-H^+ ligand.

3.3.5.3 Photo-CIDNP enhancements at $pH^{\#} \leq 1.56$

In this range of $pH^{\#}$, both the complex and the dGMP are protonated in the ground state. As investigated, the excited protonated complex has a reduction potential close to the one of the unprotonated excited complex while, on the other hand, protonation of the guanine moiety at low pH will expectedly increase the oxidation potential of the nucleobase and, therefore, have a negative effect on the exergonicity of the PET. Besides, electrostatic repulsion between protonated dGMP-H^+ and the positively charged excited complex also reduce the quenching efficiency, as observed in the luminescence experiments. Nevertheless, according to Stern-Volmer experiments (Figure 3.28a), a PET still occurs and photo-CIDNP enhancements are thus expected.

Indeed, as observed on Figure 3.30, photo-CIDNP effects on both Ir(III) complex and nucleobase were detected at low $pH^{\#}$. As the

observation of photo-CIDNP effects is a clear-cut indication for a reaction via radical pairs, previously observed luminescence quenching cannot be due to an energy transfer and are thus, as postulated, induced by the PET. Such electron transfer at low pH with a protonated guanine could not be highlighted with highly photooxidizing Ru(II) complexes such as $[Ru(TAP)_3]^{2+}$,[21] confirming our former hypothesis of a photoinduced electron transfer from protonated $[R\text{-}IrN_5C_1\text{-}H]^{3+}$ to the protonated nucleic base (equation 3.21), *i.e.* photoreduction of the guanine unit.

$$[\text{Ir(III)}(N,N'\text{-bpy})(N,N'\text{-bpy})(N,C^3\text{-bpy-H})]^{3+*} + \text{dGMP-H}^+ \rightarrow [\text{Ir(III)}(N,N'\text{-bpy})(N,N'\text{-bpy})(N,C^3\text{-bpy-H})^{\bullet+}]^{4+} + \text{dGMP-H}^{\bullet} \quad \text{eq 3.21}$$

It is noteworthy that despite the change in photoinduced electron transfer pathway, the mono-oxidized Ir(III) complex remains protonated and, hence, meets all requirements for the occurrence of photo-CIDNP enhancements.

For illustration purposes, the aromatic regions of ^{1}H NMR spectra showing the signals of $[R\text{-}IrN_5C_1]^{2+}$ and dGMP are displayed in Figure 3.34 for the sample at $pH^{\#}$ = 1.56. With respect to spectrum D1, the peaks exhibit positive photo-CIDNP enhancements of about 25% to 70% for signals H-3E, H-6′ and H-4E and a negative effect (-19%) for signal H-6E. On the other hand, H-5E, H-5′ and H-4′ exhibit a much stronger effect with enhancements of 175%, 112% and 212%, respectively. The intensity of the aromatic ^{1}H of dGMP is decreased by about 4% (negative photo-CIDNP effect, emissive polarization). In subsequent spectra recorded under sample illumination, the ^{1}H NMR signal of dGMP showed slight narrowing. The linewidth of the Ir(III) complex signals is not significantly modified but photo-CIDNP attenuation was observed (*e.g.* H-5′ and H-4′ – Figure 3.35). The

occurrence of such extinction in photo-CIDNP enhancements was reported in previous work with $[Ru(TAP)_3]^{2+}$ and indicates an accumulation of long-lived radicals species in exchange with the diamagnetic complex.[39]

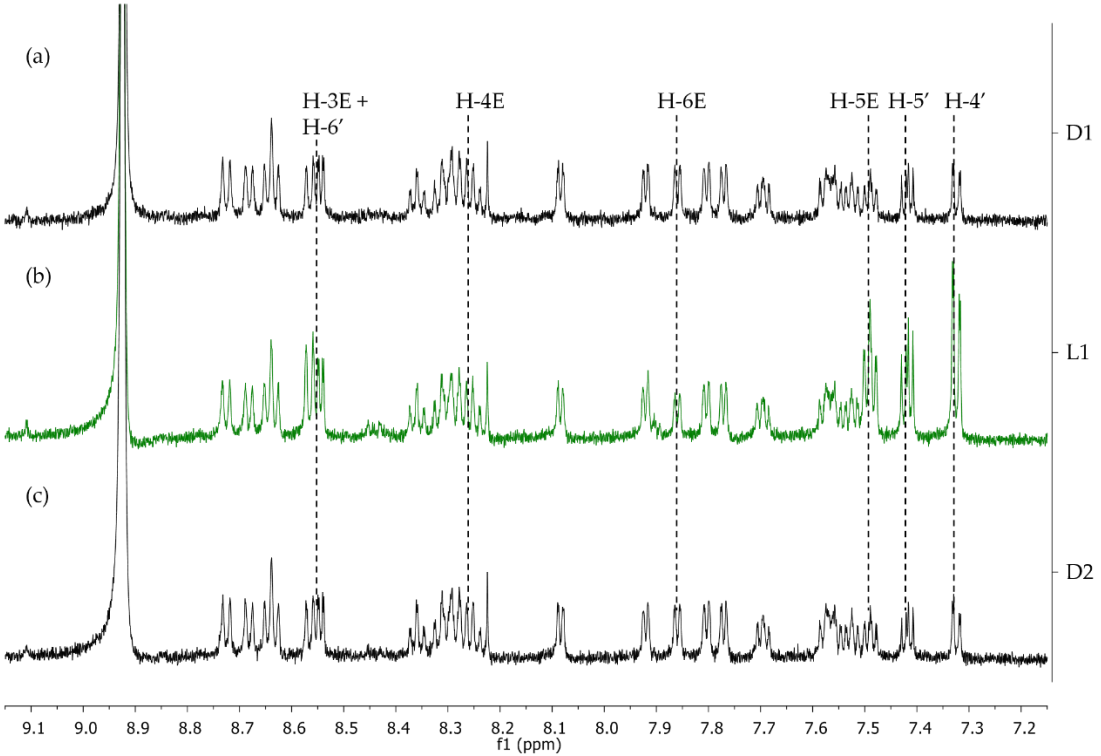

Figure 3.34 – ^{1}H NMR signals of $[R\text{-}IrN_5C_1]^{2+}$ observed for the sample at $pH^{\#}$ = 1.56: (a) equilibrium spectrum D1 recorded without illumination ; (b) spectrum L1 obtained with illumination at 405 nm ; (c) spectrum D2 recorded without illumination immediately after spectrum L1. All the ^{1}H signals exhibiting photo-CIDNP effects are displayed.

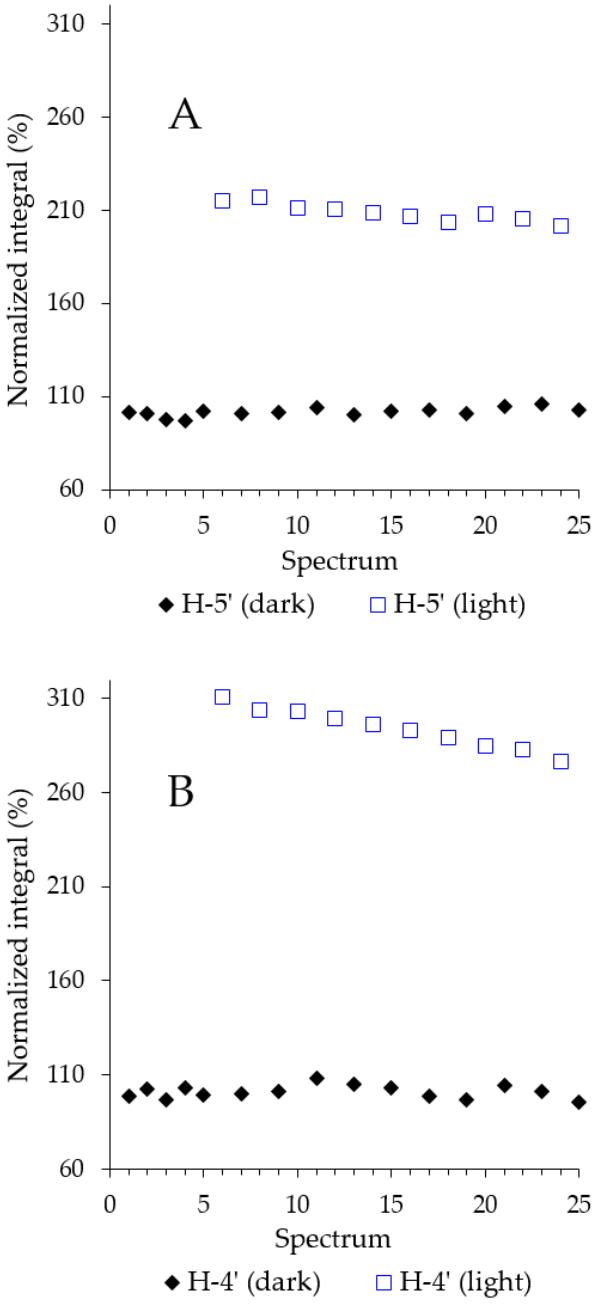

Figure 3.35 – Photo-CIDNP effect attenuation on (a) H-5′ and (b) H-4′ with increasing number of experiments

It is noteworthy to indicate that due to progressive protonation with decreasing $pH^{\#}$, some ^{1}H NMR signals are overlapped. It becomes thus extremely difficult to evaluate accurately the photo-CIDNP effects on a lone signal at $pH^{\#} = 0.21$ and 0.93. For example, H-5E, H-5′ and H-4′ from N,C^{3}-bpy ligand involved in the photo-CIDNP process are mixed with H-5C, H-5D and H-5B belonging to N,N′-bpy ligands. Enhancements are determined considering a whole area of chemical shifts under such acidic conditions. At $pH^{\#} = 0.93$, those six signals displayed an average integration of 9.108 ^{1}H under illumination *i.e.* an enhancement of 3.108 ^{1}H, whereas it is only 8.025 ^{1}H *i.e.* an enhancement of 2.025 ^{1}H at $pH^{\#} = 0.21$. As a comparison, an average enhancement of 4.546 ^{1}H for the same signals could be measured at $pH^{\#} = 1.56$. Thus, despite the overlap of signals at lower $pH^{\#}$, a net decrease of photo-CIDNP enhancement at highly acidic $pH^{\#}$ is detected. This lowering of the photo-CIDNP effect can be rationalized by an electron self-exchange mechanism between the protonated mono-oxidized complex $[Ir(N,N'\text{-bpy})_2(N,C^{3}\text{-bpy-H})^{\bullet}]^{4+}$ and the increasing amount of protonated complex at the ground state with lowering of $pH^{\#}$. However, as it is the case for high $pH^{\#}$ conditions for which electron self-exchange is also expected, no significant signal broadening can be observed on the NMR signals of the complex. Another plausible explanation for the decrease of photo-CIDNP enhancements at low $pH^{\#}$ is the ionic repulsion between both cationic protonated dGMP-H^{+} and Iridium complex. Indeed, Stern-Volmer experiments confirm the feasibility of electron transfer between both species at low pH, but low quenching rate constants attest of inhibited approach due to their respective protonation states (Table 3.4). As the electron transfer is required to observe photo-CIDNP enhancements, a decrease in photoreactivity towards PET may explain the decrease of

photo-CIDNP effects on the Ir(III) complex. This is in agreement with previously described photo-CIDNP enhancements at low $pH^{\#}$ involving $[Ru(TAP)_3]^{2+}$ when using N-acetyltyrosine or 1,4-hydroquinone as reducing agents.[21] Indeed, no photo-CIDNP effect could be detected in the presence of GMP at low $pH^{\#}$ while the use of both other non-protonable (*i.e.* uncharged) quenchers allowed the detection of radicals on the Ruthenium complex.

An electron transfer originating from residual non-protonated dGMP could be considered at low $pH^{\#}$. Nevertheless, using determined $pKa^{\#}$(dGMP), the calculated amount of non-protonated dGMP (starting with 2 mM dGMP) at $pH^{\#} = 0.21$ is ~0.0134 mM making it unlikely to detect such intense photo-CIDNP effects at this $pH^{\#}$.

As observed for $1.56 < pH^{\#} < 4.99$, no significant photo-CIDNP effect was measured for the N,N'-bpy ligands on $[R\text{-}IrN_5C_1\text{-}H]^{3+}$ but only on the protonated N,C^3-bpy-H^+ despite the change in PET pathway *i.e.* from the reduction of the complex at higher $pH^{\#}$ to its oxidation by dGMP-H^+ at $pH^{\#} < 1.56$. Indeed, due to protonation of the ground state $[R\text{-}IrN_5C_1]^{2+}$ (equation 3.22 and Figure 3.36 – step "HT"), the excited state of the complex corresponds to a ^{3}LC transition with the LUMO localized on the cyclometalated N,C^3-bpy-H^+ ligand (Figure 3.36 – step "hυ"), as confirmed by previous measurements (Chapter 2). Photoreduction of protonated dGMP-H^+ by excited $[R\text{-}IrN_5C_1\text{-}H]^{3+*}$ then occurs leading to protonated mono-oxidized complex, with remaining unpaired electron localized on the protonated cyclometalated N,C^3-bpy-H^+ ligand (equation 3.23 and Figure 3.36 – step "PET"), and photoreduced guanine residue.

$$[\text{Ir(III)}(N,N'\text{-bpy})_2(N,C^3\text{-bpy})]^{2+} + \text{H}^+ \xrightarrow{\text{HT}} [\text{Ir(III)}(N,N'\text{-bpy})_2(N,C^3\text{-bpy-H})^+]^{3+} \qquad \text{eq 3.22}$$

$$[\mathrm{Ir(III)}(N,N'\text{-bpy})_2(N,C^3\text{-bpy-H})^+]^{3+*} + \mathrm{dGMP\text{-}H^+}$$
$$\xrightarrow{\mathrm{PET}} [\mathrm{Ir(III)}(N,N'\text{-bpy})_2(N,C^3\text{-bpy-H})^{\bullet 2+}]^{4+} + \mathrm{dGMP\text{-}H^\bullet} \qquad \text{eq 3.23}$$

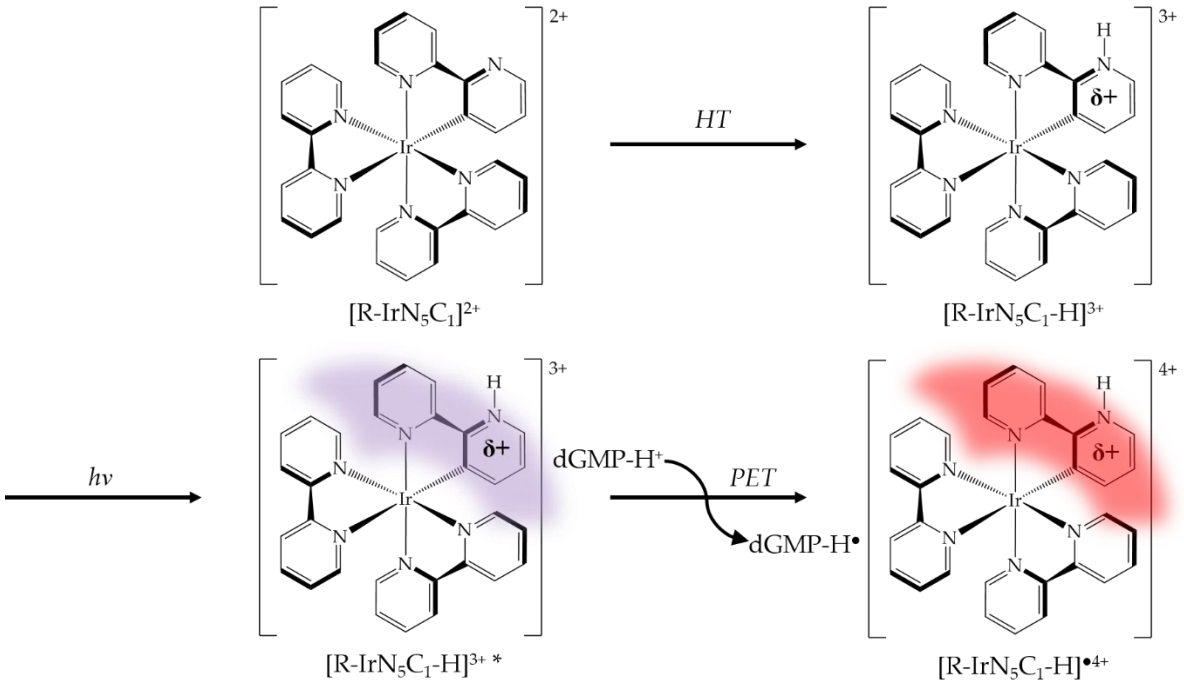

Figure 3.36 – Description of the electron transfers within $[R\text{-}IrN_5C_1\text{-}H]^{3+}$ during the photoreaction between the protonated photosensitizer and $dGMP\text{-}H^+$ at $pH^{\#} < 1.56$ with schematic localization of lone electrons on the former HOMO (*red*).

(PET = Photoinduced Electron Transfer – HT = Proton Transfer)

(*purple* describes the presence of both lone electrons on HOMO and LUMO on the same part of the complex)

3.4 Conclusion

Photo-CIDNP experiments allowed us to gain insight into the photophysics of $[R\text{-}IrN_5C_1]^{2+}$, its photoreactivity in the presence of a reducing agent and the pH dependency of a protonable Iridium complex, never observed so far. When irradiated, according to an ET-PT (Electron Transfer – Proton Transfer) mechanism, an electron from one of the bpy ligands is promoted to the π^* orbital of the same ligand. Because of the difference between pKa at the ground state and pKa of the mono-reduced complex, the ET is followed by the protonation of the cyclometalated ligand at $1.56 < pH^{\#} < 4.99$ and the latter gets a higher electron-withdrawing behaviour, generating a ^{3}LC excited state only centered on the N,C-bpy-H^+ ligand. It is worth mentioning that a PT-ET (Proton Transfer – Electron Transfer) could also occur. Indeed, pKa of the monoreduced complex and pKa of the excited complex have high values (*vide supra*); furthermore, the reduction potential of both neutral and protonated complexes are close to each other. Because of the Stern-Volmer relationships between non-protonable $[IrN_6]^{3+}$ and dGMP-H^+, a PCET mechanism involving residual neutral $[R\text{-}IrN_5C_1]^{2+}$ is unlikely.

Interestingly, a highly acidic medium led to a change in photoreactivity of $[R\text{-}IrN_5C_1]^{2+}$ towards the nucleic. Indeed, protonated dGMP-H^+ displays a high reduction potential leading to the photooxidation of the protonated complex and subsequent formation of a reduced Guanine base.

3.5 References

1. Bargon, J.; Fischer, H.; Johnsen, U., Kernresonanz-Emissionslinien während rascher Radikalreaktionen. *Zeitschrift für Naturforschung A* **1967**, *22*, 1551-1555.
2. Lawler, R. G., Chemically induced dynamic nuclear polarization. *J. Am. Chem. Soc.* **1967**, *89*, 5519-5521.
3. Roth, H. D., Chemically induced nuclear spin polarization in the study of carbene reaction mechanisms. *Acc. Chem. Res.* **1977**, *10*, 85-91.
4. Batchelor, S. N.; Fischer, H., Radical Addition Rates to Alkenes by Time-Resolved CIDNP: 2-Hydroxy-2-propyl Radicals. *J. Phys. Chem.* **1996**, *100*, 9794-9799.
5. Neshchadin, D.; Gescheidt, G., CIDNP as a tool for rapid rearrangements: New insights into cyclobutanoid 4-center/3-electron radical cations. *J. Phys. Org. Chem.* **2013**, *26*, 737-741.
6. Fischer, H.; Baer, R.; Hany, R.; Verhoolen, I.; Walbiner, M., 2,2-Dimethoxy-2-phenylacetophenone: photochemistry and free radical photofragmentation. *J. Chem. Soc., Perkin Trans. 2* **1990**, 787-798.
7. Roth, H. D., Biradicals by triplet recombination of radical ion pairs. *Photochemical & Photobiological Sciences* **2008**, *7*, 540-546.
8. Day, I. J.; Wain, R.; Tozawa, K.; Smith, L. J.; Hore, P. J., Photo-CIDNP NMR spectroscopy of a heme-containing protein. *J. Magn. Reson.* **2005**, *175*, 330-335.
9. Lee, J. H.; Cavagnero, S., A novel tri-enzyme system in combination with laser-driven NMR enables efficient nuclear polarization of biomolecules in solution. *J. Phys. Chem. B* **2013**, *117*, 6069-6081.
10. Morozova, O. B.; Yurkovskaya, A. V.; Sagdeev, R. Z.; Mok, K. H.; Hore, P. J., Time-Resolved CIDNP Study of Native-State Bovine and Human α-Lactalbumins. *J. Phys. Chem. B* **2004**, *108*, 15355-15363.
11. Mok, K., Photo-CIDNP NMR methods for studying protein folding. *Methods* **2004**, *34*, 75-87.
12. Morozova, O. B.; Yurkovskaya, A. V.; Tsentalovich, Y. P.; Forbes, M. D. E.; Hore, P. J.; Sagdeev, R. Z., Time resolved CIDNP study of electron transfer reactions in proteins and model compounds. *Mol. Phys.* **2002**, *100*, 1187-1195.
13. Yurkovskaya, A. V.; Snytnikova, O. A.; Morozova, O. B.; Tsentalovich, Y. P.; Sagdeev, R. Z., Time-resolved CIDNP and laser flash photolysis study of the photoreaction between triplet 2,2'-dipyridyl and guanosine-5'-monophosphate in water. *Phys. Chem. Chem. Phys.* **2003**, *5*, 3653-3659.
14. Perrier, S.; Mugeniwabagara, E.; Kirsch-De Mesmaeker, A. e.; Hore, P. J.; Luhmer, M., Exploring Photoreactions between Polyazaaromatic Ru(II)

Complexes and Biomolecules by Chemically Induced Dynamic Nuclear Polarization Measurements. *J. Am. Chem. Soc.* **2009**, *131*, 12458-12465.
15. Juris, A.; Balzani, V.; Barigelletti, F.; Campagna, S.; Belser, P.; von Zelewsky, A., Ru(II) polypyridine complexes: photophysics, photochemistry, eletrochemistry, and chemiluminescence. *Coord. Chem. Rev.* **1988**, *84*, 85-277.
16. Campagna, S.; Puntoriero, F.; Nastasi, F.; Bergamini, G.; Balzani, V., Photochemistry and Photophysics of Coordination Compounds: Ruthenium. *Top. Curr. Chem.* **2007**, *280*, 117-214.
17. Gicquel, E.; Boisdenghien, A.; Defrancq, E.; Moucheron, C.; Kirsch-De Mesmaeker, A., Adduct formation by photo-induced electron transfer between photo-oxidising Ru(II) complexes and tryptophan. *Chem. Commun.* **2004**, 2764-2765.
18. Elias, B.; Kirsch-De Mesmaeker, A., Photo-reduction of polyazaaromatic Ru(II) complexes by biomolecules and possible applications. *Coord. Chem. Rev.* **2006**, *250*, 1627-1641.
19. Marcélis, L.; Ghesquière, J.; Garnir, K.; Kirsch-De Mesmaeker, A.; Moucheron, C., Photo-oxidizing RuII complexes and light: Targeting biomolecules via photoadditions. *Coord. Chem. Rev.* **2012**, *256*, 1569-1582.
20. Herman, L.; Ghosh, S.; Defrancq, E.; Mesmaekera, A. K.-D., Ru(II) complexes and light: molecular tools for biomolecules. *J. Phys. Org. Chem.* **2008**, *21*, 670-681.
21. Troian-Gautier, L.; Mugeniwabagara, E.; Fusaro, L.; Moucheron, C.; Kirsch-De Mesmaeker, A.; Luhmer, M., pH Dependence of Photoinduced Electron Transfer with [Ru(TAP)3](2). *Inorg. Chem.* **2017**, *56*, 1794-1803.
22. Kaptein, R.; Oosterhoff, J. L., Chemically induced dynamic nuclear polarization II. *Chem. Phys. Lett.* **1969**, *4*, 195-197.
23. Closs, G. L., Mechanism explaining nuclear spin polarizations in radical combination reactions. *J. Am. Chem. Soc.* **1969**, *91*, 4552-4554.
24. Day, I. J.; Maeda, K.; Paisley, H. J.; Mok, K. H.; Hore, P. J., Refolding of ribonuclease A monitored by real-time photo-CIDNP NMR spectroscopy. *J. Biomol. NMR* **2009**, *44*, 77-86.
25. Tsentalovich, Y. P.; Lopez, J. J.; Hore, P. J.; Sagdeev, R. Z., Mechanisms of reactions of flavin mononucleotide triplet with aromatic amino acids. *Spectroc. Acta A* **2002**, *58*, 2043-2050.
26. Bhat, R.; Wedemeyer, W. J.; Scheraga, H. A., Proline isomerization in bovine pancreatic ribonuclease A. 2. Folding conditions. *Biochemistry* **2003**, *42*, 5722-5728.
27. Troian-Gautier, L.; Mugeniwabagara, E.; Fusaro, L.; Cauet, E.; Kirsch-De Mesmaeker, A.; Luhmer, M., Photo-CIDNP Reveals Different Protonation Sites Depending on the Primary Step of the Photoinduced Electron-/Proton-

Transfer Process with Ru(II) Polyazaaromatic Complexes. *J. Am. Chem. Soc.* **2017**, *139*, 14909-14912.
28. van Slageren, J.; Martino, D. M.; Kleverlaan, C. J.; Bussandri, A. P.; van Willigen, H.; Stufkens, D. J., FT-EPR Study of Methyl Radicals Photogenerated from [Ru(Me)(SnPh3)(CO)2(iPr-DAB)] and [Pt(Me)4(iPr-DAB)]: An Example of a Strong Excitation Wavelength Dependent CIDEP Effect. *J. Phys. Chem. A* **2000**, *104*, 5969-5973.
29. Concepcion, J. J.; Brennaman, M. K.; Deyton, J. R.; Lebedeva, N. V.; Forbes, M. D.; Papanikolas, J. M.; Meyer, T. J., Excited state quenching by proton-coupled electron transfer. *J. Am. Chem. Soc.* **2007**, *129*, 6968-6969.
30. Mugeniwabagara, E.; Fusaro, L.; Luhmer, M., Full assignment of the 1H NMR spectrum of heteroleptic polyazaaromatic Ru(II) complexes based on long-range interligand NOEs. *Magnetic Resonance Chemistry* **2013**, *51*, 308-311.
31. Costa, R. n. D.; Orti, E.; Bolink, H. J.; Graber, S.; Schaffner, S.; Neuburger, M.; Housecroft, C. E.; Constable, E. C., Archetype Cationic Iridium Complexes and Their Use in Solid-State Light-Emitting Electrochemical Cells. *Adv. Funct. Mater.* **2009**, *19*, 3456-3463.
32. Box, K.; Bevan, C.; Comer, J.; Hill, A.; Allen, R.; Reynolds, D., High-Throughput Measurement of pKaValues in a Mixed-Buffer Linear pH Gradient System. *Anal. Chem.* **2003**, *75*, 883-892.
33. Avdeef, A., pH-Metric log P. II: Refinement of Partition Coefficients and Ionization Constants of Multiprotic Substances. *J. Pharm. Sci.* **1993**, *82*, 183-190.
34. Krężel, A.; Bal, W., A formula for correlating pKa values determined in D2O and H2O. *J. Inorg. Biochem.* **2004**, *98*, 161-166.
35. Song, B.; Oswald, G.; Bastian, M.; Sigel, H.; Lippert, B., Extent of the Acidification by N7-Coordinated cis-Diammine-Platinum(II) on the Acidic Sites of Guanine Derivatives. *Met.-Based Drugs* **1996**, *3*, 131-141.
36. Steenken, S.; Jovanovic, S. V., How Easily Oxidizable Is DNA? One-Electron Reduction Potentials of Adenosine and Guanosine Radicals in Aqueous Solution. *J. Am. Chem. Soc.* **1997**, *119*, 617-618.
37. Wong, A.; Ida, R.; Spindler, L.; Wu, G., Disodium guanosine 5'-monophosphate self-associates into nanoscale cylinders at pH 8: a combined diffusion NMR spectroscopy and dynamic light scattering study. *J. Am. Chem. Soc.* **2005**, *127*, 6990-6998.
38. Balzani, V.; Ceroni, P.; Juris, A., Photochemistry and Photophysics : concepts, research, applications. **2014**.
39. Perrier, S.; Mugeniwabagara, E.; Kirsch-De Mesmaeker, A.; Hore, P. J.; Luhmer, M., Exploring photoreactions between polyazaaromatic Ru(II) complexes and biomolecules by chemically induced dynamic nuclear polarization measurements. *J. Am. Chem. Soc.* **2009**, *131*, 12458-12465.

CHAPTER 4

Photocatalytic H_2 production using Ir(III)-Co(III) dyads

4.1 Foreword

In Chapter 2, we performed the synthesis of trischelate Ir(III) complexes with ppyH and/or bpy as ligands and observed a wide range of properties due to the variation of the first coordination sphere with C/N (C-chelation *vs.* N-chelation) ratio varying from 0/6 to 3/3. Despite the promising features of complexes such as $[R\text{-}IrN_5C_1]^{2+}$, the synthesis of the $[IrN_4C_2]^{+}$-like complexes appeared to be the easiest way to obtain a wide library of complexes with highly tuned properties.

The studies performed in collaboration with Prof. G. Hanan (Université de Montréal) and presented hereafter reflect our wish to study various heteroleptic Ir(III) complexes as photosensitizers for H_2 photoproduction by varying the cyclometalated N^C ligands as well as the ancillary N^N ligand. These Ir(III) complexes can be combined with a H_2 production catalyst via the N^N ligand.

4.2 Introduction

Despite Pt(II) and Pd(II) catalysts have shown a tremendous activity regarding photoinduced reduction of two protons into H_2,[1-4] Cobalt derivatives have drawn chemists' attention as an efficient and cheap alternative.[5-6] Indeed, Cobalt-containing supramolecules *e.g.* vitamin B_{12} appeared to be among the most efficient molecular electrocatalysts for H_2 evolution[7] from an acidic solution in the presence of reducing agents and mimic of this particular compound led to the synthesis of Cobalt bis-glyoximato complexes, referred as cobaloxime (Figure 4.1).

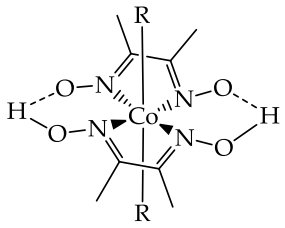

$R = H_2O, CH_3CN, Cl^-,...$

Figure 4.1 – Structure of the cobaloxime catalyst for H_2 evolution

Early studies of hydrogen production using cobaloximes as catalysts involve acidic solutions of metal salts of Eu(III) or Cr(II) used as sacrificial electron donors[8] and later with the electrons provided by a glassy carbon working electrode.[9-11] Nevertheless, as explained previously, direct conversion of solar energy to stored chemical potential by splitting water into hydrogen and oxygen is a highly attractive approach towards hydrogen evolution. This process requires the efficient coupling of the cobaloxime catalyst with a photosensitizer. The latter converts the luminous flux into a flow of electrons to be used by the catalytic center. It is worth mentioning that to allow this reaction

to proceed catalytically with respect to chromophore and catalyst, a sacrificial electron donor must be added to the system.

The proposed mechanisms for photoinduced hydrogen production within a dyad (catalyzed by Cobalt systems) are displayed in Figure 4.2.[5] All possible pathways start with the absorption of a photon by the photosensitizer (PS) yielding the excited state (PS*). From this state, a first electron transfer to acceptor Cobalt complex occurs to generate the active Co(I) species. A second electron transfer involving a sacrificial electron donor D regenerates the photosensitizer from oxidized PS^+. An alternate mechanism implies a prior reductive quenching of the photosensitizer induced by the sacrificial electron donor yielding reduced PS^- which subsequently reduces the catalyst to the Co(I) species. In the case of the Co(III) catalysts, a prior photoinduced electron transfer is mandatory to generate the Co(II) precursor which is further reduced to its Co(I) state. Protonation of the reduced Cobalt catalyst affords the active Co(III) hydride moiety from which hydrogen is released.

The establishment of the exact nature of the mechanism is dependent on the redox properties of the different couples (PS^*/PS^-, PS^+/PS, Co(III)/Co(II), Co(II)/Co(I), $D^{\bullet+}/D$) together with their relative concentration. In addition, it is noteworthy that some electrons entering the catalytic H_2 production cycle might originate from a distinct dark (*i.e.* thermal) process. Indeed, in numerous photocatalytic experiments, oxidized electron donors $D^{\bullet+}$ decompose over time and, in some cases, act like H_2-evolving catalysts.[12-13]

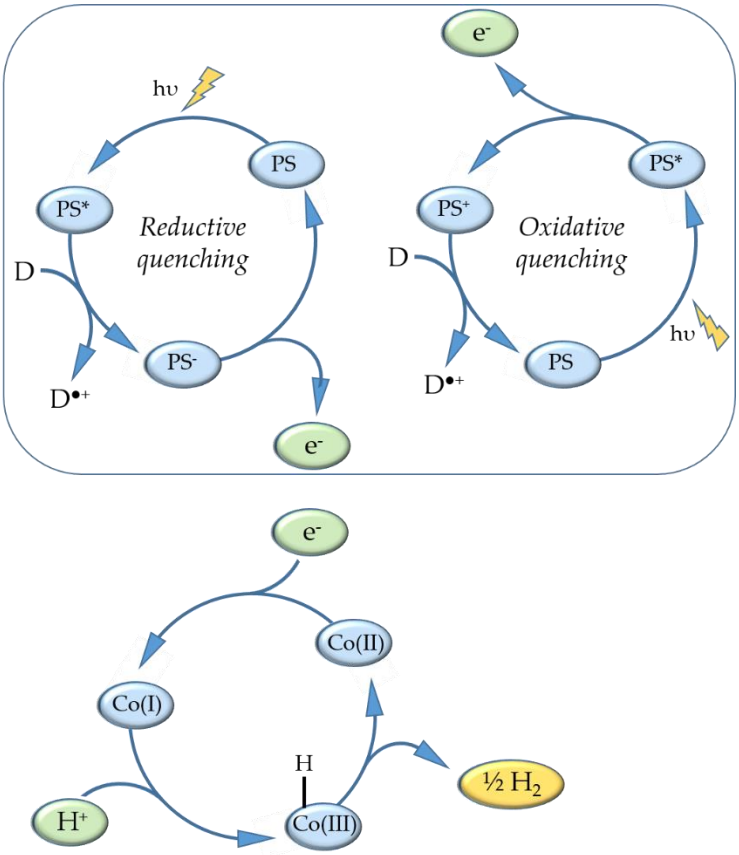

Figure 4.2 – Photosensitizer-based and Cobalt-based processes involved in photoinduced H_2 evolution catalyzed by Cobalt complexes (adapted from [5])

Cobaloxime moieties have been tethered to Pt(II), Re(I), Ru(II) and Ir(III) photosensitizer complexes.[14-16] Cationic cyclometalated Ir(III) complexes have advantages due to their higher tunability upon small variation of the first coordination sphere. Previous studies have shown that such Ir(III) complexes outperform archetypal photosensitizers such as $[Ru(bpy)_3]^{2+}$ (bpy = 2,2′-bipyridine) in H_2 photoproduction (Chapter 1).[14, 17] Furthermore, with respect to hydrogen evolution reactions, covalent linkage of the photosensitizer

to the catalyst gives in general rise to enhanced H_2 production when compared to dissociated, bimolecular systems.[14, 18]

In the literature, the covalent grafting of cobaloximes has been successively achieved on Ir(III) complexes (Figure 4.3)[14, 16] and the resulting activity is high compared to Ru(II) derivatives mostly due to the fact that (i) the stability of the Ir(III) center is higher than corresponding Ru(II) one and (ii) in the excited state, these complexes undergo faster reductive quenching.

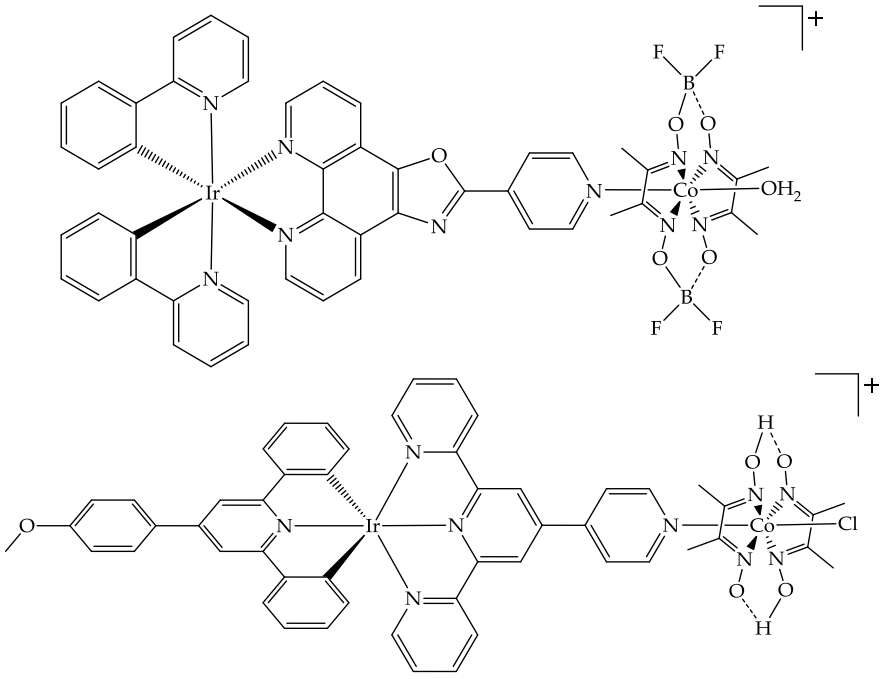

Figure 4.3 – Supramolecular [Ir-Co] dyads for photoinduced H_2 production

As literature based on [Ir-Co] dyads in the field of H_2 photoproduction only displays punctual studies on Ir(III) photosensitizers without any attempt of improvement, one of the focus of this chapter is thus to study thoroughly the influence of the Ir(III)

photosensitizers on H_2 evolution by varying the nature of the cyclometalated N^CH ligands as well as the ancillary N^N ligand connected to the Co(III) center (Figure 4.4). While the addition of electron-donating groups (methoxy-, *tert*-butyl-) onto the cyclometalated ligands is a promising approach for the reduction of protons, Bernhard and co-workers studied the influence of electron-withdrawing fluorine atoms on the cyclometalated ligands of $[Ir(ppy)_2(N^N)]^+$ derivatives and found out that the obtained complexes displayed a higher quantum yield together with an expected blue-shifted emission, in turn leading to a slightly more efficient H_2 photoproduction compared to non-fluorinated derivatives.[17, 19] In contrast, Huang and co-workers showed that using 1-phenylisoquinoline (piqH) as the cyclometalated ligand provide an enhanced conjugation of the system yielding to a higher molar absorptivity of the Ir(III) core as well as red-shifted absorption compared to 2-phenylpyridine.[20-21] Hence, in the present work, these cyclometalated ligands will also be investigated for H_2 photoproduction.

Two different terpyridines *i.e.* 2,2';4',4''-terpyridine (2244tpy) and 2,2';5',4''-terpyridine (2254tpy) have been used as bridging ligands between both Ir(III) and Co(III) centers. Indeed, despite their apparent similarity, both bridging ligands display different electron density on the pendant pyridine moiety leading to different photophysical properties (*vide infra*). The structures of the Ir(III) complexes and the resulting covalent (*i.e.* monocomponent) Ir(III)-Co(III) dyads studied in this chapter are presented in Figure 4.4. In addition, reference N^N ligand bpy will be chelated as well on Ir(III) photosensitizers to study separate (*i.e.* multicomponent) Ir(III) photosensitizer and Co(III) catalyst systems.

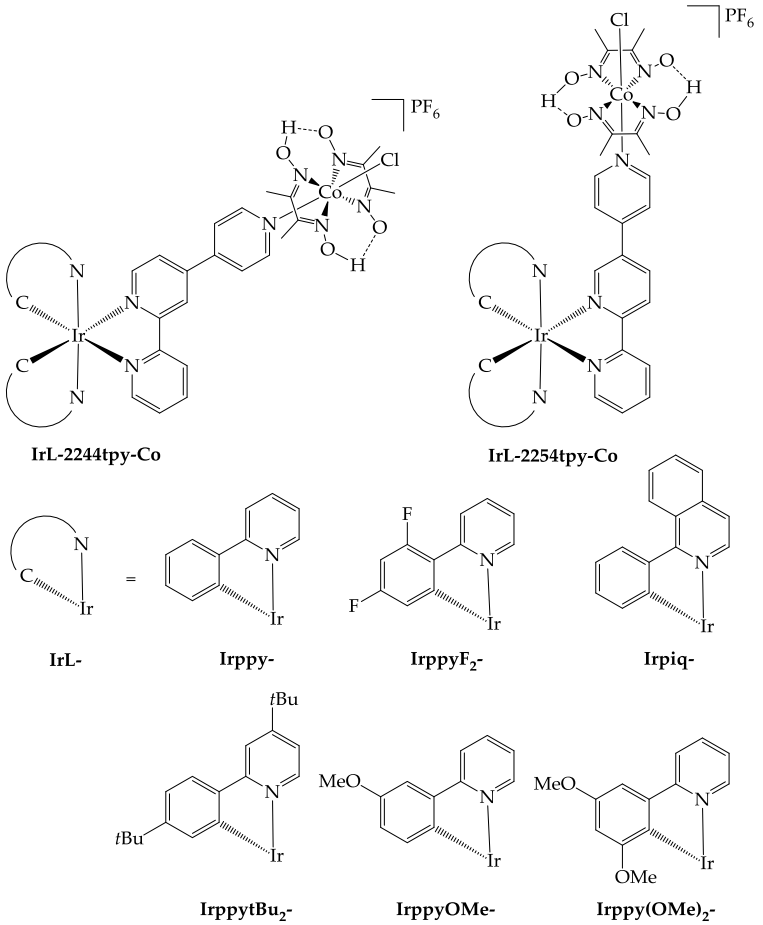

Figure 4.4 – Structures (and respective abbreviations used throughout this chapter) of the [Ir-Co] dyads

4.3 Synthesis

4.3.1 Synthesis of the aromatic ligands

2-(3′-methoxyphenyl)pyridine (*ppyOMeH*), 2-(3′,5′-dimethoxyphenyl)pyridine (*ppy(OMe)$_2$H*) and 4-(*tert*-butyl)-2-(4′-(*tert*-butyl)phenyl)pyridine (*ppytBu$_2$H*) (the latter provided by M. Abraham) are not commercially available and are synthesized via Suzuki coupling between corresponding bromopyridyl and phenylboronic acid derivatives with moderate yields (equation 4.1).

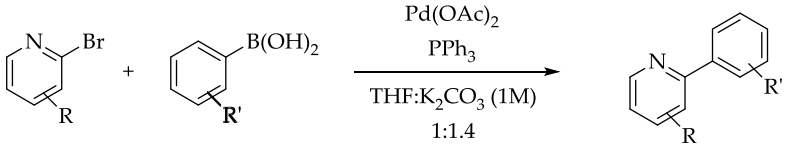

eq 4.1

R = H, R' = 3-methoxy : ppyOMeH ; *yield = 69%*
R = H, R' = 3,5-dimethoxy : ppy(OMe)$_2$H ; *yield = 49%*

The synthesis of the ancillary ligands was performed by using the same conditions with high yields (equation 4.2). Precursors 4-bromo-2,2′-bipyridine[22] and 5-bromo-2,2′-bipyridine[23] were synthesized following protocols reported in the literature.

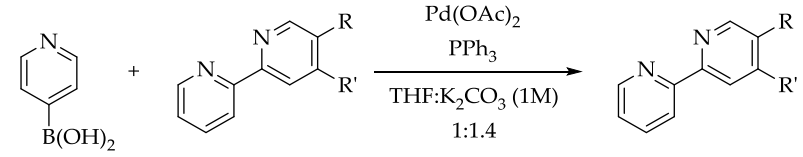

eq 4.2

R = H, R' = Br : 4-bromo-2,2'-pyridine
R = Br, R' = H : 5-bromo-2,2'-pyridine

R = H, R' = 4-pyridyl : 2244tpy ; *yield = 92%*
R = 4-pyridyl, R' = H : 2254tpy ; *yield = 82%*

4.3.2 Synthesis of the Ir(III) photosensitizers

As previously described, Ir(III) dimers [Ir(N^C)$_2$(μ-Cl)]$_2$ are obtained according to Nonoyama's method from an Iridium salt,

$IrCl_3.xH_2O$, and the desired ancillary ligands. $[Ir(ppy)_2(\mu\text{-}Cl)]_2$, $[Ir(ppyF_2)_2(\mu\text{-}Cl)]_2$, $[Ir(ppytBu_2)_2(\mu\text{-}Cl)]_2$ and $[Ir(piq)_2(\mu\text{-}Cl)]_2$ are obtained in good yields and high purity. $[Ir(ppyOMe)_2(\mu\text{-}Cl)]_2$ could not be obtained pure due to the twist of the phenyl ring orienting the methoxy substituent in *ortho* position with respect to the Ir-C bond (Figure 4.5A). As the chelation of a bpy ligand onto the Ir(III) center (*vide infra*) did not allow any easier purification, the synthesis and (photo)physical characterization of the Ir-ppy(OMe) family were abandoned. It is still noteworthy that the obtained $[Ir(ppyOMe)_2(bpy)]^+$ complex did not display any luminescence. Finally, only traces of $[Ir(ppy(OMe)_2)_2(\mu\text{-}Cl)]_2$ could be obtained, probably because of steric hindrance due to the methoxy substituent in *ortho* position with respect to the Ir-C bond (Figure 4.5B) and the Ir-ppy$(OMe)_2$ family thus will not be further studied.

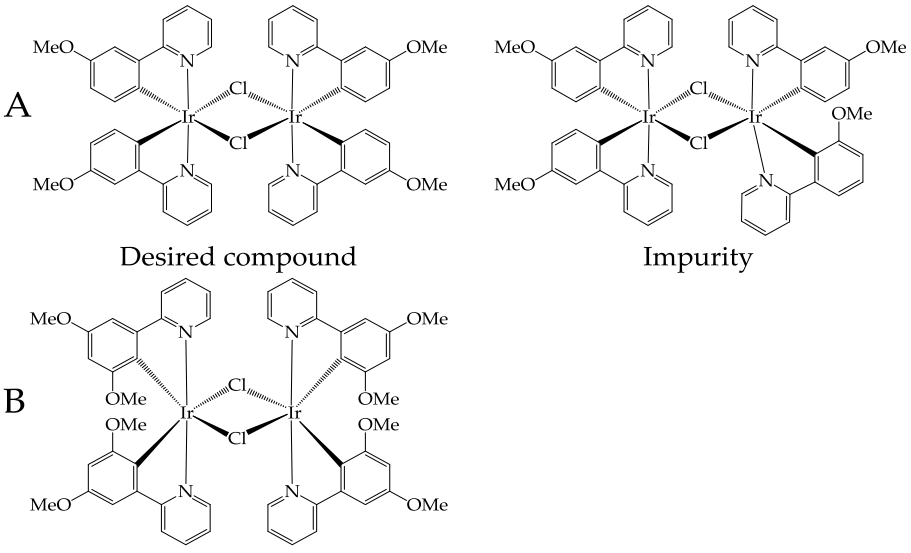

Figure 4.5 – Ir(III) dichloro-bridged dimers with (A) ppyOMeH and (B) ppy$(OMe)_2$H as cyclometalated ligands

All three N^N ligands *i.e.* bpy, 2244tpy and 2254tpy are chelated onto the Iridium dimeric precursors (with ppyH, $ppyF_2H$, $ppytBu_2H$ or piqH as cyclometalated ligands) in ethyleneglycol (equation 4.3). All the resulting complexes are obtained pure without any further purification in high yields. As $IrppytBu_2$-N^N photosensitizers display similar photophysical features compared to reference Irppy-N^N compounds (*vide infra*), they will not be further used for H_2 photoproduction.

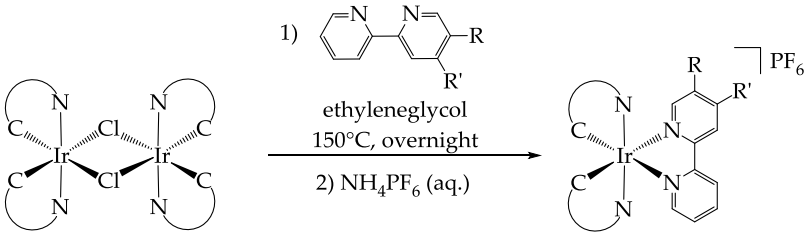

eq 4.3

R = H, R' = H : bpy ; *yield = 68-91%*
R = H, R' = 4-pyridyl : 2244tpy ; *yield = 67-92%*
R = 4-pyridyl, R' = H : 2254tpy ; *yield = 73-91%*

4.3.3 Synthesis of the Ir(III)-Co(III) dyads

The dyads [Ir-Co] are obtained via a chelation of the Cobalt precursor $Co(dmgH)(dmgH_2)Cl_2$ (synthesized according to literature)[10] on the pendant pyridine of the Ir(III) complexes bearing either 2244ty or 2254tpy in the presence of triethylamine. This synthetic pathway offers huge advantage as the reaction medium is close to the one used for H_2 photoproduction experiments, leaving the possibility of tuning both metallic centers separately and associating them subsequently *in situ* for the H_2 photoproduction experiments (*vide infra*).

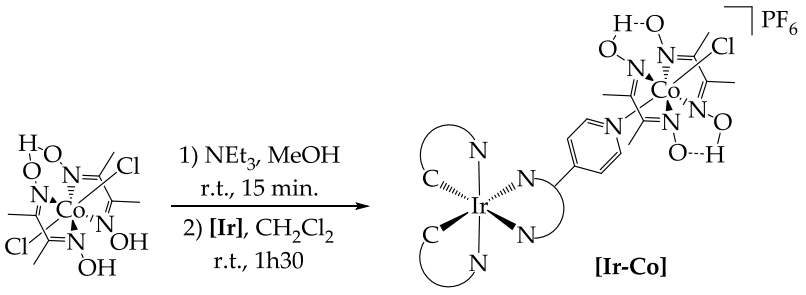

eq 4.4

IrX-2244tpy-Co : *yield = 72-81%*
IrX-2254tpy-Co : *yield = 74-79%*

4.4 Electrochemical properties

The electrochemical data for all the Ir(III) complexes and [Ir-Co] dyads have been obtained by cyclic voltammetry in dry deoxygenated acetonitrile which is a suitable solvent for photocatalytic H_2 production.[3, 16, 24-25] The voltammograms are illustrated for the [Ir-Co] dyads in Figures 4.6-4.9 while all the values are reported in Table 4.1.

All the Iridium-based complexes display only one oxidation wave in the investigated electrochemical window (see Supporting Information – Figures S4.1-S4.3). IrppyF_2-N^N complexes (N^N = 2244tpy, 2254tpy and bpy) display an anodically shifted oxidation wave compared to Irppy-N^N and Irpiq-N^N complexes ($E_{ox,IrppyF2\text{-}N^N}$ ≈ 1.72 V while $E_{ox,Irppy\text{-}N^N}$ ≈ $E_{ox,Irpiq\text{-}N^N}$ ≈ 1.37-1.43 V *vs.* Ag/AgCl) due to the electron-withdrawing effect of the fluorine atoms. In contrast, electron-donating groups in IrppytBu_2-N^N complexes generate a slight cathodic shift compared to Irppy-N^N reference compounds ($E_{ox,IrppytBu2\text{-}N^N}$ ≈ 1.27 V *vs.* Ag/AgCl). Furthermore, in each series, no substantial change in potential was observed with variation of the N^N ligand. These observations strongly suggest that the oxidation process occurs on the Iridium and/or the cyclometalated ligands fragment of the photosensitizers, irrespective of the nature of the N^N ligand. This attribution is confirmed by TD-DFT calculations showing that the HOMO has a mixed contribution of the metal (40%) and the phenyl part of the cyclometalated ligands (60%) (see Tables 4.2-4.4 for Irpiq-N^N family and Supporting information – Tables S4.1-S4.6 – for Irppy-N^N and IrppyF_2-N^N families). In the case of the dyads, chelation of the Co(III) center on the pendant pyridine does not affect the oxidation potential of the complexes, as expected since there is no contribution of this part of the complex in the HOMO level implying

an absence of communication between the two metal centers at the ground state. Another oxidation process at *ca* 1.3 V *vs.* Ag/AgCl (not displayed in Table 4.1) can be attributed to the forced reoxidation of the Co(II) center into Co(III), after reduction pathway studies (*vide infra*).

When looking at the reduction of the Ir(III) complexes, several waves have been observed (see Supporting Information – Figures S4.4-S4.6). The first reduction takes place on the N^N ligand, and, as expected from the electron-withdrawing character of the pendant pyridine and the extended conjugation of the ditopic ligand, the IrL-2244tpy and IrL-2254tpy series are easier to reduce than the IrL-bpy series ($E_{red,IrL\text{-}2244tpy}$ ≈ -1.17 V; $E_{red,IrL\text{-}2254tpy}$ ≈ -1.06 V; $E_{red,IrL\text{-}bpy}$ ≈ -1.28 V *vs.* Ag/AgCl). The theoretical models confirmed this, with slightly more delocalized electron density on the 2254tpy compared to the 2244tpy in all cases. Both IrL-2244tpy and IrL-2254tpy series display a second reduction process in contrast to the IrL-bpy series, this process corresponds to the reduction of the pyridine moiety. In the same way as it was observed for the first reduction process on the bpy residue, reduction of the pendant pyridine is slightly anodically shifted for IrL-2254tpy compared to IrL-2244tpy implying a more efficient stabilization on 5′ position of the bpy residue than on 4′ position. Irpiq-N^N complexes display a third reduction wave corresponding to the reduction of the isoquinoline part of the ancillary ligand ($E_{red,quinoline}$ ≈ -1.64 V *vs.* Ag/AgCl). When the Co(III) core is chelated onto IrL-2244tpy or IrL-2254tpy, two new reduction processes are observed at ≈-0.42 V and ≈-0.96 V *vs.* Ag/AgCl and correspond to irreversible Co(III)/Co(II) and reversible Co(II)/Co(I) reductions, respectively. The irreversibility of the first process is explained by the loss of the chloride ion from the Cobalt center upon one-electron reduction.[26] It is worth mentioning

that reduction values of the [Ir-Co] dyad are slightly less negative compared to the parent Ir(III) complexes and [Co(dmgH)$_2$PyrCl] (E_{red} = -1.10 V *vs.* Ag/AgCl in MeCN) due to the electron-withdrawing character of both metal centers in the supramolecular assembly compared to separate compounds.[27] Reduction of both bpy moiety and pendant pyridine are only slightly anodically shifted for the dyads with respect to the corresponding Ir(III) photosensitizers due to the weak stabilizing effect of the chelated reduced Cobalt center on the ligand.

Table 4.1 – Electrochemical data for the Ir(III) photosensitizers and corresponding [Ir-Co] dyads[a]

Complex	E_{ox}	E_{red}				
Irppy-2244tpy	1.37 (99)	-1.17 (100)	-1.72 (106)			
Irppy-2254tpy	1.37 (149)	-1.11 (198)	-1.62 (207)			
Irppy-bpy	1.37 (129)	-1.30 (111)				
IrppyF_2-2244tpy	1.72 (138)	-1.17 (86)	-1.72 (111)			
IrppyF_2-2254tpy	1.72 (129)	-1.06 (134)	-1.53 (166)			
IrppyF_2-bpy	1.71 (184)	-1.25 (169)				
Irpiq-2244tpy	1.42[b]	-1.16 (108)	-1.64 (114)	-1.86 (135)		
Irpiq-2254tpy	1.43[b]	-1.09 (124)	-1.60 (173)	-1.75 (131)		
Irpiq-bpy	1.36 (156)	-1.30 (128)	-1.67 (104)			
IrppytBu_2-2244tpy	1.30 (160)	-1.18 (78)	-1.77 (78)			
IrppytBu_2-2254tpy	1.26 (80)	-0.98 (87)	-1.89[b]			
IrppytBu_2-bpy	1.25 (81)	-1.31 (95)				
Irppy-2244tpy-Co	1.45[b]	-0.44[b]	-0.97 (128)	-1.14 (88)	-1.71 (96)	
Irppy-2254tpy-Co	1.46[b]	-0.44[b]	-0.95 (128)	-1.10 (71)	-1.56 (76)	
IrppyF_2-2244tpy-Co	1.67 (147)	-0.40[b]	-0.96 (98)	-1.08 (76)	-1.64 (85)	
IrppyF_2-2254tpy-Co	1.69 (144)	-0.44[b]	~ -0.95[c]		-1.49 (80)	
Irpiq-2244tpy-Co	1.43[b]	-0.42[b]	-0.95 (90)	-1.13 (86)	-1.62 (43)	-1.81 (94)
Irpiq-2254tpy-Co	1.43[b]	-0.43[b]	-0.95 (71)	-1.09 (75)	-1.55 (110)	-1.73 (77)

[a]Potentials are in volts *vs.* Ag/AgCl for acetonitrile solutions, 0.1 M in TBAP, recorded at 25°C at a sweep rate of 100 mV/s. The difference between cathodic and anodic peak potentials (millivolts) is given in parentheses. [b]Irreversible; potential is given for the cathodic wave. [c]Overlap of Cobalt and ligand reductions giving a broad unresolved wave

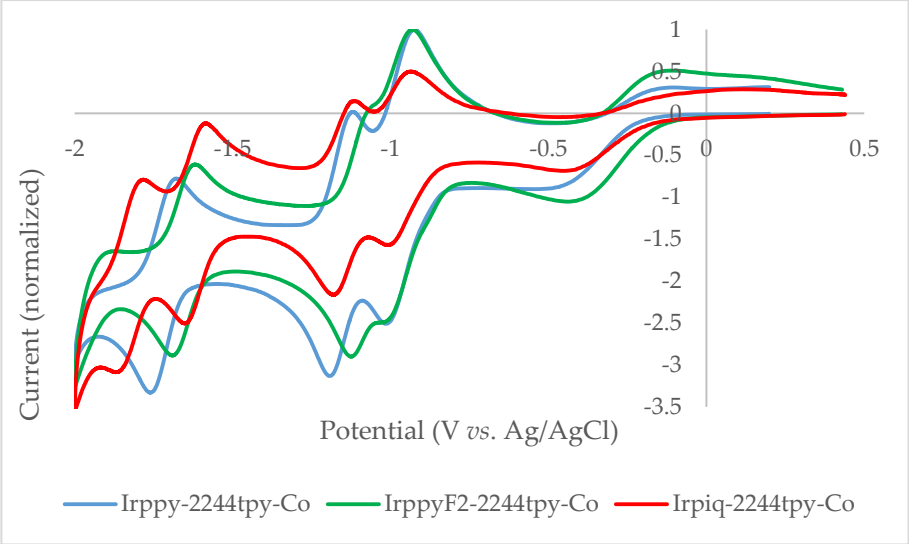

Figure 4.6 – Reduction voltammograms of Irppy-2244tpy-Co (*blue*), IrppyF$_2$-2244tpy-Co (*green*) and Irpiq-2244tpy-Co (*red*) (10^{-5} M) in acetonitrile with Bu$_4$NClO$_4$ 0.1 M as supporting electrolyte (sweeping rate = 0.1 V/s)

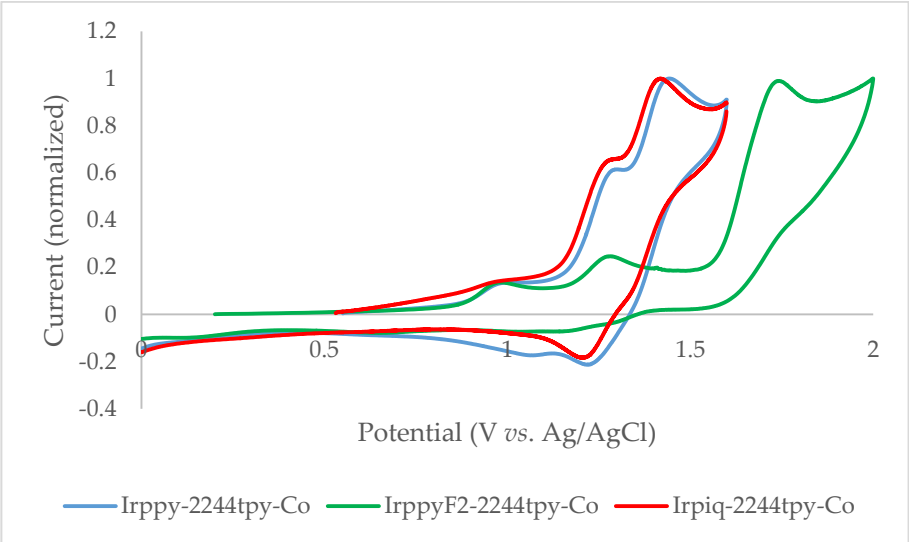

Figure 4.7 – Oxidation voltammograms of Irppy-2244tpy-Co (*blue*), IrppyF$_2$-2244tpy-Co (*green*) and Irpiq-2244tpy-Co (*red*) (10^{-5} M) in acetonitrile with Bu$_4$NClO$_4$ 0.1 M as supporting electrolyte (sweeping rate = 0.1 V/s)

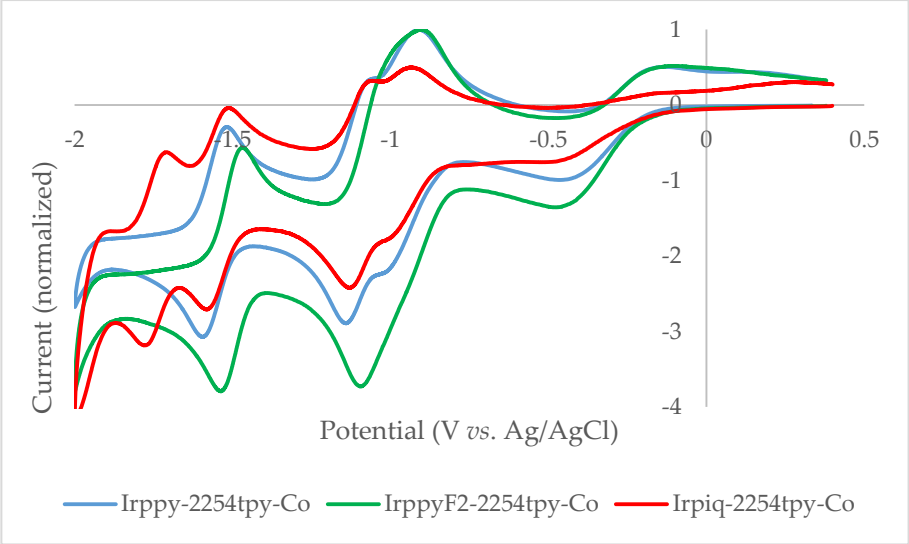

Figure 4.8 – Reduction voltammograms of Irppy-2254tpy-Co (*blue*), IrppyF$_2$-2254tpy-Co (*green*) and Irpiq-2254tpy-Co (*red*) (10^{-5} M) in acetonitrile with Bu_4NClO_4 0.1 M as supporting electrolyte (sweeping rate = 0.1 V/s)

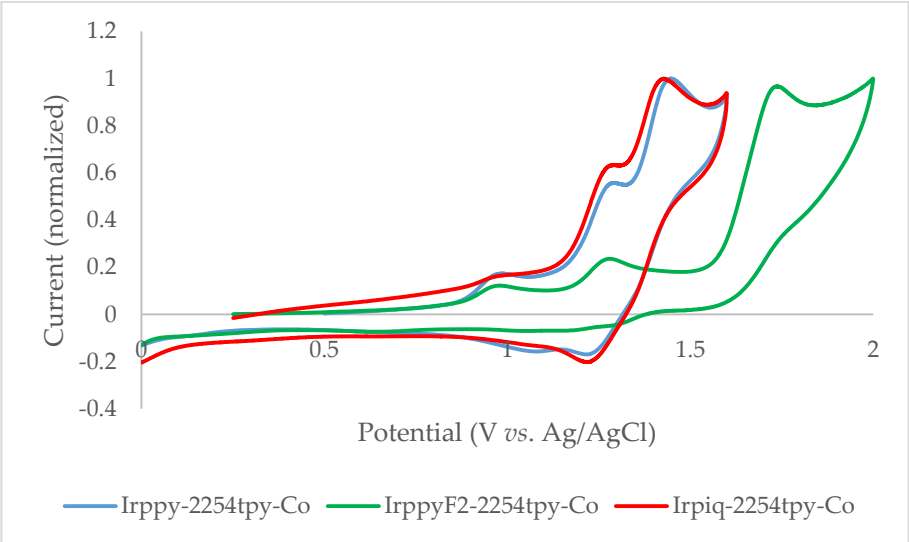

Figure 4.9 – Oxidation voltammograms of Irppy-2254tpy-Co (*blue*), IrppyF$_2$-2254tpy-Co (*green*) and Irpiq-2254tpy-Co (*red*) (10^{-5} M) in acetonitrile with Bu_4NClO_4 0.1 M as supporting electrolyte (sweeping rate = 0.1 V/s)

Table 4.2 – Contributions to MOs for Irpiq-bpy
(isovalue: 0.03 e.Å^{-3})

Orbital	Contributions	Orbital	Contributions
LUMO+4 -1.28eV 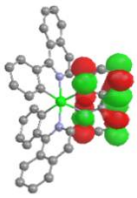	Ir : 1% piq : 2% bpy : 97%	HOMO -5.64eV 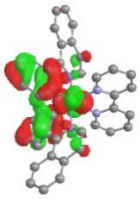	Ir : 37% piq : 62% bpy : 2%
LUMO+3 -1.51eV 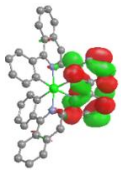	Ir : 2% piq : 10% bpy : 88%	HOMO-1 -6.05eV 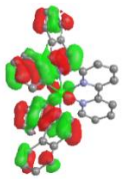	Ir : 10% piq : 89% bpy : 1%
LUMO+2 -2.13eV 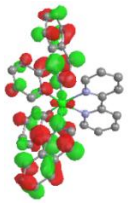	Ir : 3% piq : 96% bpy : 1%	HOMO-2 -6.22eV 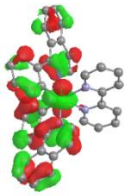	Ir : 27% piq : 72% bpy : 1%
LUMO+1 -2.22eV 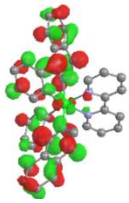	Ir : 4% piq : 91% bpy : 5%	HOMO-3 -6.5eV 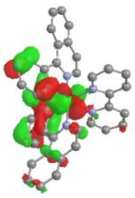	Ir : 36% piq : 59% bpy : 5%
LUMO -2.41eV 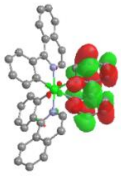	Ir : 2% piq : 5% bpy : 93%	HOMO-4 -6.58eV 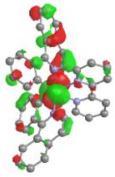	Ir : 50% piq : 45% bpy : 5%

Table 4.3 – Contributions to MOs for Irpiq-2244tpy (isovalue: 0.03 e.Å^{-3})

Orbital	Contributions	Orbital	Contributions
LUMO+4 -1.45eV 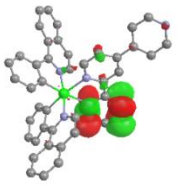	Ir : 1% piq : 9% 2244tpy : 90%	HOMO -5.65eV 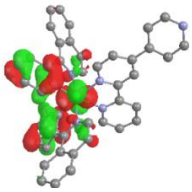	Ir : 36% piq : 62% 2244tpy : 2%
LUMO+3 -1.89eV 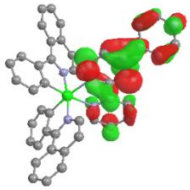	Ir : 1% piq : 3% 2244tpy : 97%	HOMO-1 -6.06eV 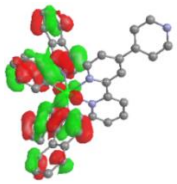	Ir : 10% piq : 89% 2244tpy : 1%
LUMO+2 -2.14eV 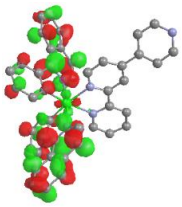	Ir : 3% piq : 95% 2244tpy : 1%	HOMO-2 -6.23eV 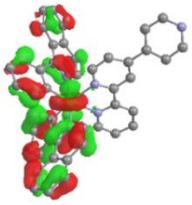	Ir : 26% piq : 72% 2244tpy : 2%
LUMO+1 -2.23eV 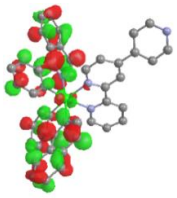	Ir : 4% piq : 94% 2244tpy : 2%	HOMO-3 -6.51eV 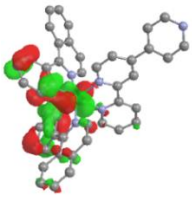	Ir : 36% piq : 59% 2244tpy : 6%
LUMO -2.57eV 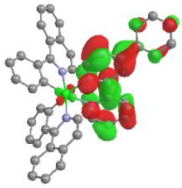	Ir : 2% piq : 2% 2244tpy : 96%	HOMO-4 -6.58eV 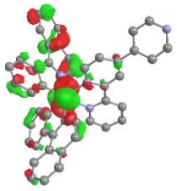	Ir : 49% piq : 44% 2244tpy : 6%

Table 4.4 – Contributions to MOs for Irpiq-2254tpy (isovalue: 0.03 e.Å^{-3})

Orbital	Contributions	Orbital	Contributions
LUMO+4 -1.35eV 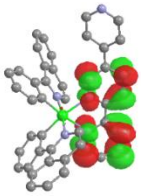	Ir : 1% piq : 3% 2254tpy : 96%	HOMO -5.66eV 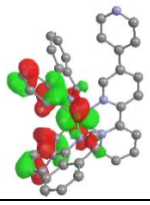	Ir : 36% piq : 62% 2254tpy : 2%
LUMO+3 -1.67eV 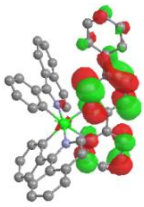	Ir : 2% piq : 5% 2254tpy : 93%	HOMO-1 -6.07eV 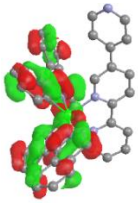	Ir : 10% piq : 89% 2254tpy : 1%
LUMO+2 -2.15eV 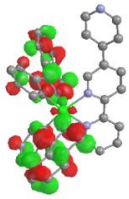	Ir : 3% piq : 85% 2254tpy : 11%	HOMO-2 -6.24eV 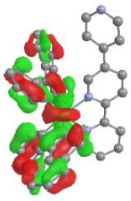	Ir : 26% piq : 72% 2254tpy : 2%
LUMO+1 -2.23eV 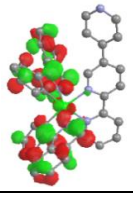	Ir : 4% piq : 94% 2254tpy : 2%	HOMO-3 -6.52eV 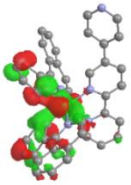	Ir : 35% piq : 59% 2254tpy : 5%
LUMO -2.62eV 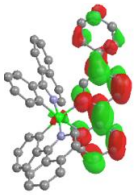	Ir : 2% piq : 2% 2254tpy : 97%	HOMO-4 -6.59eV 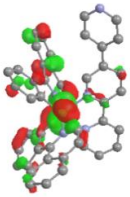	Ir : 50% piq : 44% 2254tpy : 6%

4.5 Photophysical studies

Figure 4.10 displays the UV-visible absorption spectra for the six [Ir-Co] dyads in acetonitrile (see Supporting Information – Figures S4.7-S4.9 – for Ir(III) photosensitizers). The corresponding data are gathered in Tables 4.5 and 4.6. All the compounds display absorption bands in the UV region tailing into the visible. On the basis of previous studies on cyclometalated Ir(III) complexes and the absorption of the ligands, intense absorption bands in the UV region can be ascribed to intraligand transitions (Ligand Centered – LC).[28] Absorption bands appearing in the visible region correspond to a mixture of LC and charge-transfer transitions from the cyclometalated ligand to the N^N ligand (Ligand-to-Ligand Charge Transfer – LLCT) or from the Iridium center to one of the ligands (Metal-to-Ligand Charge Transfer – MLCT). From our TD-DFT calculations on the nine Iridium complexes, the contribution for each transition above 300 nm *i.e.* the exact nature of the transition could be assessed (see Figures 4.11-4.13 for Irpiq-N^N family and Supporting Information – Figures S4.10-S4.15 – for Irppy-N^N and IrppyF_2-N^N families).

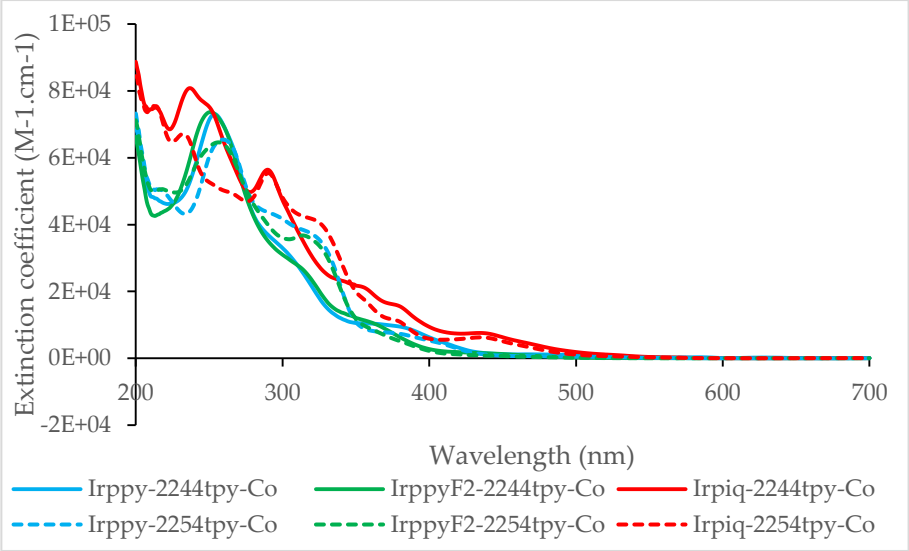

Figure 4.10 – Absorption spectra of [Ir-Co] dyads in acetonitrile

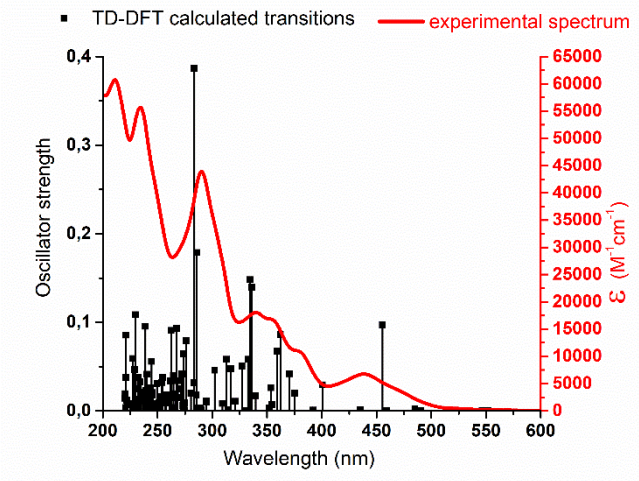

Figure 4.11 – Experimental spectrum and calculated transitions for Irpiq-bpy

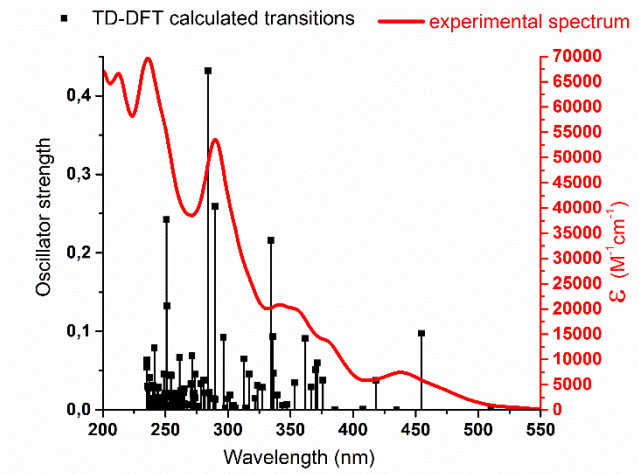

Figure 4.12 – Experimental spectrum and calculated transitions for Irpiq-2244tpy

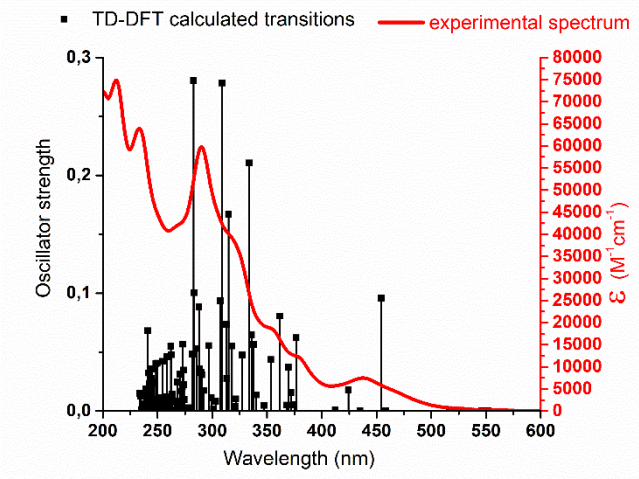

Figure 4.13 – Experimental spectrum and calculated transitions for Irpiq-2254tpy

Table 4.5 – Spectroscopic data for the [Ir-Co] dyads

Complex	λ_{abs} [nm] (ε x 10^2 M^{-1} cm^{-1})	$\lambda_{max\ em}$ [nm]	τ^b [μs]	Φ^c (Ar)	$k_r{}^d$ [x10^3 s^{-1}]
Irppy-2244tpy-Co	254 (731), 308 (291), 383 (92), 412 (44), 468 (12), 495 (10)	652	0.035 (16 %) 0.213 (84 %)	0.0030	16.3
Irppy-2254tpy-Co	215 (485), 260 (654), 294 (431), 326 (350), 377 (75), 409 (43), 468 (7), 514 (4)	661	0.034 (11 %) 0.115 (89 %)	0.0015	14.1
$IrppyF_2$-2244tpy-Co	252 (736), 312 (273), 343 (133), 360 (108), 420 (18), 445 (14)	567	0.121 (14 %) 0.384 (86 %)	0.0124	35.7
$IrppyF_2$-2254tpy-Co	258 (645), 315 (367), 331 (298), 361 (86), 421 (11), 448 (7)	572	0.196 (13 %) 0.406 (87 %)	0.0094	25.2
Irpiq-2244tpy-Co	215 (747), 238 (807), 251 (747), 291 (562), 339 (234), 355 (211), 380 (155), 437 (75), 528 (9), 567 (2)	593, 637	1.053	0.0023	2.2
Irpiq-2254tpy-Co	215 (750), 235 (664), 291 (554), 327 (398), 357 (180), 379 (111), 437 (62), 530 (5), 567 (2)	593, 637	0.705	0.0033	4.7

[a]Measurements in degassed acetonitrile at 298 K. [b]Lifetime under N_2 atmosphere. [c]Quantum yield measured by using $[Ru(bpy)_3]^{2+}$ as a reference, $\Phi_{ref} = 0.028$ in water under air. [d]Radiative rate constant determined under an inert atmosphere at 298 K ($k_r = \Phi/\tau$).

Table 4.6 (part 1) – Spectroscopic data for the Ir(III) photosensitizers

Complex	λ_{abs} [nm] (ε x 10^2 M^{-1} cm^{-1})	$\lambda_{max\ em}$ [nm]	τ^b [μs]	Φ^c (Ar)	$k_r{}^d$ [x10^3 s^{-1}]	$\lambda_{em,77\ K}$ [nm][e]
Irppy-2244tpy	256 (562), 318 (191), 383 (80), 418 (31), 468 (11)	646	0.266	0.0228	85.7	543
Irppy-2254tpy	255 (489), 270 (484), 289 (398), 321 (287), 382 (64), 467 (7)	654	0.128	0.0103	80.5	554
Irppy-bpy	257 (512), 267 (487), 310 (227), 339 (96), 376 (64), 412 (36), 467 (7)	599	0.267	0.0215	80.5	514
$IrppyF_2$-2244tpy	247 (565), 262 (489), 308 (236), 340 (97), 358 (79), 427 (11), 447 (8)	564	1.192	0.1182	99.2	502
$IrppyF_2$-2254tpy	249 (490), 263 (475), 311 (327), 324 (275), 358 (70), 428 (8), 449 (5)	567	1.272	0.1183	93.0	485, 520
$IrppyF_2$-bpy	247 (531), 262 (481), 298 (277), 310 (241), 360 (65), 423 (8), 449 (4)	539	1.274	0.0758	59.5	455, 483

[a]Measurements in degassed acetonitrile at 298 K. [b]Lifetime under N_2 atmosphere. [c]Quantum yield measured by using $[Ru(bpy)_3]^{2+}$ as a reference, $\Phi_{ref} = 0.028$ in water under air. [d]Radiative rate constant determined under an inert atmosphere at 298 K ($k_r = \Phi/\tau$).[e]measured in EtOH:MeOH / 4:1.

Table 4.6 (part 2) – Spectroscopic data for the Ir(III) photosensitizers

Complex	λ_{abs} [nm] (ε x 10^2 M^{-1} cm^{-1})	$\lambda_{max\ em}$ [nm]	τ^b [μs]	Φ^c (Ar)	$k_r{}^d$ [x10^3 s^{-1}]	$\lambda_{em,77\ K}$ [nm][e]
Irpiq-2244tpy	214 (662), 236 (696), 343 (208), 357 (195), 380 (136), 439 (74), 527 (5), 560 (2)	592, 636	1.528 (12%) 3.049 (88%)	0.0125	4.4	579, 626
Irpiq-2254tpy	212 (749), 234 (639), 291 (596), 322 (374), 357 (180), 381 (118), 438 (74), 527 (5), 565 (2)	593, 636	1.619 (43%) 2.372 (57%)	0.0130	6.3	578, 625
Irpiq-bpy	212 (606), 234 (557), 290 (440), 338 (180), 354 (168), 379 (109), 439 (67), 527 (4), 564 (1)	593, 638	1.059 (39%) 1.638 (61%)	0.0110	7.8	580, 627
IrppytBu$_2$-2244tpy	252 (562), 276 (468), 376 (83), 469 (10)	611	nd	nd	nd	nd
IrppytBu$_2$-2254tpy	252 (423), 272 (503), 323 (242), 380 (71), 471 (6)	595	nd	nd	nd	nd
IrppytBu$_2$-bpy	253 (461), 276 (516), 312 (217), 381 (79), 414 (38), 472 (7)	591	nd	nd	nd	nd

[a]Measurements in degassed acetonitrile at 298 K. [b]Lifetime under N_2 atmosphere. [c]Quantum yield measured by using $[Ru(bpy)_3]^{2+}$ as a reference, $\Phi_{ref} = 0.028$ in water under air. [d]Radiative rate constant determined under an inert atmosphere at 298 K ($k_r = \Phi/\tau$).[e]measured in EtOH:MeOH / 4:1. nd = not determined

As both contributions of the metal and the cyclometalated ligand have to be taken into account for several orbitals, many transitions are ascribed to a combination of charge transfers from the metal and the N^C ligands towards the N^N ligand, thus having MLCT and LLCT characters. These transitions will be further referred as a metal-ligand-to-ligand charge transfer (MLLCT). In a similar way, several unoccupied levels have contributions from both type of ligands, leading to population of orbitals on the N^N ligand and the N^C ligands.

The transitions in the visible region of IrppyF$_2$-N^N complexes are blue-shifted compared to those of corresponding Irppy-N^N complexes due to the electron-withdrawing ability of the fluorine atoms which stabilizes the HOMO of the complexes. The electron-donating character of the *tert*-butyl groups has almost no effect compared to reference Irppy-N^N compounds, as shown for the electrochemical properties. The higher conjugation of Irpiq-N^N complexes due to the supplementary aromatic ring on the cyclometalated ligands stabilize the system leading to a red-shift in absorption compared to Irppy-N^N complexes. When comparing the absorption spectra of the complexes in each IrL-N^N family, one can observe that there are no major difference in the position and intensities of the absorption maxima in the visible region, except a slightly higher extinction coefficient for IrL-2244tpy relative to those with IrL-2254tpy. At 320 nm, the IrL-2254tpy compound displays an additional shoulder, caused by an additional LC contribution from the N^N ligand (see TD-DFT calculations). This situation is favored by the fact that the complexes built with 2254tpy have mixed N^N and N^C contributions in the LUMO+2/+3, with varying ratio, while these levels have pure N^C contributions for all the IrL-2244tpy family.

The lowest singlet transition in all cases has an MLLCT character. However, due the strong spin-orbit coupling of the Iridium center, there is significant mixing between the singlet and triplet states, allowing for spin forbidden triplet transitions to be directly excited. Thus, for the Irppy-N^N and IrppyF_2-N^N compounds, the lowest absorption bands respectively around 500 and 450 nm corresponds to a mixed $^{1/3}$MLLCT transition. For the Irpiq-N^N series, due to the extended conjugation of the cyclometalated ligand, there are several ^{3}MLCT N^C transitions at lower energy than the mixed $^{1/3}$MLLCT transition, *i.e.* 570 and 530 nm, respectively.

Finally, the absorption spectra for [Ir-Co] dyads are almost identical to those of the corresponding photosensitizers (see Figures 4.14 and 4.15 for Irpiq-2244tpy and Irpiq-2254tpy, respectively, and Supporting Information – Figures S4.16-S4.19 – for the other dyads and corresponding photosensitizers) confirming the observation that no strong electronic interaction occurs between the metallic centers.

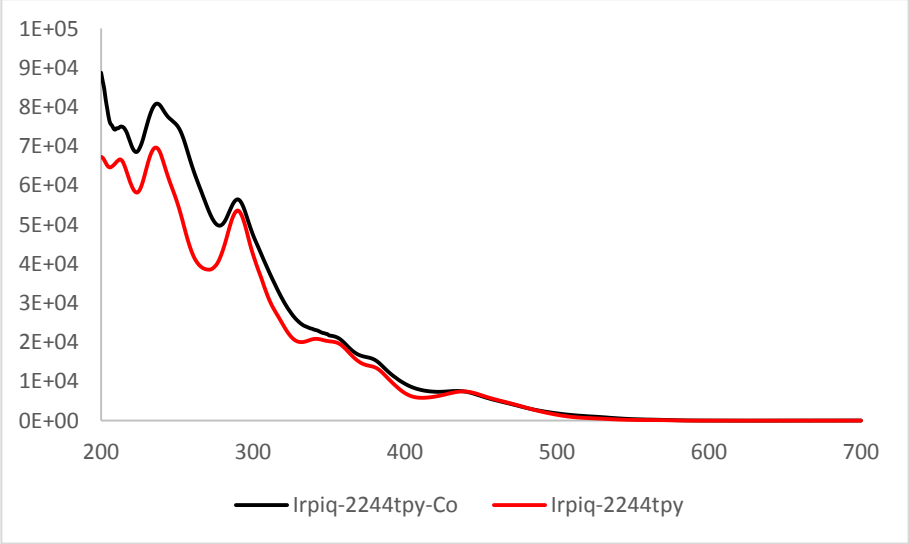

Figure 4.14 – Absorption spectra of Irpiq-2244tpy-Co (*black*) and Irpiq-2244tpy (*red*) in acetonitrile at room temperature.

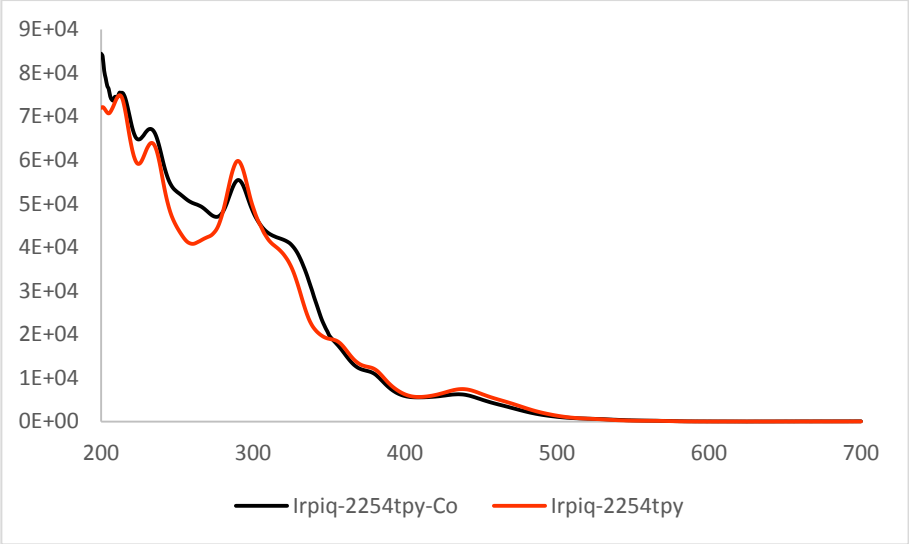

Figure 4.15 – Absorption spectra of Irpiq-2254tpy-Co (*black*) and Irpiq-2254tpy (*red*) in acetonitrile at room temperature.

The luminescence lifetimes and the quantum yields of luminescence for each dyad and photosensitizer (Irppy-N^N, IrppyF_2-N^N and Irpiq-N^N complexes) have been measured in acetonitrile under an inert atmosphere (Tables 4.5 and 4.6, respectively). While the Irppy-N^N, IrppyF_2-N^N and IrppytBu_2-N^N series display broad unstructured emission spectra, as expected from ^{3}CT-type excited states, more structured emission bands can be observed for the Irpiq-N^N series. This typical vibrational progression is implying a major ^{3}LC contribution to the excited state of the Irpiq-N^N series in addition to the expected ^{3}CT-type excited states. This interpretation is confirmed by the luminescence measurements at 77 K, as the emission maxima are only slightly blue-shifted for the Irpiq-N^N series while the Irppy-N^N and IrppyF_2-N^N series show hypsochromic shifts of ~100 and ~40 nm, respectively. It is also confirmed by the TD-DFT calculations showing that the lowest triplet state for Irppy-N^N and

IrppyF$_2$-N^N is a ^{3}MLLCT while it is a mix-state combining N^C-centered ^{3}MLCT and ^{3}LC characters for Irpiq-N^N. Unexpectedly, IrppytBu$_2$-N^N family displays a more energetic emissive transition compared to reference Irppy-N^N compounds despite a more energetic HOMO as observed with the oxidation potentials. This might be due to a less efficient stabilization of the excited state through internal conversion yielding to a more energetic LUMO.

Due to HOMO stabilization induced by the addition of fluorine atoms, emissive transitions of IrppyF$_2$-N^N compounds are more energetic compared to those of Irppy-N^N and Irpiq-N^N families. Despite the higher conjugation in the Irpiq-N^N family, the energies of the ^{3}LC/^{3}CT transitions are quite close to those of the Irppy-N^N compounds. In air-equilibrated solvents, a decrease in the luminescence intensity with respect to degassed solutions is systematically observed for every complex, indicating that a luminescence quenching by oxygen is operative (photosensitization of ^{3}O$_2$).[29] However, there is no significant difference in photosensitization between the IrL-2244tpy and IrL-2254tpy series.

Table 4.7 – Excited states oxidation and reduction potentials of Ir(III) photosensitizers

Complex	$\lambda_{max\ em}$ (nm)[a]	E_{00} (V)[b]	E_{ox}* (V *vs.* Ag/AgCl)	E_{red}* (V *vs.* Ag/AgCl)
Irppy-2244tpy	646	1.91	-0.54	0.74
Irppy-2254tpy	654	1.89	-0.52	0.78
Irppy-bpy	599	2.06	-0.69	0.76
IrppyF_2-2244tpy	564	2.19	-0.47	1.02
IrppyF_2-2254tpy	567	2.18	-0.46	1.12
IrppyF_2-bpy	539	2.29	-0.58	1.04
Irpiq-2244tpy	592	2.09	-0.67	0.93
Irpiq-2254tpy	593	2.08	-0.65	0.99
Irpiq-bpy	593	2.08	-0.72	0.78
IrppytBu_2-2244tpy	611	2.02	-0.72	0.84
IrppytBu_2-2254tpy	595	2.07	-0.81	1.09
IrppytBu_2-bpy	591	2.09	-0.84	0.78

[a]Emission maximum for the most hypsochromic band if multiband spectrum.
[b]Evaluated at the emission maximum.

The potential in the excited states (namely E_{ox}* and E_{red}*) can be estimated from the ground state potentials and the energy of the excited state corresponding to the maximum of the emission spectrum at 298 K in acetonitrile (Table 4.7). All the oxidation potentials at the excited state are evaluated above 0.7 V *vs.* Ag/AgCl meaning that the Ir(III) photosensitizers are able to reduce the Co(III) catalyst under irradiation and, hence, initiate proton reduction.

The emission maxima of the dyads in acetonitrile (Table 4.5) are close to those of the Ir(III) photosensitizers, exhibiting only a small red-shift falling within the limit of the resolution of the spectrometer. This

indicates that the Cobalt coordination does not lower significantly the energy of the radiative pathways. Nevertheless, the observed decreased lifetimes and quantum yields imply that an intramolecular electron or energy transfer from the excited Iridium unit to the Cobalt unit is at stake.

An efficient way to probe the nature of the excited states and the ability of the excited electron to reach pendant pyridine is the study of the effect of protonation upon progressive addition of an acid on IrL-2244tpy and IrL-2254tpy. Indeed, if ^{3}MLLCT transitions are predominant and the non-chelated pyridine is involved in the excited state, the corresponding absorption and emission energy should be altered by protonation[30] as predicted by TD-DFT (see Tables 4.8-4.9 for Irpiq-2244tpy and Irpiq-2254tpy and Supporting information – Tables S4.7-S4.10 – for Irppy-2244tpy, Irppy-2254tpy, IrppyF_2-2244tpy and IrppyF_2-2254tpy).

Table 4.8 – Contributions to MOs for protonated Irpiq-2244tpy-H^+ (isovalue: 0.03 e.$Å^{-3}$)

Orbital	Contributions	Orbital	Contributions
LUMO+4 -1.91eV 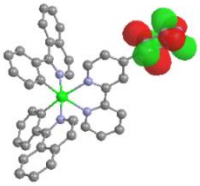	Ir : 0% piq : 0% H-2244tpy : 100%	HOMO -5.73eV 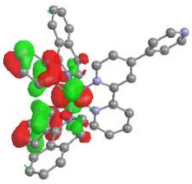	Ir : 35% piq : 63% H-2244tpy : 2%
LUMO+3 -2.2eV 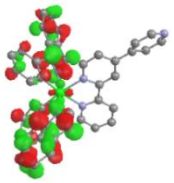	Ir : 3% piq : 1% H-2244tpy : 96%	HOMO-1 -6.12eV 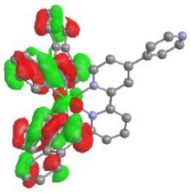	Ir : 8% piq : 91% H-2244tpy : 1%
LUMO+2 -2.28eV 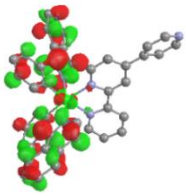	Ir : 4% piq : 92% H-2244tpy : 4%	HOMO-2 -6.3eV 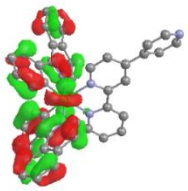	Ir : 23% piq : 76% H-2244tpy : 2%
LUMO+1 -2.5eV 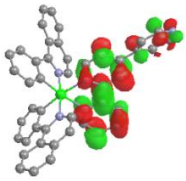	Ir : 1% piq : 4% H-2244tpy : 95%	HOMO-3 -6.59eV 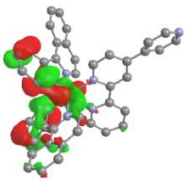	Ir : 31% piq : 64% H-2244tpy : 5%
LUMO -3.38eV 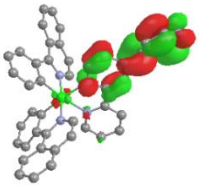	Ir : 2% piq : 0% H-2244tpy : 98%	HOMO-4 -6.68eV 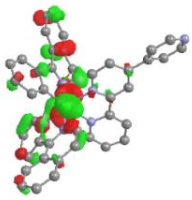	Ir : 52% piq : 43% H-2244tpy : 5%

Table 4.9 – Contributions to MOs for protonated Irpiq-2254tpy-H^+ (isovalue: 0.03 e.$Å^{-3}$)

Orbital	Contributions	Orbital	Contributions
LUMO+4 -1.91eV 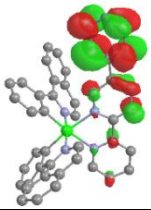	Ir : 0% piq : 2% H-2254tpy : 98%	HOMO -5.74eV 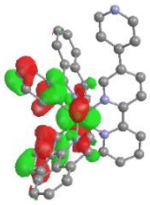	Ir : 36% piq : 63% H-2254tpy : 2%
LUMO+3 -2.2eV 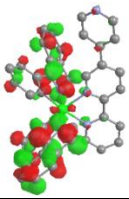	Ir : 3% piq : 89% H-2254tpy : 8%	HOMO-1 -6.13eV 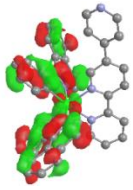	Ir : 8% piq : 91% H-2254tpy : 1%
LUMO+2 -2.3eV 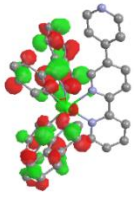	Ir : 4% piq : 95% H-2254tpy : 1%	HOMO-2 -6.31eV 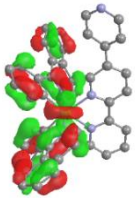	Ir : 24% piq : 75% H-2254tpy : 2%
LUMO+1 -2.34eV 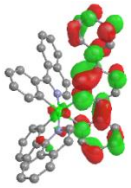	Ir : 3% piq : 13% H-2254tpy : 85%	HOMO-3 -6.6eV 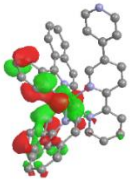	Ir : 33% piq : 62% H-2254tpy : 5%
LUMO -3.38eV 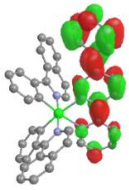	Ir : 1% piq : 12% H-2254tpy : 87%	HOMO-4 -6.69eV 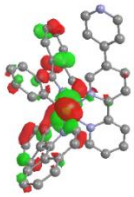	Ir : 51% piq : 44% H-2254tpy : 4%

4.6 Photochemical behavior upon addition of acid

Titration experiments were carried out in acetonitrile with two acids of different pKa values *i.e.* trifluoroacetic acid (TFA – pKa = 12.65 in CH_3CN)[31] and acetic acid (AcOH – pKa = 23.51 in CH_3CN).[32]

The luminescence quenching of Irpiq-2244tpy and Irpiq-2254tpy upon addition of trifluoroacetic acid as well as modifications of absorption bands are illustrated in Figures 4.16-4.18 and Figures 4.19-4.21 for Irpiq-2244tpy and Irpiq-2254tpy, respectively (see Supporting Information – Figures S4.20-S4.31 – for Irppy-2244tpy, Irppy-2254tpy, IrppyF_2-2244tpy and IrppyF_2-2254tpy).

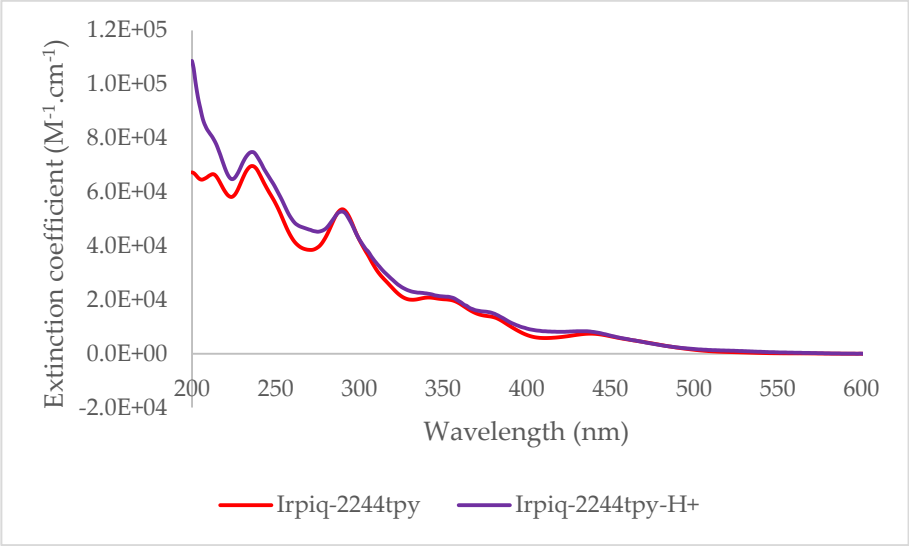

Figure 4.16 – Absorption spectra in acetonitrile for neutral (*red*) and protonated (*purple*) (obtained when solubilized in a 0.2 mM of TFA solution in acetonitrile) Irpiq-2244tpy photosensitizer

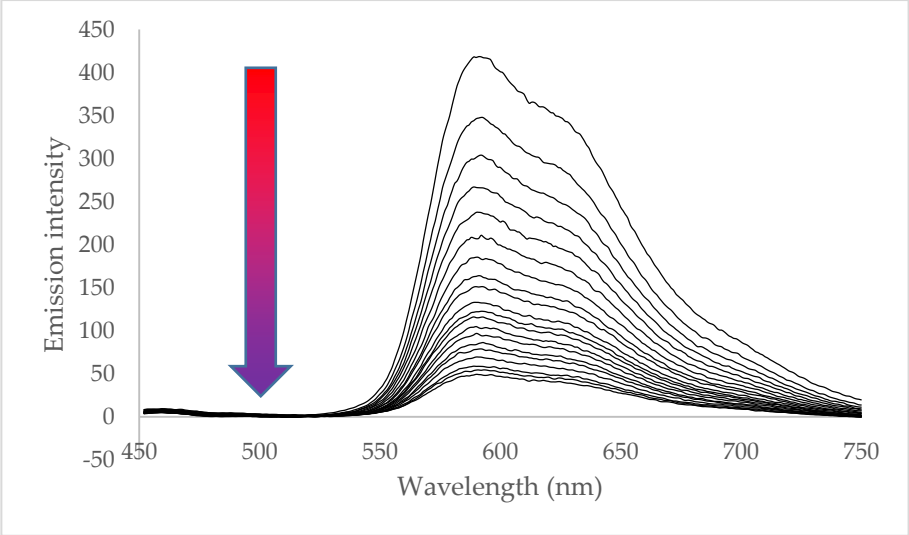

Figure 4.17 – Emission spectral changes for a 2.5 x 10^{-5} M solution of Irpiq-2244tpy in acetonitrile for increasing concentrations of TFA (10^{-4} M range)

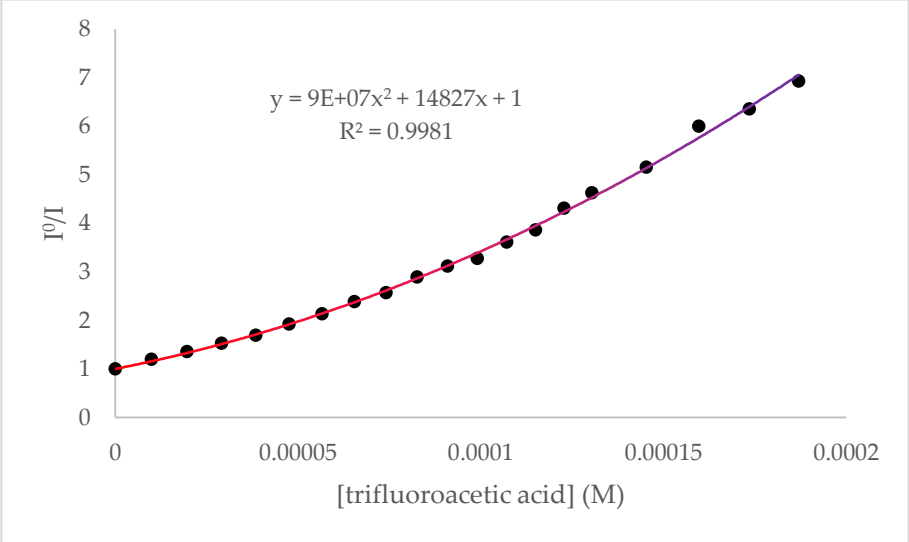

Figure 4.18 – Stern-Volmer plots of the luminescence quenching of a 2.5 x 10^{-5} M solution of Irpiq-2244tpy in acetonitrile upon the addition of TFA

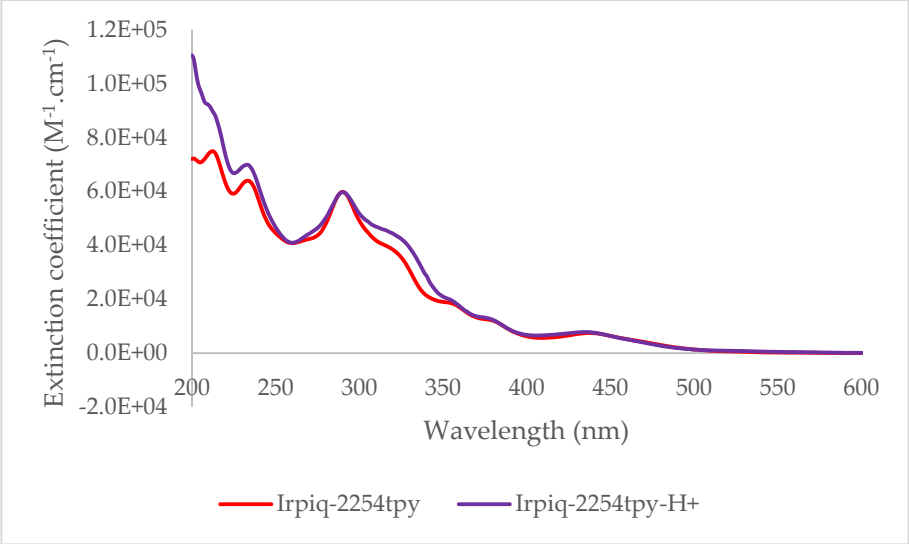

Figure 4.19 – Absorption spectra in acetonitrile for neutral (*red*) and protonated (*purple*) (obtained when solubilized in a 0.2 mM of TFA solution in acetonitrile) Irpiq-2254tpy photosensitizer

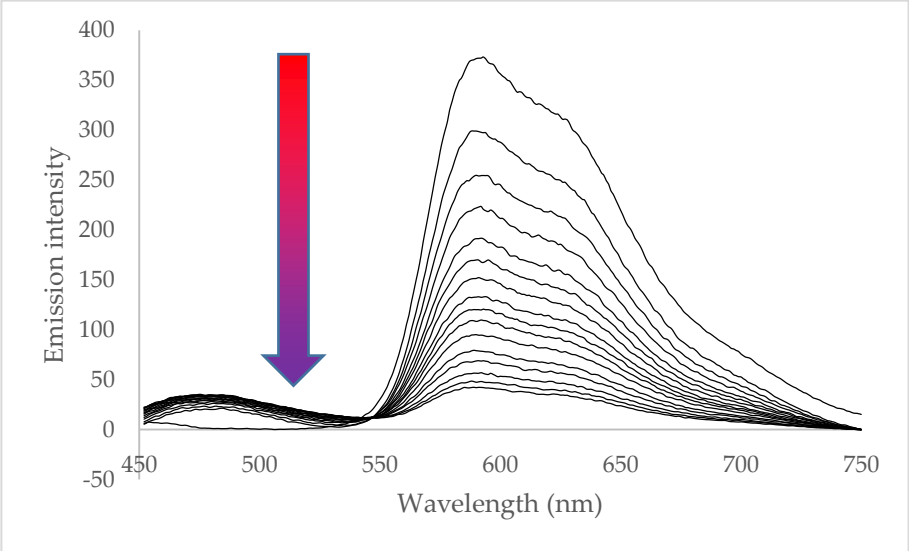

Figure 4.20 – Emission spectral changes for a 2.5 x 10^{-5} M solution of Irpiq-2254tpy in acetonitrile for increasing concentrations of TFA (10^{-4} M range)

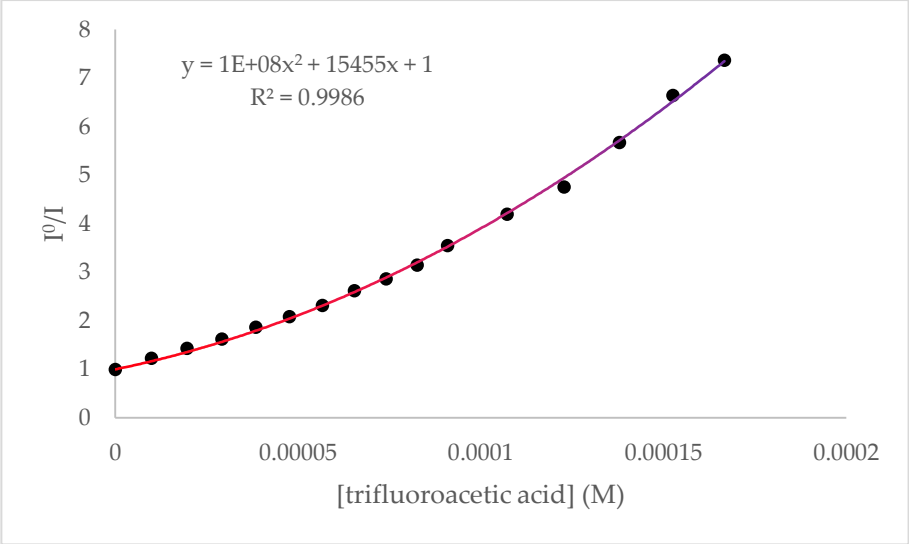

Figure 4.21 – Stern-Volmer plots of the luminescence quenching of a 2.5 x 10^{-5} M solution of Irpiq-2254tpy upon the addition of TFA

A clear red-shift of the most bathochromic absorption band upon addition of TFA can be observed, which is consistent with the protonation of the pendant pyridine residue. Indeed, once protonated, the pendant pyridine becomes a better acceptor in the ^{3}MLLCT transition due to the stabilization of a LUMO centered on 2244tpy and 2254tpy ligands for IrL-2244tpy and IrL-2254tpy complexes, respectively (*vide supra*). No observable shift was noticed for the higher energy absorption bands. The presence of several isosbestic points indicates the existence of at least two species in equilibrium.

The emission of every complex decreases dramatically with the addition of TFA, due to the additional non-radiative relaxation pathways created. Interestingly, the luminescence quenching is quite similar for the complexes of a same family, *i.e.* IrL-2244tpy and IrL-2254tpy families, showing the inertness of the cyclometalated ligands towards protonation. The luminescence quenching is more efficient for

IrL-2254tpy complexes than for IrL-2244tpy due the electron-rich character of the 5′ position on the bpy residue with respect to 4′ position which increases the basicity of the pendant 5′-pyridine of IrL-2254tpy complexes in the ground state. In the case of the Irpiq-N^N compounds, the emissive state was expected to be localized on the N^C ligand and thus should not be affected by the protonation. However, a similar behavior for the Irpiq-N^N complexes upon protonation was observed, suggesting that the lowest excited state of the protonated form Irpiq-N^N-H^+ has a predominant ^{3}MLLCT character. This has been confirmed by the TD-DFT calculations on the protonated complexes (Figures 4.22 and 4.23 and Supporting Information – Figures S4.32-S4.39 – for Irppy-2244tpy, Irppy-2254tpy, IrppyF$_2$-2244tpy and IrppyF$_2$-2254tpy).

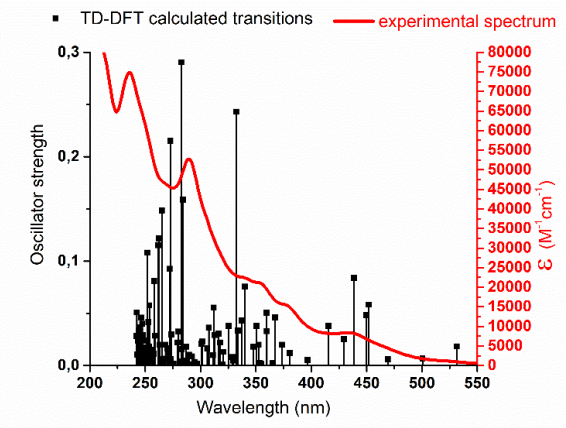

Figure 4.22 – Experimental spectrum and calculated transitions for protonated Irpiq-2244tpy-H^+

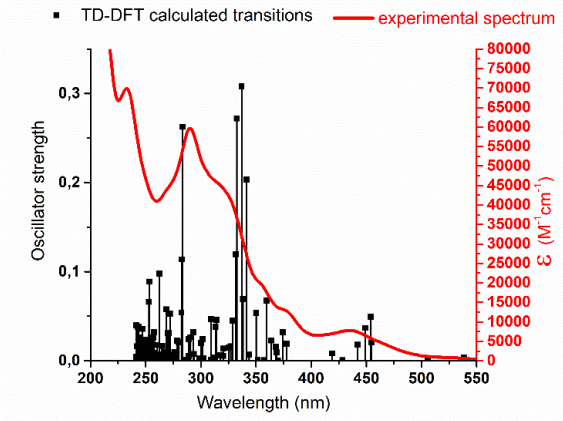

Figure 4.23 – Experimental spectrum and calculated transitions for protonated Irpiq-2254tpy-H^+

The luminescence quenching of Irpiq-2244tpy and Irpiq-2254tpy upon addition of acetic acid are illustrated in Figures 4.24-4.25 and 4.26-4.27, respectively (and Supporting Information – Figures S4.36-S4.43 – for the other families). Gradual addition of AcOH had no effect on the absorption of the complexes, even at high concentration, implying that the pendant pyridine residue cannot be protonated by this acid in the ground state. Nevertheless, luminescence quenching could still be observed upon addition of AcOH implying a contribution of the pendant pyridine on the LUMO for all the complexes. Interestingly, in contrast to the behavior of the complexes in the presence of TFA, luminescence quenching of IrL-2244tpy complexes upon increased amounts of AcOH is more efficient than with IrL-2254tpy complexes. Indeed, due to the electron-poor character of the 4' position of the bpy moiety compared to the 5' position in the ground state, the excited electron will preferentially be located on this position when the complex is irradiated, enhancing the electron density of the pendant 4'-pyridine. Furthermore, unlike what was observed upon addition of TFA, luminescence quenching due to

protonation of the excited complexes by AcOH is highly influenced by the nature of the ancillary ligands. Indeed, the luminescence of Irppy-2244tpy is more efficiently quenched than in the cases of $IrppyF_2$-2244tpy and Irpiq-2244tpy. This is due to increased contribution of the ^3LC transition on the nature of the excited state ($^3LC_{Irppy\text{-}N\hat{}N} < {}^3LC_{IrppyF2\text{-}N\hat{}N} < {}^3LC_{Irpiq\text{-}N\hat{}N}$) leading to a less efficient ^3MLLCT and, hence, a lower electron density in the excited state on the pendant pyridine residue, making Irpiq-2244tpy the least basic complex. The same observations can be made for Irppy-2254tpy, $IrppyF_2$-2254tpy and Irpiq-2254tpy.

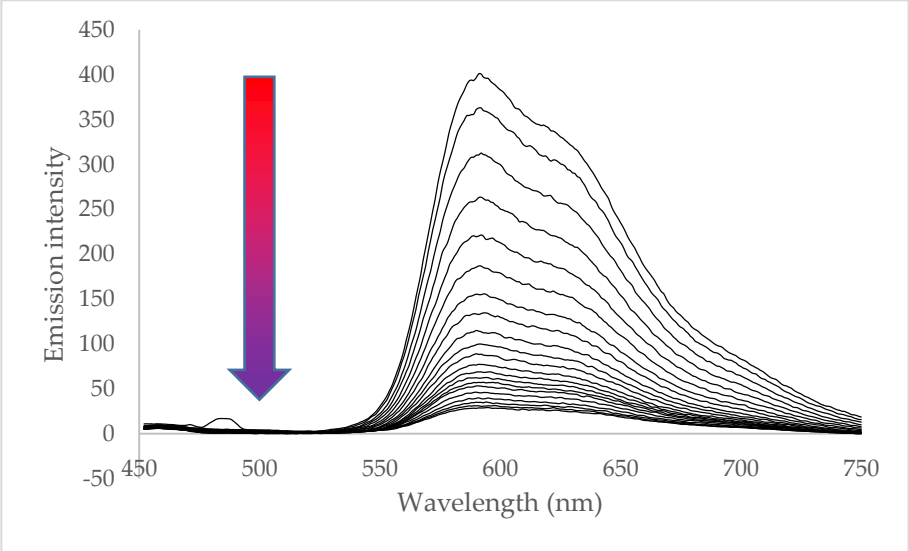

Figure 4.24 – Emission spectral changes for a 2.5 x 10^{-5} M solution of Irpiq-2244tpy in acetonitrile for increasing concentrations of AcOH (10^{-1} M range).

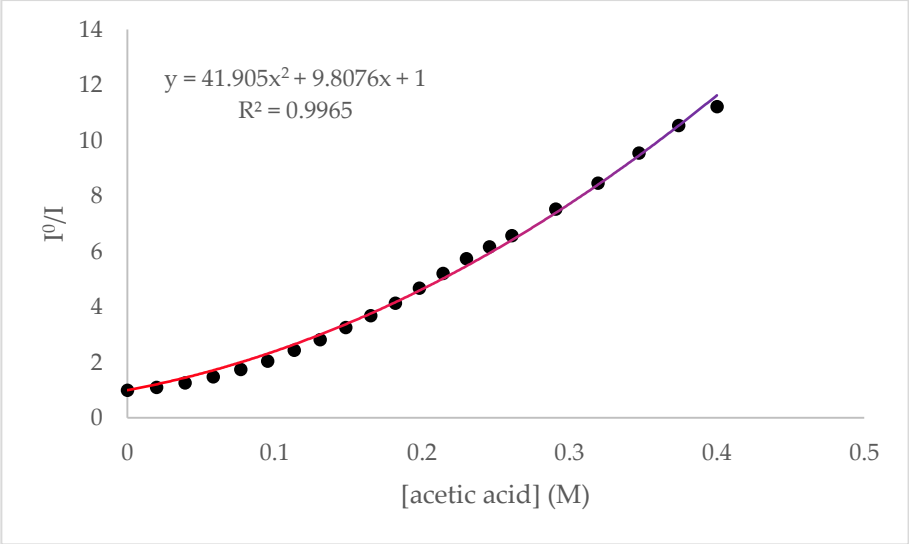

Figure 4.25 – Stern-Volmer plots of the luminescence quenching of a 2.5 x 10^{-5} M solution of Irpiq-2244tpy in acetonitrile upon the addition of AcOH.

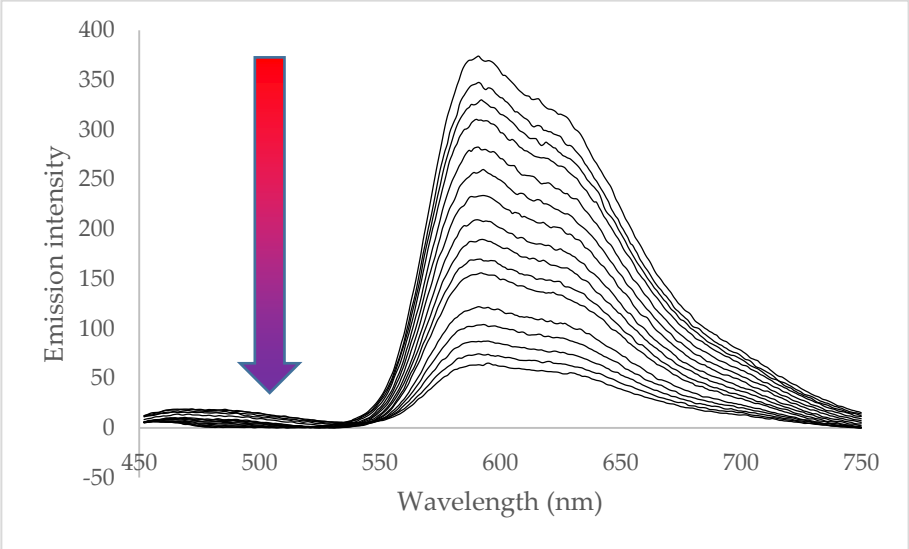

Figure 4.26 – Emission spectral changes for a 2.5 x 10^{-5} M solution of Irpiq-2254tpy in acetonitrile for increasing concentrations of AcOH (10^{-1} M range).

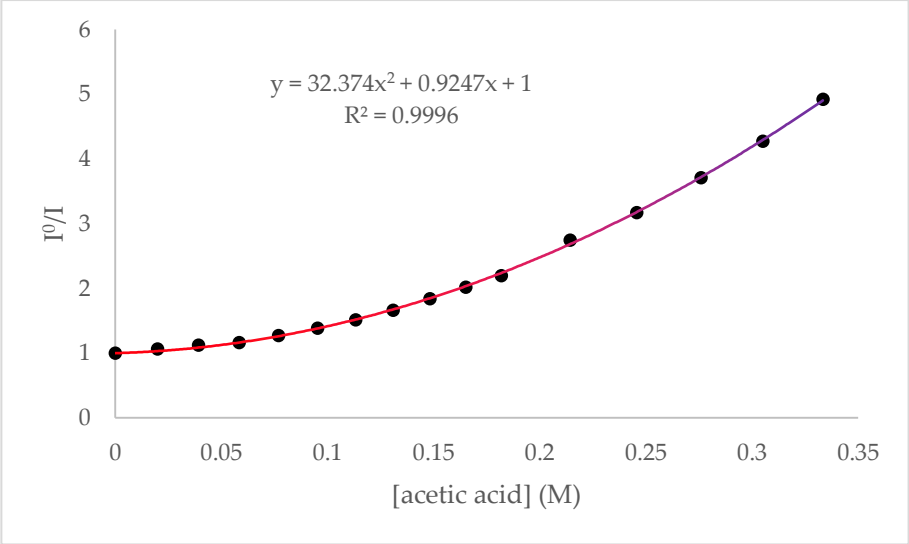

Figure 4.27 – Stern-Volmer plots of the luminescence quenching of a 2.5 x 10^{-5} M solution of Irpiq-2254tpy in acetonitrile upon the addition of AcOH.

Now we have a good idea of the photophysics of the Ir(III) photosensitizers as well as their ability to photoinduce an electron transfer to the Co(III) catalyst, and thus all the evidences to foresee an efficient H_2 photoproduction.

4.7 Hydrogen photo-evolution under various wavelengths of irradiation

Several studies aimed at the development of supramolecular assemblies[3, 14-16, 33-34] as they show increased efficiency in terms of electron transfer compared to the related multicomponent systems.[14, 17, 24, 34-38] The Ir(III) photosensitizers without the pendant pyridines have been tested for hydrogen evolution with $Co(dmgH)_2PyrCl$ under similar conditions used for the study of the [Ir-Co] dyads. The experiments consisted in the addition of either the photosensitizer and the proton reduction catalyst in 1:1 ratio or the [Ir-Co] dyad with a concentration of 10^{-4} M in acetonitrile in the presence of 0.5 M triethanolamine as the sacrificial electron donor and 0.05 M aqueous tetrafluoroboric acid as the proton source. From these, TON (TurnOver Number) *i.e.* the number of moles of substrate that a mole of catalyst can convert before being inactivated, and TOF (TurnOver Frequency) *i.e.* the turnover per unit time, have been obtained. The reaction mixture was irradiated using a light-emitting diode (LED). Four light-emitting diodes with emissions centered at 452, 525, 595 and 630 nm (Table 4.10 and Figures 4.28-4.29), have been used to evaluate the potential of photoredox processes for each systems as a function of the irradiation wavelength.[39] N_2 was continuously bubbled through the solution for stirring and transferring the produced hydrogen to a GC system to evaluate the hydrogen evolution efficiency. The error associated with the TOF and TON values is 10%.[40]

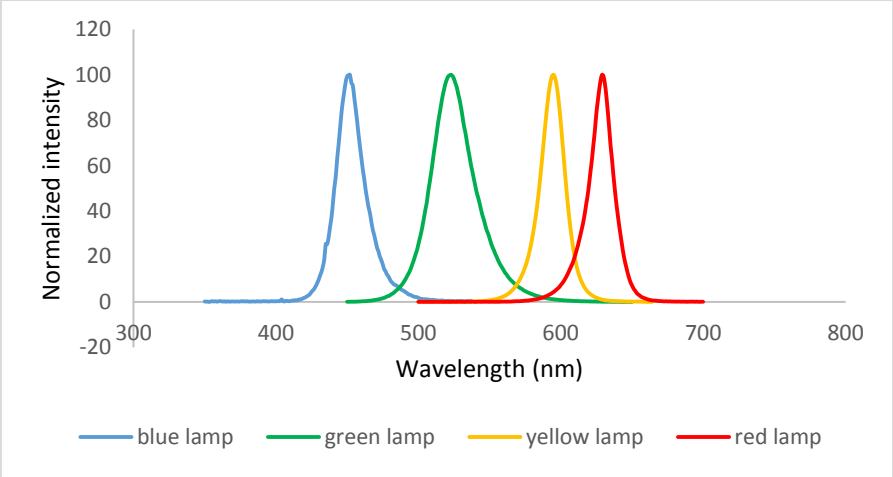

Figure 4.28 – Emission spectra of light-emitting diodes used as irradiation sources (blue, green, yellow, red)

Table 4.10 – Maxima, width band of emission spectra and photon flux of used LEDs.

	Blue	*Green*	*Yellow*	*Red*
$\lambda_{max\ em}$ (nm)	452	525	595	630
$\Delta\lambda$ (nm)	150	170	85	125
Photon flux (μEinstein.min^{-1}.cm^{-2})[a]	20.5	10.1	13.9	24.5

[a]An analog power-meter PM100A (THORLABS) associated with a compact photodiode power head with silicon detector S120C is used to evaluate the photon flux for each LEDs. Photo-diode detector is placed at the same distance from the LED surface than the bottom of illuminated vial (0.7 cm for blue, green and red LED panels and 1.2 cm for yellow LED).

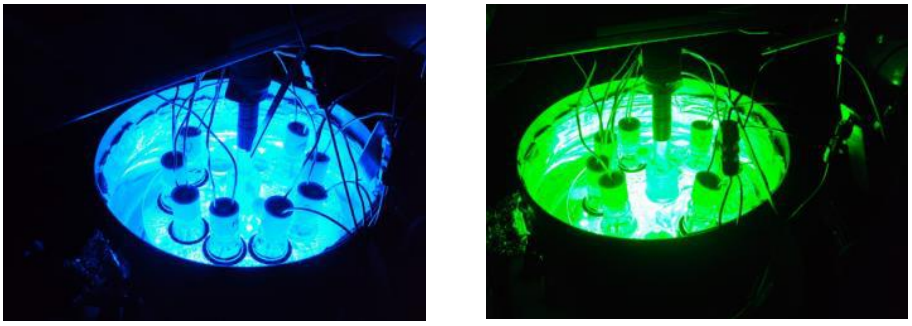

Figure 4.29 – Lamps set-up for irradiation experiments

Table 4.11 gathers the results obtained for hydrogen evolution experiments in the different conditions tested. Clearly, the dissociated systems IrL-bpy/Co(dmgH)$_2$PyrCl are less efficient than single-component ones. Spatial interactions between photosensitizer and catalyst through coordination bonding of terpyridine ligands enhance electronic transfers.[39, 41-45] Indeed, it has been shown that fast electronic transfer from the reduced photosensitizer to the catalyst could lower the probability of decomposition of the photosensitizer via ligand dissociation.[46]

Table 4.11 – Performances of photocatalytic systems under various wavelengths

	Blue LED		Green LED	
Compounds	TON	TOF_{max}	TON	TOF_{max}
Irppy-bpy/Co(dmgH)$_2$PyrCl	29 (0.5 h)	4394	16 (3.7 h)	175
Irppy-2244tpy-Co	205 (1.5 h)	6011	176 (9 h)	1090
Irppy-2254tpy-Co	251 (1.7 h)	5725	227 (12.8 h)	1223
IrppyF$_2$-bpy/Co(dmgH)$_2$PyrCl	35 (0.8 h)	4215	18 (27 h)[a]	26
IrppyF$_2$-2244tpy-Co	262 (1.3 h)	12320	167 (30.3 h)[b]	146
IrppyF$_2$-2254tpy-Co	295 (2.8 h)	8233	151 (27.3 h)	138
Irpiq-bpy/Co(dmgH)$_2$PyrCl	71 (7 h)	350	30 (16 h)	58
Irpiq-2244tpy-Co	230 (2.7 h)	5208	199 (6.8 h)	1158
Irpiq-2254tpy-Co	181 (2.3 h)	16023	251 (3.8 h)	3516
	Yellow LED		Red LED	
Compounds	TON	TOF_{max}	TON	TOF_{max}
Irppy-2244tpy-Co	43 (83 h)	17	-	-
Irppy-2254tpy-Co	66 (81.5 h)	22	-	-
Irpiq-2244tpy-Co	109 (42.8 h)	66	28 (110 h)[c,d]	5
Irpiq-2254tpy-Co	180 (17.8 h)	265	75 (110 h)[c,d]	15

TON in $mol_{H2}.mol^{-1}_{PS}$. TOF in $mmol_{H2}.mol^{-1}_{PS}.min^{-1}$. 0.5 M TEOA. 0.05 M HBF_4.

[a]15 min induction time. [b]5 min of induction time. [c]40 min of induction time. [d]production still ongoing.

Compared to the photocatalytic activity of the reference system IrL-bpy/Co(dmgH)$_2$PyrCl, [Ir-Co] dyads react faster under irradiation to reach a best TON limited by the stability of cobaloxime (*vide infra*).[41] Indeed, in the case of the dissociated systems, the addition of Ir(III) photosensitizer just after the deactivation of the system does not evolve hydrogen anymore, meaning that the cobaloxime is decomposed. In fact, addition of Co(III) catalyst should lead to hydrogen production. Considering the photo-reaction conditions, the activity of cobaloxime is enhanced towards its best performance with the use of pyridyl pendant Iridium photosensitizers. Under blue light irradiation, all photosensitizers are excited in their absorption bands and generate photoredox processes. Irppy-2254tpy-Co displays higher activity than Irppy-2244tpy-Co *i.e.* TON of 251 and 205, respectively, and TOF_{max} of 5725 $mmol_{H2}.mol^{-1}_{PS}.min^{-1}$ and 6011 $mmol_{H2}.mol^{-1}_{PS}.min^{-1}$, respectively. As similar conditions have been used for the synthesis of [Ir-Co] dyads (*vide supra*), Irppy-2244tpy and Irppy-2254tpy photosensitizers were solubilized with Co(dmgH)(dmgH$_2$)Cl$_2$ precursor yielding to similar results *i.e.* a TON of 208 after 1.5 h for Irppy-2244tpy (TOF_{max} = 5991) and a TON of 246 after 1.67 h for Irppy-2254tpy (TOF_{max} = 5586). An increase in the amount of sacrificial electron donor TEOA and proton source HBF_4 to 1 M and 0.1 M, respectively, dramatically decreased TON to 51 after 0.6 h and 63 after 1 h for Irppy-2244tpy-Co and Irppy-2254tpy-Co, respectively, with slightly lower TOF, meaning that a too concentrated media leads to decomposition of the catalyst. Regarding IrppyF$_2$- derivatives, the rate for IrppyF$_2$-2244tpy-Co is higher than that of IrppyF$_2$-2254tpy-Co, with 12320 $mmol_{H2}.mol^{-1}_{PS}.min^{-1}$ and 8233 $mmol_{H2}.mol^{-1}_{PS}.min^{-1}$, respectively, but a lower TON is observed *i.e.* 262 (1.3 h) *vs*. 295 (2.8 h). Irpiq-2254tpy-Co has a maximum rate of activity 16023 $mmol_{H2}.mol^{-}$

$^{1}_{PS}$.min^{-1} with a TON = 181 (2.3 h), while Irpiq-2244tpy-Co displays a TON of 230 after 2.7 h and TOF_{max} of 5208 $mmol_{H2}.mol^{-1}_{PS}.min^{-1}$ (Figure 4.30 and Supporting Information – Figures S4.42-S4.43 – for the other families). Thus, the best performances in TOF and TON are attributed to the IrppyF_2- and Irpiq- derivatives. The former derivatives are known to generate a powerful oxidant in the excited state[47] whereas the 1-phenylisoquinoline derivatives have been more investigated for the extending of electronic conjugation. In both series, a higher contribution of ^{3}LC in the excited state is noticed and their lifetime is raised to the microsecond range. Those photophysical particularities could account for the higher efficiency of photoredox processes.[48-49] An interesting observation concerns the high efficiency of IrppyF_2- dyads under blue light irradiation even if they exhibit low absorption in the wavelength range of blue LEDs. It is noteworthy that, in the same conditions, dissociated systems displayed dramatically lower activities and sustainabilities compared to corresponding dyads. The Irppy-bpy and IrppyF_2-bpy systems quickly reach a TOF_{max} of 4394 $mmol_{H2}.mol^{-1}_{PS}.min^{-1}$ and 4215 $mmol_{H2}.mol^{-1}_{PS}.min^{-1}$, followed by a rapid decrease of activity to reach a modest TON of 29 (0.5 h) and 35 (0.8 h). Irpiq-bpy/Co(dmgH)$_2$PyrCl system reacts much slower under blue light with a TOF_{max} of only 350 $mmol_{H2}.mol^{-1}_{PS}.min^{-1}$ but with a more sustainable activity, with a TON of 71 after 7 h.

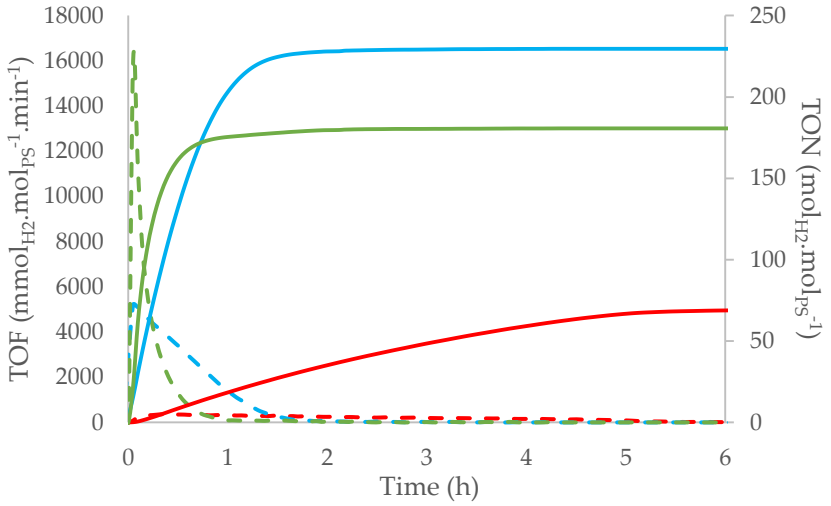

Figure 4.30 – Hydrogen evolution of 0.1 mM Irpiq-2244tpy-Co (*blue*), 0.1 mM Irpiq-2254tpy-Co (*green*) and dissociated system 0.1 mM Irpiq-bpy:[Co(dmgH)$_2$PyrCl] / 1:1 (*red*) in CH_3CN with 0.5 M TEOA as electron source and 0.05 M HBF_4 as proton source. Solid line: TON, dashed line: TOF. Irradiation centered at 452 nm, blue light.

Under green irradiation, overlaps of absorption spectra of photosensitizers and emission spectra of LEDs are worse. As a result, the systems show lower activity. For dissociated system Irppy-bpy/Co(dmgH)$_2$PyrCl, a quick deactivation occurs, to reach a TON of 16 (3.7 h) with a low TOF_{max} of 175 $mmol_{H2}.mol^{-1}{}_{PS}.min^{-1}$ as expected whereas Irppy-2244tpy-Co and Irppy-2254tpy-Co reach 176 (9 h) and 227 (12.8 h) with a TOF of 1090 and 1226 $mmol_{H2}.mol^{-1}{}_{PS}.min^{-1}$, respectively. In the case of IrppyF$_2$- derivatives, weak absorptivity in the green range of the absorption spectra involves slower reactivity but high sustainability. Indeed, IrppyF$_2$-bpy/Co(dmgH$_2$)PyrCl system holds its activity for 27 h with a low rate. IrppyF$_2$-2244tpy-Co and IrppyF$_2$-2254tpy-Co show a TON of 167 (30.3 h) and 151 (27 h) with a sustainable rate of 146 $mmol_{H2}.mol^{-1}{}_{PS}.min^{-1}$ and 138 $mmol_{H2}.mol^{-1}{}_{PS}.min^{-1}$. In the case of Irpiq- derivatives, multicomponent Irpiq-

bpy/Co(dmgH$_2$)PyrCl system displays a weak activity with a TON of 30 (16 h) with 58 mmol$_{H2}$.mol$^{-1}_{PS}$.min^{-1}. The Irpiq-2254tpy-Co dyad shows again a faster rate with 3516 mmol$_{H2}$.mol$^{-1}_{PS}$.min^{-1} to obtain a TON of 251 (3.8 h) *vs.* 1158 mmol$_{H2}$.mol$^{-1}_{PS}$.min^{-1} and 199 of TON (6.8 h) for Irpiq-2244tpy-Co (Figure 4.31 and Supporting Information – Figures S4.44-S4.45 – for the other families). Surprisingly, despite a lower molar extinction coefficient at 525 nm (green light) compared to 452 (blue light), H_2 photoproduction by Irpiq-2254tpy-Co dyad is more efficient under green light. Indeed, as green light is less energetic, the Cobalt catalyst is less solicited by the Iridium photosensitizer and, hence, displays a slower deterioration. In order to improve the stability of both Irpiq-2244tpy-Co and Irpiq-2254tpy-Co under green light irradiation, four equivalents of dmgH$_2$ ligand were added to the medium to regenerate the Cobalt catalyst. While TOF$_{max}$ were only slightly higher, *i.e.* 1192 and 3929 mmol$_{H2}$.mol$^{-1}_{PS}$.min^{-1} for Irpiq-2244tpy-Co and Irpiq-2254tpy-Co, respectively, confirming the optimized production rate of our system, TON and sustainability were dramatically increased to TON = 315 after 13.25 h and TON = 463 after 8.5 h, respectively. These results confirm the weakness of the Cobalt catalyst compared to the Iridium photosensitizer.

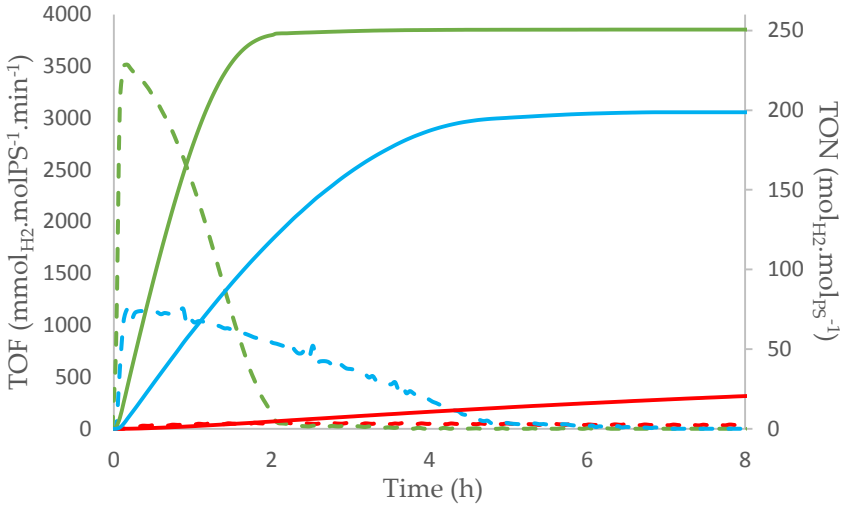

Figure 4.31 – Hydrogen evolution of 0.1 mM Irpiq-2244tpy-Co (*blue*), 0.1 mM Irpiq-2254tpy-Co (*green*) and dissociated system 0.1 mM Irpiq-bpy:[Co(dmgH)$_2$PyrCl] / 1:1 (*red*) in CH_3CN with 0.5 M TEOA as electron source and 0.05 M HBF_4 as proton source. Solid line: TON, dashed line: TOF. Irradiation centered at 525 nm, green light.

Under yellow LED irradiation, no production of dihydrogen could be detected, neither for all the dissociated systems nor for IrppyF$_2$-2244tpy-Co and IrppyF$_2$-2254tpy-Co dyads. Indeed, their absorption spectra do not overlap with the emission spectrum of the yellow LED. The Irppy-2244tpy-Co and Irppy-2254tpy-Co are active for 83 h and 81.5 h to reach a TON of 42 and 62, respectively. Irpiq-2244tpy-Co and Irpiq-2254tpy-Co generate a TON of 109 (43 h) and 180 (18 h) with a TOF_{max} of 66 and 265 $mmol_{H2}.mol^{-1}{}_{PS}.min^{-1}$, respectively (Figure 4.32 and Supporting Information – Figure S4.46 – for Irppy-N^N-Co family).

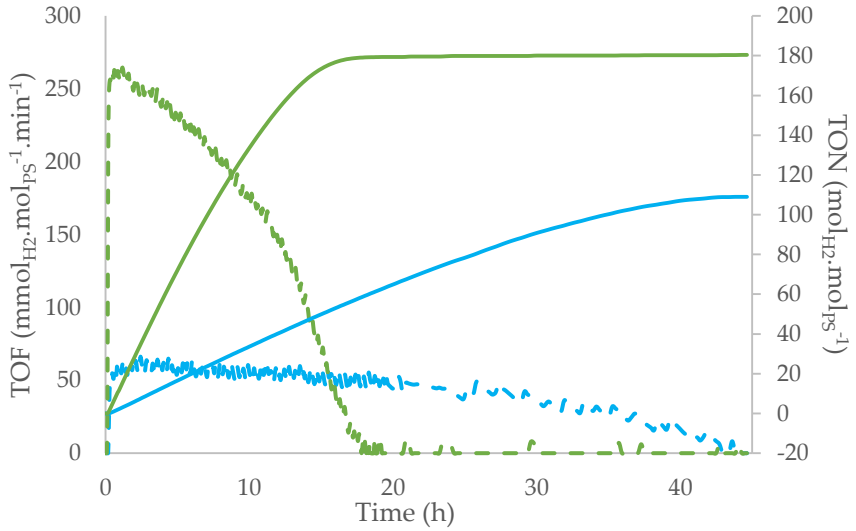

Figure 4.32 – Hydrogen evolution of 0.1 mM Irpiq-2244tpy-Co (*blue*) and 0.1 mM Irpiq-2254tpy-Co (*green*) in CH_3CN with 0.5 M TEOA as electron source and 0.05 M HBF_4 as proton source. Solid line: TON, dashed line: TOF. Irradiation centered at 595 nm, yellow light.

The tailing of the absorption spectra for Irpiq-2254tpy displays a weak absorptivity up to 590 nm *vs*. Irpiq-2244tpy at 560 nm. Under red LED irradiation centered at 630 nm, Irpiq-2254tpy-Co exhibits a somewhat slow but constant hydrogen production for more than 110 h with a TON of 75, whereas a three times lower activity for Irpiq-2244tpy is detected (TON = 28) (Figure 4.33). It is noteworthy that experiments carried out under red light irradiation required induction time before H_2 production. Indeed, in order to generate the Co(II) which is subsequently reduced to the Co(I) state, a primary photoinduced electron transfer step is mandatory but may take some time if the irradiation is energetically weak. Photoredox processes triggered by low energy photons could be enhanced by a good electronic communication between the photosensitizer and the catalyst. Indeed, direct population of the lowest $MLLCT^{1/3}$ excited in

the tailing of absorption spectra drives a constant sustainable photoactivity.

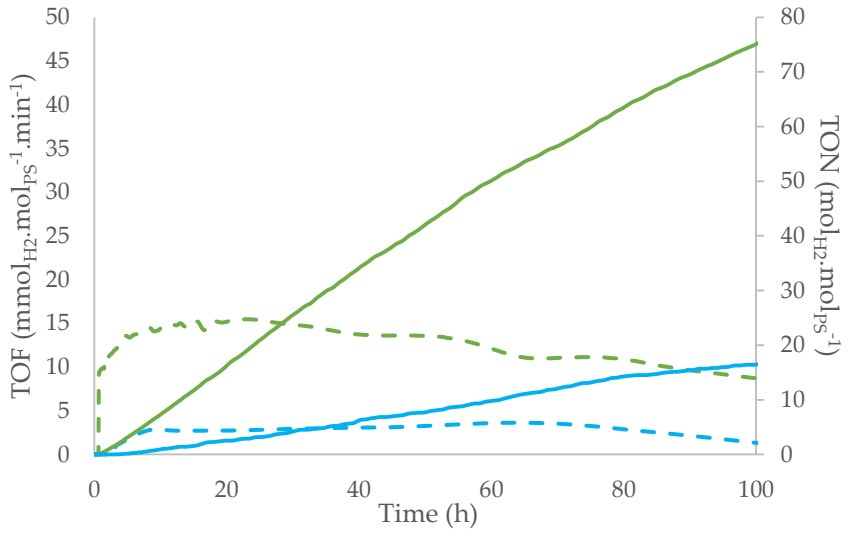

Figure 4.33 – Hydrogen evolution of 0.1 mM Irpiq-2244tpy-Co (*blue*) and 0.1 mM Irpiq-2254tpy-Co (*green*) in CH_3CN with 0.5 M TEOA as electron source and 0.05 M HBF_4 as proton source. Solid line: TON, dashed line: TOF. Irradiation centered at 630 nm, red light.

4.8 Conclusion

In this work, we managed to synthesize different families of Ir(III) photosensitizers with either electron-rich, electron-poor or highly conjugated 2-phenylpyridine derivatives. Some of these *i.e.* reference ligand ppyH, electron-poor $ppyF_2H$ allowing a high quantum yield on Ir(III) photosensitizers and conjugated piqH affording red-shifted absorption were selected for the synthesis and studies of [Ir-Co] dyads for photoinduced hydrogen evolution. Photophysical and electrochemical properties of photosensitizers and dyads were thoroughly investigated as well as the ability of the pendant pyridine to act like an electron bridge between both metallic centers by protonation studies. Progressive addition of acetic acid proved that the pyridine moiety is involved in the PET process between the photosensitizer and the proton reduction catalyst.

During H_2-evolution reactions, in different families of compounds, the bridging 2244tpy and 2254tpy influence the photo-activity of compounds and resulting [Ir-Co] dyads appear to be much more efficient than their multicomponent derivatives. The $IrppyF_2$-N^N-Co family is more active under blue light compared to the other families because of the high quantum yield of such compounds whereas under green, yellow and red irradiation, Irpiq-N^N-Co family is more active due to the higher molar extinction coefficient. Strikingly, extending electronic conjugation with phenylisoquinoline substituents in cyclometalated ligands allows for hydrogen to be produced with yellow and red light irradiations, providing the best results so far for [Ir-Co] dyads. In the investigated systems, photocatalysis under red light appears surprisingly efficient in view of the small absorptivity in the tailing of absorption spectra.

4.9 Experimental details

4.9.1 Synthesis of the ligands

ppyOMeH. Palladium(II) acetate (24.9 mg, 0.111 mmol) and triphenylphosphine (118.6 mg, 0.452 mmol) were added to dimethoxyethane (2.1 mL) under Argon atmosphere and stirred for 1 min. 2-bromopyridine (328.0 mg, 2.08 mmol), 3-methoxyphenylboronic acid (390.1 mg, 2.57 mmol) and an aqueous solution of K_2CO_3 (2 M, 2.9 mL) were successively added. The mixture was degassed and then put under Argon atmosphere. The mixture was heated to 85°C and stirred for 5 days. H_2O (20 mL) and AcOEt (20 mL) were added and the organic phase was isolated. The aqueous phase was washed with AcOEt (3 x 20 mL). The organic layers were combined, washed with H_2O (40 mL) and brine (20 mL) and dried over $MgSO_4$. A column chromatography on silica (neutralized with 1 M NEt_3 in eluent) using Cy:CH_2Cl_2 / 7:1 as eluent (266.4 mg – 69%). ^{1}H NMR ($CDCl_3$), δ/ppm: 8.70 (dd, 1H, *H-6*, $J_{6\text{-}5}$ = 4.8 Hz, $J_{6\text{-}4}$ = 1.3 Hz), 7.75 (m, 2H, *H-4* + *H-4'*), 7.57 (m, 2H, *H-3* + *H-2'*), 7.39 (dd, 1H, *H-5'*, $J_{5'\text{-}4'}$ = $J_{5'\text{-}6'}$ = 8.0 Hz), 7.24 (ddd, 1H, *H-5*, $J_{5\text{-}6}$ = 4.8 Hz, $J_{5\text{-}4}$ = 6.4 Hz, $J_{5\text{-}3}$ = 2.2 Hz), 6.98 (dd, 1H, *H-6'*, $J_{6'\text{-}5'}$ = 8.0 Hz, $J_{6'\text{-}4'}$ = 2.6 Hz, $J_{6'\text{-}2'}$ = 0.9 Hz).

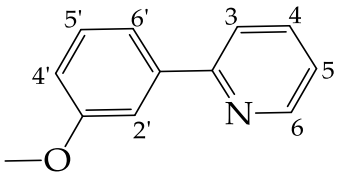

ppy(OMe)$_2$H. Palladium(II) acetate (23.1 mg, 0.103 mmol) and triphenylphosphine (109.4 mg, 0.417 mmol) were added to dimethoxyethane (2.1 mL) under Argon atmosphere and stirred for 1 min. 2-bromopyridine (318.1 mg, 2.01 mmol), 3,5-dimethoxyphenylboronic acid (443.0 mg, 2.43 mmol) and an aqueous solution of K_2CO_3 (2 M, 2.9 mL) were successively added. The mixture was degassed and then put under Argon atmosphere. The mixture was heated to 85°C and stirred for 5 days. H_2O (20 mL) and AcOEt (20 mL) were added and the organic phase was isolated. The aqueous phase was washed with AcOEt (3 x 20 mL). The organic layers were combined, washed with H_2O (40 mL) and brine (20 mL) and dried over $MgSO_4$. A column chromatography on silica (neutralized with 1 M NEt_3 in eluent) using Cy:CH_2Cl_2 / 2:1 as eluent (212.8 mg – 49%). ^{1}H NMR ($CDCl_3$), δ/ppm: 8.63 (dd, 1H, *H-6*, $J_{6\text{-}5}$ = 4.8 Hz, $J_{6\text{-}4}$ = 1.4 Hz), 7.63 (m, 2H, *H-5* + *H-3*), 7.12 (m, 3H, *H-4* + *H-2'* + *H-6'*), 6.49 (dd, 1H, *H-4'*, $J_{4'\text{-}2'}$ = $J_{4'\text{-}6'}$ = 2.3 Hz).

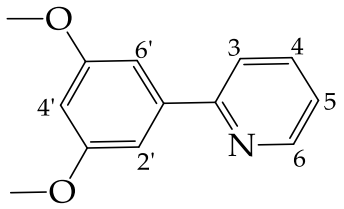

2244tpy. In a schlenck were successively added 4-bromo-2,2′-bipyridine (119.9 mg, 0.510 mmol), 1,2-dimethoxyethane (10.5 mL), water (1.4 mL), K_2CO_3 (139.7 mg, 1.01 mmol) and 4-pyridylboronic acid (82.1 mg, 0.668 mmol). The mixture was degassed and put under Argon before adding [$Pd(PPh_3)_4$] (59.4 mg, 0.0514 mmol). The reaction mixture was refluxed for 4 days. The mixture was poured onto water (30 mL). The solid was filtered on Celite® and washed successively with water and AcOEt. The organic layer was separated and the aqueous phase extracted with AcOEt (3 x 30 mL). The organic layers were combined, dried over $MgSO_4$ and concentrated under reduced pressure. The product was purified by column chromatography on silica using CH_2Cl_2:MeOH / 95:5 as eluent (108.9 mg – 92%). ^{1}H NMR ($CDCl_3$), δ/ppm: 8.77 (dd, 1H, *H-6′*, $J_{6'-5'}$ = 5.1 Hz, $J_{6'-3'}$ = 0.7 Hz), 8.74 (dd, 2H, *H-2″* + *H-6″*, $J_{2''/6''-3''/5''}$ = 4.5 Hz, $J_{2''/6''-5''/3''}$ = 1.7 Hz), 8.69 (m, 2H, *H-6* + *H-3′*), 8.45 (dd, 1H, *H-3*, J_{3-4} = 7.9 Hz, J_{3-5} = 1.1 Hz), 7.84 (ddd, 1H, *H-4*, J_{4-3} = 7.9 Hz, J_{4-5} = 7.7 Hz, J_{4-6} = 1.8 Hz), 7.64 (dd, 2H, *H-3″* + *H-5″*, $J_{3''/5''-2''/6''}$ = 4.5 Hz, $J_{5''/3''-2''/6''}$ = 1.7 Hz), 7.53 (dd, 1H, *H-5′*, $J_{5'-6'}$ = 5.1 Hz, $J_{5'-3'}$ = 1.9 Hz), 7.33 (ddd, 1H, *H-5*, J_{5-4} = 7.7 Hz, J_{5-6} = 4.8 Hz, J_{5-3} = 1.1 Hz).

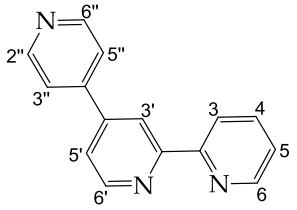

2254tpy. In a schlenck were successively added 5-bromo-2,2′-bipyridine (60.1 mg, 0.256 mmol), 1,2-dimethoxyethane (5.3 mL), water (0.7 mL), K_2CO_3 (72.9 mg, 0.528 mmol) and 4-pyridylboronic acid (42.3 mg, 0.344 mmol). The mixture was degassed and put under Argon before adding [$Pd(PPh_3)_4$] (32.1 mg, 0.0278 mmol). The reaction mixture was refluxed for 4 days. The mixture was poured onto water (30 mL). The solid was filtered on Celite® and washed successively with water and AcOEt. The organic layer was separated and the aqueous phase extracted with AcOEt (3 x 30 mL). The organic layers were combined, dried over $MgSO_4$ and concentrated under reduced pressure. The product was purified by column chromatography on silica using CH_2Cl_2:MeOH / 95:5 as eluent. The fraction with a R_f = 0.3 was collected and evaporated (48.6 mg – 82%). ^{1}H NMR ($CDCl_3$), δ/ppm: 8.97 (d, 1H, *H-6′*, $J_{6'-4'}$ = 2.4 Hz, $J_{6'-3'}$ = 0.5 Hz), 8.73 (m, 3H, *H-2″* + *H-6″* + *H-6*), 8.55 (dd, *H-3′*, $J_{3'-4'}$ = 8.3 Hz, $J_{3'-6'}$ = 0.5 Hz), 8.46 (dd, 1H, *H-3*, J_{3-4} = 7.9 Hz, J_{3-5} = 1.1 Hz), 8.08 (dd, 1H, *H-4′*, $J_{4'-3'}$ = 8.3 Hz, $J_{4'-6'}$ = 2.4 Hz), 7.86 (dd, 1H, *H-4*, J_{4-3} = 7.9 Hz, J_{4-5} = 7.6 Hz, J_{4-6} = 1.8 Hz), 7.60 (dd, 2H, *H-3″* + *H-5″*, $J_{3''/5''-2''/6''}$ = 4.5 Hz, $J_{5''/3''-2''/6''}$ = 1.7 Hz), 7.36 (1H, ddd, *H-5*, J_{5-4} = 7.6 Hz, J_{5-6} = 4.8 Hz, J_{5-3} = 1.1 Hz).

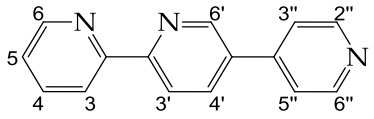

4.9.2 Synthesis of the Ir(III) photosensitizers

General procedure for Ir(III) dimer precursors. Iridium(III) chloride hydrate (1.0 eq) was suspended in a 2-ethoxyethanol:water / 3:1 mixture followed by 2-phenylpyridine (2.0 eq). The system was put under Argon and refluxed overnight. The obtained solid was centrifuged, washed successively with EtOH and acetone and dissolved in CH_2Cl_2 to remove impurities. The solvents were evaporated under reduced pressure.

$[Ir(ppy)_2Cl]_2$. Yield = 74%. ^{1}H NMR ($CDCl_3$), δ/ppm: 9.24 (dd, 4H, *H-a*, $J_{a\text{-}b}$ = 5.8 Hz, $J_{a\text{-}c}$ = 1.2 Hz), 7.87 (dd, 4H, *H-d*, $J_{d\text{-}c}$ = 8.0 Hz, $J_{d\text{-}b}$ = 1.2 Hz), 7.73 (ddd, 4H, *H-c*, $J_{c\text{-}d}$ = 8.0 Hz, $J_{c\text{-}b}$ = 7.5 Hz, $J_{c\text{-}a}$ = 1.2 Hz), 7.49 (dd, 4H, *H-e*, $J_{e\text{-}f}$ = 8.2 Hz, $J_{e\text{-}g}$ = 1.2 Hz), 6.75 (m, 8H, *H-b* + *H-f*), 6.56 (ddd, 4H, *H-g*, $J_{g\text{-}h}$ = 7.9 Hz, $J_{g\text{-}f}$ = 7.2 Hz, $J_{g\text{-}e}$ = 1.2 Hz), 5.93 (dd, 4H, *H-h*, $J_{h\text{-}g}$ = 7.9 Hz, $J_{h\text{-}f}$ = 0.8 Hz).

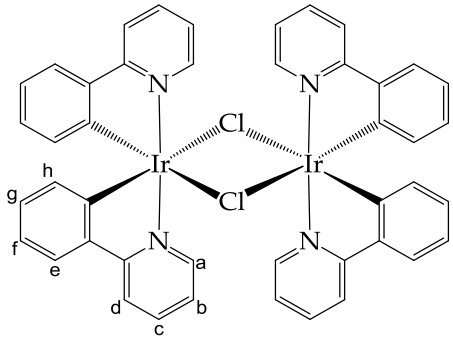

[Ir(ppyF$_2$)$_2$Cl]$_2$. Yield = 71%. ^{1}H NMR ($CDCl_3$), δ/ppm: 9.12 (dd, 4H, *H-a*, $J_{a\text{-}b}$ = 5.8 Hz, $J_{a\text{-}c}$ = 1.2 Hz), 8.31 (dd, 4H, *H-d*, $J_{d\text{-}c}$ = 8.2 Hz, $J_{d\text{-}b}$ = 0.7 Hz), 7.83 (ddd, 4H, *H-c*, $J_{c\text{-}d}$ = 8.2 Hz, $J_{c\text{-}b}$ = 7.7 Hz, $J_{c\text{-}a}$ = 1.2 Hz), 6.83 (ddd, 4H, *H-b*, $J_{b\text{-}c}$ = 7.7 Hz, $J_{b\text{-}a}$ = 5.8 Hz, $J_{b\text{-}d}$ = 0.7 Hz), 6.34 (ddd, 4H, *H-f*, $J_{f\text{-}F}$ = 12.2 Hz, $J_{f\text{-}F}$ = 9.0 Hz, $J_{f\text{-}h}$ = 2.3 Hz), 5.29 (dd, 4H, *H-h*, $J_{h\text{-}F}$ = 9.1 Hz, $J_{h\text{-}f}$ = 2.3 Hz).

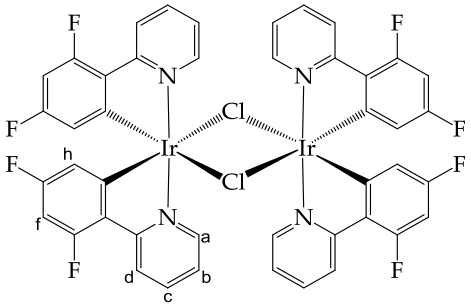

[Ir(piq)$_2$Cl]$_2$. Yield = 67%. ^{1}H NMR ($CDCl_3$), δ/ppm: 9.05 (d, 4H, *H-a*, $J_{a\text{-}b}$ = 6.3 Hz), 8.97 (d, 4H, *H-f*, $J_{f\text{-}e}$ = 8.4 Hz), 8.12 (d, 4H, *H-g*, $J_{g\text{-}h}$ = 8.0 Hz), 7.83 (m, 8H, *H-c* + *H-d*), 7.76 (ddd, 4H, *H-e*, $J_{e\text{-}f}$ = 8.4 Hz, $J_{e\text{-}d}$ = 6.6 Hz, $J_{e\text{-}c}$ = 1.7 Hz), 6.81 (ddd, 4H, *H-h*, $J_{h\text{-}g}$ = 8.0 Hz, $J_{h\text{-}i}$ = 7.1 Hz, $J_{h\text{-}j}$ = 1.2 Hz), 6.56 (d, 4H, *H-b*, $J_{b\text{-}a}$ = 6.3 Hz), 6.50 (ddd, 4H, *H-i*, $J_{i\text{-}j}$ = 8.2 Hz, $J_{i\text{-}h}$ = 6.9 Hz, $J_{i\text{-}g}$ = 1.2 Hz), 6.03 (dd, 4H, *H-j*, $J_{j\text{-}i}$ = 7.9 Hz, $J_{j\text{-}h}$ = 1.0 Hz).

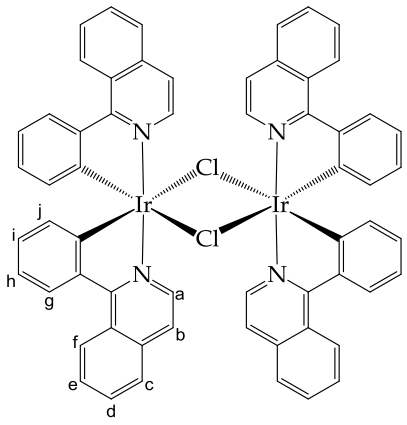

[Ir(ppytBu$_2$)$_2$Cl]$_2$. Yield = 94% (unpure). ^{1}H NMR ($CDCl_3$), δ/ppm: 9.30 (dd, 4H, *H-a*, $J_{a\text{-}b}$ = 6.1 Hz, $J_{a\text{-}c}$ = 1.2 Hz), 7.80 (d, 4H, *H-d*, $J_{d\text{-}b}$ = 2.0 Hz), 7.39 (d, 4H, *H-e*, $J_{e\text{-}f}$ = 8.2 Hz), 6.80 (dd, 4H, *H-b*, $J_{b\text{-}a}$ = 6.1 Hz, $J_{b\text{-}d}$ = 2.0 Hz), 6.75 (dd, 4H, *H-f*, $J_{f\text{-}e}$ = 8.2 Hz, $J_{f\text{-}h}$ = 1.8 Hz), 5.93 (d, 4H, *H-h*, $J_{h\text{-}f}$ = 1.8 Hz), 1.47 (s, 36H, *H-tBu-Pyr*), 0.91 (s, 36H, *H-tBu-Ph*).

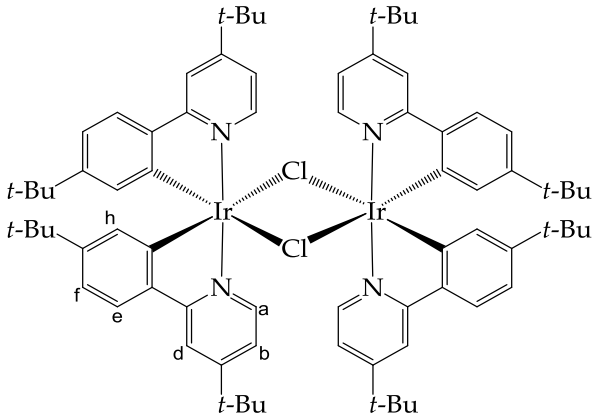

General procedure for Ir(III) trischelate complexes. Ir(III) dimer precursor (1.0 eq) and N^N ligand (N^N = bpy, 2244tpy or 2254tpy) (2.4 eq) were suspended in ethyleneglycol. The mixture was refluxed overnight under Argon. The solution was cooled to room temperature and a saturated aqueous solution of NH_4PF_6 was added for precipitation. The solid was centrifuged, washed with water (3X) and dried under reduced pressure.

Irppy-bpy. Yield = 88%. HRMS (ESI): m/z calculated for $[C_{32}H_{24}{}^{193}IrN_4 - PF_6]^+$, 657.16247 ; found: 657.16221, m/z calculated for $[C_{22}H_{16}{}^{193}IrN_2 - PF_6 - bpy]^+$, 501.09372 ; found: 501.09222. ^{1}H NMR (CD_3CN), δ/ppm: 8.53 (dd, 2H, *H-3*, $J_{3\text{-}4}$ = 8.1 Hz, $J_{3\text{-}5}$ = 1.3 Hz), 8.12 (ddd, 2H, *H-4*, $J_{4\text{-}3}$ = 8.1 Hz, $J_{4\text{-}5}$ = 7.9 Hz, $J_{4\text{-}6}$ = 1.7 Hz), 8.06 (dd, 2H, *H-d*, $J_{d\text{-}c}$ = 8.5 Hz, $J_{d\text{-}b}$ = 1.6 Hz), 7.98 (dd, 2H, *H-6*, $J_{6\text{-}5}$ = 5.5 Hz, $J_{6\text{-}4}$ = 1.7 Hz), 7.85 (ddd, 2H, *H-c*, $J_{c\text{-}d}$ = 8.5 Hz, $J_{c\text{-}b}$ = 7.6 Hz, $J_{c\text{-}a}$ = 1.6 Hz), 7.80 (dd, 2H, *H-e*, $J_{e\text{-}f}$ = 7.8 Hz, $J_{e\text{-}g}$ = 1.4 Hz), 7.60 (dd, 2H, *H-a*, $J_{a\text{-}b}$ = 5.8 Hz, $J_{a\text{-}c}$ = 1.6 Hz), 7.50 (ddd, 2H, *H-5*, $J_{5\text{-}4}$ = 7.9 Hz, $J_{5\text{-}6}$ = 5.5 Hz, $J_{5\text{-}3}$ = 1.3 Hz), 7.04 (ddd, 2H, *H-f*, $J_{f\text{-}e}$ = 7.8 Hz, $J_{f\text{-}g}$ = 7.5 Hz, $J_{f\text{-}h}$ = 1.3 Hz), 7.02 (ddd, 2H, *H-b*, $J_{b\text{-}c}$ = 7.6 Hz, $J_{b\text{-}a}$ = 5.8 Hz, $J_{b\text{-}d}$ = 1.6 Hz), 6.92 (ddd, 2H, *H-g*, $J_{g\text{-}f}$ = $J_{g\text{-}h}$ = 7.5 Hz, $J_{g\text{-}e}$ = 1.4 Hz), 6.28 (dd, 2H, *H-h*, $J_{h\text{-}g}$ = 7.5 Hz, $J_{h\text{-}f}$ = 1.3 Hz).

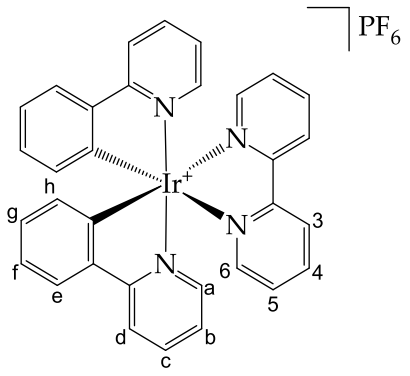

Irppy-2244tpy. Yield = 92%. HRMS (ESI): m/z calculated for $[C_{37}H_{27}{}^{193}IrN_5 - PF_6]^+$, 734.18902 ; found: 734.18860, m/z calculated for $[C_{22}H_{16}{}^{193}IrN_2 - PF_6 - 2244\text{-tpy}]^+$, 501.09372 ; found: 501.09245. ^{1}H NMR (CD_3CN), δ/ppm: 8.79 (m, 3H, *H-3′* + *H-2″* + *H-6″*), 8.71 (dd, 1H, *H*-3, J_{3-4} = 8.1 Hz, J_{3-5} = 0.5 Hz), 8.17 (ddd, 1H, *H-4*, J_{4-3} = 8.1 Hz, J_{4-5} = 7.7 Hz, J_{4-6} = 1.1 Hz), 8.08 (m, 2H, *H-d* + *H-d′*), 8.05 (d, 1H, *H-6′*, $J_{6'-5'}$ = 5.8 Hz), 8.02 (dd, 1H, *H-6*, J_{6-5} = 5.5 Hz, J_{6-4} = 1.1 Hz), 7.84 (m, 4H, *H-c* + *H-c′* + *H-e* + *H-e′*), 7.78 (m, 3H, *H-5′* + *H-3″* + *H-5″*), 7.65 (m, 2H, *H-a* + *H-a′*), 7.54 (ddd, 1H, *H-5*, J_{5-4} = 7.7 Hz, J_{5-6} = 5.5 Hz, J_{5-3} = 0.5 Hz), 7.05 (m, 4H, *H-f* + *H-f′* + *H-b* + *H-b′*), 6.94 (m, 2H, *H-g* + *H-g′*), 6.30 (m, 2H, *H-h* + *H-h′*).

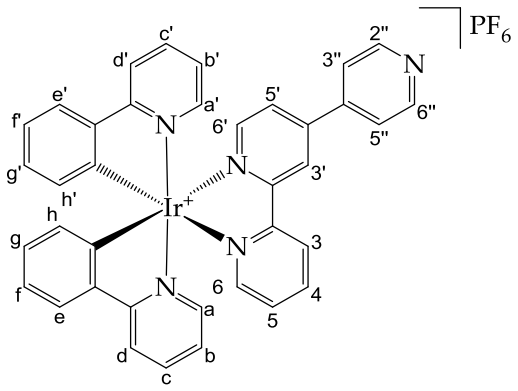

Irppy-2254tpy. Yield = 91%. HRMS (ESI): m/z calculated for $[C_{37}H_{27}{}^{193}IrN_5 - PF_6]^+$, 734.18902 ; found: 734.18906, m/z calculated for $[C_{22}H_{16}{}^{193}IrN_2 - PF_6 - 2254\text{-tpy}]^+$, 501.09372 ; found: 501.09293. ^{1}H NMR (CD_3CN), δ/ppm: 8.62 (m, 3H, *H-3′* + *H-2″* + *H-6″*), 8.57 (dd, 1H, *H-3*, $J_{3\text{-}4}$ = 8.1 Hz, $J_{3\text{-}5}$ = 0.6 Hz), 8.42 (dd, 1H, *H-4′*, $J_{4'\text{-}3'}$ = 8.5 Hz, $J_{4'\text{-}6'}$ = 2.0 Hz), 8.18 (d, 1H, *H-6′*, $J_{6'\text{-}4'}$ = 2.0 Hz), 8.15 (ddd, 1H, *H-4*, $J_{4\text{-}3}$ = 8.1 Hz, $J_{4\text{-}5}$ = 7.8 Hz, $J_{4\text{-}6}$ = 1.6 Hz), 8.07 (m, 2H, *H-d* + *H-d′*), 8.02 (dd, 1H, *H-6*, $J_{6\text{-}5}$ = 5.4 Hz, $J_{6\text{-}4}$ = 1.6 Hz), 7.84 (m, 4H, *H-c* + *H-c′* + *H-e* + *H-e′*), 7.67 (m, 2H, *H-a* + *H-a′*), 7.53 (ddd, 1H, *H-5*, $J_{5\text{-}4}$ = 7.8 Hz, $J_{5\text{-}6}$ = 5.4 Hz, $J_{5\text{-}3}$ = 0.6 Hz), 7.30 (dd, 2H, *H-3″* + *H-5″*, $J_{3''/5''\text{-}2''/6''}$ = 4.5 Hz, $J_{5''/3''\text{-}2''/6''}$ = 1.7 Hz), 7.05 (m, 4H, *H-f* + *H-f′* + *H-b* + *H-b′*), 6.94 (m, 2H, *H-g* + *H-g′*), 6.33 (m, 2H, *H-h* + *H-h′*).

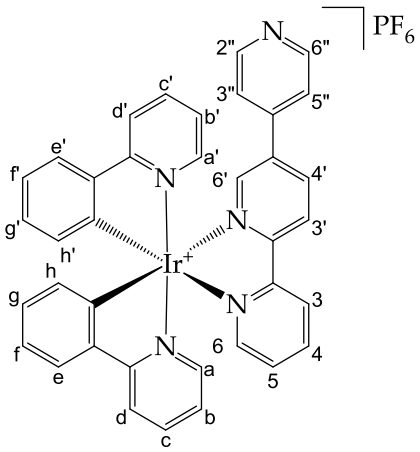

IrppyF$_2$-bpy. Yield = 91%. HRMS (ESI): m/z calculated for $[C_{32}H_{20}F_4{}^{193}IrN_4 - PF_6]^+$, 729.12478 ; found: 729.12459, m/z calculated for $[C_{22}H_{12}F_4{}^{193}IrN_2 - PF_6 - bpy]^+$, 573.05604 ; found: 573.05446. ^{1}H NMR (CD_3CN), δ/ppm: 8.53 (dd, 2H, *H-3*, J_{3-4} = 8.1 Hz, J_{3-5} = 1.1 Hz), 8.32 (dd, 2H, *H-d*, J_{d-c} = 8.4 Hz, J_{d-b} = 0.7 Hz), 8.16 (ddd, 2H, *H-4*, J_{4-3} = 8.1 Hz, J_{4-5} = 7.8 Hz, J_{4-6} = 1.4 Hz), 8.01 (dd, 2H, *H-6*, J_{6-5} = 5.5 Hz, J_{6-4} = 1.4 Hz), 7.91 (ddd, 2H, *H-c*, J_{c-d} = 8.5 Hz, J_{c-b} = 7.5 Hz, J_{c-a} = 1.2 Hz), 7.61 (dd, 2H, *H-a*, J_{a-b} = 5.8 Hz, J_{a-c} = 1.2 Hz), 7.53 (ddd, 2H, *H-5*, J_{5-4} = 7.8 Hz, J_{5-6} = 5.5 Hz, J_{5-3} = 1.1 Hz), 7.07 (ddd, 2H, *H-b*, J_{b-c} = 7.5 Hz, J_{b-a} = 5.8 Hz, J_{b-d} = 0.7 Hz), 6.71 (ddd, 2H, *H-f*, J_{f-F} = 12.7 Hz, J_{f-F} = 9.4 Hz, J_{f-h} = 2.4 Hz), 5.73 (dd, 2H, *H-h*, J_{h-F} = 8.6 Hz, J_{h-f} = 2.4 Hz).

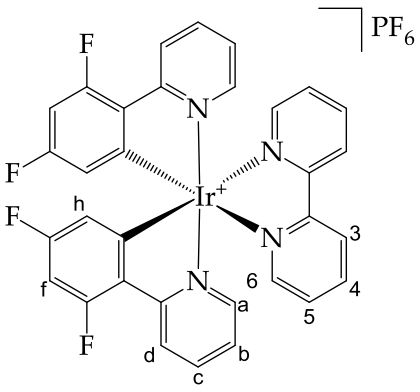

IrppyF$_2$-2244tpy. Yield = 87%. HRMS (ESI): m/z calculated for [$C_{37}H_{23}F_4{}^{193}IrN_5$ – PF_6]$^+$, 806.15133 ; found: 806.15063, m/z calculated for [$C_{22}H_{12}F_4{}^{193}IrN_2$ – PF_6 – 2244-tpy]$^+$, 573.05604 ; found: 573.05454. ^{1}H NMR (CD_3CN), δ/ppm: 8.83 (m, 3H, *H-3′* + *H-2″* + *H-6″*), 8.75 (d, 1H, *H*-3, $J_{3\text{-}4}$ = 8.1 Hz, $J_{3\text{-}5}$ = 0.6 Hz), 8.37 (m, 2H, *H-d* + *H-d′*), 8.24 (ddd, 1H, *H-4*, $J_{4\text{-}3}$ = 8.1 Hz, $J_{4\text{-}5}$ = 7.8 Hz, $J_{4\text{-}6}$ = 1.2 Hz), 8.11 (d, 1H, *H-6′*, $J_{6'\text{-}5'}$ = 5.8 Hz), 8.02 (dd, 1H, *H-6*, $J_{6\text{-}5}$ = 5.4 Hz, $J_{6\text{-}4}$ = 1.2 Hz), 7.95 (m, 2H, *H-c* + *H-c′*), 7.84 (dd, 1H, $J_{5'\text{-}6'}$ = 5.8 Hz, $J_{5'\text{-}3'}$ = 1.9 Hz), 7.82 (dd, 2H, *H-3″* + *H-5″*, $J_{3''/5''\text{-}2''/6''}$ = 4.5 Hz, $J_{5''/3''\text{-}2''/6''}$ = 1.7 Hz), 7.69 (m, 2H, *H-a* + *H-a′*), 7.61 (ddd, 1H, *H-5*, $J_{5\text{-}4}$ = 7.8 Hz, $J_{5\text{-}6}$ = 5.4 Hz, $J_{5\text{-}3}$ = 0.6 Hz), 7.12 (m, 2H, *H-b* + *H-b′*), 6.75 (m, 2H, *H-H-f* + *H-f′*), 5.79 (m, 2H, *H-h* + *H-h′*).

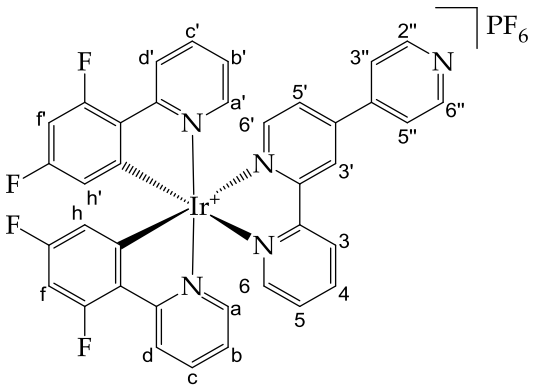

IrppyF$_2$-2254tpy. Yield = 89%. HRMS (ESI): m/z calculated for [$C_{37}H_{23}F_4{}^{193}IrN_5$ – PF_6]$^+$, 806.15133 ; found: 806.15068, m/z calculated for [$C_{22}H_{12}F_4{}^{193}IrN_2$ – PF_6 – 2254-tpy]$^+$, 573.05604 ; found: 573.04591. ^{1}H NMR (CD_3CN), δ/ppm: 8.65 (m, 3H, *H-3′* + *H-2″* + *H-6″*), 8.59 (d, 1H, *H*-3, $J_{3\text{-}4}$ = 8.1 Hz, $J_{3\text{-}5}$ = 0.4 Hz), 8.42 (dd, 1H, *H-4′*, $J_{4'\text{-}3'}$ = 8.5 Hz, $J_{4'\text{-}6'}$ = 2.1 Hz), 8.32 (m, 2H, *H-d* + *H-d′*), 8.20 (m, 2H, *H-4* + *H-6′*), 8.03 (dd, 1H, *H-6*, $J_{6\text{-}5}$ = 5.5 Hz, $J_{6\text{-}4}$ = 0.8 Hz), 7.91 (m, 2H, *H-c* + *H-c′*), 7.69 (m, 2H, *H-a* + *H-a′*), 7.53 (ddd, 1H, *H-5*, $J_{5\text{-}4}$ = 7.6 Hz, $J_{5\text{-}6}$ = 5.5 Hz, $J_{5\text{-}3}$ = 0.4 Hz), 7.40 (dd, 2H, *H-3″* + *H-5″*, $J_{3''/5''\text{-}2''/6''}$ = 4.5 Hz, $J_{5''/3''\text{-}2''/6''}$ = 1.6 Hz), 7.09 (m, 2H, *H-b* + *H-b′*), 6.71 (m, 2H, *H-f* + *H-f′*), 5.76 (m, 2H, *H-h* + *H-h′*).

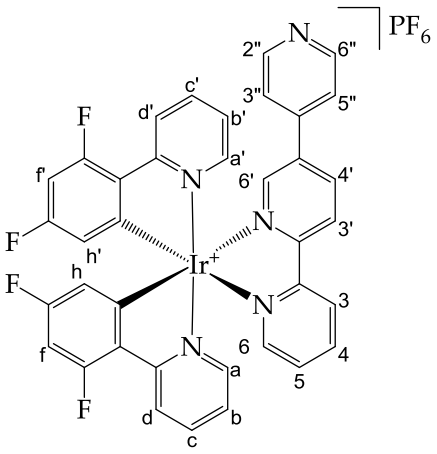

Irpiq-bpy. Yield = 87%. HRMS (ESI): m/z calculated for $[C_{40}H_{28}{}^{193}IrN_4 - PF_6]^+$, 755.19144 ; found: 755.19342, m/z calculated for $[C_{30}H_{20}{}^{193}IrN_2 - PF_6 - bpy]^+$, 601.12502 ; found: 601.12306. ^{1}H NMR (CD_3CN), δ/ppm: 9.02 (m, 2H, *H-c*/*H-f*), 8.54 (dd, 2H, *H-3*, $J_{3\text{-}4}$ = 8.1 Hz, $J_{3\text{-}5}$ = 1.0 Hz), 8.38 (dd, 2H, *H-g*, $J_{g\text{-}h}$ = 8.2 Hz, $J_{g\text{-}i}$ = 1.0 Hz), 8.11 (ddd, 2H, *H-4*, $J_{4\text{-}3}$ = 8.1 Hz, $J_{4\text{-}5}$ = 7.8 Hz, $J_{4\text{-}6}$ = 1.1 Hz), 7.99 (m, 2H, *H-f*/*H-c*), 7.87 (dd, 2H, *H-6*, $J_{6\text{-}5}$ = 5.4 Hz, $J_{6\text{-}4}$ = 1.1 Hz), 7.84 (m, 4H, *H-d* + *H*-e), 7.51 (d, 2H, *H-b*, $J_{b\text{-}a}$ = 6.4 Hz), 7.46 (ddd, 2H, *H-5*, $J_{5\text{-}4}$ = 7.8 Hz, $J_{5\text{-}6}$ = 5.4 Hz, $J_{5\text{-}3}$ = 1.0 Hz), 7.42 (d, 2H, *H-a*, $J_{a\text{-}b}$ = 6.4 Hz), 7.14 (ddd, 2H, *H-h*, $J_{h\text{-}g}$ = 8.2 Hz, $J_{h\text{-}i}$ = 7.8 Hz, $J_{h\text{-}j}$ = 1.1 Hz), 6.88 (ddd, 2H, *H-i*, $J_{i\text{-}h}$ = 7.8 Hz, $J_{i\text{-}j}$ = 7.6 Hz, $J_{i\text{-}g}$ = 1.0 Hz), 6.31 (dd, 2H, *H-j*, $J_{j\text{-}i}$ = 7.6 Hz, $J_{j\text{-}h}$ = 1.1 Hz).

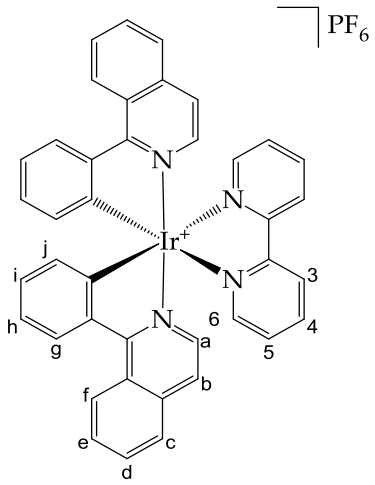

Irpiq-2244tpy. Yield = 85%. HRMS (ESI): m/z calculated for $[C_{45}H_{31}{}^{193}IrN_5 - PF_6]^+$, 834.22032 ; found: 834.21994, m/z calculated for $[C_{30}H_{20}{}^{193}IrN_2 - PF_6 - 2244tpy]^+$, 601.12502 ; found: 601.12264. ^{1}H NMR (CD_3CN), δ/ppm: 9.03 (m, 2H, *H-f* + *H-f'*), 8.81 (d, 1H, *H-3'*, $J_{3'\text{-}5'}$ = 1.6 Hz), 8.78 (dd, 2H, *H-2''* + *H-6''*, $J_{2''/6''\text{-}3''/5''}$ = 4.5 Hz, $J_{6''/2''\text{-}3''/5''}$ = 1.7 Hz), 8.74 (dd, 1H, *H-3*, $J_{3\text{-}4}$ = 8.1 Hz, $J_{3\text{-}5}$ = 0.5 Hz), 8.40 (m, 2H, *H-g* + *H-g'*), 8.16 (ddd, 1H, *H-4*, $J_{4\text{-}3}$ = 8.1 Hz, $J_{4\text{-}5}$ = 7.8 Hz, $J_{4\text{-}6}$ = 1.5 Hz), 8.00 (m, 2H, *H-c* + *H-c'*), 7.96 (d, 1H, *H-6'*, $J_{6'\text{-}5'}$ = 5.8 Hz), 7.91 (dd, 1H, *H-6*, $J_{6\text{-}5}$ = 5.6 Hz, $J_{6\text{-}4}$ = 1.5 Hz), 7.84 (m, 4H, *H-d* + *H-d'* + *H-e* + *H-e'*), 7.76 (dd, 2H, *H-3''* + *H-5''*, $J_{3''/5''\text{-}2''/6''}$ = 4.5 Hz, $J_{5''/3''\text{-}2''/6''}$ = 1.7 Hz), 7.75 (dd, 1H, *H-5'*, $J_{5'\text{-}6'}$ = 5.8 Hz, $J_{5'\text{-}3'}$ = 1.6 Hz), 7.55 (m, 2H, *H-a/b* + *H-a'/b'*), 7.50 (ddd, 1H, *H-5*, $J_{5\text{-}4}$ = 7.8 Hz, $J_{5\text{-}6}$ = 5.6 Hz, $J_{5\text{-}3}$ = 0.5 Hz), 7.44 (m, 2H, *H-b/a* + *H-b'/a'*), 7.15 (m, 2H, *H-h* + *H-h'*), 6.90 (m, 2H, *H-i* + *H-i'*), 6.32 (m, 2H, *H-j* + *H-j'*).

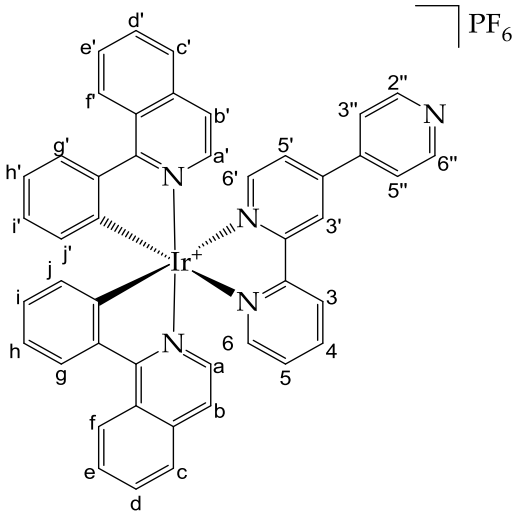

Irpiq-2254tpy. Yield = 90%. HRMS (ESI): m/z calculated for $[C_{45}H_{31}{}^{193}IrN_5 - PF_6]^+$, 832.21799 ; found: 834.21985, m/z calculated for $[C_{30}H_{20}{}^{193}IrN_2 - PF_6 - 2254tpy]^+$, 601.12502 ; found: 601.12291. ^{1}H NMR (CD_3CN), δ/ppm: 9.02 (m, 2H, *H-f* + *H-f'*), 8.65 (d, 1H, *H*-3', $J_{3'-4'}$ = 8.5 Hz), 8.59 (m, 3H, *H-3* + *H-2''* + *H-6''*), 8.41 (dd, 1H, *H*-4', $J_{4'-3'}$ = 8.5 Hz, $J_{4'-6'}$ = 2.2 Hz), 8.40 (m, 2H, *H-g* + *H-g'*), 8.14 (ddd, 1H, *H-4*, J_{4-3} = 8.0 Hz, J_{4-5} = 7.8 Hz, J_{4-6} = 1.2 Hz), 7.99 (m, 2H, *H-c* + *H-c'*), 7.96 (d, 1H, *H-6'*, $J_{6'-4'}$ = 2.2 Hz), 7.93 (dd, 1H, *H-6*, J_{6-5} = 5.4 Hz, J_{6-4} = 1.2 Hz), 7.83 (m, 4H, *H-d* + *H-d'* + *H-e* + *H-e'*), 7.57 (m, 2H, *H-a/b* + *H-a'/b'*), 7.50 (ddd, 1H, *H-5*, J_{5-4} = 7.8 Hz, J_{5-6} = 5.4 Hz, J_{5-3} = 0.6 Hz), 7.43 (m, 2H, *H-b/a* + *H-b'/a'*), 7.24 (dd, 2H, *H-3''* + *H-5''*, $J_{3''/5''-2''/6''}$ = 4.5 Hz, $J_{5''/3''-2''/6''}$ = 1.7 Hz), 7.16 (m, 2H, *H-h* + *H-h'*), 6.91 (m, 2H, *H-i* + *H-i'*), 6.34 (m, 2H, *H-j* + *H-j'*).

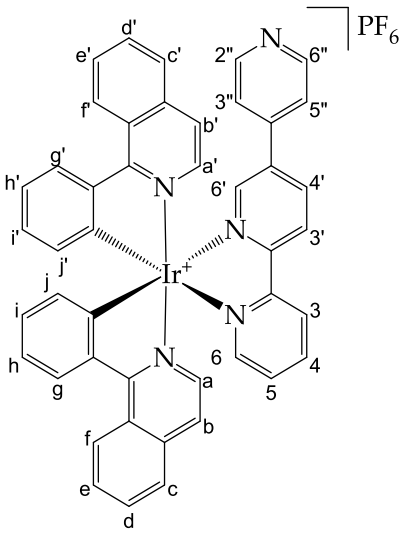

IrppytBu$_2$-bpy. Yield = 68% (from unpure precursor). HRMS (ESI): m/z calculated for [$C_{48}H_{56}{}^{193}IrN_4$ – PF_6]$^+$, 881.41287 ; found: 881.41252, m/z calculated for [$C_{38}H_{48}{}^{193}IrN_2$ – PF_6 – bpy]$^+$, 725.34412 ; found: 725.34209. ^{1}H NMR (CD_3CN), δ/ppm: 8.53 (dd, 2H, *H-3*, $J_{3\text{-}4}$ = 8.1 Hz, $J_{3\text{-}5}$ = 0.5 Hz), 8.12 (ddd, 2H, *H-4*, $J_{4\text{-}3}$ = 8.1 Hz, $J_{4\text{-}5}$ = 7.8 Hz, $J_{4\text{-}6}$ = 1.2 Hz), 7.99 (dd, 2H, *H-6*, $J_{6\text{-}5}$ = 5.3 Hz, $J_{6\text{-}4}$ = 1.2 Hz), 7.96 (d, 2H, *H-d*, $J_{d\text{-}b}$ = 2.1 Hz), 7.72 (d, 2H, *H-e*, $J_{e\text{-}f}$ = 8.3 Hz), 7.51 (ddd, 2H, *H-5*, $J_{5\text{-}4}$ = 7.8 Hz, $J_{5\text{-}6}$ = 5.3 Hz, $J_{5\text{-}3}$ = 0.5 Hz), 7.50 (d, 2H, *H-a*, $J_{a\text{-}b}$ = 6.2 Hz), 7.08 (dd, 2H, *H-f*, $J_{f\text{-}e}$ = 8.3 Hz, $J_{f\text{-}h}$ = 1.9 Hz), 7.07 (dd, 2H, *H-b*, $J_{b\text{-}a}$ = 6.2 Hz, $J_{b\text{-}d}$ = 2.1 Hz), 6.18 (d, 2H, *H-h*, $J_{h\text{-}f}$ = 1.9 Hz), 1.35 (s, 18H, *H-tBu-Pyr*), 1.07 (s, 18H, *H-tBu-Ph*).

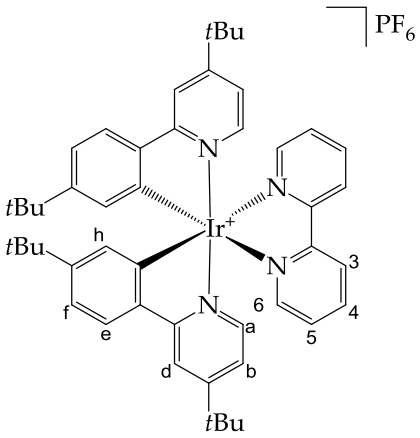

IrppytBu$_2$-2244tpy. Yield = 67% (from unpure precursor). HRMS (ESI): m/z calculated for $[C_{53}H_{59}{}^{193}IrN_5 - PF_6]^+$, 958.43942 ; found: 958.43905, m/z calculated for $[C_{38}H_{48}{}^{193}IrN_2 - PF_6 - 2244tpy]^+$, 725.34412 ; found: 725.34121. ^{1}H NMR (CD_3CN), δ/ppm: 8.80 (m, 3H, *H-3′* + *H-2″* + *H-6″*), 8.72 (dd, 1H, *H*-3, $J_{3\text{-}4}$ = 8.1 Hz, $J_{3\text{-}5}$ = 0.6 Hz), 8.16 (ddd, 1H, *H-4*, $J_{4\text{-}3}$ = 8.1 Hz, $J_{4\text{-}5}$ = 8.0 Hz, $J_{4\text{-}6}$ = 1.2 Hz), 8.06 (d, 1H, *H-6′*, $J_{6'\text{-}5'}$ = 5.7 Hz), 8.03 (dd, 1H, *H-6*, $J_{6\text{-}5}$ = 5.4 Hz, $J_{6\text{-}4}$ = 1.2 Hz), 7.98 (m, 2H, *H-d* + *H-d′*), 7.78 (m, 3H, *H-5′* + *H-3″* + *H-5″*), 7.74 (m, 2H, *H-e* + *H*-e′), 7.54 (m, 3H, *H-a* + *H-a′* + *H-5*), 7.09 (m, 4H, *H-f* + *H-f′* + *H-b* + *H-b′*), 6.20 (m, 2H, *H-h* + *H-h′*), 1.35 (2s,18H, *H-tBu-Pyr*), 1.08 (2s, 18H, *H-tBu-Ph*).

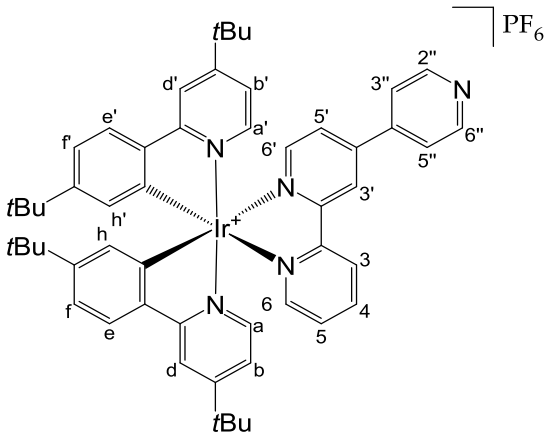

IrppytBu$_2$-2254tpy. Yield = 73% (from unpure precursor). HRMS (ESI): m/z calculated for $[C_{53}H_{59}{}^{193}IrN_5 - PF_6]^+$, 958.43942 ; found: 958.43894, m/z calculated for $[C_{38}H_{48}{}^{193}IrN_2 - PF_6 - 2254tpy]^+$, 725.34412 ; found: 725.33958. ^{1}H NMR (CD_3CN), δ/ppm: 8.62 (m, 3H, *H-3′* + *H-2″* + *H-6″*), 8.57 (d, 1H, *H*-3, $J_{3\text{-}4}$ = 8.1 Hz, $J_{3\text{-}5}$ = 0.6 Hz), 8.44 (dd, 1H, *H-4′*, $J_{4'\text{-}3'}$ = 8.5 Hz, $J_{4'\text{-}6'}$ = 2.1 Hz), 8.21 (d, 1H, *H*-6′, $J_{6'\text{-}4'}$ = 2.1 Hz), 8.16 (ddd, 1H, *H-4*, $J_{4\text{-}3}$ = 8.1 Hz, $J_{4\text{-}5}$ = 7.8 Hz, $J_{4\text{-}6}$ = 1.2 Hz), 8.06 (dd, 1H, *H-6*, $J_{6\text{-}5}$ = 5.4 Hz, $J_{6\text{-}4}$ = 1.2 Hz), 7.96 (m, 2H, *H-d* + *H-d′*), 7.74 (m, 2H, *H-e* + *H-e′*), 7.57 (m, 2H, *H-a* + *H-a′*), 7.56 (ddd, 1H, *H-5*, $J_{5\text{-}4}$ = 7.8 Hz, $J_{5\text{-}6}$ = 5.4 Hz, $J_{5\text{-}3}$ = 0.6 Hz), 7.30 (dd, 2H, *H-3″* + *H-5″*, $J_{3''/5''\text{-}2''/6''}$ = 4.5 Hz, $J_{5''/3''\text{-}2''/6''}$ = 1.7 Hz), 7.09 (m, 4H, *H-f* + *H-f′* + *H-b* + *H-b′*), 6.26 (m, 2H, *H-h* + *H-h′*), 1.34 (2s,18H, *H-tBu-Pyr*), 1.09 (2s, 18H, *H-tBu-Ph*).

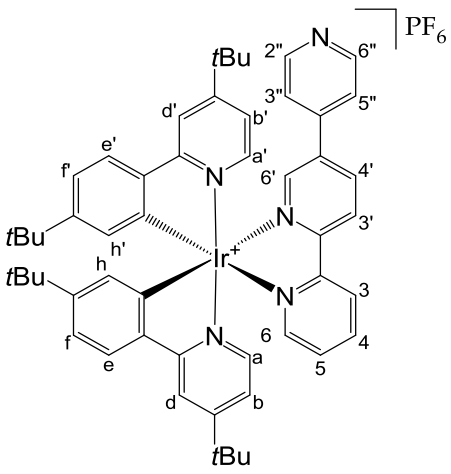

4.9.3 Synthesis of the Ir(III)-Co(III) dyads

Co(dmgH)(dmgH$_2$)Cl$_2$. To a solution of $CoCl_2.6H_2O$ (99.7 mg, 0.419 mmol) in acetone (10.0 mL) was added dimethylglyoxime (100.1 mg, 0.862 mmol). The purple solution was stirred at room temperature for 1 h. The appeared grey-green solid was centrifuged and washed with acetone (101.8 mg – 67%).

General procedure for Ir(III)-Co(III) dyads. To a suspension of Co(dmgH)(dmgH$_2$)Cl$_2$ (1.05 eq) in MeOH was added Et_3N (1.05 eq). The mixture was stirred at room temperature for 15 min. until a brown solution was obtained. A solution of Irppy-2244tpy (1.0 eq) in CH_2Cl_2 was slowly added to this solution and the mixture was stirred at room temperature for 1h30. A stream of air was passed through the solution for 15 min. and Et_2O was added for precipitation. The precipitate was centrifuged and washed with Et_2O. The product was dissolved in acetone and impurities were centrifuged. The crude product was purified by column chromatography on SiO_2 (CH_2Cl_2:MeOH / 95:5).

Irppy-2244tpy-Co. Yield = 72%. HRMS (ESI): m/z calculated for $[C_{45}H_{41}Cl^{59}Co^{193}IrN_9O_4 - PF_6]^+$, 1058.19258 ; found: 1058.19288, m/z calculated for $[C_{37}H_{27}{}^{193}IrN_5 - PF_6 - Co(dmgH)_2Cl]^+$, 734.18902 ; found: 734.18881. ^{1}H NMR (acetone-d_6), δ/ppm: 9.26 (s, 1H, *H-3′*), 9.15 (dd, 1H, *H*-3, $J_{3\text{-}4}$ = 8.0 Hz, $J_{3\text{-}5}$ = 0.7 Hz), 8.36 (d, 2H, *H-2″* + *H-6″*, $J_{2''/6''\text{-}3''/5''}$ = 6.2 Hz), 8.32 (ddd, 1H, *H-4*, $J_{4\text{-}3}$ = 8.0 Hz, $J_{4\text{-}5}$ = 7.9 Hz, $J_{4\text{-}6}$ = 1.3 Hz), 8.25 (m, 2H, *H-d* + *H-d′*), 8.21 (d, 1H, *H-6′*, $J_{6'\text{-}5'}$ = 5.8 Hz), 8.13 (dd, 1H, *H-6*, $J_{6\text{-}5}$ = 5.3 Hz, $J_{6\text{-}4}$ = 1.3 Hz), 8.04 (m, 3H, *H-5′* + *H-3″* + *H-5″*), 7.95 (m, 2H, *H-c* + *H-c′*), 7.90 (m, 2H, *H-e* + *H-e′*), 7.83 (m, 2H, *H-a* + *H-a′*), 7.75 (ddd, 1H, *H-5*, $J_{5\text{-}4}$ = 7.9 Hz, $J_{5\text{-}6}$ = 5.3 Hz, $J_{5\text{-}3}$ = 0.7 Hz), 7.13 (m, 2H, *H-b* + *H-b′*), 7.04 (m, 2H, *H-f* + *H-f′*), 6.92 (m, 2H, *H-g* + *H-g′*), 6.34 (m, 2H, *H-h* + *H-h′*), 2.33 (s, 12H, -CH_3 dmgH).

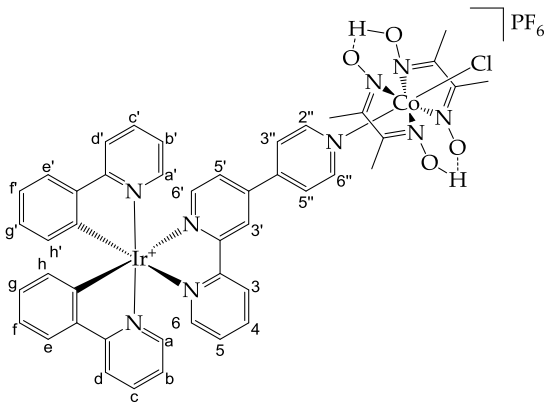

Irppy-2254tpy-Co. Yield = 74%. HRMS (ESI): m/z calculated for $[C_{45}H_{41}Cl^{59}Co^{193}IrN_9O_4 - PF_6]^+$, 1058.19258 ; found: 1058.19244, m/z calculated for $[C_{37}H_{27}{}^{193}IrN_5 - PF_6 - Co(dmgH)_2Cl]^+$, 734.18902 ; found: 734.18871. ^{1}H NMR (acetone-d_6), δ/ppm: 8.99 (d, 1H, *H-3′*, $J_{3'-4'}$ = 8.6 Hz), 8.92 (dd, 1H, *H*-3, J_{3-4} = 8.1 Hz, J_{3-5} = 0.5 Hz), 8.65 (dd, 1H, *H-4′*, $J_{4'-3'}$ = 8.6 Hz, $J_{4'-6'}$ = 2.1 Hz), 8.36 (d, 1H, *H*-6′, $J_{6'-4'}$ = 2.1 Hz), 8.32 (ddd, 1H, *H-4*, J_{4-3} = 8.1 Hz, J_{4-5} = 7.8 Hz, J_{4-6} = 1.3 Hz), 8.23 (m, 2H, *H-d* + *H-d′*), 8.19 (dd, 2H, *H-2″* + *H-6″*, $J_{2''/6''-3''/5''}$ = 5.6 Hz, $J_{2''/6''-5''/3''}$ = 1.4 Hz), 8.13 (dd, 1H, *H-6*, J_{6-5} = 5.4 Hz, J_{6-4} = 1.3 Hz), 7.91 (m, 6H, *H-a* + *H-a′* + *H-c* + *H-c′* + *H-e* + *H-e′*), 7.75 (ddd, 1H, *H-5*, J_{5-4} = 7.8 Hz, J_{5-6} = 5.4 Hz, J_{5-3} = 0.5 Hz), 7.47 (dd, 2H, *H-3″* + *H-5″*, $J_{3''/5''-2''/6''}$ = 5.6 Hz, $J_{5''/3''-2''/6''}$ = 1.4 Hz), 7.09 (m, 4H, *H-f* + *H-f′* + *H-b* + *H-b′*), 6.93 (m, 2H, *H-g* + *H-g′*), 6.36 (m, 2H, *H-h* + *H-h′*), 2.32 (s, 12H, -CH_3 dmgH).

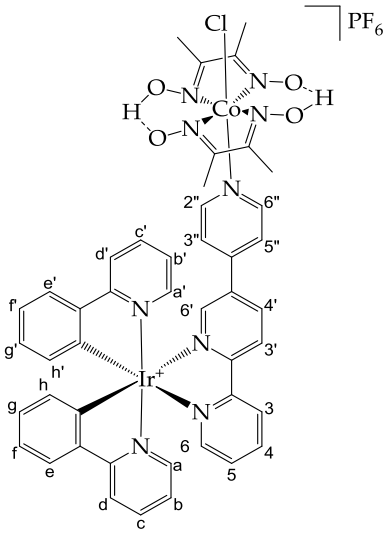

IrppyF$_2$-2244tpy-Co. Yield = 78%. HRMS (ESI): m/z calculated for [$C_{45}H_{37}Cl^{59}CoF_4{}^{193}IrN_9O_4$ – PF_6]$^+$, 1130.15489 ; found: 1130.15521, m/z calculated for [$C_{37}H_{23}F_4{}^{193}IrN_5$ – PF_6 – Co(dmgH)$_2$Cl]$^+$, 806.15133 ; found: 806.15109. ^{1}H NMR (acetone-d$_6$), δ/ppm: 9.21 (d, 1H, *H-3′*, $J_{3'-5'}$ = 1.2 Hz), 9.08 (dd, 1H, *H*-3, J_{3-4} = 8.1 Hz, J_{3-5} = 0.7 Hz), 8.37 (m, 6H, *H-2″* + *H-6″* + *H-4* +*H-d* + *H-d′* + *H-6′*), 8.24 (dd, 1H, *H-6*, J_{6-5} = 5.4 Hz, J_{6-4} = 1.2 Hz), 8.06 (m, 3H, *H-c* + *H-c′* + *H-5′*), 8.00 (dd, 3H, *H-3″* + *H-5″*, $J_{3''/5''-2''/6''}$ = 5.4 Hz, $J_{3''/5''-6''/2''}$ = 1.5 Hz), 7.92 (m, 2H, *H-a* + *H-a′*), 7.79 (ddd, 1H, *H-5*, J_{5-4} = 7.7 Hz, J_{5-6} = 5.4 Hz, J_{5-3} = 0.7 Hz), 7.22 (m, 2H, *H-b* + *H-b′*), 6.78 (m, 2H, *H-f* + *H-f′*), 5.79 (m, 2H, *H-h* + *H-h′*), 2.34 (s, 12H, -CH$_3$ dmgH).

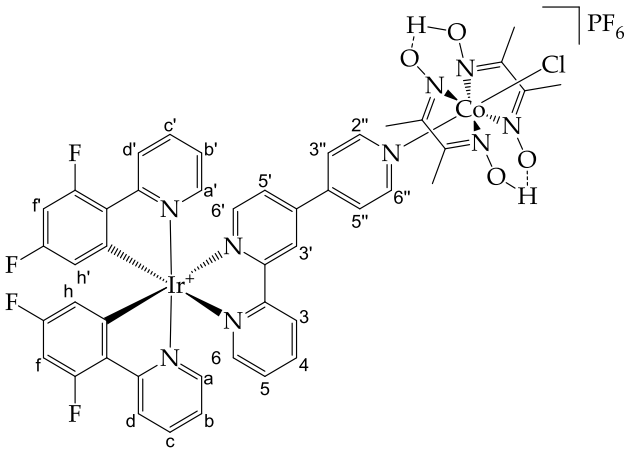

IrppyF$_2$-2254tpy-Co. Yield = 77%. HRMS (ESI): m/z calculated for [$C_{45}H_{37}Cl^{59}CoF_4{}^{193}IrN_9O_4$ – PF_6]$^+$, 1130.15489 ; found: 1130.15505, m/z calculated for [$C_{37}H_{23}F_4{}^{193}IrN_5$ – PF_6 – Co(dmgH)$_2$Cl]$^+$, 806.15133 ; found: 806.15089. ^{1}H NMR (acetone-d$_6$), δ/ppm: 9.04 (d, 1H, *H-3′*, $J_{3'-4'}$ = 8.6 Hz), 8.97 (dd, 1H, *H*-3, J_{3-4} = 8.1 Hz, J_{3-5} = 0.6 Hz), 8.72 (dd, 1H, *H-4′*, $J_{4'-3'}$ = 8.6 Hz, $J_{4'-6'}$ = 2.0 Hz), 8.52 (d, 1H, *H*-6′, $J_{6'-4'}$ = 2.0 Hz), 8.38 (m, 3H, *H-4* + *H-d* + *H-d′*), 8.24 (dd, 1H, *H-6*, J_{6-5} = 5.5 Hz, J_{6-4} = 0.9 Hz), 8.21 (dd, 2H, *H-2″* + *H-6″*, $J_{2''/6''-3''/5''}$ = 5.6 Hz, $J_{2''/6''-5''/3''}$ = 1.4 Hz), 7.97 (m, 4H, *H-a* + *H-a′* + *H-c* + *H-c′*), 7.80 (ddd, 1H, *H-5*, J_{5-4} = 7.6 Hz, J_{5-6} = 5.5 Hz, J_{5-3} = 0.6 Hz), 7.62 (dd, 2H, *H-3″* + *H-5″*, $J_{3''/5''-2''/6''}$ = 5.6 Hz, $J_{5''/3''-2''/6''}$ = 1.4 Hz), 7.20 (m, 2H, *H-b* + *H-b′*), 6.77 (m, 2H, *H-f* + *H-f′*), 5.78 (m, 2H, *H-h* + *H-h′*), 2.32 (s, 12H, -CH$_3$ dmgH).

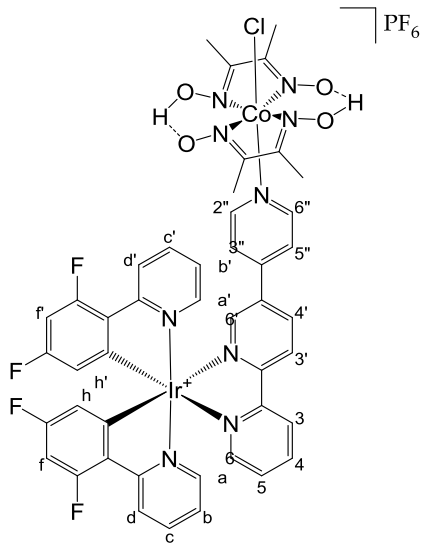

Irpiq-2244tpy-Co. Yield = 81%. HRMS (ESI): m/z calculated for $[C_{53}H_{45}{}^{37}Cl^{59}Co^{193}IrN_9O_4 - PF_6]^+$, 1158.22388 ; found: 1158.22434, m/z calculated for $[C_{45}H_{31}{}^{193}IrN_5 - PF_6 - Co(dmgH)_2Cl]^+$, 834.22032 ; found: 834.22027. ^{1}H NMR (acetone-d_6), δ/ppm: 9.24 (d, 1H, *H-3′*, $J_{3'\text{-}5'}$ = 1.6 Hz), 9.10 (m, 3H, *H-3* + *H-f* + *H-f′*), 8.43 (m, 2H, *H-g* + *H-g′*), 8.36 (d, 2H, *H-2″* + *H-6″*, $J_{2''/6''\text{-}3''/5''}$ = 6.4 Hz), 8.32 (ddd, 1H, *H-4*, $J_{4\text{-}3}$ = $J_{4\text{-}5}$ = 8.0 Hz, $J_{4\text{-}6}$ = 1.5 Hz), 8.07 (m, 3H, *H-6′* + *H-c* + *H-c′*), 7.99 (m, 4H, *H-5′* + *H-6* + *H-3″* + *H-5″*), 7.91 (m, 4H, *H-d* + *H-d′* + *H-e* + *H-e′*), 7.70 (m, 3H, *H-5* + *H-a*/*b* + *H-a′*/*b′*), 7.55 (m, 2H, *H-b*/*a* + *H-b′*/*a′*), 7.15 (m, 2H, *H-h* + *H-h′*), 6.91 (m, 2H, *H-i* + *H-i′*), 6.37 (m, 2H, *H-j* + *H-j′*), 2.33 (s, 12H, -CH_3 dmgH).

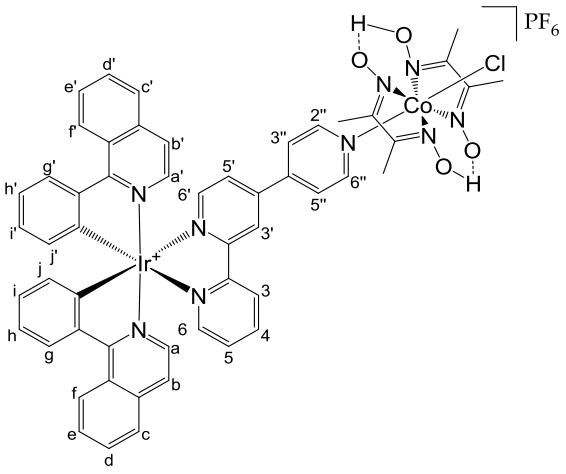

Irpiq-2254tpy-Co. Yield = 79%. HRMS (ESI): m/z calculated for $[C_{53}H_{45}{}^{37}Cl^{59}Co^{193}IrN_9O_4 - PF_6]^+$, 1158.22388 ; found: 1158.22415, m/z calculated for $[C_{45}H_{31}{}^{193}IrN_5 - PF_6 - Co(dmgH)_2Cl]^+$, 834.22032 ; found: 834.22024. ^{1}H NMR (acetone-d_6), δ/ppm: 9.10 (m, 2H, *H-f* + *H-f'*), 9.03 (d, 1H, *H*-3', $J_{3'\text{-}4'}$ = 8.6 Hz), 8.96 (d, 1H, *H*-3, $J_{3\text{-}4}$ = 8.1 Hz), 8.66 (dd, 1H, *H*-4', $J_{4'\text{-}3'}$ = 8.6 Hz, $J_{4'\text{-}6'}$ = 2.0 Hz), 8.45 (m, 2H, *H-g* + *H-g'*), 8.32 (ddd, 1H, *H-4*, $J_{4\text{-}3}$ = 8.1 Hz, $J_{4\text{-}5}$ = 8.0 Hz, $J_{4\text{-}6}$ = 1.5 Hz), 8.17 (dd, 2H, *H-2″* + *H-6″*, $J_{2''/6''\text{-}3''/5''}$ = 5.6 Hz, $J_{2''/6''\text{-}5''/3''}$ = 1.4 Hz), 8.13 (d, 1H, *H-6'*, $J_{6'\text{-}4'}$ = 2.0 Hz), 8.05 (m, 3H, *H-6* + *H-c* + *H-c'*), 7.92 (m, 4H, *H-d* + *H-d'* + *H-e* + *H-e'*), 7.75 (m, 3H, *H-5* + *H-a/b* + *H-a'/b'*), 7.54 (m, 2H, *H-b/a* + *H-b'/a'*), 7.42 (dd, 2H, *H-3″* + *H-5″*, $J_{3''/5''\text{-}2''/6''}$ = 5.6 Hz, $J_{5''/3''\text{-}2''/6''}$ = 1.4 Hz), 7.18 (m, 2H, *H-h* + *H-h'*), 6.94 (m, 2H, *H-i* + *H-i'*), 6.39 (m, 2H, *H-j* + *H-j'*), 2.30 (s, 12H, -CH_3 dmgH).

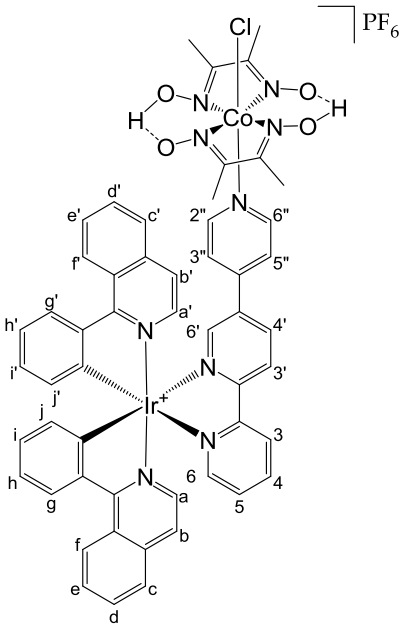

4.10 References

1. Kobayashi, M.; Masaoka, S.; Sakai, K., Photoinduced hydrogen evolution from water by a simple platinum(II) terpyridine derivative: a Z-scheme photosynthesis. *Angew. Chem. Int. Ed.* **2012**, *51*, 7431-7434.
2. Ozawa, H.; Yokoyama, Y.; Haga, M. A.; Sakai, K., Syntheses, characterization, and photo-hydrogen-evolving properties of tris(2,2'-bipyridine)ruthenium(II) derivatives tethered to a cis-Pt(II)Cl2 unit: insights into the structure-activity relationship. *Dalton Trans.* **2007**, 1197-1206.
3. Rau, S.; Schafer, B.; Gleich, D.; Anders, E.; Rudolph, M.; Friedrich, M.; Gorls, H.; Henry, W.; Vos, J. G., A supramolecular photocatalyst for the production of hydrogen and the selective hydrogenation of tolane. *Angew. Chem. Int. Ed.* **2006**, *45*, 6215-6218.
4. Tschierlei, S.; Presselt, M.; Kuhnt, C.; Yartsev, A.; Pascher, T.; Sundstrom, V.; Karnahl, M.; Schwalbe, M.; Schafer, B.; Rau, S.; Schmitt, M.; Dietzek, B.; Popp, J., Photophysics of an intramolecular hydrogen-evolving Ru-Pd photocatalyst. *Chem. Eur. J.* **2009**, *15*, 7678-7688.
5. Artero, V.; Chavarot-Kerlidou, M.; Fontecave, M., Splitting water with cobalt. *Angew. Chem. Int. Ed.* **2011**, *50*, 7238-7266.
6. Kaeffer, N.; Chavarot-Kerlidou, M.; Artero, V., Hydrogen evolution catalyzed by cobalt diimine-dioxime complexes. *Acc. Chem. Res.* **2015**, *48*, 1286-1295.
7. Schrauzer, G. N., Organocobalt chemistry of vitamin B12 model compounds (cobaloximes). *Acc. Chem. Res.* **1968**, *1*, 97-103.
8. Connolly, P.; Espenson, J. H., Cobalt-catalyzed evolution of molecular hydrogen. *Inorg. Chem.* **1986**, *25*, 2684-2688.
9. Hu, X.; Brunschwig, B. S.; Peters, J. C., Electrocatalytic hydrogen evolution at low overpotentials by cobalt macrocyclic glyoxime and tetraimine complexes. *J. Am. Chem. Soc.* **2007**, *129*, 8988-8998.
10. Razavet, M.; Artero, V.; Fontecave, M., Proton electroreduction catalyzed by cobaloximes: functional models for hydrogenases. *Inorg. Chem.* **2005**, *44*, 4786-4795.
11. Baffert, C.; Artero, V.; Fontecave, M., Cobaloximes as functional models for hydrogenases. 2. Proton electroreduction catalyzed by difluoroborylbis(dimethylglyoximato)cobalt(II) complexes in organic media. *Inorg. Chem.* **2007**, *46*, 1817-1824.
12. Kirch, M.; Lehn, J.-M.; Sauvage, J.-P., Hydrogen Generation by Visible Light Irradiation of Aqueous Solutions of Metal Complexes. An approach to the photochemical conversion and storage of solar energy. *Helv. Chim. Acta* **1979**, *62*, 1345-1384.

13. Chan, S. F.; Chou, M.; Creutz, C.; Matsubara, T.; Sutin, N., Mechanism of the formation of dihydrogen from the photoinduced reactions of poly(pyridine)ruthenium(II) and poly(pyridine)rhodium(III) complexes. *J. Am. Chem. Soc.* **1981**, *103*, 369-379.
14. Fihri, A.; Artero, V.; Pereira, A.; Fontecave, M., Efficient H2-producing photocatalytic systems based on cyclometalated iridium- and tricarbonylrhenium-diimine photosensitizers and cobaloxime catalysts. *Dalton Trans.* **2008**, 5567-5569.
15. Li, C.; Wang, M.; Pan, J.; Zhang, P.; Zhang, R.; Sun, L., Photochemical hydrogen production catalyzed by polypyridyl ruthenium–cobaloxime heterobinuclear complexes with different bridges. *J. Organomet. Chem.* **2009**, *694*, 2814-2819.
16. Jacques, A.; Schott, O.; Robeyns, K.; Hanan, G. S.; Elias, B., Hydrogen Photoevolution from a Green-Absorbing Iridium(III)-Cobalt(III) Dyad. *Eur. J. Inorg. Chem.* **2016**, *2016*, 1779-1783.
17. Goldsmith, J. I.; Hudson, W. R.; Lowry, M. S.; Anderson, T. H.; Bernhard, S., Discovery and high-throughput screening of heteroleptic iridium complexes for photoinduced hydrogen production. *J. Am. Chem. Soc* **2005**, *127*, 7502-7510.
18. Rousset, E.; Chartrand, D.; Ciofini, I.; Marvaud, V.; Hanan, G. S., Red-light-driven photocatalytic hydrogen evolution using a ruthenium quaterpyridine complex. *Chem. Commun.* **2015**, *51*, 9261-9264.
19. Lowry, M. S.; Goldsmith, J. I.; Slinker, J. D.; Rohl, R.; Pascal, R. A., Jr.; Malliaras, G. G.; Bernhard, S., Single-Layer Electroluminescent Devices and Photoinduced Hydrogen Production from an Ionic Iridium(III) Complex. *Chem. Mater.* **2005**, *17*, 5712-5719.
20. Yu, L.; Huang, Z.; Liu, Y.; Zhou, M., Photophysics, electrochemistry and electrochemiluminescence of water-soluble biscyclometalated iridium (III) complexes. *J. Organomet. Chem.* **2012**, *718*, 14-21.
21. Zhao, Q.; Liu, S.; Shi, M.; Wang, C.; Yu, M.; Li, L.; Li, F.; Yi, T.; Huang, C., Series of new cationic iridium(III) complexes with tunable emission wavelength and excited state properties: structures, theoretical calculations, and photophysical and electrochemical properties. *Inorg. Chem.* **2006**, *45*, 6152-6160.
22. Kodama, K.; Kobayashi, A.; Hirose, T., Synthesis and spectral properties of ruthenium(II) complexes based on 2,2'-bipyridines modified by a perylene chromophore. *Tetrahedron Lett.* **2013**, *54*, 5514-5517.
23. Brotschi, C.; Mathis, G.; Leumann, C. J., Bipyridyl- and biphenyl-DNA: a recognition motif based on interstrand aromatic stacking. *Chem. Eur. J.* **2005**, *11*, 1911-1923.
24. Zhang, P.; Jacques, P. A.; Chavarot-Kerlidou, M.; Wang, M.; Sun, L.; Fontecave, M.; Artero, V., Phosphine coordination to a cobalt diimine-

dioxime catalyst increases stability during light-driven H2 production. *Inorg. Chem.* **2012**, *51*, 2115-2120.
25. Soman, S.; Singh Bindra, G.; Paul, A.; Groarke, R.; Manton, J. C.; Connaughton, F. M.; Schulz, M.; Dini, D.; Long, C.; Pryce, M. T.; Vos, J. G., Wavelength dependent photocatalytic H2 generation using iridium-Pt/Pd complexes. *Dalton Trans.* **2012**, *41*, 12678-12680.
26. Panagiotopoulos, A.; Ladomenou, K.; Sun, D.; Artero, V.; Coutsolelos, A. G., Photochemical hydrogen production and cobaloximes: the influence of the cobalt axial N-ligand on the system stability. *Dalton Trans.* **2016**, *45*, 6732-6738.
27. Du, P.; Schneider, J.; Luo, G.; Brennessel, W. W.; Eisenberg, R., Visible light-driven hydrogen production from aqueous protons catalyzed by molecular cobaloxime catalysts. *Inorg. Chem.* **2009**, *48*, 4952-4962.
28. Polson, M.; Ravaglia, M.; Fracasso, S.; Garavelli, M.; Scandola, F., Iridium cyclometalated complexes with axial symmetry: time-dependent density functional theory investigation of trans-bis-cyclometalated complexes containing the tridentate ligand 2,6-diphenylpyridine. *Inorg. Chem.* **2005**, *44*, 1282-1289.
29. DeRosa, M. C.; Hodgson, D. J.; Enright, G. D.; Dawson, B.; Evans, C. E.; Crutchley, R. J., Iridium luminophore complexes for unimolecular oxygen sensors. *J. Am. Chem. Soc.* **2004**, *126*, 7619-7626.
30. Licini, M.; Gareth Williams, J. A., Iridium(III) bis-terpyridine complexes displaying long-lived pH sensitive luminescence. *Chem. Commun.* **1999**, 1943-1944.
31. Dempsey, J. L.; Brunschwig, B. S.; Winkler, J. R.; Gray, H. B., Hydrogen evolution catalyzed by cobaloximes. *Acc. Chem. Res.* **2009**, *42*, 1995-2004.
32. Kutt, A.; Leito, I.; Kaljurand, I.; Soovali, L.; Vlasov, V. M.; Yagupolskii, L. M.; Koppel, I. A., A comprehensive self-consistent spectrophotometric acidity scale of neutral Bronsted acids in acetonitrile. *J. Org. Chem.* **2006**, *71*, 2829-2838.
33. Queyriaux, N.; Jane, R. T.; Massin, J.; Artero, V.; Chavarot-Kerlidou, M., Recent Developments in Hydrogen Evolving Molecular Cobalt(II)-Polypyridyl Catalysts. *Coord. Chem. Rev.* **2015**, *304-305*, 3-19.
34. Fihri, A.; Artero, V.; Razavet, M.; Baffert, C.; Leibl, W.; Fontecave, M., Cobaloxime-based photocatalytic devices for hydrogen production. *Angew. Chem. Int. Ed.* **2008**, *47*, 564-567.
35. Whang, D. R.; Sakai, K.; Park, S. Y., Highly efficient photocatalytic water reduction with robust iridium(III) photosensitizers containing arylsilyl substituents. *Angew. Chem. Int. Ed.* **2013**, *52*, 11612-11615.
36. Hansen, S.; Pohl, M. M.; Klahn, M.; Spannenberg, A.; Beweries, T., Investigation and enhancement of the stability and performance of water

reduction systems based on cyclometalated iridium(III) complexes. *ChemSusChem* **2013**, *6*, 92-101.
37. Sakai, K.; Ozawa, H., Homogeneous catalysis of platinum(II) complexes in photochemical hydrogen production from water. *Coord. Chem. Rev.* **2007**, *251*, 2753-2766.
38. Radhakrishnan, A. N.; Rao, P. P.; Linsa, K. S.; Deepa, M.; Koshy, P., Influence of disorder-to-order transition on lattice thermal expansion and oxide ion conductivity in (Ca(x)Gd(1-x))(2)(Zr(1-x)M(x))2O7 pyrochlore solid solutions. *Dalton Trans.* **2011**, *40*, 3839-3848.
39. Rousset, E.; Chartrand, D.; Ciofini, I.; Marvaud, V.; Hanan, G. S., Red-light-driven photocatalytic hydrogen evolution using a ruthenium quaterpyridine complex. *Chem. Commun. (Camb)* **2015**, *51*, 9261-9264.
40. Lentz, C.; Schott, O.; Auvray, T.; Hanan, G.; Elias, B., Photocatalytic Hydrogen Production Using a Red-Absorbing Ir(III)-Co(III) Dyad. *Inorg. Chem.* **2017**, *56*, 10875-10881.
41. Jacques, A.; Schott, O.; Robeyns, K.; Hanan, G. S.; Elias, B., Hydrogen Photoevolution from a Green-Absorbing Iridium(III)-Cobalt-(III) Dyad. *Eur. J. Inorg. Chem.* **2016**, *2016*, 1779-1783.
42. Schulz, M.; Karnahl, M.; Schwalbe, M.; Vos, J. G., The role of the bridging ligand in photocatalytic supramolecular assemblies for the reduction of protons and carbon dioxide. *Coord. Chem. Rev.* **2012**, *256*, 1682-1705.
43. Fihri, A.; Artero, V.; Razavet, M.; Baffert, C.; Leibl, W.; Fontecave, M., Cobaloxime-based photocatalytic devices for hydrogen production. *Angew. Chem., Int. Ed.* **2008**, *47*, 564-567.
44. DiSalle, B. F.; Bernhard, S., Orchestrated photocatalytic water reduction using surface-adsorbing iridium photosensitizers. *J. Am. Chem. Soc.* **2011**, *133*, 11819-11821.
45. Fihri, A.; Artero, V.; Pereira, A.; Fontecave, M., Efficient H2-producing photocatalytic systems based on cyclometalated iridium- and tricarbonylrhenium-diimine photosensitizers and cobaloxime catalysts. *Dalton Trans.* **2008**, 5567-5569.
46. Deponti, E.; Natali, M., Photocatalytic hydrogen evolution with ruthenium polypyridine sensitizers: unveiling the key factors to improve efficiencies. *Dalton Trans.* **2016**, *45*, 9136-9147.
47. Goldsmith, J. I.; Hudson, W. R.; Lowry, M. S.; Anderson, T. H.; Bernhard, S., Discovery and High-Throughput Screening of Heteroleptic Iridium Complexes for Photoinduced Hydrogen Production. *J. Am. Chem. Soc.* **2005**, *127*, 7502-7510.
48. Eric D. Cline, S. E. A., and Stefan Bernhard, Homogeneous Catalytic System for Photoinduced Hydrogen Production Utilizing Iridium and Rhodium Complexes. *Inorg. Chem.* **2008**, *47*, 10378-10388.

49. Michael S. Lowry, J. I. G., Jason D. Slinker, Richard Rohl,; Robert A. Pascal, J., George G. Malliaras, Stefan Bernhard, Single-Layer Electroluminescent Devices and Photoinduced Hydrogen Production from an Ionic Iridium(III) Complex. *Chem. Mater.* **2005**, *17*, 5712-5719.

CHAPTER 5

Palladocatalyzed reactions: photooxidation of Pd(0) to Pd(II) by Ir(III) complexes

5.1 Foreword

In view of previous results indicating that Ir(III) complexes display tremendous properties when irradiated, and especially their ability to reduce and oxidize various well-known redox systems, new applications for those compounds are thus considered.

Over the past decades, catalytic C-H functionalization reactions using Palladium catalysts have begun to emerge as viable alternatives to traditional synthetic methods. While these reactions offer important advantages over other synthetic pathways by eliminating the requirement of prefunctionalized substrates, regeneration of the catalyst remains a main challenge especially in the field of oxidative coupling reactions where reduced Palladium catalyst has to be reoxidized for the reaction to carry on.

The studies performed in collaboration with Prof. G. Poli (Université Pierre et Marie Curie) and presented hereafter reflect our wish to implement new reaction conditions using heteroleptic Ir(III) complexes as photosensitizers for Palladium(0) reoxidation into Palladium(II) for oxidative reactions such as Wacker oxidation and acetoxylation. These preliminary studies will constitute considerable progress in the field of Pd(0) reoxidation.

5.2 Introduction

Berzelius first defined a *catalyst* as a compound that increases the rate of a chemical reaction, although is not consumed.[1] This definition allows for a cyclic system to require only sub-stoichiometric amounts of catalyst. For synthetic and economic reasons, catalyzed reactions are preferred to stoichiometric ones. Among these, Palladium-catalyzed transformations offer chemists a wide range of synthetic opportunities. Although this domain has been widely explored for decades, its interest is still far from being vanished.[2-5] Two main classes of transformations emerge, depending on the oxidation state of the metal.

5.2.1 Palladium(0)-catalyzed coupling reactions

The principle of Palladium-catalyzed cross coupling is that two organic molecules are assembled on the metal via the formation of metal-carbon bonds. In this way, both carbon atoms bound to the Palladium center are coupled, thus allowing the formation of a new carbon-carbon single bond. This reaction usually involves an electrophilic partner RX (where R is an alkyl/aryl chain and X is a leaving group) and a nucleophilic partner, which either corresponds to a non transitional organometallic compound R'-[M] (where R' is an alkyl/aryl chain and M is a transition metal – *vide infra*) (equation 5.1) or to an unsaturated C-C bond (equation 5.2).

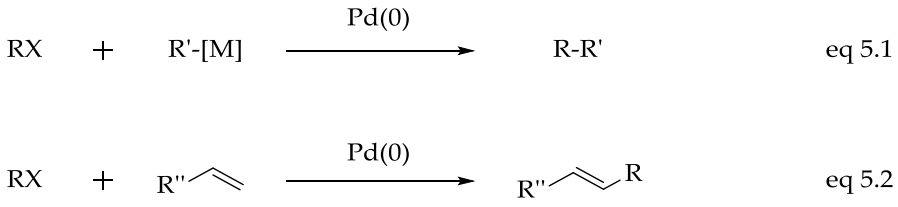

Most Palladium-catalyzed reactions are believed to share a common catalytic cycle. The catalytic species can be formed *in situ* by reducing a $Pd(II)X_2$ salt to Pd(0) or introduced as a preformed Pd(0) catalyst. Of course, the presence of appropriate dative ligands L is central for the stabilization of the above complexes. The reduced complex enters the catalytic cycle (Figure 5.1) and undergoes an oxidative addition by the electrophilic reagent generating an organopalladium complex RPd(II)X(L). This organopalladium species subsequently reacts with the nucleophilic coupling partner R'-[M] via a transmetalation reaction and finally undergoes a reductive elimination yielding a new C-C bond and the recovery of the Pd(0)L catalyst.

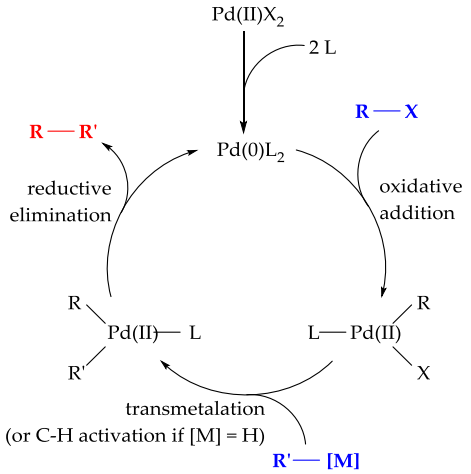

Figure 5.1 – General scheme for Palladium-catalyzed cross coupling reactions with the substrates in blue and the product in red[6]

The general reaction presented in equation 5.1 can exist under different variants according to the identity of the organometallic compound R'-[M], such as: Negishi (R'-[M] = organozinc), Suzuki (R'-[M] = organoboron), Stille (R'-[M] = organotin), Hiyama (R'-[M] = organosilane), Kumada (R'-[M] = Grignard reagent) and Sonogashira (R'-[M] = organocopper) couplings.[6]

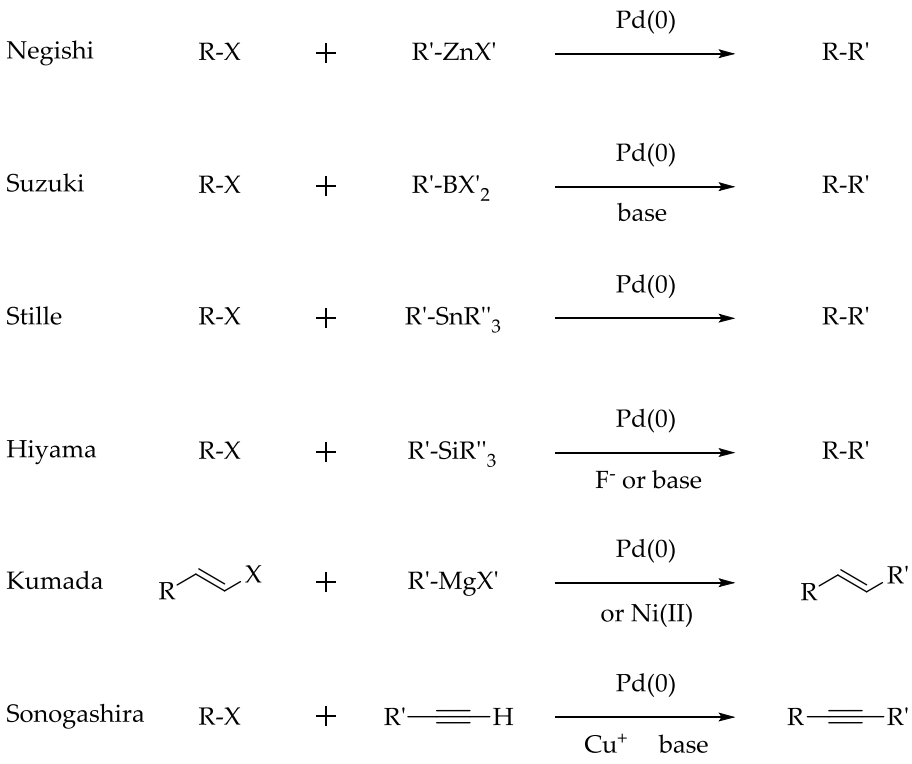

5.2.2 Palladium(II)-catalyzed reactions

Palladium(II)-catalyzed reactions can be split in two major classes: isohypsic reactions (*i.e.* without modification of the oxidation state of the metal) such as Overman rearrangement,[7] and oxidative reactions in which Pd(II) recovers its oxidation state after either

reoxidation of Pd(0) or reduction of Pd(IV) as in palladocatalyzed vicinal dioxylation or deamination.[8,9] Despite the great interest that isohypsic reactions and oxidative reactions through Pd(II)/Pd(IV) cycle represent, the main interest of this section will be mainly focused on Pd(II)/Pd(0) cycles involving a reoxidation of Pd(0) to recover the Pd(II) catalyst.

As to the Pd(II)/Pd(0) oxidative transformations, they require a terminal oxidant to regenerate the Pd(II) catalyst from reduced Pd(0) obtained after oxidation of the substrate by Pd(II) in order to close the overall catalytic cycle (Figure 5.2).[6,10,11]

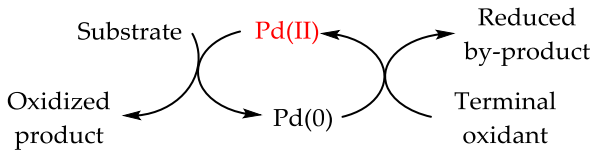

Figure 5.2 – Overall mechanism for a Pd(II)-catalyzed oxidation

Palladocatalyzed oxidative coupling reactions offer advantages over catalytic cross-coupling methods as well as traditional carbon-carbon or carbon-heteroatom bond forming reactions by eliminating the requirement of substrates such as alkyl/aryl halides or organometallic reagents. However, in order to achieve such goals, at least two conditions are required:[12]

(i) the oxidative coupling must be highly selective;
(ii) the cost and/or waste associated with the stoichiometric oxidant should not compensate for the use of a less functionalized substrate.

One of the earliest catalytic demonstrations of C-H oxidation is the selective oxidation of methane to methanol using $[Pt(IV)Cl_6]^{2-}$ as

the stoichiometric oxidant and $[Pt(II)Cl_4]^{2-}$ as the catalyst (Figure 5.3), known as Shilov reaction (equation 5.3).[13,14]

$$CH_4 + Pt(IV)Cl_6^{2-} + H_2O \xrightarrow[120°C]{Pt(II)Cl_4^{2-}} CH_3OH + Pt(II)Cl_4^{2-} + 2\,HCl \qquad \text{eq 5.3}$$

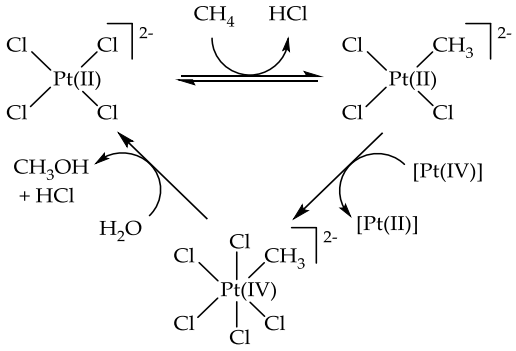

Figure 5.3 – Pathway for Shilov's cycle (adapted from [14])
(for sake of clarity, the ligands are considered to be Cl^- during the whole process)

However, depending on the release of the metal *i.e.* reductive elimination or dehydropalladation yielding [Pd(0)] and H[Pd]X, respectively, and on the nature of the terminal oxidant, the redox process can follow different paths (Figure 5.4).[15] For example, Pd(0) can readily be oxidized to PdX_2 either in the presence of quinones or directly by dioxygen. In the latter case, an η^2-peroxo complex is initially generated, and may evolve either by getting protonated or by reacting with another Pd(0) species to yield two equivalents of oxidized catalyst. On the other hand, when H[Pd]X is generated first through a dehydropalladation step, it can either undergo reductive elimination to provide Pd(0) and HX again, or oxidation by O_2 insertion followed by the release of H_2O_2.

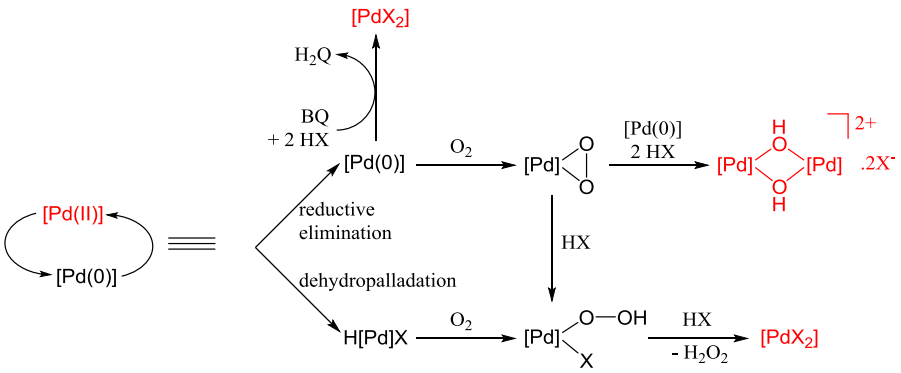

Figure 5.4 – Alternative pathways for Pd(II) regeneration (adapted from [15])

A further different oxidation path can be followed when a Cu(II)-Pd(II) heterobimetallic couple is used as the oxidizing system, as in this case the oxidation is relocated from Palladium to Copper. If the stoichiometric oxidant is dioxygen, the process is defined as aerobic. Dioxygen-based reoxidation mimics the action mechanism of oxidases, and its usage is recommended in sustainable chemistry era because dioxygen is a low cost, "green" molecule, the only side product being water. However, although the redox potential of the O_2/H_2O couple is thermodynamically appropriate to regenerate PdX_2 from Pd(0), the kinetics of this redox can be slow, and other side reactions, such as Pd(0) aggregation, can become overwhelming. To address limitations induced by the kinetically unfavored Pd(0) reoxidation, several solutions have been investigated:

(i) use high O_2 pressure[12,16] and/or temperatures;

(ii) increase the reaction rate or stabilize Pd(0) to prevent precipitation of Palladium black with particular ligands that sustain the redox step such as benzoquinone (BQ),[15,17,18] Nitrogen-based ligands,[12,19-21] NHCs[22,23] or solvent-based ligands (DMSO,…)[24,25];

(iii) use catalytic amounts of Electron Transfer Mediators (ETMs) such as complexes with a macrocyclic ligand L^m (ML^m) like iron phthalocyanine (Fe(pc))[26] or polyoxometalates like $H_3PMo_{12}O_{40}$.[27,28] Indeed, ETMs carry the electrons from the Pd(II) redox catalyst to the oxidant along a low energy pathway which competes with side reactions such as previously mentioned decomposition/precipitation of the metal. Therefore, the use of catalytic systems with ETMs extends drastically the use of O_2 as final oxidant in palladocatalyzed oxidation reactions (Figure 5.5).

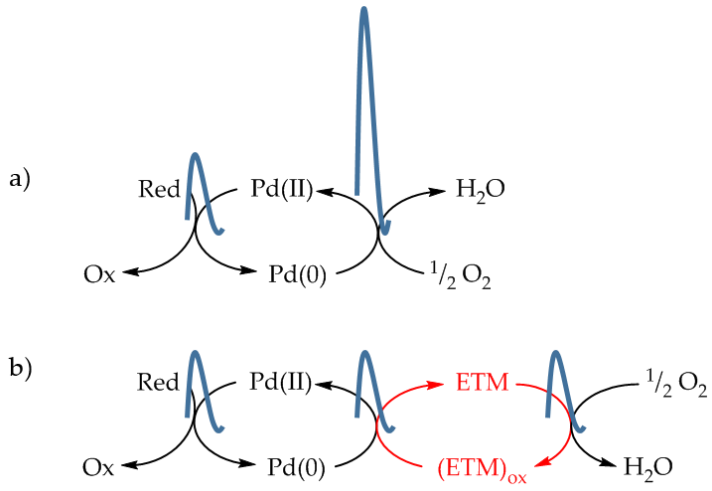

Figure 5.5 – Influence of the ETM on the energy barrier in Pd-catalyzed oxidation reactions: (a) no ETM and (b) presence of ETM

5.2.2.1 Tsuji-Wacker oxidation

The Wacker oxidation concerns the oxipalladation of terminal alkenes to the corresponding methylketones by the action of a Pd(II) catalyst under aerobic and acidic aqueous conditions, with $CuCl_2$ as

redox cocatalyst (equation 5.4). Historically, the oxipalladation of ethylene yielding acetaldehyde first observed by Philips in 1894 was conducted using stoichiometric $PdCl_2$ and acidic conditions.[29] Conditions were improved from stoichiometric to catalytic with respect to Palladium and with $CuCl_2$ as ETM in 1959 by Smidt.[30,31] Finally, in order to extend the method to other classes of substrates, dimethylformamide was employed as a co-solvent by Tsuji in 1984 yielding to the more widespread Tsuji-Wacker oxidation.[32]

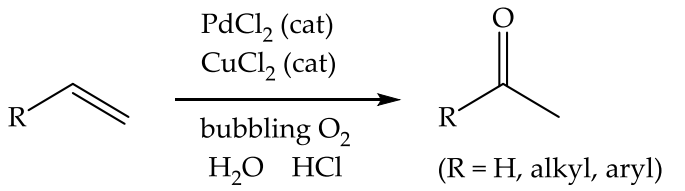

eq 5.4

The industrial production of acetaldehyde from ethylene presented in Figure 5.6 uses low chloride ion and $CuCl_2$ concentrations (< 1 M).[28,33] When using more complex olefins, (cyclic, internal,…), the systems shows low activity, with Palladium decomposition, olefin isomerization, copper waste and, because of the presence of chloride ions, chlorinated by-products, which considerably limit the oxidation.[31,32,34]

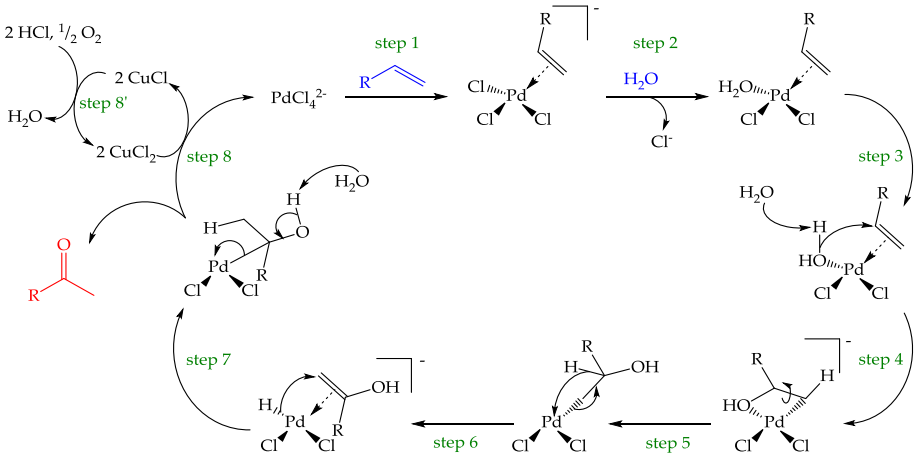

Figure 5.6 – Proposed mechanism of the industrial Wacker process

Industrial Wacker oxidation mechanism[33,35] involves the initial activation of the olefin by coordinating the C=C double bond to the Pd(II) cation (Figure 5.6 – step 1), followed by a ligand exchange reaction (Figure 5.6 – step 2) and a subsequent nucleophilic attack of water in Markovnikov position (Figure 5.6 – step 3). The resulting complex undergoes a deprotonation and then rate-determining *syn* hydroxypalladation (Figure 5.6 – step 4). Despite the commonly accepted β-hydride elimination followed by tautomerization of the obtained enol,[36,37] Palladium complex seems to undergo two hydride shifts and a water-assisted reductive elimination to provide the desired methylketone (Figure 5.6 – step 6-8).[35] The obtained Pd(0) is then reoxidized by Cu(II) to Pd(II), while Cu(II) is reduced in Cu(I) (Figure 5.6 – step 8). Cu(II) is then recovered by oxidation of Cu(I) by molecular oxygen (Figure 5.6 – step 8'). Overall, in this reaction, only dioxygen and olefin are consumed (1:1 stoechiometry) while $PdCl_2$ and $CuCl_2$ are regenerated during the reaction cycle.

Wacker-type conditions can also be used for intramolecular reactions, yielding oxygenated heterocycles. Zhang and co-workers

used this approach for the preparation of vinylchromans from *o*-allylphenol derivatives using BQ as ETM (Figure 5.7).[38] Chiral chroman derivatives have attracted much attention for their broad range of biological activities such as anti-HIV agent[39] or antioxidant.[40]

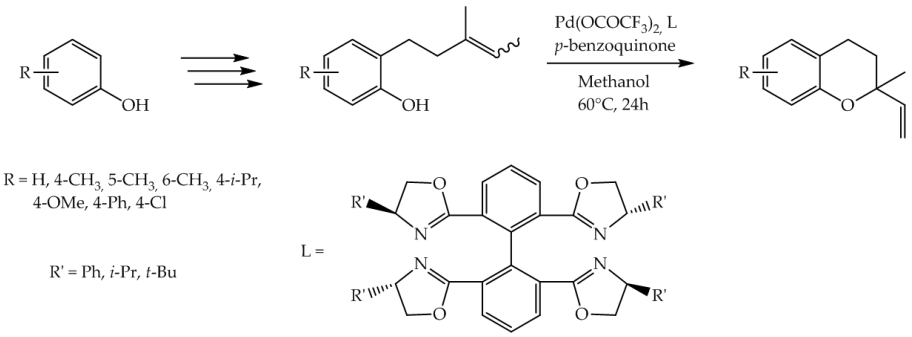

Figure 5.7 – Synthesis of chroman derivatives from *o*-allylphenol derivatives using Wacker-type cyclization

A useful application of the intramolecular Wacker oxidation outside the context of the industrial process has been described by De Koning and co-workers in the synthesis of the core of marticin from 4-(2-allyl-3,6-dimethoxyphenyl)butane-1,2,4-triol.[41] Marticin and isomarticin (Figure 5.8) are napthazirin phytotoxins produced by fungi *Fusarium solani* and *Fusarium martii*. Both can cause extensive damage to plant tissue and possess some antimicrobial activity; they were found to be active against *Staphylococcus aureus* (128 μg/mL) and *Staphylococcus pyogenes* (128 μg/mL).

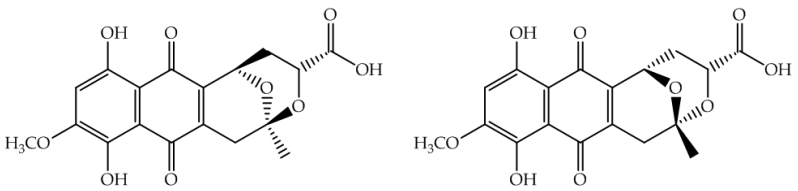

Figure 5.8 – Structure of marticin (*left*) and isomarticin (*right*)

Starting from 2,5-dihydroxyacetophenone, the authors obtained the desired triol intermediate in eight steps (Figure 5.9 – steps not shown). Wacker-type conditions using $PdCl_2$ as catalyst and $CuCl_2{\cdot}2H_2O$ as ETM under aerobic conditions allows the selective oxidation of the terminal alkene into the corresponding methylketone. The resulting methylketone underwent spontaneous ketalization with the secondary alcohols moieties.

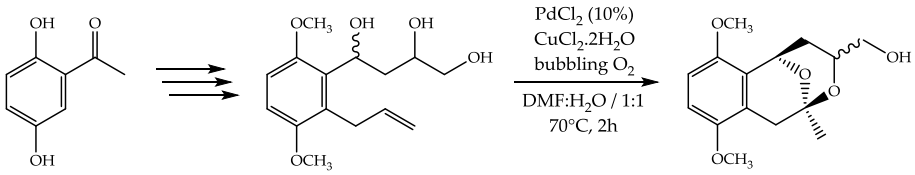

Figure 5.9 – Synthesis of the marticin core from 2,5-dihydroxyacetophenone using Wacker oxidation[41]

Quinones are well-known terminal oxidants or ETMs in Palladium-catalyzed oxidations.[15,17] However, under oxidative conditions such as those described in Figure 5.10, molecular oxygen is kinetically not very efficient to directly reoxidize the resulting hydroquinone (H_2Q). Therefore, an additional ETM is sometimes used to further lower the energy barrier of the redox cascade. The use of a complex with a macrocyclic ligand L^m (ML^m) as ETM has proven to be a highly efficient solution for chloride-free Wacker-type oxidation (Figure 5.10).

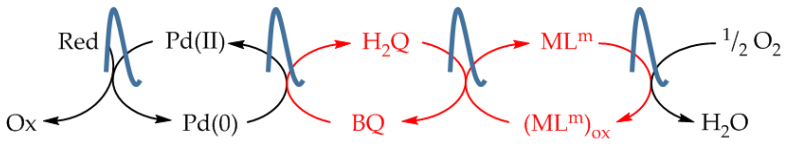

Figure 5.10 – Use of a ML^m/BQ system as ETM for oxipalladation reactions

Metal complexes such as Co(dmgH_2) derivatives,[42] Co(Salen) derivatives, Co(tpp) (where tpp = tetraphenylporphyrin) or Mn(tpp)Cl[43] are able to catalyze the oxidation of H_2Q. They can thus be used in catalytic amounts to obtain an efficient catalytic system under aerobic conditions. An easy analogy can be made between those systems and processes occurring in biological media such as the respiratory chain, as both are based on stepwise low energy electron transfer with lower redox potentials. It is noteworthy mentioning that in systems such as those presented in Figure 5.10, there are four oxidants with decreasing oxidation potentials (O_2, $(ML^m)_{ox}$, BQ and Pd(II)) and four oxidizable components (ML^m, H_2Q, Pd(0) and diene). Thus, ten different thermodynamically favored reactions could occur, but only four of these are kinetically favored due to the coordination between interacting redox couples. For example, O_2 coordinates to ML^m to form a peroxo- compound,[44] Pd(0) is known to coordinate to BQ[17,45] and Pd(II) forms a complex with the alkene.[33,35]

The best results were obtained so far by using iron phthalocyanine (Fe(pc)) as oxygen-activating complex together with Palladium(II) acetate and a catalytic amount of benzoquinone (Figure 5.11) in aqueous DMF.[26] The addition of a small amount of a strong acid helps preventing the precipitation of Pd(0), likely due to protonation of BQ, which promotes Pd(0) oxidation step. An attractive attribute of Fe(pc) is its high chemical stability, partially due to its poor solubility in most organic solvents allowing its recovery at the end of the reaction.

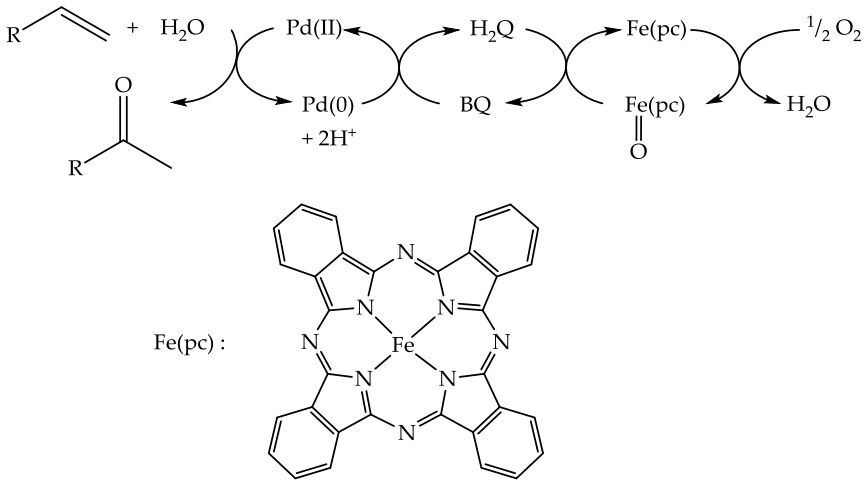

Figure 5.11 – Catalytic system for Wacker oxidation using Fe(pc) as ETM (adapted from [26])

5.2.2.2 Acetoxylation

Allylic acetoxylation of α-olefins to give the corresponding linear allylic acetates (anti-Markovnikov regioselectivity) is another synthetically interesting oxidation reaction involving C-H activation.[12,16,46,47] Independently of the discovery of the Wacker process in 1960, Moiseev and co-workers described the Pd(II)-catalyzed acetoxylation of ethylene and terminal alkenes using BQ as terminal oxidant (equation 5.5).[48]

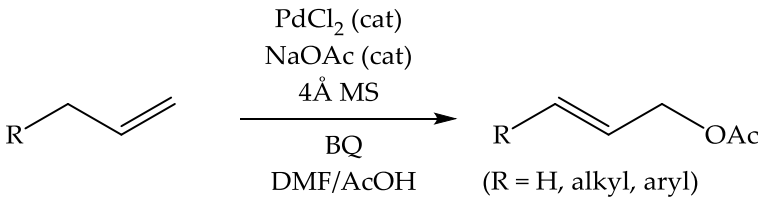

eq 5.5

The reaction conditions used for this acetoxylation are close to those used for Wacker oxidation, with acetic acid as nucleophile in

water-free solvent, to avoid the oxidation of the alkene into ketone. The mechanism of this transformation is described in Figure 5.12. Noteworthy is the double role of BQ as oxidizing agent as well as π-acid ligand. This latter feature renders the η^3-allyl complex more electrophilic, thereby facilitating the reductive elimination step.[49,50] Nevertheless, several groups recently succeeded to replace BQ for molecular oxygen.[16,46,51]

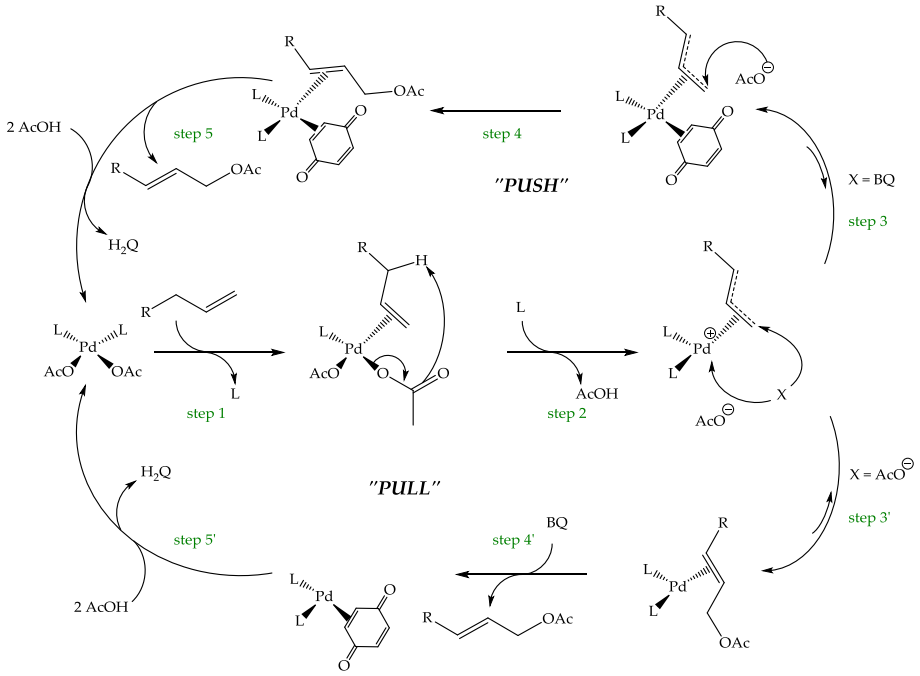

Figure 5.12 – Proposed mechanisms "push" (*up*) and "pull" (*down*) for the palladocatalyzed acetoxylation using benzoquinone as terminal oxidant (adapted from [50,52])

Complexation of the allyl function on the Palladium catalyst yields to the η^2-alkene complex (Figure 5.12 – step 1), subsequently converted to the η^3-allyl Palladium complex by intramolecular deprotonation by one of the acetate ligands (Figure 5.12 – step 2). At this step, two distinct mechanisms are considered.

(i) *"push" mechanism*:[50] BQ binds to the Pd(II) center (Figure 5.12 – step 3), which assists the subsequent reductive elimination step (Figure 5.12 – step 4), followed by reoxidation of the Pd(0) (and reduction of BQ in H_2Q) (Figure 5.12 – step 5).

(ii) *"pull" mechanism*:[52] the reductive elimination occurs releasing the acetoxylated product (Figure 5.12 – step 3'), followed by the trapping of the Pd(0) center by the BQ oxidant (Figure 5.12 – step 4') and subsequent reoxidation into Pd(II) (Figure 5.12 – step 5').

White and co-workers reported the Pd(II)-catalyzed Markovnikov allylic acetoxylation of terminal alkenes to generate the corresponding branched allylic acetate.[53-55] Although the reaction mechanism is not fully understood, they found out that the use of DMSO as co-solvent led to linear (*anti-Markovnikov*) allylic acetate (equation 5.6), whereas the presence of a 1,2-disulfoxide ligand provided the preferential branched (*Markovnikov*) product (equation 5.7).

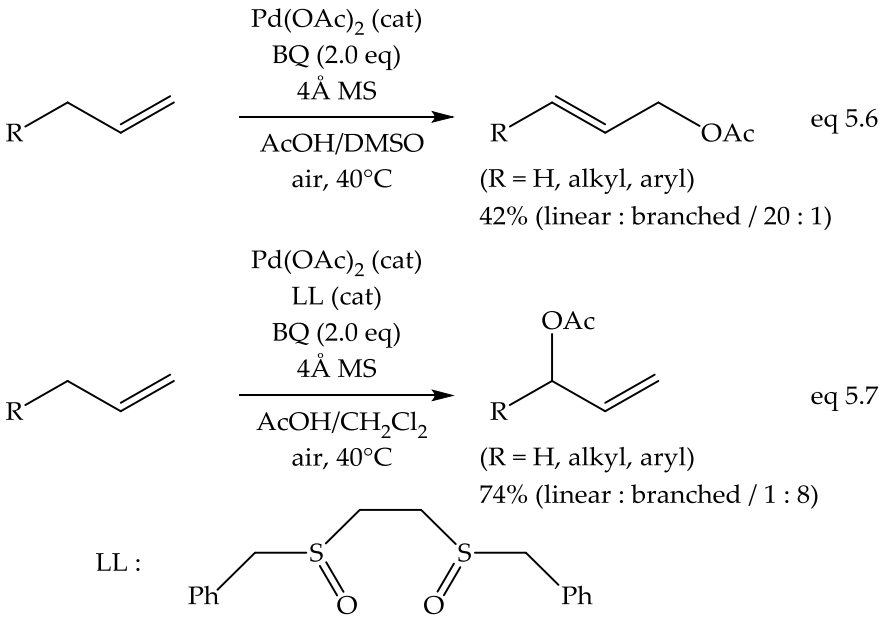

As previously described, acetoxylated compounds are useful synthetic intermediates. Maffei and co-workers investigated the acetoxylation of several allyl phosphonates for further substitution of the acetate group by amino acids derivatives (Figure 5.13).[56,57] Indeed, phosphono amino acids appear to have tremendous biological activities. For example, 2-amino-4-oxo-5-phosphonopentanoic acid (Figure 5.14 – left) is known to possess N-methyl-D-aspartate (NMDA) (*i.e.* a specific agonist of NMDA receptors mimicking the action of glutamate neurotransmitter) antagonist activity.[58] On the other hand, (*E*)-2-amino-5-phosphonopent-4-enoic acid (Figure 5.14 – right) has been reported to inhibit threonine synthase from *Escherichia Coli*.[59]

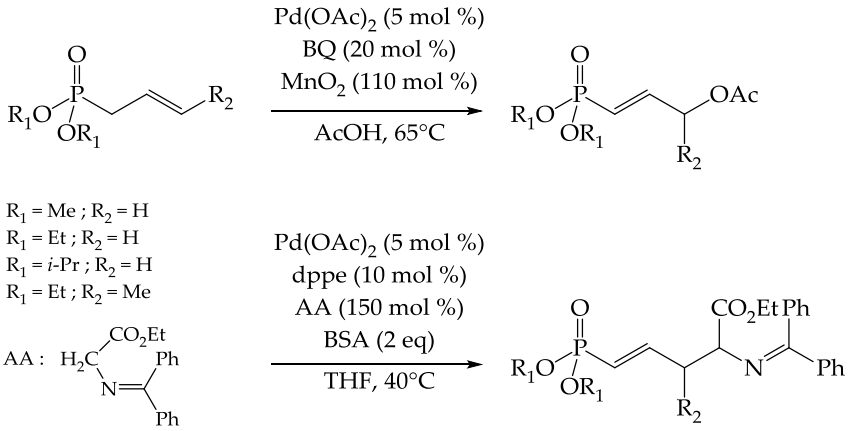

Figure 5.13 – Synthesis of phosphono amino acids derivatives[56,57]

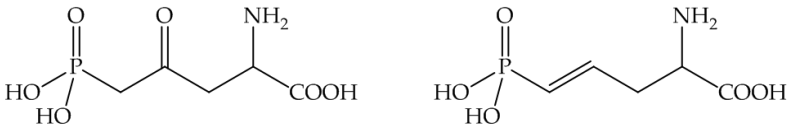

Figure 5.14 – Structure of 2-amino-4-oxo-5-phosphonopentanoic acid (*left*) and (*E*)-2-amino-5-phosphonopent-4-enoic acid (*right*)

5.2.2.3 Photoactivatable Ir(III) complexes as ETMs

Among all the ETMs described in the literature, photoactivatable transition metal complexes[60,61] including Ir(III) complexes have recently gained tremendous interest due to their enhanced redox properties upon irradiation in the field of catalysis,[62-70] including their use in palladocatalyzed reactions.

Sanford and co-workers achieved the *ortho*-directed palladocatalyzed coupling of iodonium salts with arenes under extremely mild conditions using $[Ir(ppy)_2(dtbbpy)]PF_6$ (ppyH = 2-phenylpyridine ; dtbbpy = 4,4′-di-*tert*-butyl-2,2′-bipyridine) as

cocatalyst (equation 5.8).[71] The proposed mechanism is as follows: after visible light photoexcitation of the Ir(III) cocatalyst (Figure 5.15 – step 1), the resulting excited Ir(III)* photocatalyst reduces the iodonium salts to the corresponding aryl iodide and aryl radical with concomitant formation of an Ir(IV) intermediate (Figure 5.15 – step 2). The aryl radical can in turn enter the Palladium catalytic cycle through coupling with the cyclopalladated Pd(II) complex (Figure 5.15 – step 3). The resulting Pd(III) complex can then be further oxidized into a Pd(IV) complex by the oxidized Iridium(IV) complex, regenerating the starting Ir(III) photocatalyst (Figure 5.15 – step 4). Finally, reductive elimination occurs (Figure 5.15 – step 5) yielding the diaryl product as well as the starting Pd(II) catalyst.

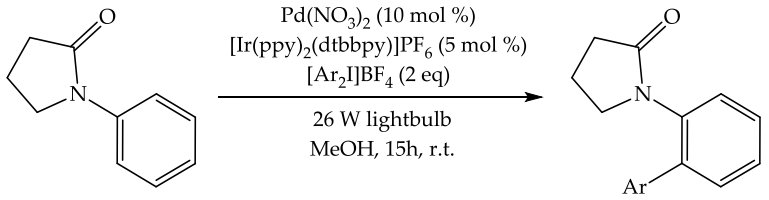

eq 5.8

(Ar = *o*/*m*/*p*-$CF_3C_6H_4$, *p*-ClC_6H_4, *p*-BrC_6H_4
o/*p*-$CH_3C_6H_4$, *p*-$CH_3OC_6H_4$,...)

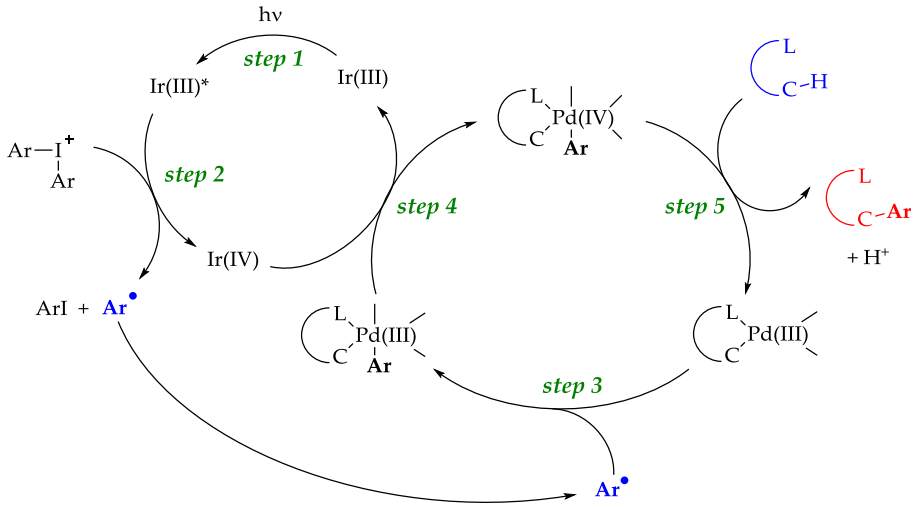

Figure 5.15 – Possible mechanism for the Pd/Ir-catalyzed C-H arylation with Ar_2I^+ (adapted from [71])

In a related work, Rueping and co-workers used a combination of Palladium catalyst and various Iridium complexes for the oxidative synthesis of indoles from arylaminoacrylic esters through an oxidative Heck reaction (equation 5.9).[61,72] With $[Ir(ppy)_2(bpy)]PF_6$ as the reference cocatalyst, electronic and steric properties of two other Iridium complexes were investigated. Surprisingly, an electron-deficient ligand on the Iridium center {$[Ir(ppyCF_3)_2(bpy)]PF_6$ ($ppyCF_3H$ = 2-(3′-trifluoromethyl)-phenylpyridine), which presumably easily reoxidizes the Pd(0), led to decreased yields compared to the reference compound (55% and 66%, respectively), whereas an electron-rich ligand {$[Ir(ppytBu)_2(bpytBu_2)]PF_6$ (ppytBuH = 2-(4′-*tert*-butyl)-phenylpyridine; $bpytBu_2$ = 4,4′-di-*tert*-butyl-2,2′-bipyridine) gave a slightly higher yield (77%).

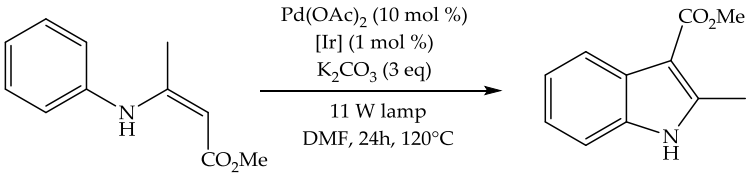

eq 5.9

[Ir] : $[Ir(ppy)_2(bpy)]PF_6$; *yield = 66%*
[Ir] : $[Ir(ppyCF_3)_2(bpy)]PF_6$; *yield = 55%*
[Ir] : $[Ir(ppytBu)_2(bpytBu_2)]PF_6$; *yield = 77%*

Based on the fact that the reaction does not occur in the absence of the photoredox catalyst, even under O_2 atmosphere, nor in the absence of light, the following mechanism is proposed (Figure 5.16): in the first step, C-H activation of the olefin by the Pd(II) catalyst takes place (Figure 5.16 – step 1) followed by the subsequent ortho-palladation of the arene (Figure 5.16 – step 2). Reductive elimination occurs releasing the desired indole and Pd(0) (Figure 5.16 – step 3), which is directly reoxidized by the photoexcited Iridium cocatalyst or by the *in situ* formed superoxide anion after reaction between reduced photosensitizer and molecular oxygen (Figure 5.16 – step 4).[73]

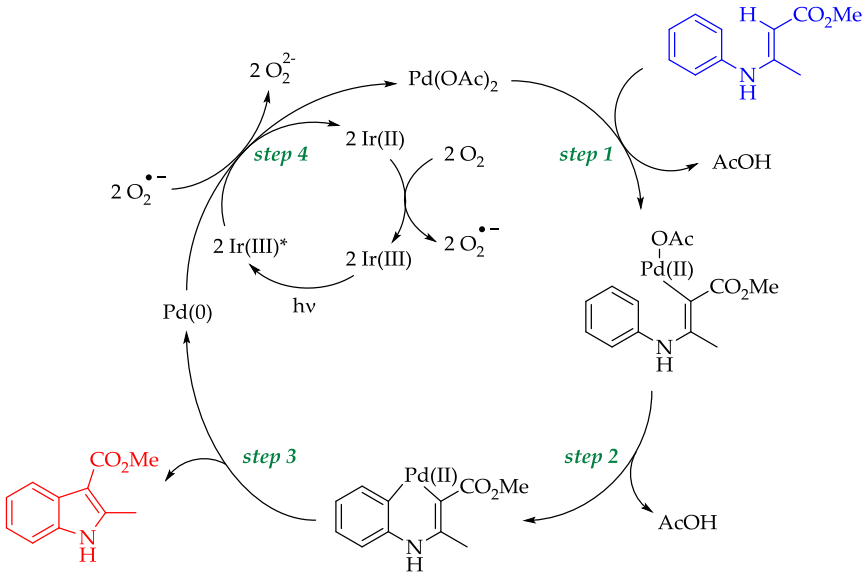

Figure 5.16 – Possible mechanism for the Pd/Ir-catalyzed intramolecular olefination reaction (adapted from [72])

To the best of our knowledge, the use of Ir(III) complexes as ETMs in Wacker oxidation and palladocatalyzed acetoxylation has never been exploited. To that purpose, in close collaboration with Prof. G. Poli (Université Pierre et Marie Curie, France), preliminary studies on both reactions have been performed using standard $[Ir(ppy)_2(bpy)]PF_6$ as photosensitizer. Upon white light irradiation, this complex is photooxidant (E^*_{red} = 0.79 V *vs.* AgCl) enough to recover the Pd(II) catalyst from reduced Pd(0) (E_{ox} = 0.15 V *vs.* Ag/AgCl)[16] (Figure 5.17).

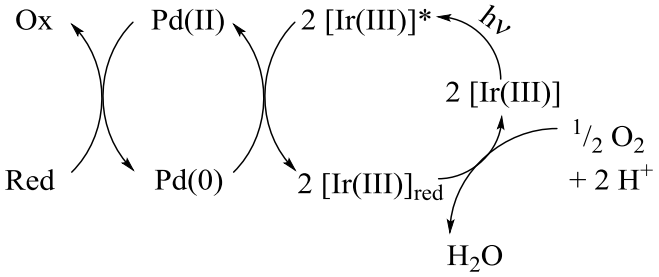

Figure 5.17 – Catalytic system for palladocatalyzed oxidation using a photoactivatable Ir(III) complex as ETM

5.3 Purpose of the study

In the light of the results presented above, we decided to study the Wacker reaction and the Palladium-catalyzed allylic acetoxylation of terminal alkenes, in the presence of catalytic amounts of Iridium complexes as possible ETMs. The idea is to verify whether in these two Pd(II)-catalyzed oxidative transformations, the presence of a photoactivated Iridium complex can speed-up the reoxidation step, and possibly improve the efficiency. In this type of reactions, the reoxidation step is often the most problematic.

5.4 Results and discussion

5.4.1 Wacker oxidation

To put our project into practice, we needed a benchmark reaction to test, as well as specific reaction conditions, to be tested and compared with and without the Iridium complexes. After a careful study of the literature, we selected the Wacker conditions reported by Kaneda and co-workers, as they were totally aerobic (use of O_2 as sole reoxidant), without the requirement of any ETM (equation 5.10).[16]

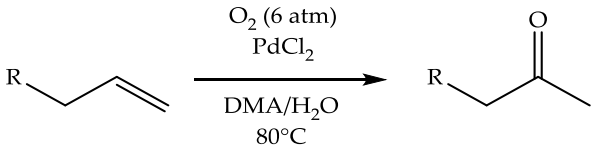

eq 5.10

In the study of Kaneda, the combination of $PdCl_2$ and DMA as co-solvent for the oxidation of 1-decene exhibited the highest catalytic activity (84% yield) compared to other solvents such as N-methyl-2-

pyrrolidone (NMP) (74%) or more common DMF (traces of product) without observation of unreactive Palladium black precipitation. This might be due to the fact that Pd(0) reoxidation is thermodynamically more favored in DMA than in NMP or DMF ($E_{ox,Pd(0)/Pd(II)}$ = -0,26 V, $E_{ox,Pd(0)/Pd(II)}$ = -0,20 V and $E_{ox,Pd(0)/Pd(II)}$ = -0,12 V *vs*. SCE, respectively). The oxidation reactions in the study of Kaneda were performed in an autoclave to maintain 6 atm of O_2 pressure. However, as irradiation of Ir(III) cocatalysts is not compatible with such device, we carried out our reactions in a glass vessel, and under atmospheric pressure of oxygen, hoping that the presence of the Ir(III) complex as ETM could compensate the reduced amount of O_2 in the reaction mixture. The Wacker oxidation being usually performed with $PdCl_2$ as Palladium source, no variation of the catalyst counteranion is expected in the experiments with the Iridium cocatalyst (equation 5.11).

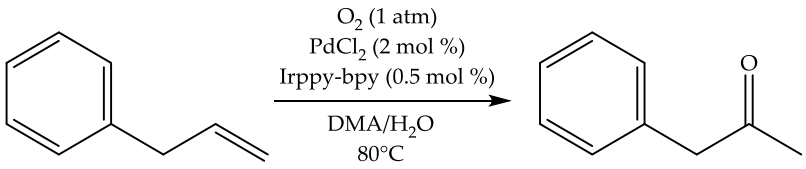

eq 5.11

Different tests using allylbenzene as the reference substrate were performed in DMA:H_2O as the solvent (Table 5.1). Because of the volatility of the compound, gas chromatography was used to follow the reaction. Under atmospheric pressure of oxygen, conversion of allylbenzene into phenylacetone in DMA:H_2O / 6:1 takes place up to 40%, after 40 h in the presence of previously described Irppy-bpy under white light irradiation, while it only reaches 12% in its absence (Table 5.1 – entries 1 and 2). Although the effect of the presence of the Ir(III) cocatalyst is noteworthy and positive, conversion of the substrate remained low. Performing the reaction in more concentrated

conditions (1 M instead of 0.1 M), while keeping the DMA:H_2O / 6:1 ratio, gave a total conversion of the substrate after 8.7 h and 11.4 h with and without Irppy-bpy, respectively (Table 5.1 – entries 3 and 4). Enhancing the DMA:H_2O ratio from 6:1 to 3.8:1 and keeping a global molarity of 1 M, total conversion of the substrate was achieved after 5.9 h and 7.5 h, in the presence and in the absence of Irppy-bpy, respectively (Table 5.1 – entries 5 and 6). Interestingly, the kinetic is influenced by the concentration of H_2O in the reaction mixture. Indeed, when the concentration of H_2O is increased (Table 5.1 – compare entries 3 and 4 *vs.* 5 and 6, respectively), the reaction time is decreased by the same factor, implying a direct proportionality between the kinetics of Wacker oxidation and the concentration of H_2O in our conditions. However, despite its importance in the reaction, such a correlation has not been addressed in industrial Wacker process.[33]

Control reactions were performed in the absence of Pd(II) catalyst, to confirm the inertness of Irppy-bpy in the oxidation of a terminal alkene to the corresponding methylketone (Table 5.1 – entries 7 and 8). Furthermore, reactions were performed under Argon atmosphere, which gave, as expected, almost no conversion of the allylbenzene (Table 5.1 – entries 9 and 10). Finally, the oxidation has been performed in the presence of the Ir(III) cocatalyst in the dark, which gave results close to those obtained in the absence of the photosensitizer (Table 5.1 – entry 11).

Table 5.1 – Experimental conditions for the photoinduced Pd(0) reoxydation by Irppy-bpy in Wacker oxidation of allylbenzene in phenylacetone

	[Alkene] (M)	[$PdCl_2$] (% mol)	[Irppy-bpy] (% mol)	DMA:H_2O	Time (h)	Conversion (%)[a]
1	0,1	2	0.5	6:1	40	40
2	0,1	2	/	6:1	40	12
3	1	2	0.5	6:1	9	> 99
4	1	2	/	6:1	9	76
5	1	2	0.5	3.8:1	6	> 99
6	1	2	/	3.8:1	6	72
7	1	/	0.5	3.8:1	22	< 2
8	1	/	/	3.8:1	22	< 2
9	1	2	0.5	3.8:1	22	< 2[b]
10	1	2	/	3.8:1	22	< 2[b]
11	1	2	0.5	3.8:1	6	71[c]

[a] Conversion was determined by GC using tridecane as external reference
[b] Under Argon atmosphere
[c] In the dark

The oxidation products obtained by using the optimized conditions (Table 5.1 – entries 5 and 6) were separated and purified by column chromatography. Interestingly, a small amount of phenylpropionaldehyde was obtained, implying a minor contribution of an anti-Markovnikov mechanism. Due to the close polarity between phenylpropionaldehyde and phenylacetone, the aldehyde could not be isolated, but its presence was unambiguously attested by ^{1}H NMR spectrum and GC analysis. The obtained yields of 32% and 8% in oxidized products in the presence and in the absence of Irppy-bpy reflects the previous observations *i.e.* Irppy-bpy successfully boosts Pd(0) reoxidation increasing the yield in terminal alkene. Despite such a promising and unambiguous improvement, global yields are still low compared to alternative reaction conditions. The same trend has

been confirmed in the oxidation of other substrates, such as styrene, which gave acetophenone in 33% and 8% yields with and without Ir(III) cocatalyst, respectively. Several reasons could account for such poor yields such as decomposition of the substrates/products, polymerization or volatility of the product. Increased amounts of $PdCl_2$ and Irppy-bpy were used to improve the kinetics and yields but no change could be noted.

As explained above, during the follow-up of the reaction, GC chromatograms revealed side products in small amounts among which phenylpropionaldehyde *i.e.* anti-Markovnikov product of the Wacker oxidation. Interestingly, the amount of aldehyde started to decrease after reaching a maximum. Such decomposition was studied using the same reaction condition with phenylpropionaldehyde as the substrate (equation 5.12).

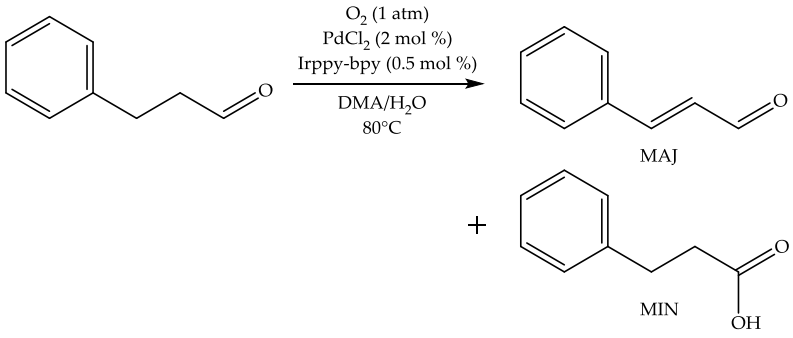

eq 5.12

The major product of the reaction is cinnamaldehyde. Such oxidation of an aldehyde yielding to an α,β-insaturation might be compared to Saegusa's reaction in which a silyl enol ether undergoes palladocatalyzed oxidation to the corresponding α,β-unsaturated ketone (equation 5.13).[74]

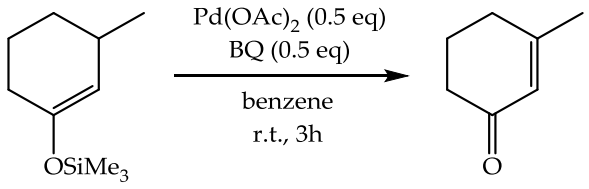

eq 5.13

Such a reactivity could be synthetically highly useful as it allows the direct oxidation of a terminal alkene into the corresponding α,β-unsaturated aldehyde. As the conversion of the alkene into aldehyde is low, other conditions have to be developed to ensure the first oxidation and subsequently the α,β-unsaturation. Grubbs and co-workers have developed appropriate anti-Markovnikov conditions to convert styrene derivatives into the corresponding aldehydes (equation 5.14). To the best of our knowledge, these conditions have not been adapted to alkyl alkenes.

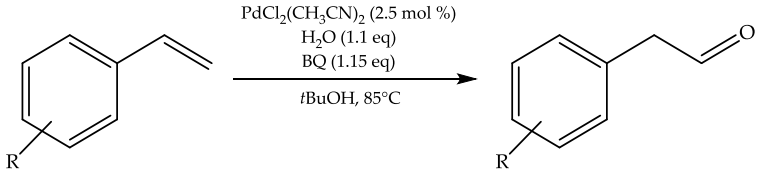

eq 5.14

5.4.2 Acetoxylation

When allylbenzene is heated at 80°C with catalytic $PdCl_2$, in the presence of AcONa, in DMA/AcOH and under O_2 atmosphere (1 atm) in the absence of any particular ligand,[15,46] the regioselective allylic acetoxylation to give cinnamyl acetate takes place (equation 5.15).

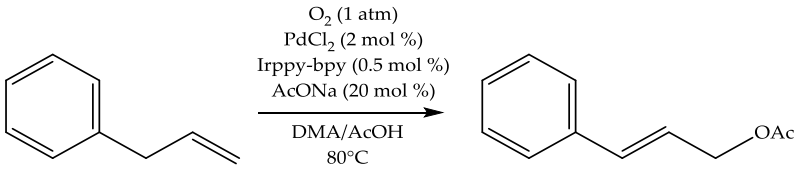

eq 5.15

This reaction gave, after 40 h stirring, 54% and 44% of cinnamyl acetate, when operating with or without Irppy-bpy, respectively, accompanied by considerable amounts of Palladium black (Table 5.2 – entries 1 and 2). Although the effect of the photosensitizer is once again clear and positive, the reaction is too slow under these conditions. An increase of the substrate concentration from 0.1 M to 1 M by modifying the proportions of the solvent *i.e.* from DMA:AcOH / 25:1 to 5:1 resulted in a slightly faster conversion of the substrate (73% and 60% after 40 h with and without Irppy-bpy, respectively) (Table 5.2 – entries 3 and 4). A higher concentrated mixture might have led to a faster reaction but also induced an easier precipitation of Palladium black. Reference reactions were also performed without Pd(II) catalyst (Table 5.2 – entries 5 and 6) and under Argon atmosphere (Table 5.2 – entries 7 and 8), confirming the need of the Palladium catalyst and aerobic conditions for the acetoxylation to occur. Reactions were also performed using styrene instead of allylbenzene, to ensure the mechanism presented in Figure 5.12 using allyl-Pd complex under our conditions and no acetate derivative could be observed by GC (Table 5.2 – entries 9 and 10).

Table 5.2 – Experimental conditions for the photoinduced Pd(0) reoxidation by Irppy-bpy in acetoxylation of allylbenzene in cinnamyl acetate

	[Alkene] (M)	[$PdCl_2$] (% mol)	[Irppy-bpy] (% mol)	DMA:AcOH	Time (h)	Conversion (%)[a]
1	0.1	2	0.5	25:1	40	54
2	0.1	2	/	25:1	40	44
3	1	2	0.5	5:1	40	73
4	1	2	/	5:1	40	60
5	1	/	0.5	5:1	40	< 2
6	1	/	/	5:1	40	< 2
7	1	2	0.5	5:1	40	< 2[b]
8	1	2	/	5:1	40	< 2[b]
9	1	2	0.5	5:1	40	0[c]
10	1	2	/	5:1	40	0[c]

[a] Conversion was determined by GC using tridecane as external reference

[b] Under Argon atmosphere

[c] With styrene as substrate

5.4 Conclusion

Having in mind that Palladium(II)-catalyzed oxidation reactions suffer from several issues such as the fast precipitation of the reduced catalyst Pd(0), we successfully managed to use the enhanced photoredox abilities of the Irppy-bpy complex to increase the rate as well as the yield for both Wacker oxidation and acetoxylation reactions. Nevertheless, a serious optimization of both systems must be performed in order to increase the yields to a satisfactory level. Indeed, Wacker oxidation of allylbenzene to phenylacetone afforded moderate yields of 32% and 8% in the presence and in the absence of Irppy-bpy, respectively. Despite the positive effect of the photoactivatable Ir(III) complex, the results are still weaker compared to experimental conditions described in the literature,[16] and so were those obtained for the palladocatalyzed acetoxylation.

An interesting perspective is the variation of the photoactivatable Ir(III) complex. Indeed, as presented in Chapters 2 and 4, the variation in the coordination sphere of an Ir(III) complex causes tremendous alterations of its (photo)physical properties.

5.5 Experimental section

5.5.1 Typical Wacker oxidation experiment

Palladium(II) chloride (0.02 eq) was solubilized in a DMA:H_2O / 6:1 (7 mL/mmol of alkene) under O_2 atmosphere (1 atm) and the solution was heated to 80°C for 2 h. The terminal alkene (1.0 eq) was added followed by the Ir(III) photosensitizer (5.10^{-3} eq). The mixture was stirred under white light for 40 h.

Work-up and purification: The solution was cooled to room temperature and the products were extracted with a Et_2O:H_2O / 1:1 mixture (2 x 60 mL/mmol of alkene). The organic phase was dried over MgSO4, filtered and concentrated under reduced pressure. The product was purified on column chromatography on silica gel using a Cy/AcOEt mixture as eluent.

5.5.2 Typical Acetoxylation experiment

Palladium(II) chloride (0.02 eq) was solubilized in DMA (5 mL/mmol of alkene) under O_2 atmosphere (1 atm), directly followed by the terminal alkene (1.0 eq), acetic acid (0.2 mL/mmol of alkene), sodium acetate (0.2 eq), 4Å molecular sieves (0.2 g/mol of alkene) and the Ir(III) photosensitizer (5.10^{-3} eq). The mixture was stirred under white light for 40 h.

5.5 References

1. Berzelius, J. J. Considerations respecting a New Power which acts in the Formation of Organic Bodies. *Edinburgh New Philosophical Journal* **1836**, *21*, 223-228.
2. Wolfe, J.; Thomas, J. Recent Developments in Palladium-Catalyzed Heterocycle Synthesis and Functionalization. *Curr. Org. Chem.* **2005**, *9*, 625-655.
3. Nakamura, I.; Yamamoto, Y. Transition-metal-catalyzed reactions in heterocyclic synthesis. *Chem. Rev.* **2004**, *104*, 2127-2198.
4. Zeni, G.; Larock, R. C. Synthesis of heterocycles via palladium pi-olefin and pi-alkyne chemistry. *Chem. Rev.* **2004**, *104*, 2285-2309.
5. Gevorgyan, V.; Rubin, M.; Sromek, A. W. New Advances in Selected Transition Metal-Catalyzed Annulations. *Synlett* **2003**, 2265-2291.
6. Liu, C.; Zhang, H.; Shi, W.; Lei, A. Bond formations between two nucleophiles: transition metal catalyzed oxidative cross-coupling reactions. *Chem. Rev.* **2011**, *111*, 1780-1824.
7. Overman, L. E.; Knoll, F. M. Palladium (II) - catalyzed rearrangement of allylic acetates. *Tetrahedron Lett.* **1979**, *20*, 321-324.
8. Bar, G. L.; Lloyd-Jones, G. C.; Booker-Milburn, K. I. Pd(II)-catalyzed intermolecular 1,2-diamination of conjugated dienes. *J. Am. Chem. Soc.* **2005**, *127*, 7308-7309.
9. Li, Y.; Song, D.; Dong, V. M. Palladium-catalyzed olefin dioxygenation. *J. Am. Chem. Soc.* **2008**, *130*, 2962-2964.
10. Chen, X.; Engle, K. M.; Wang, D. H.; Yu, J. Q. Palladium(II)-catalyzed C-H activation/C-C cross-coupling reactions: versatility and practicality. *Angew. Chem. Int. Ed.* **2009**, *48*, 5094-5115.
11. Lyons, T. W.; Sanford, M. S. Palladium-catalyzed ligand-directed C-H functionalization reactions. *Chem. Rev.* **2010**, *110*, 1147-1169.
12. Campbell, A. N.; Stahl, S. S. Overcoming the "oxidant problem": strategies to use O2 as the oxidant in organometallic C-H oxidation reactions catalyzed by Pd (and Cu). *Acc. Chem. Res.* **2012**, *45*, 851-863.
13. Shilov, A. E.; Shul'pin, G. B. Activation and Catalytic Reactions of Alkanes in Solutions of Metal Complexes. *Russ. Chem. Rev.* **1987**, *56*, 442-464.
14. Lersch, M.; Tilset, M. Mechanistic aspects of C-H activation by Pt complexes. *Chem. Rev.* **2005**, *105*, 2471-2526.
15. Liron, F.; Oble, J.; Lorion, M. M.; Poli, G. Direct Allylic Functionalization Through Pd-Catalyzed C-H Activation. *Eur. J. Org. Chem.* **2014**, *2014*, 5863-5883.
16. Mitsudome, T.; Umetani, T.; Nosaka, N.; Mori, K.; Mizugaki, T.; Ebitani, K.; Kaneda, K. Convenient and Efficient Pd-Catalyzed Regioselective

Oxyfunctionalization of Terminal Olefins by Using Molecular Oxygen as Sole Reoxidant. *Angew. Chem. Int. Ed.* **2006**, *45*, 481-485.
17. Popp, B. V.; Stahl, S. S. Palladium-Catalyzed Oxidation Reactions: Comparison of Benzoquinone and Molecular Oxygen as Stoichiometric Oxidants. *Topics in Organometallic Chemistry* **2007**, *22*, 149-189.
18. Zhang, G.; Xie, X.; Wang, Y.; Wen, X.; Zhao, Y.; Ding, C. Highly selective Wacker reaction of styrene derivatives: a green and efficient aerobic oxidative process promoted by benzoquinone/NaNO2/HClO4 under mild conditions. *Org. Biomol. Chem.* **2013**, *11*, 2947-2950.
19. Sigman, M. S.; Jensen, D. R. Ligand-modulated palladium-catalyzed aerobic alcohol oxidations. *Acc. Chem. Res.* **2006**, *39*, 221-229.
20. Cornell, C. N.; Sigman, M. S. Discovery of a Practical Direct O2-Coupled Wacker Oxidation with Pd[(−)-sparteine]Cl2. *Org. Lett.* **2006**, *8*, 4117-4120.
21. Brink, G. t.; Arends, I. W. C. E.; Sheldon, R. A. Green, Catalytic Oxidation of Alcohols in Water. *Science* **2000**, *287*, 1636-1639.
22. Muñiz, K. Palladium-Carbene Catalysts for Aerobic, Intramolecular Wacker-Type Cyclisation Reactions. *Adv. Synth. Catal.* **2004**, *346*, 1425-1428.
23. Kantchev, E. A.; O'Brien, C. J.; Organ, M. G. Palladium complexes of N-heterocyclic carbenes as catalysts for cross-coupling reactions--a synthetic chemist's perspective. *Angew. Chem. Int. Ed.* **2007**, *46*, 2768-2813.
24. Larock, R. C.; Hightower, T. R. Synthesis of unsaturated lactones via palladium-catalyzed cyclization of alkenoic acids. *J. Org. Chem.* **1993**, *58*, 5298-5300.
25. van Benthem, R. A. T. M.; Hiemstra, H.; Michels, J. J.; Speckamp, W. N. Palladium(II)-catalysed oxidation of allylic amines with molecular oxygen. *J. Chem. Soc., Chem. Commun.* **1994**, 357-359.
26. Bäckvall, J.-E.; Hopkins, R. B. Multi-step catalysis for the oxidation of olefins to ketones by molecular oxygen in chloride free media. *Tetrahedron Lett.* **1988**, *29*, 2885-2888.
27. Kim, Y.; Kim, H.; Lee, J.; Sim, K.; Han, Y.; Paik, H. A modified Wacker catalysis using heteropolyacid: Interaction of heteropolyanion with Cu(II) in cyclohexene oxidation. *Applied Catalysis A: General* **1997**, *155*, 15-26.
28. Melgo, M. S.; Lindner, A.; Schuchardt, U. Wacker oxidation of cyclohexene in the presence of Pd(NO3)2/CuSO4/H3PMo12O40. *Applied Catalysis A: General* **2004**, *273*, 217-221.
29. Phillips, F. C. Untersuchungen über die chemischen Eigenschaften von Gasen. I. Mitteilung. Erscheinungen bei der Oxydation von Wasserstoff und Kohlenwasserstoffen. *Zeitschrift für anorganische Chemie* **1894**, *6*, 213-228.
30. Smidt, J.; Hafner, W.; Jira, R.; Sedlmeier, J.; Sieber, R.; Rüttinger, R.; Kojer, H. Katalytische Umsetzungen von Olefinen an Platinmetall-

Verbindungen Das Consortium-Verfahren zur Herstellung von Acetaldehyd. *Angew. Chem.* **1959**, *71*, 176-182.
31. Smidt, J.; Hafner, W.; Jira, R.; Sieber, R.; Sedlmeier, J.; Sabel, A. The Oxidation of Olefins with Palladium Chloride Catalysts. *Angew. Chem. Int. Ed.* **1962**, *1*, 80-88.
32. Tsuji, J.; Nagashima, H.; Nemoto, H. A General Synthetic Method for the Preparation of Methyl Ketones from Terminal Olefins: 2-Decanone. *Organic Syntheses* **1984**, *62*, 9.
33. Keith, J. A.; Nielsen, R. J.; Oxgaard, J.; Goddard, W. A., 3rd. Unraveling the Wacker oxidation mechanisms. *J. Am. Chem. Soc.* **2007**, *129*, 12342-12343.
34. Stangl, H.; Jira, R. Die durch palladium(II)chlorid und kupfer(II)chlorid katalysierte oxychlorierung von äthylen zu äthylenchlorhydrin. *Tetrahedron Lett.* **1970**, *11*, 3589-3592.
35. Keith, J. A.; Oxgaard, J.; Goddard, W. A., 3rd. Inaccessibility of beta-hydride elimination from -OH functional groups in Wacker-type oxidation. *J. Am. Chem. Soc.* **2006**, *128*, 3132-3133.
36. Sigman, M. S.; Schultz, M. J. The renaissance of palladium(II)-catalyzed oxidation chemistry. *Org. Biomol. Chem.* **2004**, *2*, 2551-2554.
37. Baiju, T. V.; Gravel, E.; Doris, E.; Namboothiri, I. N. N. Recent developments in Tsuji-Wacker oxidation. *Tetrahedron Lett.* **2016**, *57*, 3993-4000.
38. Liu, Q.; Wen, K.; Zhang, Z.; Wu, Z.; Zhang, Y. J.; Zhang, W. Pd(II)-catalyzed asymmetric Wacker-type cyclization for the preparation of 2-vinylchroman derivatives with biphenyl tetraoxazoline ligands. *Tetrahedron* **2012**, *68*, 5209-5215.
39. Kashiwada, Y.; Yamazaki, K.; Ikeshiro, Y.; Yamagishi, T.; Fujioka, T.; Mihashi, K.; Mizuki, K.; Cosentino, L. M.; Fowke, K.; Morris-Natschke, S. L.; Lee, K.-H. Isolation of rhododaurichromanic acid B and the anti-HIV principles rhododaurichromanic acid A and rhododaurichromenic acid from Rhododendron dauricum. *Tetrahedron* **2001**, *57*, 1559-1563.
40. Tietze, L. F.; Sommer, K. M.; Zinngrebe, J.; Stecker, F. Palladium-catalyzed enantioselective domino reaction for the efficient synthesis of vitamin E. *Angew. Chem. Int. Ed.* **2004**, *44*, 257-259.
41. Pillay, A.; Rousseau, A. L.; Fernandes, M. A.; de Koning, C. B. Wacker oxidation methodology for the synthesis of the benzo-fused acetal core of marticin. *Tetrahedron* **2012**, *68*, 7116-7121.
42. Németh, S.; Szeverényi, Z.; Simándi, L. I. Catalytic oxidations with molecular oxygen in the presence of cobaloxime(II) derivatives. *Inorg. Chim. Acta* **1980**, *44*, L107-L109.
43. Frostin-Rio, M.; Pujol, D.; Bied-Charreton, C.; Perrée-Fauvet, M.; Gaudemer, A. Oxidation of phenols by molecular oxygen catalysed by

transition metal complexes. Comparison between the activity of various cobalt and manganese complexes and the role of peroxy intermediates. *J. Chem. Soc., Perkin Trans. 1* **1984**, 1971-1979.
44. Meunier, B.; de Visser, S. P.; Shaik, S. Mechanism of oxidation reactions catalyzed by cytochrome p450 enzymes. *Chem. Rev.* **2004**, *104*, 3947-3980.
45. Grennberg, H.; Gogoll, A.; Baeckvall, J. E. Acid-induced transformation of palladium(0)-benzoquinone complexes to palladium(II) and hydroquinone. *Organometallics* **1993**, *12*, 1790-1793.
46. Campbell, A. N.; White, P. B.; Guzei, I. A.; Stahl, S. S. Allylic C-H acetoxylation with a 4,5-diazafluorenone-ligated palladium catalyst: a ligand-based strategy to achieve aerobic catalytic turnover. *J. Am. Chem. Soc.* **2010**, *132*, 15116-15119.
47. Frost, C. G.; Howarth, J.; Williams, J. M. J. Selectivity in palladium catalysed allylic substitution. *Tetrahedron: Asymmetry* **1992**, *3*, 1089-1122.
48. Moiseev, I. I.; Vargaftik, M. N. Allylic oxidation of alkenes with palladium catalysts. *Coord. Chem. Rev.* **2004**, *248*, 2381-2391.
49. Baeckvall, J. E.; Nordberg, R. E.; Wilhelm, D. Dual stereoselectivity in the nucleophilic attack on (p-allyl)palladium complexes. *J. Am. Chem. Soc.* **1985**, *107*, 6892-6898.
50. Diao, T.; Stahl, S. S. O2-Promoted Allylic Acetoxylation of Alkenes: Assessment of "Push" vs. "Pull" Mechanisms and Comparison between O2 and Benzoquinone. *Polyhedron* **2014**, *84*, 96-102.
51. Liu, G.; Yin, G.; Wu, L. Palladium-catalyzed intermolecular aerobic oxidative amination of terminal alkenes: efficient synthesis of linear allylamine derivatives. *Angew. Chem. Int. Ed.* **2008**, *47*, 4733-4736.
52. Lin, B.-L.; Labinger, J. A.; Bercaw, J. E. Mechanistic investigations of bipyrimidine-promoted palladium-catalyzed allylic acetoxylation of olefins. *Can. J. Chem.* **2009**, *87*, 264-271.
53. Chen, M. S.; Prabagaran, N.; Labenz, N. A.; White, M. C. Serial ligand catalysis: a highly selective allylic C-H oxidation. *J. Am. Chem. Soc.* **2005**, *127*, 6970-6971.
54. Chen, M. S.; White, M. C. A sulfoxide-promoted, catalytic method for the regioselective synthesis of allylic acetates from monosubstituted olefins via C-H oxidation. *J. Am. Chem. Soc.* **2004**, *126*, 1346-1347.
55. Delcamp, J. H.; White, M. C. Sequential hydrocarbon functionalization: allylic C-H oxidation/vinylic C-H arylation. *J. Am. Chem. Soc.* **2006**, *128*, 15076-15077.
56. Principato, B.; Maffei, M.; Siv, C.; Buono, G.; Peiffer, G. Palladium catalysed allylic acetoxylation of dialkyl allyl phosphonates. *Tetrahedron* **1996**, *52*, 2087-2096.

57. Attolini, M.; Maffei, M.; Principato, B.; Pfeiffer, G. A Palladium Catalyzed Synthesis of Precursors of 2-Amino-5-Phosphonopentanoic Acid and Related Compounds. *Synlett* **1997**, *1997*, 384-386.
58. Rudisill, D. E.; Whitten, J. P. Synthesis of (R)-4-Oxo-5-phosphononorvaline, an N-Methyl-D-aspartic Acid Receptor Selective β-Keto Phosphonate. *Synthesis* **1994**, *1994*, 851-854.
59. Harde, C.; Neff, K.-H.; Nordhoff, E.; Gerbling, K.-P.; Laber, B.; Pohlenz, H.-D. Syntheses of homoserine phosphate analogs as potential inhibitors of bacterial threonine synthase. *Bioorg. Med. Chem. Lett.* **1994**, *4*, 273-278.
60. Shaw, M. H.; Twilton, J.; MacMillan, D. W. Photoredox Catalysis in Organic Chemistry. *J. Org. Chem.* **2016**, *81*, 6898-6926.
61. Fabry, D. C.; Rueping, M. Merging Visible Light Photoredox Catalysis with Metal Catalyzed C-H Activations: On the Role of Oxygen and Superoxide Ions as Oxidants. *Acc. Chem. Res.* **2016**, *49*, 1969-1979.
62. Nagib, D. A.; MacMillan, D. W. Trifluoromethylation of arenes and heteroarenes by means of photoredox catalysis. *Nature* **2011**, *480*, 224-228.
63. You, Y.; Nam, W. Photofunctional triplet excited states of cyclometalated Ir(III) complexes: beyond electroluminescence. *Chem. Soc. Rev.* **2012**, *41*, 7061-7084.
64. Lowry, M. S.; Goldsmith, J. I.; Slinker, J. D.; Rohl, R.; Pascal, R. A., Jr.; Malliaras, G. G.; Bernhard, S. Single-Layer Electroluminescent Devices and Photoinduced Hydrogen Production from an Ionic Iridium(III) Complex. *Chem. Mater.* **2005**, *17*, 5712-5719.
65. Hansen, S.; Pohl, M. M.; Klahn, M.; Spannenberg, A.; Beweries, T. Investigation and enhancement of the stability and performance of water reduction systems based on cyclometalated iridium(III) complexes. *ChemSusChem* **2013**, *6*, 92-101.
66. Angeles-Boza, A. M.; Roth, J. P. Oxygen kinetic isotope effects upon catalytic water oxidation by a monomeric ruthenium complex. *Inorg. Chem.* **2012**, *51*, 4722-4729.
67. Matsumoto, T.; Periana, R. A.; Taube, D. J.; Yoshida, H. Regioselective hydrophenylation of olefins catalyzed by an Ir(III) complex. *J. Mol. Catal. A: Chem.* **2002**, *180*, 1-18.
68. Govindaswamy, P.; Canivet, J.; Therrien, B.; Süss-Fink, G.; Štěpnička, P.; Ludvík, J. Mono and dinuclear rhodium, iridium and ruthenium complexes containing chelating 2,2'-bipyrimidine ligands: Synthesis, molecular structure, electrochemistry and catalytic properties. *J. Organomet. Chem.* **2007**, *692*, 3664-3675.
69. Goldsmith, J. I.; Hudson, W. R.; Lowry, M. S.; Anderson, T. H.; Bernhard, S. Discovery and High-Throughput Screening of Heteroleptic Iridium Complexes for Photoinduced Hydrogen Production. *J. Am. Chem. Soc.* **2005**, *127*, 7502-7510.

70. Tanaka, R.; Yamashita, M.; Nozaki, K. Catalytic hydrogenation of carbon dioxide using Ir(III)-pincer complexes. *J. Am. Chem. Soc.* **2009**, *131*, 14168-14169.
71. Neufeldt, S. R.; Sanford, M. S. Combining Transition Metal Catalysis with Radical Chemistry: Dramatic Acceleration of Palladium-Catalyzed C-H Arylation with Diaryliodonium Salts. *Adv. Synth. Catal.* **2012**, *354*, 3517-3522.
72. Zoller, J.; Fabry, D. C.; Ronge, M. A.; Rueping, M. Synthesis of Indoles Using Visible Light: Photoredox Catalysis for Palladium-Catalyzed C-H Activation. *Angew. Chem. Int. Ed.* **2014**, *53*, 13264-13268.
73. Prier, C. K.; Rankic, D. A.; MacMillan, D. W. Visible light photoredox catalysis with transition metal complexes: applications in organic synthesis. *Chem. Rev.* **2013**, *113*, 5322-5363.
74. Ito, Y.; Hirao, T.; Saegusa, T. Synthesis of .alpha.,.beta.-unsaturated carbonyl compounds by palladium(II)-catalyzed dehydrosilylation of silyl enol ethers. *J. Org. Chem.* **1978**, *43*, 1011-1013.

CHAPTER 6

Conclusion and prospects

6.1 Conclusion

This Ph.D. thesis was mainly focused on the development, studies and applications of novel photoactive systems for the regeneration of catalysts involved in various redox processes. In that purpose, Ir(III) complexes were tuned for photooxidation or photoreduction of the investigated catalysts by modification of the first and/or second coordination spheres.

In Chapter 2, a novel study on the effects of the variation of the first coordination sphere of reference Ir(III) complexes was performed. Indeed, despite the use of standard complexes such as *fac*-[Ir(ppy)$_3$] or [Ir(ppy)$_2$(bpy)]$^+$ in organic light-emitting diodes (OLEDs),[1-4] biolabeling agents,[5-7] photocatalysts for solar energy conversion[8-9] and in organic reactions,[10-13] no clear-cut comparative study on their photophysical and photochemical properties had been described in the literature. Hence, we successfully synthesized a library of Ir(III) complexes with various N/C ratio (from 3/3 to 6/0) of the first coordination sphere (*i.e.* a ppyH/bpy ratio from 3/0 to 0/3) leading to four references complexes: [IrN$_3$C$_3$], [IrN$_4$C$_2$]$^+$, [IrN$_5$C$_1$]$^{2+}$ and [IrN$_6$]$^{3+}$ (Figure 6.1). As the two latter complexes displayed tremendous properties, an intermediary complex [R-IrN$_5$C$_1$]$^{2+}$ with three bpy ligands but a N/C ratio of 5/1 and, hence, a protonable non-chelating N, was designed. Substituting cyclometalated ppy ligand with polyimine bpy ligand lead to an increase of ^{3}LC contribution in the nature of the excited state of the complexes. Having established their photophysical properties, their photochemical behavior was investigated through their ability to photoinduce an electron transfer in the presence of a well-known redox system *i.e.* hydroquinone H$_2$Q and benzoquinone BQ. Surprisingly, all the Ir(III) complexes were able

to photoreduce BQ under irradiation despite the electron-poor character of $[IrN_5C_1]^{2+}$, $[IrN_6]^{3+}$ and both neutral and protonated $[R\text{-}IrN_5C_1]^{2+}$. As all ligands of protonated $[R\text{-}IrN_5C_1\text{-}H]^{3+}$ are electrodeficient, the exact attribution of the nature of the excited state is unsure and needs to be investigated by more specific techniques, such as photo-CIDNP experiments.

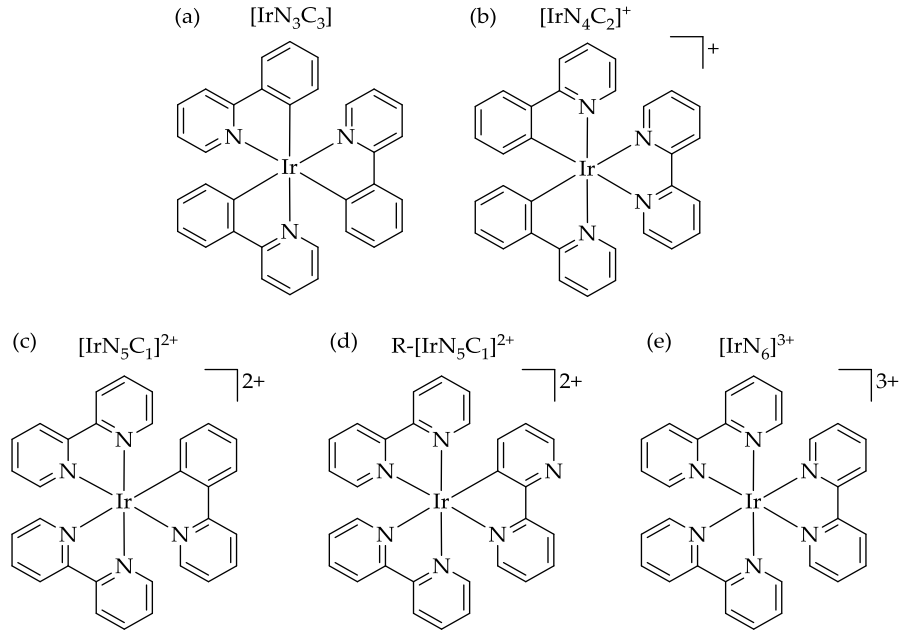

Figure 6.1 – Structures of the trischelate Ir(III) complexes: (a) *fac*-$[Ir(ppy)_3]$ ($[IrN_3C_3]$) ; (b) $[Ir(N,N'\text{-}bpy)(ppy)_2]^+$ ($[IrN_4C_2]^+$) ; (c) $[Ir(N,N'\text{-}bpy)_2(ppy)]^{2+}$ ($[IrN_5C_1]^{2+}$) ; (d) $[Ir(N,N'\text{-}bpy)_2(N,C^3\text{-}bpy)]^{2+}$ ($R\text{-}[IrN_5C_1]^{2+}$) ; (e) $[Ir(N,N'\text{-}bpy)_3]^{3+}$ ($[IrN_6]^{3+}$)

Chapter 3 describes the first photophysical and photochemical studies of an Ir(III) photosensitizer ($[R\text{-}IrN_5C_1]^{2+}$) by photo-CIDNP experiments in the presence of a nucleic base to provide an unambiguous attribution of the nature of its excited state. The radical induced by the PET process between both compounds induces a variation of Boltzmann distribution of nuclear spins leading to

absorptive or emissive enhancements of NMR signals of ^1H in its neighborhood. Hence, a variation of intensity of ^1H NMR signals is a clear-cut confirmation of the presence of a radical and of the nature of the excited state of the complex. An intensive study of ^1H attribution of asymmetric $[R\text{-}IrN_5C_1]^{2+}$ was first performed to allow the distinction between ^1H of the different ligands. As the complex can be protonated, the pKa of ground state, excited state and mono-reduced complex were found to be 2.07, 3.45 and 6.14, respectively. Luminescence quenching of neutral and protonated $[R\text{-}IrN_5C_1]^{2+}$ were studied at various pH, confirming that either energy or electron transfer occurs under irradiation, even under highly acidic (pH = 0) and basic (pH = 11) conditions. Subsequent photo-CIDNP studies revealed unambiguously the presence of a radical on the protonated N,C^3-bpy-H^+ ligand confirming the nature of the excited state. The electronic distribution over the whole cyclometalated N,C^3-bpy ligand confirms the manifold of excited states, which differs from other photosensitizers such as $[Ru(TAP)_3]^{2+}$ or $[Ru(TAP)_2(phen)]^{2+}$.[14-15] Furthermore, these studies highlighted an unexpected change in photochemical behavior of the Ir(III) photosensitizer in the presence of the nucleic base when protonated *i.e.* from the photooxidation of dGMP at high pH to its photoreduction at low pH.

As $[IrN_4C_2]^+$ derivatives are easily synthesized and tunable, several photosensitizers were synthesized in Chapter 4 using a terpyridine (2244tpy or 2254tpy) as bridging ligand between the Iridium(III) center and the Cobalt(III) catalyst. Amongst a whole library of cyclometalated ligands, ppyH, $ppyF_2H$ and piqH were selected for H_2 photoproduction (Figure 6.2). All the obtained [Ir-Co] dyads and corresponding photosensitizers were extensively characterized and the photophysical properties were investigated. As

the ability of the dyads to transfer an electron from Ir(III) to Co(III) under irradiation was confirmed by acid titrations of the photosensitizers, all dyads were tested for H_2 photo-evolution. In all investigated productions, corresponding multicomponent reference systems displayed lower catalytic activities compared to the monocomponent systems. Interestingly, IrppyF_2-based dyads produced more efficiently hydrogen under green light than under blue light despite the lower energetic irradiation probably because of combination of the good quantum yield of the Iridium center and the low stability of the Cobalt catalyst. Nevertheless, no production could be detected under yellow light nor red light. Irpiq-based dyads displayed tremendous activities under all irradiation wavelengths, especially with similar turnover number under blue and yellow lights. More importantly, those dyads allowed the H_2 photoproduction for more than 110 h under red light irradiation, which makes them the best [Ir-Co] dyads described in the literature to date. It is worth mentioning that under green light, upon addition of dmgH_2 ligand (4 equivalents) for Cobalt catalyst stabilization, the obtained TON of 463 corresponds to more than 90% conversion of the proton source in the medium. All these features make Irpiq-2254tpy-Co dyad the best [Ir-Co] system ever described in the literature.

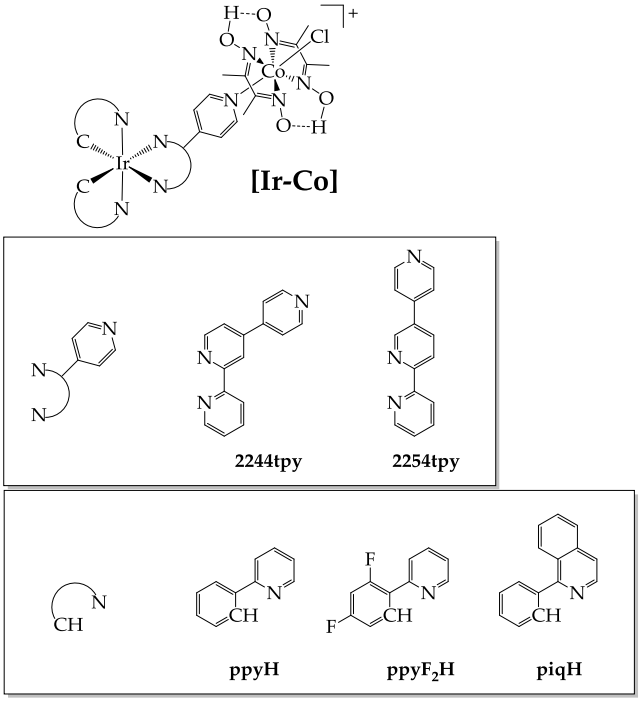

Figure 6.2 – Schematic representation of all investigated [Ir-Co] dyads

Based on the compatibility of Ir(III) photosensitizers with other catalytic systems, their ability to transfer an electron under irradiation and our experience in the field of photoredox catalysis, we decided to perform preliminary investigation of the Palladium-catalyzed C-H oxidation of aromatic allyl groups and more specifically Wacker oxidation and acetoxylation, using Ir(III) photosensitizer for photoinduced regeneration of a Pd(II) catalyst from reduced Pd(0) (Chapter 5). In that purpose, experiments were conducted with reference Irppy-bpy (= $[IrN_4C_2]^+$) as photooxidizing agent for Pd(0) reoxidation under aerobic conditions and revealed the viability of our system for both investigated reactions. Indeed, both kinetics and yield were significantly improved compared to the reference system without any ETM. These preliminary results constitute a tremendous progress

in the field of Pd(0) reoxidation and further improvements will allow the design of highly efficient Iridium-based photocatalytic regeneration systems for the reoxidation of Pd(0) into Pd(II).

In that purpose, a Master thesis performed by R. Bevernaegie was started during my Ph.D. and consisted in the synthesis and photophysical studies of a whole library of complexes (Figure 6.3). Such photosensitizers would reoxidize Pd(0) more efficiently and drastically improve the C-H oxidation yield.

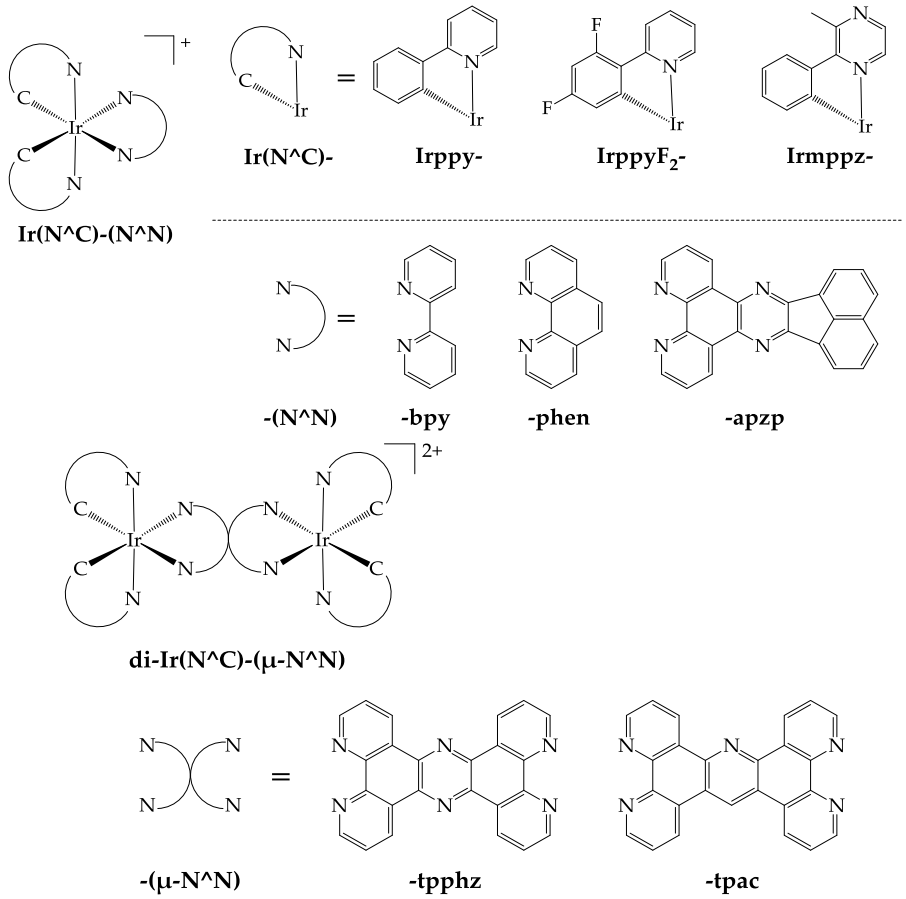

Figure 6.3 – Schematic structure of all the investigated Ir(III) complexes

6.2 Prospects

From the results unveiled in this Ph.D. thesis, this is clear that further improvements can be applied in the field of photocatalysis.

Despite the tremendous results obtained in Chapter 4 with [Ir-Co] dyads, the Cobalt catalyst stability has to be enhanced for an optimal H_2 photoproduction. In that purpose, new dioxime ligands directly combined to the Ir(III) photosensitizer can be investigated. Chelation of a 1,10-phenanthroline-5,6-dioxime (phendioxime) on an Ir(III) center has been achieved during this Ph.D. thesis (*not shown*) and a subsequent chelation on a Co(III) would yield to a new kind of [Ir-Co-Ir] triade (Figure 6.4). This variation still allows the photosensitizer to be tuned with diverse cyclometalated ligands, though ligands with extended conjugation are expected to be more efficient when visible light is used for the activation.

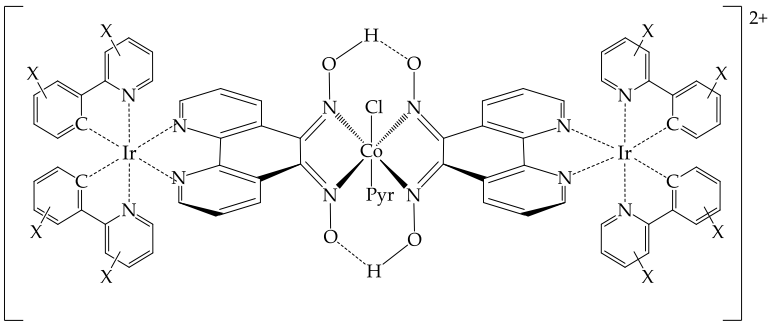

Figure 6.4 – New [Ir-Co-Ir] triad with phendioxime bridges for H_2 photoproduction

Another possibility for a better stability of the proton reduction catalyst is the design of new systems with a higher Co/Ir ratio. While a PET from the Iridium center to the Cobalt, the other center can be properly regenerated. Hence, two Cobalt catalysts can be linked to the

photosensitizer by a quaterpyridine ligand (Figure 6.5). Due to the higher activity of IrL-2254tpy-Co dyads compared to IrL-2244tpy-Co, a similar position of pendant pyridine moieties is expected to provide more active systems.

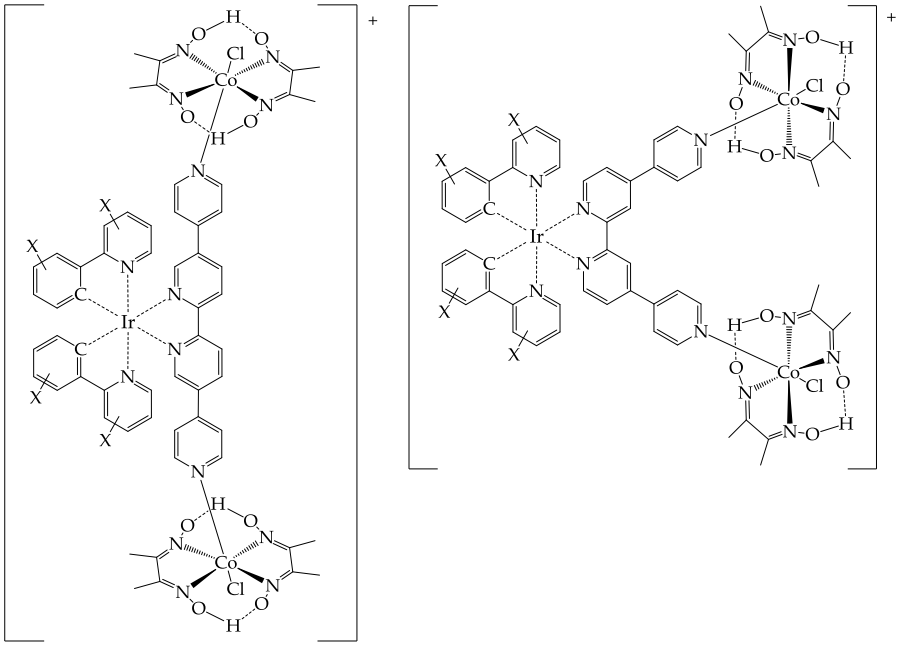

Figure 6.5 – New [Ir-Co_2] triad with quaterpyridine bridge for H_2 photoproduction

As water splitting is one of the most promising strategy for clean and low-cost hydrogen production, an Ir(III) photosensitizer connected to a hydrophilic moiety can be designed to produce H_2 and O_2 in aqueous medium. Because of its various properties involving hydrosolubility and electron conductivity,[16-18] DNA would be the ideal candidate as bridging ligand between the photosensitizer and a proton reduction catalyst. Despite multicomponent systems implying transition metal complexes intercalated within a double DNA strand are well described in the literature,[19-22] monocomponent Ir-DNA

systems are expected to work more efficiently. In that purpose, a bpy and a ppy moieties are added on a Cytidine residue and the obtained ligands are chelated to an Ir(III) center to afford $[IrN_4C_2]^+$ and $[IrN_3C_3]$ derivatives, respectively (Figure 6.6). The synthesis of both compounds has been explored and is now part of Michaël Abraham Ph.D. thesis.

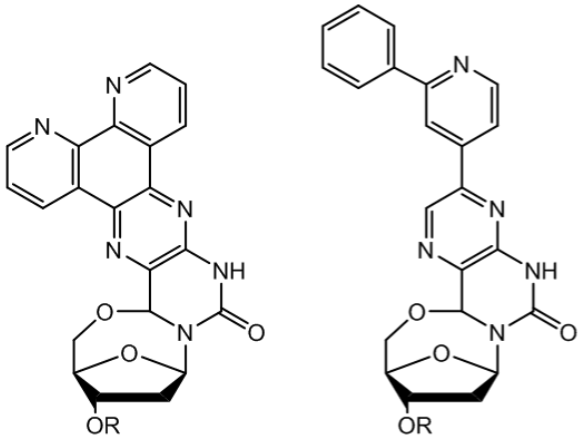

Figure 6.6 – Modified Cytidine with diimine (*left*) and cyclometalated (*right*) ligand for the synthesis of $[IrN_4C_2]^+$ and $[IrN_3C_3]$ derivatives, respectively

6.3 References

1. Jung, S.; Kang, Y.; Kim, H.-S.; Kim, Y.-H.; Lee, C.-L.; Kim, J.-J.; Lee, S.-K.; Kwon, S.-K., Effect of Substitution of Methyl Groups on the Luminescence Performance of IrIII Complexes: Preparation, Structures, Electrochemistry, Photophysical Properties and Their Applications in Organic Light-Emitting Diodes (OLEDs). *Eur. J. Inorg. Chem.* **2004**, *2004*, 3415-3423.
2. Baranoff, E.; Curchod, B. F.; Frey, J.; Scopelliti, R.; Kessler, F.; Tavernelli, I.; Rothlisberger, U.; Gratzel, M.; Nazeeruddin, M. K., Acid-induced degradation of phosphorescent dopants for OLEDs and its application to the synthesis of tris-heteroleptic iridium(III) bis-cyclometalated complexes. *Inorg. Chem.* **2012**, *51*, 215-224.
3. Mauro, M.; Schuermann, K. C.; Prétôt, R.; Hafner, A.; Mercandelli, P.; Sironi, A.; De Cola, L., Complex Iridium(III) Salts: Luminescent Porous Crystalline Materials. *Angew. Chem. Int. Ed.* **2010**, *49*, 1222-1226.
4. Ren, X.; Kondakova, M. E.; Giesen, D. J.; Rajeswaran, M.; Madaras, M.; Lenhart, W. C., Coumarin-based, electron-trapping iridium complexes as highly efficient and stable phosphorescent emitters for organic light-emitting diodes. *Inorg. Chem.* **2010**, *49*, 1301-1303.
5. Leung, K. H.; He, H. Z.; Ma, V. P.; Chan, D. S.; Leung, C. H.; Ma, D. L., A luminescent G-quadruplex switch-on probe for the highly selective and tunable detection of cysteine and glutathione. *Chem. Commun.* **2013**, *49*, 771-773.
6. Wu, Z.; Mu, J.; Wang, Q.; Chen, X.; Jensen, L.; Yi, C.; Li, M.-J., Hydroxyl and amino functionalized cyclometalated Ir(III) complexes: Synthesis, characterization and cytotoxicity studies. *J. Organomet. Chem.* **2015**, *791*, 175-182.
7. Steunenberg, P.; Ruggi, A.; van den Berg, N. S.; Buckle, T.; Kuil, J.; van Leeuwen, F. W.; Velders, A. H., Phosphorescence imaging of living cells with amino acid-functionalized tris(2-phenylpyridine)iridium(III) complexes. *Inorg. Chem.* **2012**, *51*, 2105-2114.
8. Fihri, A.; Artero, V.; Pereira, A.; Fontecave, M., Efficient H2-producing photocatalytic systems based on cyclometalated iridium- and tricarbonylrhenium-diimine photosensitizers and cobaloxime catalysts. *Dalton Trans.* **2008**, 5567-5569.
9. DiSalle, B. F.; Bernhard, S., Orchestrated photocatalytic water reduction using surface-adsorbing iridium photosensitizers. *J. Am. Chem. Soc.* **2011**, *133*, 11819-11821.
10. Zoller, J.; Fabry, D. C.; Ronge, M. A.; Rueping, M., Synthesis of Indoles Using Visible Light: Photoredox Catalysis for Palladium-Catalyzed C-H Activation. *Angew. Chem. Int. Ed.* **2014**, *53*, 13264-13268.

11. Govindaswamy, P.; Canivet, J.; Therrien, B.; Süss-Fink, G.; Štěpnička, P.; Ludvík, J., Mono and dinuclear rhodium, iridium and ruthenium complexes containing chelating 2,2'-bipyrimidine ligands: Synthesis, molecular structure, electrochemistry and catalytic properties. *J. Organomet. Chem.* **2007**, *692*, 3664-3675.
12. Xuan, J.; Zeng, T.-T.; Feng, Z.-J.; Deng, Q.-H.; Chen, J.-R.; Lu, L.-Q.; Xiao, W.-J.; Alper, H., Redox-Neutral α-Allylation of Amines by Combining Palladium Catalysis and Visible-Light Photoredox Catalysis. *Angew. Chem. Int. Ed.* **2015**, *54*, 1625-1628.
13. Hoffmann, N., Combining Photoredox and Metal Catalysis. *ChemCatChem* **2015**, *7*, 393-394.
14. Troian-Gautier, L.; Mugeniwabagara, E.; Fusaro, L.; Moucheron, C.; Kirsch-De Mesmaeker, A.; Luhmer, M., pH Dependence of Photoinduced Electron Transfer with [Ru(TAP)3](2). *Inorg. Chem.* **2017**, *56*, 1794-1803.
15. Troian-Gautier, L.; Mugeniwabagara, E.; Fusaro, L.; Cauet, E.; Kirsch-De Mesmaeker, A.; Luhmer, M., Photo-CIDNP Reveals Different Protonation Sites Depending on the Primary Step of the Photoinduced Electron-/Proton-Transfer Process with Ru(II) Polyazaaromatic Complexes. *J. Am. Chem. Soc.* **2017**, *139*, 14909-14912.
16. Delaney, S.; Barton, J. K., Long-range DNA charge transport. *J. Org. Chem.* **2003**, *68*, 6475-6483.
17. Boynton, A. N.; Marcelis, L.; Barton, J. K., [Ru(Me4phen)2dppz](2+), a Light Switch for DNA Mismatches. *J. Am. Chem. Soc.* **2016**, *138*, 5020-5023.
18. Sontz, P. A.; Mui, T. P.; Fuss, J. O.; Tainer, J. A.; Barton, J. K., DNA charge transport as a first step in coordinating the detection of lesions by repair proteins. *Proc. Natl. Acad. Sci. USA* **2012**, *109*, 1856-1861.
19. Stimpson, S.; Jenkinson, D. R.; Sadler, A.; Latham, M.; Wragg, A.; Meijer, A. J.; Thomas, J. A., Tuning the excited state of water-soluble Ir(III)-based DNA intercalators that are isostructural with [Ru(II)(NN)2(dppz)] light-switch complexes. *Angew. Chem. Int. Ed.* **2015**, *54*, 3000-3003.
20. Gill, M. R.; Thomas, J. A., Ruthenium(II) polypyridyl complexes and DNA--from structural probes to cellular imaging and therapeutics. *Chemical Society Reviews* **2012**, *41*, 3179-3192.

21. Ahmad, H.; Wragg, A.; Cullen, W.; Wombwell, C.; Meijer, A. J.; Thomas, J. A., From intercalation to groove binding: switching the DNA-binding mode of isostructural transition-metal complexes. *Chem. Eur. J.* **2014**, *20*, 3089-3096.

22. Vargiu, A. V.; Magistrato, A., Detecting DNA mismatches with metallo-insertors: a molecular simulation study. *Inorg. Chem.* **2012**, *51*, 2046-2057.

CHAPTER 7

Instrumental techniques

7.1 Chapter 2 - Tris-bidentate Ir(III) polypyridyl and cyclometalated complexes: synthesis and comparative photoredox behavior

7.1.1 Nuclear Magnetic Resonance (^{1}H NMR)

^{1}H NMR spectra have been recorded on a Bruker AC-300 Avance II (^{1}H: 300 MHz), a Varian GEMINI-2000 (^{1}H: 300 MHz) or a Bruker AM-500 (^{1}H: 500 MHz). Spectra were obtained in $CDCl_3$, CD_3CN and $(CD_3)_2CO$. The chemical shifts (given in ppm) were measured versus the residual peak of solvent as the internal standard. The constants coupling (J) are given in Hertz. Multiplicity is given as follows: s = singlet, d = doublet, t = triplet, q = quadruplet, m = multiplet, br = broad.

7.1.2 Mass Spectrometry

HRMS were recorded on a Q-Extractive orbitrap from ThermoFisher. Samples were ionized either by ESI or by APCI (positive mode) (capillary temperature: 250 °C, vaporizer temperatures: 250 °C or 400 °C, sheath gas flow rate: 20).

7.1.3 UV-visible Absorption Spectrophotometry

UV-vis absorption spectra were recorded on a Shimadzu UV-1700. Data were converted and transferred to a PC computer. A halogen lamp from Narva-light (12V/20 W) was used to generate light

in the visible range. Near-UV light was produced from a Shimadzu deuterium lamp.

7.1.4 Determination of Molar Extinction Coefficient

Molar extinction coefficients were determined by measuring absorbance of different solutions with known complex concentrations in the appropriate solvent (by weighting). A linear relation was found when absorbance of these solutions in function of concentration was plotted. The molar extinction coefficient was given by the slope of this plot according to the Beer-Lambert equation ($A = \varepsilon.l.C$ where A is the absorbance of the solution, ε is the molar extinction coefficient, l is the optical path length and C is the concentration).

7.1.5 Emission Spectroscopy

Room temperature luminescence spectra were recorded on Varian Cary Eclipse. Excitation source was a Xe lamp and a phototube was used for detection. Luminescence emission at 77 K was recorded on a FluoroLog3 FL3-22 from Jobin Yvon equipped with an 18V 450W Xenon Short Arc lamp and an R928P photomultiplier, using an Oxford Instrument Optistat DN nitrogen cryostat controlled by an Oxford Intelligent Temperature Controller (ITC503S) instrument. Data were converted and transferred to a PC computer.

7.1.6 Luminescence Lifetime

Luminescence lifetimes were measured with a modified Applied Photophysics laser kinetic spectrometer by exciting the samples at 355 nm with a Nd-YAG pulsed laser (Continuum NY 61-10). Emitted light as a function of time was detected with a R-928 Hamamatsu photomultiplier tube whose output was applied to a digital oscilloscope (Hewlett-Packard HP 54200A) interfaced with a Dell Dimension DE051 computer. Signals were averaged over at least 16 shots and corrected for baseline. Igor 6.1 software was used for the decay analyses.

7.1.7 Cyclic Voltammetry

Cyclic voltammetry was carried out in a one-compartment cell, using a glassy carbon disk working electrode (approximate area = 0.03 cm^2), a platinum wire as counter electrode and an Ag/AgCl electrode as reference electrode. The potential of the working electrode was controlled by an Autolab PGSTAT 100 potentiostat through a PC interface. The cyclic voltammograms were recorded with a sweep rate of 100 or 400 mV.s-1, either in dried acetonitrile (Acros, HPLC grade) or in dried DMF (Sigma-Aldrich, HPLC grade). Tetrabutylammonium perchlorate (0.1 M) was used as supporting electrolyte and the samples were purged by Argon before each measurement.

7.1.8 Stern-Volmer Measurements

Stern-Volmer measurements were performed under air in a quartz cell of 5 mm optical path length that was filled with 700 μL of 0.1 mM Ir(III) photosensitizer solution in acetonitrile with increasing amounts of quencher. Absorption and emission spectra were recorded as previously described. The spectra were corrected for the instrument response.

7.2 Chapter 3 - Exploring photoreactions between pH sensitive [R-IrN_5C_1]$^{2+}$ and dGMP by photo-Chemically Induced Dynamic Nuclear Polarization (photo-CIDNP)

7.2.1 Materials

[R-IrN_5C_1]$^{2+}$ was synthesized and purified as previously described. 2'-deoxyguanosine-5'-monophosphate (dGMP) disodium salt was purchased from Sigma-Aldrich and used without further purification. 4,4-dimethyl-4-silapentane-1-sulfonic acid sodium salt (DSS) was purchased from Sigma Aldrich and was used as received. For the NMR measurements, concentrated acetate-phosphate buffers (20 mmol.L^{-1}) were prepared in D_2O for every measurements using D_3PO_4 (Sigma), CD_3COOD (Sigma), DCl (Sigma) and NaOD (Sigma). The pH of the solutions was measured using a Consort P601 pH meter. The solutions were deoxygenated upon Argon bubbling (Air Liquide) for at least 30 min. For the Stern-Volmer measurements, the same conditions were used with non-deuterated reagents and solvents.

7.2.2 NMR Measurements

Samples were prepared by mixing suitable volumes of aqueous (D_2O) stock solutions of [R-IrN_5C_1]Cl_2, dGMP, DSS and acetate-phosphate buffer. The pH* which is a direct reading in D_2O solution of a H_2O-calibrated pH-meter was adjusted to the desired value using NaOD or DCl. D_2O was then added to reach a volume of 600 µL and the following concentrations: ~ 0.1 mM [R-IrN_5C_1]Cl_2, ~ 2 mM dGMP, 0.1 mM DSS and 20 mM acetate-phosphate buffer. A different sample

was prepared for each pH value. It was transferred into a standard 5 mm NMR tube and thoroughly deoxygenated prior to careful introduction of the optical fiber required for the photo-CIDNP experiment and sealed with Parafilm®. The samples were illuminated in the NMR magnet, from above, via a 1 mm diameter optical fiber positioned inside a coaxial insert (Wilmad WGS 5BL) whose tip was about 3 mm above the top of the NMR receiver coil, as illustrated in Figure 7.1.

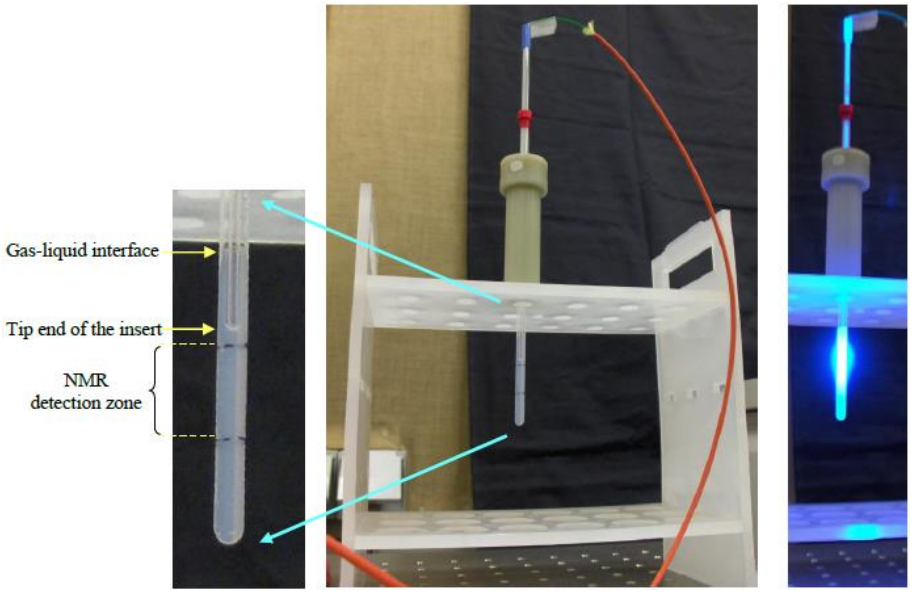

Figure 7.1 – Sample set-up for photo-CIDNP experiment (a dilute polymer colloid was used to get strong light dispersion).

The NMR measurements were carried out at 298 K on a 600 MHz Varian VNMRS spectrometer equipped with a standard 5 mm Triple Inverse z-Gradient probe. The pulse sequence used for the ^{1}H photo-CIDNP experiments is depicted in Figure 7.2. The illumination period of 100 ms was followed by a short delay prior to the non-selective ^{1}H RF pulse and subsequent acquisition of the free induction

decay (FID).The spectral width was about 16 ppm centered at the signal of the solvent (HDO). The processing of the NMR spectra comprised exponential apodization of the FID (lb = 2 Hz), zero-filling (spectrum digital resolution of 0.07 Hz/point) and calibration of the chemical shift scale with respect to the methyl signal of DSS (δ = 0.00 ppm).

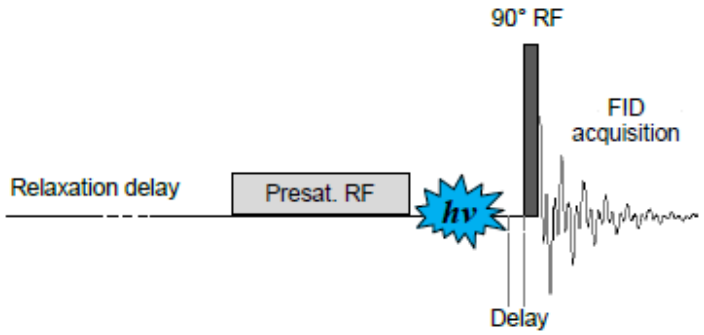

Figure 7.2 – ^{1}H NMR pulse sequence used for the photo-CIDNP experiments. The duration of the successive components is not represented on scale: the relaxation delay is followed by (i) continuous-wave radio frequency (RF) irradiation for presaturation of the signal of the solvent, (ii) blue-light illumination for photo-CIDNP spectra or a corresponding waiting delay for control spectra, (iii) a short delay intended to allow radical recombination so as to avoid paramagnetic broadening of the NMR signals, (iv) high-power non-selective RF and (v) acquisition of the FID. The sequence pulse was repeated 12 times.

7.3 Chapter 4 - Photocatalytic H_2 production using Ir(III)-Co(III) dyads

7.3.1 Theoretical studies

All complexes were studied by DFT[1-4] and TD-DFT[5-7] using Gaussian9.[8] The B3LYP[9-11] method and two basis set (6-31G*[12] for C, H, and N / VDZ (valence double ζ) with the SBKJC effective core potential basis set[13-16] for Ir) were used. Geometry optimizations were conducted without symmetry constraints. Frequency calculations on each optimized structure confirmed that energy minima had been reached in all cases. The energy, oscillator strength, and related MO contributions for the 100 lowest singlet–singlet and 10 lowest singlet–triplet excitations were obtained from the TD-DFT/singlets and the TD-DFT/triplets output files, respectively, for the S_0-optimized geometry. GaussView5.09,[17] GaussSum3.0[18] and Chemissian4.43[19] were used for data analysis, visualization and surface plots. All calculations were performed in MeCN solution by use of the polarized continuum (PCM) solvation model as implemented in Gaussian 09.[20-21]

7.3.3 Set-up for gas chromatography

Monitoring of hydrogen evolution is measured using a Perkin Elmer Clarus-480 gas chromatograph (GC) with a thermal conductivity detector, Argon as carrier and eluent gas, a 7′ HayeSep N 60/80 pre-column, a 9′ molecular sieve 13x45/60 column and a 2 mL injection loop. Three distinct solutions for photosensitizer, for catalyst and lastly for sacrificial donor and acid source (HBF_4 48% water) (or

two solutions when [Ir-Co] dyads are used) are mixed together to obtain 5 mL of sample solutions in standard 20 mL headspace vials. Those vials are placed on LED panel in a thermostatic bath set at 20°C. They were sealed with a rubber septum pierced with two stainless steel tubes. The first tube carried an Argon flow pre-bubbled in solvent. The flow was set to 10 mL/min adjusted with a manual flow controller (Porter, 1000) and referenced with a digital flowmeter (Perkin Elmer FlowMark). The second tube leads the flow through a 2 mL overflow protection vial, then through an 8-port stream select valve (VICCI) and finally to the GC sample loop. A microprocessor (Arduino Uno) coupled with a custom PC interface allowed for timed injections. For general calibration of the H_2 production, certified Argon stock cylinders at 500 ppm, 100 ppm and 50 ppm of hydrogen are set to deliver a specific flow (inserted at the pre-bubbler, to keep the vapor matrix consistent). The measured results, independent of flow rate (under same pressure) can be easily converted into a rate of hydrogen according to equation 7.1.

$$H_2 \text{ rate } (\mu L/min) = [H_2 \text{ standard}] \text{ (ppm)} \times \text{ Ar flow rate (mL/min)} \qquad \text{eq 7.1}$$

For a specific Argon flow, a syringe pump (New Era Pump) equipped with a gas-tight syringe (SGE) and a 26s gauge needle (Hamilton) was used to bubble different rates of 500 ppm hydrogen in Argon gas into the sample, to a minimum of 0.1 mL/minute. This gave a linear fit for peak area of H_2 versus the flow rates of H_2 (Figure 7.3).

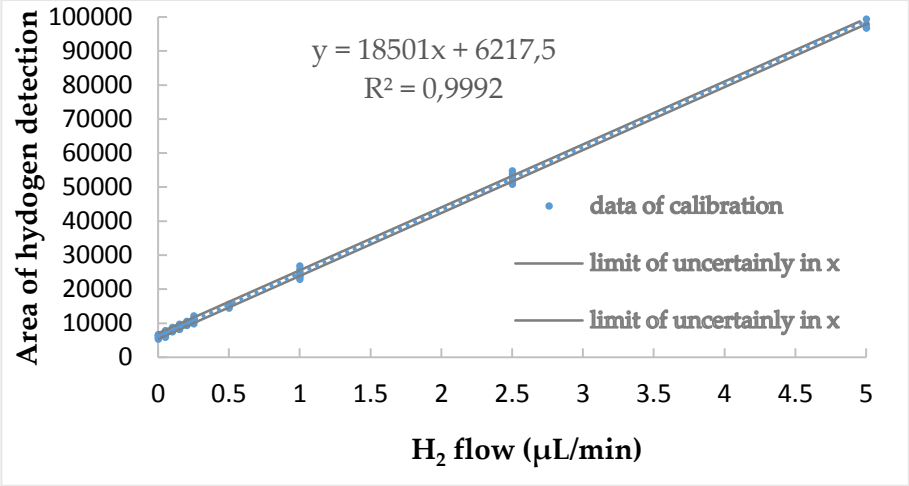

Figure 7.3 – Calibration curve of hydrogen flux in 10 mL/min of carrier gas Argon (0 to 5 μL_{H2}/min). The two grey lines show the uncertainly in x of the calibration curve. The uncertainly in x is ± 0.045 μL_{H2}/min.

7.4 References

1. Parr, R. G.; Weitao, Y., *Density-Functional Theory of Atoms and Molecules*. Oxford University Press: **1994**.
2. Salahub, D. R.; Zerner, M. C., *The Challenge of d and f Electrons*. **1989**; Vol. 394.
3. Hohenberg, P.; Kohn, W., Inhomogeneous Electron Gas. *Physical Review* **1964**, *136*, B864-B871.
4. Kohn, W.; Sham, L. J., Self-Consistent Equations Including Exchange and Correlation Effects. *Physical Review* **1965**, *140*, A1133-A1138.
5. Bauernschmitt, R.; Ahlrichs, R., Treatment of electronic excitations within the adiabatic approximation of time dependent density functional theory. *Chem. Phys. Lett.* **1996**, *256*, 454-464.
6. Casida, M. E.; Jamorski, C.; Casida, K. C.; Salahub, D. R., Molecular excitation energies to high-lying bound states from time-dependent density-functional response theory: Characterization and correction of the time-dependent local density approximation ionization threshold. *The Journal of Chemical Physics* **1998**, *108*, 4439-4449.
7. Stratmann, R. E.; Scuseria, G. E.; Frisch, M. J., An efficient implementation of time-dependent density-functional theory for the calculation of excitation energies of large molecules. *The Journal of Chemical Physics* **1998**, *109*, 8218-8224.
8. Frisch, M. J.; Trucks, G. W.; Schlegel, H. B.; Scuseria, G. E.; Robb, M. A.; Cheeseman, J. R.; Scalmani, G.; Barone, V.; Mennucci, B.; Petersson, G. A.; Nakatsuji, H.; Caricato, M.; Li, X.; Hratchian, H. P.; Izmaylov, A. F.; Bloino, J.; Zheng, G.; Sonnenberg, J. L.; Hada, M.; Ehara, M.; Toyota, K.; Fukuda, R.; Hasegawa, J.; Ishida, M.; Nakajima, T.; Honda, Y.; Kitao, O.; Nakai, H.; Vreven, T.; Montgomery Jr., J. A.; Peralta, J. E.; Ogliaro, F.; Bearpark, M. J.; Heyd, J. J.; Brothers, E. N.; Kudin, K. N.; Staroverov, V. N.; Kobayashi, R.; Normand, J.; Raghavachari, K.; Rendell, A. P.; Burant, J. C.; Iyengar, S. S.; Tomasi, J.; Cossi, M.; Rega, N.; Millam, J. M.; Klene, M.; Knox, J. E.; Cross, J. B.; Bakken, V.; Adamo, C.; Jaramillo, J.; Gomperts, R.; Stratmann, R. E.; Yazyev, O.; Austin, A. J.; Cammi, R.; Pomelli, C.; Ochterski, J. W.; Martin, R. L.; Morokuma, K.; Zakrzewski, V. G.; Voth, G. A.; Salvador, P.; Dannenberg, J. J.; Dapprich, S.; Daniels, A. D.; Farkas, O.; Foresman, J. B.; Ortiz, J. V.; Cioslowski, J.; Fox, D. J. *Gaussian 09, Revision E.01*, Gaussian, Inc., Wallingford, CT, 2009.
9. Miehlich, B.; Savin, A.; Stoll, H.; Preuss, H., Results obtained with the correlation energy density functionals of becke and Lee, Yang and Parr. *Chem. Phys. Lett.* **1989**, *157*, 200-206.
10. Becke, A. D., Density-functional thermochemistry. III. The role of exact exchange. *The Journal of Chemical Physics* **1993**, *98*, 5648-5652.

11. Lee, C.; Yang, W.; Parr, R. G., Development of the Colle-Salvetti correlation-energy formula into a functional of the electron density. *Physical Review B* **1988**, *37*, 785-789.
12. Mitin, A. V.; Baker, J.; Pulay, P., An improved 6-31G* basis set for first-row transition metals. *J. Chem. Phys.* **2003**, *118*, 7775-7782.
13. Stevens, W. J.; Krauss, M.; Basch, H.; Jasien, P. G., Relativistic compact effective potentials and efficient, shared-exponent basis sets for the third-, fourth-, and fifth-row atoms. *Can. J. Chem.* **1992**, *70*, 612-630.
14. Cundari, T. R.; Stevens, W. J., Effective core potential methods for the lanthanides. *The Journal of Chemical Physics* **1993**, *98*, 5555-5565.
15. Stevens, W. J.; Basch, H.; Krauss, M., Compact effective potentials and efficient shared-exponent basis sets for the first- and second-row atoms. *The Journal of Chemical Physics* **1984**, *81*, 6026-6033.
16. Binkley, J. S.; Pople, J. A.; Hehre, W. J., Self-consistent molecular orbital methods. 21. Small split-valence basis sets for first-row elements. *J. Am. Chem. Soc.* **1980**, *102*, 939-947.
17. Dennington, R.; Keith, J. A.; Millam, J. M. *GaussView, Version 5.09*, Shawnee Mission, KS, 2009.
18. O'Boyle, N. M.; Tenderholt, A. L.; Langner, K. M., cclib: a library for package-independent computational chemistry algorithms. *J. Comput. Chem.* **2008**, *29*, 839-845.
19. Skripnikov, L. *Chemissian, V4.43*, 2005-2016.
20. Miertuš, S.; Scrocco, E.; Tomasi, J., Electrostatic interaction of a solute with a continuum. A direct utilization of AB initio molecular potentials for the prevision of solvent effects. *Chem. Phys.* **1981**, *55*, 117-129.
21. Tomasi, J.; Mennucci, B.; Cammi, R., Quantum mechanical continuum solvation models. *Chem. Rev.* **2005**, *105*, 2999-3093.

CHAPTER 8

Supporting information

8.1 Chapter 2 – Tris-bidentate Ir(III) polypyridyl and cyclometalated complexes: synthesis and comparative photoredox behavior

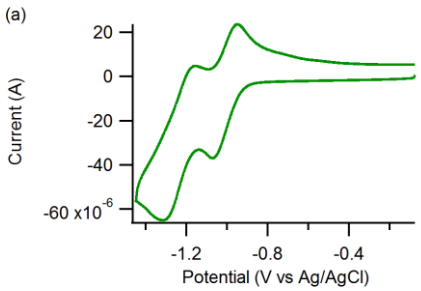

Figure S2.1 – Voltammogram of $[IrN_4Cl_2]^+$ measured by cyclic voltammetry in dry acetonitrile with Bu_4NClO_4 0.1 M as supporting electrolyte (sweeping rate = 0.1 V/s) for reduction (no oxidation wave detected)

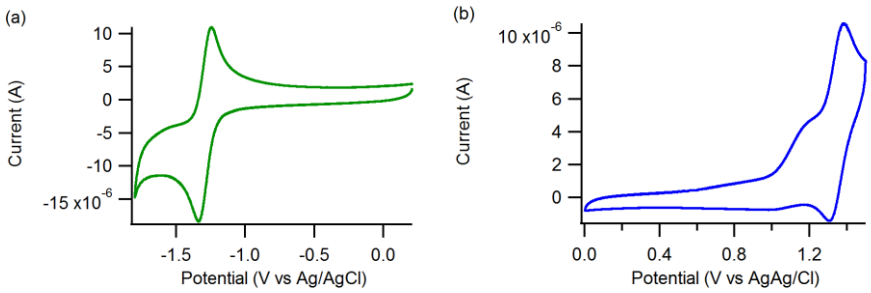

Figure S2.2 – Voltammogram of $[IrN_3C_1Cl_2]$ measured by cyclic voltammetry in dry acetonitrile with Bu_4NClO_4 0.1 M as supporting electrolyte (sweeping rate = 0.1 V/s) for (a) reduction (b) oxidation

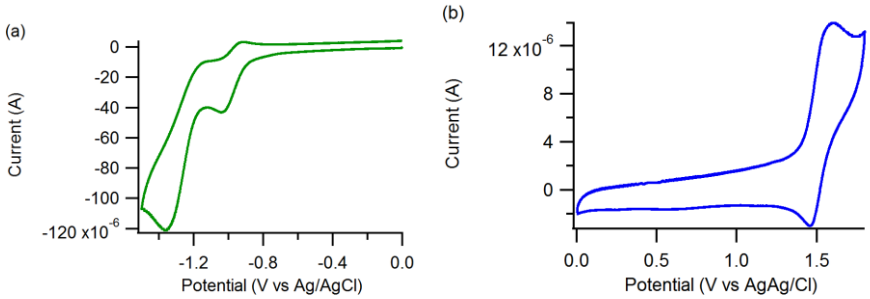

Figure S2.3 – Voltammogram of protonated $[IrN_3C_1Cl_2\text{-}H]^+$ measured by cyclic voltammetry in dry acetonitrile with Bu_4NClO_4 0.1 M as supporting electrolyte (sweeping rate = 0.1 V/s) for (a) reduction (b) oxidation.

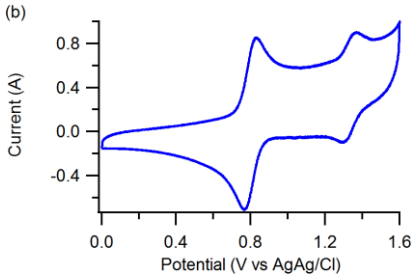

Figure S2.4 – Voltammogram of complex $[IrN_3C_3]$ measured by cyclic voltammetry in dry acetonitrile with Bu_4NClO_4 0.1 M as supporting electrolyte (sweeping rate = 0.1 V/s) for oxidation (no reduction wave detected)

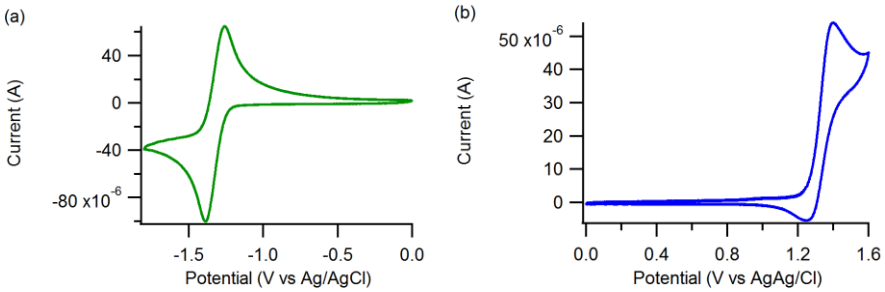

Figure S2.5 – Voltammogram of complex $[IrN_4C_2]^+$ measured by cyclic voltammetry in dry acetonitrile with Bu_4NClO_4 0.1 M as supporting electrolyte (sweeping rate = 0.1 V/s) for (a) reduction and (b) oxidation

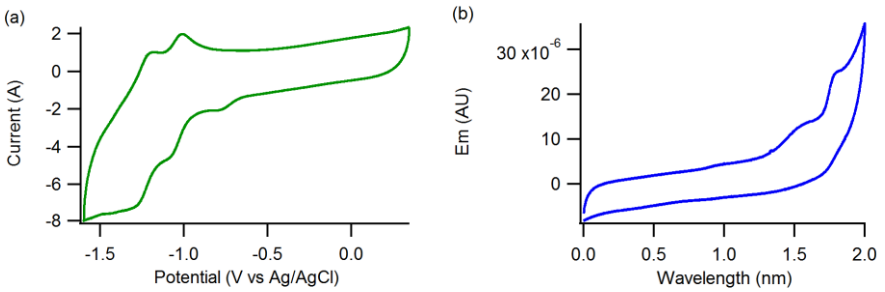

Figure S2.6 – Voltammogram of complex $[IrN_5C_1]^{2+}$ measured by cyclic voltammetry in dry acetonitrile with Bu_4NClO_4 0.1 M as supporting electrolyte (sweeping rate = 0.1 V/s) for (a) reduction and (b) oxidation

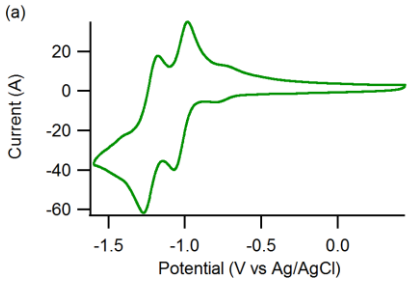

Figure S2.7 – Voltammogram of complex $[R\text{-}IrN_5C_1]^{2+}$ measured by cyclic voltammetry in dry acetonitrile with Bu_4NClO_4 0.1 M as supporting electrolyte (sweeping rate = 0.1 V/s) for reduction (no oxidation wave detected)

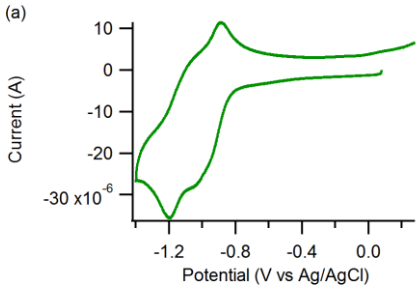

Figure S2.8 – Voltammogram of protonated complex $[R\text{-}IrN_5C_1\text{-}H]^{3+}$ measured by cyclic voltammetry in dry acetonitrile with Bu_4NClO_4 0.1 M as supporting electrolyte (sweeping rate = 0.1 V/s) for reduction (no oxidation wave detected)

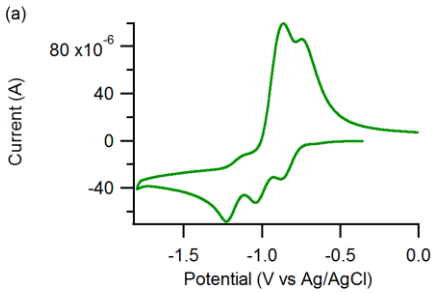

Figure S2.9 – Voltammogram of complex $[IrN_6]^{3+}$ measured by cyclic voltammetry in dry acetonitrile with Bu_4NClO_4 0.1 M as supporting electrolyte (sweeping rate = 0.1 V/s) for reduction (no oxidation wave detected)

$$I(\tilde{\nu}) = \sum_{\nu_m=0}^{\infty} \sum_{\nu_n=0}^{\infty} \left[\left(\frac{E_0 - \nu_m * \hbar * \omega_m - \nu_n * \hbar * \omega_n}{E_0} \right)^4 \right) * \frac{S_M^{\nu_m}}{\nu_m!} * \frac{S_N^{\nu_n}}{\nu_n!} *$$

$$\exp\{-4\ln 2[(\tilde{\nu} - E_0 + \nu_m * \hbar * \omega_m + \nu_n * \hbar * \omega_n)/\Delta\tilde{\nu}_{1/2}]^2\} \Big] \qquad \text{eq S2.1}$$

Table S2.1 – Emission parameters for Ir(III) complexes evaluated by Franck-Condon line-shape analysis according to equation S2.1.

Complex	E_{00} (cm^{-1}) [nm]	$\hbar * \omega_m$ (cm^{-1})	S_M	$\hbar * \omega_n$ (cm^{-1})	S_N	$\Delta\upsilon_{1/2}$ (cm^{-1})
$[IrN_3C_3]$	20259 [493]	1227	0.87	378	2.39	936
$[IrN_4C_2]^+$	17552 [570]	793	1.42	4486	0.26	2434
$[IrN_5C_1]^{2+}$	21221 [471]	990	1.84	962	0.84	1431
$[R\text{-}IrN_5C_1]^{2+}$	21565 [464]	1375	1.27	732	0.86	860
$[R\text{-}IrN_5C_1\text{-}H]^{3+}$	20707 [483]	1411	1.13	734	0.70	853
$[IrN_6]^{3+}$	22163 [451]	1424	1.57	830	0.88	812

8.2 Chapter 3 – Exploring photoreactions between pH sensitive [R-IrN_5C_1]$^{2+}$ and dGMP by photo-Chemically Induced Dynamic Nuclear Polarization

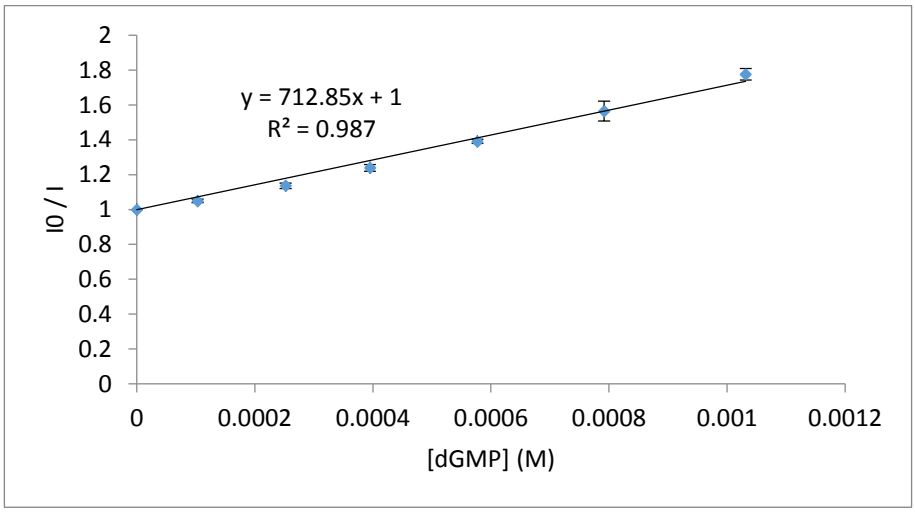

Figure S3.1 – Stern-Volmer plots of the luminescence quenching (hypsochromic band) of a 10^{-4} M solution of [R-IrN_5C_1]$^{2+}$ in aqueous acetate-phosphate buffer upon the addition of dGMP at pH = 0.22

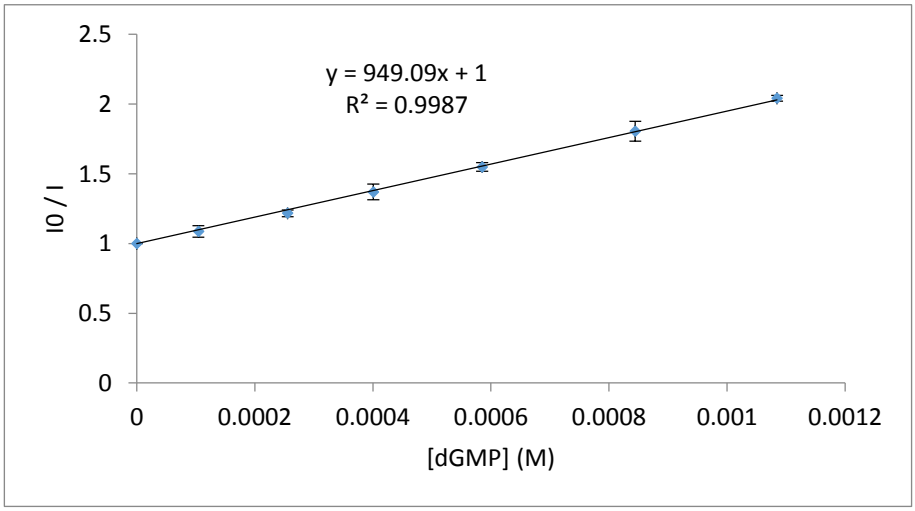

Figure S3.2 – Stern-Volmer plots of the luminescence quenching (hypsochromic band) of a 10^{-4} M solution of [R-IrN_5C_1]$^{2+}$ in aqueous acetate-phosphate buffer upon the addition of dGMP at pH = 0.99

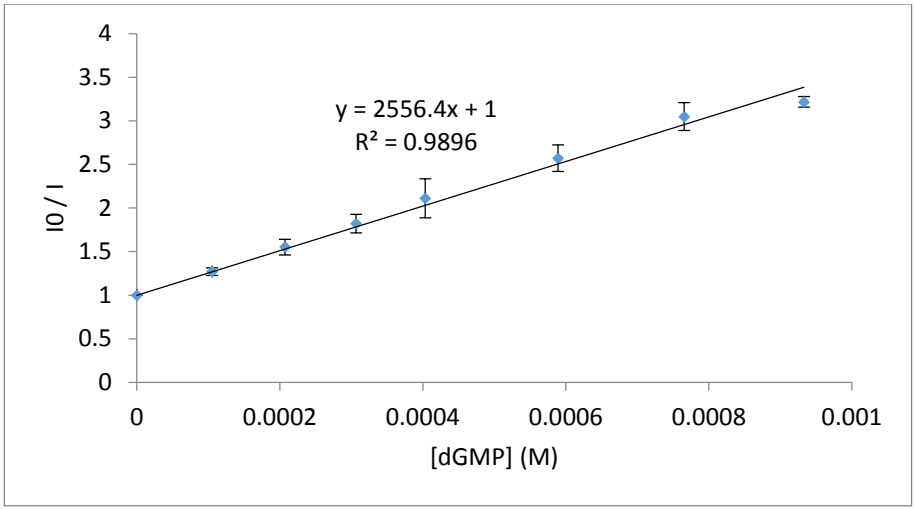

Figure S3.3 – Stern-Volmer plots of the luminescence quenching (hypsochromic band) of a 10^{-4} M solution of $[R\text{-}IrN_5C_1]^{2+}$ in aqueous acetate-phosphate buffer upon the addition of dGMP at pH = 1.43

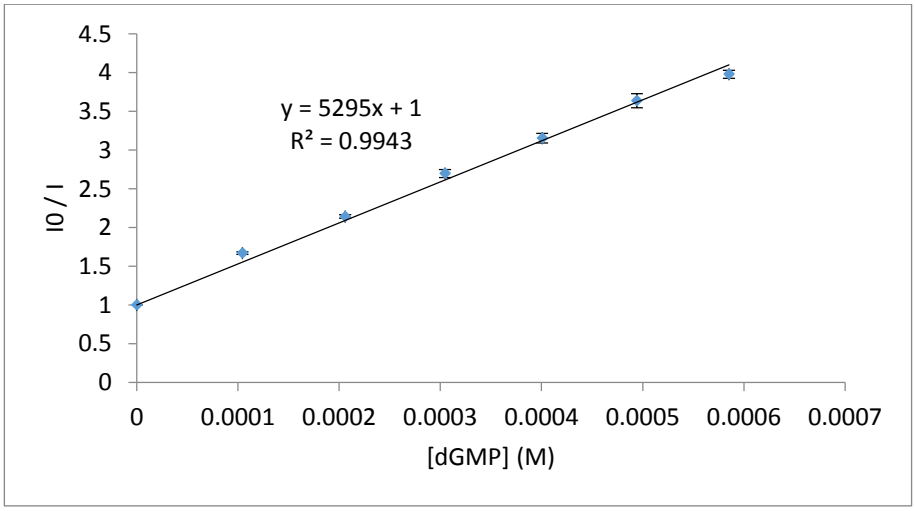

Figure S3.4 – Stern-Volmer plots of the luminescence quenching (hypsochromic band) of a 10^{-4} M solution of $[R\text{-}IrN_5C_1]^{2+}$ in aqueous acetate-phosphate buffer upon the addition of dGMP at pH = 2.55

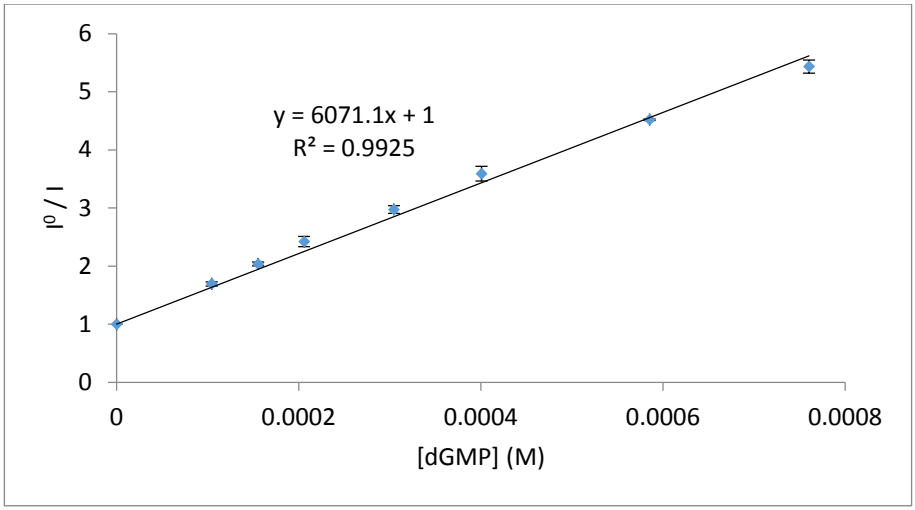

Figure S3.5 – Stern-Volmer plots of the luminescence quenching (hypsochromic band) of a 10^{-4} M solution of $[R\text{-}IrN_5C_1]^{2+}$ in aqueous acetate-phosphate buffer upon the addition of dGMP at pH = 3.43

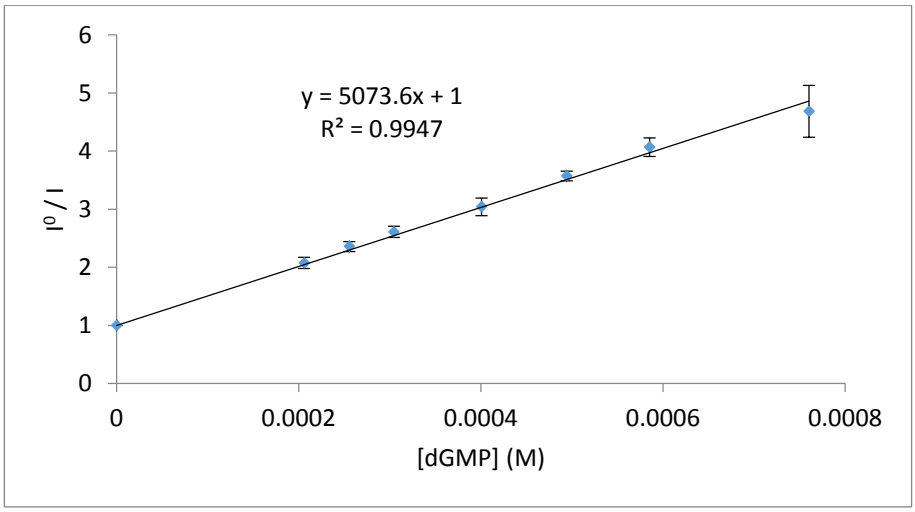

Figure S3.6 – Stern-Volmer plots of the luminescence quenching (hypsochromic band) of a 10^{-4} M solution of $[R\text{-}IrN_5C_1]^{2+}$ in aqueous acetate-phosphate buffer upon the addition of dGMP at pH = 5.04

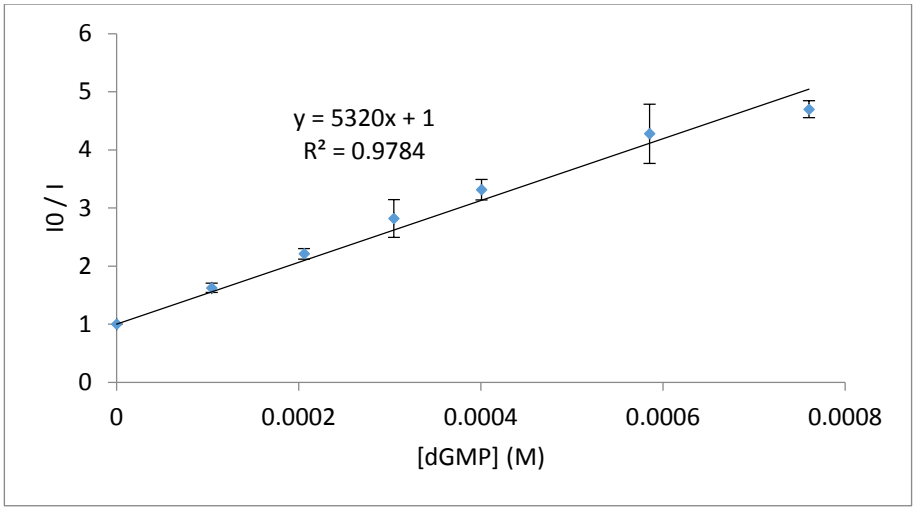

Figure S3.7 – Stern-Volmer plots of the luminescence quenching (hypsochromic band) of a 10^{-4} M solution of $[R\text{-}IrN_5C_1]^{2+}$ in aqueous acetate-phosphate buffer upon the addition of dGMP at pH = 6.92

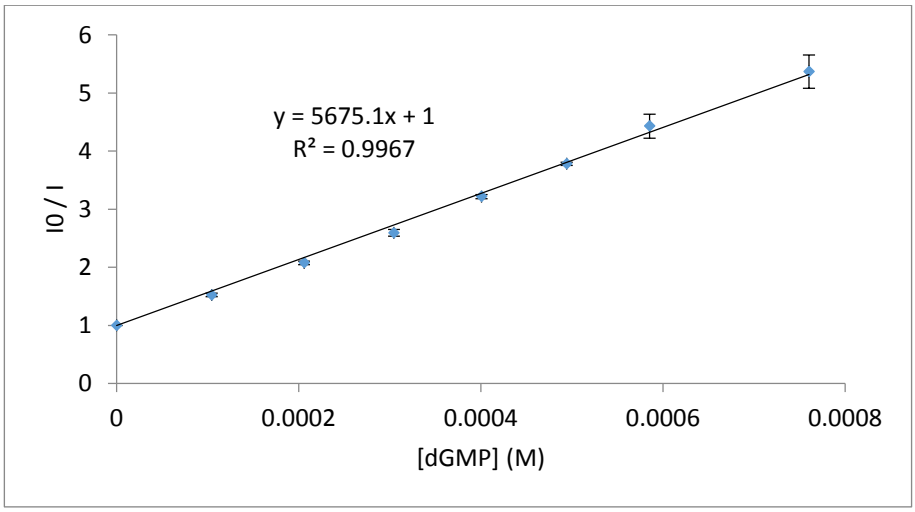

Figure S3.8 – Stern-Volmer plots of the luminescence quenching (hypsochromic band) of a 10^{-4} M solution of $[R\text{-}IrN_5C_1]^{2+}$ in aqueous acetate-phosphate buffer upon the addition of dGMP at pH = 7.97

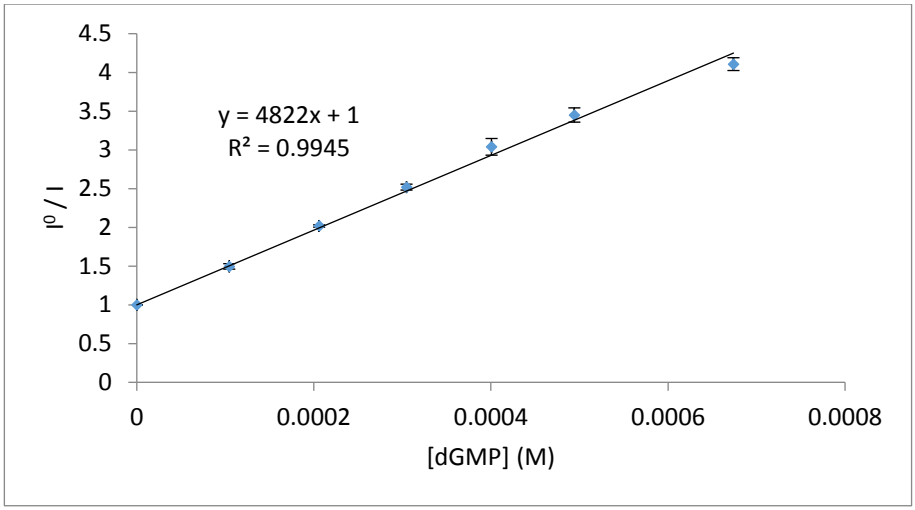

Figure S3.9 – Stern-Volmer plots of the luminescence quenching (hypsochromic band) of a 10^{-4} M solution of $[R\text{-}IrN_5C_1]^{2+}$ in aqueous acetate-phosphate buffer upon the addition of dGMP at pH = 9.49

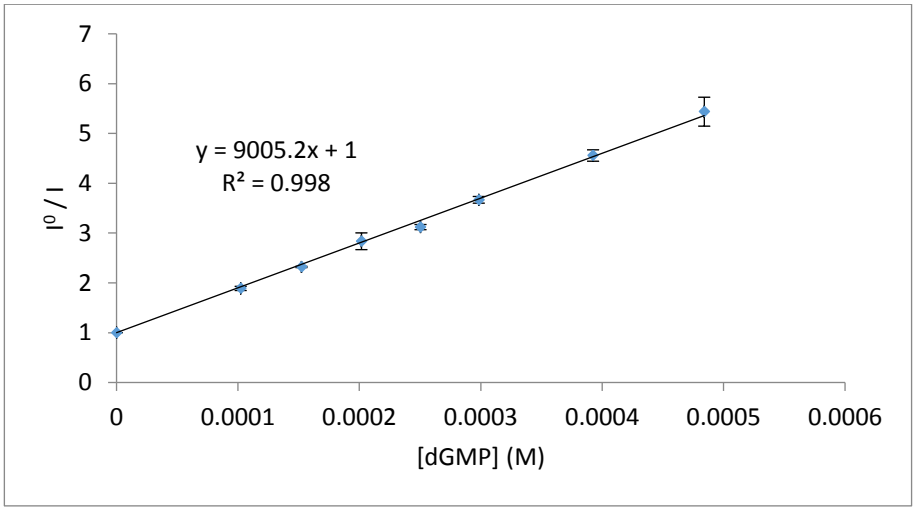

Figure S3.10 – Stern-Volmer plots of the luminescence quenching (hypsochromic band) of a 10^{-4} M solution of $[R\text{-}IrN_5C_1]^{2+}$ in aqueous acetate-phosphate buffer upon the addition of dGMP at pH = 11.15

8.3 Chapter 4 – Photocatalytic H_2 production using Ir(III)-Co(III) dyads

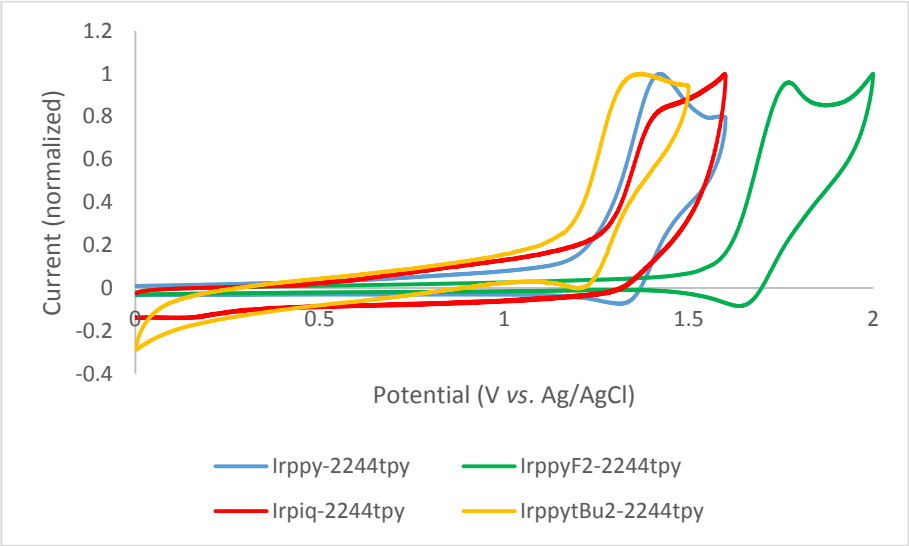

Figure S4.1 – Oxidation voltammograms of Irppy-2244tpy (*blue*), IrppyF$_2$-2244tpy (*green*), Irpiq-2244tpy (*red*) and IrppytBu$_2$-2244tpy (*orange*) (10^{-5} M) in acetonitrile with Bu_4NClO_4 0.1 M as supporting electrolyte (sweeping rate = 0.1 V/s).

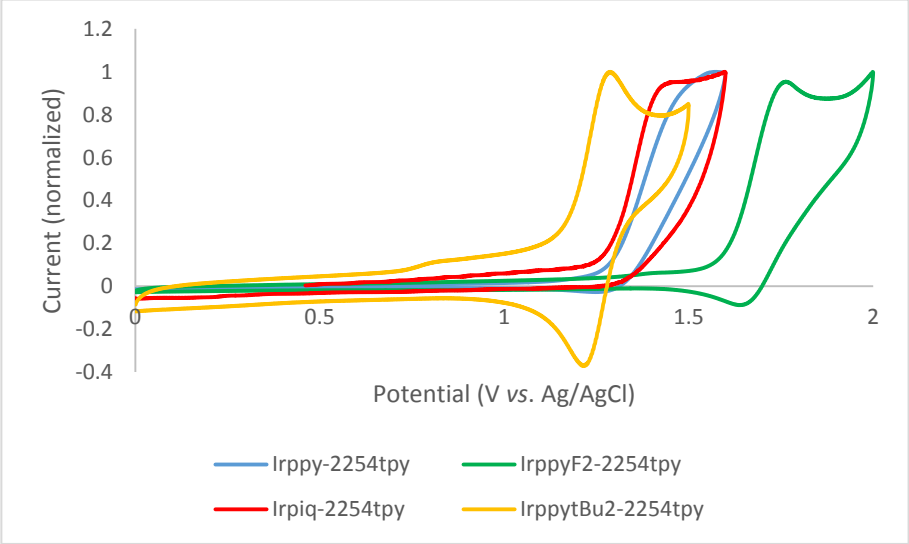

Figure S4.2 – Oxidation voltammograms of Irppy-2254tpy (*blue*), IrppyF$_2$-2254tpy (*green*), Irpiq-2254tpy (*red*) and IrppytBu$_2$-2254tpy (*orange*) (10^{-5} M) in acetonitrile with Bu_4NClO_4 0.1 M as supporting electrolyte (sweeping rate = 0.1 V/s).

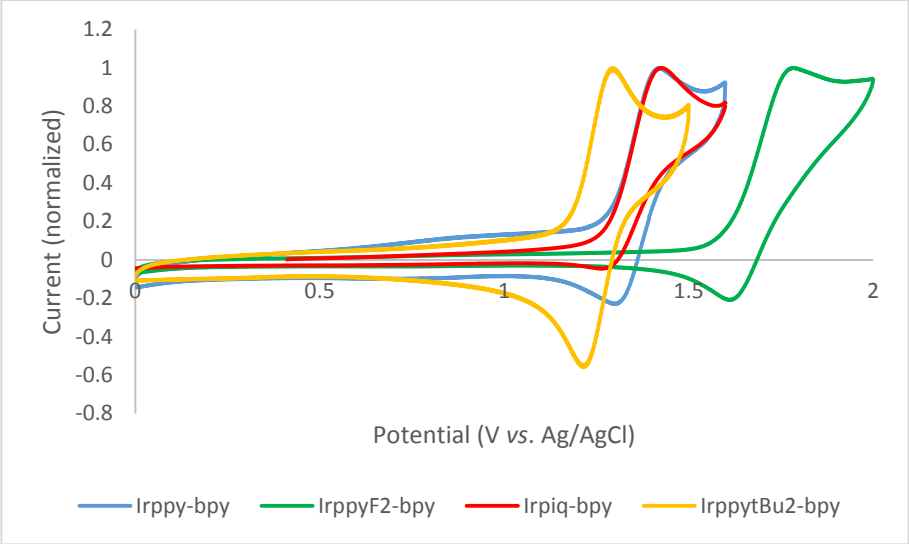

Figure S4.3 – Oxidation voltammograms of Irppy-bpy (*blue*), $IrppyF_2$-bpy (*green*), Irpiq-bpy (*red*) and $IrppytBu_2$-bpy (*orange*) (10^{-5} M) in acetonitrile with Bu_4NClO_4 0.1 M as supporting electrolyte (sweeping rate = 0.1 V/s).

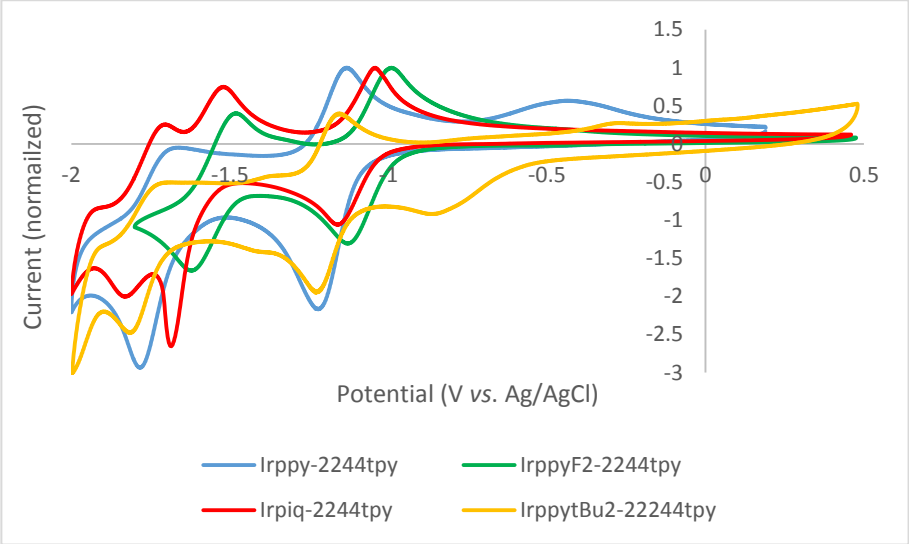

Figure S4.4 – Reduction voltammograms of Irppy-2244tpy (*blue*), $IrppyF_2$-2244tpy (*green*), Irpiq-2244tpy (*red*) and $IrppytBu_2$-2244tpy (*orange*) (10^{-5} M) in acetonitrile with Bu_4NClO_4 0.1 M as supporting electrolyte (sweeping rate = 0.1 V/s).

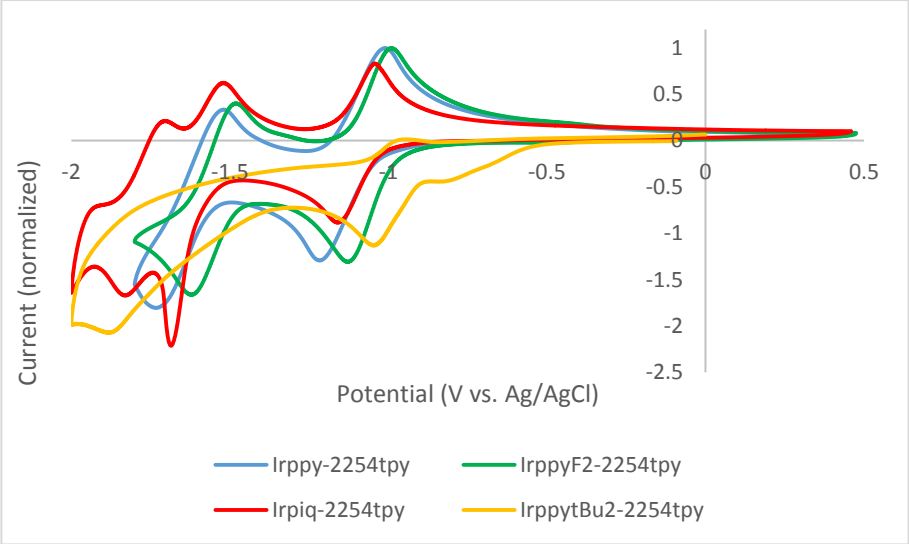

Figure S4.5 – Reduction voltammograms of Irppy-2254tpy (*blue*), IrppyF$_2$-2254tpy (*green*), Irpiq-2254tpy (*red*) and IrppytBu$_2$-2254tpy (*orange*) (10^{-5} M) in acetonitrile with Bu$_4$NClO$_4$ 0.1 M as supporting electrolyte (sweeping rate = 0.1 V/s).

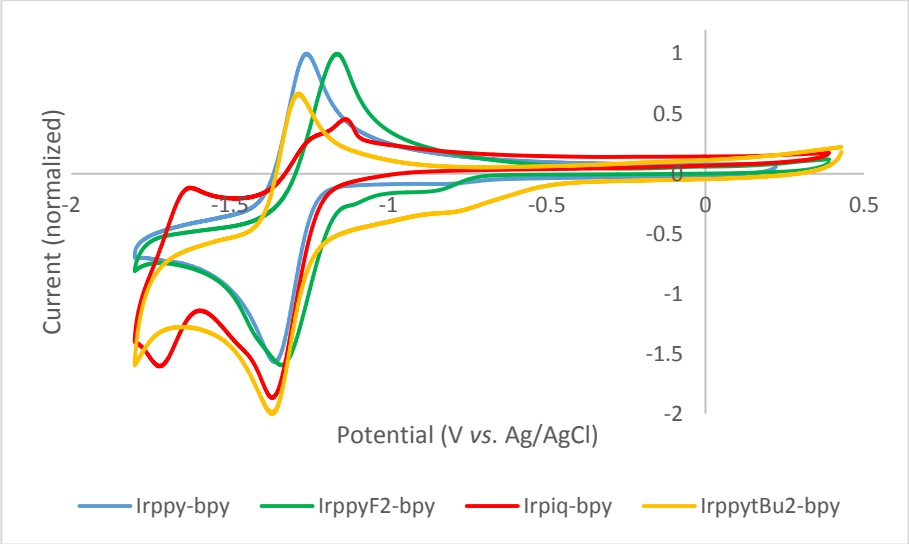

Figure S4.6 – Reduction voltammograms of Irppy-bpy (*blue*), IrppyF$_2$-bpy (*green*), Irpiq-bpy (*red*) and IrppytBu$_2$-bpy (*orange*) (10^{-5} M) in acetonitrile with Bu$_4$NClO$_4$ 0.1 M as supporting electrolyte (sweeping rate = 0.1 V/s).

Table S4.1 – Contributions to MOs for Irppy-bpy (isovalue: 0.03 e.Å^{-3})

Orbital	Contributions	Orbital	Contributions
LUMO+4 -1.27eV 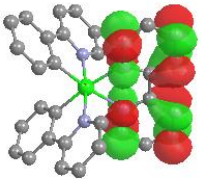	Ir : 1% ppy : 2% bpy : 97%	HOMO -5.66eV 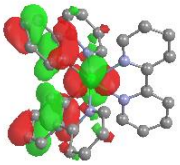	Ir : 40% ppy : 58% bpy : 2%
LUMO+3 -1.53eV 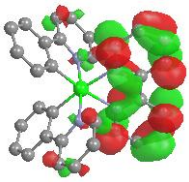	Ir : 1% ppy : 15% bpy : 83%	HOMO-1 -6.28eV 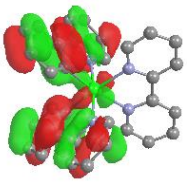	Ir : 8% ppy : 91% bpy : 1%
LUMO+2 -1.66eV 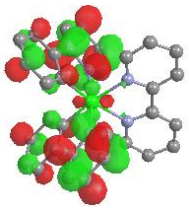	Ir : 4% ppy : 94% bpy : 2%	HOMO-2 -6.43eV 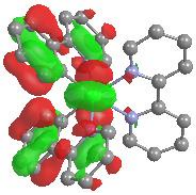	Ir : 48% ppy : 49% bpy : 4%
LUMO+1 -1.75eV 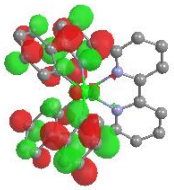	Ir : 2% ppy : 95% bpy : 1%	HOMO-3 -6.54eV 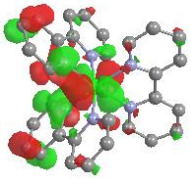	Ir : 48% ppy : 45% bpy : 7%
LUMO -2.4eV 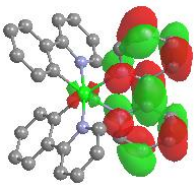	Ir : 2% ppy : 1% bpy : 97%	HOMO-4 -6.61eV 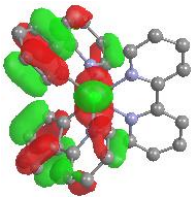	Ir : 30% ppy : 67% bpy : 3%

Table S4.2 – Contributions to MOs for Irppy-2244py (isovalue: 0.03 e.Å^{-3})

Orbital	Contributions	Orbital	Contributions
LUMO+4 -1.46eV 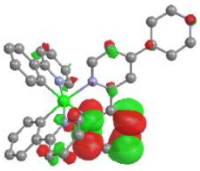	Ir : 1% ppy : 13% 2244tpy : 86%	HOMO -5.68eV 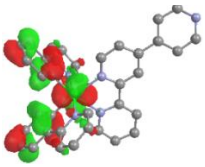	Ir : 39% ppy : 59% 2244tpy : 2%
LUMO+3 -1.67eV 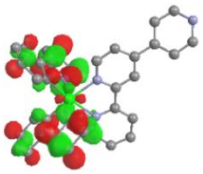	Ir : 4% ppy : 94% 2244tpy : 3%	HOMO-1 -6.29eV 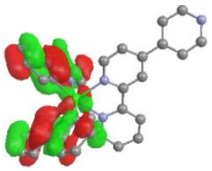	Ir : 8% ppy : 91% 2244tpy : 1%
LUMO+2 -1.76eV 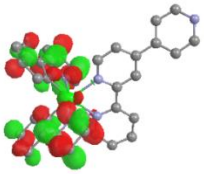	Ir : 4% ppy : 95% 2244tpy : 1%	HOMO-2 -6.44eV 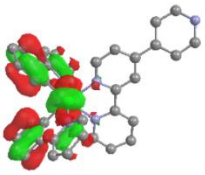	Ir : 47% ppy : 49% 2244tpy : 4%
LUMO+1 -1.9eV 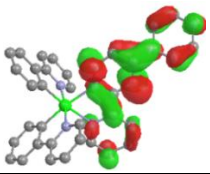	Ir : 2% ppy : 1% 2244tpy : 97%	HOMO-3 -6.55eV 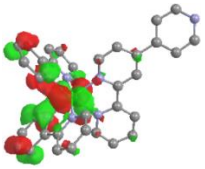	Ir : 47% ppy : 45% 2244tpy : 8%
LUMO -2.57eV 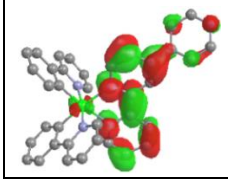	Ir : 2% ppy : 1% 2244tpy : 97%	HOMO-4 -6.62eV 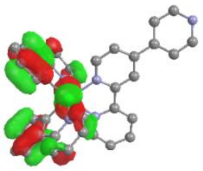	Ir : 30% ppy : 66% 2244tpy : 4%

Table S4.3 – Contributions to MOs for Irppy-2254py (isovalue: 0.03 e.Å^{-3})

Orbital	Contributions	Orbital	Contributions
LUMO+4 -1.34eV 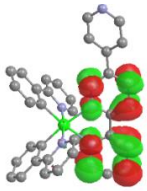	Ir : 1% ppy : 3% 2254tpy : 96%	HOMO -5.68eV 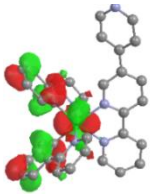	Ir : 39% ppy : 59% 2254tpy : 2%
LUMO+3 -1.66eV 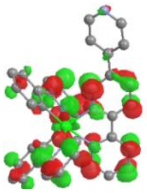	Ir : 3% ppy : 58% 2254tpy : 39%	HOMO-1 -6.3eV 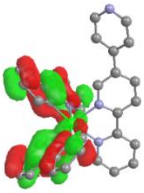	Ir : 8% ppy : 91% 2254tpy : 1%
LUMO+2 -1.7eV 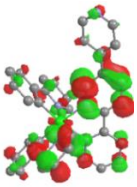	Ir : 3% ppy : 44% 2254tpy : 53%	HOMO-2 -6.45eV 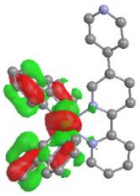	Ir : 46% ppy : 50% 2254tpy : 4%
LUMO+1 -1.76eV 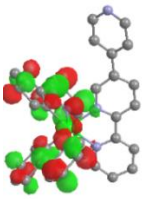	Ir : 4% ppy : 93% 2254tpy : 3%	HOMO-3 -6.56eV 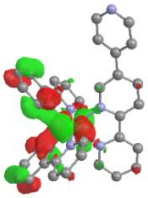	Ir : 46% ppy : 47% 2254tpy : 7%
LUMO -2.62eV 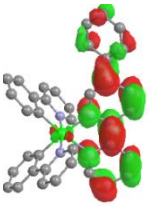	Ir : 2% ppy : 1% 2254tpy : 98%	HOMO-4 -6.63eV 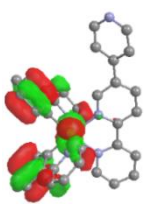	Ir : 30% ppy : 65% 2254tpy : 5%

Table S4.4 – Contributions to MOs for IrppyF_2-bpy (isovalue: 0.03 e.Å^{-3})

Orbital	Contributions	Orbital	Contributions
LUMO+4 -1.34eV 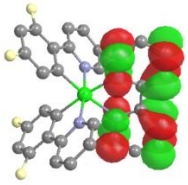	Ir : 0% ppyF_2 : 2% bpy : 98%	HOMO -5.98eV 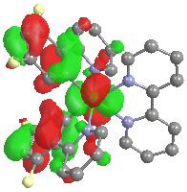	Ir : 38% ppyF_2 : 60% bpy : 2%
LUMO+3 -1.59eV 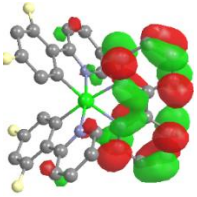	Ir : 2% ppyF_2 : 13% bpy : 85%	HOMO-1 -6.42eV 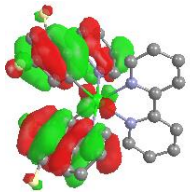	Ir : 6% ppyF_2 : 93% bpy : 1%
LUMO+2 -1.77eV 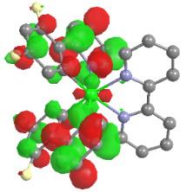	Ir : 4% ppyF_2 : 94% bpy : 2%	HOMO-2 -6.53eV 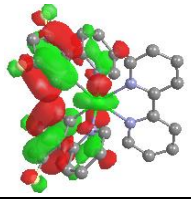	Ir : 15% ppyF_2 : 84% bpy : 1%
LUMO+1 -1.85eV 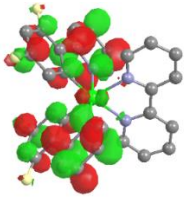	Ir : 4% ppyF_2 : 95% bpy : 1%	HOMO-3 -6.75eV 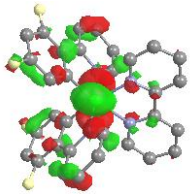	Ir : 62% ppyF_2 : 31% bpy : 7%
LUMO -2.48eV 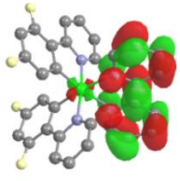	Ir : 2% ppyF_2 : 1% bpy : 97%	HOMO-4 -6.79eV 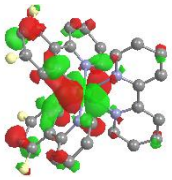	Ir : 51% ppyF_2 : 41% bpy : 8%

Table S4.5 – Contributions to MOs for IrppyF_2-2244tpy (isovalue: 0.03 e.Å^{-3})

Orbital	Contributions	Orbital	Contributions
LUMO+4 -1.52eV 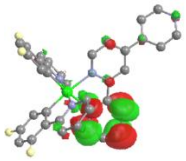	Ir : 1% ppyF_2 : 10% 2244tpy : 88%	HOMO -6.00eV 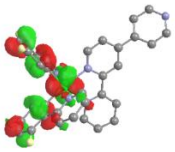	Ir : 38% ppyF_2 : 60% 2244tpy : 2%
LUMO+3 -1.77eV 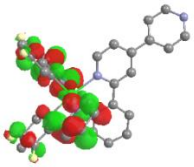	Ir : 4% ppyF_2 : 94% 2244tpy : 2%	HOMO-1 -6.43eV 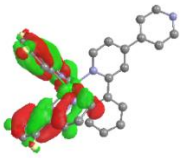	Ir : 6% ppyF_2 : 93% 2244tpy : 1%
LUMO+2 -1.86eV 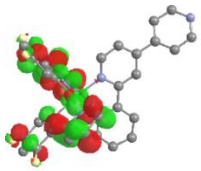	Ir : 4% ppyF_2 : 95% 2244tpy : 1%	HOMO-2 -6.54eV 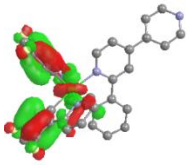	Ir : 15% ppyF_2 : 84% 2244tpy : 1%
LUMO+1 -1.96eV 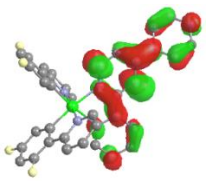	Ir : 1% ppyF_2 : 3% 2244tpy : 97%	HOMO-3 -6.76eV 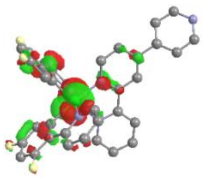	Ir : 60% ppyF_2 : 31% 2244tpy : 9%
LUMO -2.64eV 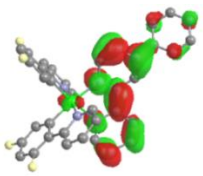	Ir : 2% ppyF_2 : 1% 2244tpy : 97%	HOMO-4 -6.8eV 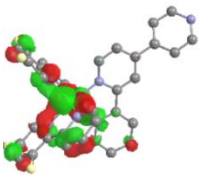	Ir : 52% ppyF_2 : 39% 2244tpy : 9%

Table S4.6 – Contributions to MOs for IrppyF_2-2254tpy (isovalue: 0.03 e.Å^{-3})

Orbital	Contributions	Orbital	Contributions
LUMO+4 -1.41eV 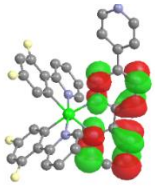	Ir : 1% ppyF_2 : 3% 2254tpy : 97%	HOMO -6.01eV 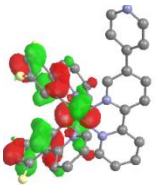	Ir : 38% ppyF_2 : 60% 2254tpy : 2%
LUMO+3 -1.74eV 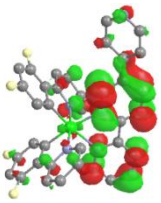	Ir : 2% ppyF_2 : 20% 2254tpy : 78%	HOMO-1 -6.44eV 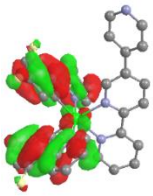	Ir : 6% ppyF_2 : 93% 2254tpy : 1%
LUMO+2 -1.79eV 	Ir : 4% ppyF_2 : 80% 2254tpy : 16%	HOMO-2 -6.55eV 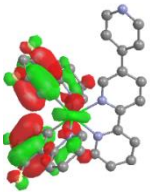	Ir : 15% ppyF_2 : 84% 2254tpy : 1%
LUMO+1 -1.86eV 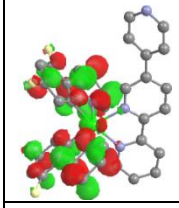	Ir : 4% ppyF_2 : 95% 2254tpy : 1%	HOMO-3 -6.77eV 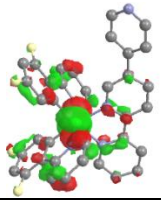	Ir : 60% ppyF_2 : 29% 2254tpy : 10%
LUMO -2.69eV 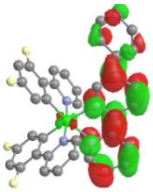	Ir : 2% ppyF_2 : 1% 2254tpy : 98%	HOMO-4 -6.81eV 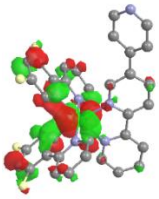	Ir : 48% ppyF_2 : 45% 2254tpy : 8%

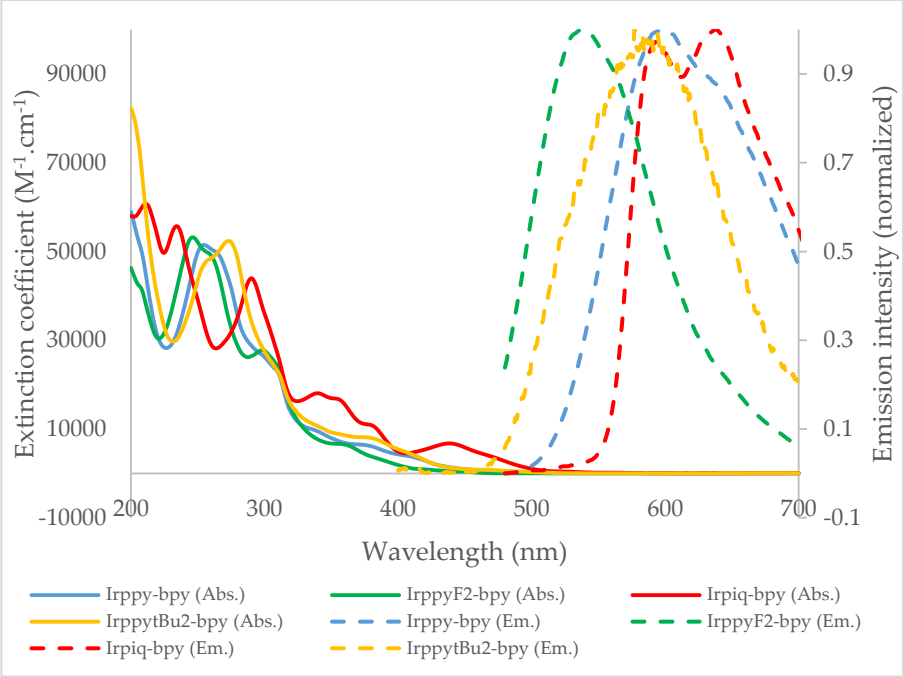

Figure S4.7 –Absorption spectra of IrX-bpy photosensitizers in acetonitrile

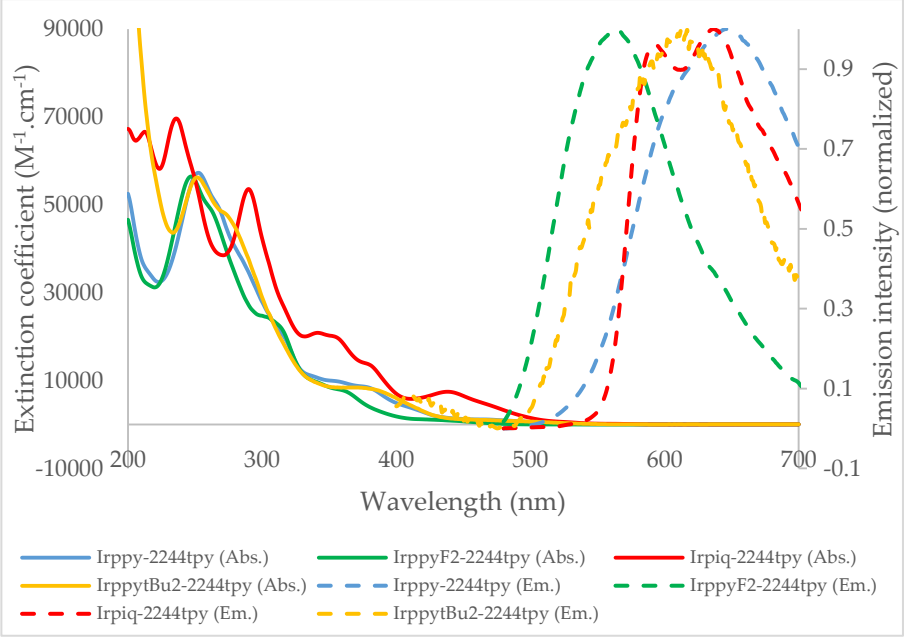

Figure S4.8 –Absorption spectra of IrX-2244tpy photosensitizers in acetonitrile

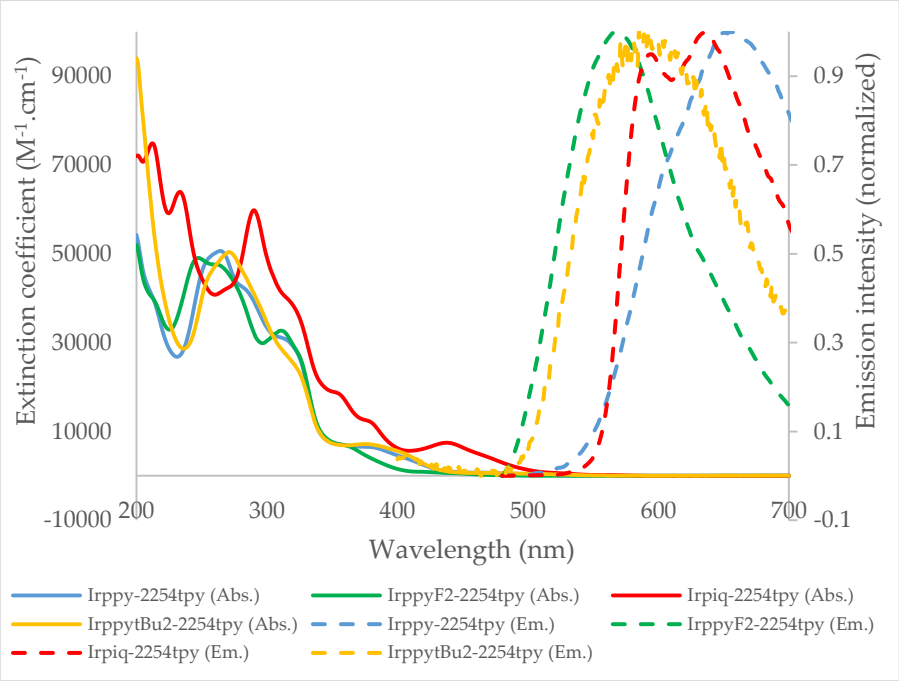

Figure S4.9 –Absorption spectra of IrX-2254tpy photosensitizers in acetonitrile

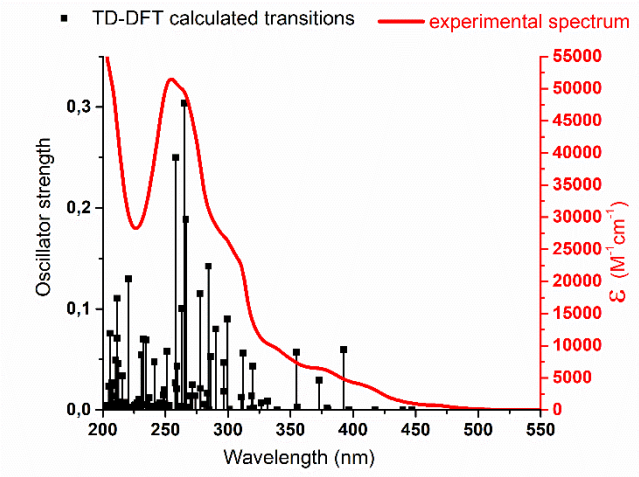

Figure S4.10 – Experimental spectrum and calculated transitions for Irppy-bpy

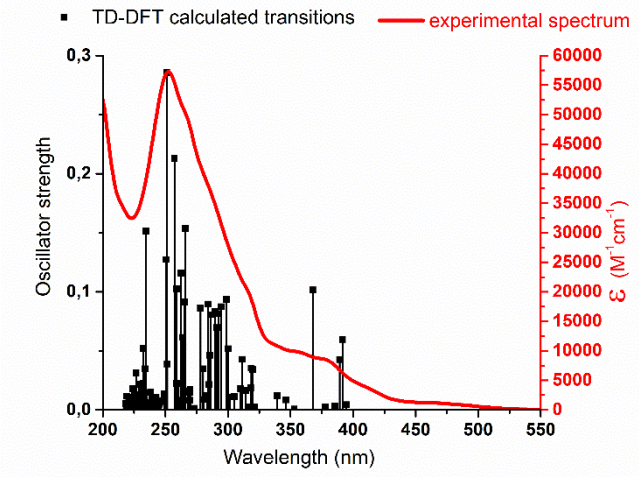

Figure S4.11 – Experimental spectrum and calculated transitions for Irppy-2244tpy

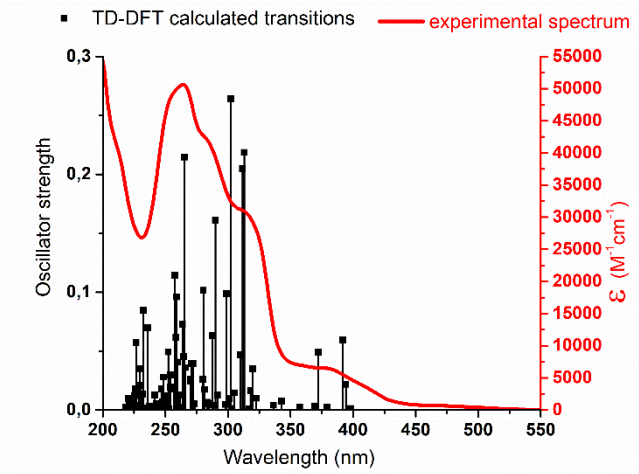

Figure S4.12 – Experimental spectrum and calculated transitions for Irppy-2254tpy

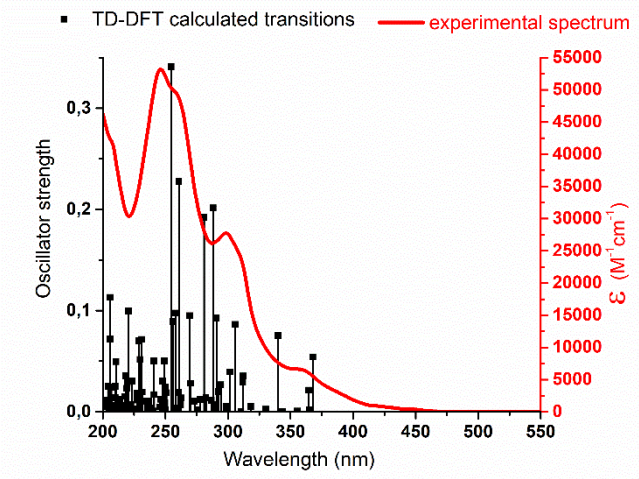

Figure S4.13 – Experimental spectrum and calculated transitions for IrppyF_2-bpy

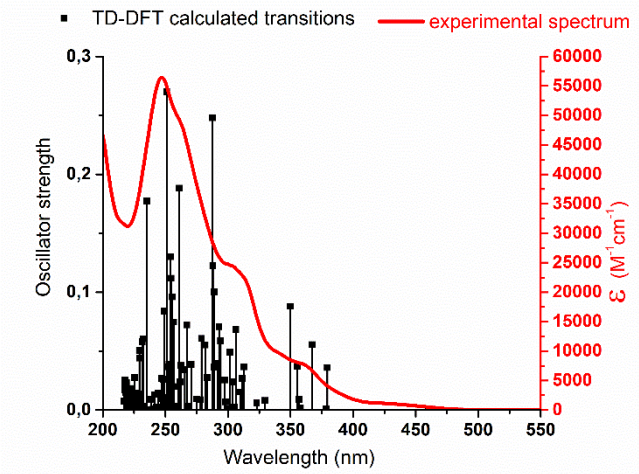

Figure S4.14 – Experimental spectrum and calculated transitions for IrppyF$_2$-2244tpy

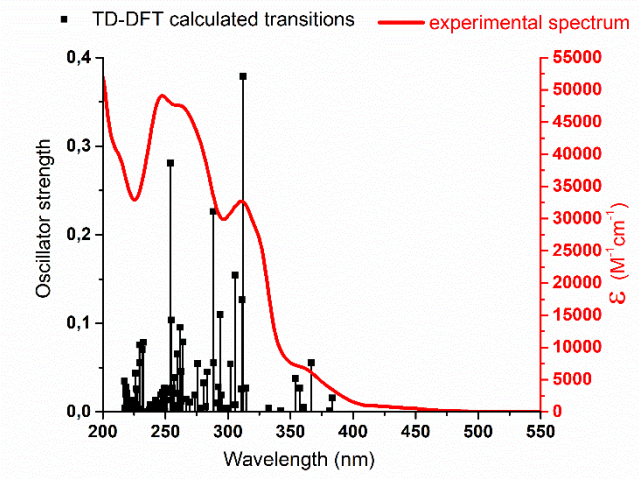

Figure S4.15 – Experimental spectrum and calculated transitions for IrppyF$_2$-2254tpy

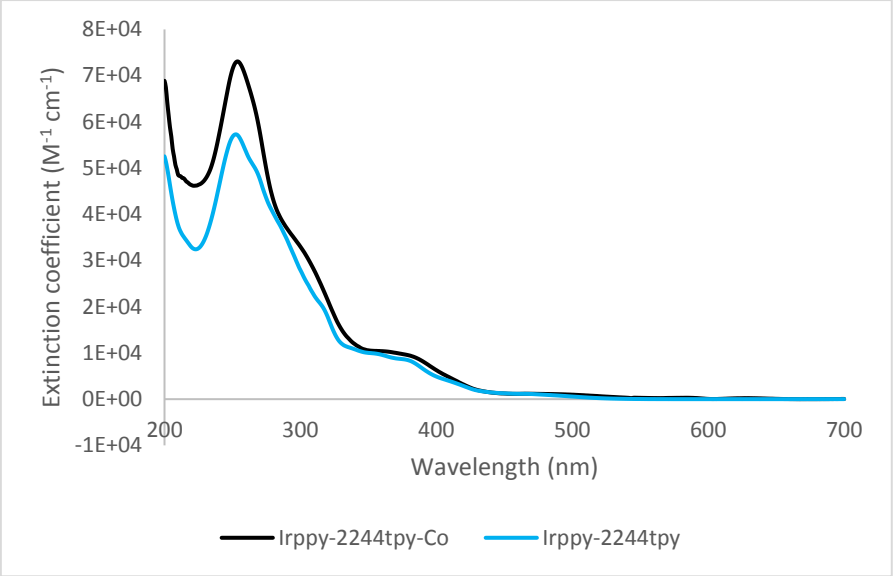

Figure S4.16 – Absorption spectra of Irppy-2244tpy-Co (*black*) and Irppy-2244tpy (*blue*) in acetonitrile at room temperature

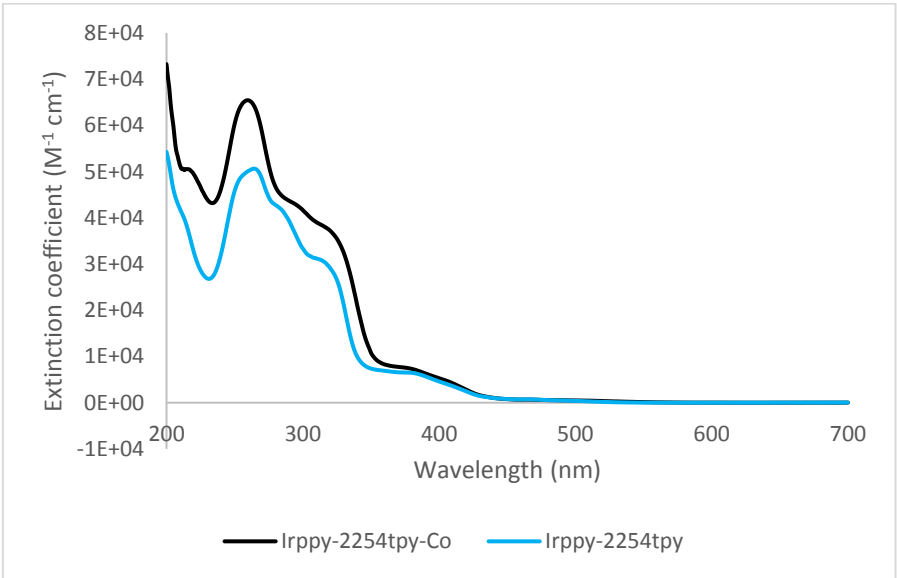

Figure S4.17 – Absorption spectra of Irppy-2254tpy-Co (*black*) and Irppy-2254tpy (*blue*) in acetonitrile at room temperature

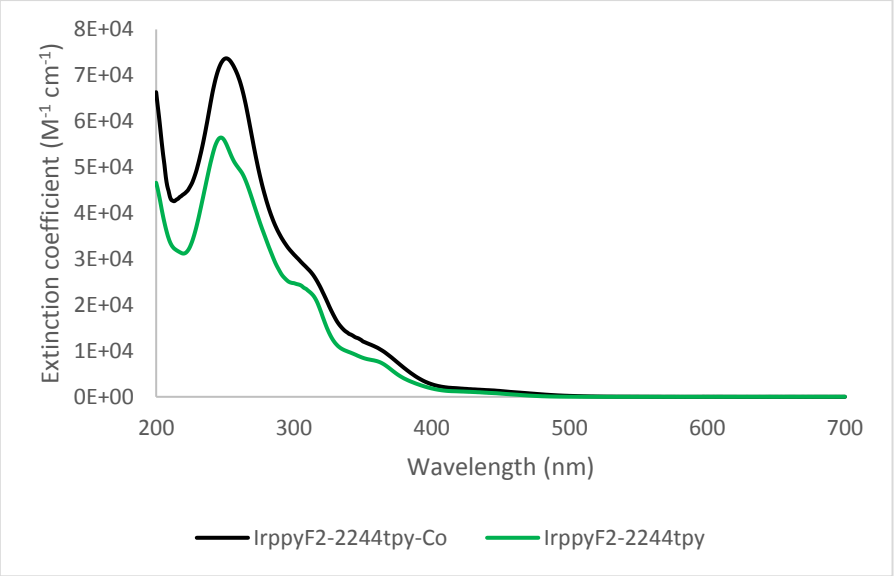

Figure S4.18 – Absorption spectra of IrppyF$_2$-2244tpy-Co (*black*) and IrppyF$_2$-2244tpy (*green*) in acetonitrile at room temperature

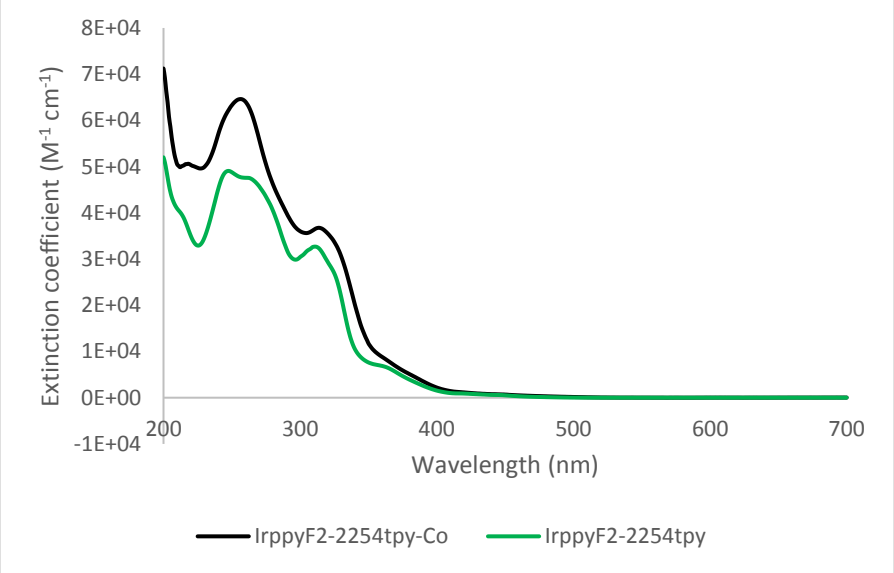

Figure S4.19 – Absorption spectra of IrppyF$_2$-2254tpy-Co (*black*) and IrppyF$_2$-2254tpy (*green*) in acetonitrile at room temperature

Table S4.7 – Contributions to MOs for protonated Irppy-2244tpy (isovalue: 0.03 e.Å^{-3})

Orbital	Contributions	Orbital	Contributions
LUMO+4 -1.73eV 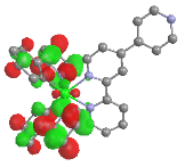	Ir : 4% ppy : 94% 2244tpy-H : 2%	HOMO -5.76eV 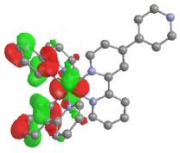	Ir : 39% ppy : 59% 2244tpy-H : 2%
LUMO+3 -1.82eV 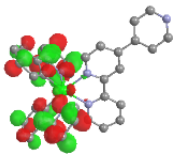	Ir : 4% ppy : 94% 2244tpy-H : 2%	HOMO-1 -6.36eV 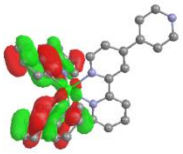	Ir : 6% ppy : 93% 2244tpy-H : 1%
LUMO+2 -1.92eV 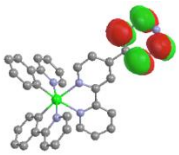	Ir : 0% ppy : 2% 2244tpy-H : 98%	HOMO-2 -6.52eV 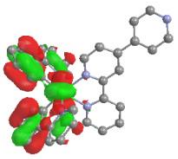	Ir : 36% ppy : 61% 2244tpy-H : 3%
LUMO+1 -2.5eV 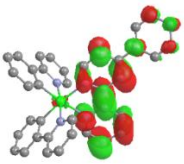	Ir : 1% ppy : 3% 2244tpy-H : 96%	HOMO-3 -6.65eV 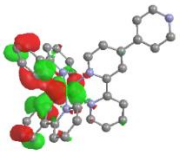	Ir : 39% ppy : 55% 2244tpy-H : 6%
LUMO -3.36eV 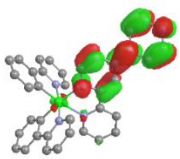	Ir : 2% ppy : 14% 2244tpy-H : 85%	HOMO-4 -6.7eV 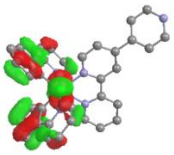	Ir : 41% ppy : 55% 2244tpy-H : 4%

Table S4.8 – Contributions to MOs for protonated Irppy-2254tpy (isovalue: 0.03 e.Å^{-3})

Orbital	Contributions	Orbital	Contributions
LUMO+4 -1.75eV 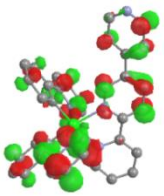	Ir : 3% ppy : 69% 2254tpy-H : 28%	HOMO -5.76eV 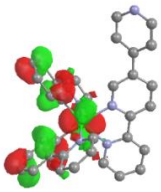	Ir : 39% ppy : 59% 2254tpy-H : 2%
LUMO+3 -1.83eV 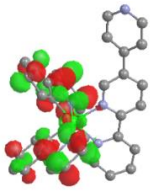	Ir : 4% ppy : 92% 2254tpy-H : 4%	HOMO-1 -6.37eV 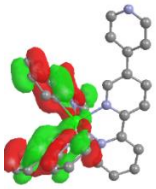	Ir : 7% ppy : 92% 2254tpy-H : 1%
LUMO+2 -1.91eV 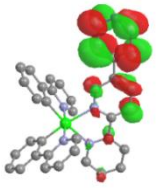	Ir : 0% ppy : 4% 2254tpy-H : 96%	HOMO-2 -6.53eV 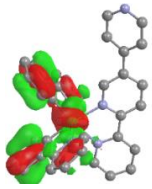	Ir : 38% ppy : 59% 2254tpy-H : 3%
LUMO+1 -2.33eV 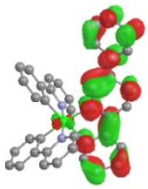	Ir : 2% ppy : 6% 2254tpy-H : 91%	HOMO-3 -6.66eV 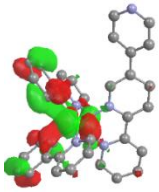	Ir : 41% ppy : 53% 2254tpy-H : 6%
LUMO -3.37eV 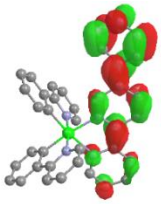	Ir : 1% ppy : 12% 2254tpy-H : 87%	HOMO-4 -6.71eV 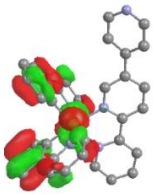	Ir : 40% ppy : 57% 2254tpy-H : 3%

Table S4.9 – Contributions to MOs for protonated IrppyF$_2$-2244tpy (isovalue: 0.03 e.Å^{-3})

Orbital	Contributions	Orbital	Contributions
LUMO+4 -1.84eV 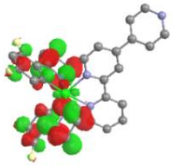	Ir : 4% ppyF$_2$: 94% 2244tpy-H : 2%	HOMO -6.07eV 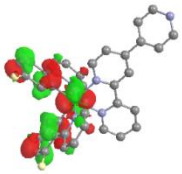	Ir : 37% ppyF$_2$: 61% 2244tpy-H : 2%
LUMO+3 -1.91eV 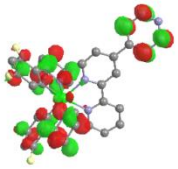	Ir : 3% ppyF$_2$: 72% 2244tpy-H : 25%	HOMO-1 -6.49eV 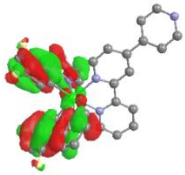	Ir : 5% ppyF$_2$: 94% 2244tpy-H : 1%
LUMO+2 -1.94eV 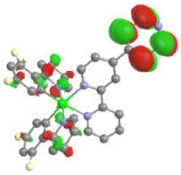	Ir : 1% ppyF$_2$: 24% 2244tpy-H : 75%	HOMO-2 -6.61eV 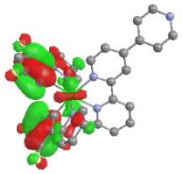	Ir : 12% ppyF$_2$: 87% 2244tpy-H : 1%
LUMO+1 -2.56eV 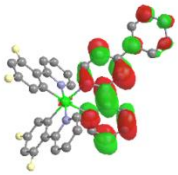	Ir : 1% ppyF$_2$: 3% 2244tpy-H : 96%	HOMO-3 -6.87eV 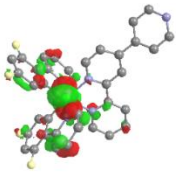	Ir : 66% ppyF$_2$: 28% 2244tpy-H : 6%
LUMO -3.42eV 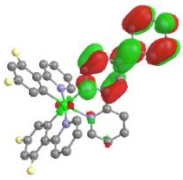	Ir : 2% ppyF$_2$: 13% 2244tpy-H : 85%	HOMO-4 -6.9eV 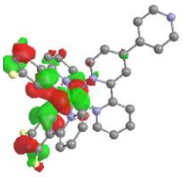	Ir : 37% ppyF$_2$: 57% 2244tpy-H : 6%

Table S4.10 – Contributions to MOs for protonated IrppyF$_2$-2254tpy (isovalue: 0.03 e.Å^{-3})

Orbital	Contributions	Orbital	Contributions
LUMO+4 -1.85eV 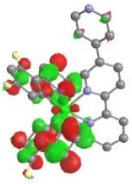	Ir : 4% ppyF$_2$: 91% 2254tpy-H : 6%	HOMO -6.09eV 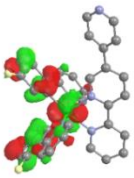	Ir : 37% ppyF$_2$: 61% 2254tpy-H : 2%
LUMO+3 -1.92eV 	Ir : 3% ppyF$_2$: 64% 2254tpy-H : 33%	HOMO-1 -6.5eV 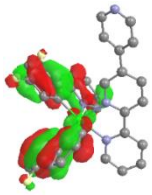	Ir : 5% ppyF$_2$: 94% 2254tpy-H : 1%
LUMO+2 -1.94eV 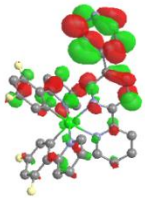	Ir : 2% ppyF$_2$: 34% 2254tpy-H : 64%	HOMO-2 -6.62eV 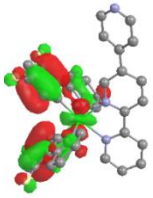	Ir : 12% ppyF$_2$: 87% 2254tpy-H : 1%
LUMO+1 -2.39eV 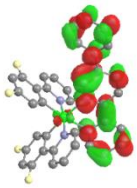	Ir : 2% ppyF$_2$: 6% 2254tpy-H : 91%	HOMO-3 -6.87eV 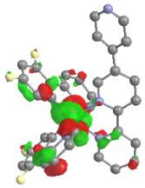	Ir : 65% ppyF$_2$: 29% 2254tpy-H : 6%
LUMO -3.41eV 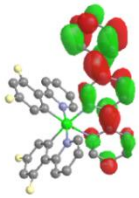	Ir : 1% ppyF$_2$: 12% 2254tpy-H : 88%	HOMO-4 -6.91eV 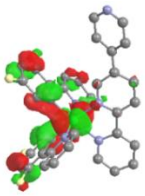	Ir : 40% ppyF$_2$: 54% 2254tpy-H : 6%

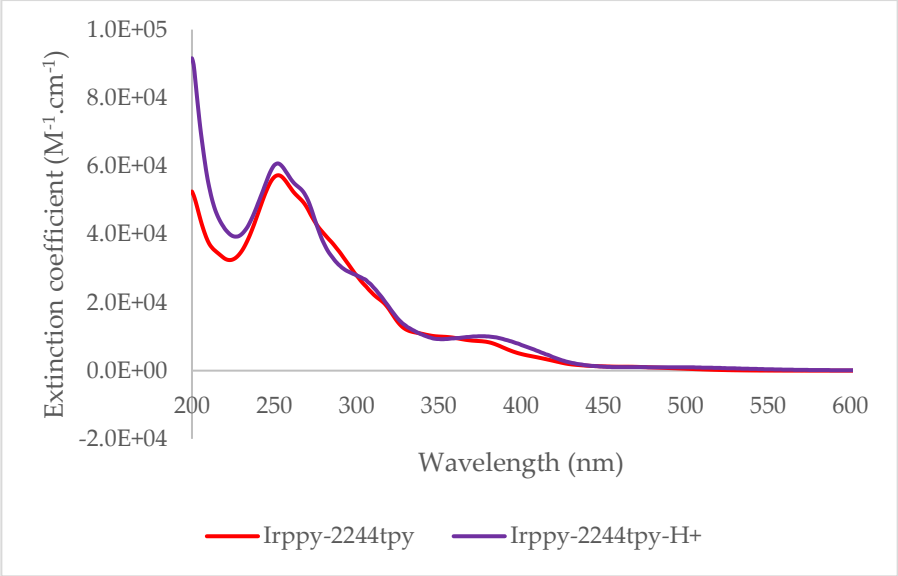

Figure S4.20 – Absorption spectra in acetonitrile for neutral (*red*) and protonated (*purple*) (obtained when solubilized in a 0.2 mM of TFA solution in acetonitrile) Irppy-2244tpy photosensitizer

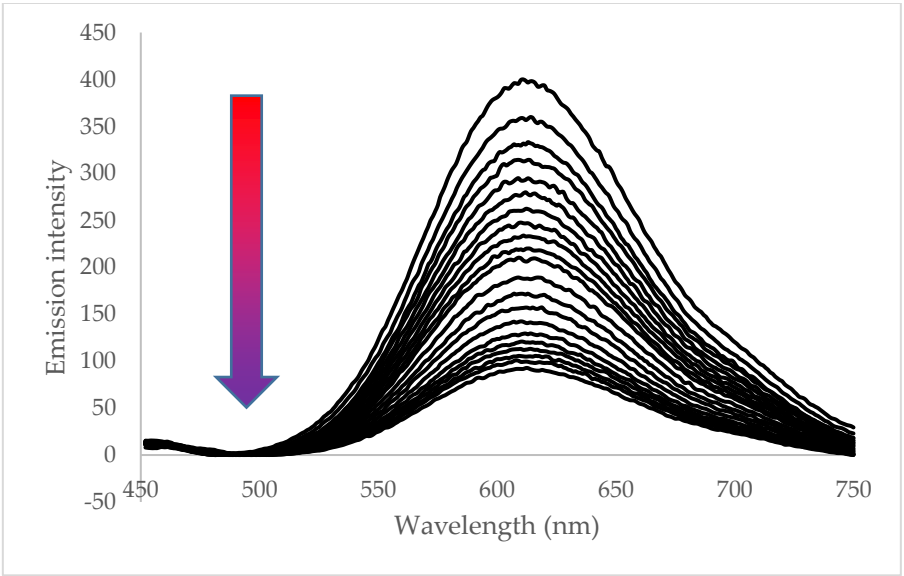

Figure S4.21 – Emission spectral changes for a 2.5 x 10^{-5} M solution of Irppy-2244tpy in acetonitrile for increasing concentrations of trifluoroacetic acid (10^{-4} M range)

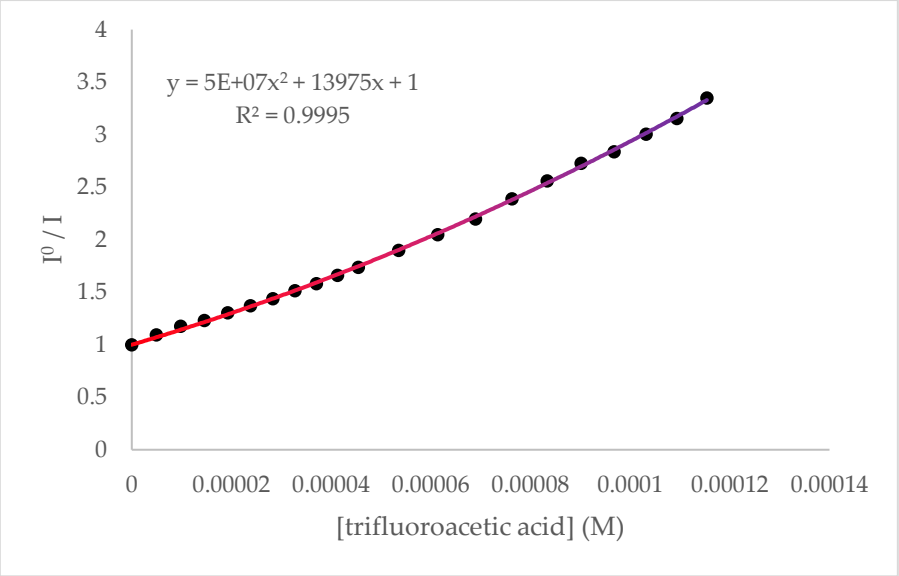

Figure S4.22 – Stern-Volmer plots of the luminescence quenching of a 2.5 x 10^{-5} M solution of Irppy-2244tpy in acetonitrile upon the addition of trifluoroacetic acid

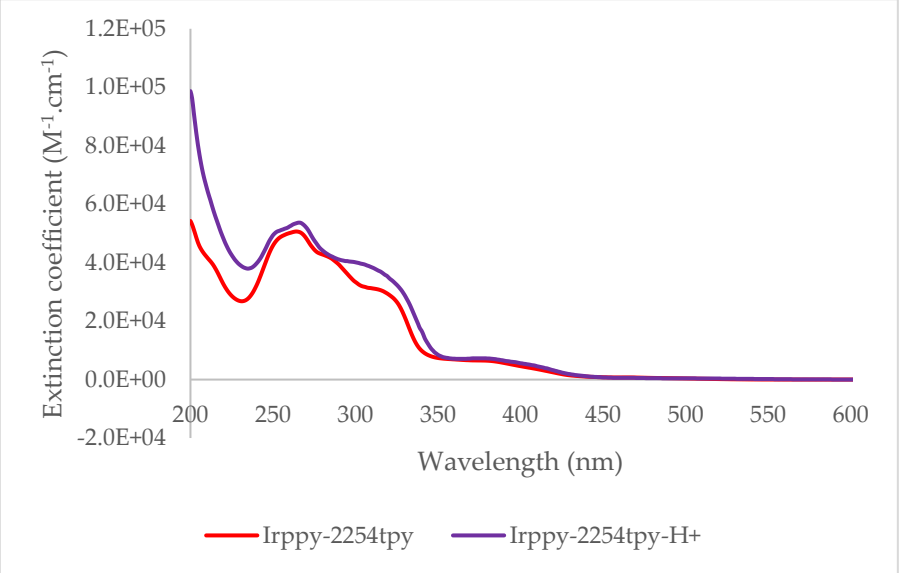

Figure S4.23 – Absorption spectra in acetonitrile for neutral (*red*) and protonated (*purple*) (obtained when solubilized in a 0.2 mM of TFA solution in acetonitrile) Irppy-2254tpy photosensitizer

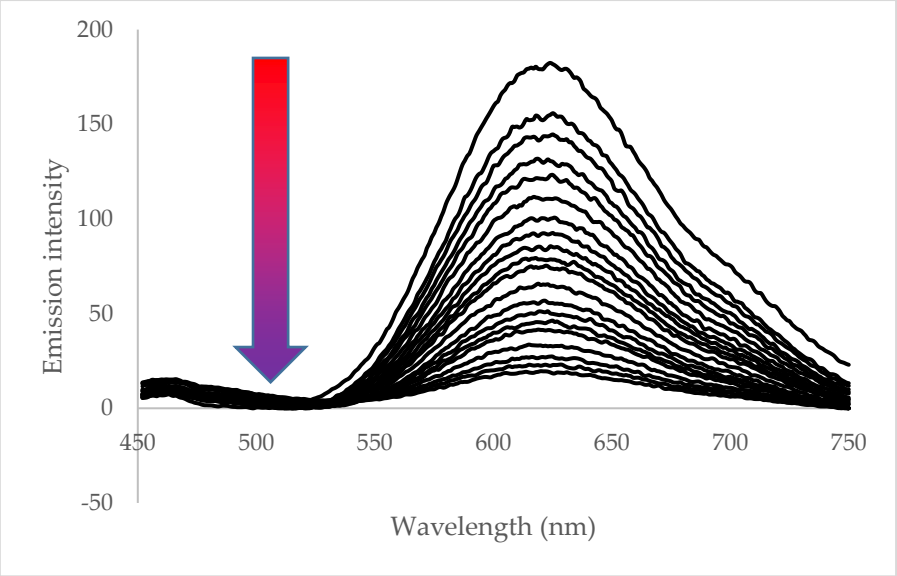

Figure S4.24 – Emission spectral changes for a 2.5 x 10^{-5} M solution of Irppy-2254tpy in acetonitrile for increasing concentrations of trifluoroacetic acid (10^{-4} M range)

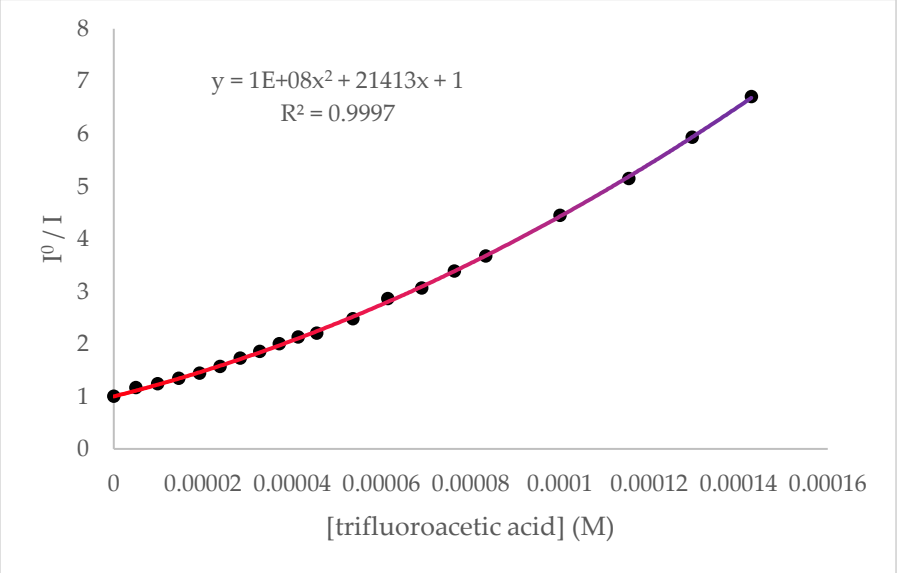

Figure S4.25 – Stern-Volmer plots of the luminescence quenching of a 2.5 x 10^{-5} M solution of Irppy-2254tpy in acetonitrile upon the addition of trifluoroacetic acid

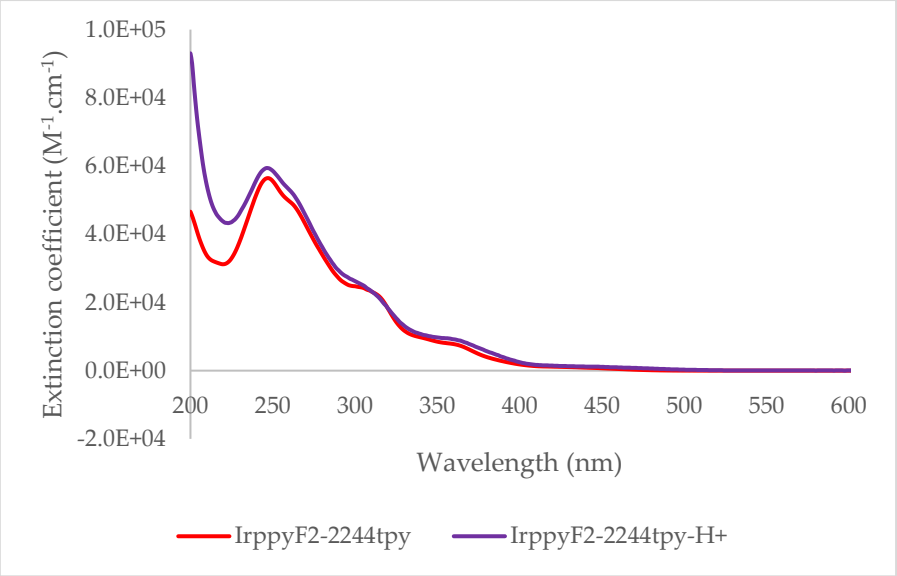

Figure S4.26 – Absorption spectra in acetonitrile for neutral (*red*) and protonated (*purple*) (obtained when solubilized in a 0.2 mM of TFA solution in acetonitrile) IrppyF_2-2244tpy photosensitizer

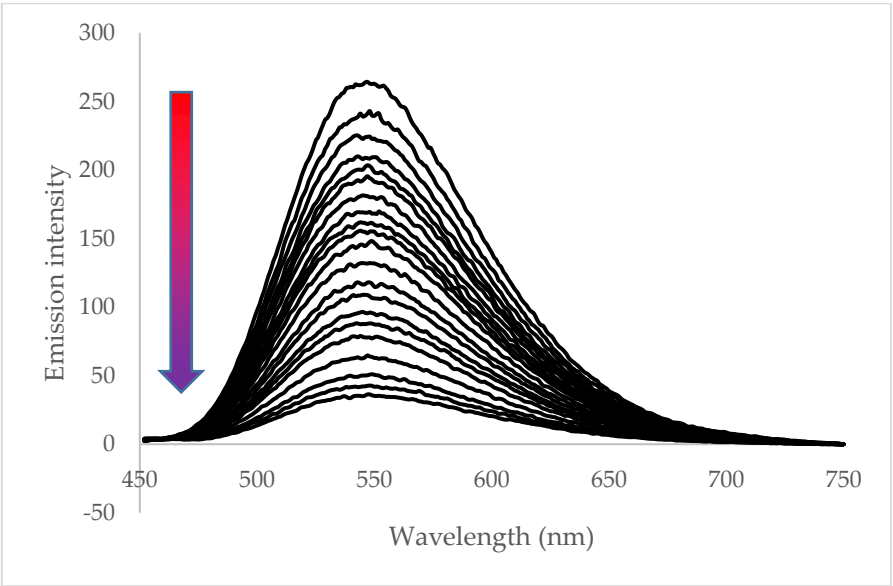

Figure S4.27 – Emission spectral changes for a 2.5 x 10^{-5} M solution of IrppyF_2-2244tpy in acetonitrile for increasing concentrations of trifluoroacetic acid (10^{-4} M range)

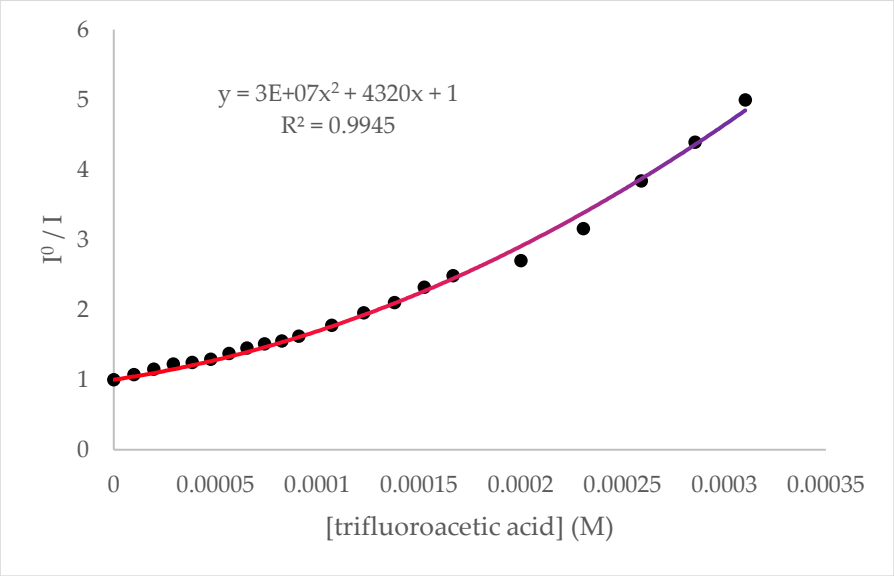

Figure S4.28 – Stern-Volmer plots of the luminescence quenching of a 2.5 x 10^{-5} M solution of IrppyF$_2$-2244tpy in acetonitrile upon the addition of trifluoroacetic acid

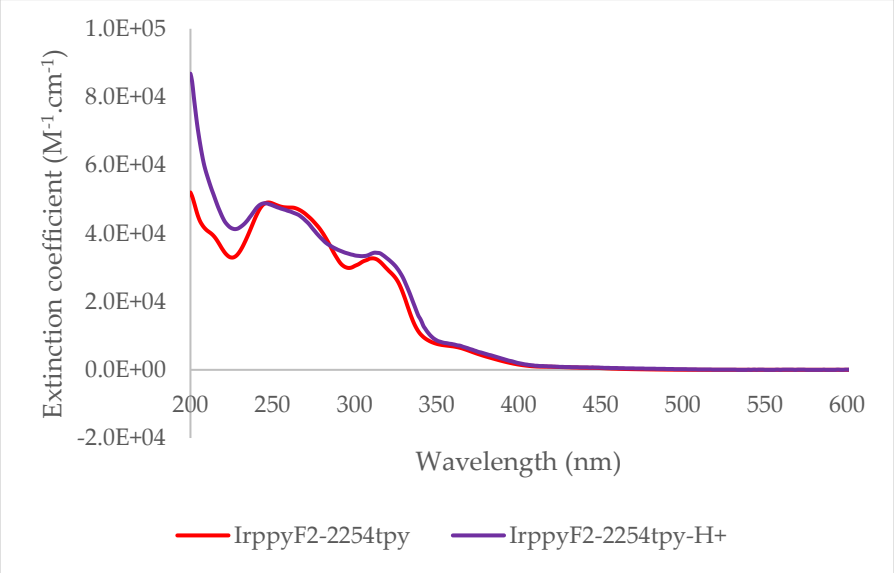

Figure S4.29 – Absorption spectra in acetonitrile for neutral (*red*) and protonated (*purple*) (obtained when solubilized in a 0.2 mM of TFA solution in acetonitrile) IrppyF$_2$-2254tpy photosensitizer

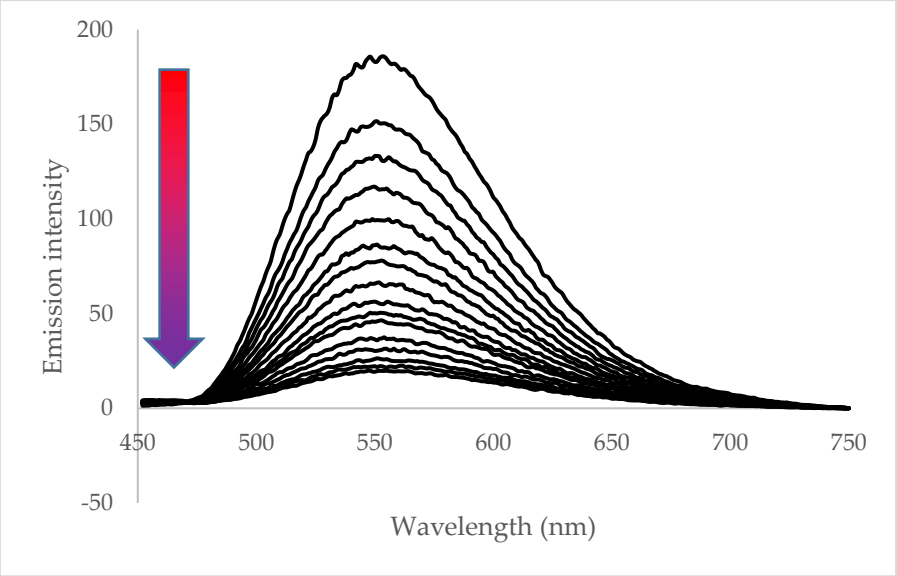

Figure S4.30 – Emission spectral changes for a 2.5 x 10^{-5} M solution of IrppyF$_2$-2254tpy in acetonitrile for increasing concentrations of trifluoroacetic acid (10^{-4} M range)

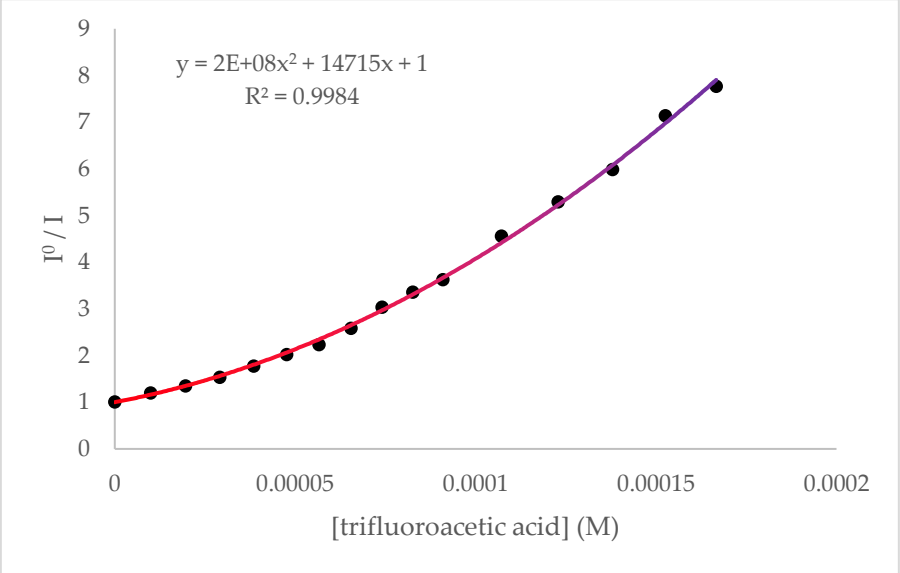

Figure S4.31 – Stern-Volmer plots of the luminescence quenching of a 2.5 x 10^{-5} M solution of IrppyF$_2$-2254tpy in acetonitrile upon the addition of trifluoroacetic acid

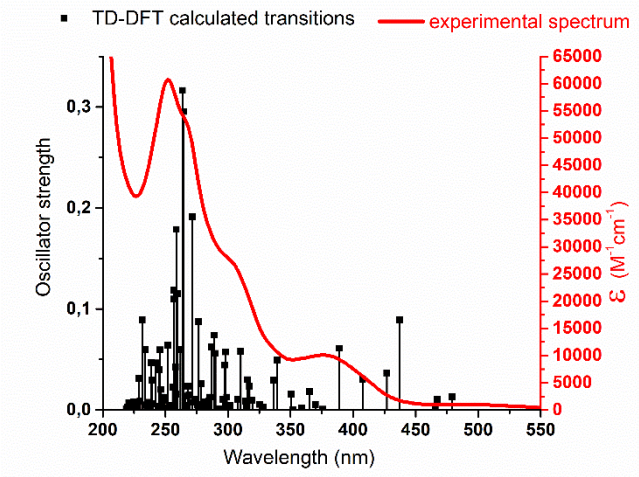

Figure S4.32 – Experimental spectrum and calculated transitions for Irppy-2244tpy-H$^+$

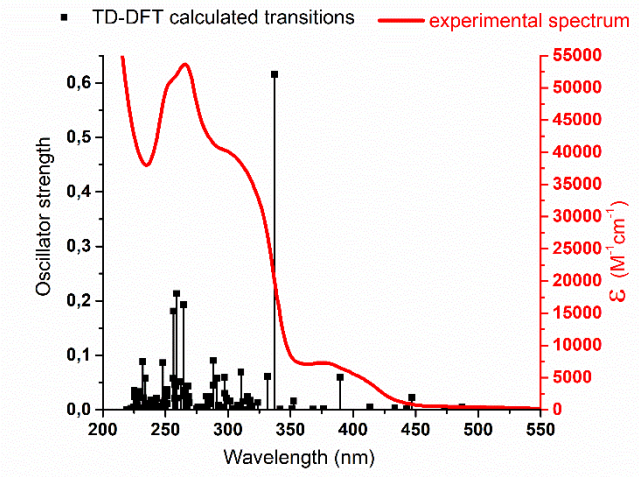

Figure S4.33 – Experimental spectrum and calculated transitions for Irppy-2254tpy-H$^+$

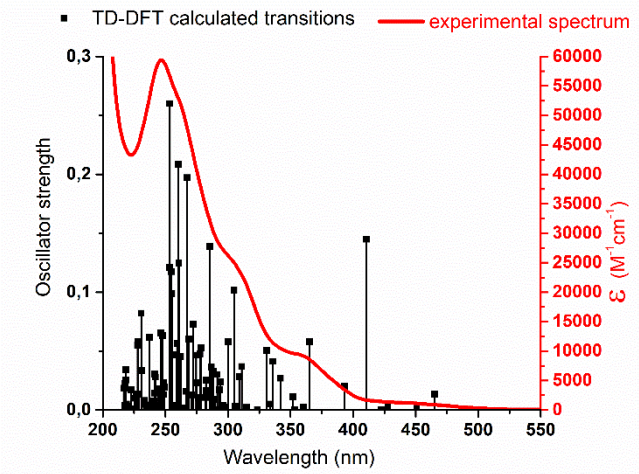

Figure S4.34 – Experimental spectrum and calculated transitions for $IrppyF_2$-2244tpy-H^+

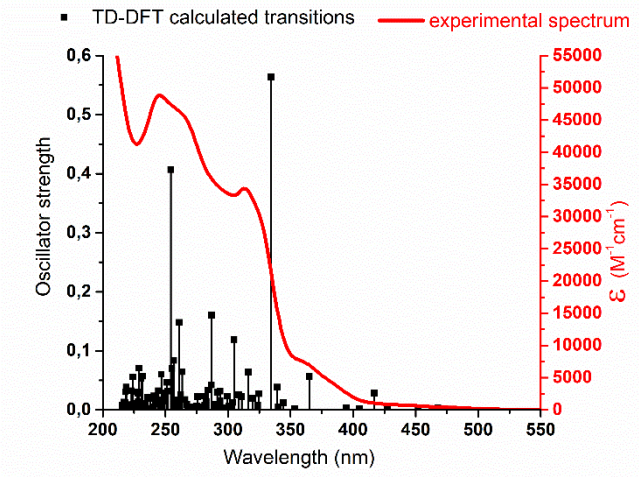

Figure S4.35 – Experimental spectrum and calculated transitions for $IrppyF_2$-2254tpy-H^+

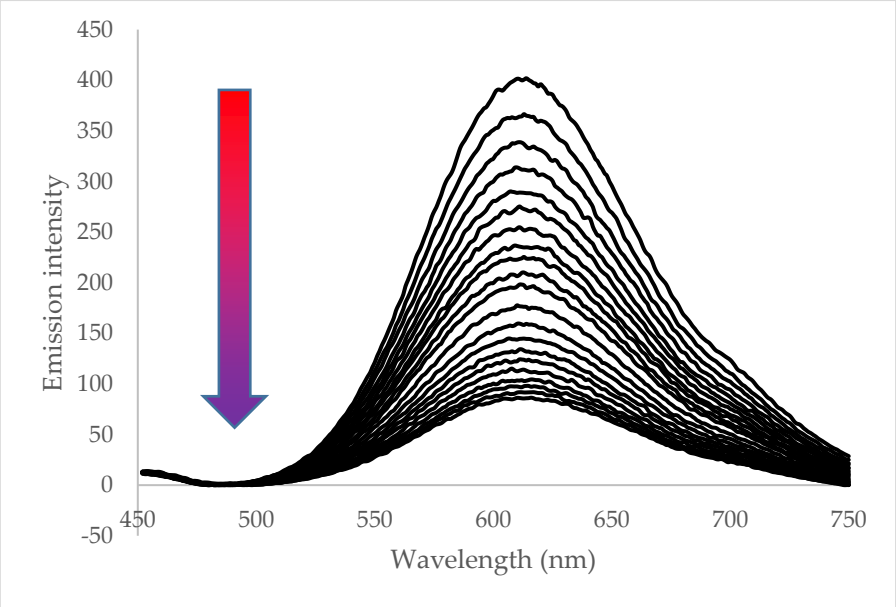

Figure S4.36 – Emission spectral changes for a 2.5 x 10^{-5} M solution of Irppy-2244tpy in acetonitrile for increasing concentrations of AcOH (1 M range)

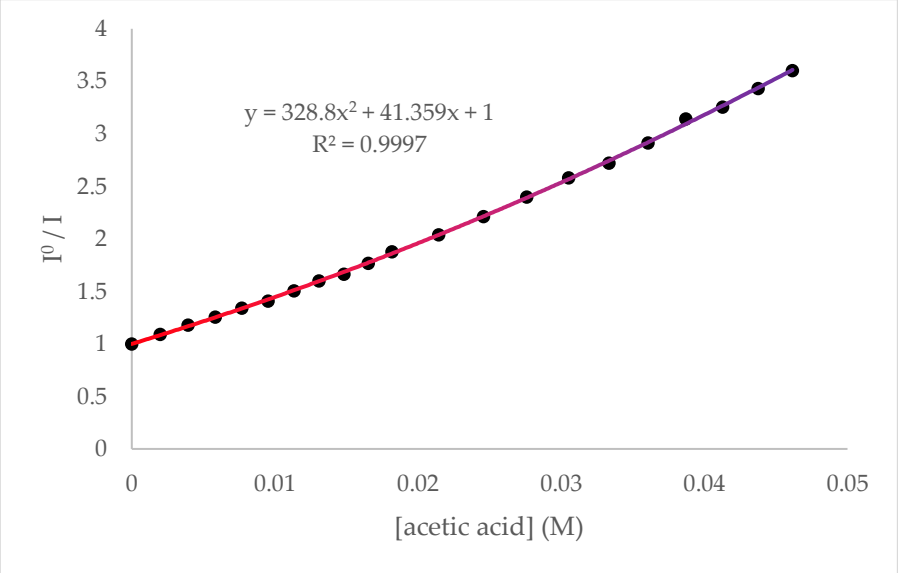

Figure S4.37 – Stern-Volmer plots of the luminescence quenching of a 2.5 x 10^{-5} M solution of Irppy-2244tpy in acetonitrile upon the addition of acetic acid

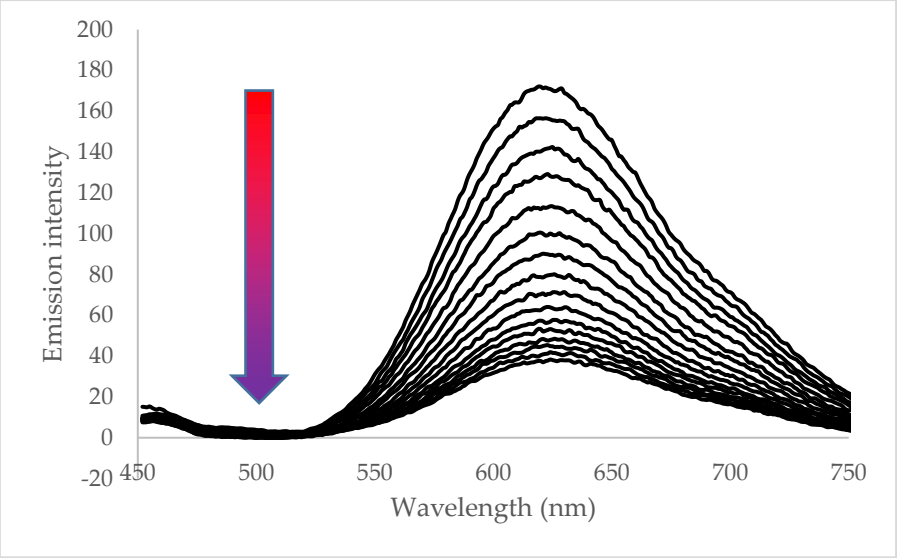

Figure S4.38 – Emission spectral changes for a 2.5 x 10^{-5} M solution of Irppy-2254tpy in acetonitrile for increasing concentrations of AcOH (1 M range)

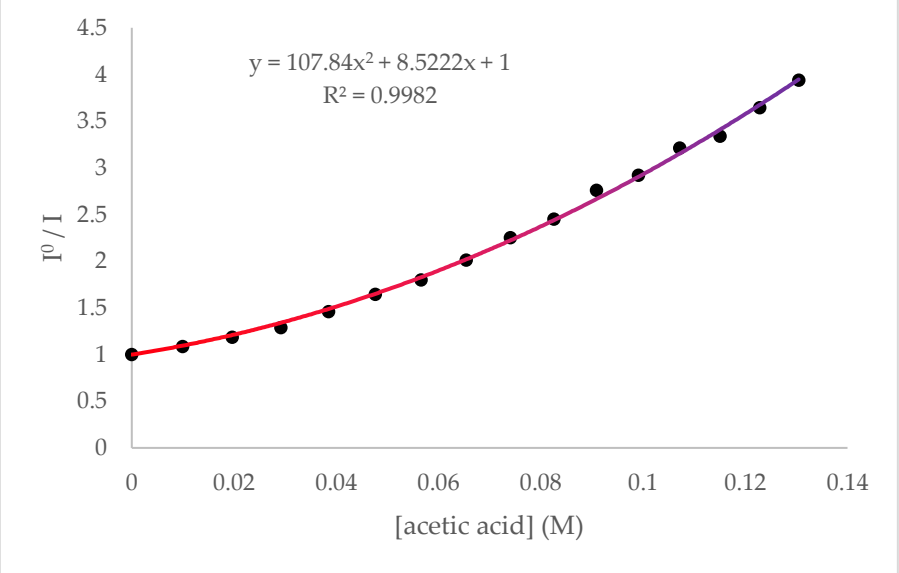

Figure S4.39 – Stern-Volmer plots of the luminescence quenching of a 2.5 x 10^{-5} M solution of Irppy-2254tpy in acetonitrile upon the addition of acetic acid

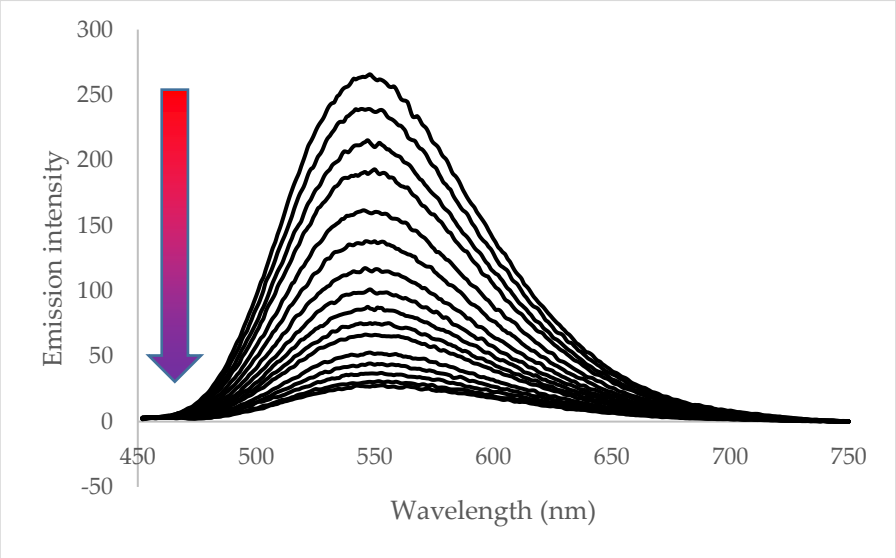

Figure S4.40 – Emission spectral changes for a 2.5 x 10^{-5} M solution of IrppyF_2-2244tpy in acetonitrile for increasing concentrations of AcOH (1 M range)

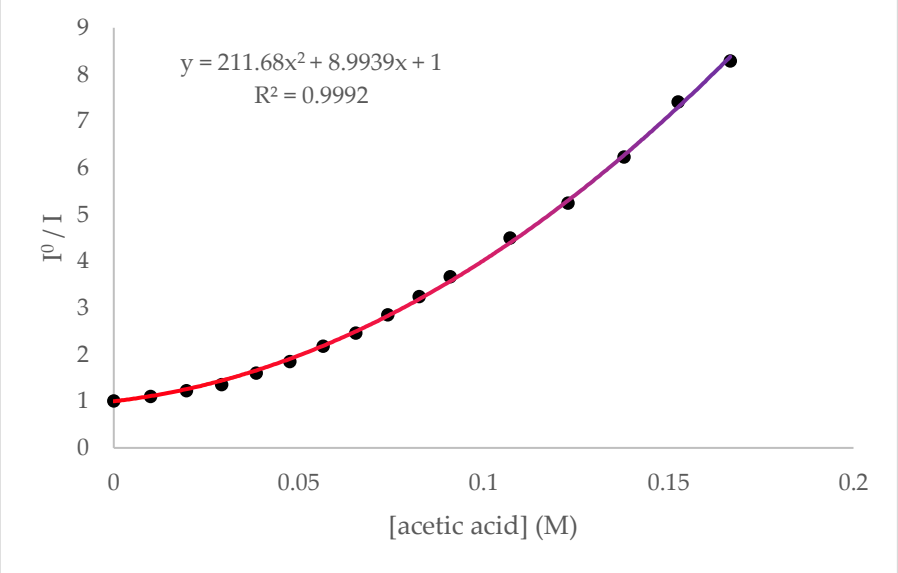

Figure S4.41 – Stern-Volmer plots of the luminescence quenching of a 2.5 x 10^{-5} M solution of IrppyF_2-2244tpy in acetonitrile upon the addition of acetic acid

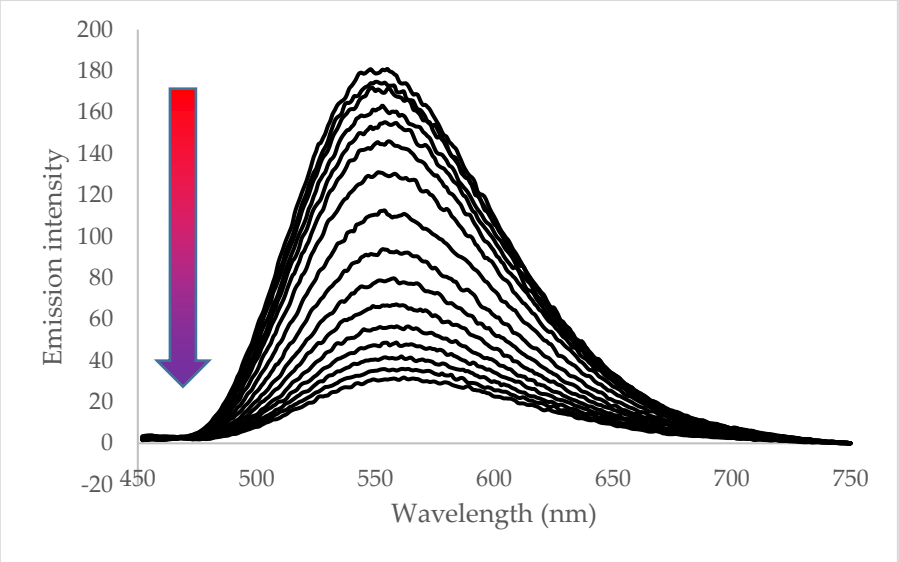

Figure S4.42 – Emission spectral changes for a 2.5 x 10^{-5} M solution of IrppyF$_2$-2254tpy in acetonitrile for increasing concentrations of AcOH (1 M range)

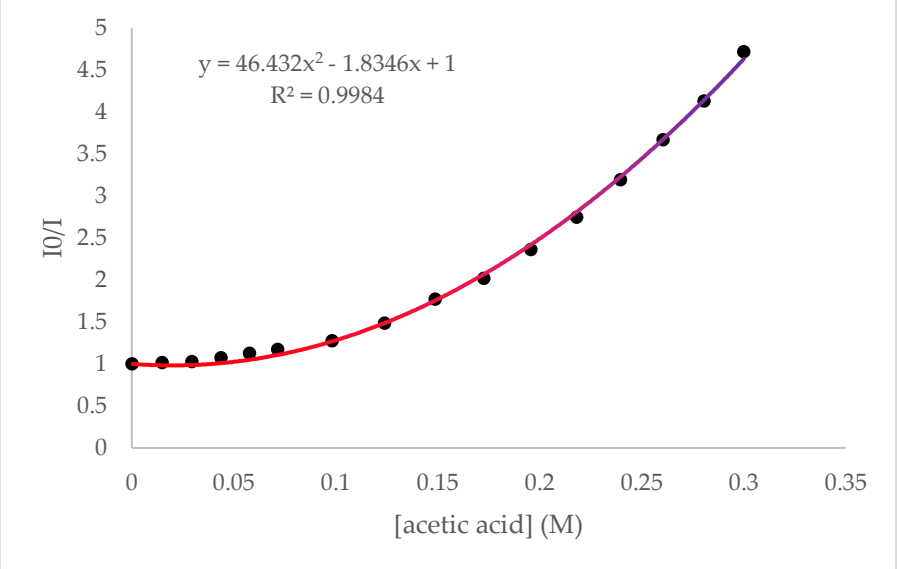

Figure S4.43 – Stern-Volmer plots of the luminescence quenching of a 2.5 x 10^{-5} M solution of IrppyF$_2$-2254tpy in acetonitrile upon the addition of acetic acid

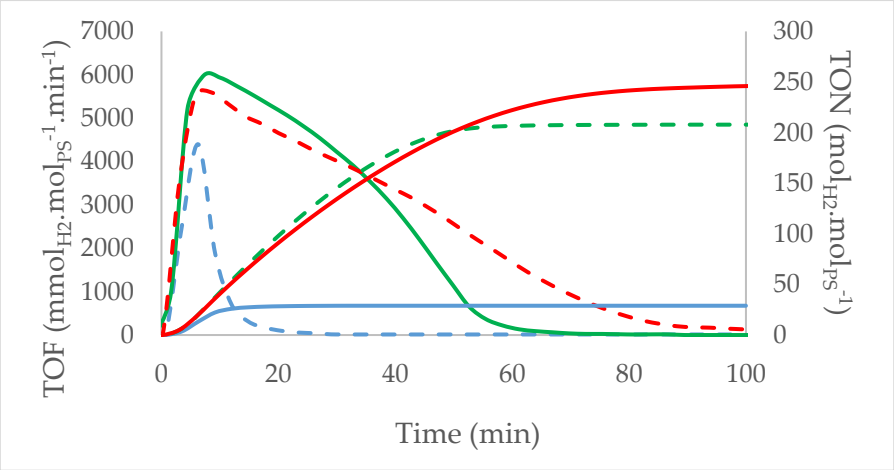

Figure S4.42 – Hydrogen evolution of 0.1 mM Irppy-2244tpy-Co (*blue*), 0.1 mM Irppy-2254tpy-Co (*green*) and dissociated system 0.1 mM Irppy-bpy:[Co(dmgH)$_2$PyrCl] / 1:1 (*red*) in CH_3CN with 0.5 M TEOA as electron source and 0.05 M HBF_4 as proton source. Solid line: TON, dashed line: TOF. Irradiation centered at 452 nm, blue light

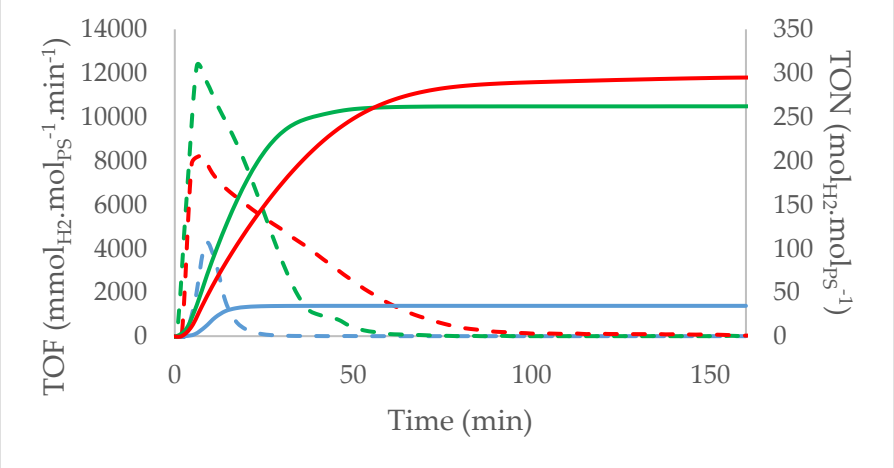

Figure S4.43 – Hydrogen evolution of 0.1 mM IrppyF$_2$-2244tpy-Co (*blue*), 0.1 mM IrppyF$_2$-2254tpy-Co (*green*) and dissociated system 0.1 mM IrppyF$_2$-bpy:[Co(dmgH)$_2$PyrCl] / 1:1 (*red*) in CH_3CN with 0.5 M TEOA as electron source and 0.05 M HBF_4 as proton source. Solid line: TON, dashed line: TOF. Irradiation centered at 452 nm, blue light

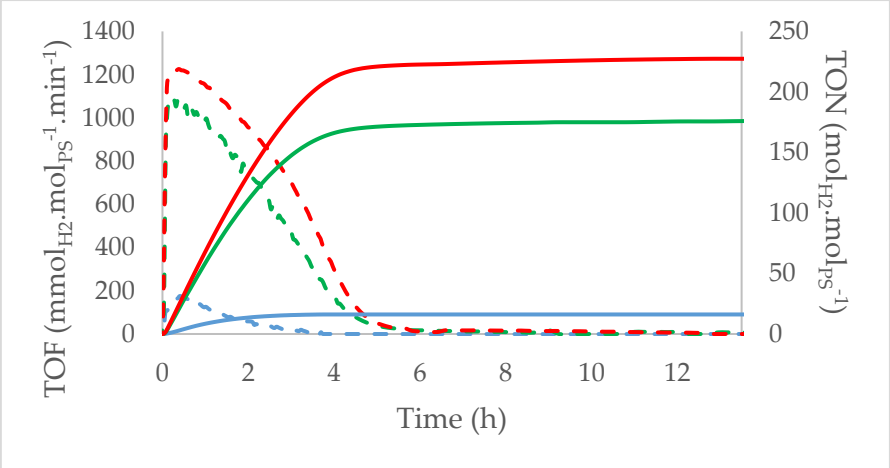

Figure S4.44 – Hydrogen evolution of 0.1 mM Irppy-2244tpy-Co (*blue*), 0.1 mM Irppy-2254tpy-Co (*green*) and dissociated system 0.1 mM Irppy-bpy:[Co(dmgH)$_2$PyrCl] / 1:1 (*red*) in CH_3CN with 0.5 M TEOA as electron source and 0.05 M HBF_4 as proton source. Solid line: TON, dashed line: TOF. Irradiation centered at 525 nm, green light

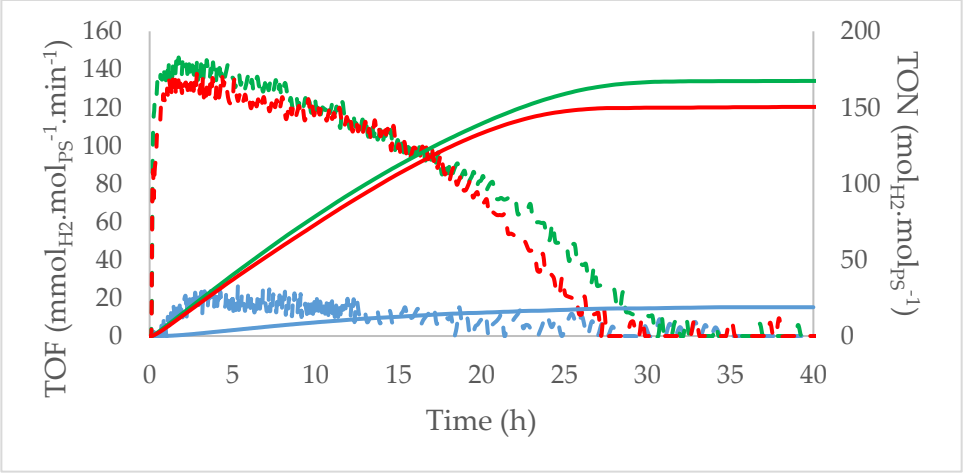

Figure S4.45 – Hydrogen evolution of 0.1 mM IrppyF$_2$-2244tpy-Co (*blue*), 0.1 mM IrppyF$_2$-2254tpy-Co (*green*) and dissociated system 0.1 mM IrppyF$_2$-bpy:[Co(dmgH)$_2$PyrCl] / 1:1 (*red*) in CH_3CN with 0.5 M TEOA as electron source and 0.05 M HBF_4 as proton source. Solid line: TON, dashed line: TOF. Irradiation centered at 525 nm, green light

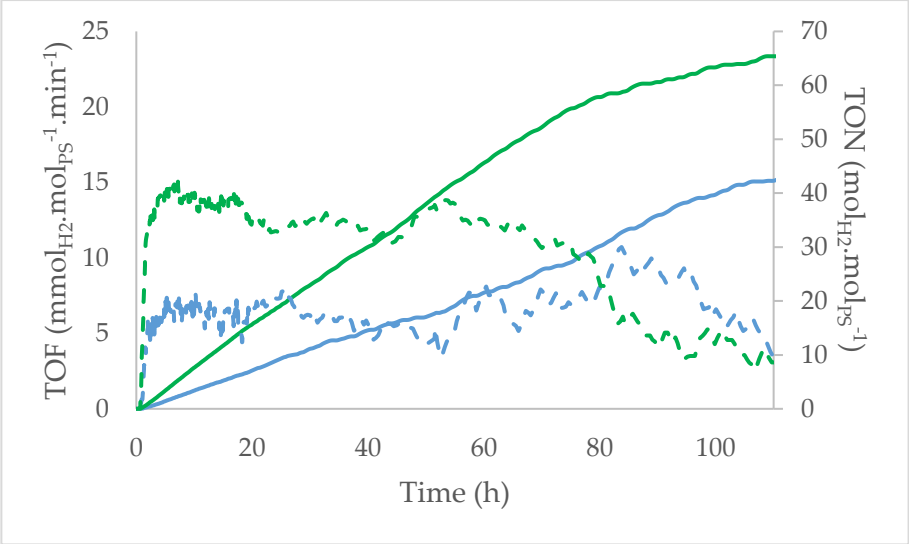

Figure S4.46 – Hydrogen evolution of 0.1 mM Irppy-2244tpy-Co (*blue*) and 0.1 mM Irppy-2254tpy-Co (*green*) in CH_3CN with 0.5 M TEOA as electron source and 0.05 M HBF_4 as proton source. Solid line: TON, dashed line: TOF. Irradiation centered at 595 nm, yellow light